PERFORMANCE OF A MEMS HEAT EXCHANGER FOR A CRYOSURGICAL PROBE

By

Michael J. White

A thesis submitted in partial fulfillment of

the requirements for the degree of

Master of Science
(Mechanical Engineering)

at the

UNIVERSITY OF WISCONSIN-MADISON

2008

Abstract

This thesis presents the experimental test results for a 2nd generation Micro-Electro-Mechanical-Systems (MEMS) heat exchanger that is a composite of silicon plates with micro-machined flow passages interleaved with glass spacers. The MEMS heat exchangers are designed for use as the recuperative heat exchanger within a Joule-Thomson (J-T) cycle used to energize a cryosurgical probe.

The MEMS heat exchangers were tested using two different methods. The first method utilized a cryocooler to provide the cooling at the cold end of the heat exchanger. This method allows a large temperature difference to be applied to the heat exchanger with a minimal pressure difference between the streams and therefore allows accurate testing with little risk of failure. The second test method incorporates the heat exchanger into a J-T cycle using either a micro-valve or orifice to create the isenthalpic pressure drop. A numerical model that includes estimated parasitic heat loads, axial conduction, and internal fluid leakage was used to predict heat exchanger performance. The results of the numerical model are compared with experimental test results over a range of conditions. Two of the MEMS heat exchangers were fabricated with integrated platinum resistance thermometers (PRTs). Therefore, test results include spatially resolved internal temperature distributions, allowing detailed comparisons with the numerical model.

Acknowledgments

I am deeply indebted to the many people throughout my life that have supported me in my efforts to fulfill my dreams. First and foremost credit belongs to my parents who gave me the drive to explore the world and the curiosity to keep learning. Without all the time and energy they spent on me I would not be the person that I am today. Special thanks belongs to my father, who's unceasing compulsion to build and disassemble things surely led me into a career as an engineer.

In my path towards becoming an engineer I have benefited tremendously from two sets of advisors. Arkadiy Klebaner and Jay Theilacker, my former and future supervisors at Fermilab, were instrumental in teaching me how to adapt to a research environment where almost every problem requires an original and unique solution. Even more important was their emphasis on the human elements of engineering problems and their ability to see the big picture.

My second set of advisors, Greg Nellis and Sandy Klein, have spent many hours offering comments and suggestions on how to improve my experimental setups, numerical model, and writing. My thesis has been vastly improved by their contributions. I also have to thank them as teachers. In the many classes I have taken with them as instructors I have learned how to solve complex problems clearly and efficiently. Perhaps most important was their emphasis on the need for engineers to use their technical expertise to push for positive changes in energy and environmental policies. Too often today's engineering marvels become tomorrow's environmental disasters and I hope that I can do my part to reverse that trend.

I am also very grateful for the help of my colleague Weibin Zhu at the University of Michigan. He worked many long hours side-by-side with me trying to meet conference deadlines and lost a lot of sleep checking on the experiments in the middle of the night. Gathering as much data as I did would not have been possible without his help.

Lastly I would like to thank my fellow SEL lab-mates and friends who are too numerous to mention here but have been invaluable in helping me complete my thesis. Whether it was forcing me into a lunch time break or showing me around the lab, they made graduate school fun and rewarding.

Table of Contents

Abstract ii
Acknowledgments iii
Table of Contents iv
List of Tables vii
List of Figures xvi
List of Symbols xxix
1. Background 1
1.0 Introduction 1
1.1 Cryosurgery 1
1.2 Joule-Thomson Cycle 2
1.3 First Generation MEMS Heat Exchanger 4
2. MEMS Components 7
2.0 Introduction 7
2.1 Heat Exchanger Assembly 7
2.2 Valve & Orifice Assembly 29
3. Experimental Setups 36
3.0 Introduction 36
3.1 Cryogenic Test Facility 36
3.1.1 Modes of Operation 36
3.1.2 Flow Schematics 39
3.1.3 Equipment 44
3.1.4 Design 48
3.1.3 Equipment 48
3.1.5 Construction 53
3.2 Prototype Cryosurgical Probe Assembly 61
3.2.1 Flow Schematics 61
3.2.2 Construction 63
4. Numerical Model for a Perforated Plate Heat Exchanger 69
4.0 Introduction 69
4.1 Numerical Model of Standard Heat Exchanger 69
4.2 Numerical Model of Perforated Plate Heat Exchanger 75

4.3 Effect of Parasitic Losses on Perforated Plate Heat Exchanger Performance 81
5. MEMS Heat Exchanger Design Model 108
5.0 Introduction 108
5.1 Die Geometry 108
5.2 Material Properties 114
5.3 Laminar Flow Heat Transfer and Pressure Drop Correlations 123
5.4 Turbulent Flow Heat Transfer and Pressure Drop Correlations 136
5.5 Fin Effectiveness 140
5.6 Thermal Resistances 144
5.7 Axial Conduction 149
5.8 Parasitic Heat Loads 153
5.9 Integration of General Model with MEMS Heat Exchanger Procedures 165
5.10 Components External to Heat Exchanger 175
6. Comparison of Experimental Results with a Numerical Model 178
6.0 Introduction 178
6.1 Integrated PRT Calibration 178
6.2 Pressure Drop Test Results for the Micro-Valve 189
6.3 Pressure Drop Test Results for the MEMS Heat Exchangers 196
6.4 Applied-Cooling Experimental Results 201
6.5 Applied-Cooling Numerical Modeling Results 214
6.6 Cryogenic Test Facility Self-Cooling Results 220
6.7 Cryosurgical Probe Prototype Results 232
References 239
Appendicies 241
A. Experimental Uncertainty Review 241
B. Sixteen Die 10 mm Heat Exchanger External Cooling Results 248
C. Sixteen Die 10 mm Heat Exchanger Self-Cooling Results 251
D. Sixteen Die 10 mm Heat Exchanger Pressure Drop Results 253
E. Integrated PRT Die Calibration 257
F. Forty-three Die 10 mm Heat Exchanger Integrated PRT Calibration 260

G. Thirty-Seven Die 20 mm Heat Exchanger Integrated PRT Calibration 263
H. Micro-Valve Flow Rate Testing 265
I. Forty-three Die 10 mm Heat Exchanger Pressure Drop Testing.....269
J. Thirty-Seven Die 20 mm Heat Exchanger Pressure Drop Testing.....273
K. Forty-three Die 10 mm Heat Exchanger Cryosurgical Probe Tests.....279
L. Forty-three Die 10 mm Heat Exchanger Effectiveness Tests 292
M. Thirty-seven Die 20 mm Heat Exchanger Effectiveness Tests 297
N. Forty-three Die 10 mm Heat Exchanger Self-Cooling Tests.....301
O. Forty-three Die 10 mm Heat Exchanger Load Curve Tests 314

List of Tables

Table 2.1.1: Thermal conductivity of common metals used in cryogenic wiring as a function of temperature 19
Table 2.1.2: Electrical resistivity of common metals used in cryogenic wiring as a function of temperature 20
Table 2.1.3: Heat conducted to a die PRT through various wire diameters and wire materials for a 0.3 m wire lead length, a 10 μA current, and a 150 K die temperature. 22
Table 2.1.4: Heat conducted to a die PRT through various wire diameters and wire materials for a 1 m wire lead length, a 10 μA current, and a 150 K die temperature. 23
Table 2.1.5: Heat conducted to a die PRT through various wire diameters and wire materials for a 0.3 m wire lead length, a 10 μA current, and a 250 K die temperature. 24
Table 2.1.6: Heat conducted to a die PRT through various wire diameters and wire materials for a 1 m wire lead length, a 10 μA current, and a 250 K die temperature. 25
Table 2.1.7: Location of working normal and reference PRTs within the two heat exchangers with integrated PRTs 28
Table 2.2.1: Available orifice sizes and their respective flow factors 30
Table 3.1.1: Values of Cconvert for various gasses at multiple pressures 46
Table 4.3.1: The specific heats and thermal resistances for a heat exchanger with no axial conduction (Case 1), axial conduction only in perforated plates (Case 2), and axial conduction in both the perforated plates and the spacers (Case 3) 82
Table 4.3.2: Variations of the hypothetical heat exchanger used to show the effect of conduction to and from the heat exchanger ends. 87
Table 4.3.3: Variations of the hypothetical heat exchanger used to show the effect of parasitic heat loads. 92
Table 4.3.4: Variations of a hypothetical heat exchanger used for showing the effect of leak location on heat exchanger effectiveness 95

Table 4.3.5: Variations of a hypothetical heat exchanger used for showing the effect of leak location on heat exchanger effectiveness 96
Table 4.3.6: Variations of a hypothetical heat exchanger used for showing the effect of leak location on heat exchanger effectiveness. 100
Table 4.3.7: Variations of a hypothetical heat exchanger used for showing the effect of leak location on heat exchanger effectiveness 101
Table 4.3.8: Four heat exchanger variations used to show the effect of hot side pressure on heat exchangers with internal leakage 104
Table 4.3.9: Three heat exchanger variations used to demonstrate the effect of internal leakage on J-T cycle performance. 106
Table 5.1.1: Dimensions in millimeters for 10x10 mm and 20x20 mm heat exchanger silicon plates 110
Table 5.1.2: Dimensions in millimeters for 10x10 mm and 20x20 mm heat exchanger glass spacers 111
Table 5.1.3: Hydraulic diameter and aspect ratio for both the 10x10 mm and 20x20 mm heat exchangers 112
Table 5.2.1: Values used for calculating the thermal conductivity of copper and stainless steel [19] 115
Table 5.2.2: Key characteristics of the silicon samples shown in Fig. 5.2.3 119
Table 5.2.3: The values in EES Lookup Tables used for interpolating thermal conductivity of various heat exchanger materials. 122
Table 5.3.1: Comparison of apparent friction factors derived using two different methods. 126
Table 5.3.2: Fully developed Nusselt numbers for constant wall temperature NuT,fd,lam and constant heat flux NuH,fd,lam for both the 10 mm and 20 mm heat exchangers 128
Table 5.3.3: Average simultaneously developing constant temperature Nusselt numbers for parallel plates from two different authors 129
Table 5.3.4: The constant wall temperature and constant wall heat flux Nusselt numbers as a function of thermal entrance length and rectangular duct aspect ratio for air (Pr = 0.72). 133

Table 5.3.5: Estimated constant wall temperature Nusselt number as a function of dimensionless entrance length for both the 10 mm and 20 mm heat exchangers. 134
Table 5.3.5: Estimated constant wall temperature Nusselt number as a function of dimensionless entrance length for both the 10 mm and 20 mm heat exchangers. 134
Table 5.4.1: Critical Reynolds number for transition to turbulent flow in smooth rectangular ducts 136
Table 5.5.1: Constants required for analytical solution of Eq. 5.5.7 -5.5.10 142
Table 5.7.1: Integrated thermal conductivity values based off a reference temperature of 100 K for stainless steel. 152
Table 5.8.1: Heat load to the heat exchanger as a function of the temperature difference between the ends of the lead wire. 159
Table A.1: Common abbreviations used in tables and figures in the appendices 241
Table A.2: Table of PRT resistances as a function of temperature. 245
Table B.1: Experimental temperature measurements for the sixteen die 10 mm heat exchanger operating in external cooling mode with helium as the working fluid 248
Table B.2: Experimental measurements of the mass flow rate and pressures for the sixteen die 10 mm heat exchanger operating in external cooling mode with helium as the working fluid. 249
Table B.3: Calculation of heat exchanger effectiveness based on the experimental measurements shown in Table B.1 249
Table B.4: Calculation of mass flow rate and pressures based on the experimental data shown in Table B.2. 250
Table C.1: Experimental measurements for the self-cooling test on the sixteen die 10 mm heat exchanger. 251
Table C.2: Calculations of maximum temperature difference (Th,in – Tc,in) and pressure difference (Ph,in – Pc,in) based on the experimental data in Table C.1. 251

Table C.3: Calculations of heat exchanger effectiveness and mass flow rate based on the experimental data in Table C.1. 252
Table D.1: Experimental data collected for the pressure drop testing of the sixteen die 10 mm heat exchanger with helium as the working fluid 253
Table D.2: Experimental data collected for the pressure drop testing of the sixteen die 10 mm heat exchanger with air as the working fluid 253
Table D.3: Experimental data collected for the pressure drop testing of the sixteen die 10 mm heat exchanger with ethane as the working fluid 254
Table D.4: Experimental data collected for the leak testing of the sixteen die 10 mm heat exchanger with helium as the working fluid 254
Table D.5: Calculated results from Table D.1 255
Table D.6: Calculated results from Table D.2 255
Table D.7: Calculated results from Table D.3 256
Table D.8: Calculated results from Table D.4 256
Table E.1: Experimental data from the calibration of individual dies with integrated PRT dies. 257
Table F.1: Mass flow rate, temperature, and pressure measurements for the PRTs that were tested in both wiring arrangements during the calibration of the forty-three die 10 mm heat exchanger. 260
Table F.2: The voltages of every die PRT that was tested in both wiring arrangements during the calibration of the forty-three die 10 mm heat exchanger. 260
Table F.3: The voltages of every die PRT that was tested only in the first wiring arrangement during the calibration of the forty-three die 10 mm heat exchanger. 261
Table F.4: The voltages of every die PRT that was tested only in the second wiring arrangement during the calibration of the forty-three die 10 mm heat exchanger 261
Table F.5: PRT resistances as a function of temperature for PRTs 1 through 6 on the forty-three die 10 mm heat exchanger. 261

Table F.6: PRT resistances as a function of temperature for PRTs 9 through 15 on the forty-three die 10 mm heat exchanger. 262
Table F.7: Mass flow rate, heat leak, and temperatures for all calibration points 262
Table G.1: Steady-state mass flow rate, temperature, and pressure measurements for the thirty-seven die 20 mm heat exchanger during the calibration test. . 263
Table G.2: Measured steady-state voltages on the integrated PRTs of the thirty-seven die 20 mm heat exchanger during the calibration test. 263
Table G.3: PRT resistances as a function of temperature for PRTs 1 through 5 on the thirty-seven die 20 mm heat exchanger. 263
Table G.4: PRT resistances as a function of temperature for PRTs 6 through 9 on the thirty-seven die 20 mm heat exchanger. 264
Table G.5: Mass flow rate, heat leak, and temperatures for all calibration points 264
Table H.1: Experimental data measuring the pressure drop characteristics of the micro-valve. 265
Table H.2: Calculated values from the experimental data shown in Table H.1. ... 267
Table I.1: Experimental data collected for the through gasket pressure drop test on the forty-three die 10 mm heat exchanger 269
Table I.2: Experimental data collected for the 0.015” orifice gasket pressure drop test on the forty-three die 10 mm heat exchanger 270
Table I.3: Experimental data collected for the blank gasket pressure drop test on the forty-three die 10 mm heat exchanger 270
Table I.4: Calculated results from the experimental data listed in Table I.1 271
Table I.5: Calculated results from the experimental data listed in Table I.2 271
Table I.6: Calculated results from the experimental data listed in Table I.3 272
Table J.1: Experimental data collected for the through gasket pressure drop test on the thirty-seven die 20 mm heat exchanger 273
Table J.2: Experimental data collected for the 0.013” orifice gasket pressure drop test on the thirty-seven die 20 mm heat exchanger 274
Table J.3: Experimental data collected for the blank gasket pressure drop test on the thirty-seven die 20 mm heat exchanger 275

Table J.4: Calculated results from the experimental data listed in Table J.1 276
Table J.5: Calculated results from the experimental data listed in Table J.2 277
Table J.6: Calculated results from the experimental data listed in Table J.3 278
Table K.1: Locations of the integrated PRTs within the forty-three die 10 mm heat exchanger during the self-cooling tests performed in the cryosurgical probe prototype 279
Table K.2: Experimental data for the cryosurgical probe with the forty-three die 10 mm heat exchanger installed. The working fluid was ethane and the orifice diameters tested include 0.010", 0.013", and 0.015"..... 280
Table K.3: Integrated RTD voltages for the cryosurgical probe prototype with the forty-three die 10 mm heat exchanger installed. The working fluid was ethane and the orifice diameters tested include 0.010", 0.013", and 0.015" 281
Table K.4: Experimental data for the cryosurgical probe with the forty-three die 10 mm heat exchanger installed. The working fluid was ethane and the voltages applied to the valve include -30 V, 0 V, and 30 V...... 282
Table K.5: Integrated RTD voltages for the cryosurgical probe prototype with the forty-three die 10 mm heat exchanger installed. The working fluid was ethane and the voltages applied to the valve include -30 V, 0 V, and 30 V...... 283
Table K.6: Experimental data for the cryosurgical probe with the forty-three die 10 mm heat exchanger installed. The working fluid was ethane and the voltages applied to the valve include 60 V, 80 V, and 100 V...... 284
Table K.7: Integrated RTD voltages for the cryosurgical probe prototype with the forty-three die 10 mm heat exchanger installed. The working fluid was ethane and the voltages applied to the valve include 60 V, 80 V, and 100 V...... 285
Table K.8: Calculated results from Table K.1 286
Table K.9: Calculated results from Table K.2 287
Table K.10: Calculated results from Table K.3 288
Table K.11: Calculated results from Table K.4 289
Table K.12: Calculated results from Table K.5 290
Table K.13: Calculated results from Table K.6 291

Table L.1: Locations of the integrated PRTs within the forty-three die 10 mm heat exchanger applied-cooling tests performed in the cryogenic testing facility 292
Table L.2: Experimental temperature measurements at the inlets and outlets for the forty-three die 10 mm heat exchanger as it was being tested in applied-cooling mode in the cryogenic test facility. Helium was the working fluid.. 293
Table L.3: Experimental mass flow rate and pressure measurements for the forty-three die 10 mm heat exchanger as it was being tested in applied-cooling mode in the cryogenic test facility. Helium was the working fluid. 293
Table L.4: Experimental temperature measurements for the integrated PRTs of the forty-three die 10 mm heat exchanger as it was being tested in applied-cooling mode in the cryogenic test facility. Helium was the working fluid.. 293
Table L.5: Experimental temperature measurements at the inlets and outlets for the forty-three die 10 mm heat exchanger as it was being tested in applied-cooling mode in the cryogenic test facility. Ethane was the working fluid.. 294
Table L.6: Experimental mass flow rate and pressure measurements for the forty-three die 10 mm heat exchanger as it was being tested in applied-cooling mode in the cryogenic test facility. Ethane was the working fluid. 294
Table L.7: Experimental temperature measurements for the integrated PRTs of the forty-three die 10 mm heat exchanger as it was being tested in applied-cooling mode in the cryogenic test facility. Ethane was the working fluid.. 294
Table L.8: Calculated results from experimental data shown in Table L.2 295
Table L.9: Calculated results from experimental data shown in Table L.3 295
Table L.10: Calculated results from experimental data shown in Table L.4 295
Table L.11: Calculated results from experimental data shown in Table L.5 296
Table L.12: Calculated results from experimental data shown in Table L.6 296
Table L.13: Calculated results from experimental data shown in Table L.7 296
Table M.1: Locations of the integrated PRTs within the thirty-seven die 20 mm heat exchanger for the applied-cooling tests performed in the cryogenic testing facility 297

Table M.2: Experimental temperature measurements at the inlets and outlets for the thirty-seven die 20 mm heat exchanger as it was being tested in applied-cooling mode in the cryogenic test facility. Helium was the working fluid.. 298
Table M.3: Experimental mass flow rate and pressure measurements for the thirty-seven die 20 mm heat exchanger as it was being tested in applied-cooling mode in the cryogenic test facility. Helium was the working fluid.. 298
Table M.4: Experimental temperature measurements for the integrated PRTs of the thirty-seven die 20 mm heat exchanger as it was being tested in applied-cooling mode in the cryogenic test facility. Helium was the working fluid.. 299
Table M.5: Calculated results from the experimental data in Table M.2..... 299
Table M.6: Calculated results from the experimental data in Table M.3..... 299
Table M.7: Calculated results from the experimental data in Table M.4..... 300
Table N.1: Locations of the integrated PRTs within the forty-three die 10 mm heat exchanger self-cooling tests performed in the cryogenic testing facility..... 301
Table N.2: Experimental data for the forty-three die 10 mm heat exchanger installed in the cryogenic test facility. The working fluid was ethane and the orifice diameters tested include 0.010”, 0.015”, and 0.020”..... 302
Table N.3: Integrated RTD voltages for the forty-three die 10 mm heat exchanger installed in the cryogenic test facility. The working fluid was ethane and the orifice diameters tested include 0.010”, 0.015”, and 0.020”..... 303
Table N.4: Experimental data for the forty-three die 10 mm heat exchanger installed in the cryogenic test facility. The working fluid was ethane and the voltages applied to the valve include -30 V, 0 V, and 30 V...... 304
Table N.5: Integrated RTD voltages for the forty-three die 10 mm heat exchanger installed in the cryogenic test facility. The working fluid was ethane and the voltages applied to the valve include -30 V, 0 V, and 30 V..... 305
Table N.6: Experimental data for the forty-three die 10 mm heat exchanger installed in the cryogenic test facility. The working fluid was ethane and the voltages applied to the valve include 60 V, 80 V, and 100 V...... 306

Table N.7: Integrated RTD voltages for the forty-three die 10 mm heat exchanger installed in the cryogenic test facility. The working fluid was ethane and the voltages applied to the valve include 60 V, 80 V, and 100 V. 307
Table N.8: Calculated results from Table N.2 308
Table N.9: Calculated results from Table N.3 309
Table N.10: Calculated results from Table N.4 310
Table N.11: Calculated results from Table N.5 311
Table N.12: Calculated results from Table N.6 312
Table N.13: Calculated results from Table N.7 313
Table O.1: Locations of the integrated PRTs within the forty-three die 10 mm heat exchanger self-cooling tests performed in the cryogenic testing facility 314
Table O.2: Experimental data for the forty-three die 10 mm heat exchanger installed self-cooling mode in the cryogenic test facility with ethane as the working fluid. 315
Table O.3: Integrated RTD voltages for the forty-three die 10 mm heat exchanger installed in self-cooling mode in the cryogenic test facility with ethane as the working fluid. 315
Table O.4: Calculated results from Table O.2 315
Table O.5: Calculated results from Table O.2 316

List of Figures

Fig. 1.1.1: Photograph of the cryoablation of cancerous cells in the liver [2]. 1
Fig. 1.1.2: Photograph of a finned tube heat exchanger used in conventional cryosurgical probes [3]. 2
Fig. 1.2.1: Flow schematic for a J-T cycle 3
Fig. 1.2.2: T-s diagram showing representative states of a J-T cycle for ethane as the working fluid. The numbered states are shown on the flow schematic in Fig. 1.2.1 3
Fig. 1.3.1: Geometric model the first generation MEMS heat exchanger [7]. 4
Fig. 1.3.2: Photograph of the first generation MEMS heat exchanger [5]. 4
Fig. 1.3.3: Experimental setup used for testing the first generation MEMS heat exchanger [5]. 5
Fig. 1.3.4: Geometric model of the heat exchanger (left) and a photograph of a heat exchanger before bonding with the headers (right) 6
Fig. 2.1.1: 20 mm heat exchanger die before thermal shock test (left) and after being immersed suddenly in a liquid nitrogen bath (right) 8
Fig. 2.1.2: 10 mm heat exchanger die before thermal shock test (left) and after being immersed suddenly in a liquid nitrogen bath (right) 8
Fig. 2.1.3: Sixteen dies were epoxied together to form the first 10 mm heat exchanger. This heat exchanger was tested in both the room temperature experimental setup and the cryogenic test facility. 9
Fig. 2.1.4: Eight dies were epoxied together to form the first 20 mm heat exchanger. This heat exchanger was tested only in the room temperature experimental setup and was broken before any useful experimental data was obtained. 10
Fig. 2.1.5: The flow passages in these 10 mm dies were partially blocked by excess epoxy 10
Fig. 2.1.6: 20 mm G10 header with the heat exchanger side shown on the left and the fluid connection side shown on the right. 11
Fig. 2.1.7: 10 mm G10 header with the heat exchanger side shown on the left and the fluid connection side shown on the right. 11

Fig. 2.1.8: Photographs of the 10 mm (left) and 20 mm (right) heat exchanger assemblies before epoxy is applied 12
Fig. 2.1.9: VCR glands silver brazed to copper tubing which is epoxied to 10 mm header 13
Fig. 2.1.10: Final assembly of the 10 mm heat exchanger 14
Fig. 2.1.11: Final assembly of 20 mm heat exchanger with externally mounted thermocouples 14
Fig. 2.1.12: Comparison of the initial header design (left) and the improved design (right) 15
Fig. 2.1.13: 23 die 20 mm heat exchanger assembly using stainless steel headers. 16
Fig. 2.1.14: Final header design for the 20 mm heat exchanger 17
Fig. 2.1.15: Photograph showing both an ordinary die and a gold plated die with integrated PRTs 17
Fig. 2.1.16: Simplified drawing of the silicon fin plate with platinum resistor wires used for temperature measurement 18
Fig 2.1.17: 10 mm die with built-in PRT for assembly into a heat exchanger 19
Fig 2.1.18: 10 mm heat exchanger before assembly with headers. 26
Fig 2.1.19: Thirty-seven die, 20 mm heat exchanger before assembly with headers 26
Fig. 2.1.20: Thirty-seven die, 20 mm heat exchanger assembly with integrated PRTs with headers installed 27
Fig. 2.1.21: Forty-three die, 10 mm heat exchanger assembly with integrated PRTs with headers installed. 27
Fig. 2.2.1: Various methods of mounting jewel orifices in VCR gaskets. 29
Fig. 2.2.2: Exponential relationship between the flow factor Cv and the inner diameter of the orifice 31
Fig. 2.2.3: Linear relationship between the flow factor Cv and the cross sectional area of the orifice 31
Fig. 2.2.4: Geometric model of the cryogenic micro valve [9]. 33
Fig. 2.2.5: Photograph of the PZT stack before valve assembly 34

Fig. 2.2.6: Photograph of the valve housing before valve assembly. 34
Fig. 2.2.7: Photograph of a fully assembled cryogenic micro valve. The valve housing was later covered in epoxy to increase the strength and durability of the housing. 35
Fig. 3.1.1: Expected temperature difference across a valve or orifice due to isenthalpic expansion 39
Fig. 3.1.2: Flow schematic of the Cryogenic Test Facility showing all components external to the Dewar 41
Fig. 3.1.3: Flow schematic of the Cryogenic Test Facility showing all components internal to the Dewar 42
Fig. 3.1.4: Heat exchanger effectiveness as a function of mass flow rate for the 20x20 mm heat exchanger assuming testing in applied mode with helium from 300 K to 150 K. 43
Fig. 3.1.5: Heat exchanger effectiveness as a function of mass flow rate for the 10x10 mm heat exchanger assuming testing in active mode with helium from 300 K to 150 K. 43
Fig. 3.1.6: Photograph of compressor to be used in the cryogenic test facility 44
Fig. 3.1.7: Photograph of Mass Flow Meter to be used in the Cryogenic Test Facility 44
Fig. 3.1.8: Mass flow rate as a function of mass flow sensor voltage signal for various fluids at 202 kPa 47
Fig. 3.1.9: Relative uncertainty of mass flow rates for various fluids at 202 kPa .. 47
Fig. 3.1.10: Geometric solid model of instrumentation inside the Dewar 49
Fig. 3.1.11: Photograph of internal components of PRT measurement tee 50
Fig. 3.1.12: Photograph showing how the PRTs are inserted into a tee to directly measure the fluid temperature 50
Fig. 3.1.13: Photograph of type E thermocouple to be used in cryogenic test facility 50
Fig. 3.1.14: Geometric solid model of the cryocooler heat exchanger assembly .. 51
Fig. 3.1.15: Vacuum feedthrough for thermocouple wires 52

Fig. 3.1.16: Geometric solid model of the entire Dewar tubing assembly (left), the entire Dewar assembly (middle), and a photograph of the entire Dewar assembly (right) 53
Fig. 3.1.17: Warm end of heat exchanger and instrumentation assembly to be used in the cryogenic test facility. 54
Fig. 3.1.18: Cold end of heat exchanger and instrumentation assembly to be used in the cryogenic test facility 55
Fig. 3.1.19: The entire heat exchanger and instrumentation assembly to be used in the cryogenic test facility. 56
Fig. 3.1.20: The cryocooler heat exchanger is attached to the second stage of the cryocooler, which has a higher cooling capacity than the first stage at temperatures typical of cryosurgery (150 K – 200 K). 57
Fig. 3.1.21: Photograph of the heater used to control the cryocooler heat exchanger temperature. 58
Fig. 3.1.22: Dewar assembly for the cryogenic test facility. 59
Fig. 3.1.23: Top view of the Dewar assembly. 60
Fig. 3.1.24: Pressure regulator used to control the inlet pressure to the Dewar assembly 61
Fig. 3.2.1: Flow schematic for components external to the cryosurgical probe prototype 62
Fig. 3.2.2: Flow schematic of components internal to the cryosurgical probe prototype housing. 63
Fig. 3.2.3: Photograph of the thirty-seven die 20 mm heat exchanger attached to the cryosurgical probe assembly 64
Fig. 3.2.4: Photograph of the valve and orifice installed in parallel. The orifice size is chosen so that the valve can modulates the flow higher and lower than the optimal flow rate. 65
Fig. 3.2.5: Photograph of the cryosurgical probe prototype tip. 65
Fig. 3.2.6: Photograph of all components internal to the cryosurgical probe prototype. 66

Fig. 3.2.7: Photograph of cryosurgical probe while an experiment is in progress. 67
Fig. 3.2.8: A photograph of the entire cryosurgical probe while an experiment is in progress 68
Fig. 4.1.1: Location of nodes used for computational grid in heat exchanger numerical model 72
Fig. 4.1.2: Energy balance for the hot stream in the ith section of the heat exchanger 72
Fig. 4.1.3: Energy balance for the cold stream in the ith section of the heat exchanger 73
Fig. 4.1.4: Energy balance for the wall in the ith section of the heat exchanger ... 73
Fig. 4.2.1: Numbering system for perforated plates (PP) and spacers (SP) in the numerical model of a perforated plate heat exchanger with N plates. 76
Fig. 4.2.2: Plot of a representative dimensionless temperature distribution within a perforated plate heat exchanger. 78
Fig. 4.2.3: Energy balance on the spacer used to determine the inlet temperature of the cold fluid to the jth perforated plate in the heat exchanger. 79
Fig. 4.3.1: Temperature distribution for Case 1 which has no axial conduction in the perforated plates or spacers 83
Fig. 4.3.2: Temperature distribution for Case 2 which has axial conduction in perforated plates 84
Fig. 4.3.3: Temperature distribution for Case 3 which has axial conduction in perforated plates and spacers 85
Fig. 4.3.4: Effectiveness as a function of the total number of transfer units for the three variations of the hypothetical heat exchanger listed in Table 4.3.1 86
Fig. 4.3.5: Comparison of effectiveness for Case 3 (adiabatic ends) and Case 4 (heat conducted to the warm end) as a function of total NTU 88
Fig. 4.3.6: Comparison of effectiveness for Case 3 (adiabatic ends) and Case 5 (heat conducted from the warm end) as a function of total NTU 89
Fig. 4.3.7: Comparison of effectiveness for Case 3 (adiabatic ends) and Case 5 (heat conducted from the cold end) as a function of total NTU 90

Fig. 4.3.7: Comparison of effectiveness for Case 3 (adiabatic ends) and Case 7 (heat conducted to the cold end) as a function of total NTU..... 91
Fig. 4.3.8: Plot comparing the effectiveness for Case 3 (no heat load) and Case 8 (heat load on hot fluid) as a function of the total number of transfer units.... 92
Fig. 4.3.9: Plot comparing the effectiveness for Case 3 (no heat load) and Case 9 (heat load on cold fluid) as a function of the total number of transfer units .. 93
Fig. 4.3.8: Plot comparing the effectiveness for Case 3 (no heat load) and Case 10 (heat load on wall) as a function of the total number of transfer units 94
Fig. 4.3.9: Plot of effectiveness as a function of total NTU for all the cases listed in Table 4.3.4. In all cases the leaking fluid is assumed to have no thermal interaction with the wall. 96
Fig. 4.3.10: Plot of effectiveness as a function of total NTU for all the cases listed in Tables 4.3.4 and 4.3.5 with leaks located in the first spacer...... 97
Fig. 4.3.11: Plot of effectiveness as a function of total NTU for all the cases listed in Tables 4.3.4 and 4.3.5 with leaks located in the second spacer. 98
Fig. 4.3.12: Joule-Thomson Coefficient as a function of temperature for helium and ethane at 100 kPa and 1000 kPa...... 99
Fig. 4.3.13: Plot of effectiveness as a function of total NTU for all the cases listed in Table 4.3.6. In all cases the leaking fluid is assumed to have no thermal interaction with the wall. 100
Fig. 4.3.14: Plot of effectiveness as a function of total NTU for all the cases listed in Tables 4.3.6 and 4.3.7 with leaks located in the first spacer...... 102
Fig. 4.3.15: Plot of effectiveness as a function of total NTU for all the cases listed in Tables 4.3.6 and 4.3.7 with leaks located in the second spacer. 103
Fig. 4.3.16: Plot showing the effect of the hot side pressure on heat exchangers with internal leakage...... 105
Fig. 4.3.17: Plot showing the effect of internal leakage on the hot side effectiveness of a heat exchanger and the refrigeration load of a J-T cycle. 107
Fig. 5.1.1: Simplified geometric model of 20 mm heat exchanger [7]..... 109
Fig. 5.1.2: Simplified drawing of the silicon plate..... 110
Fig. 5.1.3: Simplified drawing of glass spacer..... 111

Fig. 5.2.1: Comparison of the thermal conductivity of copper [19], stainless steel [19], pure silicon [20], and pyrex [21]. 116
Fig. 5.2.2: Diagram of specular and diffuse reflection of phonons off the walls of a silicon sample. 117
Fig. 5.2.3: Plot of the thermal conductivity of silicon for a number of different samples. The characteristics of each sample can be found in Table 5.2.2. Data from [20]. 119
Fig. 5.2.4: Figure 5.2.2 with curves C, G, and H removed and re-plotted from 100 K to 300 K. 120
Fig. 5.2.5: Thermal conductivity of borosilicate glass as a function of temperature. 121
Fig. 5.3.1: Fully developed Nusselt number as a function of aspect ratio for both parallel plates and rectangular ducts 128
Fig. 5.3.2: Average simultaneously developing constant wall temperature Nusselt numbers for parallel plates as a function of thermal dimensionless length from two different authors 130
Fig. 5.3.3: Prandtl number as a function of temperature at 101.3 kPa for various fluids. 131
Fig. 5.3.4: Mean simultaneously developing constant temperature Nusselt number NuT,m,pp for parallel plate ducts as a function of Reynolds number for Prandtl number values of 0.65, 0.72, and 0.8. 132
Fig. 5.3.5: Geometric model of the 10 mm heat exchanger silicon fin (drawn to scale) 133
Fig. 5.3.6: Comparison of two methods for estimating the simultaneously developing Nusselt number as a function of Reynolds number for the 10 mm heat exchanger ducts. 135
Fig. 5.4.1: Diagram of inlet geometries for rectangular ducts 136
Fig. 5.4.2: Comparison of two different correlations prediction of simultaneously developing turbulent Nusselt numbers for Pr = 2.5 in the 10mm heat exchanger. 138

Fig. 5.4.3: Fully developed and apparent friction factors for as a function of Reynolds number for a fluid with Pr = 0.72 in the 10mm heat exchanger..... 139
Fig. 5.5.1: Comparison of the numerical results of Nellis and Klein with the conventional rectangular fin equation Eq. 5.6 in the limit that NTU → 0. Figure is from [31]...... 143
Fig. 5.5.2: Dependence of fin effectiveness on the aspect ratio of the ducts for selected values of NTU and β. Figure is from [31]. 144
Fig. 5.6.1: Diagram of the four resistances acting series to resist heat conduction between the hot stream and cold stream in the heat exchanger 145
Fig. 5.8.1: Schematic showing the distribution of the temperature nodes (top text) and the element locations (bottom text). 155
Fig. 5.8.2: Energy balance for the ith element of the measurement lead wire. 155
Fig. 5.8.3: Heat load to the heat exchanger as a function of the temperature difference between the ends of the lead wire. 158
Fig. 6.1.1: Photograph of the setup used for calibrating individual dies with integrated PRTs...... 179
Fig. 6.1.2: Plot of the adapter plate temperature as function of time during calibration of individual dies with integrated PRTs. 180
Fig. 6.1.3: PRT resistance as a function of temperature. Nearly identical results were obtained using the thermocouple or the PRT as the temperature standard...... 181
Fig. 6.1.4: Normalized resistance of integrated PRTs as a function of adapter plate temperature. The normalized resistance is defined as the resistance divided by the resistance at room temperature 182
Fig. 6.1.5: Normalized resistance of integrated PRTs as a function of adapter plate temperature above 150 K. 183
Fig. 6.1.6: Resistance of the PRTs integrated into the heat exchanger dies as function of temperature for the forty-three die 10 mm heat exchanger. 184
Fig. 6.1.7: Normalized resistance (PRT resistance/PRT resistance at room temperature) as a function of temperature for the forty-three die 10 mm heat exchanger. 185

Fig. 6.1.8: Parasitic heat loads on the heat exchanger during calibration tests of the forty-three die 10 mm heat exchanger. 186
Fig. 6.1.9: Resistance of the PRTs integrated into the heat exchanger dies as function of temperature for the thirty-seven die 20 mm heat exchanger. 187
Fig. 6.1.10: Normalized resistance (PRT resistance/PRT resistance at room temperature) as a function of temperature for the thirty-seven die 20 mm heat exchanger. 188
Fig. 6.1.10: Parasitic heat loads on the heat exchanger during calibration tests of the thirty-seven die 20 mm heat exchanger. 189
Fig. 6.2.1: Experimental setup used to test pressure drop behavior of the micro-valve, thirty-seven die 20 mm heat exchanger, and the forty-three die 10 mm heat exchanger. 190
Fig. 6.2.2: Mass flow rate of ethane as a function of valve voltage for the various pressure differences shown in the legend. The valve outlet pressure ranged from 100 kPa to 105 kPa. 191
Fig. 6.2.3: Plot of mass flow rate versus valve voltage while inlet and outlet pressures are held constant. 192
Fig. H.4: Plot of mass flow rate as a function of valve voltage. This figure shows that both the differential pressure across the valve and the outlet pressure of the valve are important. 193
Fig. 6.2.5: Plot of mass flow rate through the valve as a function of the pressure difference across the valve for various valve settings. 194
Fig. 6.2.6: Comparison of the fully open and fully closed valve positions with jewel orifice calculated flow rates. The valve outlet pressure ranged from 100 kPa to 105 kPa. 195
Fig. 6.2.7: The data in Fig. 6.2.3 re-plotted with the expected flow rates through a jewel orifice. 196
Fig. 6.3.1: Pressure drop across the sixteen die 10 mm heat exchanger using helium as the working fluid. 197
Fig. 6.3.2: Pressure drop across the sixteen die 10 mm heat exchanger using air as the working fluid. 198

Fig. 6.3.3: Pressure drop across the sixteen die 10 mm heat exchanger using ethane as the working fluid. Both the pressure drop across the entire heat exchanger assembly and across the low pressure side of the heat exchanger were measured. 199

Fig. 6.3.4: Pressure difference between the high pressure inlet and the low pressure outlet of the forty-three die 10 mm heat exchanger for various configurations. The blank orifice forced entire flow rate to pass through the internal leaks 200

Fig. 6.3.5: Pressure difference between the high pressure inlet and the low pressure outlet of the forty-three die 10 mm heat exchanger for various configurations. 201

Fig. 6.4.1: Experimentally measured heat exchanger effectiveness as a function of mass flow rate for the sixteen die 10 mm heat exchanger tested in external cooling mode in the cryogenic test facility. 202

Fig. 6.4.2. Experimentally measured pressures and pressure differences as a function of mass flow rate. Contaminants from the compressor freeze out in the heat exchanger if the cold end temperature goes below 200 K. 203

Fig. 6.4.3: Experimental measurements of heat exchanger effectiveness as a function of helium mass flow rate for the forty-three die 10 mm heat exchanger tested in applied-cooling mode in the cryogenic test facility. 204

Fig. 6.4.4: Experimental measurements of heat exchanger effectiveness as a function of ethane mass flow rate for the forty-three die 10 mm heat exchanger tested in applied-cooling mode in the cryogenic test facility. 205

Fig. 6.4.5: Experimental measurements of the pressure difference across the heat exchanger assembly (Php,in – Plp,out) as function of mass flow rate 206

Fig. 6.4.6: Experimentally measured temperature distribution within the forty-three die 10 mm heat exchanger for the smallest helium mass flow rate (0.008 g/s) shown in Fig. 6.4.3. 207

Fig. 6.4.7: Experimentally measured temperature distribution within the forty-three die 10 mm heat exchanger for the largest helium mass flow rate (0. 08 g/s) shown in Fig. 6.4.3. 208

Fig. 6.4.8: Experimentally measured temperature distribution within the forty-three die 10 mm heat exchanger for the smallest ethane mass flow rate (0.04 g/s) shown in Fig. 6.4.4. 209
Fig. 6.4.9: Experimentally measured temperature distribution within the forty-three die 10 mm heat exchanger for the largest ethane mass flow rate (0.17 g/s) shown in Fig. 6.4.4. 210
Fig. 6.4.10: Experimental measurements of heat exchanger effectiveness as a function of helium mass flow rate for the thirty-seven die 20 mm heat exchanger tested in applied-cooling mode in the cryogenic test facility. 211
Fig. 6.4.11: Experimental measurements of the pressure difference across the heat exchanger assembly (Php,in – Plp,out) as function of helium mass flow rate for the applied cooling tests on the thirty-seven die 20 mm heat exchanger. 212
Fig. 6.4.12: Experimentally measured temperature distribution within the thirty-seven die 20 mm heat exchanger for the smallest helium mass flow rate (0.030 g/s) shown in Fig. 6.4.10. 213
Fig. 6.4.13: Experimentally measured temperature distribution within the thirty-seven die 20 mm heat exchanger for the smallest helium mass flow rate (0.135 g/s) shown in Fig. 6.4.10. 214
Fig. 6.5.1: Comparison of experimentally measured and numerically modeled heat exchanger effectiveness as a function of helium mass flow rate for the 16 die 10 mm heat exchanger 215
Fig. 6.5.2: Comparison of experimentally measured and numerically modeled heat exchanger effectiveness as a function of helium mass flow rate for the 43 die 10 mm heat exchanger. 216
Fig. 6.5.3: Comparison of the experimentally measured and numerically modeled temperature distribution for the smallest mass flow rate data point shown in Fig. 6.5.2 217
Fig. 6.5.4: Comparison of the experimentally measured and numerically modeled temperature distribution for the largest mass flow rate data point shown in Fig. 6.5.2 217

Fig. 6.5.5: Comparison of experimentally measured and numerically modeled heat exchanger effectiveness as a function of helium mass flow rate for the 43 die 10 mm heat exchanger. 219
Fig. 6.5.6: Comparison of the experimentally measured and numerically modeled temperature distribution for the smallest mass flow rate data point shown in Fig. 6.5.5..... 219
Fig. 6.5.6: Comparison of the experimentally measured and numerically modeled temperature distribution for the largest mass flow rate data point shown in Fig. 6.5.5..... 220
Fig. 6.6.1: Temperature difference measured across the length of the heat exchanger as a function of the pressure drop across the heat exchanger assembly...... 221
Fig. 6.6.2: Measured effectiveness as a function of the mass flow rate of ethane. 222
Fig. 6.6.2: Fig. 6.6.2 re-plotted without error bars for increased clarity 222
Fig. 6.6.3: Experimental setup showing the new self-cooling cold end. The setup using jewel orifices is shown to the left and the setup incorporating the micro-valve is shown to the right. 223
Fig. 6.6.4: Temperature difference between the heat exchanger inlet streams as a function of pressure difference applied across the forty-three die 10 mm heat exchanger assembly...... 224
Fig. 6.6.5: Temperature difference between the heat exchanger inlet streams as a function of pressure difference applied across the forty-three die 10 mm heat exchanger assembly...... 225
Fig. 6.6.6: Temperature difference between the heat exchanger inlet streams as a function of pressure difference applied across the forty-three die 10 mm heat exchanger assembly...... 226
Fig. 6.6.7: Heat exchanger effectiveness as a function of mass flow rate for the data set shown in Figs. 6.6.4 and 6.6.5. 227
Fig. 6.6.8: Fig. 6.6.7 re-plotted without error bars for increased clarity 227

Fig. 6.6.9: Plot of the temperature distribution with the forty-three die 10 mm heat exchanger when tested with a 0.010" orifice for the data point with the maximum temperature difference. 228
Fig. 6.6.10: Plot of the temperature distribution with the forty-three die 10 mm heat exchanger when tested with a 0.015" orifice for the data point with the maximum temperature difference. 229
Fig. 6.6.11: Plot of the temperature distribution with the forty-three die 10 mm heat exchanger when tested with a 0.020" orifice for the data point with the maximum temperature difference. 230
Fig. 6.6.12: Temperature difference across the heat exchanger (Tc,in – Th,in) as a function of heater power. 231
Fig. 6.6.13: Heat exchanger effectiveness as a function of heater power for the data shown in Fig. 6.5.12. 232
Fig. 6.7.1: Temperature difference between the heat exchanger inlet streams as a function of pressure difference applied across the forty-three die 10 mm heat exchanger assembly. 233
Fig. 6.7.2: Heat exchanger effectiveness as a function of mass flow rate for the data set shown in Fig. 6.7.1. 234
Fig. 6.7.3: Figure 6.7.2 re-plotted with out error bars for increased clarity 234
Fig. 6.7.4: Plot of the temperature distribution with the forty-three die 10 mm heat exchanger when tested with a 0.010" orifice for the data point with the maximum temperature difference. 236
Fig. 6.7.5: Plot of the temperature distribution with the forty-three die 10 mm heat exchanger when tested with a 0.013" orifice for the data point with the maximum temperature difference. 237
Fig. 6.7.6: Plot of the temperature distribution with the forty-three die 10 mm heat exchanger when tested with a 0.015" orifice for the data point with the maximum temperature difference. 238

List of Symbols

Symbol	Description	Units
α	Aspect Ratio of Duct	-
A	Area	m^2
β	Fin Constant	-
χ	Dimensionless Heat Load	-
$\dot{C}$	Stream Capacity Rate	W/K
$C_{convert}$	Mass Flow Meter Conversion Factor	-
Cp	Isobaric Specific Heat	J/kg-K
C_v	Valve or Orifice Flow Factor	gal/min-psi$^{0.5}$
ΔP	Pressure Difference	psid
ΔT	Temperature Difference	K
D	Diameter	m
ε	Heat Exchanger Effectiveness	-
e	Emissivity	-
η	Efficiency	-
F_e	Emissivity Factor	-
F_{12}	Radiation View Factor	-
$Frac_{leak}$	Fraction of Hot Stream Leaking to Cold Stream	-
γ	Element Concentration Factor	-
h	Fluid Enthalpy	J
H_{die}	Height of Die	m
H_{duct}	Height of Duct	m
H_{fin}	Height of Fin Material between Duct Rows	m
H_{gw}	Height of Glass Spacer Window	m
htc	Heat Transfer Coefficient	W/m^2-K
I	Electrical Current	A
k	Thermal Conductivity	W/m-K
λ	Axial Conduction Parameter	-
L	Length	m
μ	Hot Side Dimensionless Capacity Rate	-
μ	Fluid Viscosity	kg/m-s
μ_{JT}	Joule-Thomson Coefficient	K/kPa
$\dot{m}$	Mass Flow Rate	kg/s
υ	Cold Side Dimensionless Capacity Rate	-
N	Number of Finite Elements	-
NTU	Number of Transfer Units	-
N_{column}	Number of Duct Columns	-
N_{duct}	Number of Ducts in each Columns	-
Nu	Nusselt Number	-
P	Fluid Pressure	kPa
Pe	Peclet Number	-

Pr	Prandtl Number	-
$\dot{q}$	Heat Transfer Rate	W
ρ	Fluid Density	kg/m^3
ρ	Electrical Resistivity	Ω-m
R	Thermal Resistance	K/W
R_e	Electrical Resistance	Ω/m
Re	Reynolds Number	-
σ	Stefan-Boltzmann Constant	W/ m^2-K^4
SA	Surface Area	-
SG	Specific Gravity	-
θ	Dimensionless Temperature	-
T	Fluid Temperature	K
t_{fin}	Thickness of Silicon Plate	m
U	Overall Heat Transfer Coefficient	W/m^2-K
V	Fluid Velocity	m/s
$\dot{V}$	Volumetric Flow Rate	gal/min
W_{die}	Width of Die	m
W_{duct}	Width of Duct	m
$W_{g,stream}$	Width of Glass between Fluid Streams	m
W_{gw}	Width of Glass Spacer Window	m
$W_{si,stream}$	Width of Silicon between Fluid Streams	m
W_{web}	Width of Webbing between Duct Columns	m
Z	Dimensionless Length of Heat Exchanger	-
X	Length of Heat Exchanger	m
x^+	Hydrodynamic Dimensionless Length	-
x^*	Thermal Dimensionless Length	-
	Subscripts	
ac	Axial Conduction	
act	Actual	
app	Apparent	
bolt	Bolt	
c	Cold Side	
cl	Centerline	
cond	Thermal Conduction	
cont	Contraction	
crit	Critical	
cu	Copper	
exp	Expansion	
fd	Fully Developed	
fin	Fin	
gen	Generated	
glass	Glass	
h	Hot Side	

H	Constant Wall Heat Flux Boundary Condition	
hp	High Pressure	
htr	Heater	
hyd	Hydraulic	
in	Inlet	
lam	Laminar	
leak	Leaking Fluid	
lp	Low Pressure	
m	Mean average	
max	Maximum	
min	Minimum	
MLI	Multi-Layer Insulation	
net	Net	
out	Outlet	
pp	Parallel Plate	
PRT	Platinum Resistance Thermometer	
rad	Radiation	
si	Silicon	
sp	Spacer	
ss	Stainless Steel	
T	Constant Wall Temperature Boundary Condition	
tot	Total	
turb	Turbulent	
w	Wall	
wire	Wire	
wire	Wire	

Chapter 1: Background

1.0 Introduction

This chapter provides the background information that is necessary to understand the scope and history of the project. The chapter begins with a brief introduction to cryosurgery, which is the intended application of the Micro-Electro-Mechanical-Systems (MEMS) heat exchangers studied for this thesis. The next section of the chapter describes the Joule-Thomson (J-T) cycle, which is the standard thermodynamic cycle that is used to operate cryosurgical probes. The chapter concludes with a brief history of the ongoing collaboration between the University of Wisconsin-Madison and the University of Michigan-Ann Arbor directed at the development of a MEMS based cryosurgical probe.

1.1 Cryosurgery

Cryosurgery is a medical procedure in which malignant tissue such as cancer is destroyed by rapid freezing [1]. The procedure involves cooling the cells to a temperature below -50°C in repeated freeze/thaw cycles in order to ensure that all of the malignant tissue has been destroyed. The benefit of cryosurgery over other cancer treatment options is that tissue damage is localized and blood loss is minimal. A photograph of a cryosurgical probe being used to ablate cancerous cells in the liver is shown in Fig. 1.1.1 [2].

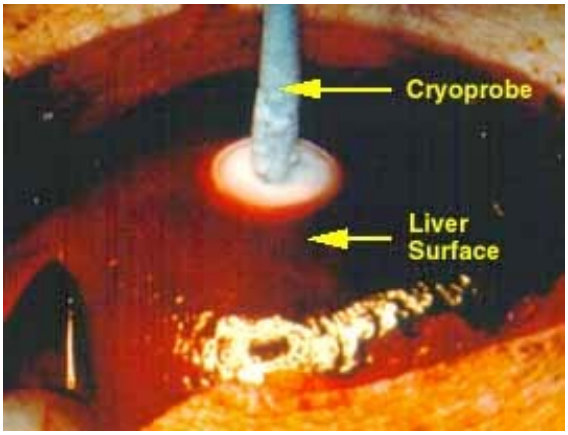

Fig. 1.1.1: Photograph of the cryoablation of cancerous cells in the liver [2].

Conventional cryosurgical probes typically operate on a J-T cycle [3], which will be discussed in detail in Section 1.2. A coiled finned tube wound around a small mandrel is generally used for the recuperative heat exchanger and a fixed orifice is used to provide the isenthalpic expansion required for the cycle. An example of a typical cryosurgical probe heat exchanger is shown in Fig. 1.1.2. The size of the metallic finned tube heat exchangers cannot easily be reduced further. Utilization of MEMS based heat exchanger may enable the size and weight of the heat exchanger to be further reduced and/or the cooling power to be increased, thereby increasing the efficacy of cryosurgery.

Fig. 1.1.2: Photograph of a finned tube heat exchanger used in conventional cryosurgical probes [3].

The heat exchanger must be lightweight and compact so that the probe can be easily held in the surgeon's hand. MRI-compatibility is a potential benefit of MEMS based heat exchangers since one of the current drawbacks to cryosurgery is that the surgeon can only estimate the size and location of the iceball formed at the probe tip using ultrasound. An MRI machine could be used to provide more accurate, real-time feedback to the surgeon regarding the status of the iceball if non-metallic materials are used to fabricate the cryosurgical probe.

1.2 Joule-Thomson Cycle

Conventional cryosurgical probes operate on a J-T cycle. A schematic of a J-T cycle is presented in Fig. 1.2.1 and representative state points in the cycle are shown on a T-s diagram for ethane in Fig. 1.2.2. High pressure gas is delivered from a remotely located compressor to the high pressure inlet of the recuperative heat exchanger (State 1). The working fluid is pre-cooled as it passes through the heat exchanger by the low pressure fluid after it has absorbed a heat load. Upon exiting the heat exchanger (State 2) the high pressure fluid is isenthalpically expanded using a valve or orifice. The isenthalpic expansion results in a cooling of the fluid (State 3), which is then used to absorb a heat load. After absorbing the heat load (State 4) the low pressure fluid is used to pre-cool the incoming high pressure fluid. Upon exiting the heat exchanger (State 5) the low pressure fluid is returned to the compressor.

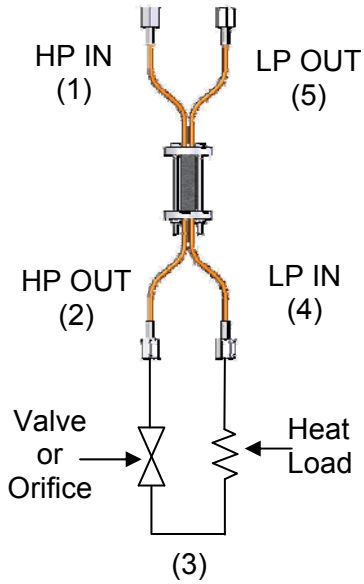

Fig. 1.2.1: Flow schematic for a J-T cycle

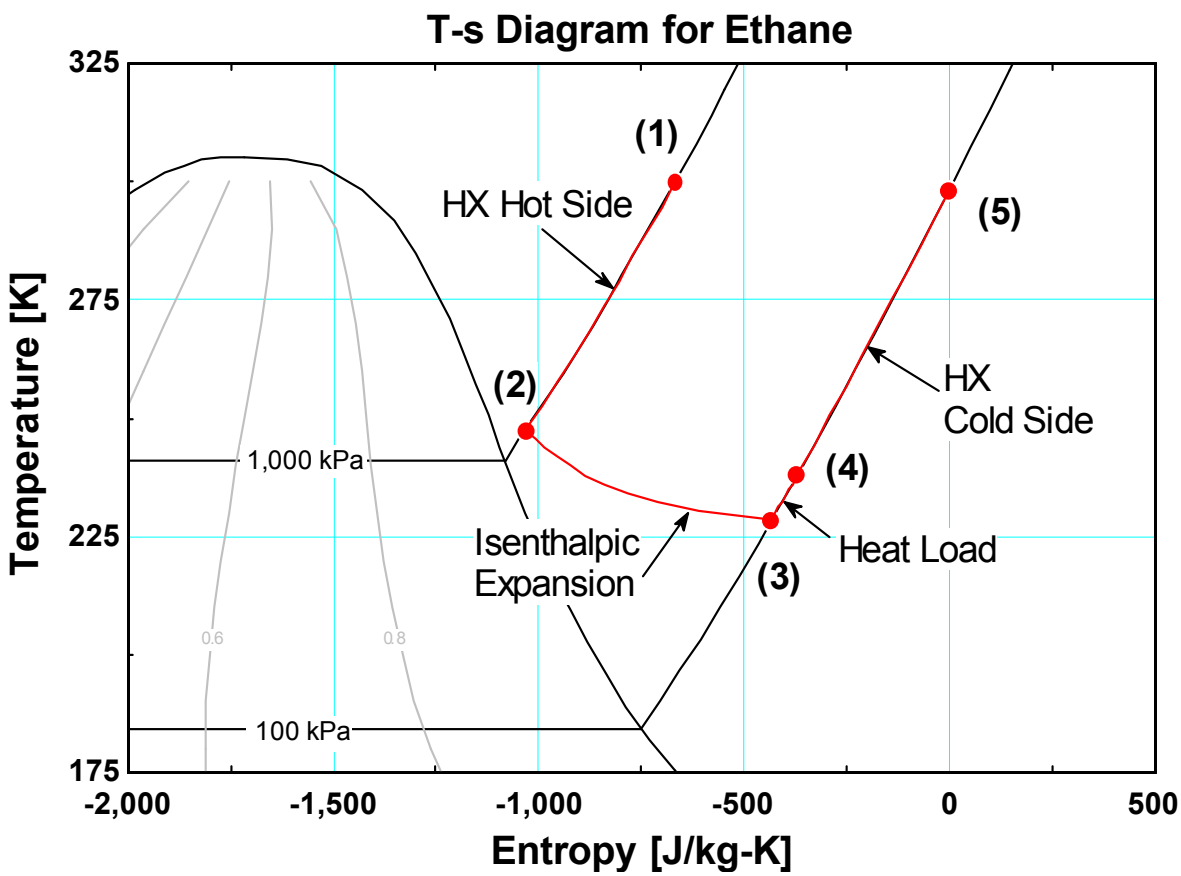

Fig. 1.2.2: T-s diagram showing representative states of a J-T cycle for ethane as the working fluid. The numbered states are shown on the flow schematic in Fig. 1.2.1

1.3 First Generation MEMS Heat Exchanger

The first generation MEMS heat exchanger was designed and tested before the author joined the project and further information regarding this heat exchanger can be found in the literature [4-7]. The first generation heat exchanger was fabricated by anodically bonding silicon wafers to both sides of a thin Pyrex plate and micromachining the silicon to form rows of silicon fins. Pyrex caps are bonded to both sides of the Pyrex base plate to force all of the fluid to flow through the silicon fins. A geometric model of the first generation heat exchanger is shown in Fig. 1.3.1 and a photograph is shown in Fig. 1.3.2.

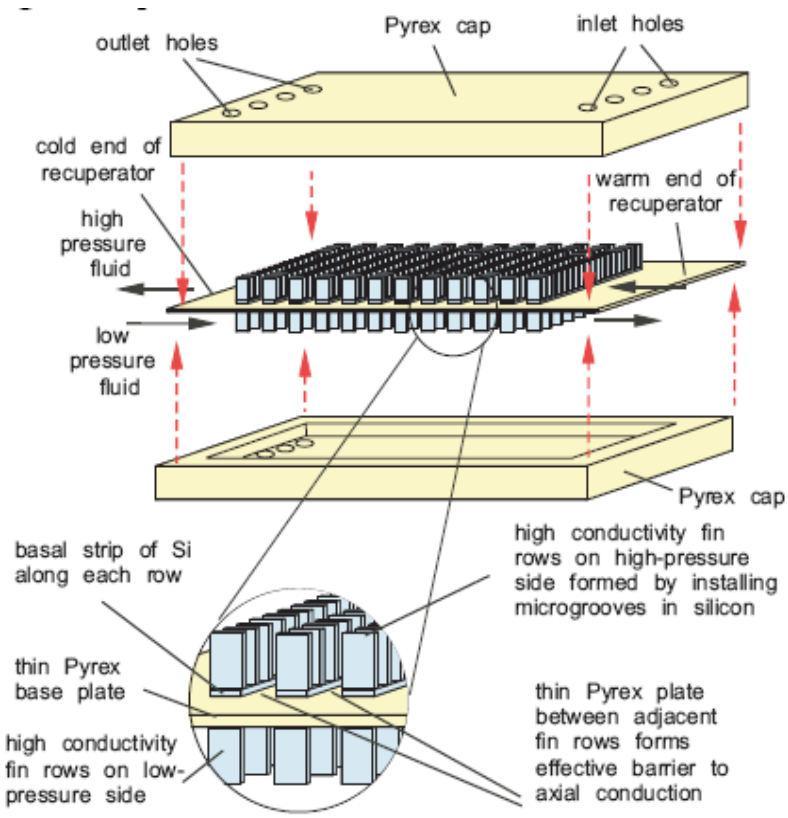

Fig. 1.3.1: Geometric model the first generation MEMS heat exchanger [7].

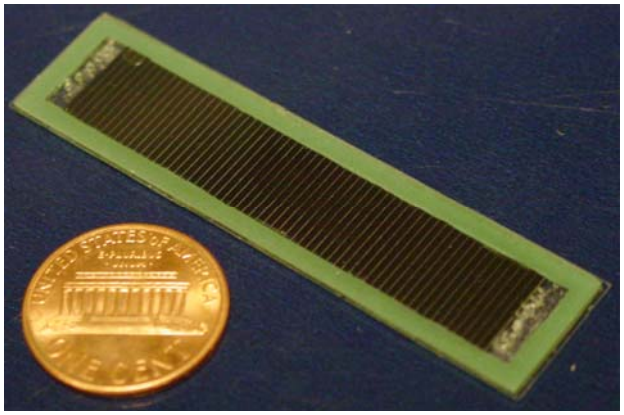

Fig. 1.3.2: Photograph of the first generation MEMS heat exchanger [5].

Silicon, which has a thermal conductivity that is almost as high as copper, was used to fabricate the fins in order to provide good stream-to-stream conductance. Pyrex has a thermal conductivity that is roughly an order of magnitude less than stainless steel. The Pyrex base plate was kept thin so that that heat exchanger has low stream-to-stream resistance but high axial conduction resistance.

The experimental setup used for testing the first generation heat exchanger is shown in Fig. 1.3.3. The heat exchanger design was very fragile and the heat exchangers frequently broke due to handling or upon applying even a very small pressure difference. The addition of a G10 support structure improved the reliability of the first generation heat exchanger enough to allow some experimental data to be collected. However, the allowable pressure differences were still so small that temperature differences of only a few Kelvin could be produced across the length of the heat exchanger when it was installed and operated in a J-T cycle.

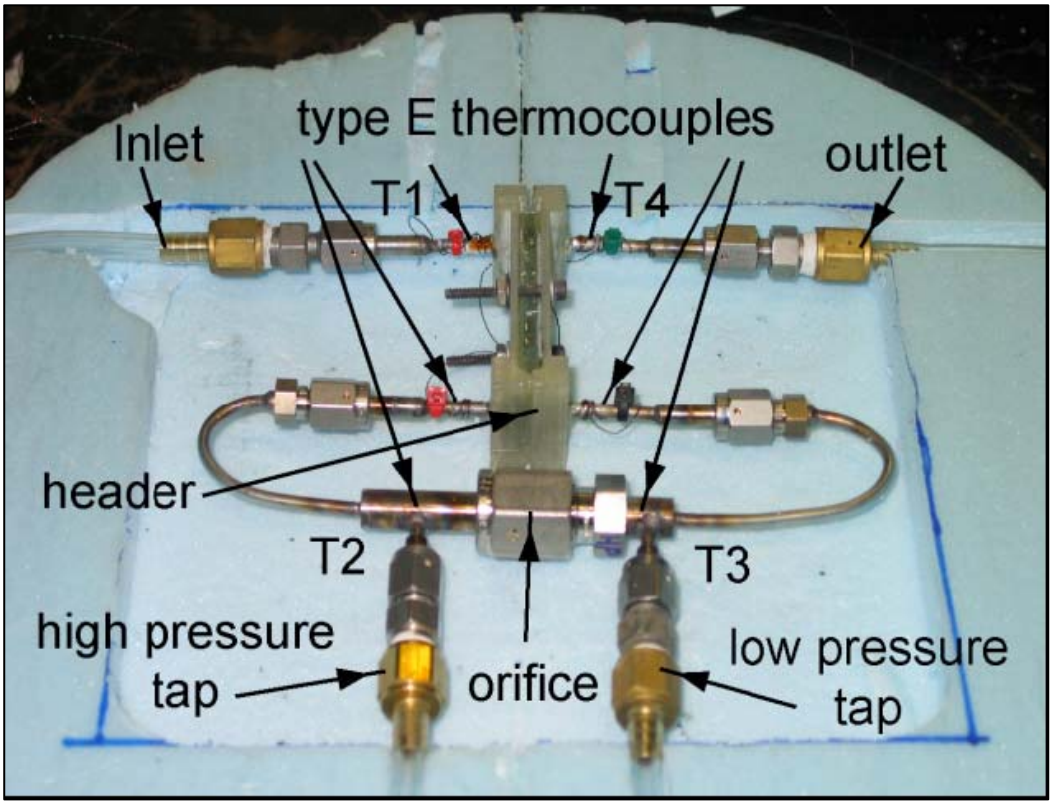

Fig. 1.3.3: Experimental setup used for testing the first generation MEMS heat exchanger [5].

A more robust perforated plate design was chosen for the second generation heat exchanger. Silicon and borosilicate glass, which are common MEMS materials, were also used to fabricate the second generation heat exchanger. The perforated plate design has the advantage over the first generation design in that the brittle glass is supported on either side by the silicon. The disadvantage of the perforated plate design is that it requires a large number of bonds, which increases the likelihood of internal fluid leakage. A simplified geometric model and a photograph of the second generation heat exchanger are shown in Fig. 1.3.4.

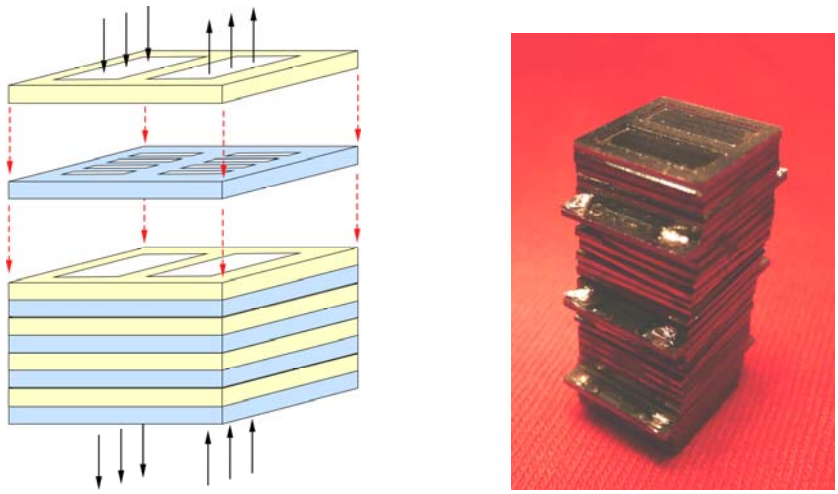

Fig. 1.3.4: Geometric model of the heat exchanger (left) and a photograph of a heat exchanger before bonding with the headers (right)

MEMS device fabrication typically involves repeated masking and etching steps, which is effective for creating holes or trenches on a flat surface. However, creating large or complicated 3-D structures can be quite difficult using standard MEMS technology. Multiple perforated plates can be etched simultaneously on a single silicon wafer using a single masking and etching step. Instead of trying to fabricate the heat exchanger as a single complicated component, the heat exchanger is fabricated by making large number of perforated plates and spacers and bonding them together. Therefore, perforated plate heat exchangers take advantage of the strengths of MEMS processes and should be suitable for mass fabrication. The assembly of the second generation heat exchangers is discussed in Chapter 2.

Chapter 2: MEMS Components

2.0 Introduction

This chapter starts with a discussion of how the heat exchangers were assembled and prepared for experimental testing. The second section of the chapter shows how the valves and orifices were assembled and how they have been used in conjunction with the heat exchanger in order to implement a Joule-Thomson refrigeration cycle.

Some of the work described in this chapter was not performed by the present author and credit should be given to others who have also worked on this project. The original design of the heat exchanger dies was a collaborative effort between Dan Hoch, who was at UW-Madison, and Weibin Zhu, who is at UM-Ann Arbor. All of the heat exchanger dies and heat exchanger stacks were manufactured and assembled by Weibin Zhu. The micro-valve was borrowed from another experiment being conducted in the same laboratory that the MEMS heat exchangers were being tested in. The valve project is also a collaborative effort between the UW-Madison and the UM-Ann Arbor.

2.1 Heat Exchanger Assembly

A key requirement for any cryogenic heat exchanger is that it must be able to withstand structural loads that are imposed by thermal expansion resulting from temperature changes and pressure differences experienced during operation. Temperature changes can impose high thermal stresses due to mismatches in the coefficient of thermal expansion associated with different materials that lead to uneven rates of contraction. The bonds between dissimilar materials are generally the regions of highest concern since the bonds often have the smallest maximum allowable stress and can be characterized by three different expansion coefficients, one for each of the bonding materials and one for the bonding medium.

A large amount of time and labor would be lost if a thermal shock test were carried out using a full heat exchanger assembly and resulted in damage. Therefore, rather than thermally shocking an entire heat exchanger assembly, only individual dies that had been previously damaged during shipping or manufacture were tested in this way. A die consists of one silicon plate that has been anodically bonded to a glass plate. Figures 2.1.1 through 2.1.2 show a 20 mm die and a 10 mm die before and after they are suddenly immersed in a liquid nitrogen bath. The thermal shock associated with the sudden immersion in liquid nitrogen produced no visually detectable damage to either die (either to the bond or the individual plates).

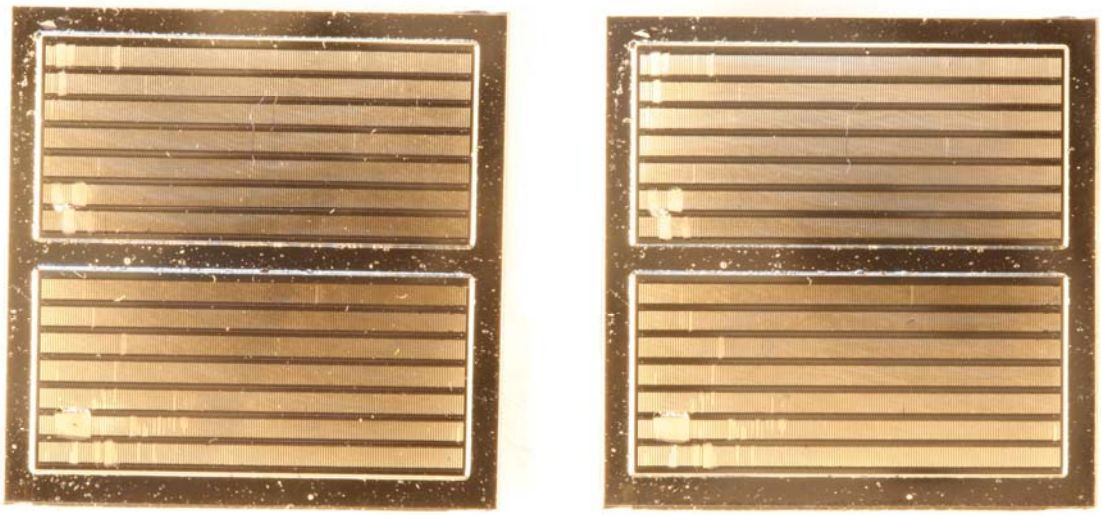

Fig. 2.1.1: 20 mm heat exchanger die before thermal shock test (left) and after being immersed suddenly in a liquid nitrogen bath (right)

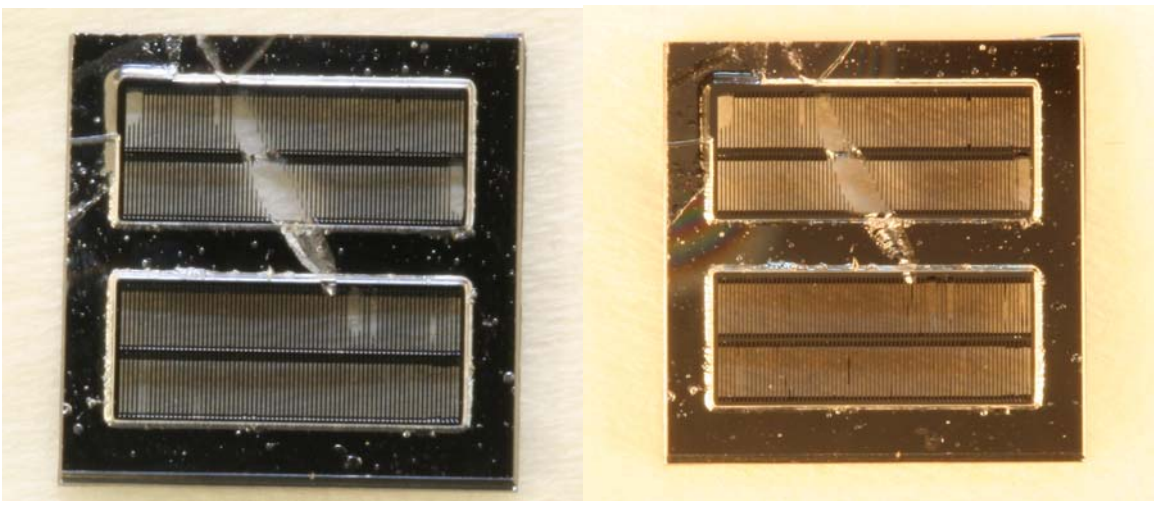

Fig. 2.1.2: 10 mm heat exchanger die before thermal shock test (left) and after being immersed suddenly in a liquid nitrogen bath (right)

Two heat exchangers were fabricated for experimental testing at room temperature; these are shown in Fig. 2.1.3 and 2.1.4. The heat exchangers were fabricated by bonding individual dies to one another using epoxy in order to form a stack of dies.

There are several drawbacks to using epoxy for fabricating the heat exchanger. One major drawback to using epoxy is illustrated in Fig. 2.1.5. If too much epoxy is applied to the dies, the epoxy is likely to seep out the sides of the heat exchanger and plug the flow passages within the heat exchanger. Conversely, if too little epoxy is applied there can be both internal and external fluid leaks. The external fluid leaks can be fixed by applying a coat of epoxy over the outer surface; this has the drawback of decreasing the resistance of the heat exchanger structure to axial conduction. Internal leaks can not be fixed but can be reduced by compressing the heat

exchanger axially. However, the application of an axial compressive force on the heat exchanger can generate cracks in the fragile glass layers, which leads to even larger internal leaks.

The other major disadvantage associated with using epoxy to assemble the heat exchanger is that it is a time consuming and inefficient manufacturing technique. The process of mixing and then degassing the epoxy in a vacuum chamber takes time if done carefully, yet these steps are necessary in order to create the strongest and most reliable bond. The epoxy also takes close to 24 hours to fully cure, which means that it takes many days to assemble a heat exchanger (a single heat exchanger requires that dies be assembled in groups of 2 and then 4 and then 8, etc., so that only one new epoxy bond is created during each process). The dies also have a tendency to shift before the epoxy becomes rigid. To minimize this problem, only one bond is epoxied at a time and small weight is place on top of the heat exchanger stack. The process of building a large heat exchanger proceeds by assembling multiple small stacks in parallel and combining them into bigger stacks. An alignment fixture would have been beneficial, but the epoxy seeping out the sides would bond the heat exchanger to the fixture. As a result of the shifting during assembly, there is some misalignment between the dies and therefore less bonding area between the dies than originally intended. If future projects continue to use epoxy as a bonding medium then searching for a suitable material that an alignment fixture could be fabricated from that would not bond to the epoxy would be very beneficial.

The eight die, 20 mm heat exchanger in Fig. 2.1.4 was broken before any useful experimental results were obtained. The epoxy joints in this heat exchanger were later dissolved and the unbroken dies were cleaned and used to fabricate a new heat exchanger. The sixteen die, 10 mm heat exchanger shown in Fig. 2.1.3 was tested in both the room temperature and cryogenic temperature experimental test facilities. The experimental results for the sixteen die, 10 mm heat exchanger at room temperature are not presented in this thesis due to the large volume of more accurate and useful data collected in the cryogenic test facility. The experimental test results for the cryogenic test facility are presented in Chapter 6.

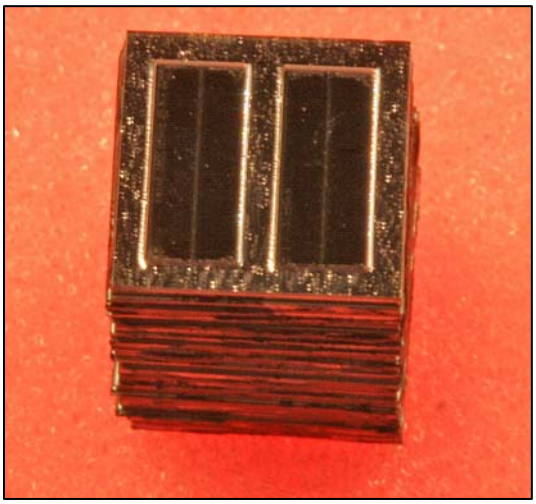

Fig. 2.1.3: Sixteen dies were epoxied together to form the first 10 mm heat exchanger. This heat exchanger was tested in both the room temperature experimental setup and the cryogenic test facility.

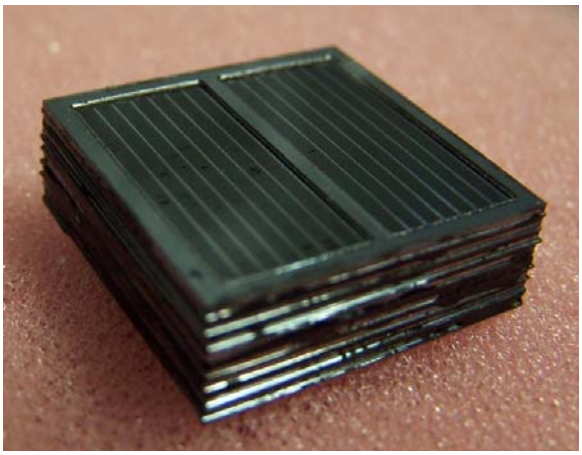

Fig. 2.1.4: Eight dies were epoxied together to form the first 20 mm heat exchanger. This heat exchanger was tested only in the room temperature experimental setup and was broken before any useful experimental data was obtained.

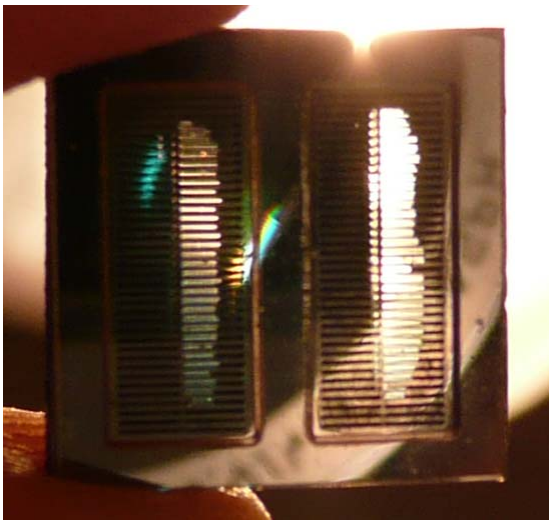

Fig. 2.1.5: The flow passages in these 10 mm dies were partially blocked by excess epoxy

Headers were manufactured in order to provide an interface between the heat exchanger and the tubing in the experimental setup. The side of the header that is bonded to the heat exchanger is shown in Fig. 2.1.6 for the 10 mm and in Fig. 2.1.7 for the 20 mm heat exchanger. There is a shallow indentation that aligns the heat exchanger with the header during the epoxy bonding stage of assembly. The heat exchangers are very light and can slide on the film of epoxy if they are not held in place during the curing process. There are two large ducts milled into both sides of the header that allow flow to enter and exit the heat exchanger uniformly. Flow maldistribution is not generally a severe problem for a perforated plate type heat exchanger; however, the heat exchangers that are tested are relatively short and therefore it is important to allow adequate space for flow distribution in the headers. Flow maldistribution will result in some parts of the heat exchanger (specifically, those passages that are furthest from the inlet and exit ports) being underutilized and will therefore decrease the effectiveness of the heat exchanger.

The opposite side of the heat exchanger header, shown in Fig. 2.1.6 for the 10 mm and Fig. 2.1.7 for the 20 mm heat exchanger, has six holes drilled through it. The two holes near the center are for the fluid connections. A small section of 1/8" tubing is silver-soldered to a VCR gland on one end and the other end of the tube is epoxied to the header, as shown in Fig. 2.1.9 for the 10 mm heat exchanger assembly. The four holes that are 90° apart and installed towards the outer radius of the header accommodate the bolts that connect the warm end header to the cold end header. These bolts have four functions: (1) guiding the top header as it is lowered onto the bottom header during the process of joining the heat exchanger assembly to the header with epoxy, (2) allowing a compressive force to be applied to the assembly during the curing process, (3) resisting forces that might be exerted by the tubing connections, and (4) bearing the load associated with expansion due to internal pressurization.

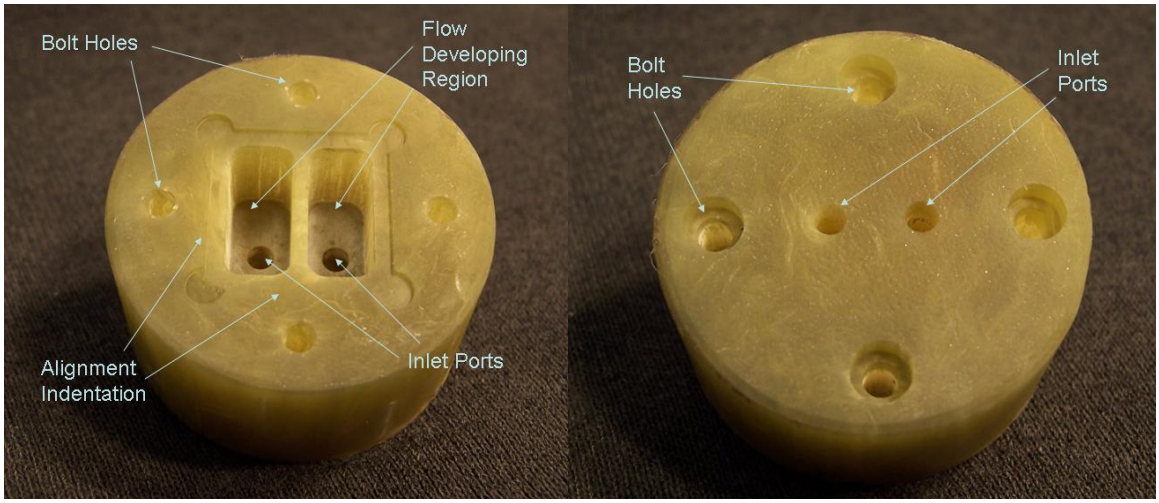

Fig. 2.1.6: 20 mm G10 header with the heat exchanger side shown on the left and the fluid connection side shown on the right.

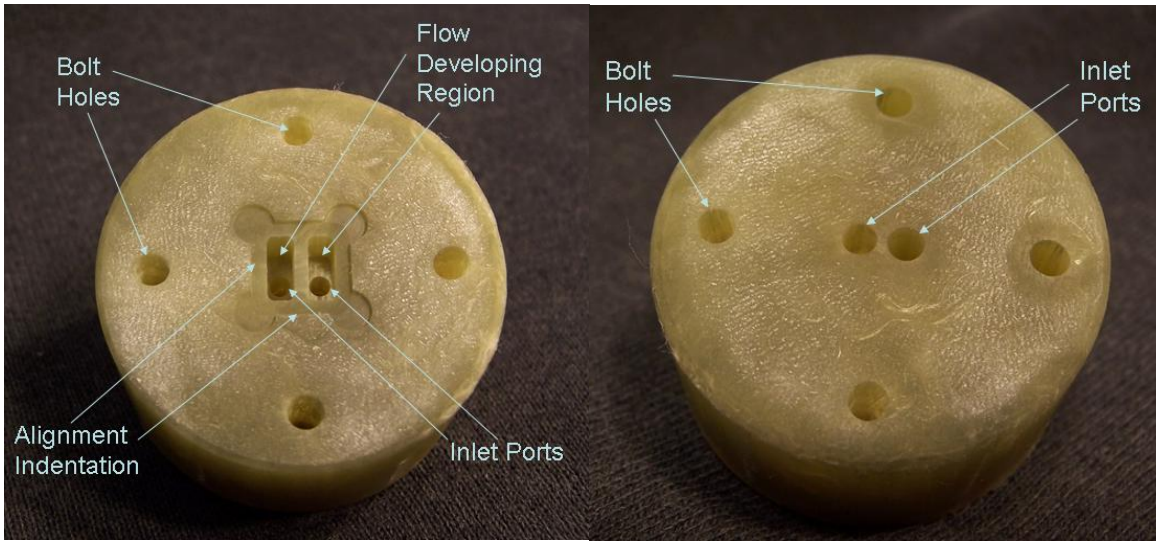

Fig. 2.1.7: 10 mm G10 header with the heat exchanger side shown on the left and the fluid connection side shown on the right.

There are a few major drawbacks to choosing G10 as the header material. The first is that all joints in the header itself must be epoxied. Epoxy joints are generally much weaker and more fragile than brazed or welded joints. Instead of producing chips as most metallic materials do when machined, G10 produces a fine abrasive powder of glass and epoxy. The glass powder can quickly dull or destroy bits if a machining lubricant isn't used. More importantly, these G10 particles can become airborne and entrained in the lungs of the machinist or others in the vicinity of the machining operation. This health hazard can be significantly reduced by using a machining lubricant and a fine grade particulate face mask.

Photographs of the heat exchanger assembly process are shown in Fig. 2.1.8. The heat exchanger is first installed in the bottom header using an epoxy joint. The bolts are then inserted into the bottom header and used to guide the top header into its position as it is installed using another epoxy joint. Once the heat exchanger has been epoxied to both headers, the bolts are gently tightened. After the heat exchanger has been compressed slightly, epoxy is applied to the external surface of the heat exchanger in order to prevent any external leaks.

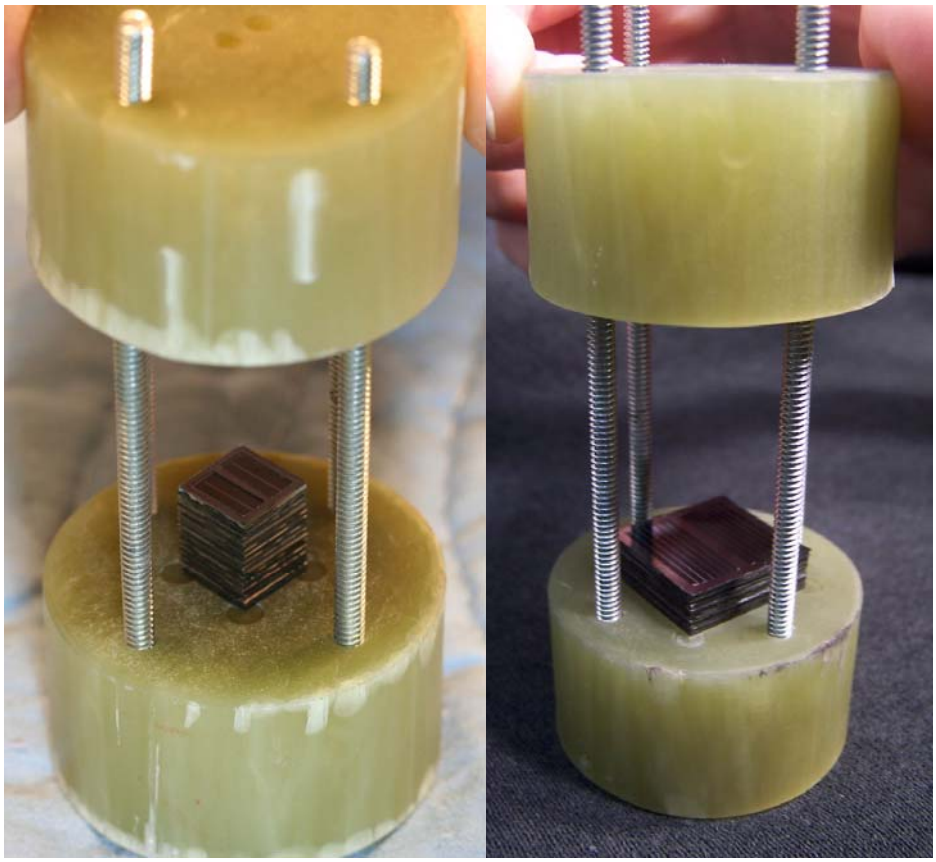

Fig. 2.1.8: Photographs of the 10 mm (left) and 20 mm (right) heat exchanger assemblies before epoxy is applied

The fluid connections used in the experiment are made with VCR fittings. VCR fittings have a metal ridge that bites into a metal gasket in order to create a seal. VCR fittings were chosen because of their reliability and their ability to making robust, helium leak-tight seals; these are necessary for testing in a cryogenic, vacuum environment. The VCR fittings are silver-soldered

to short lengths of 1/8” copper tubing and the tubing is epoxied to the header, as shown in Fig. 2.1.9.

Fig. 2.1.9: VCR glands silver brazed to copper tubing which is epoxied to 10 mm header

Photographs of the final assemblies for the 10 mm and 20 mm heat exchangers for room temperature testing are shown in Fig. 2.1.10 and 2.1.11 respectively. The room temperature testing relied on thermocouples that were attached to the external surface of the tubing, as shown in Fig. 2.1.11. The first set of thermocouples was soldered directly to the tube; this led to a large amount of electrical noise in the temperature measurements. The second set of thermocouples had a small solder bead junction that was covered by epoxy in order to electrically isolate the thermocouple from the tube. This method of installation reduced the thermocouple noise by several orders of magnitude and therefore allowed more accurate measurements to be made. The 10 mm heat exchanger was tested after the 20 mm heat exchanger using thermocouples that penetrated into the fluid stream using a tee joint rather than using externally mounted thermocouples.

Fig. 2.1.10: Final assembly of the 10 mm heat exchanger

Fig. 2.1.11: Final assembly of 20 mm heat exchanger with externally mounted thermocouples

A new header design was developed and is shown in Fig. 2.1.12. This header design is improved based on the experience gained from room temperature testing. There were two primary objectives associated with the new design. The first objective was to improve the robustness of the joint between the tubing and the header (a location that was prone to failure in the older design) and the second is to reduce the required cool down time by reducing the thermal mass of the header. Stainless steel was selected as the header material because it allowed the tubes to be welded or silver-soldered, leading to a much stronger joint than epoxy could provide. The overall size and therefore thermal mass of the headers was reduced in order to help reduce the time required to reach a steady state test condition. The reduction in the thermal mass came by removing the plenum that was previously incorporated in the header to allow fluid distribution to become uniform prior to entering the heat exchanger. It is expected that the flow will be uniform after passing through the first few dies and so issues relative to flow distribution were much larger for the initial, shorter heat exchangers that were tested using the older header than for the longer heat exchangers tested using the improved headers in the cryogenic test facility.

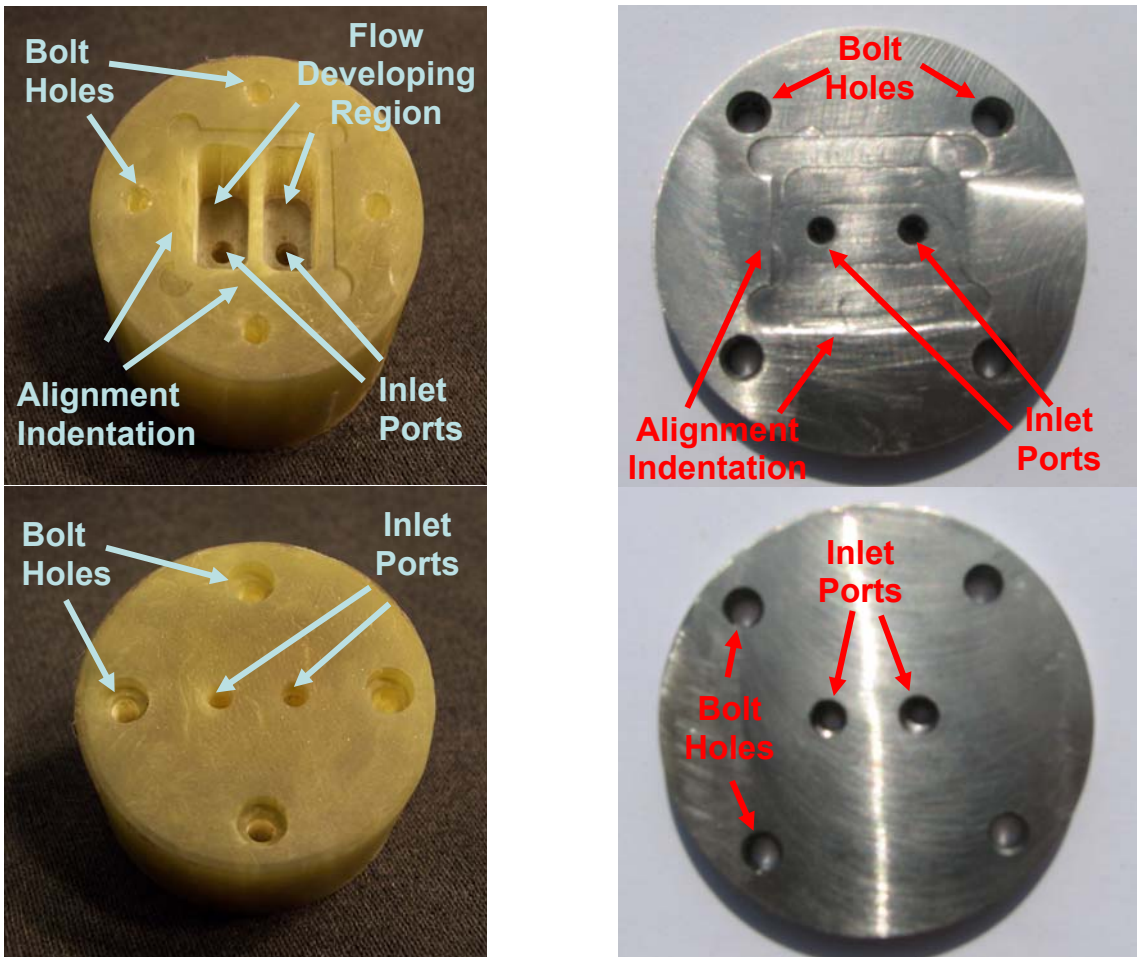

Fig. 2.1.12: Comparison of the initial header design (left) and the improved design (right)

A new process was also developed for bonding the heat exchanger dies to one another. Instead of using epoxy to create the bond between adjacent heat exchanger dies, a gold diffusion bond was developed. Gold was deposited on both sides of the die and the dies were stacked together and heated under pressure. Unfortunately, the gold bonds were found to be much weaker, less reliable, and less hermetic than the epoxy bonds. Shown in Fig. 2.1.13 is an example of a gold bonded heat exchanger that is 23 dies in length. The heat exchangers that were built with gold-bonding could be easily and accidentally broken by hand. The heat exchanger shown in Fig. 2.1.13 appeared to be the strongest of the gold bonded heat exchangers since it did not easily break by touching. However, even this heat exchanger was characterized by internal and external leaks that were large enough to make any meaningful testing impossible. No gold bonded heat exchangers were tested and the final two heat exchangers that were built were joined using the original epoxy technique.

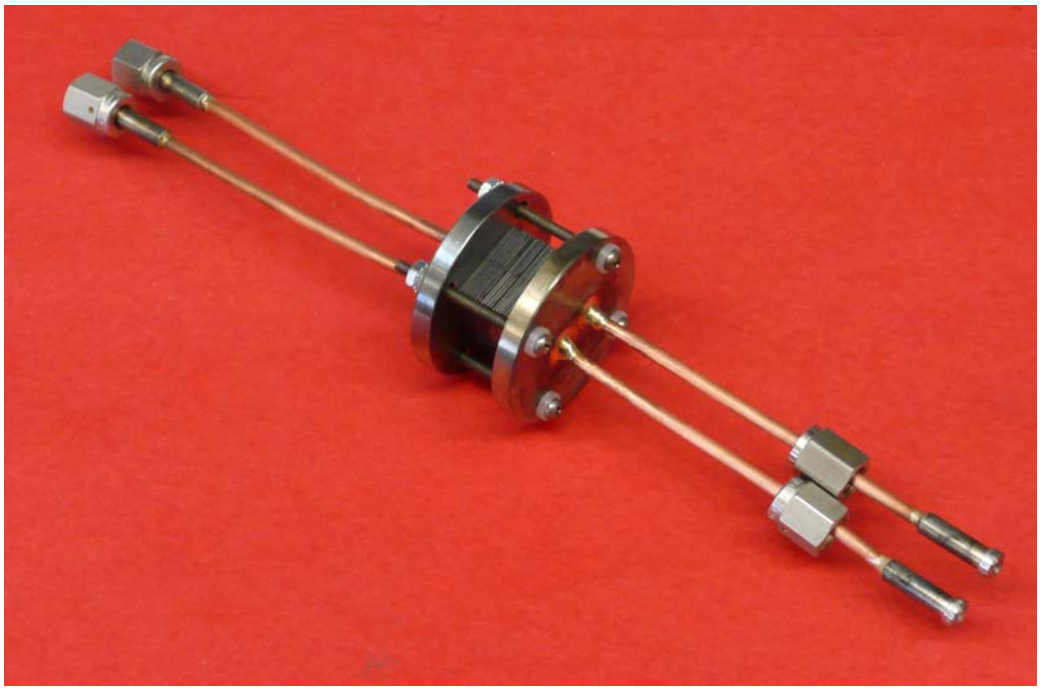

Fig. 2.1.13: 23 die 20 mm heat exchanger assembly using stainless steel headers.

Two additional improvements were made for the final header design, which is shown in Fig. 2.1.14. The first is that thermocouple penetrations were installed in the header. This addition allows temperature measurements to be taken without the use of an external VCR tee joint in which a penetration thermocouple is installed. This external VCR fitting is bulky and therefore has a large thermal mass relative to the amount of cooling produced by the heat exchanger installed in a J-T cycle. The second improvement is that the VCR fittings are attached directly to the heat exchanger header. This allows the heat exchangers to be easily moved from the cryogenic test facility to the cryosurgical probe housing. In the cryogenic test facility short adapter tubes are required to connect each of the ports on the heat exchanger to the experimental setup.

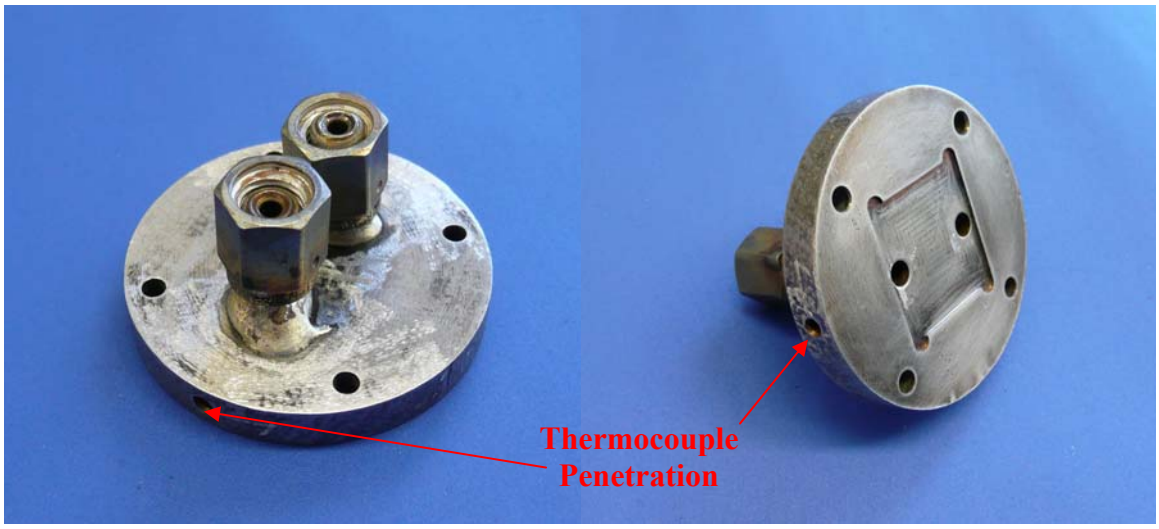

Fig. 2.1.14: Final header design for the 20 mm heat exchanger

The final two heat exchangers that were constructed had platinum resistance thermometers (PRTs) integrated into several of the dies. A photograph that compares a standard die to a die that has an integrated PRT is shown in Fig. 2.1.15. The PRT dies have the same height as the standard dies but are slightly wider in order to allow a reference resistor to be installed on the outside of each fluid stream, as shown in Fig. 2.1.16. The temperature of the reference resistor should be close to the average temperature of the fluid stream as it crosses the die. A second set of resistors have been deposited on the fins to measure the average fin temperature and are shown as the normal resistors in Fig. 2.1.16.

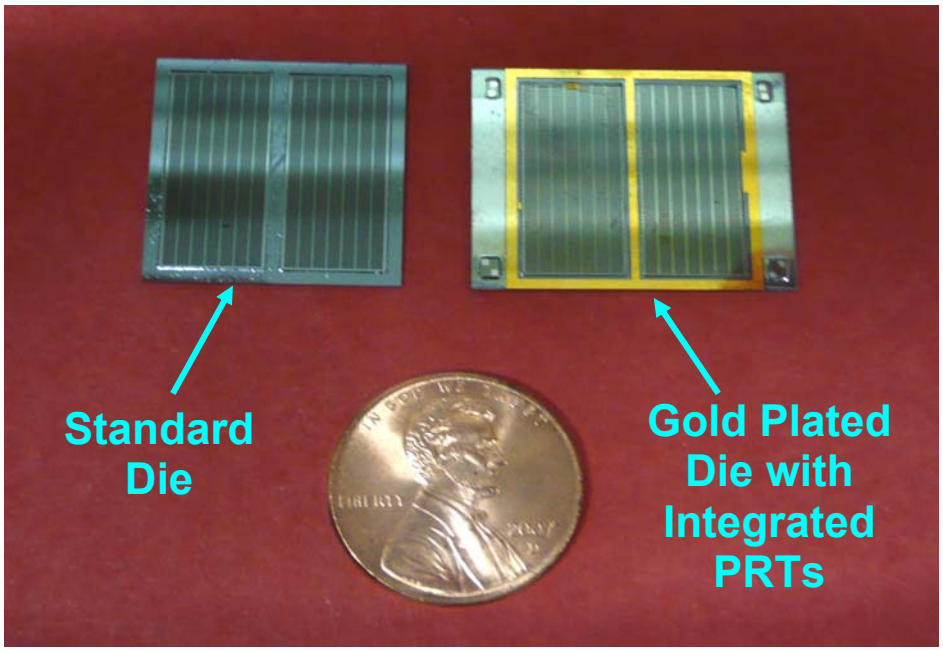

Fig. 2.1.15: Photograph showing both an ordinary die and a gold plated die with integrated PRTs

The PRTs are deposited before the dies have been diced and before the glass wafer has been bonded to the silicon wafer. All of the PRTs on an individual wafer are made simultaneously. The first step is to spin photoresist over the entire wafer and then pattern the photoresist using photolithography to expose the silicon surface with the exact dimensions of the resistor. The second step is to deposit a layer of titanium that is 50 Å thick over the entire silicon wafer. The titanium serves as a bonding agent because platinum bonds well to titanium but does not bond well to silicon. A layer of platinum 1000 Å thick is deposited on top of the titanium. The next step is to remove the remaining photoresist, which also removes all the titanium and platinum from undesired areas as the photoresist underneath dissolves. The result is that each resistor is 30 μm wide and 69 cm long for the 20 mm die and 20 μm wide and 12 cm long for the 10 mm dies.

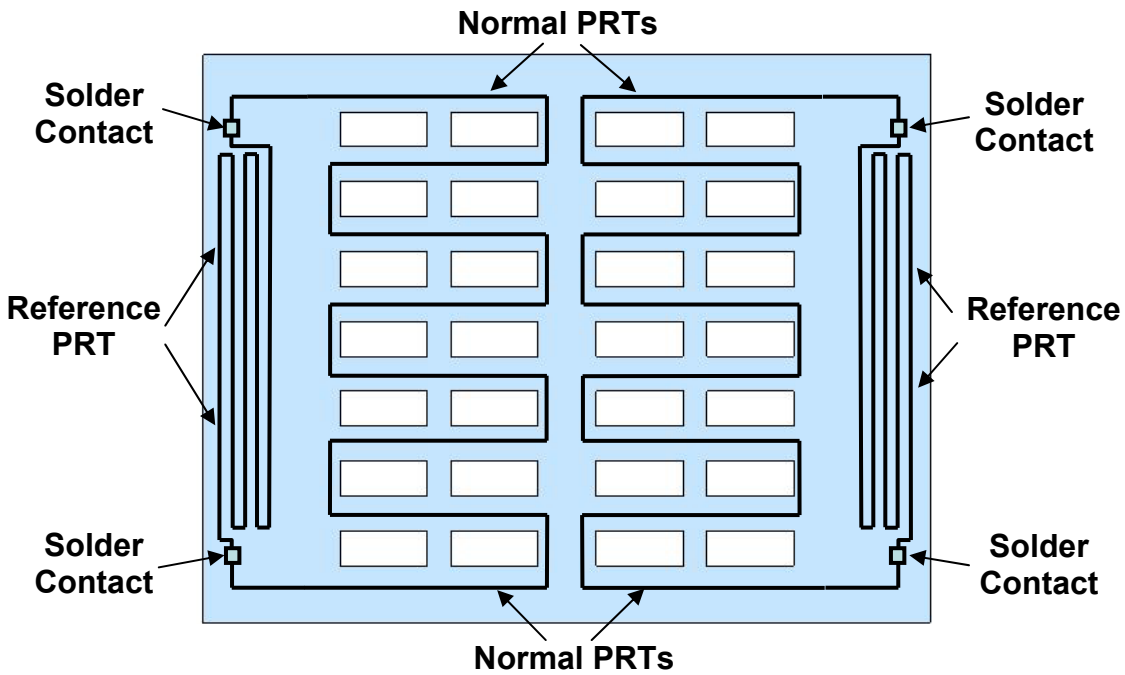

Fig. 2.1.16: Simplified drawing of the silicon fin plate with platinum resistor wires used for temperature measurement

All of the resistances are measured using a four-wire measurement technique. The current flows through one wire lead, then through the resistor, and finally out of another lead attached to the other solder contact. The voltage is measured using the other two wire leads so that the lead wire resistance does not effect the measurement of the PRT resistance. The current running through the resistor is kept very small, typically at 10 μA. The typical PRT resistance at room temperature is between 20 to 50 kΩ for the 20 mm dies and 5 to 7 kΩ for the 10 mm dies. The electrical power dissipation in a PRT is therefore in the range of 2 to 5 μW for the 20 mm dies and 0.5 to 0.7 μW for the 10 mm dies. The resistivity of platinum decreases as temperature decreases, so power dissipation will also decrease as temperature decreases. The power dissipation will cause the temperature of the PRT wire to rise with respect to the surrounding plate material and this leads to a measurement error known as self-heating. Power dissipation should be kept as low as is reasonably possible (given limits related to voltage measurement resolution and noise) in order to reduce the self-heating temperature measurement error.

A photograph showing a 10 mm PRT die with wire leads is shown in Fig. 2.1.17. The leads are soldered using indium and are covered with epoxy in order to improve their strength. The indium solder joint is not strong and will detach from the solder contact if the die is thermally or mechanically shocked. In addition, it is impractical to solder wire leads to both the normal and the reference platinum wires for the same fluid stream due to the small dimensions and close proximity of the two solder contacts. Therefore, the undesired contact must be scratched off because the entire solder contact depression must be filled with solder to ensure that the joint is sufficiently strong that it holds until it can be epoxied.

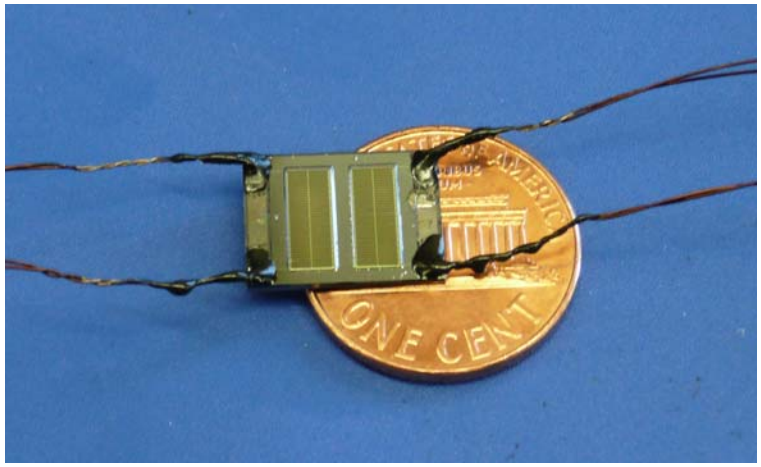

Fig 2.1.17: 10 mm die with built-in PRT for assembly into a heat exchanger

Another possible temperature measurement error is related to heat conducted through the wire leads; this conduction heat transfer will also cause the PRT wire to increase in temperature relative to its surroundings. The lead wires will conduct heat into the junction due to the thermal communication with the vacuum feed-through as well as thermal energy generation in the wires due to ohmic dissipation. The thermal conductivity of some common metals that are used for cryogenic wiring are summarized in Table 2.1.1 and the electrical resistivity for the same metals are shown in Table 2.1.2. The conductivity and resistivity values are from a manufacturer of cryogenic temperature sensors [8].

Table 2.1.1: Thermal conductivity of common metals used in cryogenic wiring as a function of temperature

Temperature	Thermal Conductivity			
[K]	*Copper* [W/m-K]	*Phosphor Bronze* [W/m-K]	*Manganin* [W/m-K]	*Nichrome* [W/m-K]
4	300	1.6	0.5	0.25
10	700	4.6	2	0.7
20	1100	10	3.3	2.6
80	600	25	13	8
150	410	34	16	9.5
300	400	48	22	12

Table 2.1.2: Electrical resistivity of common metals used in cryogenic wiring as a function of temperature

Temperature	Electrical Resistivity			
	Copper	*Phosphor Bronze*	*Manganin*	*Nichrome*
[K]	[μΩ-cm]	[μΩ-cm]	[μΩ-cm]	[μΩ-cm]
4.2	0.015	10.8	43.8	107.5
77	0.2	11.1	46.3	108.1
305	1.6	13	49.1	110

The rate of heat conducted to the die PRTs can be calculated approximately using Eqs. 2.1.1 to 3.1.3. The first equation, Eq. 2.1.1, is used to calculate the thermal conduction through a wire from the room temperature vacuum feed-through.

$$\dot{Q}_{cond} = \frac{\Delta T_{lead}}{R_{t,lead}} = \frac{k_{wire}\left(\frac{\pi}{4}D_{wire}^2\right)\Delta T_{lead}}{L_{wire}} \tag{2.1.1}$$

where $\dot{Q}_{cond}$ is the rate of thermal conduction through the wire, ΔT_{lead} is the temperature difference across the lead, $R_{t,lead}$ is the thermal resistance of the wire, D_{wire} is the metal conductor diameter, L_{wire} is the wire length, and k_{wire} is the wire thermal conductivity at the average lead temperature.

The rate of heat generated by ohmic dissipation can be calculated using Eq. 2.1.2:

$$\dot{Q}_{elec} = R_{e,lead}\ I_{wire}^2 = \frac{\rho_{wire}\ L_{wire}\ I_{wire}^2}{\left(\frac{\pi}{4}D_{wire}^2\right)} \tag{2.1.2}$$

where $\dot{Q}_{elec}$ is the electrical power dissipated in the wire lead, $R_{e,lead}$ is the electrical resistance of the wire, I_{wire} is the current flowing through the wire, and ρ_{wire} is the electrical resistivity of the wire at the average lead temperature.

The total rate of heat conducted to a die PRT, $\dot{Q}_{PRTleads}$, can be calculated using Eq. 2.1.3. Note that in fact the conduction and thermal energy generation problems are coupled with the ohmic dissipation affecting the temperature distribution. However, this decoupled solution technique provides a reasonable indication of the magnitude of this effect. There are four wires thermally conducting heat to the PRT and there are two wires that are dissipating electrical power. Radiation to the wires has been neglected.

$$\dot{Q}_{PRTleads} = 4\dot{Q}_{cond} + 2\dot{Q}_{elec} \tag{2.1.3}$$

There are tradeoffs to using different types of wire in cryogenic applications. Copper is an excellent electrical conductor but also an excellent heat conductor, which means that the heat leak due to electrical losses will be low, but the heat leak due to thermal conduction will be high. Copper is theoretically the optimal material to use; however, the wire diameters required to achieve this optimal balance between thermal and electrical loads is impractically small. The cryogenic test facility and cryosurgical probe prototype need to be frequently disassembled and reassembled, so the wires need to be sufficiently large and strong that they can withstand occasional stretching or tugging.

Nichrome, commonly used for heater wires, is a poor electrical conductor and a moderate heat conductor. The heat generated from resistive heating alone makes nichrome a poor choice for the measurement leads. Nichrome is used as a resistive heating wire in the cryogenic test facility. The phosphor bronze has a higher thermal conductivity but a lower electrical resistivity than manganin. As a general rule, manganin is better for applications with shorter leads and high temperature gradients and phosphor bronze is better for applications where longer leads can be used and therefore the temperature gradients are lower. For many cryogenic 4-wire measurements the best choice of lead conductors would be to use manganin for the voltage leads and phosphor bronze for the current leads.

A parametric study was performed on the four cryogenic wire choices over a range of conditions that correspond to what the die PRTs might see during testing. The results are shown in Tables 2.1.3 to 2.1.6. The range of wire diameters studied was 30-36 AWG, with 36 AWG being approximately the limit; smaller wires were not considered as they would break too easily. Two different cold end temperatures were examined. The coldest temperatures that PRTs are expected to encounter is about 150 K; therefore, 150 K was chosen as the temperature extreme case and 250 K was chosen as a more typical PRT temperature. In addition, two wire lengths were examined. The wire lead length in the cryosurgical probe assembly can only be about 0.3 m due to space constraints whereas the wire lead length in the cryogenic test facility can be about 1 m.

The results show that phosphor bronze is the best choice for all scenarios if only one type of conductor must be used for all leads. The 36 gauge (0.127 mm diameter) was the best for the 0.3 m lead lengths and the 32 gauge (0.203 mm diameter) was best for the 1 m lead lengths. This analysis of the wire material and size was carried out after the wire leads had already been soldered to the die PRTs. The wire leads that were actually used are 32 gauge (0.203 mm) manganin wires; these were initially chosen because manganin had the lowest thermal conductivity and was readily available in the lab. The actual wire choice is indicated in boldface font and is underlined whereas the best wire choice is indicated in boldface font and is italicized in Tables 2.1.3 to 2.1.6. For all scenarios examined, manganin had the lowest overall heat conduction to the PRT for the voltage leads and phosphor bronze had the lowest overall heat conduction to the PRT for the current leads.

Table 2.1.3: Heat conducted to a die PRT through various wire diameters and wire materials for a 0.3 m wire lead length, a 10 µA current, and a 150 K die temperature.

Conductor [-]	D_{wire} [mm]	T_{cold} [K]	L_{wire} [m]	Q_{cond} [W]	Q_{elec} [W]	$Q_{PRTleads}$ [W]	Aboslute Difference [W]	Percent Increase from Best [%]
Copper	0.254	150	0.3	7.23E-05	6.56E-08	2.89E-04	2.77E-04	2215.2
	0.203	150	0.3	4.62E-05	1.03E-07	1.85E-04	1.73E-04	1380.0
	0.16	150	0.3	2.87E-05	1.65E-07	1.15E-04	1.03E-04	820.8
	0.127	150	0.3	1.81E-05	2.63E-07	7.28E-05	6.03E-05	482.4
Phosphor Bronze	0.254	150	0.3	6.70E-06	7.30E-07	2.82E-05	1.57E-05	125.6
	0.203	150	0.3	4.30E-06	1.10E-06	1.94E-05	6.90E-06	55.2
	0.16	150	0.3	2.70E-06	1.80E-06	1.43E-05	1.80E-06	14.4
	0.127	***150***	***0.3***	***1.70E-06***	***2.90E-06***	***1.25E-05***	***0.00E+00***	***0.0***
Manganin	0.254	150	0.3	2.80E-06	2.80E-06	1.68E-05	4.30E-06	34.4
	0.203	**150**	**0.3**	**1.80E-06**	**4.50E-06**	**1.60E-05**	**3.50E-06**	**28.0**
	0.16	150	0.3	1.10E-06	7.20E-06	1.88E-05	6.30E-06	50.4
	0.127	150	0.3	6.95E-07	1.14E-05	2.56E-05	1.31E-05	104.8
Nichrome	0.254	150	0.3	1.50E-06	6.50E-06	1.93E-05	6.80E-06	54.4
	0.203	150	0.3	1.00E-06	1.01E-05	2.43E-05	1.18E-05	94.4
	0.16	150	0.3	6.30E-07	1.63E-05	3.51E-05	2.26E-05	180.8
	0.127	150	0.3	3.97E-07	2.59E-05	5.34E-05	4.09E-05	327.2

Table 2.1.4: Heat conducted to a die PRT through various wire diameters and wire materials for a 1 m wire lead length, a 10 µA current, and a 150 K die temperature.

Conductor [-]	D_{wire} [mm]	T_{cold} [K]	L_{wire} [m]	Q_{cond} [W]	Q_{elec} [W]	$Q_{PRTleads}$ [W]	Aboslute Difference [W]	Percent Increase from Best [%]
Copper	0.254	150	1	2.17E-05	2.19E-07	8.72E-05	7.44E-05	581.3
	0.203	150	1	1.39E-05	3.43E-07	5.61E-05	4.33E-05	338.3
	0.16	150	1	8.60E-06	5.52E-07	3.55E-05	2.27E-05	177.3
	0.127	150	1	5.40E-06	8.75E-07	2.34E-05	1.06E-05	82.8
Phosphor Bronze	0.254	150	1	2.00E-06	2.40E-06	1.29E-05	1.00E-07	0.8
	0.203	***150***	***1***	***1.20E-06***	***3.80E-06***	***1.28E-05***	***0.00E+00***	***0.0***
	0.16	150	1	7.97E-07	6.10E-06	1.55E-05	2.70E-06	21.1
	0.127	150	1	5.02E-07	9.70E-06	2.15E-05	8.70E-06	68.0
Manganin	0.254	150	1	8.34E-07	9.50E-06	2.23E-05	9.50E-06	74.2
	0.203	**150**	**1**	**5.32E-07**	**1.49E-05**	**3.19E-05**	**1.91E-05**	**149.2**
	0.16	150	1	3.31E-07	2.39E-05	4.92E-05	3.64E-05	284.4
	0.127	150	1	2.08E-07	3.80E-05	7.68E-05	6.40E-05	500.0
Nichrome	0.254	150	1	4.76E-07	2.16E-05	4.51E-05	3.23E-05	252.3
	0.203	150	1	3.04E-07	3.38E-05	6.88E-05	5.60E-05	437.5
	0.16	150	1	1.89E-07	5.44E-05	1.10E-04	9.67E-05	755.5
	0.127	150	1	1.19E-07	8.63E-05	1.73E-04	1.60E-04	1252.3

Table 2.1.5: Heat conducted to a die PRT through various wire diameters and wire materials for a 0.3 m wire lead length, a 10 µA current, and a 250 K die temperature.

Conductor [-]	D_{wire} [mm]	T_{cold} [K]	L_{wire} [m]	Q_{cond} [W]	Q_{elec} [W]	$Q_{PRTleads}$ [W]	Aboslute Difference [W]	Percent Increase from Best [%]
Copper	0.254	250	0.3	7.30E-05	8.38E-08	2.92E-04	2.78E-04	2047.1
	0.203	250	0.3	4.66E-05	1.31E-07	1.87E-04	1.73E-04	1272.8
	0.16	250	0.3	2.89E-05	2.11E-07	1.16E-04	1.03E-04	754.4
	0.127	250	0.3	1.82E-05	3.35E-07	7.36E-05	6.00E-05	441.2
Phosphor Bronze	0.254	250	0.3	7.50E-06	7.55E-07	3.16E-05	1.80E-05	132.4
	0.203	250	0.3	4.80E-06	1.10E-06	2.16E-05	8.00E-06	58.8
	0.16	250	0.3	3.00E-06	1.90E-06	1.57E-05	2.10E-06	15.4
	0.127	***250***	***0.3***	***1.90E-06***	***3.00E-06***	***1.36E-05***	***0.00E+00***	***0.0***
Manganin	0.254	250	0.3	3.20E-06	2.90E-06	1.87E-05	5.10E-06	37.5
	0.203	**250**	**0.3**	**2.10E-06**	**4.50E-06**	**1.73E-05**	**3.70E-06**	**27.2**
	0.16	250	0.3	1.20E-06	7.30E-06	1.97E-05	6.10E-06	44.9
	0.127	250	0.3	8.06E-07	1.15E-05	2.63E-05	1.27E-05	93.4
Nichrome	0.254	250	0.3	1.80E-06	6.50E-06	2.01E-05	6.50E-06	47.8
	0.203	250	0.3	1.10E-06	1.02E-05	2.49E-05	1.13E-05	83.1
	0.16	250	0.3	7.07E-07	1.64E-05	3.56E-05	2.20E-05	161.8
	0.127	250	0.3	4.46E-07	2.60E-05	5.38E-05	4.02E-05	295.6

Table 2.1.6: Heat conducted to a die PRT through various wire diameters and wire materials for a 1 m wire lead length, a 10 µA current, and a 250 K die temperature.

Conductor [-]	D_{wire} [mm]	T_{cold} [K]	L_{wire} [m]	Q_{cond} [W]	Q_{elec} [W]	$Q_{PRTleads}$ [W]	Aboslute Difference [W]	Percent Increase from Best [%]
Copper	0.254	250	1	2.19E-05	2.79E-07	8.81E-05	7.45E-05	547.8
	0.203	250	1	1.40E-05	4.37E-07	5.68E-05	4.32E-05	317.6
	0.16	250	1	8.70E-06	7.04E-07	3.61E-05	2.25E-05	165.4
	0.127	250	1	5.50E-06	1.10E-06	2.41E-05	1.05E-05	77.2
Phosphor Bronze	0.254	250	1	2.30E-06	2.50E-06	1.40E-05	4.00E-07	2.9
	0.203	***250***	***1***	***1.40E-06***	***3.90E-06***	***1.36E-05***	***0.00E+00***	***0.0***
	0.16	250	1	8.94E-07	6.30E-06	1.63E-05	2.70E-06	19.9
	0.127	250	1	5.64E-07	1.01E-05	2.24E-05	8.80E-06	64.7
Manganin	0.254	250	1	9.67E-07	9.60E-06	2.31E-05	9.50E-06	69.9
	0.203	**250**	**1**	**6.18E-07**	**1.51E-05**	**3.26E-05**	**1.90E-05**	**139.7**
	0.16	250	1	3.84E-07	2.42E-05	5.00E-05	3.64E-05	267.6
	0.127	250	1	2.42E-07	3.85E-05	7.79E-05	6.43E-05	472.8
Nichrome	0.254	250	1	5.35E-07	2.17E-05	4.55E-05	3.19E-05	234.6
	0.203	250	1	3.42E-07	3.39E-05	6.92E-05	5.56E-05	408.8
	0.16	250	1	2.12E-07	5.46E-05	1.10E-04	9.64E-05	708.8
	0.127	250	1	1.34E-07	8.66E-05	1.74E-04	1.60E-04	1177.9

Two heat exchanger stacks were constructed using the dies that have integrated PRTs. The first stack that was assembled is the thirty-seven die, 20 mm heat exchanger shown in Fig. 2.1.19. The headers shown in Fig. 2.1.14 were epoxied to the exchanger and thermocouples were placed in the thermocouple penetrations, as shown in Fig. 2.1.20. The second heat exchanger constructed was the forty-three die, 10 mm heat exchanger shown in Fig. 2.1.21. An example of a 10 mm heat exchanger with PRT dies is shown in Fig. 2.1.18. The heat exchanger shown in Fig. 2.1.18 had an internal (stream-to-stream) leakage rate that was too large and was therefore dissolved to salvage dies for use in constructing the forty-three die, 10 mm heat exchanger shown in Fig. 2.1.21.

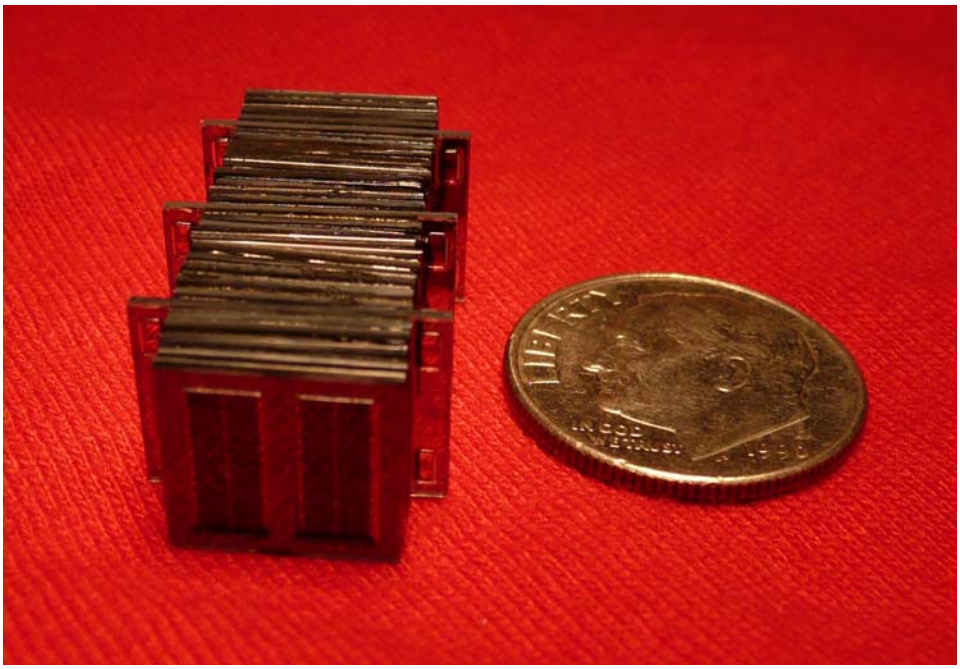

Fig 2.1.18: 10 mm heat exchanger before assembly with headers.

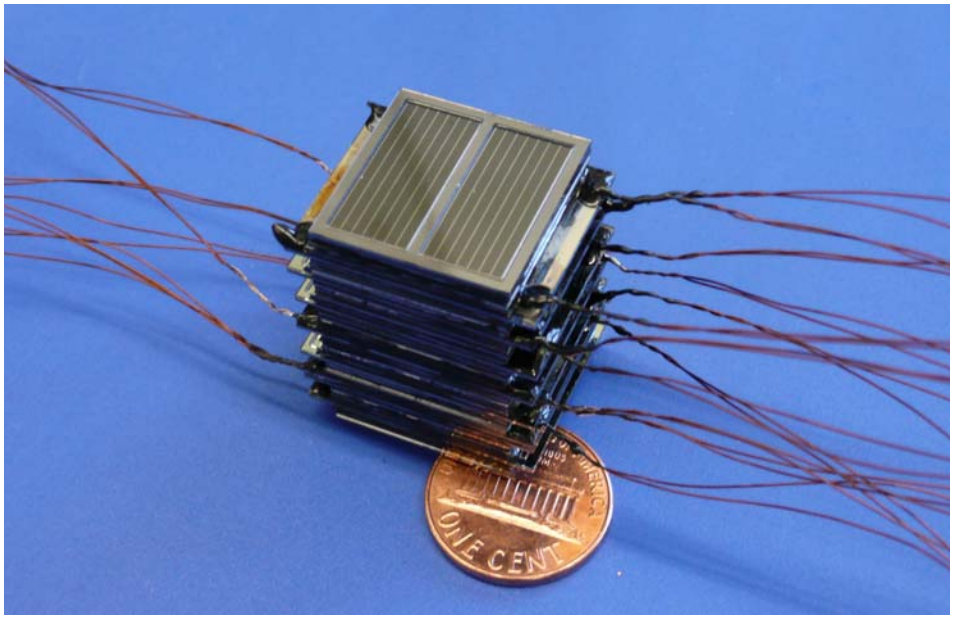

Fig 2.1.19: Thirty-seven die, 20 mm heat exchanger before assembly with headers

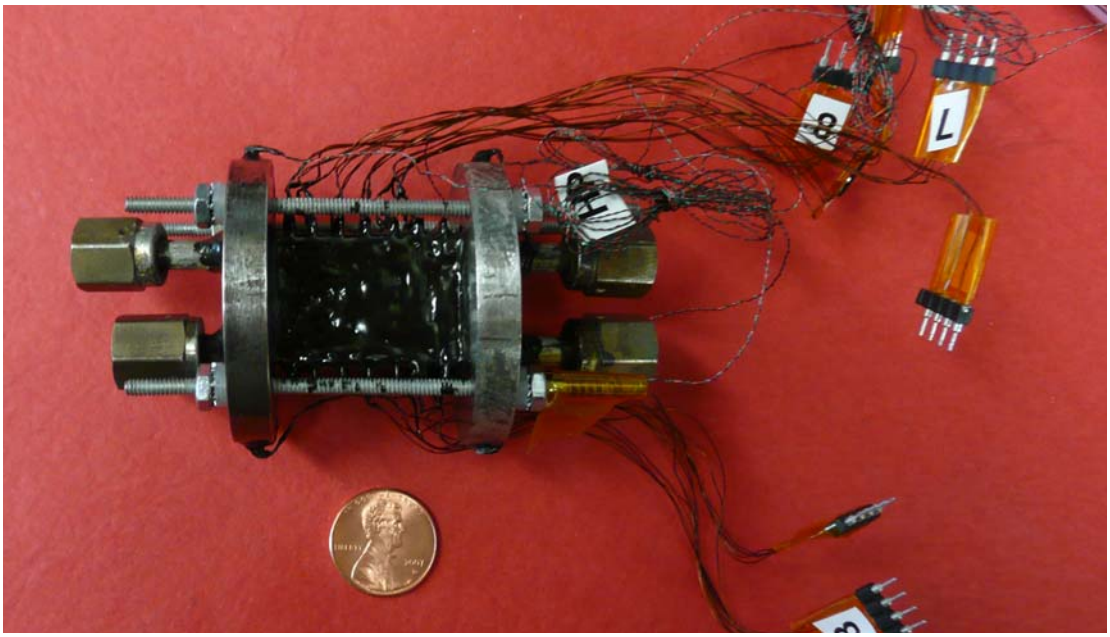

Fig. 2.1.20: Thirty-seven die, 20 mm heat exchanger assembly with integrated PRTs with headers installed

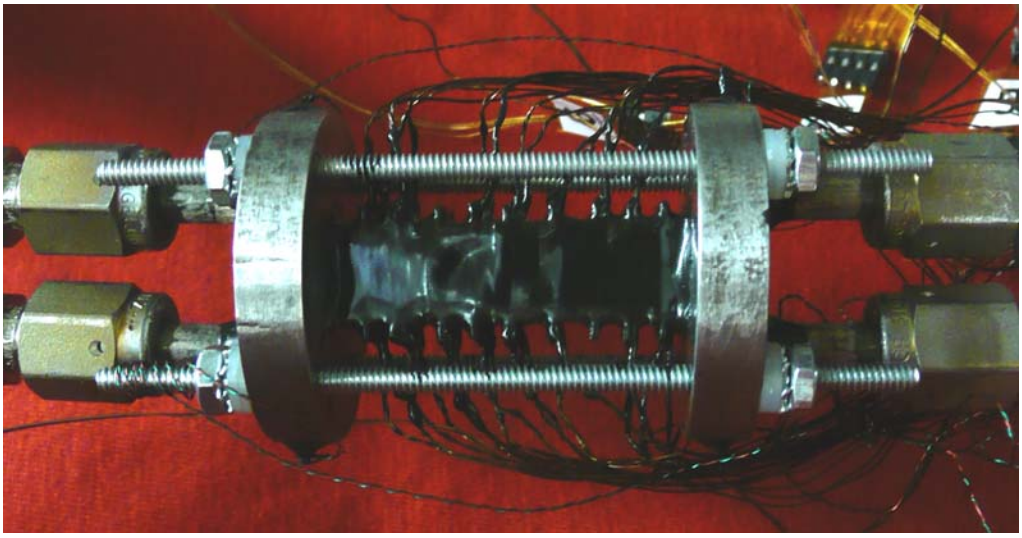

Fig. 2.1.21: Forty-three die, 10 mm heat exchanger assembly with integrated PRTs with headers installed.

The process of depositing PRTs on the silicon wafer is not consistent. The PRT resistance varies by a factor of 2 or 3 between different plates. A number of the PRTs were also found to be open circuited, indicating that the wire was not continuous. In addition, either the normal or the reference resistor but not both could be practically measured due to the small size of the solder contact. As a result of these issues, a number of working PRTs could not be used. Table 2.1.7 shows the die location of all the measurable PRTs and the type of resistors present on that die for the 10 mm and 20 mm heat exchangers fabricated using the dies with the integrated PRTs.

Table 2.1.7: Location of working normal and reference PRTs within the two heat exchangers with integrated PRTs

2cm Heat Exchanger				1cm Heat Exchanger			
Die No.	Die Type	RTD Type	RTD Type	Die No.	Die Type	RTD Type	RTD Type
		LP OUTLET	HP INLET			LP OUTLET	HP INLET
1	Normal	-	-	1	Normal	-	-
2	Normal	-	-	2	Normal	-	-
3	Normal	-	-	3	Normal	-	-
4	Normal	-	-	4	Normal	-	-
5	RTD	Ref	-	5	RTD	Ref	Ref
6	Normal	-	-	6	Normal	-	-
7	Normal	-	-	7	Normal	-	-
8	Normal	-	-	8	RTD	-	-
9	RTD	Norm	-	9	RTD	Norm	Norm
10	Normal	-	-	10	Normal	-	-
11	Normal	-	-	11	Normal	-	-
12	Normal	-	-	12	Normal	-	-
13	Normal	-	-	13	Normal	-	-
14	RTD	Ref	-	14	RTD	-	Norm
15	Normal	-	-	15	Normal	-	-
16	Normal	-	-	16	Normal	-	-
17	Normal	-	-	17	Normal	-	-
18	Normal	-	-	18	RTD	Norm	Ref
19	RTD	Norm	Norm	19	Normal	-	-
20	Normal	-	-	20	Normal	-	-
21	Normal	-	-	21	Normal	-	-
22	Normal	-	-	22	RTD	Norm	Norm
23	Normal	-	-	23	Normal	-	-
24	RTD	Ref	-	24	Normal	-	-
25	Normal	-	-	25	Normal	-	-
26	Normal	-	-	26	Normal	-	-
27	Normal	-	-	27	RTD	Ref	Norm
28	RTD	Ref	Norm	28	Normal	-	-
29	RTD	-	-	29	Normal	-	-
30	Normal	-	-	30	Normal	-	-
31	Normal	-	-	31	Normal	-	-
32	Normal	-	-	32	RTD	Norm	-
33	RTD	-	Ref	33	Normal	-	-
34	Normal	-	-	34	Normal	-	-
35	Normal	-	-	35	Normal	-	-
36	Normal	-	-	36	RTD	Norm	Norm
37	Normal	-	-	37	Normal	-	-
		LP INLET	HP OUTLET	38	Normal	-	-
				39	Normal	-	-
				40	RTD	-	Norm
				41	Normal	-	-
				42	Normal	-	-
				43	Normal	-	-
						LP INLET	HP OUTLET

2.2 Valve & Orifice Assembly

A Joule-Thomson cycle relies on an isenthalpic pressure drop that is produced by an orifice or control valve. The experimental testing of the MEMS heat exchangers utilized both jewel orifices and active control valves. This section will first explain how the orifices were installed in the test facility and discuss the expected pressure-flow behavior of the orifices. The second part of this section will describe the design and operation of the micro-control valve that was also installed; this valve was the result of another project.

The jewel orifices are small ruby disks that have very precise orifice sizes bored into their center using diamond coated wire. In order to be used in an experiment, the jewels orifices must be mounted so that all of the fluid is forced to pass through the orifice. This was accomplished by installing them into blank stainless-steel VCR gaskets. A shallow counterbore is machined into the center of the VCR gasket; the diameter of the counterbore is slightly larger than the outer diameter of the jewel and the depth of the counterbore approximately matched the thickness of the jewel (note that the gasket thickness was larger than the thickness of the jewel). A through-hole was drilled through the center of the gasket. The through hole was large enough (0.038") that the orifice sizes were always significantly smaller than the through-hole size; therefore, the geometry of the through-hole should have little effect on the fluid flow. The final step was to epoxy or superglue the jewel orifice into the counterbored hole.

Examples of jewel orifices mounted on VCR gaskets are shown in Fig. 2.2.1. The 1/8" VCR gaskets are only large enough to allow one orifice to be installed. The ¼" inch VCR gaskets can accommodate up to 3 orifices in parallel. The superglue or epoxy can be dissolved quickly and therefore many different orifice sizes can be tested using only a few gaskets. However, the VCR gaskets have a limited lifetime and will stop sealing after they have been compressed too many times.

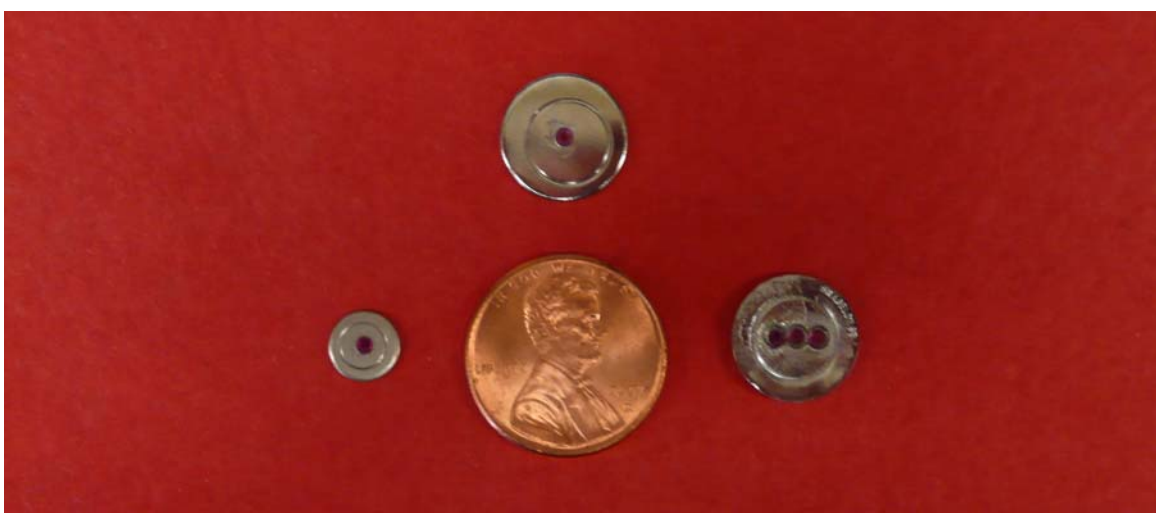

Fig. 2.2.1: Various methods of mounting jewel orifices in VCR gaskets. The 1/8" VCR gaskets only allow for a single orifice to be mounted, but ¼" inch VCR gaskets can accommodate up to 3 orifices in parallel.

The manufacturer of the precision orifices recommends using the Eq. 2.2.1 to calculate the flow through an orifice:

$$\dot{V} = C_v \sqrt{\frac{\Delta P_{orifice}}{SG}} \tag{2.2.1}$$

where $\dot{V}$ is the volumetric flow rate in units of gal/min, C_v is flow factor in units of gal/min-psi$^{0.5}$, $\Delta P_{orifice}$ is the differential pressure across the orifice in units of psid, and SG is the specific gravity of the fluid relative to liquid water (a dimensionless number). A wide variety of diameter orifice sizes were either ordered or were already available in the lab; these are summarize in Table 2.2.1 along with the manufacturer provided flow factor (C_v).

Table 2.2.1: Available orifice sizes and their respective flow factors

Orifice ID *[in]*	Orifice ID *[mm]*	Orifice Area *[in^2]*	Orifice Area *[mm^2]*	Cv *[gal/min-psi^0.5]*
0.0008	0.020	502.7E-9	324.3E-6	0.00001
0.0014	0.036	1.5E-6	993.1E-6	0.00004
0.0020	0.051	3.1E-6	2.0E-3	0.00009
0.0025	0.064	4.9E-6	3.2E-3	0.00013
0.0030	0.076	7.1E-6	4.6E-3	0.0002
0.0040	0.102	12.6E-6	8.1E-3	0.00035
0.0060	0.152	28.3E-6	18.2E-3	0.00086
0.0080	0.203	50.3E-6	32.4E-3	0.0015
0.0090	0.229	63.6E-6	41.0E-3	0.0019
0.0100	0.254	78.5E-6	50.7E-3	0.0025
0.0110	0.279	95.0E-6	61.3E-3	0.0028
0.0120	0.305	113.1E-6	73.0E-3	0.0034
0.0130	0.330	132.7E-6	85.6E-3	0.0038
0.0140	0.356	153.9E-6	99.3E-3	0.0043
0.0150	0.381	176.7E-6	114.0E-3	0.005
0.0175	0.445	240.5E-6	155.2E-3	0.007
0.0200	0.508	314.2E-6	202.7E-3	0.0088
0.0225	0.572	397.6E-6	256.5E-3	0.0115
0.0250	0.635	490.9E-6	316.7E-3	0.014
0.0280	0.711	615.8E-6	397.3E-3	0.018

The flow factor has been plotted as a function of orifice diameter in Fig. 2.1.2 and as a function of orifice flow area in Fig. 2.1.3. The flow factor of the orifice is approximately a linear function of the orifice flow area. Therefore, the flow factor for any orifice size can be easily calculated. In addition, this correlation allows the equivalent flow factor for multiple orifices to be quickly calculated based on the total flow area.

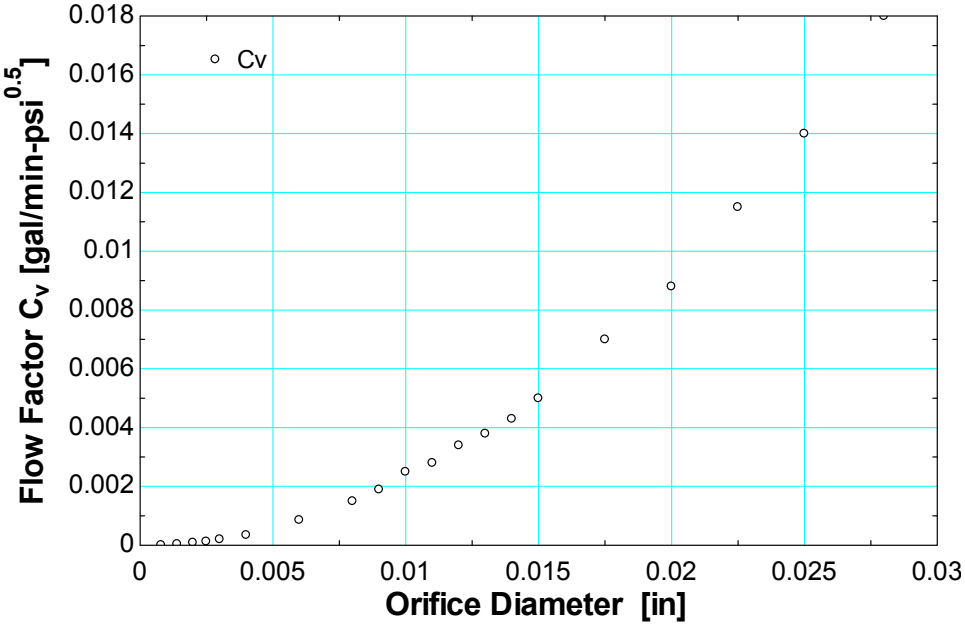

Fig. 2.2.2: Exponential relationship between the flow factor C_v and the inner diameter of the orifice

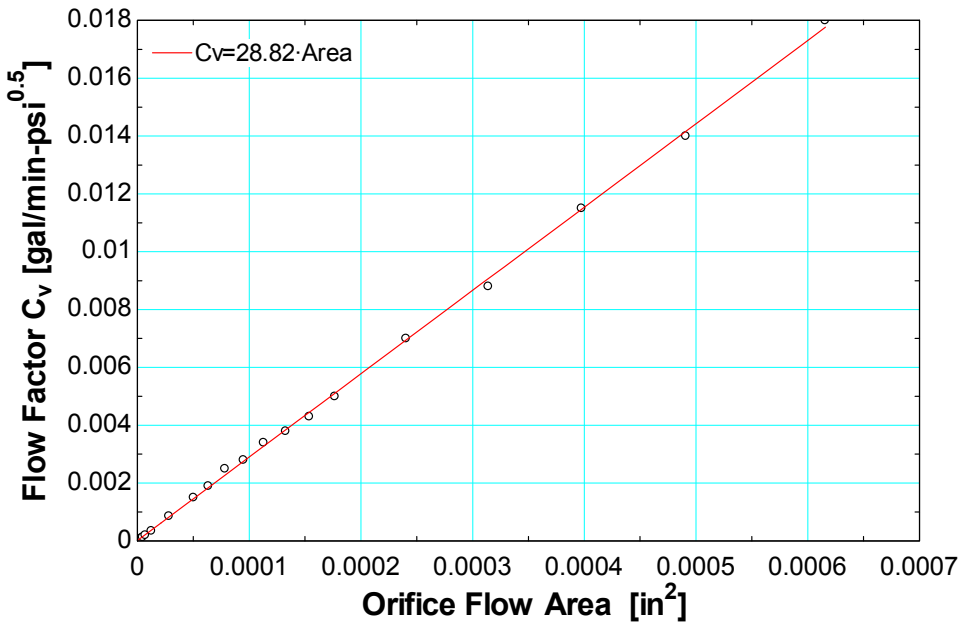

Fig. 2.2.3: Linear relationship between the flow factor C_v and the cross sectional area of the orifice

In the same lab used to test the MEMS heat exchangers another collaborative project between UM-Ann Arbor and UW-Madison was being carried out. This project involved modeling and testing an actively controlled cryogenic micro-valve [9]. The valve was designed for providing distributed cooling on NASA satellites and is also an attractive option for the control valve in a cryogenic J-T cycle. A prototype valve from this project was used as the J-T valve with the MEMS heat exchangers.

The first attractive feature of this valve is that it was designed to operate at cryogenic temperatures and in vacuum environments. Very few commercially available valves are capable of doing this due to issues related to leakage, freezing of lubricants, or heat conduction to the working fluid. Even specially designed cryogenic valves almost always require a mechanical connection to an actuator outside of the vacuum chamber; this connection introduces a significant heat conduction path. The micro-valve is actuated by a piezoelectric transducer (PZT) stack and is controlled by a 0-100 V DC voltage signal and requires no mechanical connection to the outside of the vacuum chamber. The power dissipation in the PZT from the applied voltage signal is on the order of nanowatts and can be considered negligible. As discussed in Chapter 2.1, the heat conduction through the electrical leads to the integrated PRTs is on the order of microwatts and can also be considered negligible in most applications.

The valve is constructed almost entirely from non-metallic materials. The benefit of using non-metallic materials is that the valve could potentially be used as part of a cryosurgical probe that is compatible with an MRI machine in order to obtain real time images of the ice ball development inside a human. The drawback of the non-metallic materials is that some of them are brittle and therefore the valve is vulnerable to damage due to thermal or mechanical loads.

A geometric model of the valve is shown in Fig. 2.2.4. Flow goes through the high pressure inlet port in the Pyrex substrate, flows between the grooves in the silicon plate, and finally flows out the low pressure outlet port. The PZT stack adjusts the distance between the silicon plate and the Pyrex substrate, which in turn modulates the flow rate.

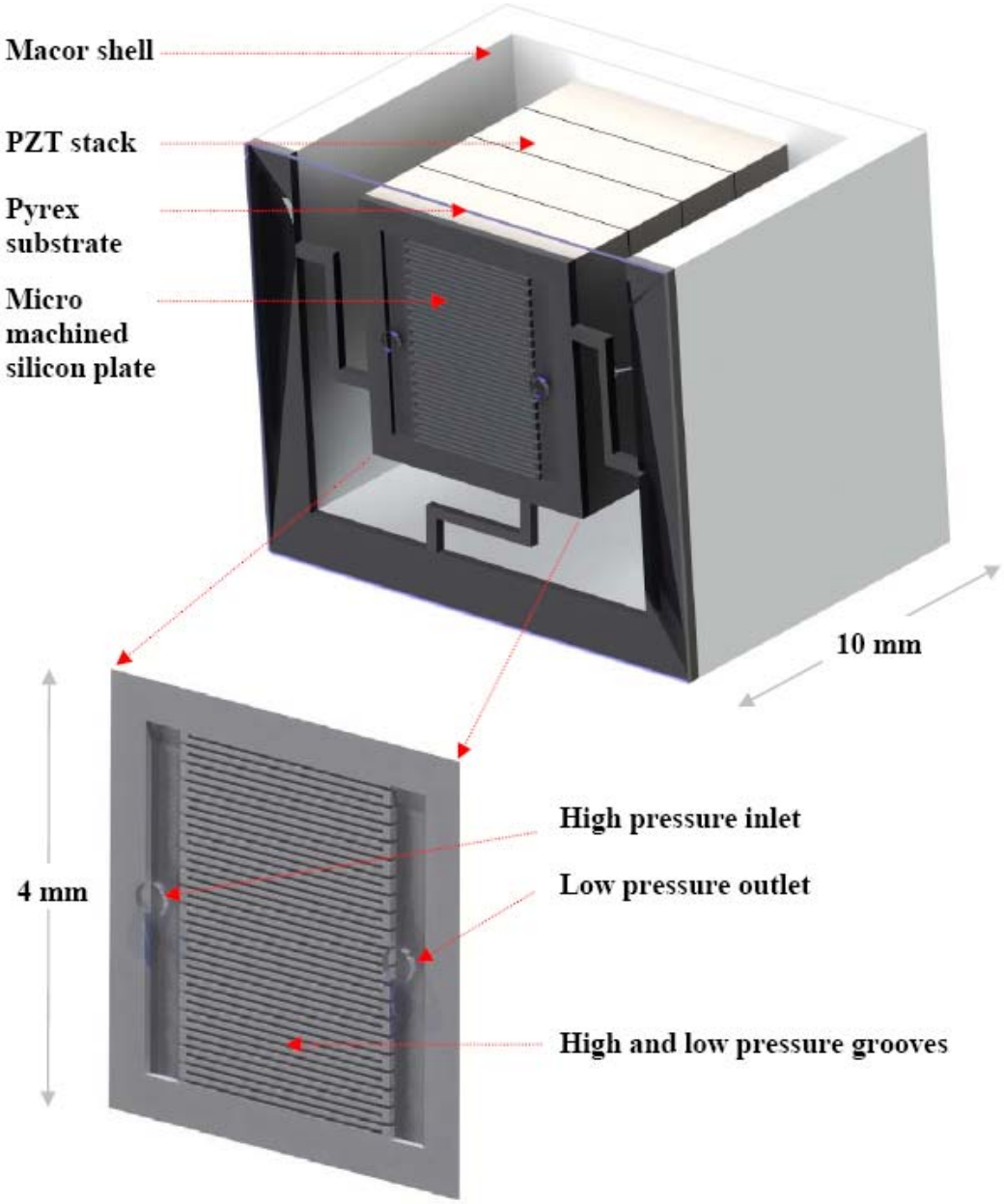

Fig. 2.2.4: Geometric model of the cryogenic micro valve [9].

A photograph of the PZT stack before it has been epoxied to the valve housing is shown in Fig. 2.2.5. The valve housing is shown in Fig. 2.2.6. The valve housing is made of Macor, a type of machinable ceramic. Macor has several beneficial material properties for cryogenic applications including low porosity, low outgassing rates, and a small coefficient of thermal expansion. The major drawback to Macor is its brittleness. Several small chips have been knocked off the Macor housing shown in the photograph even though it was machined by a professional machinist with experience machining ceramics. There is a significant likelihood that many more microscopic cracks were generated during the machining process.

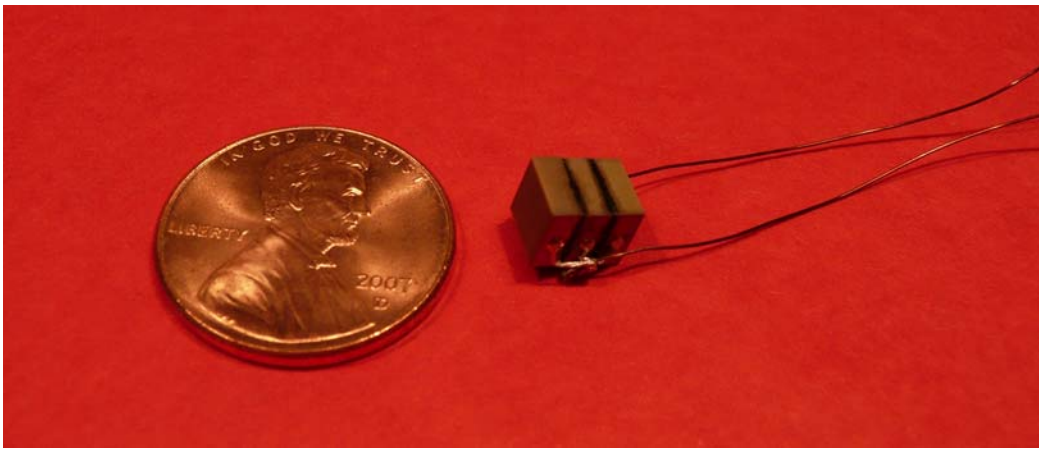

Fig. 2.2.5: Photograph of the PZT stack before valve assembly

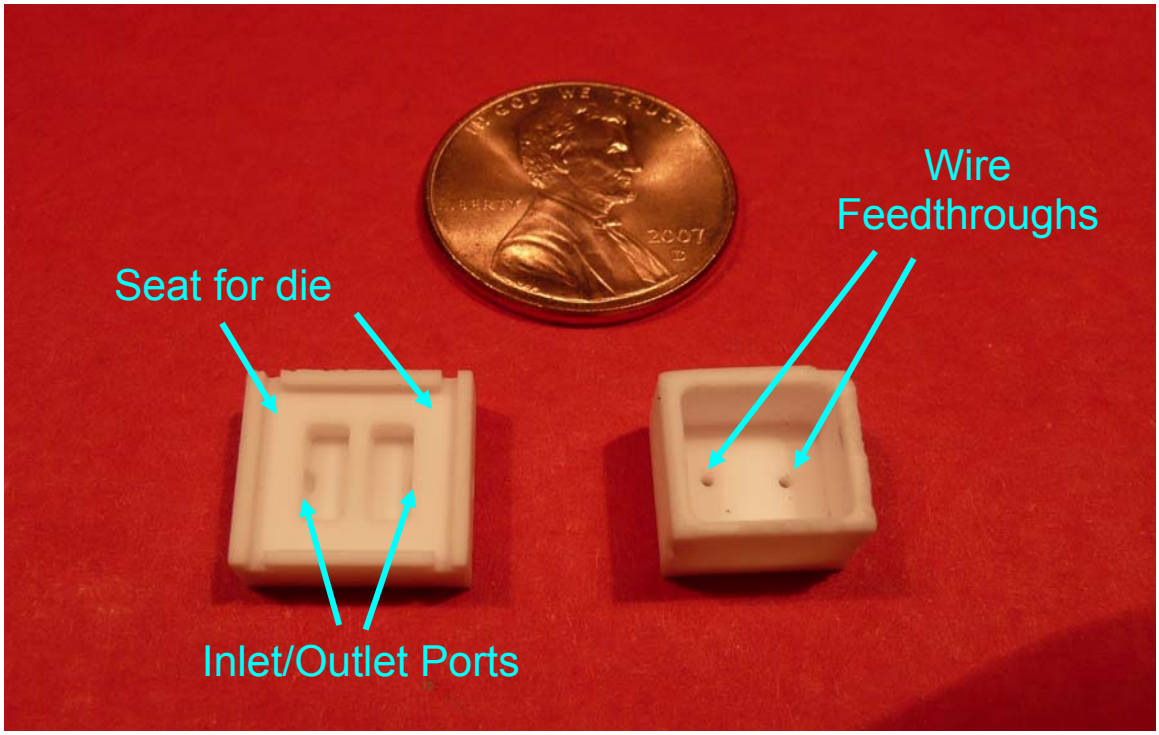

Fig. 2.2.6: Photograph of the valve housing before valve assembly.

A photograph of a fully assembled cryogenic micro valve is presented in Fig. 2.2.7. The valve housing was covered with epoxy after the picture was taken in order to increase the strength and durability of the valve housing. The fittings shown are 1/8" VCR fittings with 1/16" tube connections. The tube is epoxied to both the VCR fittings and the valve housing. The plastic sheath on the wire leads was later partially removed and replaced with epoxy in order to prevent fluid leakage between the wires and the plastic sheath to the vacuum chamber.

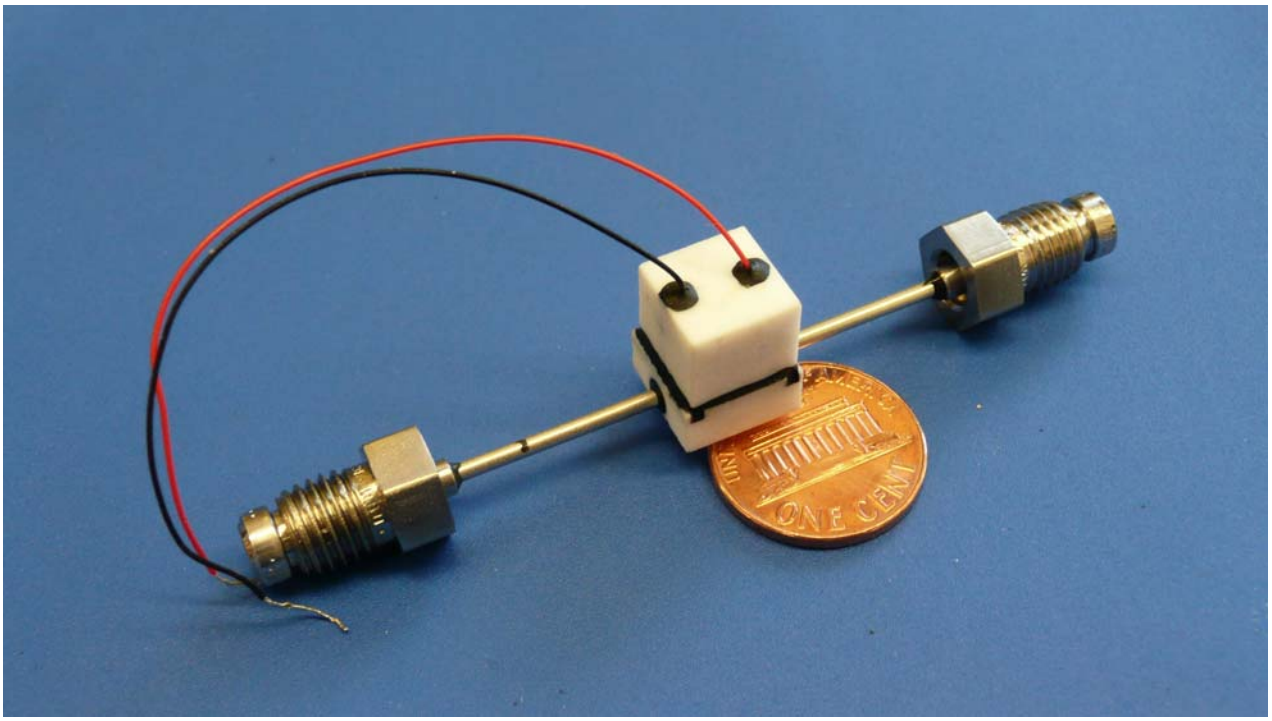

Fig. 2.2.7: Photograph of a fully assembled cryogenic micro valve. The valve housing was later covered in epoxy to increase the strength and durability of the housing.

Chapter 3: Experimental Setups

3.0 Introduction

This chapter describes the two experimental test facilities that were used to test the MEMS heat exchanger. The first and primary setup was the cryogenic test facility, which tested the heat exchanger in a large Dewar. The second experimental setup was a prototype cryosurgical probe.

As with Chapter 2, not all work described in this chapter was performed by the present author. Dan Hoch's design model [5] was slightly modified by the present author to include fluid and material properties evaluated at average temperature in the heat exchanger. The modified version of Hoch's model was used to generate the plots shown in Figs. 3.1.4 and 3.3.5, not the present author's model that is described in Chapters 4 and 5. The Hoch model, which is less accurate but much simpler, was used to determine the effect of temperature measurement uncertainty when designing the cryogenic test facility. The plots are intended to show how the cryogenic test facility was designed are not meant to be the most accurate estimate of heat exchanger performance.

The cryogenic test facility, including the heat exchanger headers, was designed, manufactured, and assembled at UW-Madison. The cryosurgical probe setup was designed primarily at UM-Ann Arbor and was assembled primarily at UW-Madison.

3.1 Cryogenic Test Facility

A cryogenic test facility was designed and constructed in order to provide more controlled test conditions and therefore more accurate measurements of the heat exchanger performance than was possible in the room temperature tests. The first part of this section will discuss the different types of tests that the experimental setup is designed for. The second part will show the flow schematics and explain how the experimental system operates. The third part is a discussion of the equipment that is used to run the cryogenic test facility. The last sections will discuss the mechanical design of the components in the test facility and show how they were assembled.

3.1.1 Modes of Operation in the Cryogenic Test Facility

There are three types of tests that the cryogenic test facility is designed to carry out; these include tests with no external cooling or self-cooling, tests with applied cooling, and tests with self-cooling.

The no external cooling mode of operation circulates working fluid at essentially a constant temperature through the heat exchanger in order to measure the pressure drop characteristics of the system. The pressure drop in the heat exchanger can be measured as a function of mass flow rate, fluid, and inlet pressure. The ability of the design model to predict pressure drop in the absence of any fluid temperature change can therefore be verified before any heat transfer measurements are taken. The design model is discussed in detail in Chapters 4 and 5.

The applied cooling mode of operation utilizes a cryocooler to produce large temperature differences across the heat exchanger with minimal pressure differences (i.e., the fluid is not required to expand from high to low pressure in order to produce a temperature drop). The applied cooling tests can therefore be performed at low pressure and low pressure differences

which minimizes the risk of damaging the heat exchanger and ensures that heat transfer data can be taken over a wide range of operating conditions using single-phase, simple fluids such as helium. Helium has well-defined properties and the flow of single-phase helium is well-understood. The large temperature differences produced by the cryocooler will enable the effectiveness of the heat exchanger to be measured accurately because the uncertainty in the temperature measurements are small relative to the temperature differences that must be measured to compute the effectiveness.

To understand why large temperature differences allow the effectiveness to be measured more accurately it is helpful to examine the standard equation by which effectiveness is calculated for counterflow heat exchangers [10], shown in Eq 3.1.1.

$$\varepsilon = \frac{\dot{q}_{act}}{\dot{q}_{\max}} = \frac{\dot{C}_h (T_{h,in} - T_{h,out})}{\dot{C}_{min} (T_{h,in} - T_{c,in})} \tag{3.1.1}$$

where ε is the heat exchanger effectiveness, $\dot{q}_{act}$ is the actual amount of heat transferred in the heat exchanger, $\dot{q}_{max}$ is the maximum possible heat transfer rate in the heat exchanger, $\dot{C}_h$ is the hot fluid capacity rate, $\dot{C}_{min}$ is the minimum capacity rate of the two fluids, $T_{h,in}$ is the inlet temperature of the hot fluid, $T_{h,out}$ is the outlet temperature of the hot fluid, and $T_{c,in}$ is the inlet temperature of the cold fluid. The capacity rate for a fluid is defined as the product of its mass flow rate and the specific heat at constant pressure.

The heat exchanger effectiveness is a function of three different temperatures and each of the temperature measurements has an uncertainty associated with it. The sensitivity of heat exchanger effectiveness to changes in temperature can be found by taking the partial derivative of Eq. 3.1.1 with respect to each of the individual fluid temperatures, which yields Eq. 3.1.2-3.1.4:

$$\frac{\partial \varepsilon}{\partial T_{h,in}} = \frac{\dot{C}_h}{\dot{C}_{min} (T_{h,in} - T_{c,in})} - \frac{\dot{C}_h (T_{h,in} - T_{h,out})}{\dot{C}_{min} (T_{h,in} - T_{c,in})^2} \tag{3.1.2}$$

$$\frac{\partial \varepsilon}{\partial T_{h,out}} = -\frac{\dot{C}_h}{\dot{C}_{min} (T_{h,in} - T_{c,in})} \tag{3.1.3}$$

$$\frac{\partial \varepsilon}{\partial T_{c,in}} = \frac{\dot{C}_h (T_{h,in} - T_{h,out})}{\dot{C}_{min} (T_{h,in} - T_{c,in})^2} \tag{3.1.4}$$

As the temperature difference between the two fluid inlet temperatures increases each of the partial derivatives shown in Eq. 3.1.2-3.1.4 decreases. Therefore, the sensitivity of the effectiveness to changes in measured fluid temperature decreases with larger temperature differences across the heat exchanger. If the measurement uncertainties are random and

uncorrelated, the total uncertainty in heat exchanger effectiveness can be calculated using Eq. 3.1.5 [11]:

$$U_{\varepsilon} = \sqrt{\left(\frac{\partial \varepsilon}{\partial T_{h,in}}\right)^2 \left(U_{T_{h,in}}\right)^2 + \left(\frac{\partial \varepsilon}{\partial T_{h,out}}\right)^2 \left(U_{T_{h,out}}\right)^2 + \left(\frac{\partial \varepsilon}{\partial T_{c,in}}\right)^2 \left(U_{T_{c,in}}\right)^2} \qquad (3.1.5)$$

Where U_{ε} is the total uncertainty in heat exchanger effectiveness and $U_{Th,in}$, $U_{Th,out}$, and U_{Tcin} are the temperature measurement uncertainties of the hot inlet, hot outlet, and cold inlet fluid streams respectively. The total effectiveness uncertainty is plotted in Fig. 3.1.3 for the 20 mm heat exchanger and Fig. 3.1.4 for the 10 mm heat exchanger.

The initial fluids to be used when testing with the cryocooler include helium, nitrogen, and argon. The advantage of these fluids is that they are inert, readily available, and will not condense or solidify under the expected operating temperatures and pressures. However, any water or oil that remains in the system will freeze; therefore, proper care must be taken to ensure that all contaminants are removed prior to testing.

In self-cooling mode, the heat exchanger is used as part of a Joule-Thomson (J-T) cycle just as it would be for a cryosurgical application. High pressure fluid will flow through one side of the heat exchanger and then undergo an insenthalpic expansion through an orifice that results in a reduction in the temperature of the fluid. The fluid then returns through the heat exchanger to pre-cool the high pressure fluid. This test will ideally be performed last because it involves the most risk of damaging the heat exchanger due to the higher operating pressures and pressure differences involved.

A fluid must be chosen for the self-cooling (or J-T cycle) mode of operation. The first factor to consider is the temperature drop due to the isenthalpic expansion of the fluid across a valve or orifice. Figure 3.1.1 shows the isenthalpic temperature difference produced for various fluids as a function of pressure difference (assuming an inlet temperature of 300 K and an exit pressure of 1 atm). Note that in general, the closer a fluid is to its saturation point the larger the isenthalpic temperature drop. Based on this fact alone, n-butane would appear to be the optimal choice to use for the self-cooling tests.

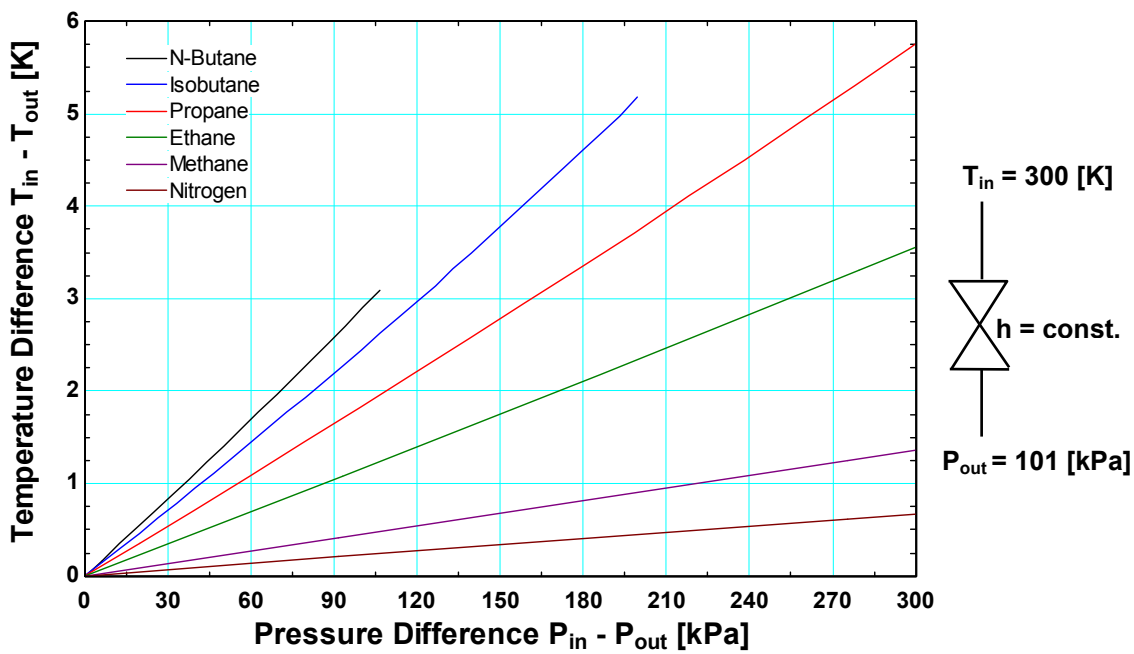

Fig. 3.1.1: Expected temperature difference across a valve or orifice due to isenthalpic expansion

However, n-butane may not be the optimal choice of fluid due to other constraints. In a closed loop circuit, the low pressure exhaust fluid leaving the heat exchanger must be compressed. The highest pressure reached in the compressor must be below the saturation pressure of the fluid at room temperature or there is a risk that liquid droplets will form in the compression chamber resulting in damage to the compressor. The compressor for the cryogenic test facility is cooled by room temperature water; therefore, if the pressure inside the compressor exceeds the saturation pressure at room temperature the vapor will begin to condense. This is a problem because liquid n-butane will be trapped in the oil removal system of the compressor. Lighter hydrocarbons such as ethane have been used as the test fluid so that higher compressor outlet pressures can be obtained.

3.1.2 Flow Schematics for the Cryogenic Test Facility

All of the components external to the Dewar that will be used as part of the cryogenic test facility are shown in the flow schematic in Fig. 3.1.2. The procedure to be used for operating the facility is as follows:

1. Roughing vacuum pump is used to evacuate gas lines

2. Gas lines are filled with working fluid to pressure slightly above atmospheric

3. Gas lines are evacuated and filled several times to remove any contaminants

4. Valves 2 and 3 are closed to prevent any pressure oscillations from damaging the heat exchanger

5. Gas lines are filled to a pressure above 50 psig, which is the minimum pressure required for compressor operation

6. Valve 1 is opened to allow flow to bypass the dewar

7. The compressor is turned on and allowed to reach steady state

8. Valve 1 is adjusted so that the compressor suction pressure is slightly above atmospheric pressure

9. Valve 3 is opened to so that the heat exchanger low pressure outlet is roughly equal to the compressor suction pressure

10. With regulator 1 completely backed out, valve 2 is opened

11. Regulator 1 is adjusted so that the high pressure inlet of the heat exchanger is at the desired level

12. After making sure that valves 4 and 7 are closed, valves 5 and 6 are opened

13. The roughing pump is turned and allowed to run until the insulating vacuum pressure stops dropping

14. The turbo vacuum pump is turned on to further reduce the insulating vacuum pressure

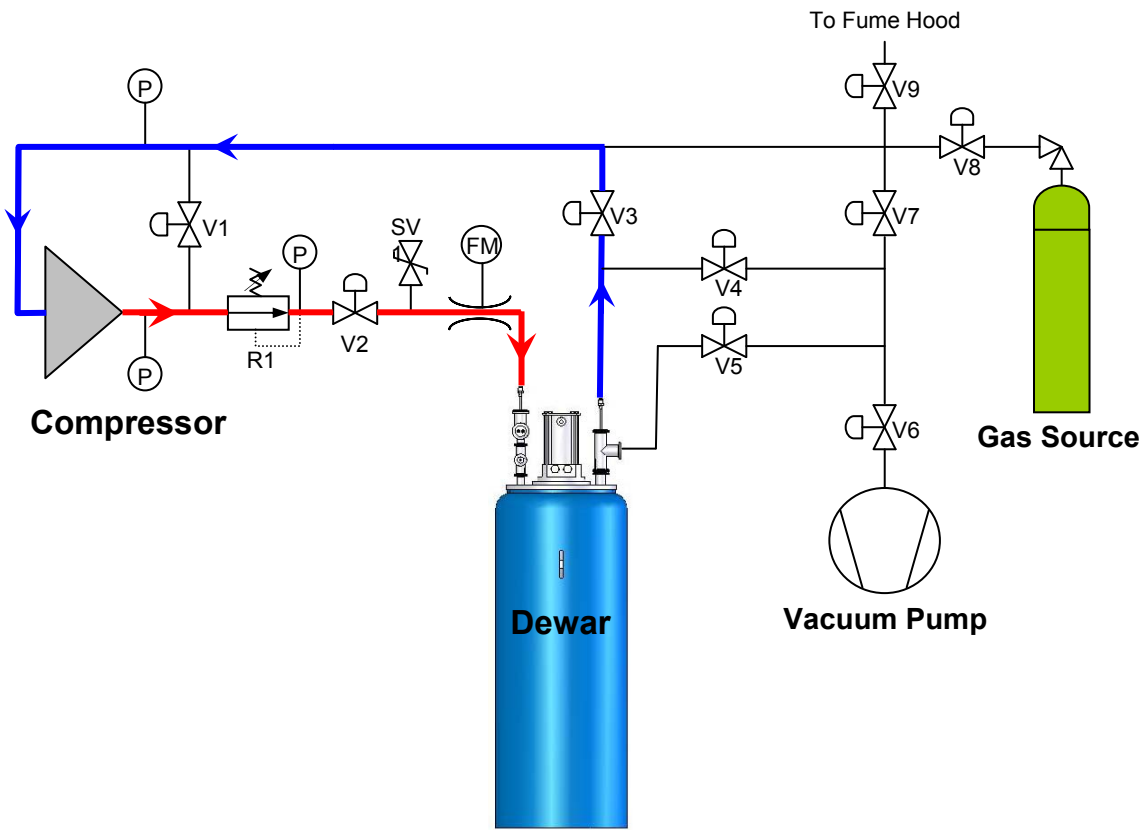

Fig. 3.1.2: Flow schematic of the Cryogenic Test Facility showing all components external to the Dewar

Figure 3.1.3 illustrates a flow schematic for the components located inside of the Dewar. To operate in the self-cooling mode, an orifice is installed between the high pressure outlet and low pressure inlet of the test heat exchanger at location A and flow to the cryocooler heat exchanger will be prevented by disconnecting the VCR fittings at locations B and C and replacing them with blank VCR gaskets. To operate in the cryocooler mode, a blank VCR gasket is installed at location A (where the orifice would normally be placed) and the fluid streams will be connected to the cryocooler heat exchanger by connecting the VCR fittings at locations B and C.

The fluid temperatures are measured at each inlet and outlet of the test heat exchanger for a total of four measurement locations. At each measurement location, there are two methods of measuring the fluid temperature. The first is a platinum resistor that is inserted directly into the flow. The second temperature measurement is obtained using the same thermocouples that were used for room temperature testing of the prototype heat exchangers (also penetration temperature measurements). An absolute pressure measurement will be taken at both fluid inlets to the heat exchanger and the differential pressure across each side of the heat exchanger will be measured.

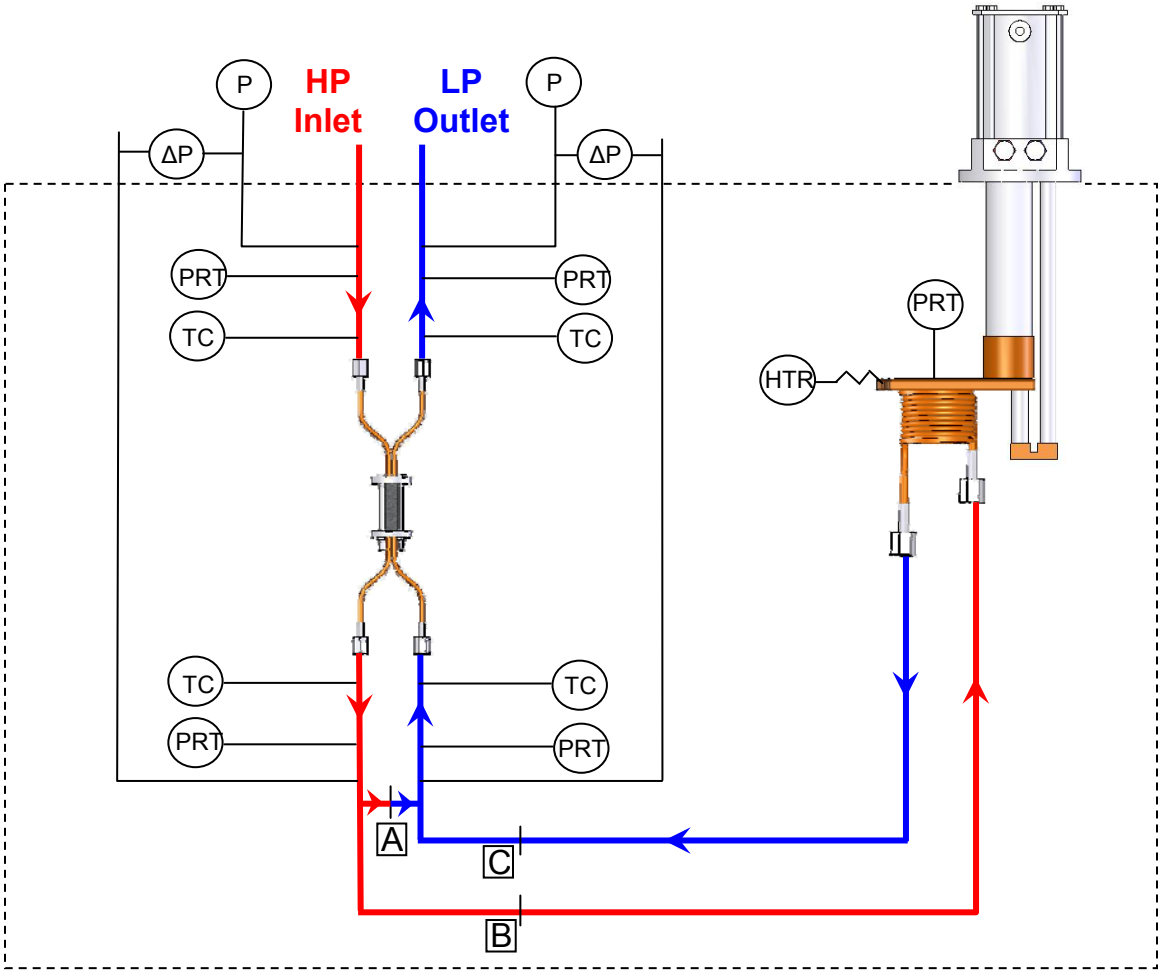

Fig. 3.1.3: Flow schematic of the Cryogenic Test Facility showing all components internal to the Dewar

The penetration platinum resistors have undergone a two-point calibration by the manufacturer at 77 K and 300 K. Because of platinum's well known and repeatable resistivity over that temperature span, the uncertainty of a temperature measurement made in this range is 0.25 K. Figures 3.1.4 and 3.1.5 illustrate the predicted effectiveness for the 20x20 mm and 10x10 mm heat exchangers, respectively, as a function of the mass flow rate assuming that the facility is operating in active cooling mode with helium over a temperature span from room temperature to 150 K. The model used to predict performance was originally developed by Hoch et al. [5].

The uncertainties in the measured effectiveness at these operating conditions associated with the temperature measurements are shown by the vertical error bars. In all cases, the uncertainties are less than 1% and near the peak effectiveness they are less than 0.5%. The effectiveness uncertainty due to temperature measurements is so small that the error bars are barely visible in Figs. 3.1.4 and 3.1.5. As a secondary measurement method, type E thermocouples have also been installed at the four heat exchanger ports. Type E thermocouples have a rated temperature range of -200°C to 900°C and an absolute uncertainty of 1.7°C. The horizontal error bars are due to the uncertainty of the mass flow meter, which will be discussed in Section 3.1.3 on cryogenic test facility equipment.

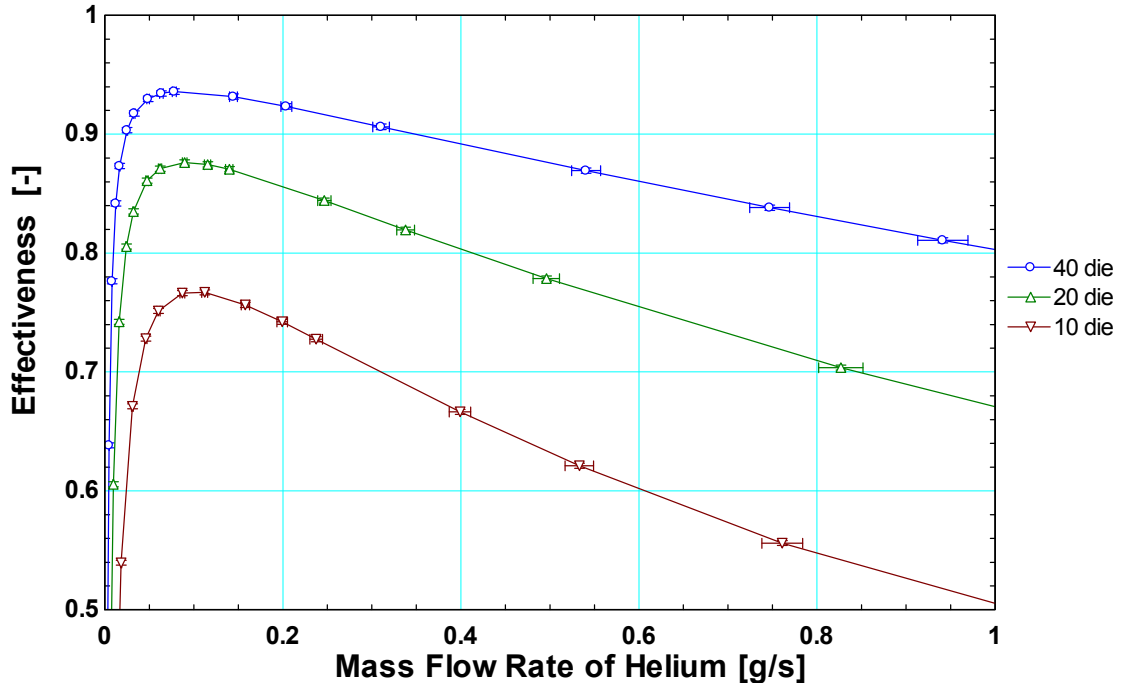

Fig. 3.1.4: Heat exchanger effectiveness as a function of mass flow rate for the 20x20 mm heat exchanger assuming testing in applied mode with helium from 300 K to 150 K. The error bars shown in the figure correspond to the uncertainty in a measured effectiveness at this operating condition due to the instrumentation uncertainty of the facility.

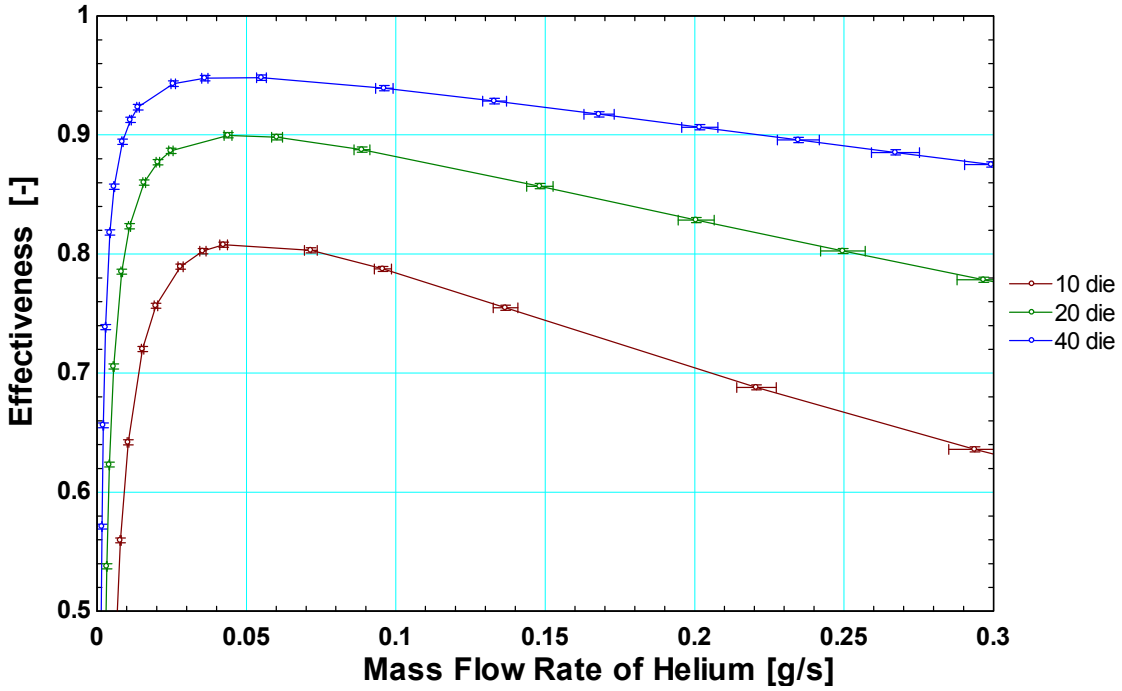

Fig. 3.1.5: Heat exchanger effectiveness as a function of mass flow rate for the 10x10 mm heat exchanger assuming testing in active mode with helium from 300 K to 150 K. The error bars shown in the figure correspond to the uncertainty in a measured effectiveness at this operating condition due to the instrumentation uncertainty of the facility.

3.1.3 Equipment for the Cryogenic Test Facility

The compressor that was used as part of the cryogenic test facility is the HC-2D helium compressor manufactured by APD Cryogenics shown in Fig. 3.1.6. The compressor is a single stage, water-cooled, oil lubricated rotary compressor that is designed to deliver high pressure helium to a cryogenic refrigerator. The compressor has an oil removal system that prevents oil from entering the rest of the system. The compressor can deliver gas at pressures up 2400 kPa.

Fig. 3.1.6: Photograph of compressor to be used in the cryogenic test facility

The flow meter that was used in the cryogenic test facility is a Bronkhorst F-132M mass flow meter shown in Fig. 3.1.7. The mass flow meter separates the flow into two streams, with the majority passing through a laminar flow device and a small percentage flowing through a capillary tube. The two flows remain proportional to each other across the entire calibrated range of the flow meter. The flow meter senses the flow rate by adding a small amount of heat to the capillary flow and measuring the temperature rise.

Fig. 3.1.7: Photograph of Mass Flow Meter to be used in the Cryogenic Test Facility

The mass flow meter has a voltage output of 0 to 5 V that corresponds to a flow rate of 0 to 100 standard liters/min of nitrogen. The manufacturer recommends using Eq. 3.1.6 to determine the mass flow rate ($\dot{m}_{actual}$) based on output voltage (V_{signal}).

$$\dot{m}_{actual} = V_{signal}\ K\ C_{convert} \tag{3.1.6}$$

where $\dot{m}_{actual}$ is the mass flow rate of the fluid in standard liters per minute, K is the conversion factor from voltage to flow rate (100 standard liters per minute divided by 5 volts), and $C_{convert}$ is the conversion factor used when operating the flow meter for fluids, temperatures, and pressures other than the calibration conditions. The conversion factor can be calculated by Eq. 3.1.7.

$$C_{convert} = \frac{Cp_1\ \rho_1}{Cp_2\ \rho_2} \tag{3.1.7}$$

where Cp_1 is the specific heat of nitrogen evaluated at 400 bar and 70°C (the calibration temperature plus 50°C), ρ_1 is the density of nitrogen evaluated at 20°C and 101.325 kPa, Cp_2 is the specific heat of the test fluid evaluated the inlet pressure and inlet temperature plus 50°C, and ρ_2 is the density of the test fluid evaluated at 20°C and 101.325 kPa. The mass flow meter is calibrated for nitrogen at 400 bar absolute and 20°C. The reason that the specific heats are evaluated at 50°C higher than the average fluid temperature is because of the heater in the capillary tube raises the fluid temperature. The 50°C is used so that the specific heat is evaluated at the average fluid temperature in the capillary tube. The mass flow sensor has been calibrated to less than 0.2% error under calibration conditions. The percent error associated with the conversion factor is shown by Eq. 3.1.8:

$$\begin{aligned} Error &= (2\%)\cdot C_{convert} \quad \text{if } C_{convert} > 1 \\ Error &= \frac{(2\%)}{C_{convert}} \quad \text{if } C_{convert} < 1 \end{aligned} \tag{3.1.8}$$

The conversion factor $C_{convert}$ has been tabulated for various gasses that the heat exchanger may be tested with for multiple pressures in Table 3.1.1. The further the gas is from an ideal gas at room temperature the more the conversion factor depends on the fluid pressure in the mass flow meter.

Table 3.1.1: Values of $C_{convert}$ for various gasses at multiple pressures

	$C_{convert}$			
	1 bar	2 bar	5 bar	10 bar
Helium	1.750	1.750	1.751	1.751
Nitrogen	1.244	1.243	1.239	1.232
Argon	1.746	1.743	1.734	1.720
Methane	0.963	0.961	0.956	0.948
Ethane	0.619	0.616	0.608	0.594
Propane	0.430	0.427	0.417	0.396
Isobutane	0.321	0.318	0.307	0.274
N-butane	0.316	0.312	0.298	0.220

The mass flow rate as a function of the output voltage signal for a number of different fluids is shown in Fig. 3.1.8. A pressure of 202 kPa (2 atm) was chosen for this plot because it represents the high end of the range of pressures that were used in room temperature testing. The vertical error bars represent the combination of both the calibration error and the conversion factor error. There were a number of fluids of interest such as ethane, propane, and isobutane that are not shown separately because these fluids behave essentially the same as n-butane and would be indiscernible on the plot. The reason that the uncertainties for n-butane, isobutane, and propane are larger than the uncertainty associated with other fluids is that their conversion factor is small, around 0.3. Fluids with a density and specific heat close to that of nitrogen will have small conversion errors and fluids with significantly different specific heats and densities will have much larger conversion errors.

The relative uncertainties of the mass flow rates as a function of voltage signal are shown in Fig. 3.1.9. The relative uncertainty as the mass flow rates approach zero is quite large and any measurement taken in this range is not accurate. A mass flow sensor with a smaller range would have to be used to make measurements at the low end of this range. The relative uncertainty for a number of fluids of interest such as nitrogen, argon, and helium were not plotted because their relative uncertainties would be indistinguishable from that of methane on the plot.

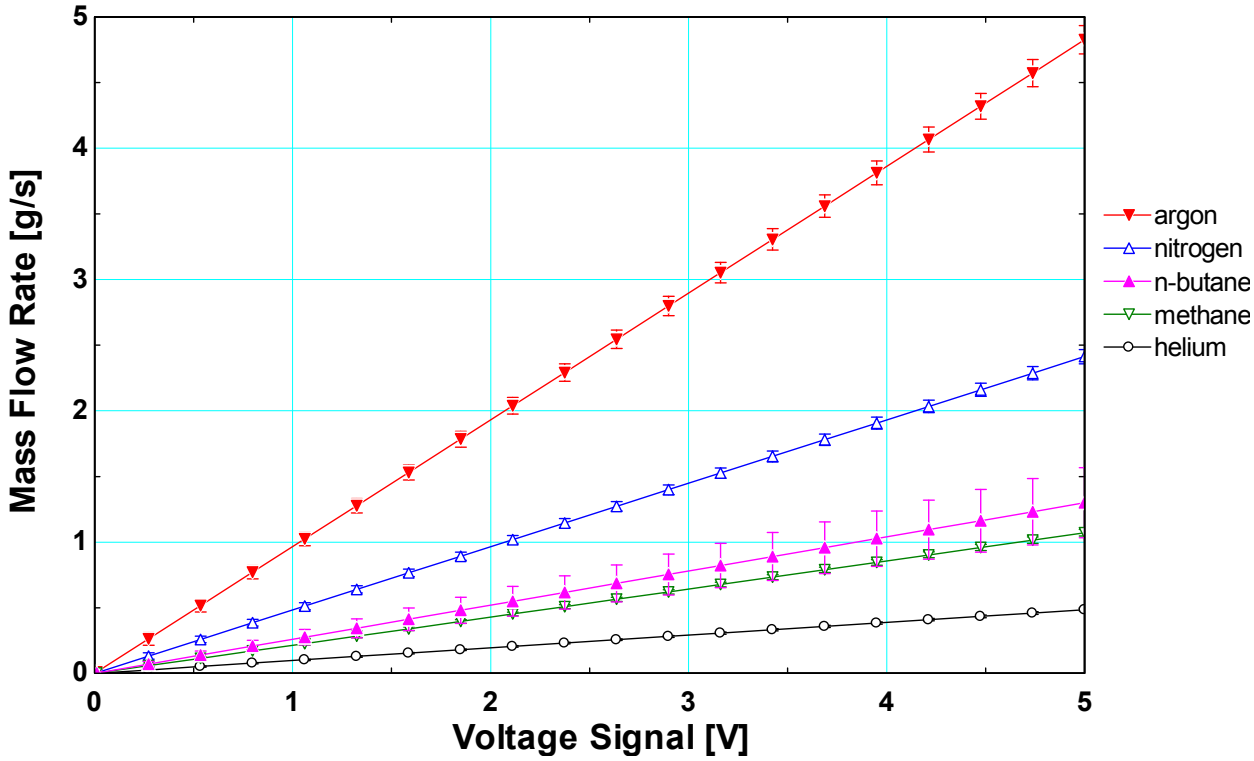

Fig. 3.1.8: Mass flow rate as a function of mass flow sensor voltage signal for various fluids at 202 kPa

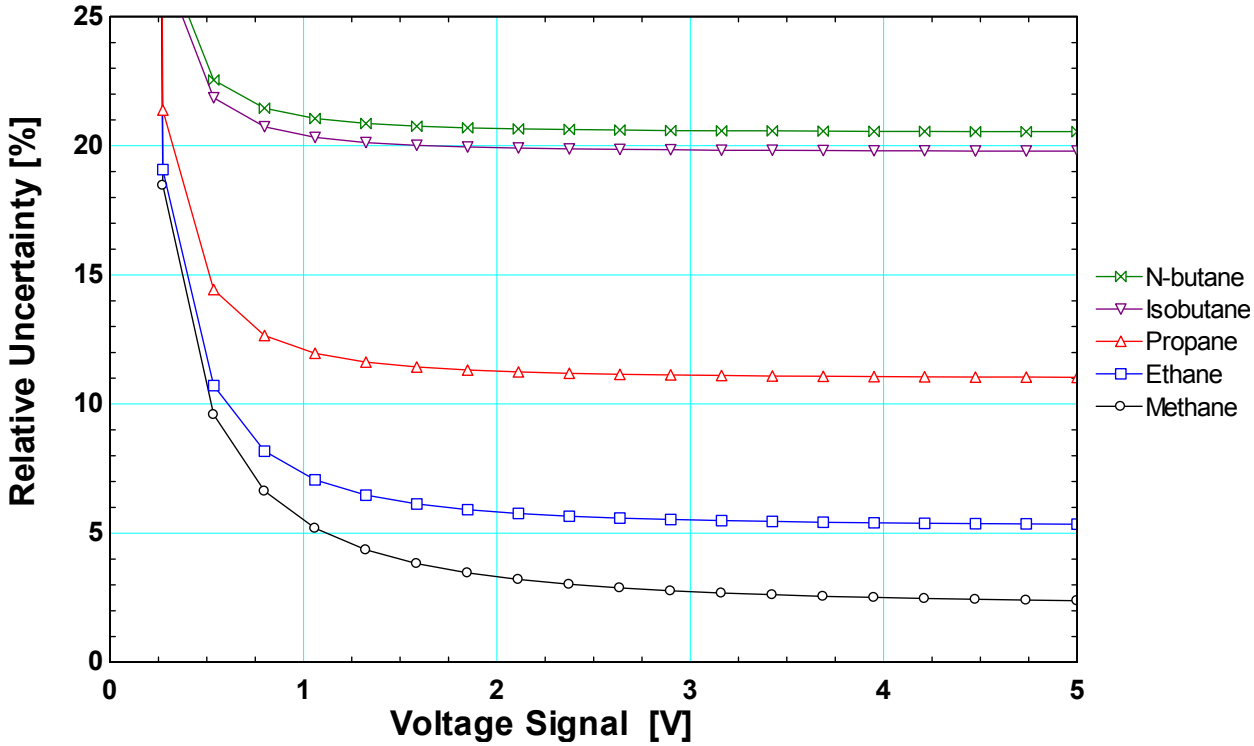

Fig. 3.1.9: Relative uncertainty of mass flow rates for various fluids at 202 kPa

3.1.4 Design of the Cryogenic Test Facility

3.1.4 Design the Cryogenic Test Facility

A geometric model of the internal Dewar assembly has been created and is shown in Fig. 3.1.10. The internal Dewar assembly consists of the heat exchanger, instrumentation, the cryocooler, and the cryocooler heat exchanger. High pressure fluid flows through the assembly in the direction of the red arrows and the low pressure stream flows through the assembly in the direction of the blue arrows.

After entering the Dewar, the pressure of the high pressure stream is measured using a pressure tap that is connected to a pressure sensor located outside the Dewar. The high pressure stream then passes over a platinum resistor thermometer (PRT) that penetrates into the fluid stream and is fixed in place inside a stainless steel tee. Next the fluid passes by a thermocouple which is also inserted directly into the flowing fluid through the use of a VCR tee.

After passing through the warm end instrumentation, the high pressure stream enters the heat exchanger. The high pressure stream leaving the cold end of the heat exchanger passes through a set of instrumentation that is identical to the temperature and pressure sensors at the high pressure inlet. At this point, the fluid can travel in two different directions depending on which mode the heat exchanger is being tested in. If testing is taking place in self-cooling mode then the high pressure stream will continue on to the jewel orifice where it will undergo an isenthalpic expansion. If the heat exchanger is being tested in applied cooling mode, then the stream will travel to a heat exchanger connected to a cryocooler.

The low pressure stream, which is shown by the blue arrows in Fig. 3.1.10, comes from either the jewel orifice or the cryocooler heat exchanger depending on the mode of testing. The low pressure stream will pass through another set of temperature and pressure instrumentation (identical to those previously discussed) before entering the low pressure inlet of the heat exchanger. Once inside the heat exchanger, the low pressure stream pre-cools the high pressure stream. The low pressure stream exiting the hot end of the heat exchanger stream passes through a fourth set of temperature and pressure instrumentation.

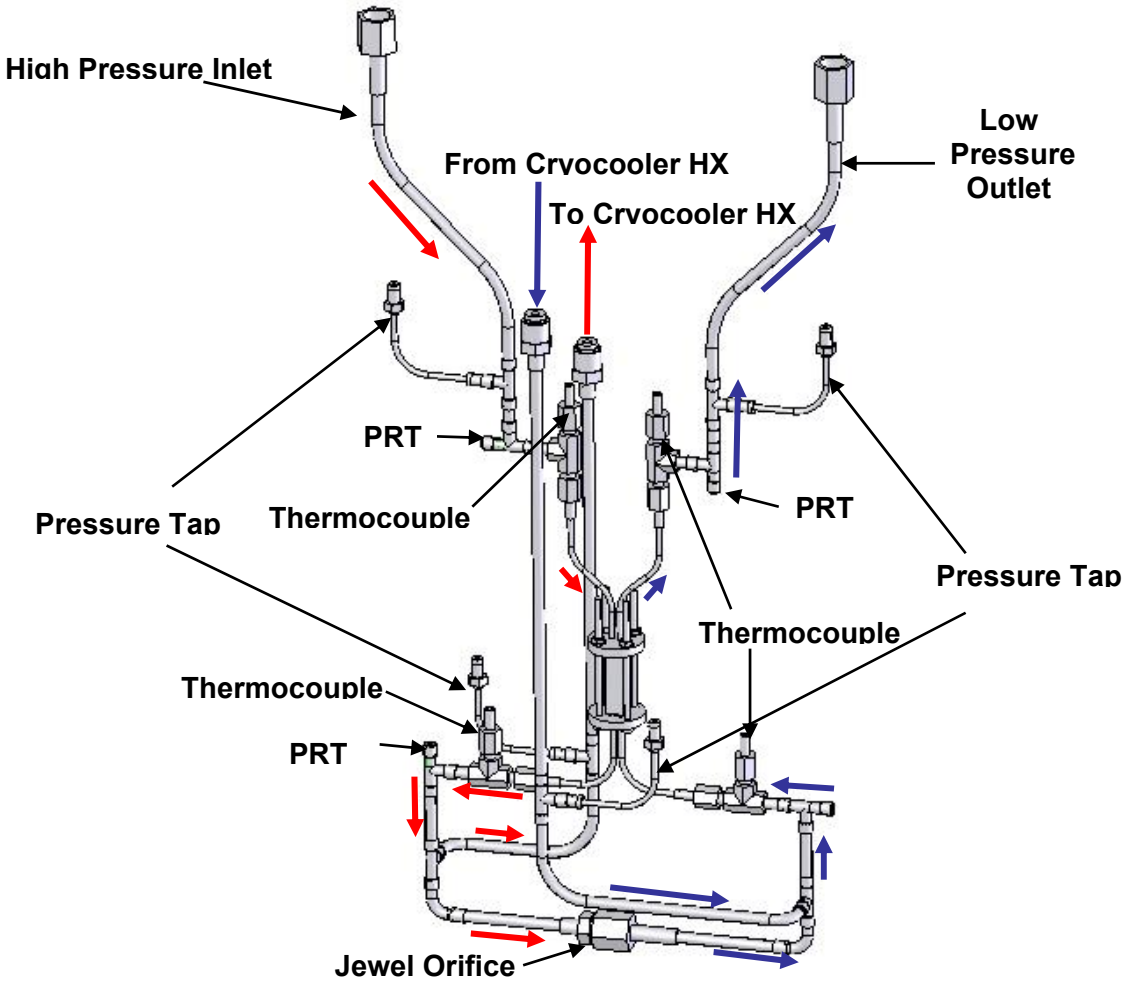

Fig. 3.1.10: Geometric solid model of instrumentation inside the Dewar

Photographs showing how the PRT is held directly in the fluid flow are provided in Figs. 3.1.11 and 3.1.12. The PRTs have been calibrated by the manufacturer using a two point calibration at 77 K and 300 K. The PRTs absolute temperature measurement uncertainty within the range of 77 K to 300 K is reported to be 0.25 K by the manufacturer. The leads have been covered in shrink wrap to provide electrical insulation and extra support in attaching the PRT to the support wire. A G10 plug was used to thermally and electrically isolate the PRT from the tubing tee. The joint with the G10 plug was sealed using epoxy after the photograph in Fig. 3.1.12 was taken. This style of PRT mounting had been previously and successfully used to measure temperatures in a test facility for measuring heat transfer coefficients [12].

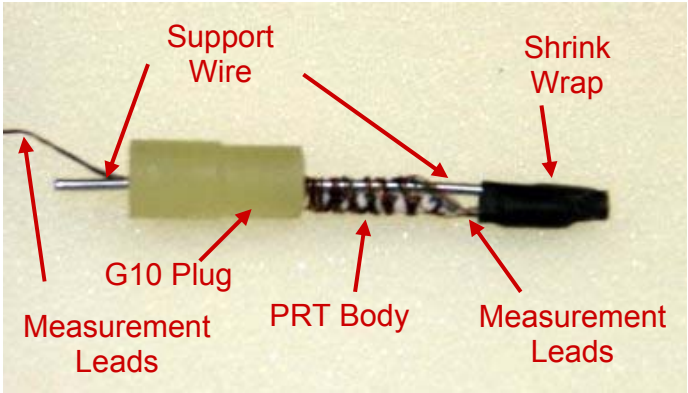

Fig. 3.1.11: Photograph of internal components of PRT measurement tee

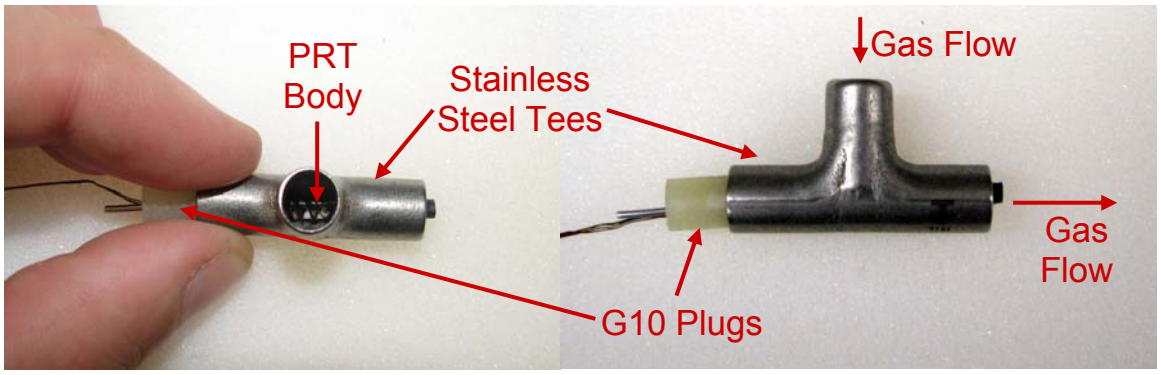

Fig. 3.1.12: Photograph showing how the PRTs are inserted into a tee to directly measure the fluid temperature

The thermocouple wire junctions were joined by a small bead of solder and covered by epoxy to electrically isolate the thermocouple from the tube. The thermocouple lead wire was then epoxied to a VCR gland as shown in Fig. 3.1.13. The thermocouple wire length was chosen so that the small solder bead would be in the center of the flowing fluid when the VCR gland was connected to a VCR tee.

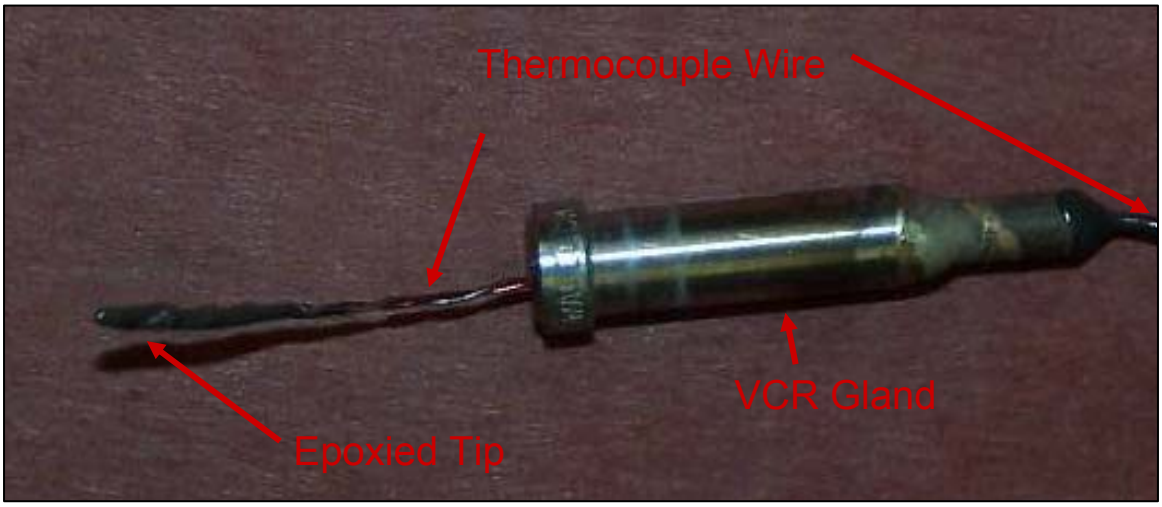

Fig. 3.1.13: Photograph of type E thermocouple to be used in cryogenic test facility

The cryocooler heat exchanger assembly is shown in Fig. 3.1.14. The cryocooler used to provide external cooling is a two-stage Cryomech GB04 cryocooler which operates on a Gifford-McMahon cycle. In a typical application, the first stage of the cryocooler would be used as an 80 K radiation heat shield to intercept the majority of the heat being conducted or radiated from the environment to an object of interest. The second stage of the cryocooler would then be used to cool the object of interest to the desired temperature, which might be around 20 K. However, such low temperatures are not needed for testing the heat exchanger. Instead, a larger heat load is required at a higher temperature, such as 150 K. Therefore, the cryocooler heat exchanger is attached to the first stage of the cryocooler in order to take advantage of the higher heat load capacity associated with the first stage. The second stage is insulated using multi-layer insulation (MLI) so that it does not reduce the cooling power of the first stage.

The cryocooler operates at a single speed; therefore, it is not possible to control the cold end temperature by modulating the power provided to the cryocooler. Instead, a heater is attached to the adapter plate in order to adjust the cold end temperature to the desired temperature. The amount of heat that must be dissipated in the electrical heater will vary depending on the mass flow rate and type of fluid passing through the cryocooler heat exchanger.

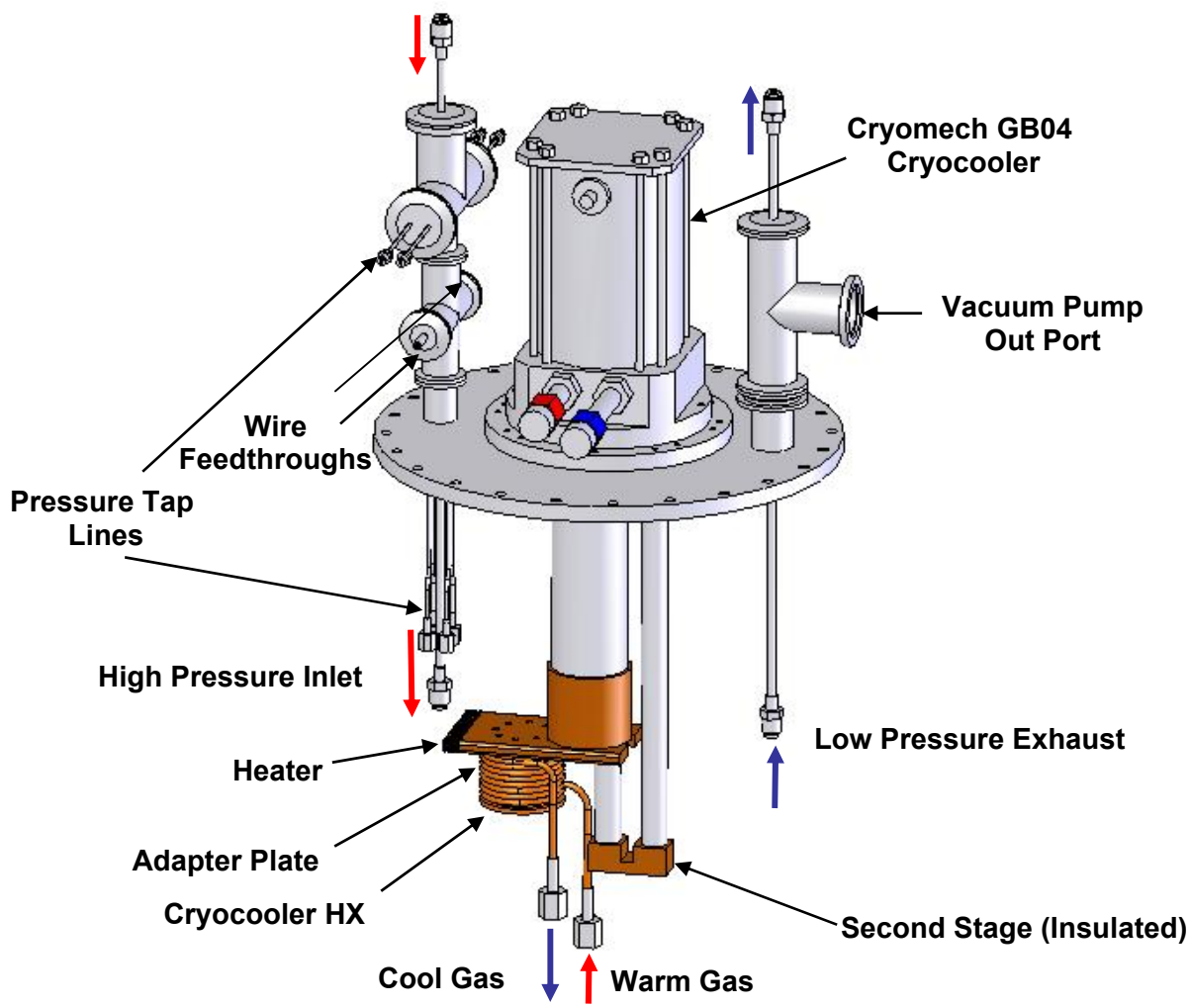

Fig. 3.1.14: Geometric solid model of the cryocooler heat exchanger assembly

The electrical wires for the thermocouples and PRTs are brought out of the Dewar through the KF fittings labeled as wire feedthroughs in Fig. 3.1.14. Shown in Fig. 3.1.15 is a photograph of the thermocouple feedthrough. A hole was drilled in a blank KF-25 fitting and a ¼" tube was epoxied to the hole in the KF fitting. The thermocouple wires are passed through the inside of the tube and then the tube is filled with epoxy. The fitting was verified to be leak tight using a helium leak detector. The method used for the PRT feedthroughs was exactly the same.

Fig. 3.1.15: Vacuum feedthrough for thermocouple wires

The geometric solid model of the entire Dewar tubing assembly and how it fits into the entire Dewar assembly are shown side by side in Fig. 3.1.16. Also shown in Fig. 3.1.16 is a photograph of the Dewar.

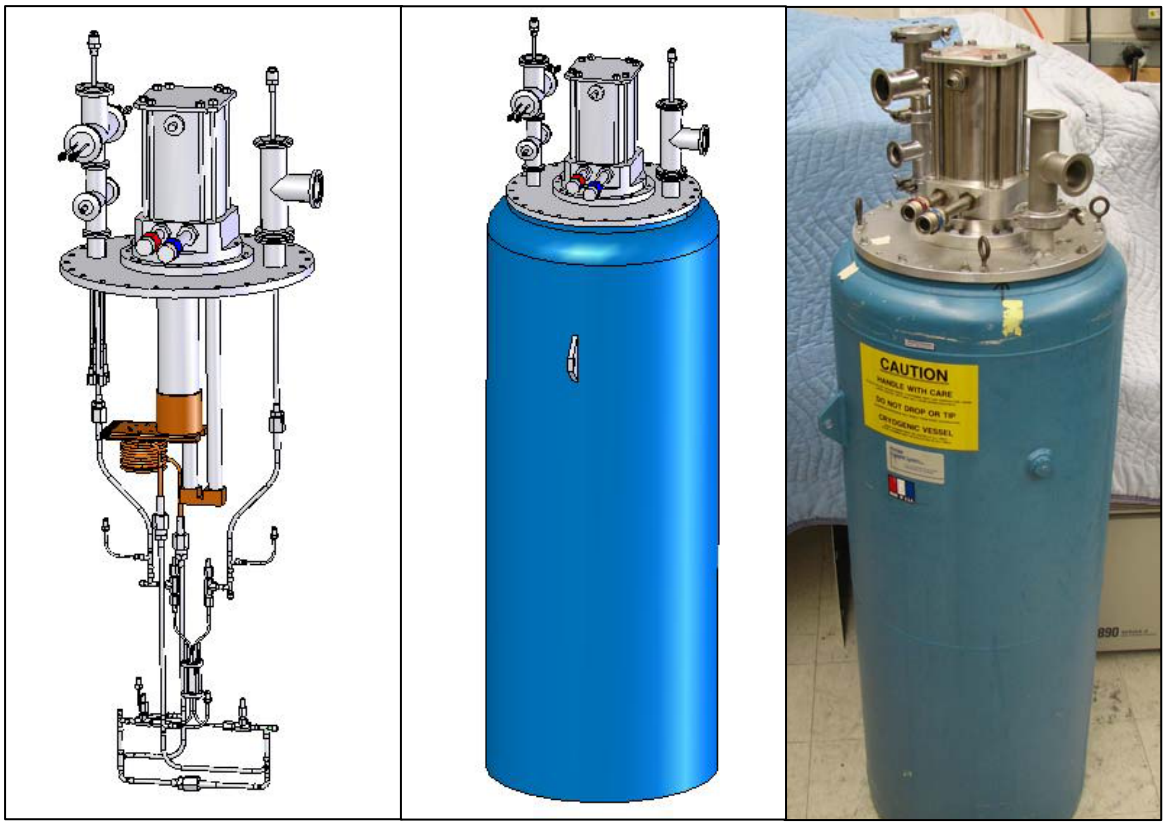

Fig. 3.1.16: Geometric solid model of the entire Dewar tubing assembly (left), the entire Dewar assembly (middle), and a photograph of the entire Dewar assembly (right)

3.1.5 Construction of the Cryogenic Test Facility

The design of the cryogenic test facility was discussed in Section 3.1.4 and this section details the construction of the cryogenic test facility. The section begins with short descriptions and photographs of components of the internal Dewar assembly. The section ends with a discussion of the components that are located outside of the Dewar. The compressor, mass flow meter, and instrumentation are discussed in Section 3.1.4.

Figure 3.1.17 shows the instrumentation at the warm end of the heat exchanger. The red arrows show the direction of flow for the high pressure stream and the blue arrows show the direction of flow for the low pressure stream. There are redundant methods of temperature measurement for increased reliability and increased confidence in the accuracy of the fluid temperature measurement. Each stream's temperature is measured with a calibrated platinum resistance thermometer (PRT) and a type E thermocouple that are both inserted directly into the flowing fluid. In addition, there is a pressure tap for monitoring the pressure of each fluid stream.

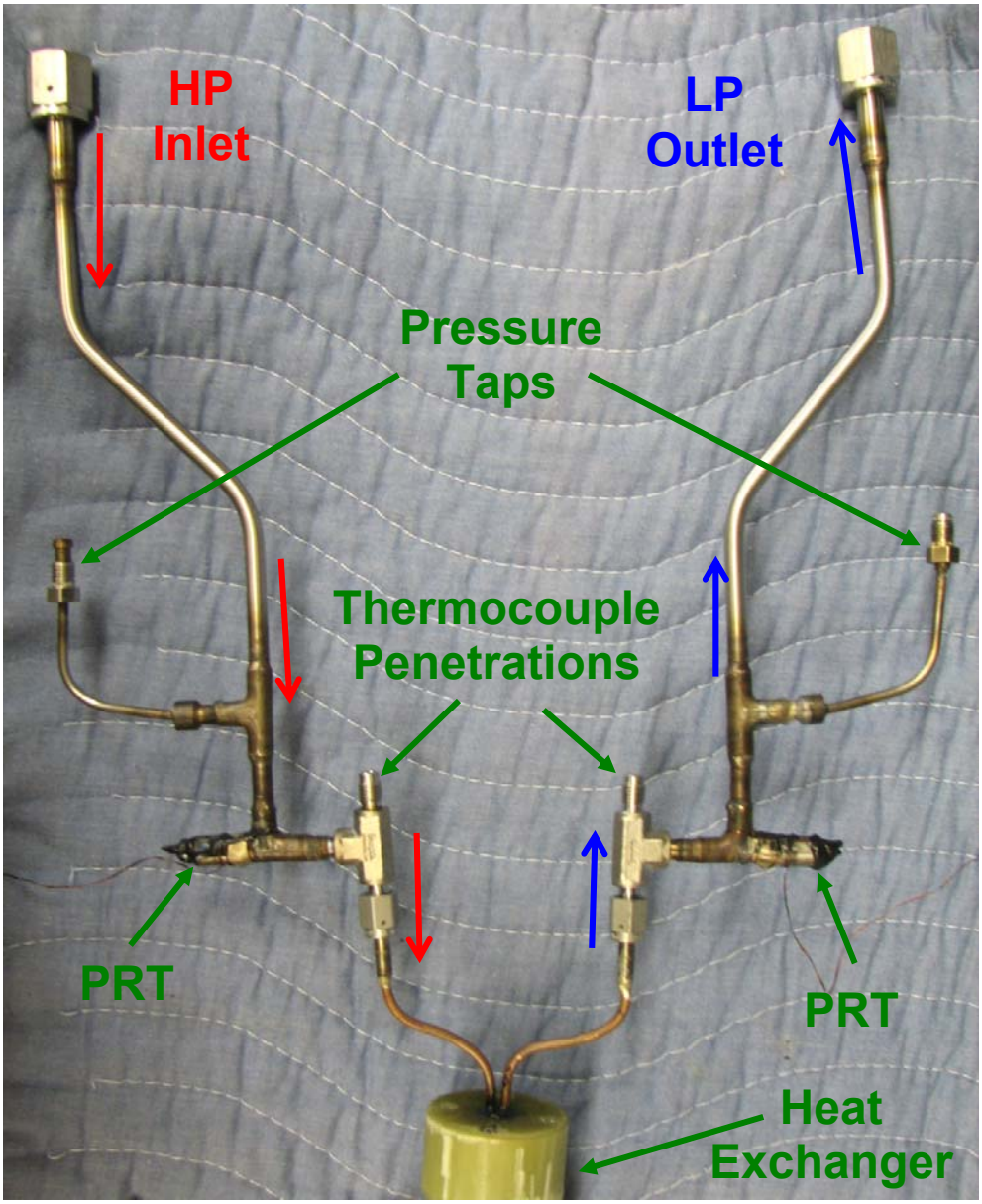

Fig. 3.1.17: Warm end of heat exchanger and instrumentation assembly to be used in the cryogenic test facility. Red arrows show the high pressure gas flow path and blue arrows shown the low pressure gas flow path

The cold end instrumentation for the heat exchanger is shown in Fig. 3.1.18. Like the warm end instrumentation, there are PRTs and thermocouples inserted into the fluid flow path and a pressure tap for each stream. There are two possible flow paths for the working fluid through the cold end assembly. If the heat exchanger is in self-cooling mode then the fluid flows through the jewel orifice while the tubes leading to the cryocooler heat exchanger are disconnected. Alternatively, if the heat exchanger is operating in applied cooling mode, then the fluid flows to the cryocooler heat exchanger while a blank VCR gasket prevents fluid flow through the jewel orifice location.

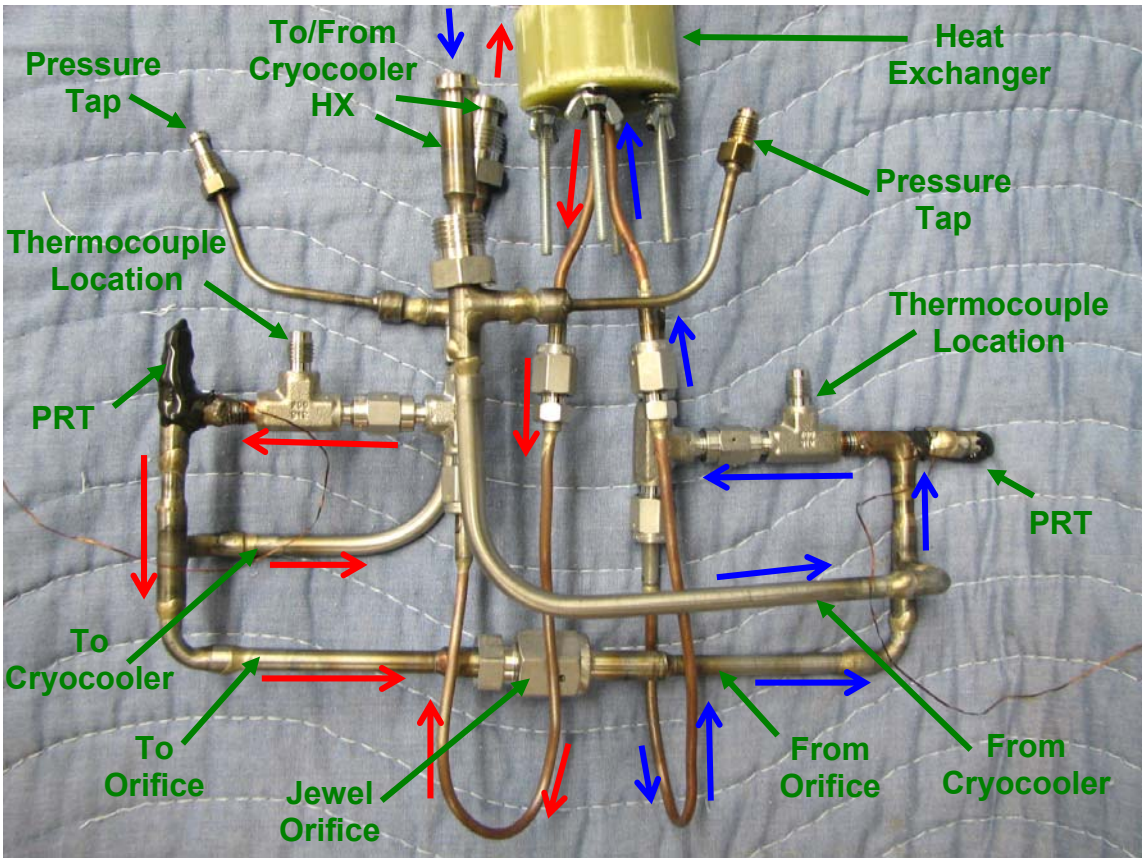

Fig. 3.1.18: Cold end of heat exchanger and instrumentation assembly to be used in the cryogenic test facility. Red arrows show the high pressure gas flow path and blue arrows shown the low pressure gas flow path

A photograph of the entire heat exchanger instrumentation assembly is shown in Fig. 3.1.19. The entire assembly is normally inside the Dewar where it is in an evacuated space, reducing convection heat loss and therefore reducing parasitic heat loads. Testing in a high vacuum environment provides a more accurate method to measure the heat exchanger effectiveness than the room temperature testing does due to reduction of parasitic heat loads to the heat exchanger. All joints were leak checked with a helium leak detector in order to ensure that a high vacuum can be achieved within the Dewar.

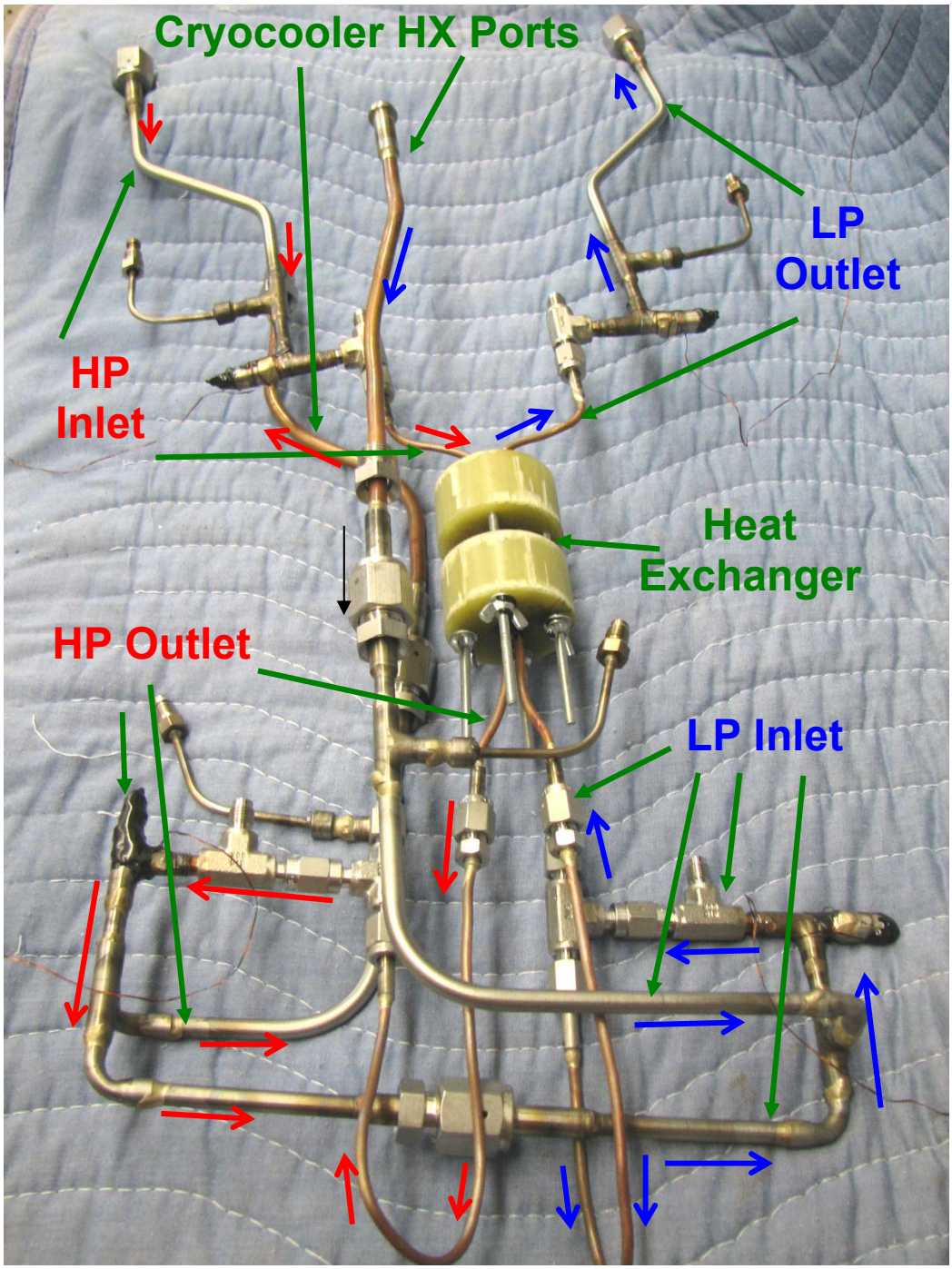

Fig. 3.1.19: The entire heat exchanger and instrumentation assembly to be used in the cryogenic test facility. Red arrows show the high pressure gas flow path and blue arrows shown the low pressure gas flow path

The entire heat exchanger instrumentation assembly shown in Fig. 3.1.19 is connected to the cryocooler and the top flange of the Dewar, which is shown in Fig. 3.1.20. The cryocooler heat exchanger was designed and fabricated by Corey Hughes [12]. A plate of ¾" thick copper was machined to provide a thermal conduit between the cryocooler heat exchanger and the cryocooler. A thin layer of indium was used to reduce the contact resistance between the

cryocooler, adapter plate, and cryocooler heat exchanger. The copper plate was attached to the first stage of the cryocooler in order to utilize the larger cooling power provided by the cooling power. The second stage was later wrapped in MLI because a small heating load on the second stage can reduce the cooling power of the first stage by a large amount.

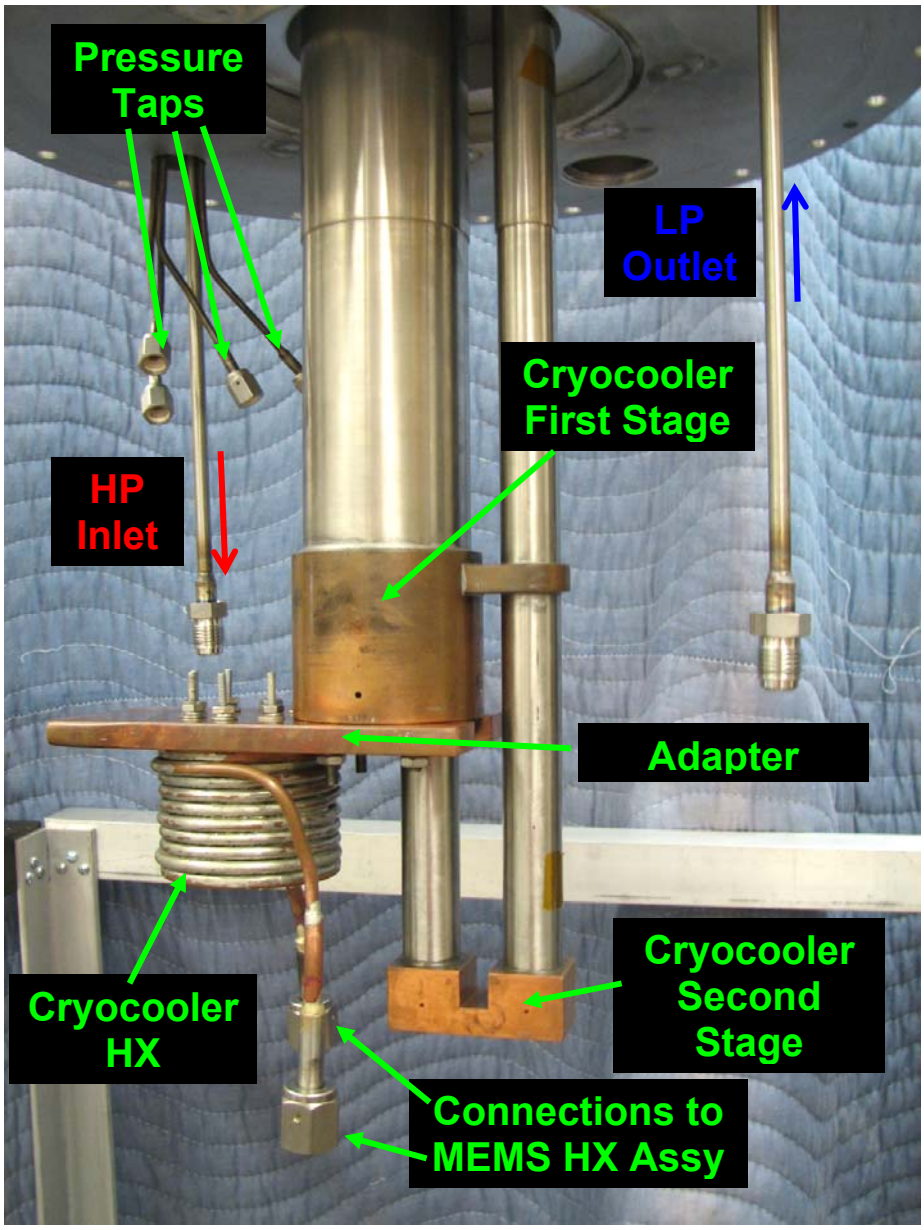

Fig. 3.1.20: The cryocooler heat exchanger is attached to the second stage of the cryocooler, which has a higher cooling capacity than the first stage at temperatures typical of cryosurgery (150 K – 200 K). The second stage was well insulated with multi-layer insulation (MLI) and was not used for testing the MEMS heat exchangers. Also shown are the fluid inlet and outlet ports and the pressure tap connections.

The adapter plate between the cryocooler heat exchanger and the cryocooler is shown again in Fig. 3.1.21. The photograph shows individual dies with integrated PRTs mounted to the adapter

plate for calibration. The calibration and experimental results of the integrated PRTs are presented in App. E. A heater was fabricated to control the temperature of the adapter plate because the cryocooler has no built-in temperature control. A layer of paper was varnished to the adapter plate in order to provide electrical insulation between the heater and the plate. Nichrome wire was wrapped around the plate and varnished to the insulation paper. The high electrical resistance of the nichrome wire provides the heating power through ohmic dissipation. The heater was controlled and powered by a 0-30 VDC power supply located outside the Dewar.

Two separate methods of measuring the adapter plate temperature are available. A commercial PRT was inserted into a hole at the top of the cryocooler heat exchanger; the thermal communication between the PRT and the heat exchanger is improved using thermal grease. In addition, one of the spare thermocouples can be installed on the plate using one of the cryocooler heat exchanger bolts.

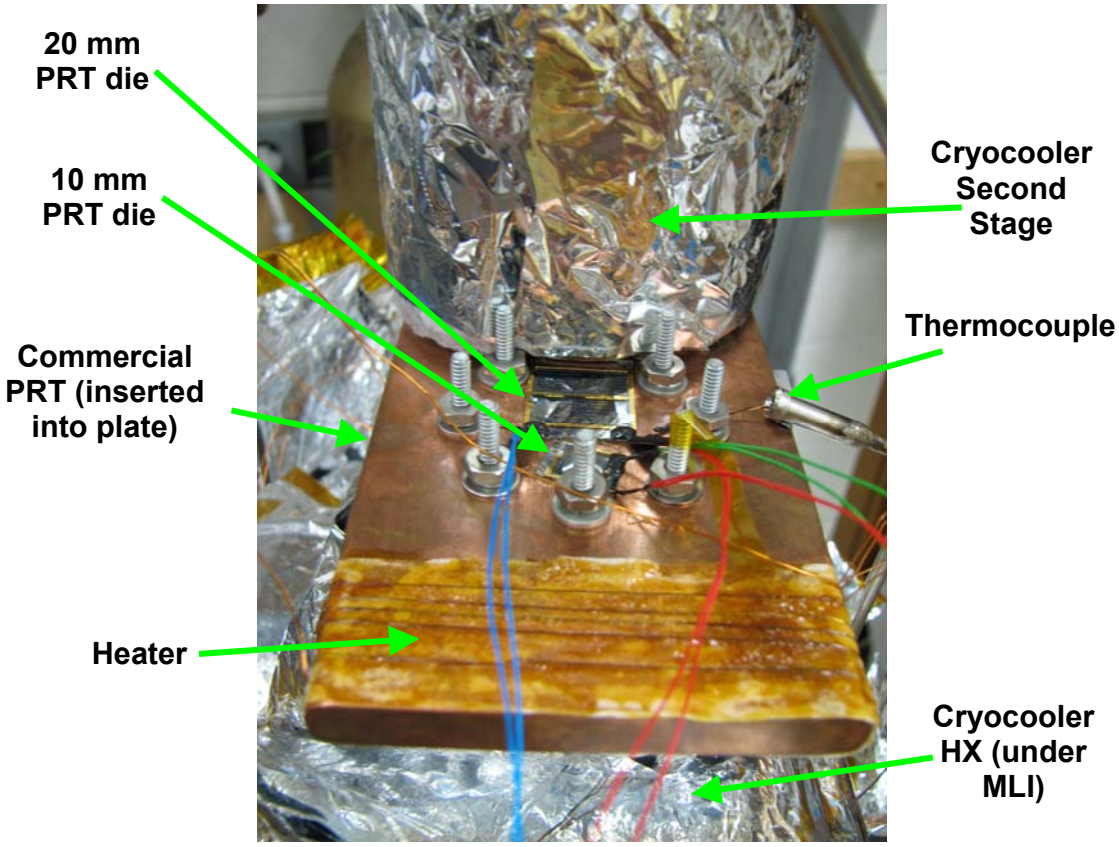

Fig. 3.1.21: Photograph of the heater used to control the cryocooler heat exchanger temperature. A commercial PRT was inserted into a small hole between the adapter plate and the heat exchanger to measure the cryocooler heat exchanger temperature. A thermocouple was used to check that the PRT was measuring correctly. The photograph was taken just prior to calibrating two individual dies with integrated PRTs.

A support stand was constructed using 1½" aluminum and steel 90° angle bars in order to the lift the top flange of the Dewar and provide easy access to the internal Dewar assembly. A photograph of the support stand with the top flange of the Dewar in the raised position is presented in Fig. 3.1.22. The entire assembly is lowered into the Dewar by using the two pulleys

attached to the top of the support stand and a steel cable. The photograph in Fig. 3.1.22 shows the assembly while it was being leak checked and before any MLI was applied. The MLI significantly reduces the heat radiated onto the cold surfaces but completely blocks the internal components from view. Therefore, pictures before the application of MLI are presented.

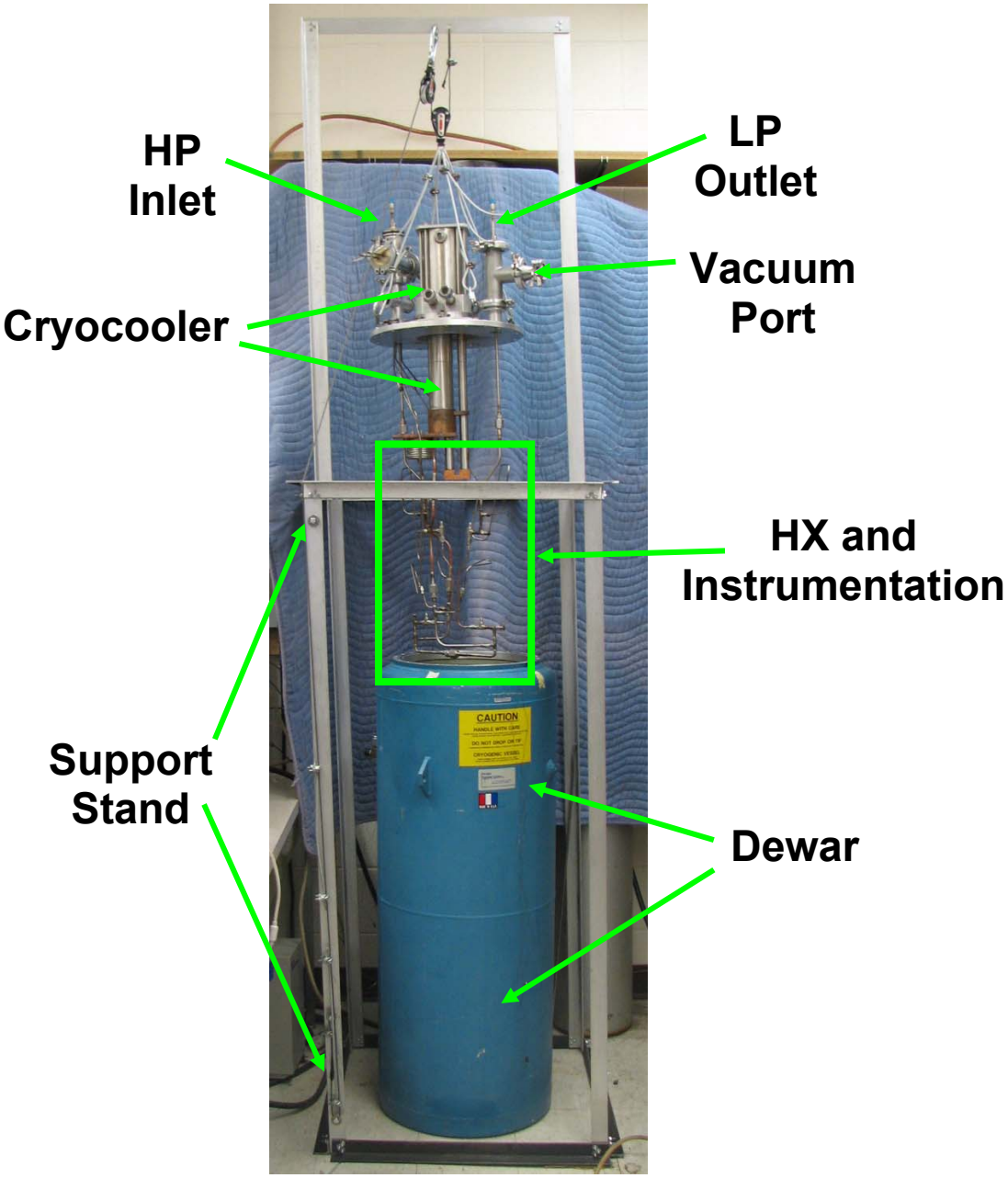

Fig. 3.1.22: Dewar assembly for the cryogenic test facility. During normal operation all components would be wrapped in multi-layer insulation (MLI). This photograph was taken when all the components were initially being leak checked.

A photograph of the internal Dewar assembly completely lowered into the Dewar is shown in Fig. 3.1.23. The photograph shows how the Dewar appears when an experiment is in progress. The high pressure gas comes from the compressor, flows through the mass flow meter, and

enters the Dewar through the high pressure inlet port. The low pressure fluid exits the Dewar from the low pressure port and flows towards the compressor. Also shown in Fig. 3.3.23 are the pressure tap tubes that connect to the pressure transducers to each of the heat exchanger inlet and outlet fluid streams.

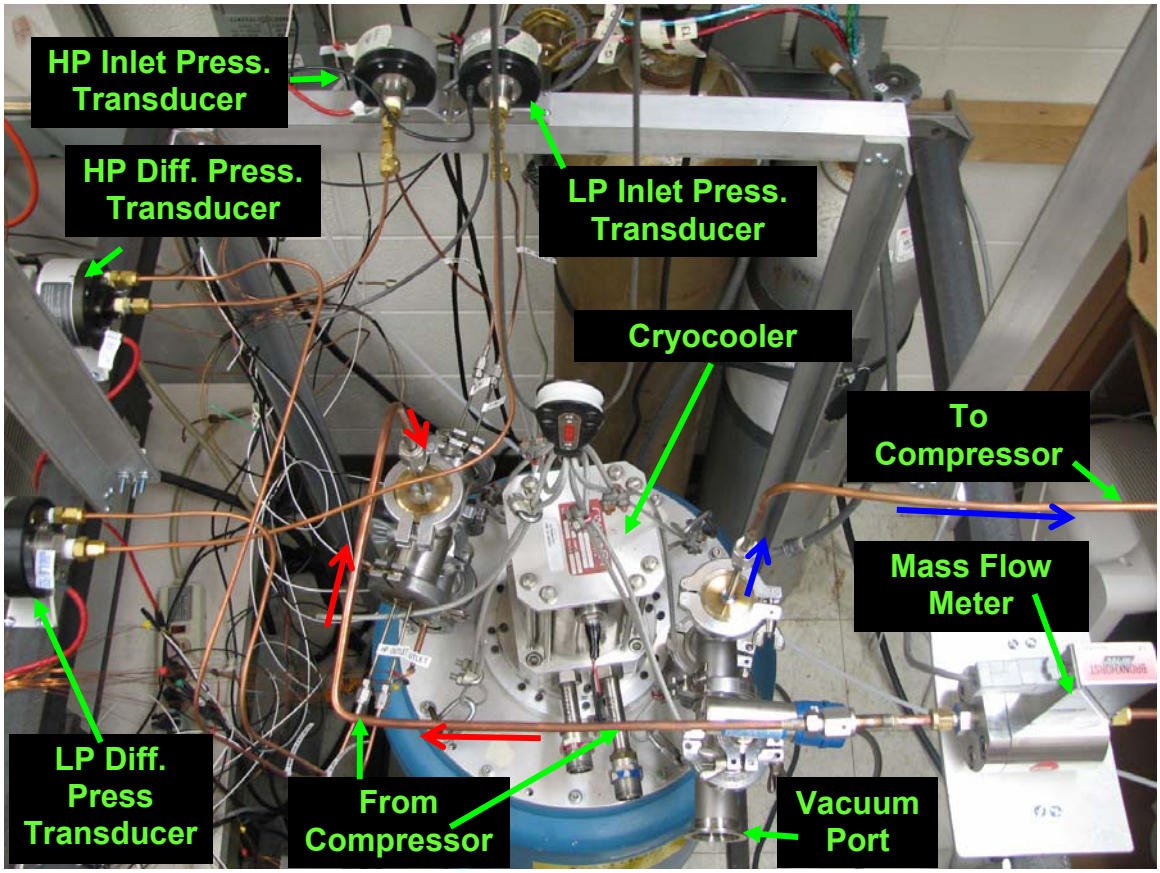

Fig. 3.1.23: Top view of the Dewar assembly. High pressure fluid flows in the direction of the red arrows and low pressure fluid flows in the direction of the blue arrows.

In between the compressor and the mass flow sensor is a pressure regulator, which is shown in Fig. 3.1.24. The pressure regulator allows the high pressure inlet pressure to be tightly controlled and easily modified. An adjustable pressure relief valve is used to prevent the pressure in the heat exchanger from increasing beyond a pre-set limit (generally 90 psig). Also shown in Fig. 3.1.24 is an evacuation/fill port that is used when only the Dewar side of the cryogenic test facility must be evacuated or filled. This allows the compressor to maintain its gas charge during the frequent openings of the Dewar.

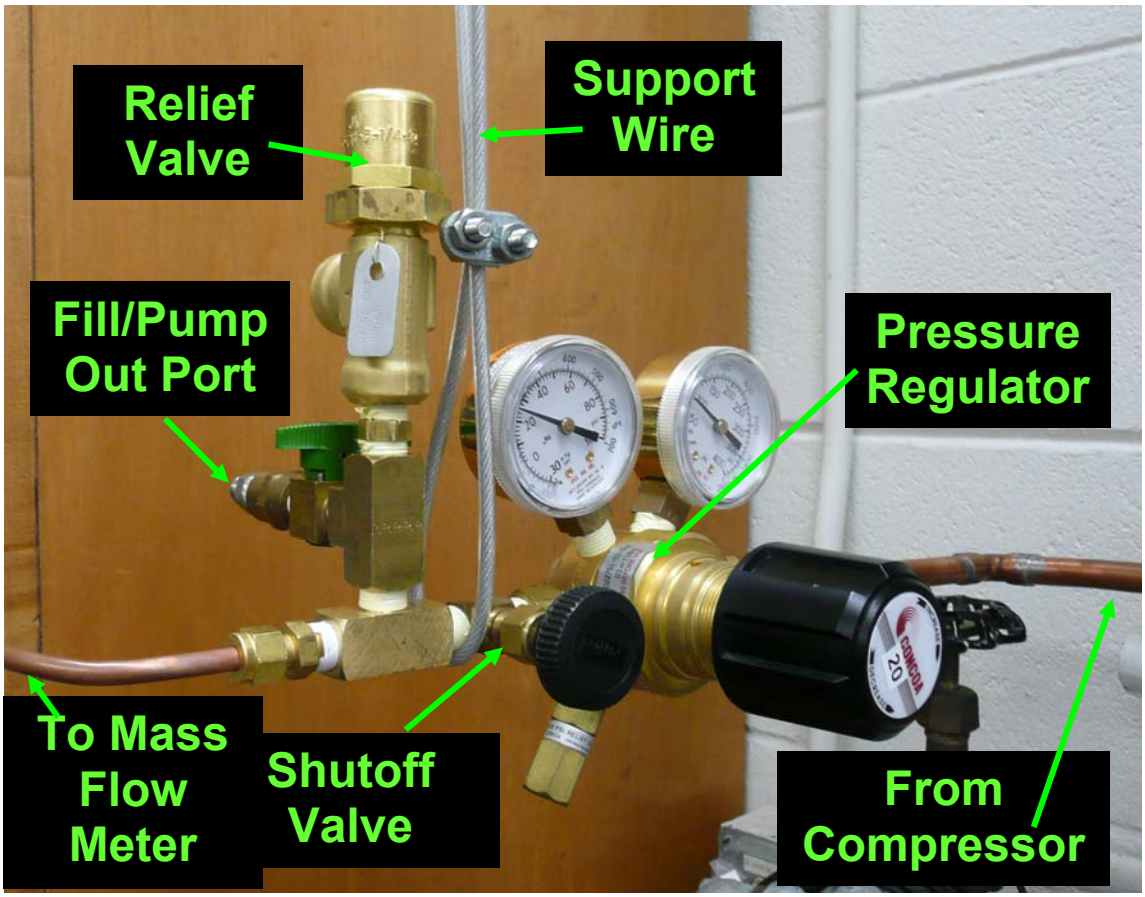

Fig. 3.1.24: Pressure regulator used to control the inlet pressure to the Dewar assembly. A relief valve set at 90 psig was used to prevent pressure spikes that might damage the heat exchanger. Also shown is a filling/pump out port used when only the Dewar side of the cryogenic test facility needs to be evacuated and/or pressurized.

3.2 Prototype Cryosurgical Probe Assembly

A prototype cryosurgical probe assembly was designed in order to demonstrate the use of a J-T cycle implemented with MEMS components in a small device that could be handheld. The MEMS heat exchangers were discussed in Chapter 2.1 and the MEMS valve was discussed in Chapter 2.2.

The cryosurgical probe assembly was developed jointly by the present author and Weibin Zhu of UM-Ann Arbor during his time at the UW-Madison. Weibin Zhu was responsible for the detailed design of the prototype cryosurgical probe and therefore the detailed design will not be discussed here. The probe was assembled at UW-Madison in a joint effort between the present author and Weibin Zhu.

3.2.1 Flow Schematics for the Cryosurgical Probe Prototype

The cryosurgical probe prototype was designed to take advantage of as much of the existing cryogenic test facility infrastructure as possible. As shown in Fig. 3.2.1, the flow schematic for the components external to the cryosurgical probe is almost identical to the flow schematic for components external to the Dewar. The only difference is that the Dewar has been replaced by

the probe prototype and new tubing connections are made in order to accommodate the altered physical location of the probe prototype.

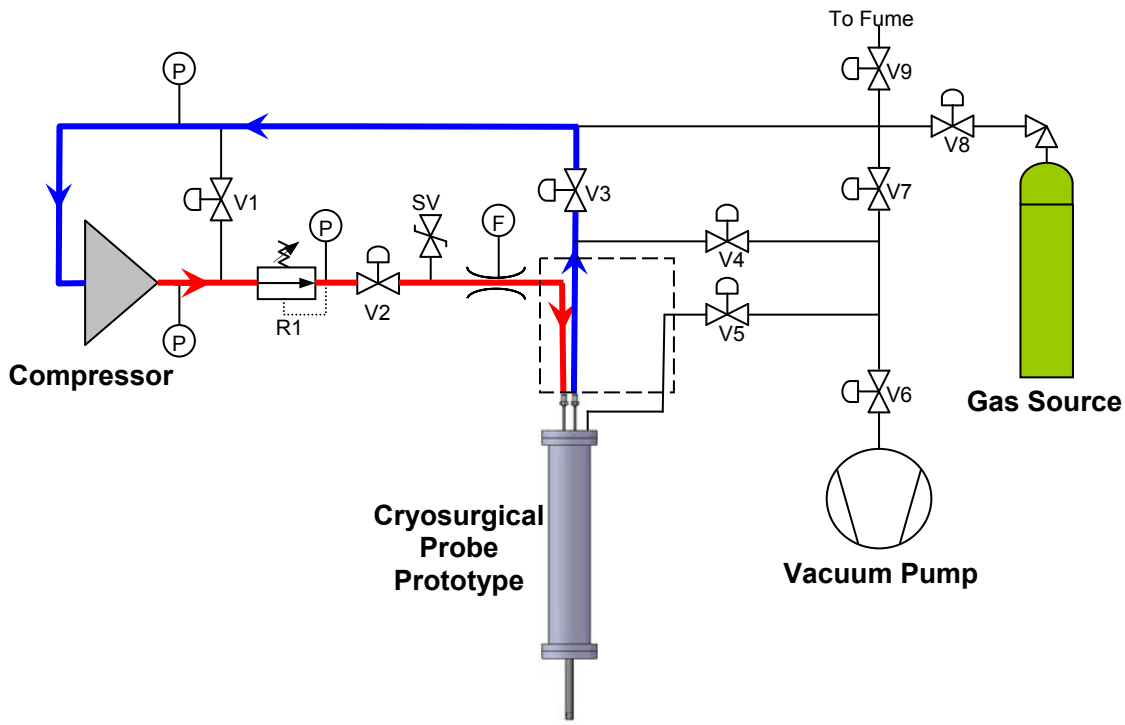

Fig. 3.2.1: Flow schematic for components external to the cryosurgical probe prototype. The flow schematic is exactly the same as the cryogenic test facility (Fig. 3.1.2) except the Dewar was replaced by the cryosurgical probe prototype and the tubing in the dotted box was replaced to account for the new testing location in the laboratory room.

However, the internal assembly of the cryosurgical probe prototype is significantly different from the internal assembly of the Dewar. The flow schematic for the internal components of the probe prototype is shown in Fig. 3.2.2. The first significant difference is the method for producing an isenthalpic pressure drop. The flow rate that can be provided by the current design of the micro-valve was thought to be too small for a viable J-T cycle even in the fully open position. Therefore, an orifice is installed in parallel with the valve in order to increase the total flow rate. The orifice provides a base flow that does not change when the valve is modulated and the valve provides a smaller flow that can be modulated. By using the orifice and valve together, the total flow rate can be modulated in a small range around the optimal flow rate. This method for creating an isenthalpic pressure drop could potentially save significant amounts of time disassembling and reassembling the probe to adjust orifice sizes. Later testing showed that the fully open position of the valve was able to provide adequate flow rates and that testing with the valve and orifice in parallel was unnecessary.

There are a few other notable differences with the cryosurgical probe. Only the high pressure inlet and low pressure outlet pressures are measured in order to save space and reduce the parasitic heat load to the heat exchanger cold end. Commercial PRTs were not used in the probe prototype; however, all of the heat exchangers tested in the probe had integrated PRTs. The thermocouples measuring the heat exchanger inlet and outlet temperatures were built directly

into the heat exchanger headers. Thermocouples were also used to measure the orifice outlet, valve outlet, and probe tip temperatures.

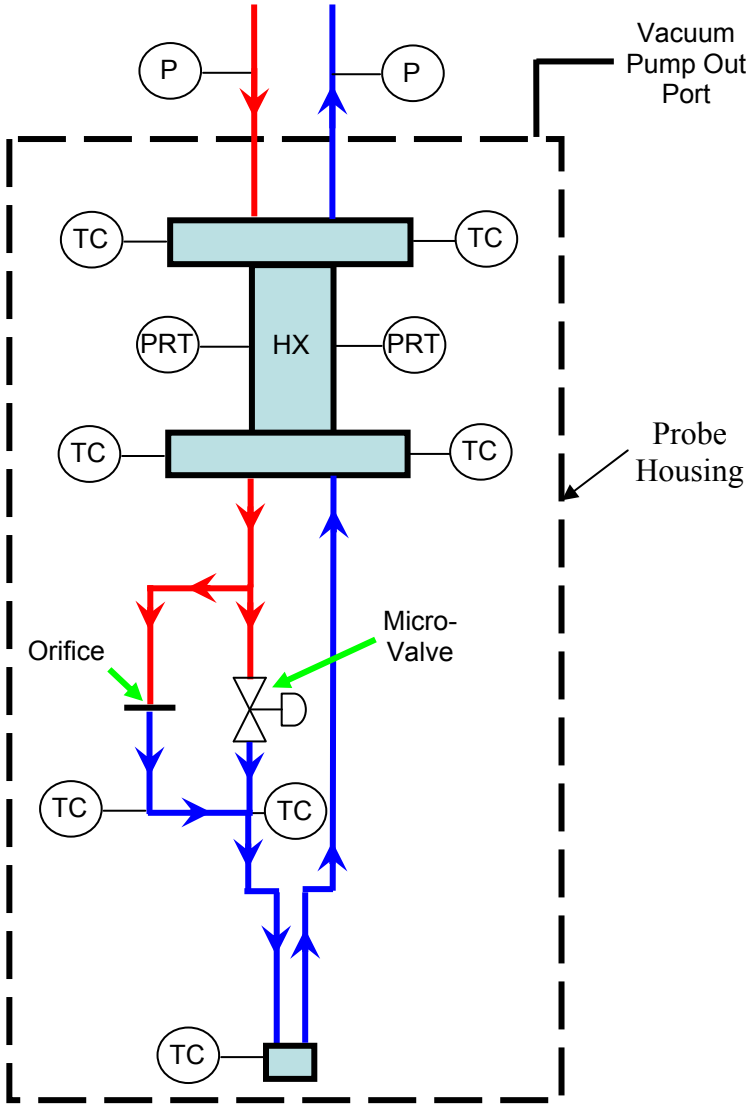

Fig. 3.2.2: Flow schematic of components internal to the cryosurgical probe prototype housing. Red arrows indicate the flow direction of the high pressure fluid and blue arrows indicated the flow direction of the low pressure fluid. The locations marked PRT represent all of the integrated PRTs in the heat exchanger. The number of integrated PRTs varies from heat exchanger to heat exchanger.

3.2.2 Cryosurgical Probe Prototype Construction

A photograph of the cryosurgical probe prototype assembly process is shown in Fig. 3.2.3. Note the short conduction length of the PRT leads as well as the small amount of space available between the outer surface of the heat exchanger and the probe housing (the probe housing itself is not shown; however, the probe housing has an outer diameter smaller than the bolt pattern on the top flange). On numerous occasions, wires were broken during the process of disassembling and reassembling the probe. Also, the limited space between the heat exchanger and the probe

housing was too small to permit the use of MLI. All of these conditions led to larger than optimal parasitic heat leak to the probe.

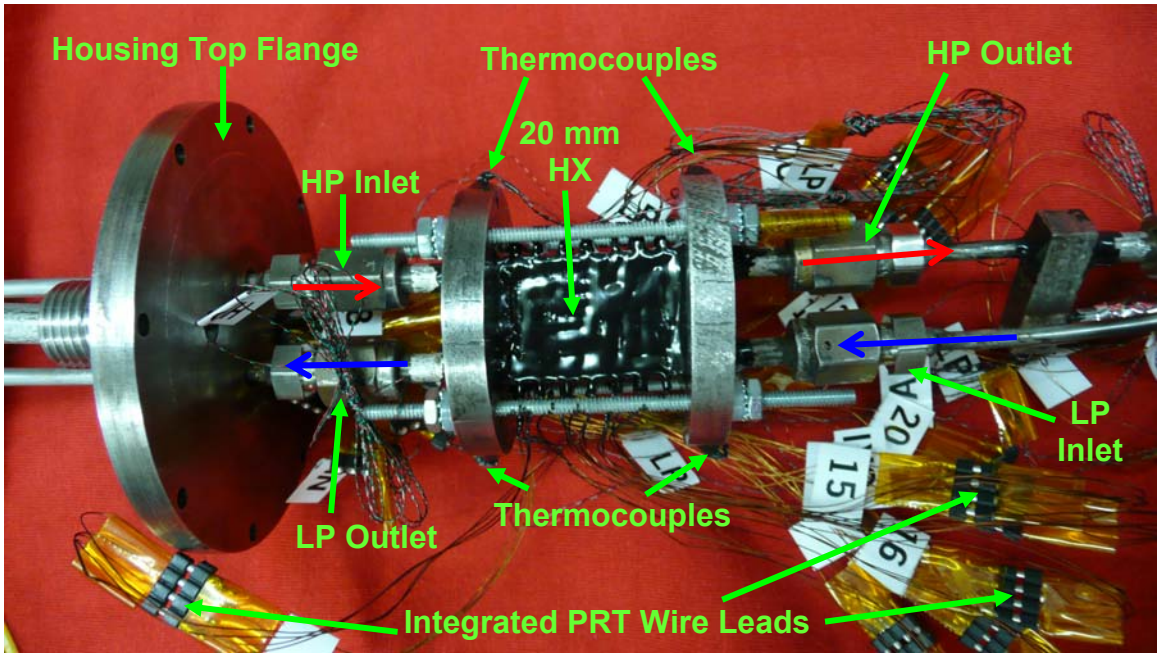

Fig. 3.2.3: Photograph of the thirty-seven die 20 mm heat exchanger attached to the cryosurgical probe assembly

The valve and orifice location are shown in Fig. 3.2.4. The valve and orifice act in parallel to create the isenthalpic pressure drop that is required for a J-T cycle. Type-E penetration thermocouples are used to measure the outlet temperature of the fluid leaving both the valve and the orifice. Unlike the cryogenic test facility where the thermocouple junctions were made with a small solder bead, all thermocouple junctions in the cryosurgical probe prototype were made using a thermocouple welder.

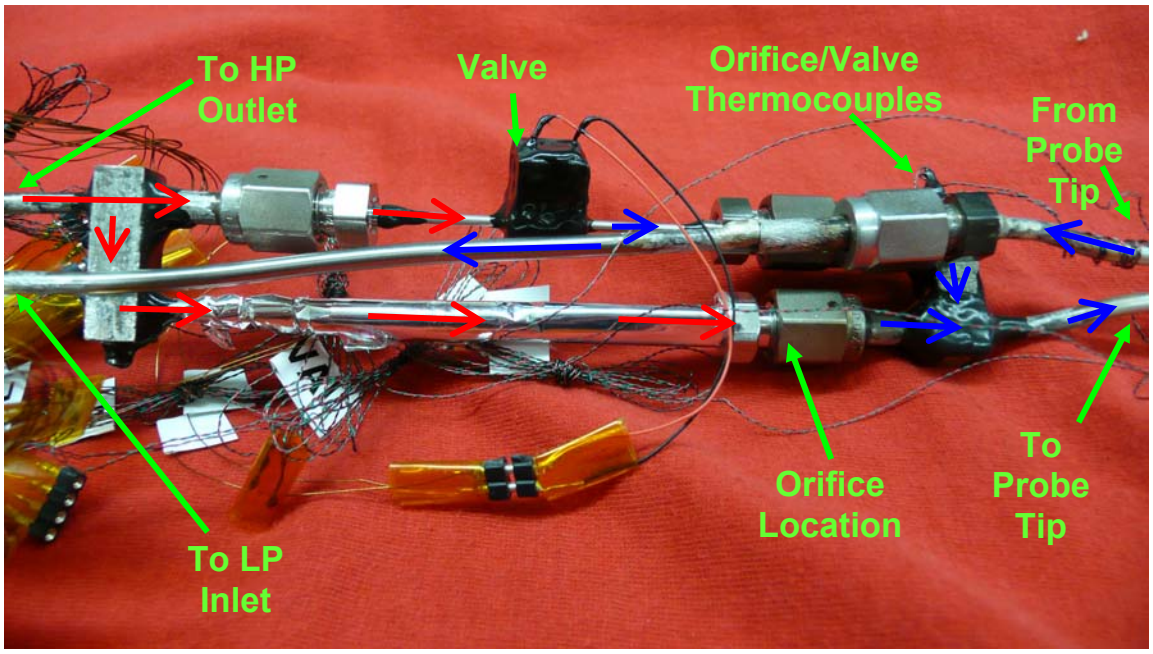

Fig. 3.2.4: Photograph of the valve and orifice installed in parallel. The orifice size is chosen so that the valve can modulates the flow higher and lower than the optimal flow rate.

The tip of the cryosurgical probe prototype is shown in Fig. 3.2.5. A thermocouple was epoxied to the top of the tip in order to measure the tip temperature.

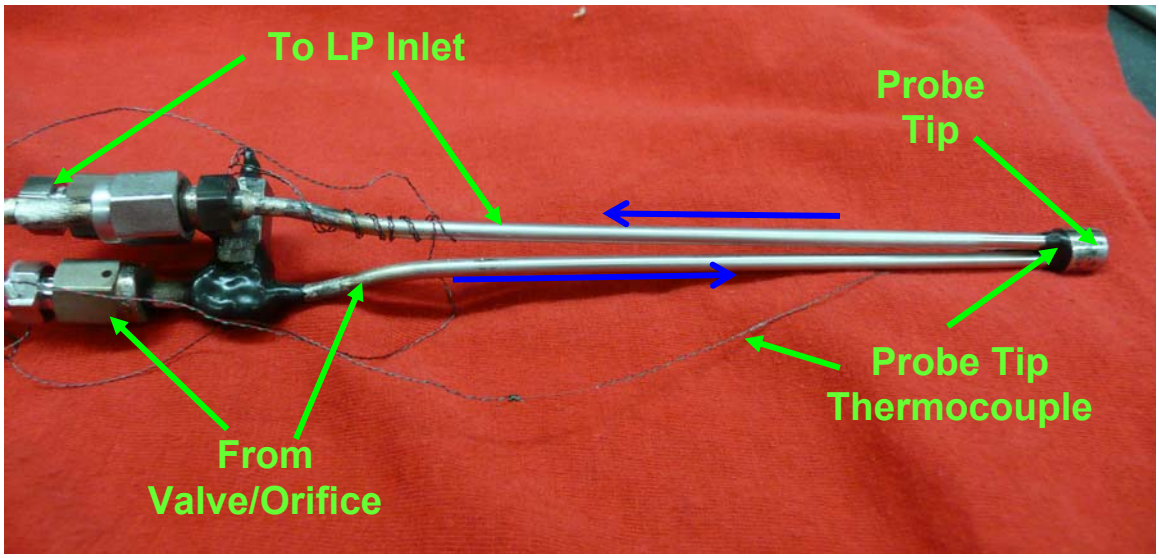

Fig. 3.2.5: Photograph of the cryosurgical probe prototype tip.

A photograph of the entire internal assembly of the cryosurgical probe is shown in Fig. 3.2.6. There is significant room for improvement in the design, particularly with respect to reducing the overall size and mass of the cryosurgical probe prototype which would make the handling of the probe easier and the cool down times faster. If the probe were to be used in a non-experimental application then all of the VCR fittings could be replaced by welds which would significantly

reduce the size and mass of the assembly. The bolts might also be unnecessary, since the probe would not be opened very frequently and the heat exchanger would be subject to less handling. The last area for improvement would be the use of concentric tubes for the tip. In the prototype, two separate tubes were used to bring the fluid into and out of the tip; this approach prevents heat transfer between the streams and therefore allows accurate measurements of the fluid temperature. The drawback to this approach is the tubes near the tip have a tendency to touch the outer wall of the housing and this in turn introduced a significant heat leak. By making the tubes concentric, the tip could made be significantly thinner.

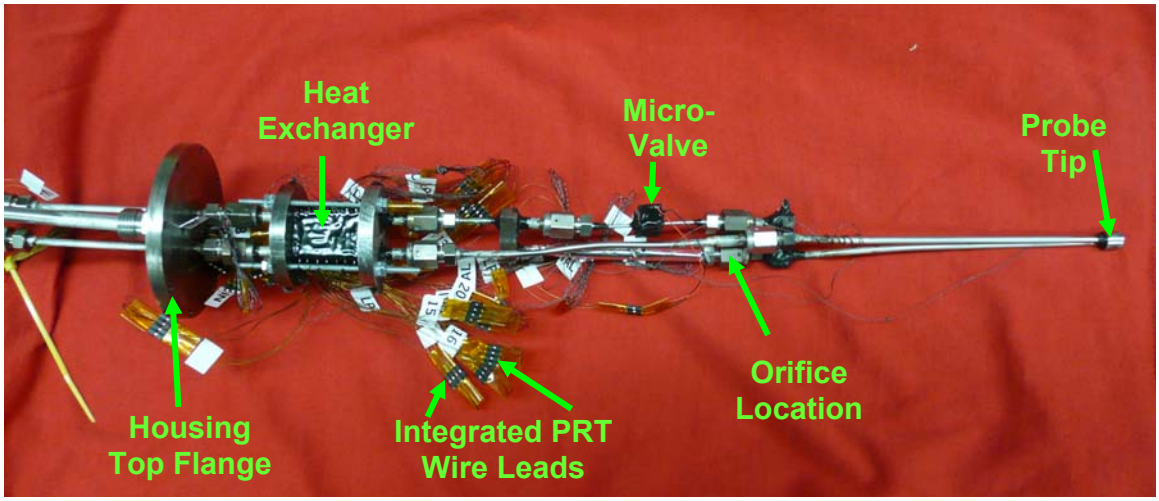

Fig. 3.2.6: Photograph of all components internal to the cryosurgical probe prototype.

A photograph showing the probe housing during an experiment is shown in Fig. 3.2.7. The pressure taps are located close to the probe housing so that the pressures measured are close to the actual pressures at the warm end of the heat exchanger. All of the instrumentation wiring passes through an epoxied feedthrough that is similar to those made for the cryogenic test facility. A VCR fitting is used to connect the vacuum insulation space of the probe to the vacuum pump.

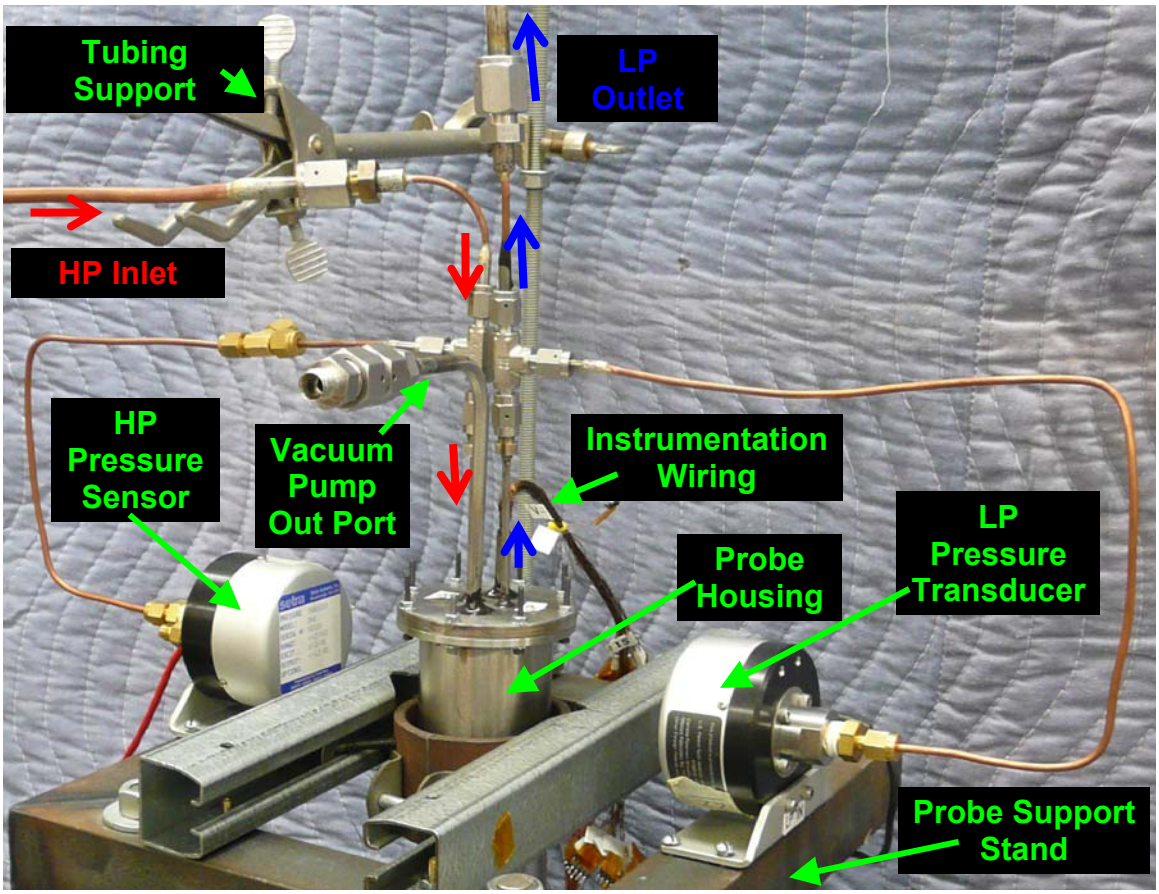

Fig. 3.2.7: Photograph of cryosurgical probe while an experiment is in progress.

Figure 3.2.8 is a photograph of the entire cryosurgical probe prototype. The original tip diameter of the housing was too small to accommodate the probe tip and therefore an adapter flange had to be machined and a larger tube used for the housing tip. Even with the larger housing tip, the internal tubing still appears to be touching the housing. The heat leaks to the cryosurgical probe setup will be discussed in more detail in Chap. 6.

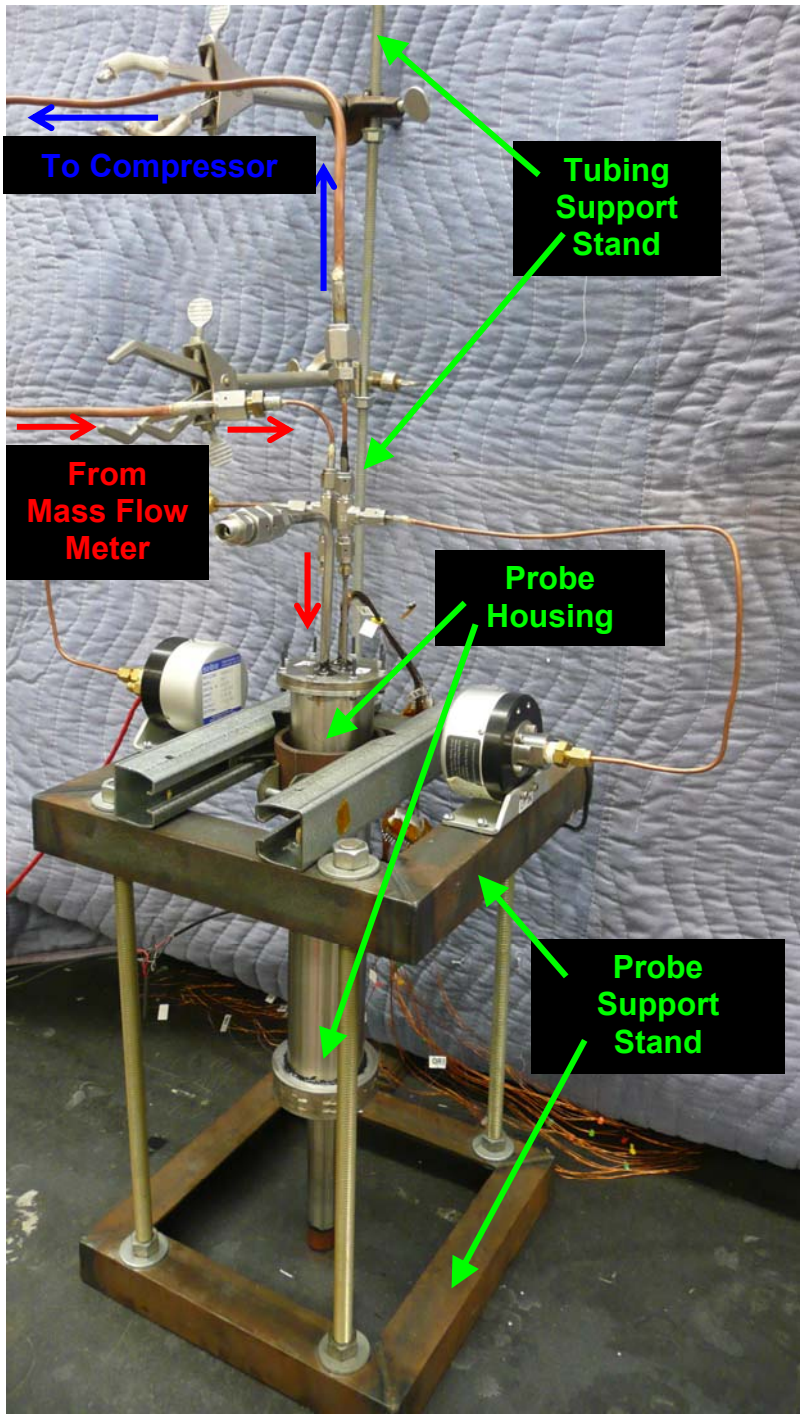

Fig. 3.2.8: A photograph of the entire cryosurgical probe while an experiment is in progress

Chapter 4: Numerical Model for a Perforated Plate Heat Exchanger

4.0 Introduction

A numerical model was written to estimate the performance of a perforated plate heat exchanger. This model is based upon the numerical model described by Nellis [13]. The Nellis model has been verified through comparison with analytical solutions for axial conduction [14] and parasitic heat loads [15, 16]. This chapter begins with a summary of the Nellis model so that the reader is familiar with the necessary energy balances and nomenclature. The second section of the chapter describes the modifications that were made to the Nellis model by the present author in order to accurately model perforated plate heat exchangers. The third section of this chapter uses the numerical model to investigate the effects of axial conduction, parasitic heat loads, and internal fluid leakage on the performance of a perforated plate heat exchanger.

4.1 Numerical Model of Standard Heat Exchanger

Nellis presented his model in both dimensional and non-dimensional forms. Only the non-dimensional model will be discussed in this section so that results are general for all heat exchangers. The Nellis model was written in order to allow the inclusion of temperature-dependent thermophysical properties; however, for this summary the properties are assumed to be constant. The reasons for this simplification will be discussed in detail in Section 4.2. The hot fluid (θ_h), cold fluid (θ_c), and wall (θ_w) dimensionless temperatures are defined using Eq. 4.1.1:

$$\theta = \frac{T - T_{c,in}}{T_{h,in} - T_{c,in}} \tag{4.1.1}$$

where T is the dimensional temperature, θ is the dimensionless temperature, $T_{h,in}$ is the hot fluid inlet temperature, and $T_{c,in}$ is the cold fluid inlet temperature. The dimensionless axial distance from the hot end of the heat exchanger (Z) is defined using Eq. 4.1.2:

$$Z = \frac{X}{L} \tag{4.1.2}$$

where X is the axial distance from the hot end of the heat exchanger and L is the total length of the heat exchanger. In order to accomplish the numerical solution, the heat exchanger is divided into a number of small but finite elements. An energy balance is written for the hot fluid, cold fluid and wall for each of these elements in order to yield a system of algebraic equations. The dimensionless width of an individual element can be calculated using Eq. 4.1.3:

$$\Delta Z = \frac{\Delta X}{L} \tag{4.1.3}$$

where ΔX is the dimensional width of the element. In order to increase the computational efficiency of the numerical model, Nellis used an exponentially distributed grid of nodes with the

recommendation that elements be concentrated towards the heat exchanger ends. The width of an individual element ΔZ_i can be calculated using Eq. 4.1.4.

$$\Delta Z_i = \frac{\exp\left(-\gamma\left(1-2\ i/N\right)\right)}{2\sum_{i=1}^{n/2}\exp\left(-\gamma\left(1-2\ i/N\right)\right)} \tag{4.1.4}$$

where N is the number of elements and γ is the grid concentration factor. If the grid concentration factor γ is equal to 0 then the grid is equally distributed across the length of the heat exchanger. Positive values of γ result in the elements being concentrated near the heat exchanger ends and negative values result in the elements being concentrated in the middle of the heat exchanger.

The capacity rate of a fluid stream is defined as the product of the mass flow rate and the specific heat. Unequal fluid capacity rates will affect performance of the heat exchanger and can be accounted for using the parameters shown in Eq. 4.1.5 and 4.1.6:

$$\mu = \frac{\dot{C}_h}{\dot{C}_{min}} \tag{4.1.5}$$

$$\upsilon = \frac{\dot{C}_c}{\dot{C}_{min}} \tag{4.1.6}$$

where μ is the hot side dimensionless capacity rate, $\dot{C}_h$ is the hot side capacity rate, $\dot{C}_{min}$ is the minimum capacity rate of the two fluid streams, υ is the cold side dimensionless capacity rate, and $\dot{C}_c$ is the cold side capacity rate.

An important parameter for determining heat exchanger performance is the total number of transfer units (*NTU*), which is the ratio of the conductance between the streams (UA_{tot}) to the minimum capacity rate ($\dot{C}_{min}$). For a heat exchanger with axial conduction through the wall separating the fluids, it is necessary to define the number of transfer units relative to each of the individual fluid streams using Eq. 4.1.7 and 4.1.8:

$$NTU_h = \frac{U_h\ A_{s,h}}{\dot{C}_{min}} = \frac{1}{R_h\ \dot{C}_{min}} \tag{4.1.7}$$

$$NTU_c = \frac{U_c\ A_{s,c}}{\dot{C}_{min}} = \frac{1}{R_c\ \dot{C}_{min}} \tag{4.1.8}$$

where the subscripts h and c refer to the hot and cold streams, U is the overall heat transfer coefficient, A_s is the heat transfer surface area, and R is the stream-to-wall thermal resistance. The axial conduction parameter λ is the dimensionless parameter that captures the importance of

axial conduction. The axial conduction parameter is approximately equal to thee ratio of the heat conducted axially to the heat conducted stream-to-stream and is defined using Eq. 4.1.9.

$$\lambda = \frac{k_w \, A_w}{L \, \dot{C}_{min}} = \frac{1}{R_{ac} \, \dot{C}_{min}} \tag{4.1.9}$$

where k_w is the wall thermal conductivity, A_w is the cross sectional area for axial conduction, and R_{ac} is the axial thermal resistance. Parasitic heat loads from ambient will also degrade the performance of cryogenic heat exchangers. Three dimensionless terms are used to account for the parasitic heat loads on the hot stream (χ_h), the cold stream (χ_c), and the wall (χ_w) in Eqs. 4.1.10 - 4.1.12:

$$\chi_h = \frac{\dot{q}_h}{\dot{C}_{min}\left(T_{h,in} - T_{c,in}\right)} \tag{4.1.10}$$

$$\chi_c = \frac{\dot{q}_c}{\dot{C}_{min}\left(T_{h,in} - T_{c,in}\right)} \tag{4.1.11}$$

$$\chi_w = \frac{\dot{q}_w}{\dot{C}_{min}\left(T_{h,in} - T_{c,in}\right)} \tag{4.1.12}$$

where $\dot{q}_h$ is the hot side parasitic heat load, $\dot{q}_c$ is the cold side parasitic heat load, and $\dot{q}_w$ is the wall parasitic heat load. Parasitic heat loads on the MEMS heats exchangers include radiation from the Dewar wall, thermal conduction through the measurement leads for the integrated PRTs, and ohmic dissipation in the integrated PRTs. Parasitic heat loads will result in more heat being transferred to the cold fluid and less heat being transferred from the hot fluid. The purpose of cryogenic heat exchangers is to remove heat from the hot stream, so in cryogenic applications external heat loads are always a penalty.

The locations of the nodes used for the computational grid are shown in Fig. 4.1.1. Each section has a width described by Eq. 4.1.4. The fluid nodes are located at the edges of each section and the wall nodes are located at the center of each element. An extra wall node is placed at both ends of the heat exchanger for the application of wall boundary conditions.

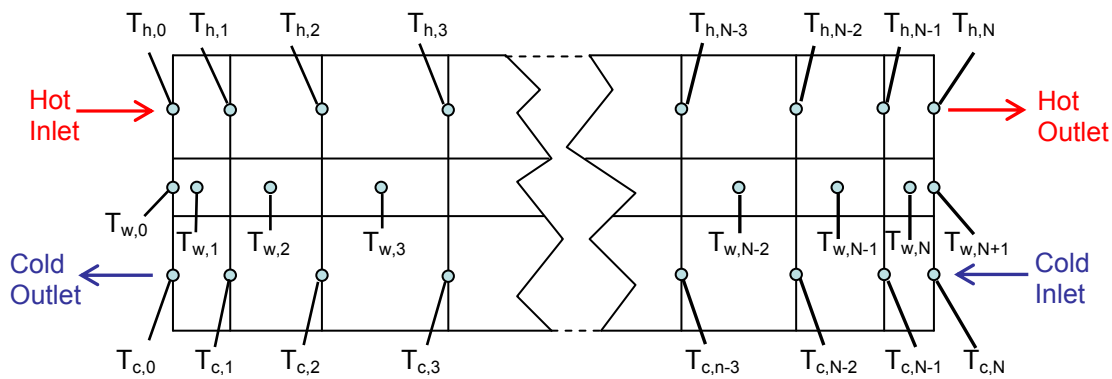

Fig. 4.1.1: Location of nodes used for computational grid in heat exchanger numerical model

The dimensionless hot side energy balance for an arbitrary internal section is presented in Fig. 4.1.2 and leads to Eq. 4.1.13.

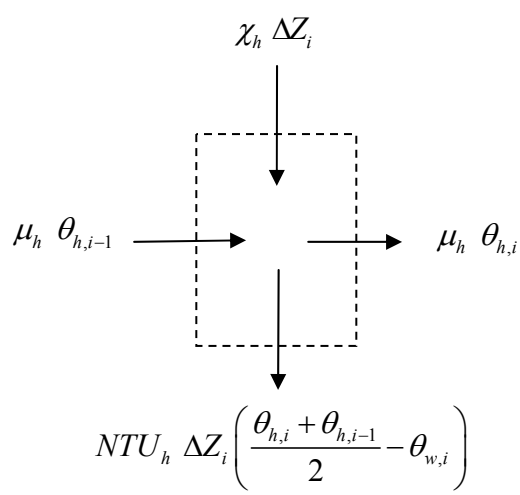

Fig. 4.1.2: Energy balance for the hot stream in the *i*th section of the heat exchanger

$$\mu_h \ \theta_{h,i-1} + \chi_h \ \Delta Z_i = \mu_h \ \theta_{h,i} + NTU_h \ \Delta Z_i \left(\frac{\theta_{h,i} + \theta_{h,i-1}}{2} - \theta_{w,i} \right) \tag{4.1.13}$$

The dimensionless cold side energy balance for an internal section is presented in Fig. 4.1.3 and leads to Eq. 4.1.14.

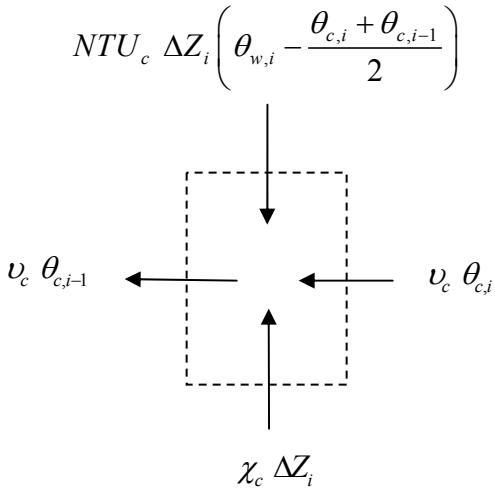

Fig. 4.1.3: Energy balance for the cold stream in the *i*th section of the heat exchanger

$$\chi_c\ \Delta Z_i+\upsilon_c\ \theta_{c,i}+NTU_c\ \Delta Z_i\left(\theta_{w,i}-\frac{\theta_{c,i}+\theta_{c,i-1}}{2}\right)=\upsilon_c\ \theta_{c,i-1} \tag{4.1.14}$$

The dimensionless wall energy balance for an internal section is presented in Fig. 4.1.4 and leads to Eq. 4.1.15.

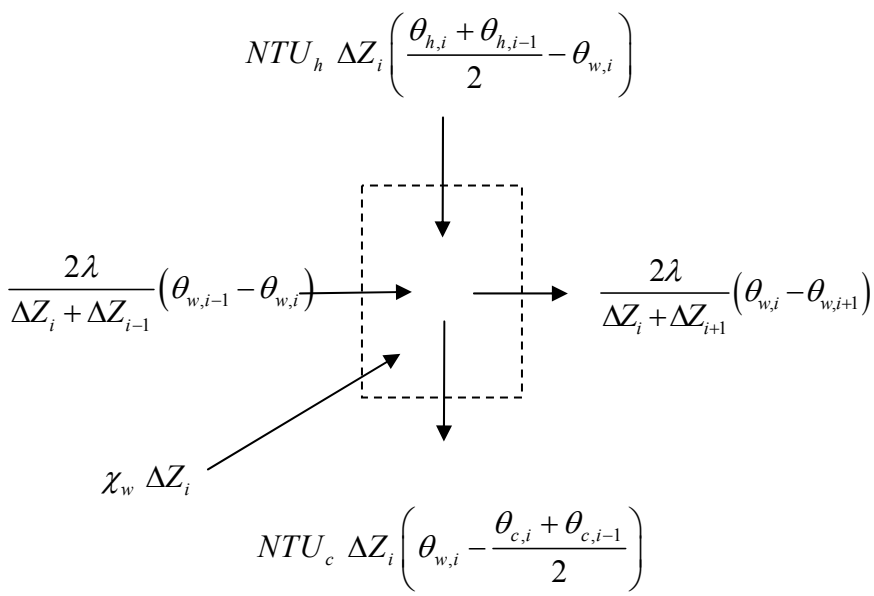

Fig. 4.1.4: Energy balance for the wall in the *i*th section of the heat exchanger

$$\begin{aligned}&\chi_w\ \Delta Z_i+NTU_h\ \Delta Z_i\left(\frac{\theta_{h,i}+\theta_{h,i-1}}{2}-\theta_{w,i}\right)+\frac{2\lambda}{\Delta Z_i+\Delta Z_{i-1}}\left(\theta_{w,i-1}-\theta_{w,i}\right)=\\&NTU_c\ \Delta Z_i\left(\theta_{w,i}-\frac{\theta_{c,i}+\theta_{c,i-1}}{2}\right)+\frac{2\lambda}{\Delta Z_i+\Delta Z_{i+1}}\left(\theta_{w,i}-\theta_{w,i+1}\right)\end{aligned} \tag{4.1.15}$$

The wall elements at the ends of the heat exchanger must be treated separately from the internal nodes due to the decreased axial conduction length. The energy balance on the first wall element is shown in Eq. 4.1.16 and the last wall element is shown in Eq. 4.1.17:

$$\begin{aligned}&\chi_w\ \Delta Z_1 + NTU_h\ \Delta Z_1\left(\frac{\theta_{h,1}+\theta_{h,0}}{2}-\theta_{w,1}\right)+\frac{\lambda}{\Delta Z_0}\left(\theta_{w,0}-\theta_{w,1}\right)=\\&NTU_c\ \Delta Z_i\left(\theta_{w,1}-\frac{\theta_{c,1}+\theta_{c,0}}{2}\right)+\frac{2\lambda}{\Delta Z_1+\Delta Z_2}\left(\theta_{w,1}-\theta_{w,2}\right)\end{aligned} \tag{4.1.16}$$

$$\begin{aligned}&\chi_w\ \Delta Z_N + NTU_h\ \Delta Z_N\left(\frac{\theta_{h,N}+\theta_{h,N-1}}{2}-\theta_{w,N}\right)+\frac{2\lambda}{\Delta Z_N+\Delta Z_{N-1}}\left(\theta_{w,N-1}-\theta_{w,N}\right)=\\&NTU_c\ \Delta Z_N\left(\theta_{w,N}-\frac{\theta_{c,N}+\theta_{c,N-1}}{2}\right)+\frac{\lambda}{\Delta Z_{N+1}}\left(\theta_{w,N}-\theta_{w,N+1}\right)\end{aligned} \tag{4.1.17}$$

Four boundary conditions are required to complete the set of algebraic equations. Two boundary conditions are defined by the fluid inlet temperatures and are shown in Eq. 4.1.18 and 4.1.19:

$$\theta_{h,i=0} = 1 \tag{4.1.18}$$

$$\theta_{c,i=N} = 0 \tag{4.1.19}$$

Nellis presented equations for two different types of wall boundary conditions. If the heat exchanger ends are adiabatic, then by definition there is no axial heat flow into the ends which is accomplished by setting the end temperatures equal to the temperature of the adjacent wall node as shown in Eq 4.1.20 and 4.1.21:

$$\theta_{w,i=0} = \theta_{w,i=1} \tag{4.1.20}$$

$$\theta_{w,i=N} = \theta_{w,i=N+1} \tag{4.1.21}$$

The wall ends could also be fixed to specified temperatures for the final two boundary conditions. The specified temperature boundary condition equations are shown in Eq. 4.1.22 and 4.1.23:

$$\theta_{w,i=0} = \theta_{w,hot} \tag{4.1.22}$$

$$\theta_{w,i=N+1} = \theta_{w,cold} \tag{4.1.23}$$

where $\theta_{w,hot}$ is the wall hot end temperature and $\theta_{w,cold}$ is the wall cold end temperature. The system of equations can be solved using the energy balances for each element and the four boundary conditions to yield the temperature distribution within the heat exchanger.

4.2 Numerical Model of Perforated Plate Heat Exchanger

Numerical models of cryogenic heat exchangers generally require the use of temperature-dependent fluid and material properties in order to maintain sufficient accuracy. This is because thermophysical properties are often highly temperature dependent at cryogenic temperatures and also because these heat exchangers typically span a large range of temperatures. The drawbacks to using temperature-dependent properties are increased computing time and the fact that the nonlinearity introduced by the temperature-dependence will often prevent the model from converging to the solution. If the initial guess values are too far from the correct values, then the thermophysical properties are evaluated at the wrong temperatures and this may cause the model to adjust the heat exchanger temperature distribution in the wrong direction. Eventually, this can lead to a "runaway" situation in which the model moves further and further from the correct solution.

Perforated plate heat exchangers are fabricated using interleaving layers of high-conductivity plates and low-conductivity spacers. The fluid temperature difference across an individual plate within the heat exchanger is likely to be very small (1 to 2 K). Therefore, only small errors are introduced if fluid and material properties evaluated at the average temperature for each plate and then are assumed to be constant across each plate.

The perforated plate heat exchanger is modeled as a series of constant property heat exchangers, with each heat exchanger being a single perforated plate. The constant property Nellis model described in Section 4.1 is used to calculate the temperature distribution within each plate (i.e., for each die). Solving this set of implicit equations is facilitated by the use of an iterative equation solver such as EES [17] and a set of reasonable initial guess values. The surface area of the spacers is so small and the thermal conductivity is so low relative to the perforated plates that stream-to-stream heat transfer in the spacers can be neglected with minimal error introduction. This is a conservative assumption as any small additional heat transfer that occurs between the plates will improve the heat exchanger performance.

Even though the stream-to-stream heat transfer is neglected in the spacers, there will be a finite and important heat transfer that is conducted axially between each perforated plate along the spacers. Therefore, the ends of each perforated plate are neither adiabatic nor do they have constant wall temperature. The wall boundary conditions that are used in the Nellis model must be adjusted to account for heat being conducted to and from each plate. Two new dimensionless parameters were defined in order to account for heat transfer to and from the ends of a heat exchanger. Similar to the parasitic heat loads, the dimensionless wall end conduction parameters were defined by dividing the specified edge conduction rates by the maximum possible stream-to-stream heat transfer rate, as shown in Eq. 4.2.1 and 4.2.2:

$$\chi_{w,h} = \frac{\dot{q}_{w,h}}{\dot{C}_{min}\left(T_{h,in} - T_{c,in}\right)} = \frac{\lambda\left(\theta_{w,0} - \theta_{w,1}\right)}{\Delta Z_0} \tag{4.2.1}$$

$$\chi_{w,c} = \frac{\dot{q}_{w,c}}{\dot{C}_{min}\left(T_{h,in} - T_{c,in}\right)} = \frac{\lambda\left(\theta_{w,N} - \theta_{w,N+1}\right)}{\Delta Z_{N+1}} \tag{4.2.2}$$

where $\chi_{w,h}$ and $\dot{q}_{w,h}$ are the dimensionless and dimensional quantities of heat conducted to the hot end of the heat exchanger, respectively, and $\chi_{w,c}$ and $\dot{q}_{w,c}$ are the dimensionless and dimensional quantities of heat conducted from the cold end of the heat exchanger, respectively.

A schematic showing the numbering system for a perforated plate heat exchanger with *N* plates is shown in Fig. 4.2.1. Spacers are located between each perforated plate and therefore there are a total of *N*-1 spacers in the heat exchanger. The MEMS heat exchangers studied for this thesis were fabricated from an equal number of spacers and plates. This configuration would have required an additional spacer on one of the heat exchanger ends. The MEMS heat exchangers were not marked during the assembly process to indicate which end had the additional spacer. The addition of an end spacer should improve the performance of the heat exchanger slightly. Therefore, the model was written with the conservative assumption that there was no spacer on either end of the heat exchanger.

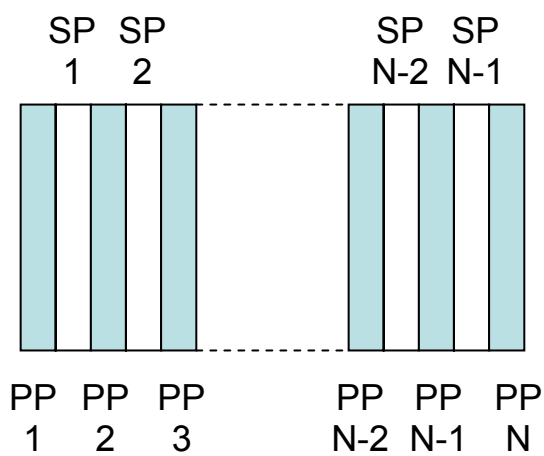

Fig. 4.2.1: Numbering system for perforated plates (PP) and spacers (SP) in the numerical model of a perforated plate heat exchanger with *N* plates. The plates are represented by the solid boxes and the spacers are represented by the white boxes.

The quantity of heat conducted to and from the ends of the jth plate of the heat exchanger can be calculated using the axial resistance of the spacer using Eqs. 4.2.3 and 4.2.4:

$$\dot{q}_{w,h,j} = \frac{\left(T_{w,c,j-1} - T_{w,h,j}\right)}{R_{sp,j-1}} \tag{4.2.3}$$

$$\dot{q}_{w,c,j} = \frac{\left(T_{w,c,j} - T_{w,h,j+1}\right)}{R_{sp,j}} \tag{4.2.4}$$

where the subscript j refers to the plate or spacer location, R_{sp} is the axial resistance of the spacer, $T_{w,h}$ is the wall temperature at the hot end of the plate, and $T_{w,c}$ is the wall temperature at the cold end of the plate.

The model accounts for the parasitic losses typically included in cryogenic heat exchanger models such as axial conduction and radiant heat loads. However, perforated plate heat exchangers can have an additional parasitic heat load that is not typically accounted for in cryogenic heat exchanger models. Internal fluid leakage is a common problem in perforated plate heat exchangers due to the large number of joints separating the two streams.

The probability of leakage through a joint is significantly higher than leakage due to one of the plates or spacers physically breaking. Therefore, all fluid leaks are assumed to only occur at joint locations. The heat exchangers being studied for this thesis are all intended for use in a Joule-Thomson (JT) cycle. The JT cycle requires that the hot fluid be at a substantially higher pressure than the cold fluid. Therefore, for the remainder of this thesis it will be assumed that the hot fluid always leaks to the cold fluid rather than the other way around. However, in other applications the leakage may be in the opposite direction and it should be noted that the model could have easily been written to simulate leakage in either direction.

The joint where the leak occurs must be specified. However, the characteristics of the leak are not readily known. The leak passage might be short and straight or long and jagged. The channel could have a constant cross sectional area or a variable cross sectional area. The model should be written in a way that as few variables as possible need to be specified. Figure 4.2.2 is a representative plot of the dimensionless temperature distribution within a perforated plate heat exchanger. The heat exchanger shown in Fig. 4.2.2 includes three perforated plates and two spacers, with each plate and spacer having a dimensionless length of one. Two possible leak locations are considered for each perforated plate. The hot side of the middle plate is labeled as Location 1 and the cold side of the middle plate is labeled Location 2 in Fig. 4.2.2. An unknown quantity of heat will be transferred from the hot fluid to the perforated plate as it passes through the leakage channel. The lower limit of thermal interaction between the fluid and wall is that no heat is transferred so that the fluid enters the cold stream at the same temperature that it left the hot stream. The upper limit of thermal interaction is that the leaking fluid reaches the wall temperature and enters the cold stream at the wall temperature.

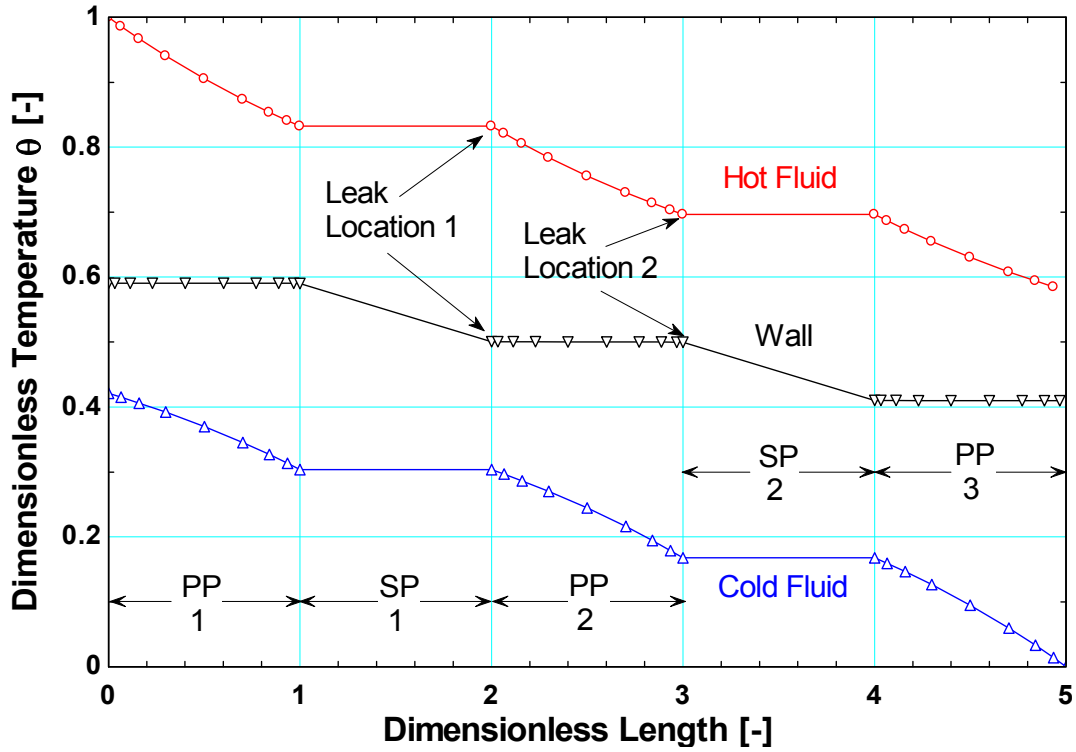

Fig. 4.2.2: Plot of a representative dimensionless temperature distribution within a perforated plate heat exchanger. The heat exchanger shown in the plot has three perforated plates (PP) and two spacers (SP), with each plate and spacer assumed to have a dimensionless length of one.

The quantity of heat transferred from the leaking fluid to the wall for the *j*th plate in a heat exchanger can be calculated using Eq. 4.2.5 if it is on the hot end of the plate and Eq. 4.2.6 if it is on the cold end of the plate:

$$\dot{q}_{h,leak,j} = Frac_{heat}\ \dot{m}_{h,leak,j}\ Cp_{h,j}\left(T_{h,in,j} - T_{w,h,j}\right) \tag{4.2.5}$$

$$\dot{q}_{c,leak,j} = Frac_{heat}\ \dot{m}_{c,leak,j}\ Cp_{h,j}\left(T_{h,out,j} - T_{w,c,j}\right) \tag{4.2.6}$$

where $\dot{q}_{h,leak,j}$ is the heat load on the hot end of the plate due to the leakage (not to be confused with the heat load from the adjacent plate due to conduction through the spacer), $\dot{m}_{h,leak,j}$ is the mass flow rate of the hot fluid through the leak channel on the hot end of the plate, $Cp_{h,j}$ is the specific heat of the hot fluid, $T_{h,in,j}$ is the hot fluid inlet temperature for the perforated plate, $T_{w,h,j}$ is the hot end temperature of the wall, $\dot{q}_{c,leak,j}$ is the heat load on the cold end of the plate due to leakage, $\dot{m}_{c,leak,j}$ is the mass flow rate of the hot fluid through the leak channel on the cold end of the perforated plate, $T_{h,out,j}$ is the hot fluid outlet temperature for the plate, and $T_{w,c,j}$ is the cold end wall temperature. The variable $Frac_{heat}$ is the fraction of the maximum possible thermal interaction between the fluid and the plate; this quantity is varied between 0 and 1 in order to

simulate no thermal interaction and the maximum possible heat transfer between the leak stream and the wall, respectively.

The quantity of heat conducted to and from the ends of the heat exchanger, originally shown in Eq. 4.2.3 and Eq. 4.2.4, must be modified to include the heat loads from the internal leakage. The actual quantity of heat conducted to and from the ends of the *j*th plate can be calculated using Eq. 4.2.7 and 4.2.8:

$$\dot{q}_{w,h,j} = \frac{\left(T_{w,c,j-1} - T_{w,h,j}\right)}{R_{sp,j-1}} + \dot{q}_{h,leak,j} \tag{4.2.7}$$

$$\dot{q}_{w,c,j} = \frac{\left(T_{w,c,j} - T_{w,h,j+1}\right)}{R_{sp,j}} - \dot{q}_{c,leak,j} \tag{4.2.8}$$

One of the assumptions for the perforated plate model was that there was no stream-to- stream heat transfer in the spacers. Thus the temperature of the fluid leaving one plate is identical to the temperature of the fluid entering the next plate in the direction of the fluid flow. However, this is not the case if internal leakage is present since part of the hot stream will be mixing with the cold stream and can result in a very large stream-to-stream interaction. The hot stream is assumed to be isothermal while flowing across the spacer since there is no stream-to-stream heat transfer and no fluid is added to the hot stream. However, an energy balance must be used to determine the temperature change of the cold fluid as it flows from plate to plate. An energy balance for the *j*th spacer of a perforated plate heat exchanger is shown schematically in Fig. 4.2.3 and leads to Eq. 4.2.9:

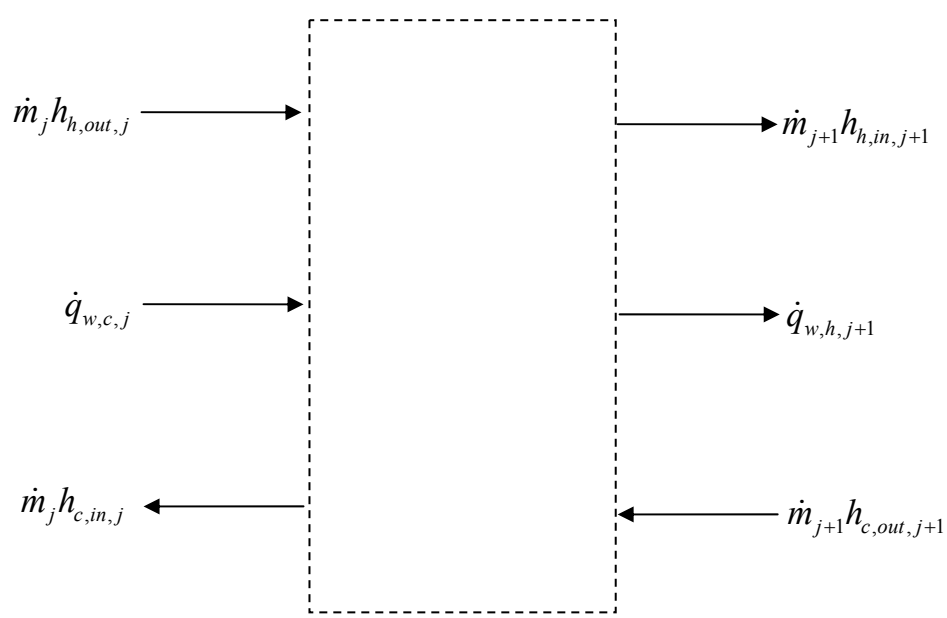

Fig. 4.2.3: Energy balance on the spacer used to determine the inlet temperature of the cold fluid to the *j*th perforated plate in the heat exchanger.

$$\dot{m}_j \; h_{h,out,j} + \dot{q}_{w,c,j} + \dot{m}_{j+1} \; h_{c,out,j+1} = \dot{m}_{j+1} \; h_{h,in,j+1} + \dot{m}_j \; h_{c,in,j} + \dot{q}_{w,h,j+1} \tag{4.2.9}$$

where $h_{h,out,j}$ is the hot fluid specific enthalpy at the outlet of the jth plate, $h_{h,in,j+1}$ is the hot fluid specific enthalpy at the inlet to the $j+1$th plate, $h_{c,out,j+1}$ is the cold fluid specific enthalpy at the outlet of the j+1th plate, and $h_{c,in,j}$ is the cold fluid specific enthalpy at the inlet to the jth plate. A mass balance on the flow passing through the region between the plates leads to:

$$\dot{m}_j = \dot{m}_{j+1} + \dot{m}_{c,leak,j} + \dot{m}_{h,leak,j+1} \tag{4.2.9}$$

where $\dot{m}_j$ is the mass flow rate through the jth plate, $\dot{m}_{j+1}$ is the mass flow rate through the j+1th plate, $\dot{m}_{c,leak,j}$ is the mass flow rate of the leak on the cold end of the jth plate, and $\dot{m}_{h,leak,j+1}$ is the mass flow rate of the leak on the hot end of the j+1th plate.

The heat exchanger effectiveness for any particular plate can be defined based on the cooling provided to the hot stream (Eq. 4.2.10) or the heating provided to the cold stream (Eq. 4.2.11) normalized by the maximum possible heat transfer rate. The effectiveness of the jth plate in the heat exchanger can be calculated using Eq. 4.2.10 for the hot side effectiveness ($\boldsymbol{\varepsilon}_{h,j}$) and Eq. 4.2.11 for the cold side effectiveness ($\boldsymbol{\varepsilon}_{c,j}$).

$$\varepsilon_{h,j} = \frac{\dot{C}_{h,j}\left(T_{h,in,j} - T_{h,out,j}\right)}{\dot{C}_{min,j}\left(T_{h,in,j} - T_{c,in,j}\right)} = \mu_j\left(1 - \theta_{h,out,j}\right) \tag{4.2.10}$$

$$\varepsilon_{c,j} = \frac{\dot{C}_{c,j}\left(T_{c,out,j} - T_{c,in,j}\right)}{\dot{C}_{min,j}\left(T_{h,in,j} - T_{c,in,j}\right)} = \upsilon_j\left(\theta_{c,out,j}\right) \tag{4.2.11}$$

The definition of effectiveness becomes more complicated when the entire perforated plate heat exchanger is considered due to the temperature-dependent specific heats and the potential for changing mass flow rates due to leakage. If the specific heat is constant across the length of the heat exchanger and there is no internal fluid leakage then the hot and cold side effectiveness can be calculated using the standard definition of heat exchanger effectiveness shown in Eq. 4.2.12 and 4.2.13:

$$\varepsilon_h = \frac{\dot{q}_{h,net}}{\dot{q}_{max}} = \frac{\dot{C}_h\left(T_{h,in,1} - T_{h,out,N}\right)}{\dot{C}_{min}\left(T_{h,in,1} - T_{c,in,N}\right)} \tag{4.2.12}$$

$$\varepsilon_c = \frac{\dot{q}_{c,net}}{\dot{q}_{max}} = \frac{\dot{C}_c\left(T_{c,out,1} - T_{c,in,N}\right)}{\dot{C}_{min}\left(T_{h,in,1} - T_{c,in,N}\right)} \tag{4.2.13}$$

where $\dot{q}_{h,net}$ is the net heat transfer from the hot fluid, $\dot{q}_{c,net}$ is the net heat transfer to the cold fluid, and $\dot{q}_{max}$ is the maximum possible heat transfer in the heat exchanger. If the specific heats vary across the length of the heat exchanger but no internal fluid leakage is present the total effectiveness can be calculated using Eq. 4.2.14 and Eq. 4.2.15:

$$\varepsilon_h = \frac{\dot{q}_{h,net}}{\dot{q}_{max}} = \frac{\sum_{j=1}^{j=N} \dot{m}_j Cp_{h,j}\left(T_{h,in,j} - T_{h,out,j}\right)}{\dot{m}_1 \min\left[\left(h_{h,in} - h_{h,out,min}\right), \left(h_{c,out,max} - h_{c,in}\right)\right]} \tag{4.2.14}$$

$$\varepsilon_c = \frac{\dot{q}_{c,net}}{\dot{q}_{max}} = \frac{\sum_{j=1}^{j=N} \dot{m}_j Cp_{c,j}\left(T_{c,out,j} - T_{c,in,j}\right)}{\dot{m}_1 \min\left[\left(h_{h,in} - h_{h,out,min}\right), \left(h_{c,out,max} - h_{c,in}\right)\right]} \tag{4.2.15}$$

where $h_{h,in}$ and $h_{c,in}$ are the hot and cold fluid enthalpies at the inlet to the heat exchanger respectively, $h_{h,out,min}$ is hot fluid enthalpy evaluated at the cold fluid inlet temperature and hot fluid outlet pressure, and $h_{c,out,max}$ is the fluid enthalpy evaluated at the hot fluid inlet temperature and cold fluid outlet pressure. The enthalpies $h_{h,out,min}$ and $h_{c,out,max}$ are evaluated at the outlet pressures of their respective fluids so that the calculated heat exchanger effectiveness is a measure of the thermal performance of the heat exchanger. The fluid pressure and mass flow rate at the hot fluid outlet of the heat exchanger both affect the performance of a J-T cycle and will be discussed in Chapter 4.3.

The hot side effectiveness (Eq. 4.2.14) remains valid if internal fluid leakage is present since no heat is transferred in the spacers and leak is assumed to always be from the hot fluid to the cold fluid. However, the cold side fluid temperature can increase across the spacer due to mixing with the leaking hot fluid. A new definition of cold side effectiveness that accounts for the energy gain across the spacers from internal leakage is shown in Eq. 4.2.16:

$$\varepsilon_c = \frac{\dot{q}_{c,net}}{\dot{q}_{max}} = \frac{\sum_{j=1}^{j=N}\left[\dot{m}_j Cp_{c,j}\left(T_{c,out,j} - T_{c,in,j}\right)\right] + \sum_{j=1}^{j=N-1}\left[\dot{m}_j h_{c,in,j} - \dot{m}_{j+1} h_{c,out,j+1}\right]}{\dot{m}_1 \min\left[\left(h_{h,in} - h_{h,out,min}\right), \left(h_{c,out,max} - h_{c,in}\right)\right]} \tag{4.2.16}$$

4.3 Effect of Parasitic Losses on Perforated Plate Heat Exchanger Performance

This section begins with a discussion of the effects of axial conduction on the temperature distribution and effectiveness of perforated plate heat exchangers. Conduction to and from the ends of the heat exchanger will also be covered as part of the axial conduction discussion. The effects of parasitic heat loads on the hot fluid, wall, and cold fluid on the heat exchanger effectiveness will be examined. The discussion of axial conduction and parasitic heat loads will be facilitated by modeled results for a hypothetical heat exchanger with assumed fluid properties and thermal resistances. The thermal resistances chosen are within the range of expected thermal resistances in the MEMS heat exchangers.

The final topic of this section will be the effect of internal leakage on J-T heat exchangers. The section on internal leakage will assume constant thermal resistances but will consider two real fluids, helium and ethane. Helium and ethane were chosen due to their significantly different J-T coefficients, with helium exhibiting slight warming and ethane exhibiting significant cooling while undergoing isenthalpic expansion.

To demonstrate the effects of axial conduction in perforated plates and spacers, three variations of a hypothetical heat exchanger were modeled. The thermal resistances and fluid properties of the three heat exchangers are shown in Table 4.3.1. For all cases there were no parasitic heat loads, no internal leakage, and the mass flow rate was held constant at 0.05 g/s. Each heat exchanger was assumed to have three plates and two spacers, with each plate and spacer having a dimensionless length of 1.

Table 4.3.1: The specific heats and thermal resistances for a heat exchanger with no axial conduction (Case 1), axial conduction only in perforated plates (Case 2), and axial conduction in both the perforated plates and the spacers (Case 3) for the plots shown in Figs. 4.3.1-4.3.4. All values are for the *j*th perforated plate or spacer and are constant for all plates and spacers.

Case	$R_{h,j}$ [K/W]	$R_{c,j}$ [K/W]	$Cp_{h,j}$ [J/kg-K]	$Cp_{c,j}$ [J/kg-K]	$R_{ac,j}$ [K/W]	$R_{sp,j}$ [K/W]
1	5	5	5000	5000	9999	9999
2	5	5	5000	5000	0.05	9999
3	5	5	5000	5000	0.05	10

The temperature distribution for Case 1 is shown in Fig. 4.3.1. Case 1 has very high thermal resistances in the axial direction for both the perforated plates and spacers. Therefore, the temperature distributions within the plates of the heat exchanger are linear and parallel for the hot fluid, cold fluid, and wall. The wall and fluid temperatures remain nearly constant across the spacers. This heat exchanger has no loss mechanisms and represents the best possible performance for this heat exchanger with the stream-to-stream resistances and fluid specific heats shown in Table 4.3.1.

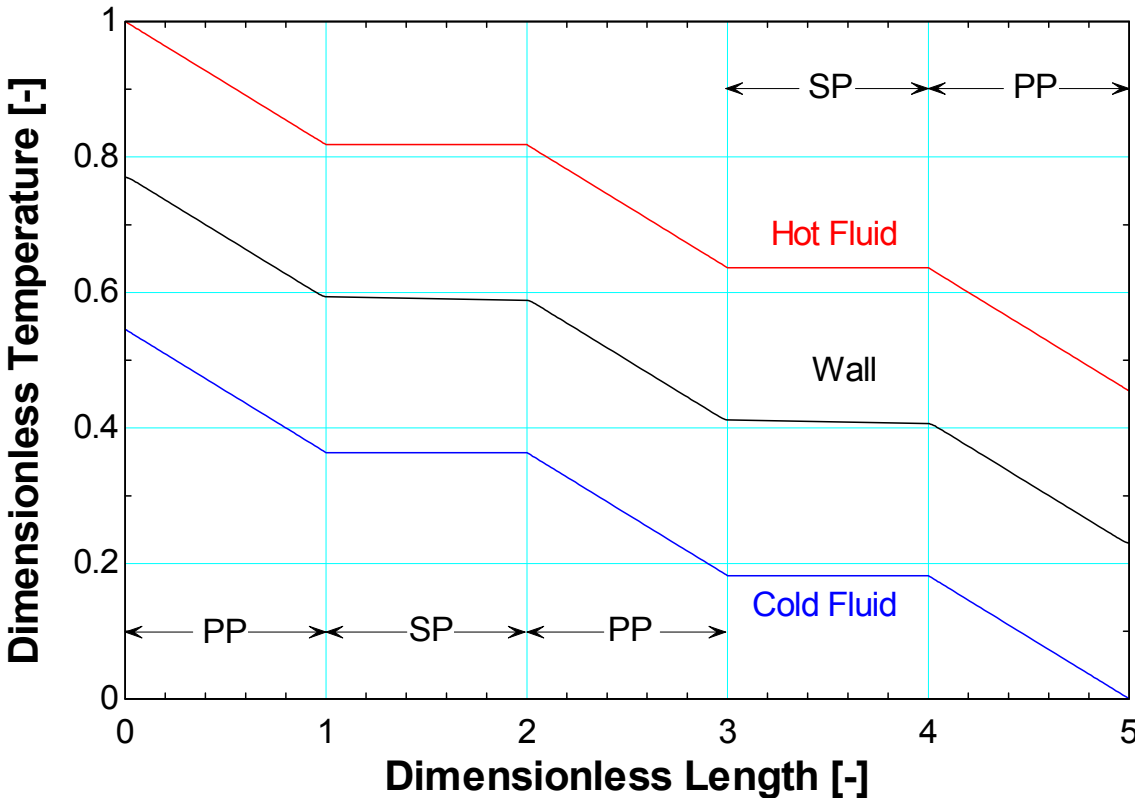

Fig. 4.3.1: Temperature distribution for Case 1 which has no axial conduction in the perforated plates or spacers

The temperature distribution for Case 2 is shown in Fig. 4.3.2. Case 2 is identical to Case 1 except that the thermal resistance of the perforated plates in the axial direction has been significantly reduced. Therefore, the wall temperature within the plate is essentially constant and the fluid temperatures asymptotically approach the wall temperature as the fluids flow across the plate in either direction. The fluid temperature remains constant across the spacers (due to the assumption of no stream-to-stream heat transfer in the spacers), but now there is a substantial temperature gradient across the axial length of the spacers.

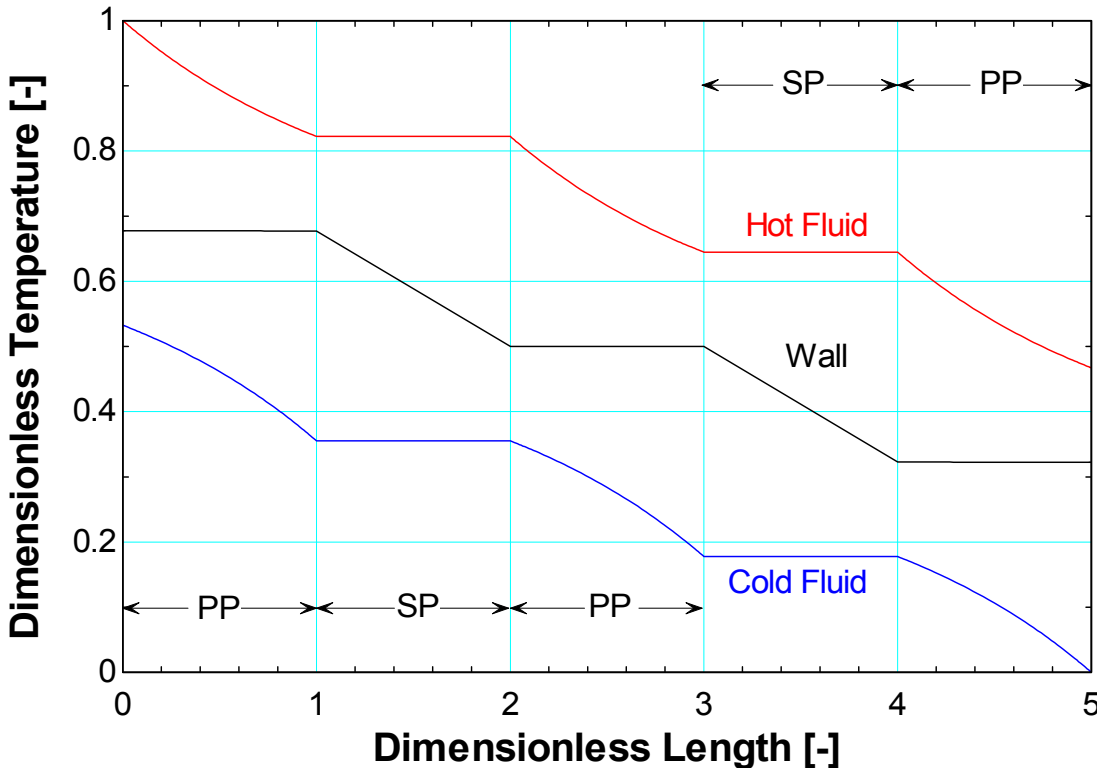

Fig. 4.3.2: Temperature distribution for Case 2 which has axial conduction in perforated plates

The temperature distribution for Case 3 is shown in Fig. 4.3.3. Case 3 is identical to Case 2 except that the axial resistance of the spacers has been significantly reduced. The temperature distributions for Case 2 and Case 3 look very similar. However, the wall temperature is closer to the hot fluid at the cold end and closer to the cold fluid at the hot end of the heat exchanger in Case 3. Axial conduction reduces the temperature difference between the hot end and cold end wall temperatures by conducting heat along the length of the heat exchanger, which lowers the hot end temperature and raises the cold end temperature of the wall.

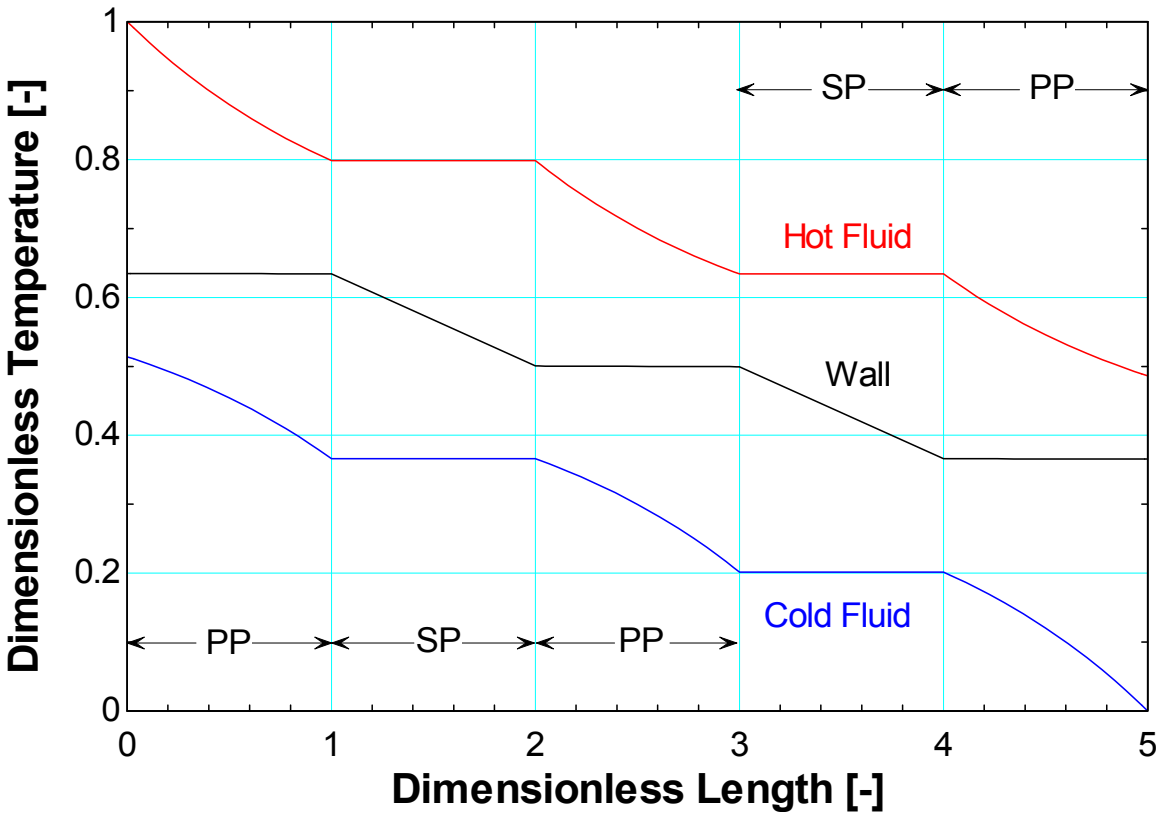

Fig. 4.3.3: Temperature distribution for Case 3 which has axial conduction in perforated plates and spacers

The modeled results of the heat exchanger effectiveness as a function of the total number of transfer units for all three variations of the hypothetical heat exchanger are shown in Fig. 4.3.4. At high mass flow rates (low *NTU*) the effects of axial conduction are very small, but at low mass flow rates (high *NTU*) the effects of axial conduction can be quite large. The modeled results show that axial conduction in both the perforated plates and the spacers reduce the performance of the heat exchanger.

At low *NTU*, the amount of heat conducted axially is small relative to the total amount of heat transferred in the heat exchanger and therefore the effects of axial conduction are minor. At high *NTU* the amount of heat conducted axially is large relative to the total amount of heat transferred in the heat exchanger, so the effects of axial conduction on a can be quite large. As shown in Fig. 4.3.4, Case 1 (which has no loss mechanisms) has an effectiveness that continues to increase as the mass flow rate is reduced (*NTU* is increased). In contrast, Case 3 (which has axial conduction in plates and spacers) has an effectiveness that peaks around *NTU* = 4 and then starts decreasing as the mass flow rate is reduced (increasing *NTU*).

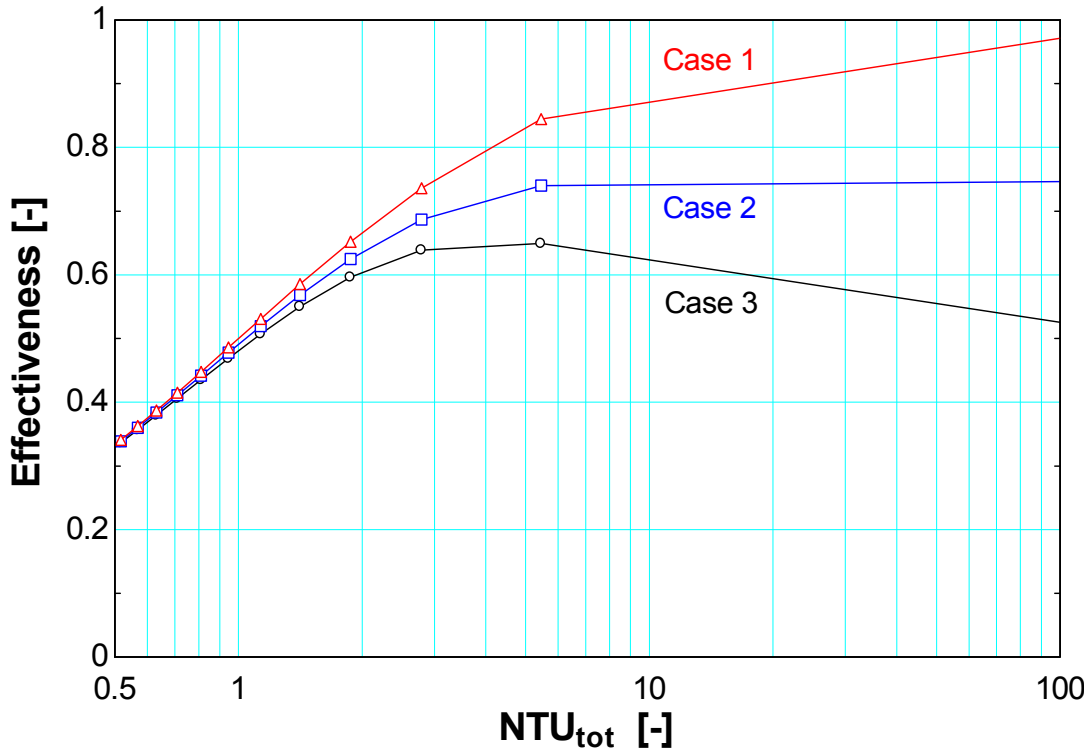

Fig. 4.3.4: Effectiveness as a function of the total number of transfer units for the three variations of the hypothetical heat exchanger listed in Table 4.3.1

The next point to consider is conduction to and from the ends of the heat exchanger. Heat exchangers will always have some type of fluid connection at the ends that will allow at least small quantities of heat to be conducted to or from the heat exchanger. Conduction to and from the ends of the heat exchanger can increase or decrease the performance depending on the direction of heat flow and the application of the heat exchanger.

Shown in Table 4.3.2 are variations of the hypothetical heat exchanger that will be used to demonstrate the effects of end conduction. Case 3 is considered to be the baseline case with adiabatic ends. The dimensionless end conduction rates $\chi_{w,h}$ and $\chi_{w,c}$ are defined by Eq. 4.2.1 and Eq. 4.2.2. The end conduction rate, if applied, was chosen to be 5% of the maximum possible stream-to-stream heat transfer rate in the heat exchanger so that the effects would be clearly visible on plots. Case 4 has heat conducted to the warm end, Case 5 has heat conducted from the warm end, Case 6 has heat conducted from the cold end, and Case 7 has heat conducted to the cold end.

Heat can be conducted to or from heat exchanger ends for number of reasons. The MEMS heat exchangers will have heat conducted directly from the warm end to the cold end through the support bolts. Heat exchangers have fluid connections at either end that may allow thermal communication with cryocoolers, heaters, or the environment. Allowing heat to be conducted to or from the ends of the heat exchanger increases the flexibility of the numerical model.

Table 4.3.2: Variations of the hypothetical heat exchanger used to show the effect of conduction to and from the heat exchanger ends. Case 3 is a heat exchanger with adiabatic ends, Case 4 has heat conducted to the warm end, Case 5 has heat conducted from the warm end, Case 6 has heat conducted from the cold end, and Case 7 has heat conducted to the cold end.

Case	$R_{h,j}$ [K/W]	$R_{c,j}$ [K/W]	$Cp_{h,j}$ [J/kg-K]	$Cp_{c,j}$ [J/kg-K]	$R_{ac,j}$ [K/W]	$R_{sp,j}$ [K/W]	$X_{w,h}$ [-]	$X_{w,c}$ [-]
3	5	5	5000	5000	0.05	10	0	0
4	5	5	5000	5000	0.05	10	0.05	0
5	5	5	5000	5000	0.05	10	-0.05	0
6	5	5	5000	5000	0.05	10	0	0.05
7	5	5	5000	5000	0.05	10	0	-0.05

The plot shown in Fig. 4.3.5 compares the effectiveness for Case 3 (adiabatic ends) and Case 4 (heat conducted to the warm end) as a function of total *NTU*. Since additional heat is being conducted to the heat exchanger, the cold fluid is expected to be heated to a higher temperature. The cold fluid will be at a higher average temperature, which will result in a smaller average temperature difference between the fluid streams, so less heat will be transferred from the hot fluid. The expected results then are that the cold side effectiveness will increase by from the baseline case (Case 3) and that the hot side effectiveness will decrease from the baseline case. These results are clearly shown in Fig. 4.3.5.

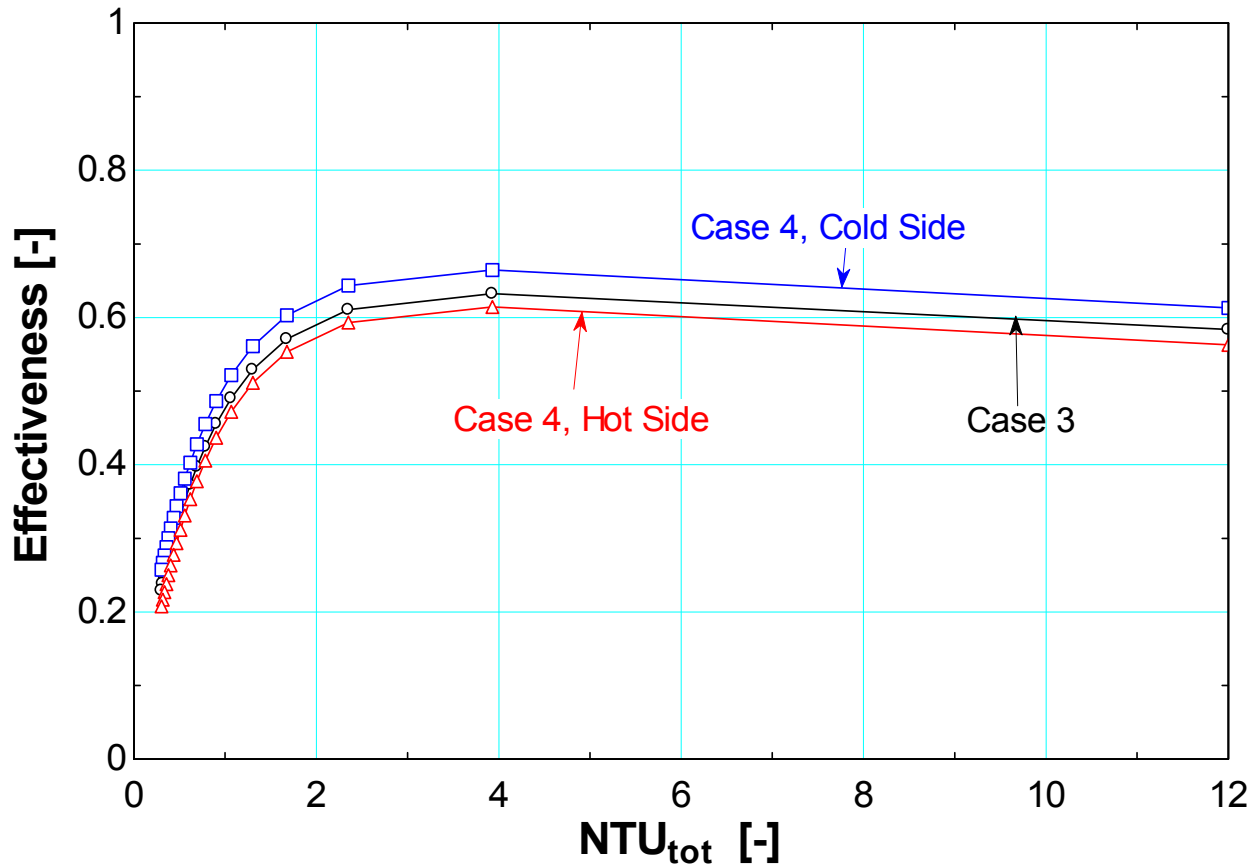

Fig. 4.3.5: Comparison of effectiveness for Case 3 (adiabatic ends) and Case 4 (heat conducted to the warm end) as a function of total NTU

Case 5 is the opposite of Case 4 since the heat is conducted from the warm end instead of to the warm end. Removing heat from the warm end should result in more cooling to the hot stream and less heating to the cold stream. The effectiveness of Case 5 is compared with the baseline Case 3 on the plot in Fig. 4.3.6 as a function of total *NTU*. Again the model shows results in the direction that is expected.

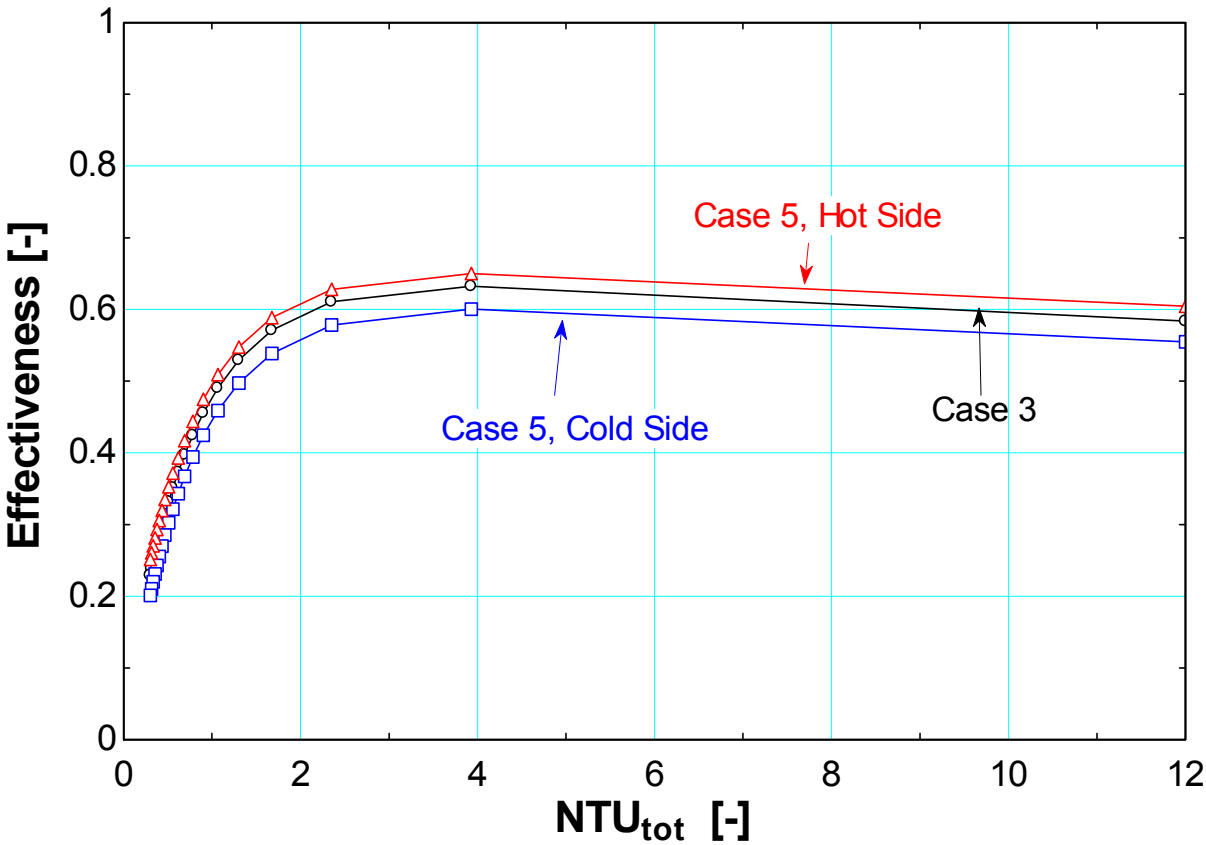

Fig. 4.3.6: Comparison of effectiveness for Case 3 (adiabatic ends) and Case 5 (heat conducted from the warm end) as a function of total NTU

The plot in Fig. 4.3.7 compares Case 6 (heat conducted from the cold end) to the baseline Case 3. Conducting heat from the cold end should increase the amount of cooling to the hot stream but reduce the heating to the cold stream. These expected results are shown in Fig. 4.3.7. Examining Figs. 4.3.5-4.3.7 shows an important consideration regarding heat flow to and from the heat exchanger ends. The cold stream is much more sensitive to heat flow at the warm end of the heat exchanger and the hot stream is much more sensitive to heat flow at the cold end of the heat exchanger. Axial conduction reduces the wall temperature at the warm end and increases the wall temperature at the cold end, which means that the wall temperature is generally much closer to the outlet fluid temperature at the heat exchanger ends. Changing the end wall conditions on one end will therefore change the effectiveness more for the stream exiting at that end than the stream entering that end.

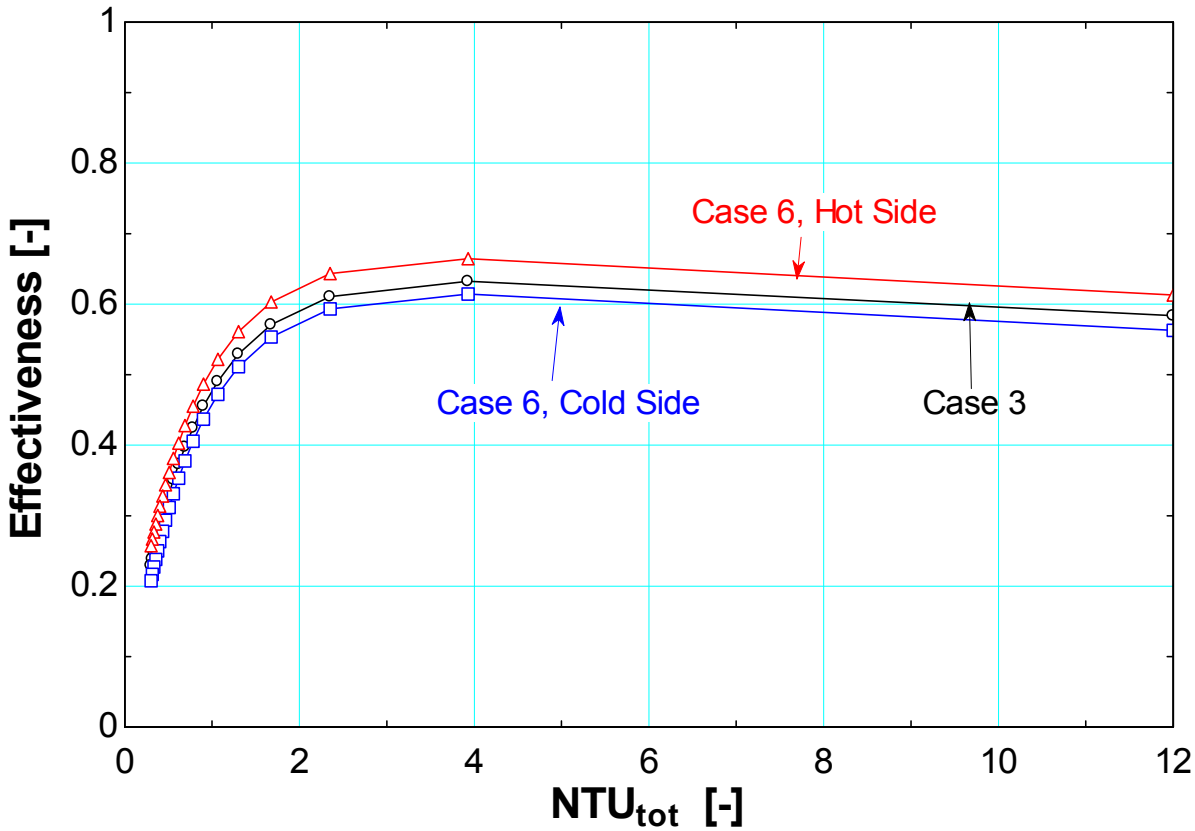

Fig. 4.3.7: Comparison of effectiveness for Case 3 (adiabatic ends) and Case 5 (heat conducted from the cold end) as a function of total NTU

The plot in Fig. 4.3.8 compares Case 6 (heat conducted to the cold end) to the baseline Case 3. Conducting heat to the cold end of the heat exchanger should result in less cooling to the hot stream and more heating to the cold stream. In addition, the hot stream should be more sensitive to the heat conduction since it is at the hot stream hot outlet. Both of these expected trends are exhibited in Fig. 4.3.8.

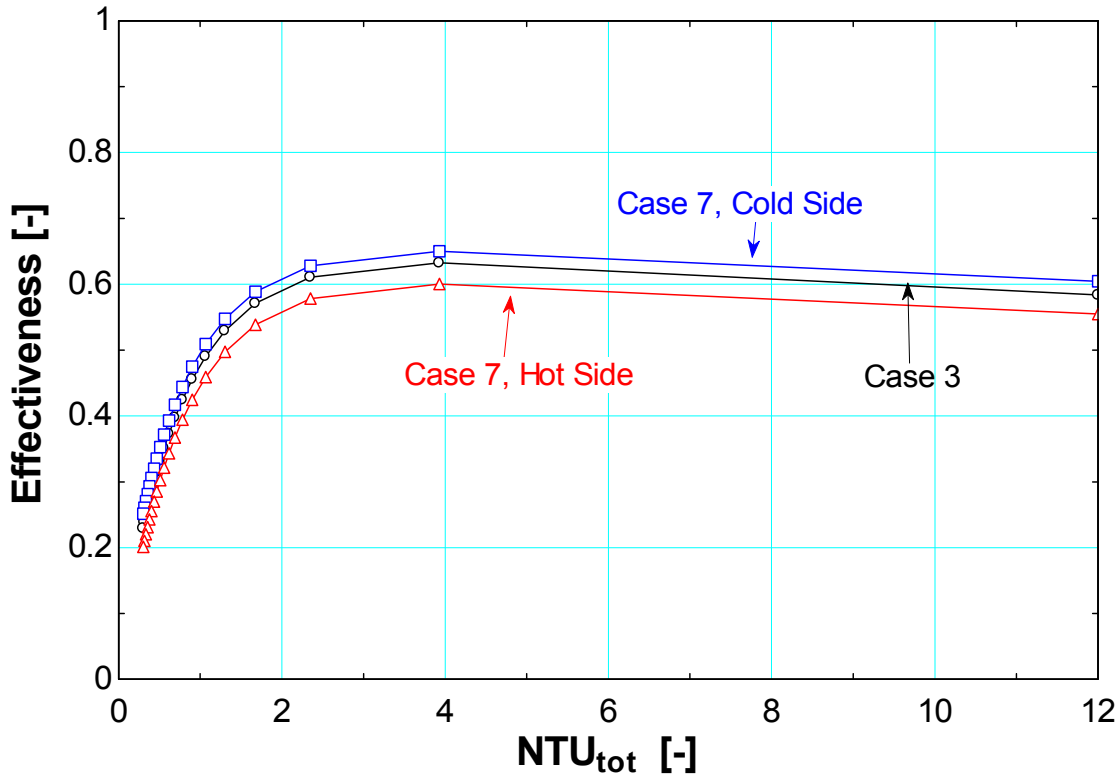

Fig. 4.3.7: Comparison of effectiveness for Case 3 (adiabatic ends) and Case 7 (heat conducted to the cold end) as a function of total NTU

Another issue that must be considered for cryogenic heat exchangers is parasitic heat loads to the heat exchanger from the ambient. Heat loss to ambient must also be considered if the heat exchanger is operated at temperatures higher than ambient. Depending on the design of the heat exchanger, the parasitic heat loads can be on the hot fluid, cold fluid, the wall, or any combination of the three. Similar to heat flow to the ends of the heat exchanger, heat flow along the length of the heat exchanger can be a gain or loss depending on the direction of flow and the application of the heat exchanger.

Shown in Table 4.3.3 are four variants of a hypothetical heat exchanger that will be used to discuss heat loads on heat exchanger. Case 3 is considered to be the baseline case with axial conduction, adiabatic ends, and no parasitic heat loads. Case 8 has a heat load only on the hot fluid, Case 9 has a heat load only on the cold fluid, and Case 10 has a heat load only on the wall. The dimensionless heat loads for the hot stream ($\chi_{h,j}$), the cold stream ($\chi_{c,j}$), and the wall ($\chi_{w,j}$) can be calculated using Eqs. 4.1.10 - 4.1.12 respectively. The heat loads were assumed to be 5% of the maximum possible heat exchanged in each die so that the effects would be clearly visible on plots.

Table 4.3.3: Variations of the hypothetical heat exchanger used to show the effect of parasitic heat loads. Case 3 is a heat exchanger with no heat loads, Case 8 has a heat load on the hot fluid, Case 9 has a heat load on the cold fluid, and Case 10 has a heat load on the wall.

Case	$R_{h,j}$ [K/W]	$R_{c,j}$ [K/W]	$Cp_{h,j}$ [J/kg-K]	$Cp_{c,j}$ [J/kg-K]	$R_{ac,j}$ [K/W]	$R_{sp,j}$ [K/W]	$X_{h,j}$ [-]	$X_{c,j}$	$X_{w,j}$ [-]
3	5	5	5000	5000	0.05	10	0	0	0
8	5	5	5000	5000	0.05	10	0.05	0	0
9	5	5	5000	5000	0.05	10	0	0.05	0
10	5	5	5000	5000	0.05	10	0	0	0.05

Case 3 (no heat loads) and Case 8 (heat load on hot fluid) are compared on a plot of effectiveness as a function of total *NTU* in Fig. 4.3.8. Similar plots are shown in Fig. 4.3.9 for Case 9 (heat load on the cold fluid) and in Fig. 4.3.10 for Case 10 (heat load on the wall). In all cases the additional heat being added to the heat exchanger should result in more heating to the cold fluid and less cooling to the hot fluid. This is shown in all the plots in Fig. 4.3.8-4.3.10.

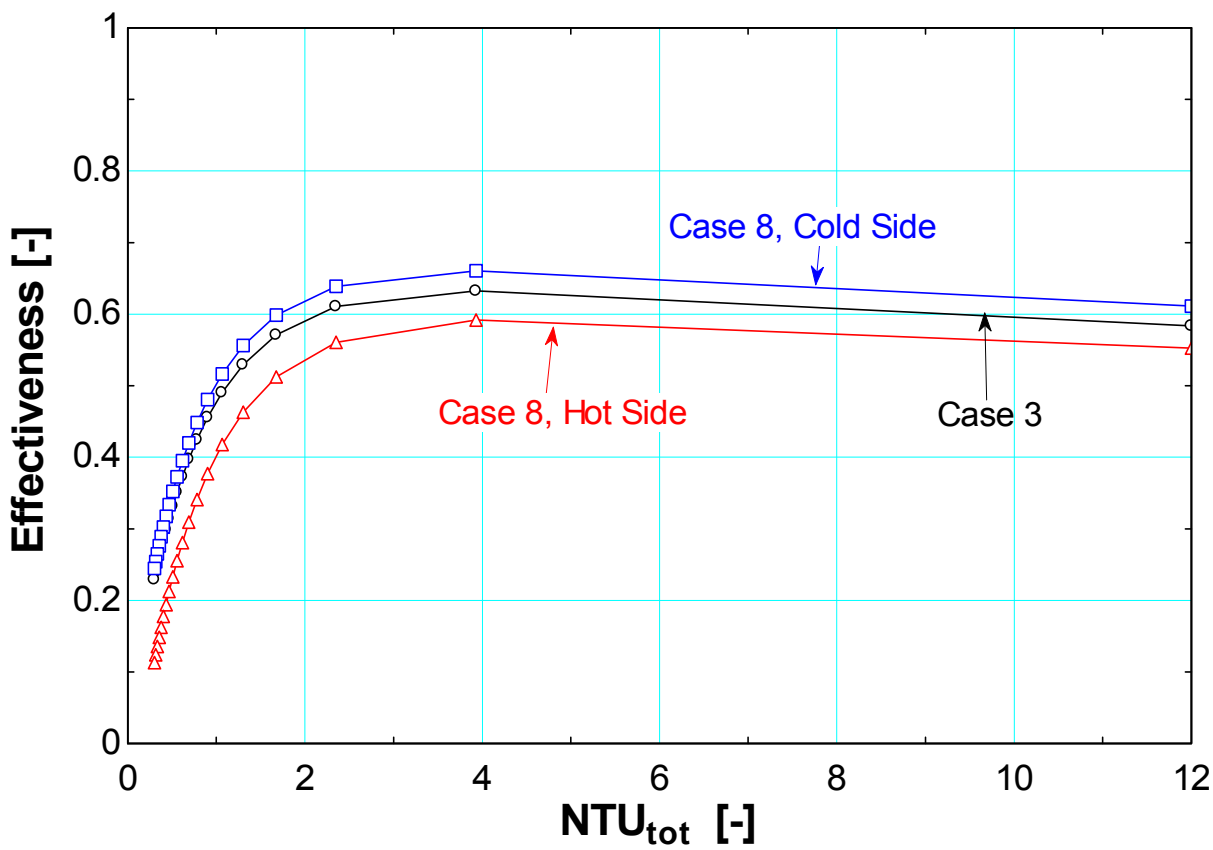

Fig. 4.3.8: Plot comparing the effectiveness for Case 3 (no heat load) and Case 8 (heat load on hot fluid) as a function of the total number of transfer units.

Comparing Fig. 4.3.8 to Fig. 4.3.9 reveals an important observation. For the same heat load on the heat exchanger, the hot fluid is cooled less if the heat load is placed directly on the hot fluid when compared to the heat load being placed on the cold fluid. The reverse holds true for the cold fluid. The cold fluid is heated more if the heat load is placed directly on the cold fluid rather than on the hot fluid. These differences are more pronounced at low *NTU* due to high stream-to-stream resistances relative to the fluid capacity rates. At high *NTU* a heat load on either stream produces the same results since the fluid stream has a low stream-to-stream resistance relative to the fluid capacity rates.

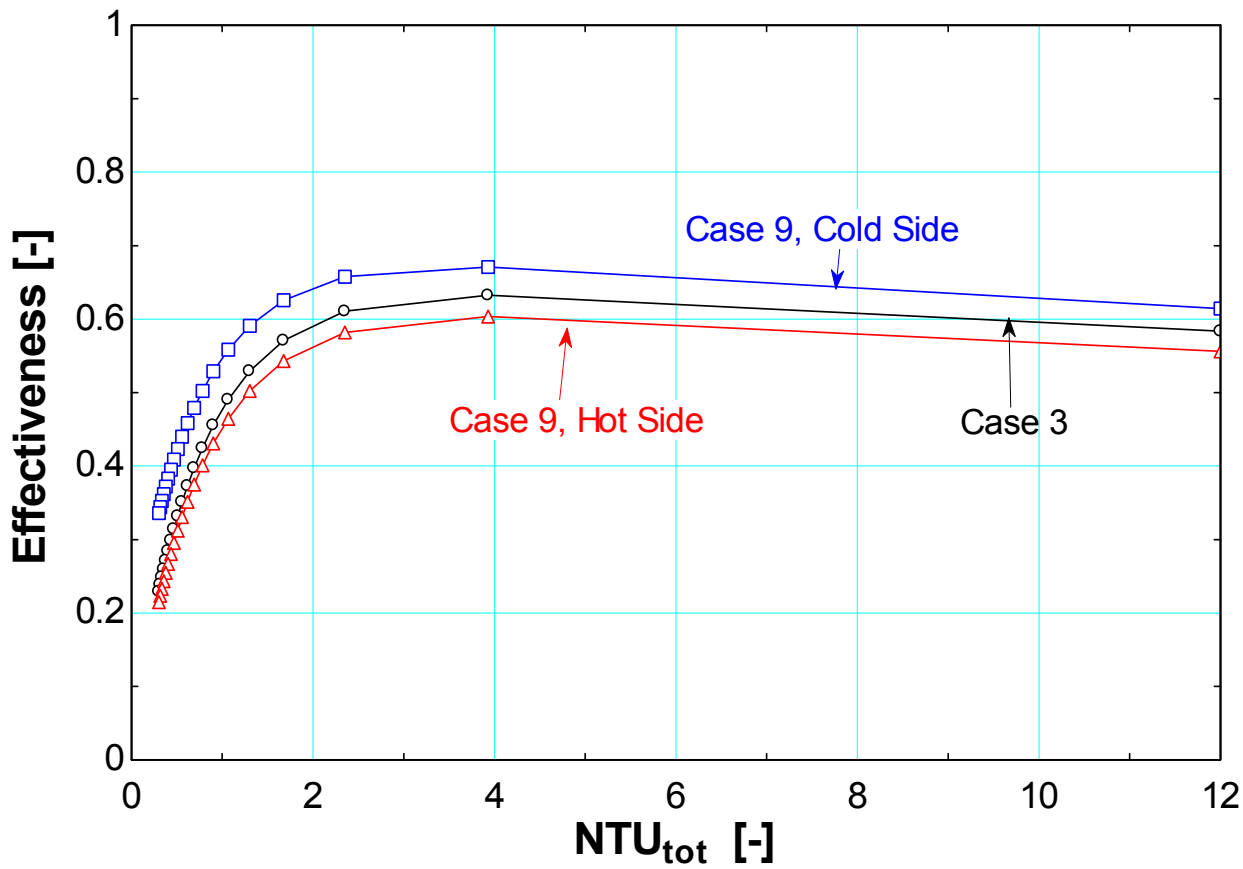

Fig. 4.3.9: Plot comparing the effectiveness for Case 3 (no heat load) and Case 9 (heat load on cold fluid) as a function of the total number of transfer units

The plot shown in Fig. 4.3.10 reveals another important observation. If the heat load is placed on the wall, the amount of additional heating provided to the cold stream will equal the reduction in cooling to the hot stream. For most perforated plate heat exchangers, the load will be placed on the hot fluid or the cold fluid since the internal wall has little direct thermal communication with the ambient.

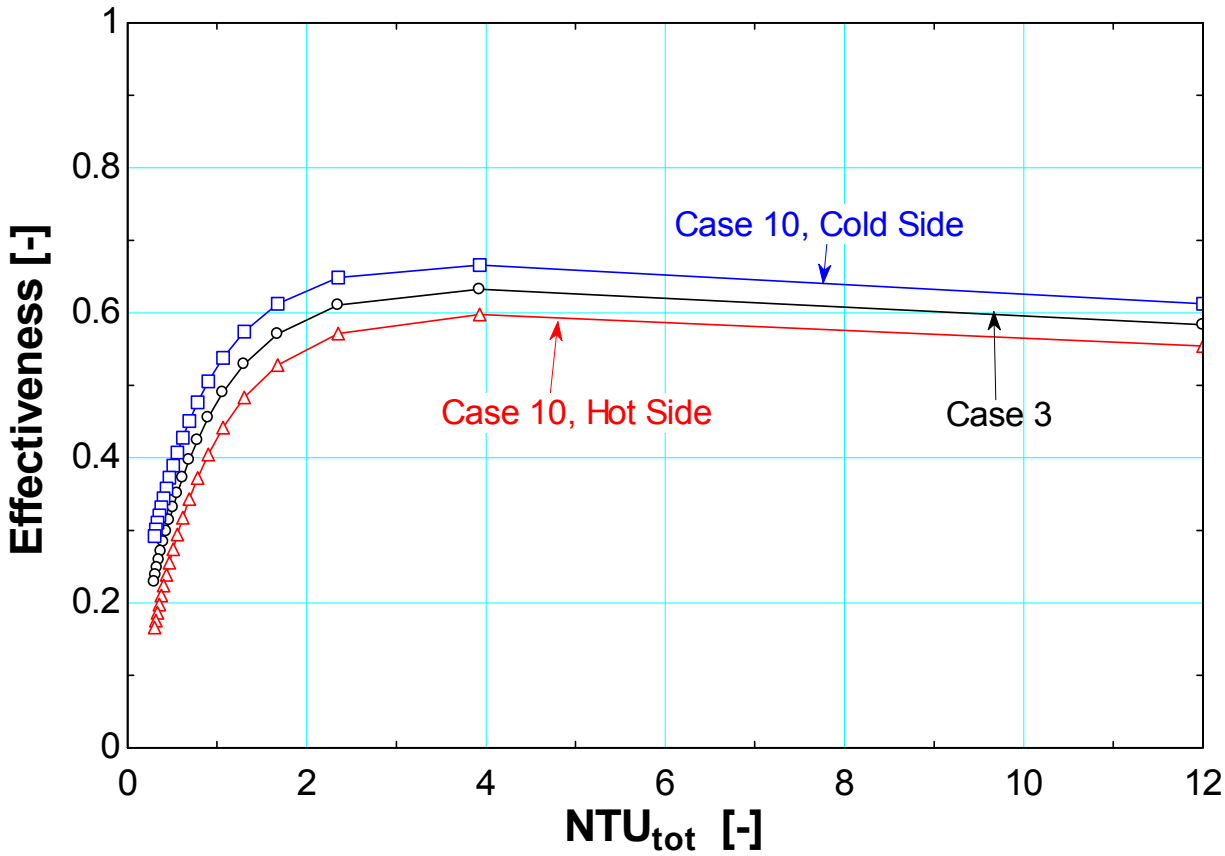

Fig. 4.3.8: Plot comparing the effectiveness for Case 3 (no heat load) and Case 10 (heat load on wall) as a function of the total number of transfer units

The final loss mechanism that should be examined for perforated plate heat exchangers is internal fluid leakage. To demonstrate the effects of internal fluid leakage another set of hypothetical heat exchangers will be examined. All of the heat exchangers used for studying internal leakage are assumed to have three perforated plates, two spacers, constant thermal resistances, no parasitic heat loads, and adiabatic ends. In addition, a hot inlet temperature of 300 K and a cold inlet temperature of 295 K were assumed. The temperature difference across the length of the heat exchanger was kept small so that the assumption of constant fluid and material properties for each plate would still be valid. Both fluids were assumed to be isobaric across the heat exchanger, with the hot fluid at 200 kPa and the cold fluid at 100 kPa. Internal fluid leaks, if present, were assumed to be 20% of the total flow so that any effects will be clearly visible on plots.

The heat exchanger model requires the use of a real fluid for predicting the results of internal leakage. The streams that are mixing are at different temperatures and pressures and require the use of the fluid's enthalpy, as shown by the energy balance in Fig. 4.2.3. Helium was used as the first fluid for modeling since its behavior very closely matches that of an ideal gas at standard conditions. For the first set of variations, which are listed in Table 4.3.4, the leaking fluid was assumed to have no thermal interaction with the wall ($Frac_{Heat}$=0). The location of the leak is specified by the parallel plate number ($Leak_{PP,Loc}$) and the spacer number ($Leak_{SP,Loc}$) since the leaks are assumed to occur only at the joints between the plates and spacers.

Table 4.3.4: Variations of a hypothetical heat exchanger used for showing the effect of leak location on heat exchanger effectiveness. All cases listed in the table assume no thermal interaction between the leaking fluid and the heat exchanger wall.

Case	Fluid	$R_{h,j}$ [K/W]	$R_{c,j}$ [K/W]	$R_{ac,j}$ [K/W]	$R_{sp,j}$ [K/W]	$P_{h,j}$ [kPa]	$P_{c,j}$ [kPa]	$Frac_{Leak}$ [-]	$Frac_{Heat}$ [-]	$Leak_{PP,Loc}$ [-]	$Leak_{SP,Loc}$ [-]
11	helium	5	5	0.05	10	200	100	0	-	-	-
12	helium	5	5	0.05	10	200	100	0.2	0	1	1
13	helium	5	5	0.05	10	200	100	0.2	0	2	1
14	helium	5	5	0.05	10	200	100	0.2	0	2	2
15	helium	5	5	0.05	10	200	100	0.2	0	3	2

The results of modeling the cases listed in Table 4.3.4 are shown in a plot of effectiveness as a function of the total *NTU* in Fig. 4.3.9. The calculation of the total number of transfer units uses the minimum average specific heat in the entire heat exchanger and the mass flow rate at the hot fluid inlet. Since the leaking fluid has no thermal interaction with the wall it does not matter which side of an individual spacer that the fluid leak is on. However, there is a significant difference between a leak in the first spacer and the second spacer. A leak in the first spacer is much more detrimental to the effectiveness than the second spacer. This is because a leak in the first spacer significantly reduces the mass flow rate throughout the rest of the heat exchanger whereas a leak in the second spacer only reduces the mass flow rate in the third perforated plate.

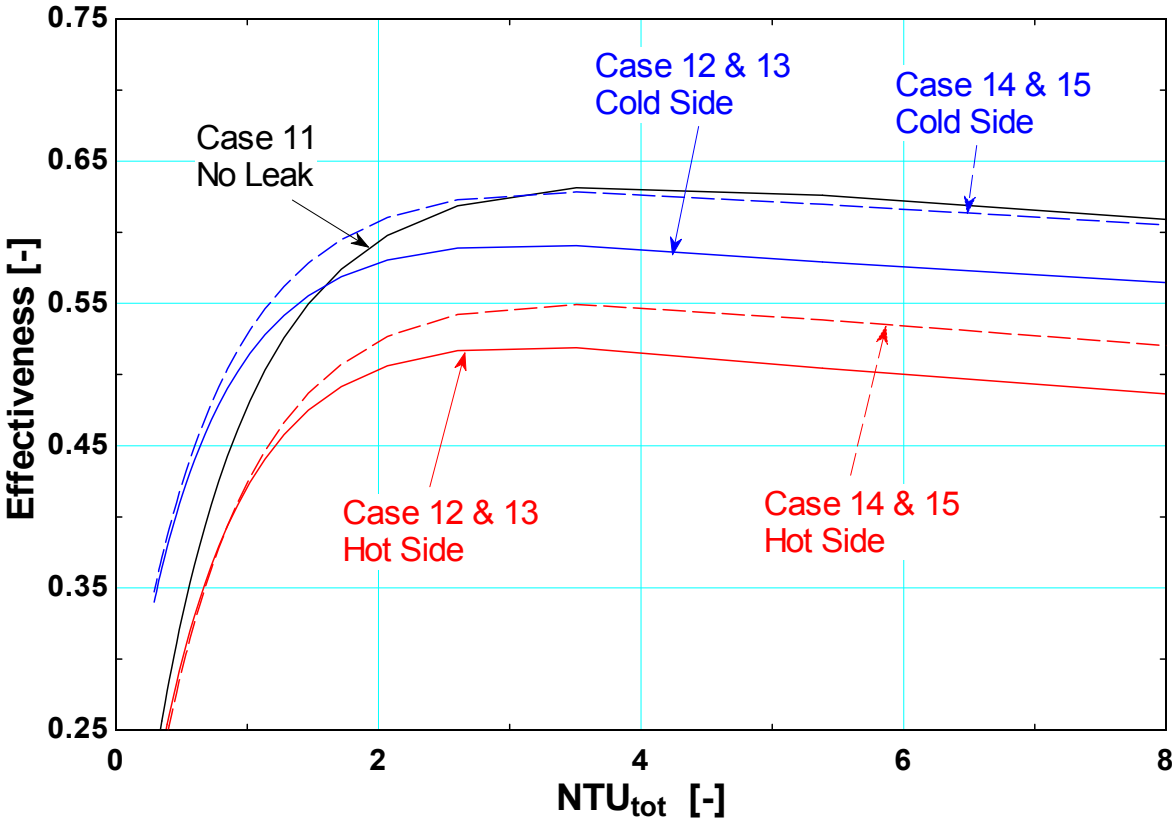

Fig. 4.3.9: Plot of effectiveness as a function of total NTU for all the cases listed in Table 4.3.4. In all cases the leaking fluid is assumed to have no thermal interaction with the wall. Case 11 is the baseline with no leakage, Cases 12 and 13 have leaks located in the first spacer and Cases 14 and 15 have leaks located in the second spacer.

Another set of variations of leak location on a hypothetical heat exchanger are shown in Table 4.3.5. For these cases the leaking hot fluid was assumed to be cooled completely to the wall temperature. All other conditions remain the same as those listed in Table 4.3.4.

Table 4.3.5: Variations of a hypothetical heat exchanger used for showing the effect of leak location on heat exchanger effectiveness. All cases listed in the table assume that the leaking fluid is cooled to the wall temperature.

Case	Fluid	$R_{h,j}$ [K/W]	$R_{c,j}$ [K/W]	$R_{ac,j}$ [K/W]	$R_{sp,j}$ [K/W]	$P_{h,j}$ [kPa]	$P_{c,j}$ [kPa]	$Frac_{Leak}$ [-]	$Frac_{Heat}$ [-]	$Leak_{PP,Loc}$ [-]	$Leak_{SP,Loc}$ [-]
11	helium	5	5	0.05	10	200	100	0	-	-	-
16	helium	5	5	0.05	10	200	100	0.2	1	1	1
17	helium	5	5	0.05	10	200	100	0.2	1	2	1
18	helium	5	5	0.05	10	200	100	0.2	1	2	2
19	helium	5	5	0.05	10	200	100	0.2	1	3	2

The cases where the leak location is on either side of the first spacer are shown in Fig. 4.3.10, which includes cases where the fluid has no thermal interaction with the wall (Cases 12 & 13)

and where the fluid is cooled to the wall temperature (Cases 16 & 17). The cases where the leak location is on either side of the second spacer are shown in Fig. 4.3.11, which includes cases where the fluid has no thermal interaction with the wall (Cases 14 & 15) and where the fluid is cooled the wall temperature (Cases 18 & 19). The most important observations from Figs. 4.3.10 and 4.3.11 are that the quantity of heat exchanged between the leaking fluid and the wall has almost no effect on heat exchanger effectiveness and that it makes almost no difference which side of the spacer that the leak occurs on.

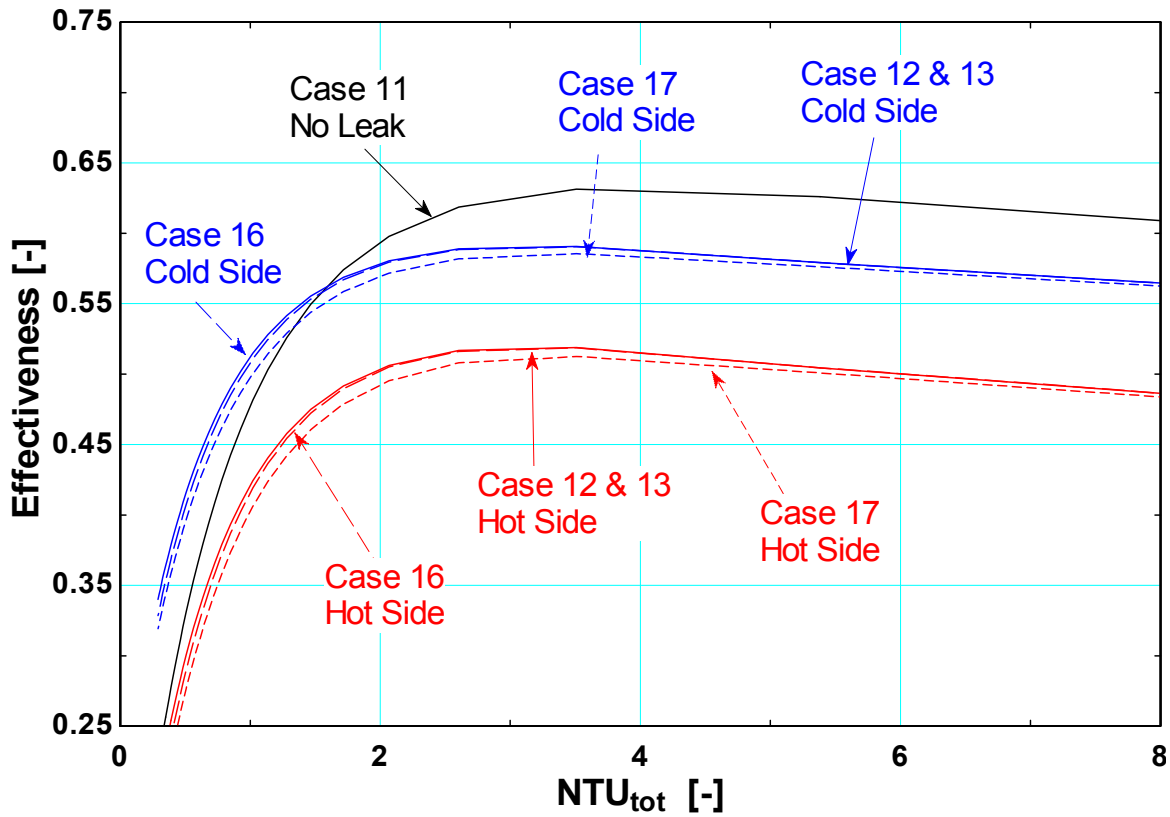

Fig. 4.3.10: Plot of effectiveness as a function of total NTU for all the cases listed in Tables 4.3.4 and 4.3.5 with leaks located in the first spacer. Case 11 is the baseline with no leakage, Cases 12 & 13 have identical results and no thermal interaction with the wall, Case 16 has the leaking hot fluid cooled to the wall temperature and is located just before the first spacer, and Case 17 has the leaking hot fluid cooled to the wall temperature and is located just after the first spacer.

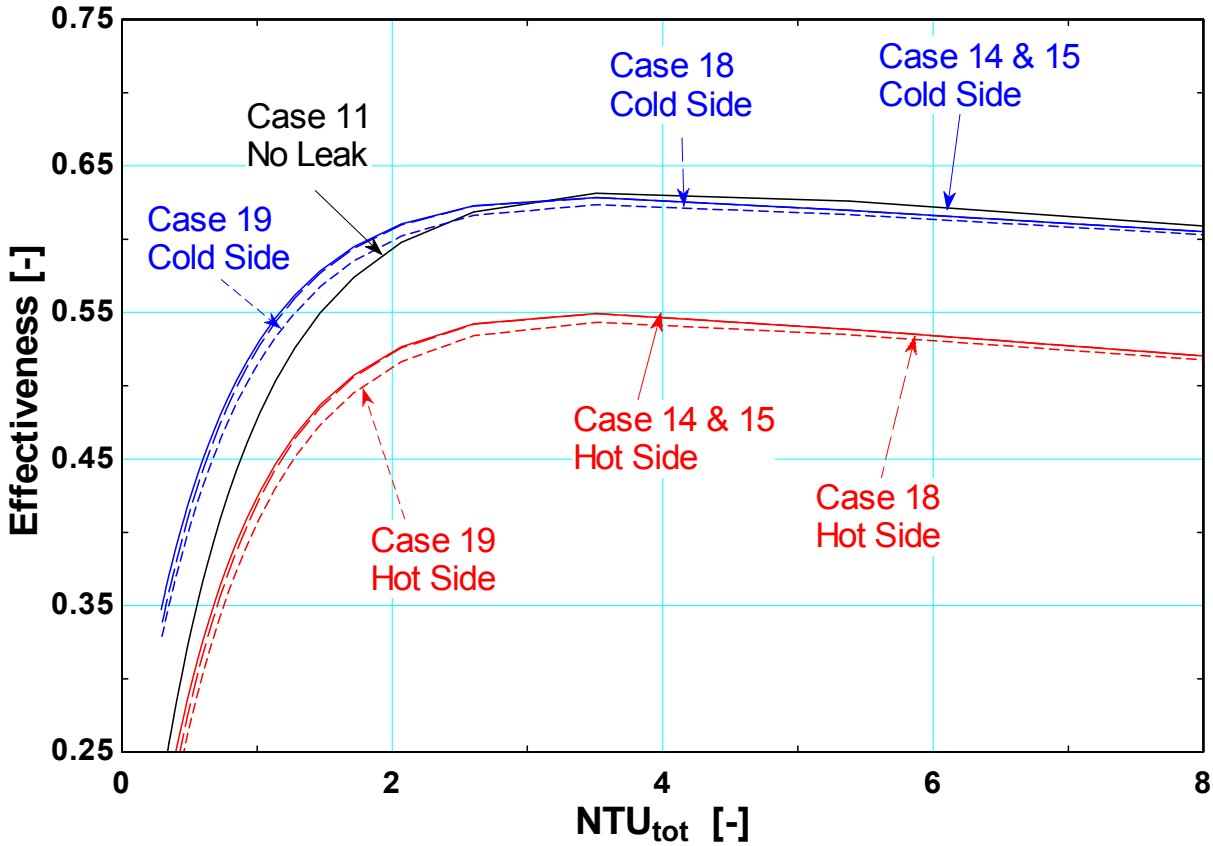

Fig. 4.3.11: Plot of effectiveness as a function of total NTU for all the cases listed in Tables 4.3.4 and 4.3.5 with leaks located in the second spacer. Case 11 is the baseline with no leakage, Cases 14 & 15 have identical results and no thermal interaction with the wall, Case 18 has the leaking hot fluid cooled to the wall temperature and is located just before the second spacer, and Case 19 has the leaking hot fluid cooled to the wall temperature and is located just after the second spacer.

The first fluid chosen for the internal leakage study was helium due to its nearly ideal gas behavior. However, heat exchangers are frequently used to condense gasses and evaporate liquids. Fluid behavior near the vapor dome on a T-s or P-v diagram is certainly far from that of an ideal gas. One of the major differences between an ideal gas and a real gas near the vapor dome is its Joule-Thomson (J-T) coefficient. The J-T coefficient (μ_{JT}) is defined as the change in temperature due to a change in pressure at constant enthalpy [4]. The J-T coefficient is shown in mathematical form by Eq. 4.3.1:

$$\mu_{JT} = \left.\frac{\partial T}{\partial P}\right|_{H} \tag{4.3.1}$$

A perfectly ideal gas has a J-T coefficient of zero, meaning that it neither cools nor warms upon an isenthalpic expansion. Helium, which is very far from the vapor dome at standard conditions, has a slightly negative J-T coefficient and will warm slightly after an isenthalpic expansion. Ethane, which is much closer to the vapor dome at standard conditions, has a positive J-T coefficient and will cool after an isenthalpic expansion. The J-T coefficient for both helium and

ethane as a function of temperature are shown in Fig. 4.3.12. The reason that the J-T coefficient might be important is that the high pressure hot fluid will expand as it leaks into the low pressure cold fluid. Ethane was chosen as the next fluid for the study of internal leakage to show the impact of using fluids that will cool while they expand from a high pressure to a low pressure.

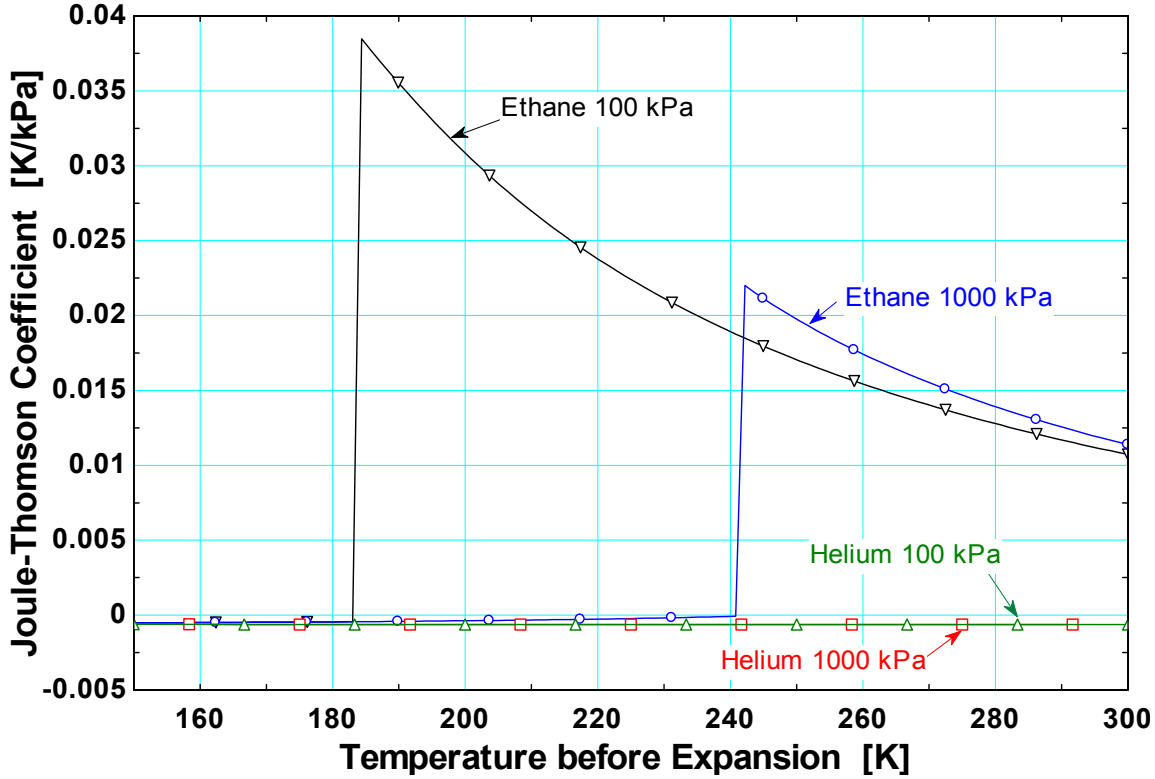

Fig. 4.3.12: Joule-Thomson Coefficient as a function of temperature for helium and ethane at 100 kPa and 1000 kPa. Positive Joule-Thomson coefficients result in the fluid cooling while it undergoes an isenthalpic expansion and negative J-T coefficients result in the fluid warming while it undergoes an isenthalpic expansion.

The same modeling tests on internal leakage were run using ethane as the working fluid as were done with helium. Shown in Table 4.3.6 are a set of cases with the assumption of no thermal interaction between the leaking fluid and the wall. The cases in Table 4.3.6 are identical to those in Table 4.3.4 except that ethane is used as the working fluid. Case 20 is the new baseline case for no internal leakage. Cases 21 through 24 are used to show the effect of leaks in all four joints.

Table 4.3.6: Variations of a hypothetical heat exchanger used for showing the effect of leak location on heat exchanger effectiveness. All cases listed in the table assume no thermal interaction between the leaking fluid and the heat exchanger wall.

Case	Fluid	$R_{h,j}$ [K/W]	$R_{c,j}$ [K/W]	$R_{ac,j}$ [K/W]	$R_{sp,j}$ [K/W]	$P_{h,j}$ [kPa]	$P_{c,j}$ [kPa]	$Frac_{Leak}$ [-]	$Frac_{Heat}$ [-]	$Leak_{PP,Loc}$ [-]	$Leak_{SP,Loc}$ [-]
20	ethane	5	5	0.05	10	200	100	0	-	-	-
21	ethane	5	5	0.05	10	200	100	0.2	0	1	1
22	ethane	5	5	0.05	10	200	100	0.2	0	2	1
23	ethane	5	5	0.05	10	200	100	0.2	0	2	2
24	ethane	5	5	0.05	10	200	100	0.2	0	3	2

A plot of effectiveness as a function of total NTU for all the cases listed in Table 4.3.6 is shown in Fig. 4.3.12. Similar to the helium cases, it doesn't matter which side of the spacer the leak is on, but a leak in the first spacer is more detrimental to heat exchanger effectiveness than a leak in the second spacer.

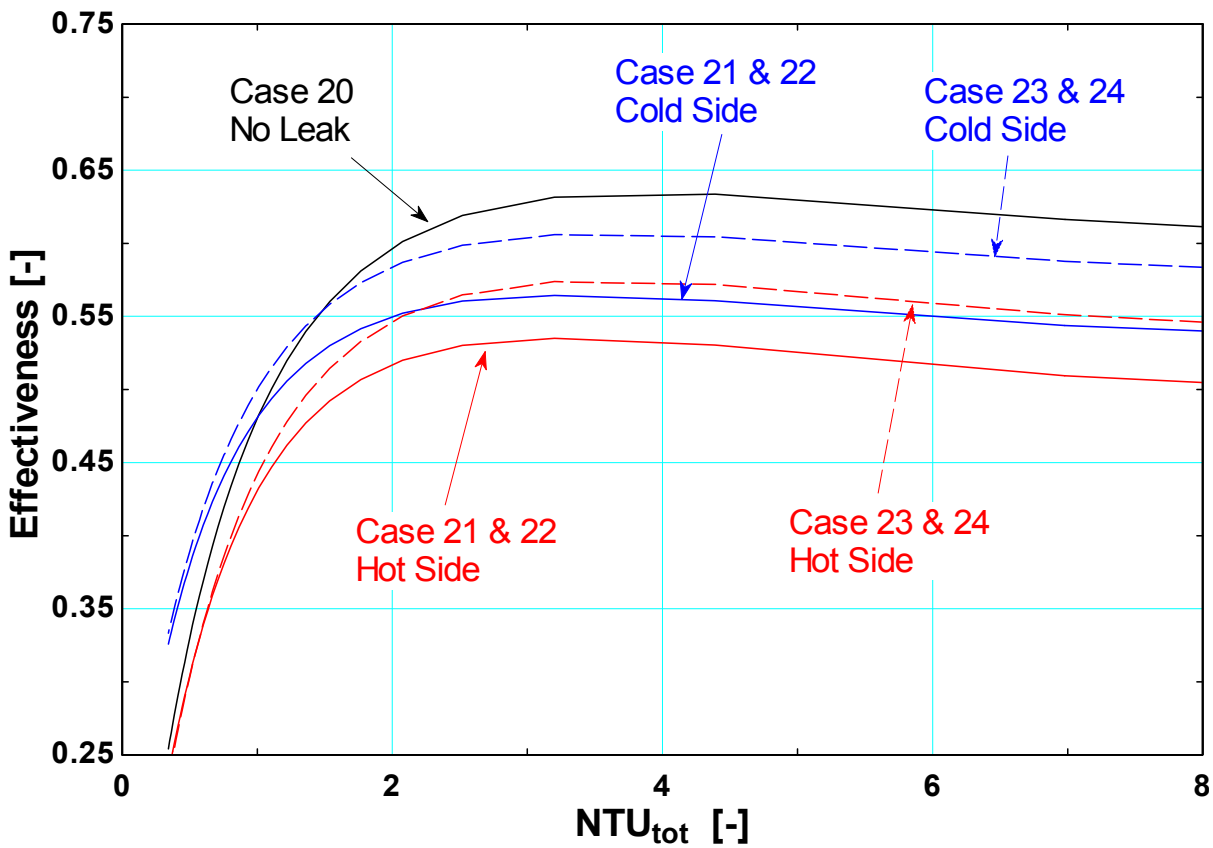

Fig. 4.3.13: Plot of effectiveness as a function of total NTU for all the cases listed in Table 4.3.6. In all cases the leaking fluid is assumed to have no thermal interaction with the wall. Case 20 is the baseline with no leakage, Cases 21 and 22 have leaks located in the first spacer and Cases 23 and 24 have leaks located in the second spacer.

Another set of modeling tests was run assuming that the leaking fluid was cooled to the wall temperature. The conditions for the tests are shown in Table 4.3.7, which is identical to Table 4.3.5 except that now ethane is working fluid.

Table 4.3.7: Variations of a hypothetical heat exchanger used for showing the effect of leak location on heat exchanger effectiveness. All cases listed in the table assume that the leaking fluid is cooled to the wall temperature.

Case	Fluid	$R_{h,j}$ [K/W]	$R_{c,j}$ [K/W]	$R_{ac,j}$ [K/W]	$R_{sp,j}$ [K/W]	$P_{h,j}$ [kPa]	$P_{c,j}$ [kPa]	$Frac_{Leak}$ [-]	$Frac_{Heat}$ [-]	$Leak_{PP,Loc}$ [-]	$Leak_{SP,Loc}$ [-]
20	ethane	5	5	0.05	10	200	100	0	-	-	-
25	ethane	5	5	0.05	10	200	100	0.2	1	1	1
26	ethane	5	5	0.05	10	200	100	0.2	1	2	1
27	ethane	5	5	0.05	10	200	100	0.2	1	2	2
28	ethane	5	5	0.05	10	200	100	0.2	1	3	2

A plot of effectiveness as a function of total NTU is shown in Fig. 4.3.14 for all cases where the leak occurs in the first spacer and in Fig. 4.3.15 for all cases where the leak occurs in the second spacer. As with the helium cases, the side of the spacer which the leak occurs and the quantity of heat transferred to the wall have very little effect.

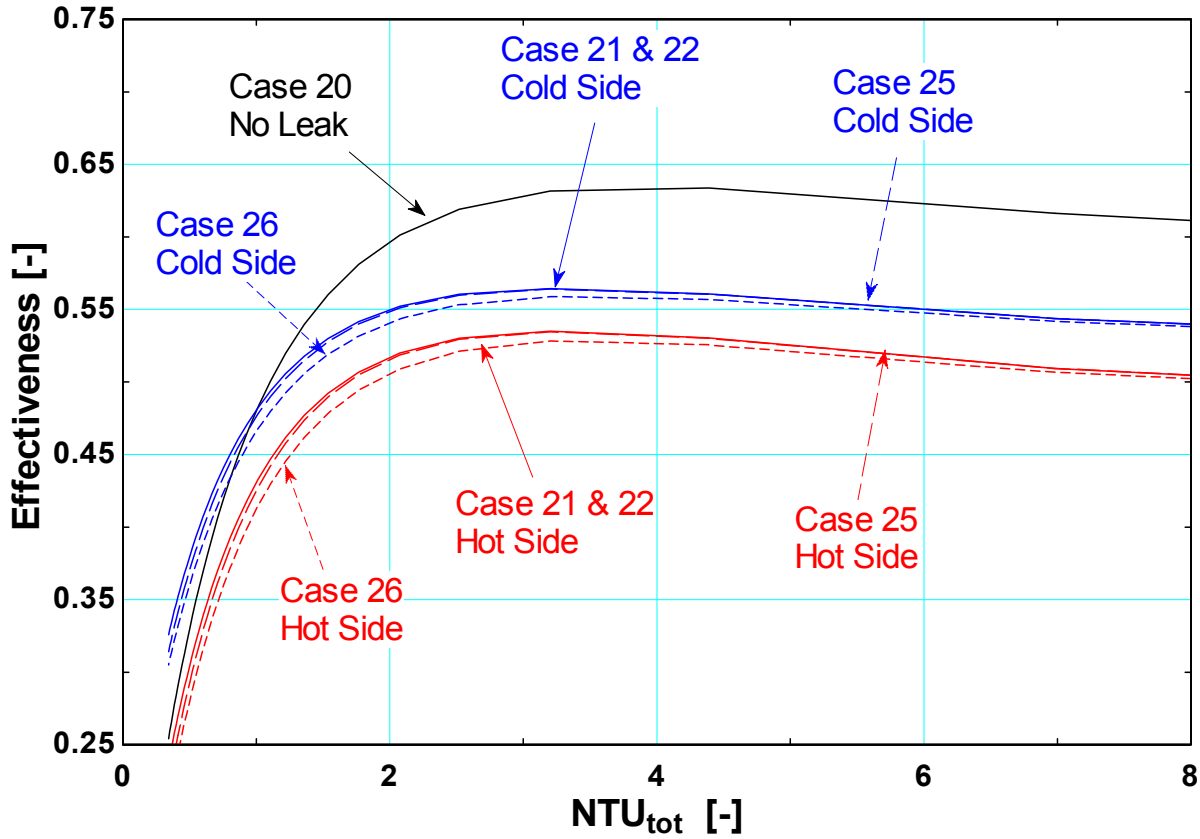

Fig. 4.3.14: Plot of effectiveness as a function of total NTU for all the cases listed in Tables 4.3.6 and 4.3.7 with leaks located in the first spacer. Case 20 is the baseline with no leakage, Cases 21 & 22 have identical results and no thermal interaction with the wall, Case 25 has the leaking hot fluid cooled to the wall temperature and is located just before the first spacer, and Case 26 has the leaking hot fluid cooled to the wall temperature and is located just after the first spacer.

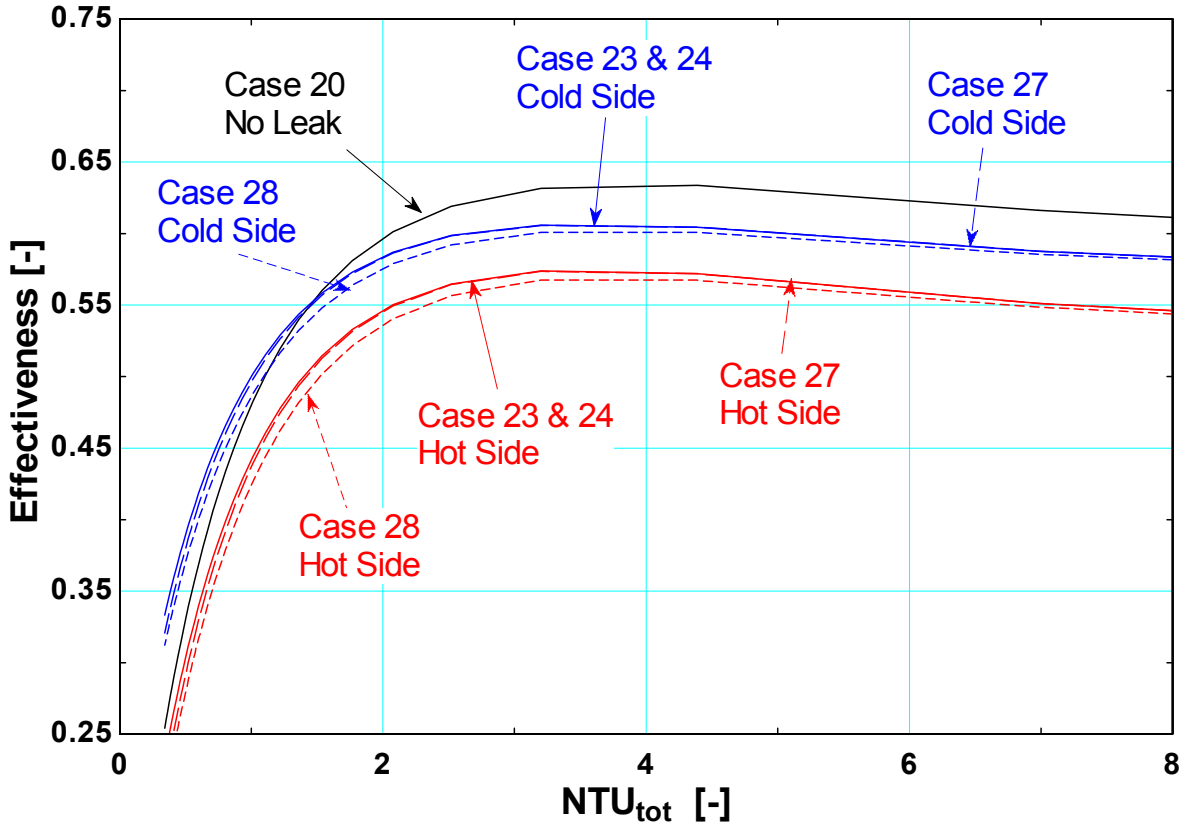

Fig. 4.3.15: Plot of effectiveness as a function of total NTU for all the cases listed in Tables 4.3.6 and 4.3.7 with leaks located in the second spacer. Case 20 is the baseline with no leakage, Cases 23 & 24 have identical results and no thermal interaction with the wall, Case 27 has the leaking hot fluid cooled to the wall temperature and is located just before the second spacer, and Case 28 has the leaking hot fluid cooled to the wall temperature and is located just after the second spacer.

The plots shown for ethane in Figs. 4.3.13-4.3.15 suggest that an internal fluid leak will always decrease the hot side effectiveness from the case where there is no internal leakage. The plot in Fig. 4.3.12 shows that the J-T coefficient at 300 K is roughly 0.01 K/kPa. Since the hot side pressure is 200 kPa and the cold side pressure is 100 kPa, the leaking fluid would cool roughly 1 K if it were isenthalpically expanded. The leaking fluid could cool much more if the hot side pressure were significantly higher.

To show the effect of higher hot side pressures on heat exchangers with internal leakage the four cases listed in Table 4.3.8 were considered. Case 20 is the no leakage case for a hot side pressure of 200 kPa and Case 29 is the no leakage case for a hot side pressure of 1200 kPa. Cases 28 and 30 both have leaks in the last spacer, with Case 28 having a hot side pressure of 200 kPa and Case 30 having a hot side pressure of 1200 kPa.

Table 4.3.8: Four heat exchanger variations used to show the effect of hot side pressure on heat exchangers with internal leakage. Case 20 is the no leakage case for a hot side pressure of 200 kPa and Case 29 is the no leakage case for a hot side pressure of 1200 kPa. Cases 28 and 30 both have leaks in the last spacer, with Case 28 having a hot side pressure of 200 kPa and Case 30 having a hot side pressure of 1200 kPa.

Case	Fluid	$R_{h,j}$ [K/W]	$R_{c,j}$ [K/W]	$R_{ac,j}$ [K/W]	$R_{sp,j}$ [K/W]	$P_{h,j}$ [kPa]	$P_{c,j}$ [kPa]	$Frac_{Leak}$ [-]	$Frac_{Heat}$ [-]	$Leak_{PP,Loc}$ [-]	$Leak_{SP,Loc}$ [-]
20	ethane	5	5	0.05	10	200	100	0	-	-	-
28	ethane	5	5	0.05	10	200	100	0.2	1	3	2
29	ethane	5	5	0.05	10	1200	100	0	1	3	2
30	ethane	5	5	0.05	10	1200	100	0.2	1	3	2

The modeling results for the cases listed in Table 4.3.8 are plotted in Fig. 4.3.16. The hot side pressure has only a minor effect on heat exchanger effectiveness for the no leakage cases (Case 20 and Case 29). The plot shown in Fig. 4.3.13 illustrated that internal leakage negatively impacts the hot side effectiveness over the entire range of NTU if the hot side pressure is 200 kPa. The plot in Fig. 4.3.16 shows that the opposite is true if the hot side pressure is 1200 kPa. More heat can be removed from the hot stream in a heat exchanger with a leak than an identical heat exchanger with no leak if the hot side pressure is high enough. At high mass flow rates (low NTU) the cold stream can actually leave the heat exchanger colder than it entered, which is shown by the negative effectiveness below 0.5 NTU for the Case 30 cold stream.

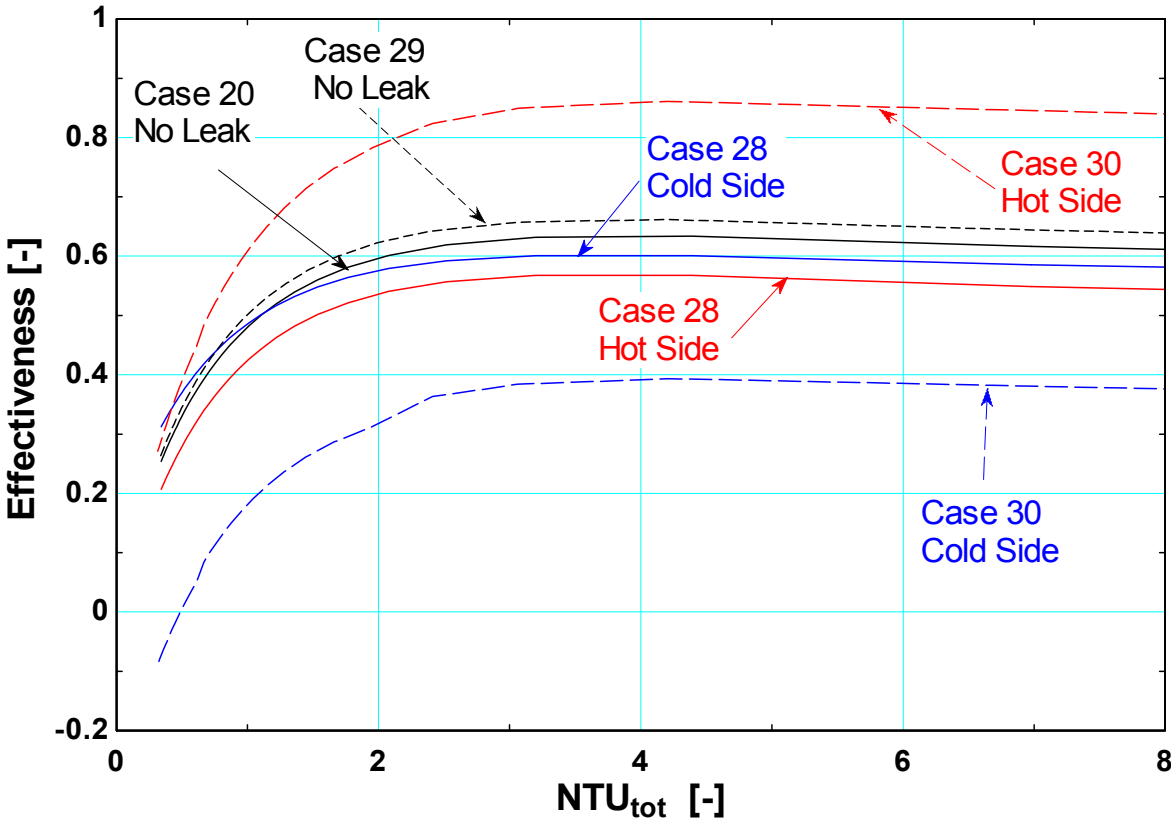

Fig. 4.3.16: Plot showing the effect of the hot side pressure on heat exchangers with internal leakage. Case 20 is the baseline case with no leakage, Case 28 has a hot side pressure of 200 kPa, and Case 29 has a hot side pressure of 1200 kPa.

The plot in Fig. 4.3.16 shows that is possible to remove more heat from the hot stream in a heat exchanger with internal leakage than an identical heat exchanger with no internal leakage. However, it is important to consider how the internal leakage may effect the entire J-T cycle. Internal leakage may improve the performance of the heat exchanger but reduce the refrigeration load that the cycle can provide. The refrigeration load can be calculated using Eq. 4.3.2:

$$\dot{q}_{load} = \dot{m}_{j=N}\left(h_{h,out,j=N} - h_{c,in,j=N}\right) \tag{4.3.2}$$

where $\dot{q}_{load}$ is the cycle refrigeration load, $\dot{m}_{j=N}$ is the mass flow rate through the last plate in the heat exchanger, $h_{c,in,j=N}$ is the fluid enthalpy at the cold inlet of the last plate, and $h_{h,out,j=N}$ is the fluid enthalpy at the hot outlet of the last plate. Greater mass flow rates through internal leaks in the heat exchanger reduce the mass flow rate used to absorb the refrigeration load.

To demonstrate the effect of internal leakage on J-T cycle performance the three cases listed in Table 4.3.9 were considered. Case 29 is the baseline case with no leakage. Cases 30 and 31 are identical to Case 29 except for the internal leakage of 20% of the fluid flow. Case 30 has a leak located in the last spacer and Case 31 has a leak located in the first spacer.

Table 4.3.9: Three heat exchanger variations used to demonstrate the effect of internal leakage on J-T cycle performance. Case 29 is the baseline case with no leakage. Cases 30 and 31 are identical to Case 29 except for the internal leakage of 20% of the fluid flow. Case 30 has a leak located in the last spacer and Case 31 has a leak located in the first spacer.

Case	Fluid	$R_{h,j}$ [K/W]	$R_{c,j}$ [K/W]	$R_{ac,j}$ [K/W]	$R_{sp,j}$ [K/W]	$P_{h,j}$ [kPa]	$P_{c,j}$ [kPa]	$Frac_{Leak}$ [-]	$Frac_{Heat}$ [-]	$Leak_{PP,Loc}$ [-]	$Leak_{SP,Loc}$ [-]
29	ethane	5	5	0.05	10	1200	100	0	1	3	2
30	ethane	5	5	0.05	10	1200	100	0.2	1	3	2
31	ethane	5	5	0.05	10	1200	100	0.2	1	1	1

The application of the J-T cycle was assumed to be the cooling of an object to less than 295 K. The cold fluid was assumed to be returned to the heat exchanger at 295 K and 100 kPa. The compressor was assumed to have an aftercooler that maintained the hot inlet temperature at 300 K. The plot shown in Fig. 4.3.17 shows the effect of internal leakage on the performance of the heat exchanger and the J-T cycle refrigeration load. For both Case 30 and 31 the internal leak improved the hot side effectiveness of the heat exchanger. However, in both cases internal leakage resulted in a decrease in the cycle refrigeration power from the no leakage case. Another point to note is that the location of the leak is relatively unimportant from a cycle perspective since the refrigeration load curves for Case 30 and 31 are indistinguishable on the plot in Fig. 4.3.17.

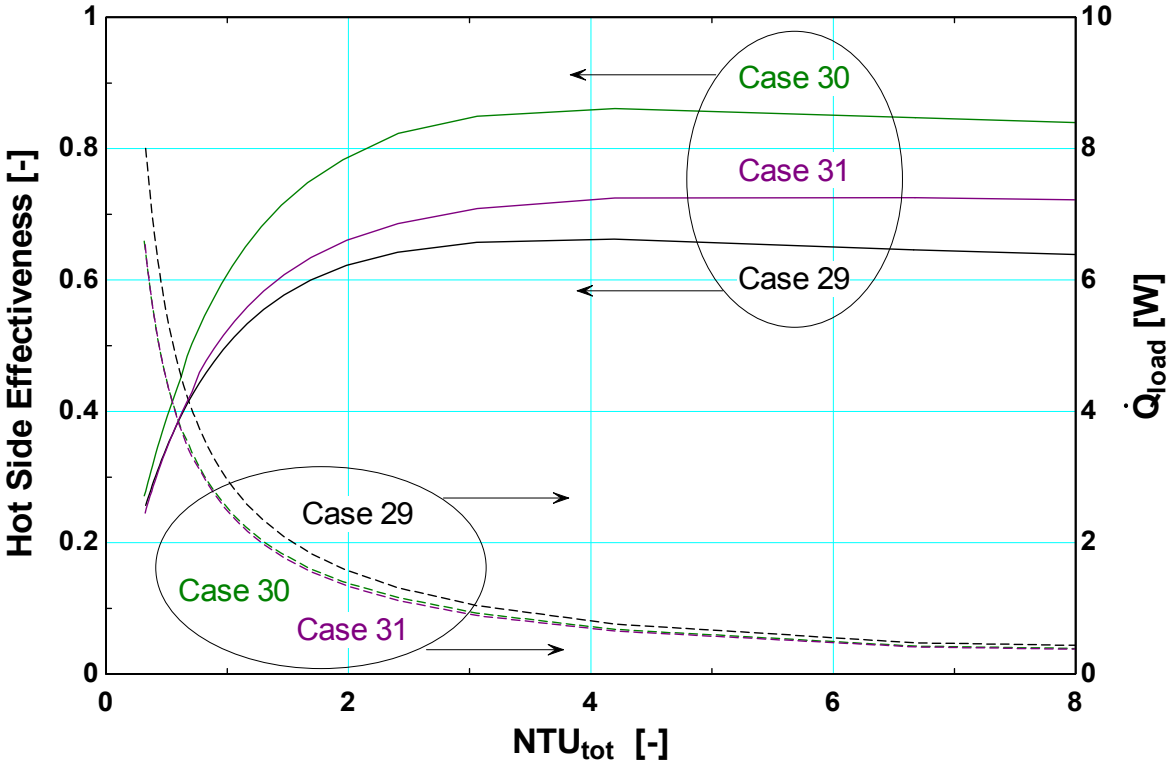

Fig. 4.3.17: Plot showing the effect of internal leakage on the hot side effectiveness of a heat exchanger and the refrigeration load of a J-T cycle.

Several conclusions can be reached from the study of internal leakage in this chapter. For fluids with near ideal gas behavior, leakage from the hot fluid to the cold fluid will reduce the amount of heat transferred from the hot fluid. The stream-to-stream pressure difference and J-T coefficient need to be large for an internal leak from the hot stream to improve the hot side effectiveness of a heat exchanger. In J-T cycle applications, an internal leak can decrease the hot outlet temperature of the heat exchanger but carries the penalty of reducing the total refrigeration load.

Chapter 5: MEMS Heat Exchanger Design Model

5.0 Introduction

This chapter takes the general perforated plate heat exchanger model that was developed in Chapter 4 and applies it to the MEMS heat exchangers that are the focus of this thesis. The chapter begins with a detailed description of the geometry within the MEMS heat exchangers. The next section of the chapter shows how the material properties for the heat exchanger were determined. The next two sections detail how the heat transfer coefficients and pressure drops were calculated for laminar and turbulent flow. Knowledge of the geometry, material properties, and heat transfer coefficients is used to calculate the stream-to-stream and axial thermal resistances for each perforated plate and spacer. Estimates of the parasitic heat loads on the heat exchanger are also covered.

The final section of this chapter will show how the general perforated plate model described in Chapter 4 is connected to the portions of the model that are specific to the MEMS heat exchangers that are described in Chapter 5. Included in the final section will be guidelines for setting up guess values so that the model will reliably converge on the solution. The final section will also provide suggestions for future improvements to the model, which include modeling fluid mixtures and two-phase fluids.

5.1 Die Geometry

Briefly describing the manufacturing process by which the heat exchanger is constructed aids in understanding how heat is conducted inside the exchanger. A geometric model of the 20 mm heat exchanger is presented in Fig. 5.1.1. The 10 mm heat exchanger is similar but with a smaller cross sectional area. A silicon wafer and a glass wafer are etched and anodically bonded to each other. The bonded wafer is then diced to form what is referred to as a “die”. A layer of epoxy is applied to both sides of the die and the dies are stacked on top of each other to form a heat exchanger. Then the heat exchanger stack is epoxied to headers that interface with the cryogenic test facility. The last step is to coat the outside of the heat exchanger stack with another layer of epoxy in order to eliminate any remaining leaks between the heat exchanger and the insulating vacuum. The result is a perforated plate heat exchanger with a high stream-to-stream conductance due to the high-conductivity silicon fins and a high axial thermal resistance due to the low-conductivity glass spacers.

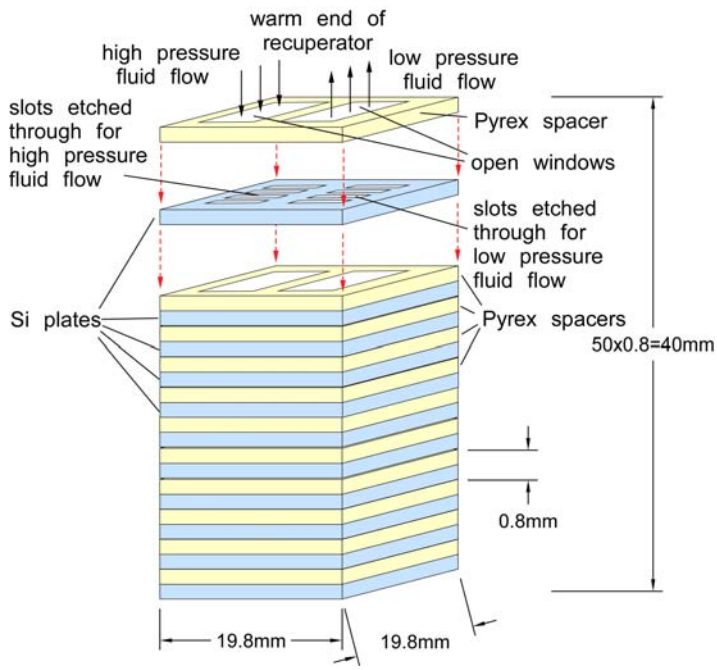

Fig. 5.1.1: Simplified geometric model of 20 mm heat exchanger [7]

The nomenclature used to specify the various dimensions of the heat exchanger is defined in Fig. 5.1.2, which provides a schematic of the silicon plate. There are two clusters of ducts represented by the dashed lines. High pressure fluid flows through one cluster of ducts and low pressure fluid returns through the other cluster of ducts. The distance between the two sets of passages is defined as $W_{si,stream}$ and this material is used for bonding the plate to the glass spacer in order to prevent leakage between the streams. The outer dimensions of the heat exchanger are represented as W_{die} for the die width and H_{die} for the die height. Both the silicon plate and the glass spacer have the same outer dimensions. The etched ducts have a width W_{duct} and a height H_{duct}. Webs between the fins have been added for structural support; the thickness of the webs is W_{web}. The fins formed by the material between adjacent ducts have a conduction length defined as W_{fin} and the cross sectional area for conduction through the fin is the product of H_{fin} and t_{fin}, where H_{fin} is the height of the fin and t_{fin} is the thickness of the silicon plate. The variable N_{column} defines the number of columns in each cluster of ducts and N_{duct} defines the number of ducts in each column. The numerical values of each dimension and the associated tolerance are presented in Table 5.1.1 for both the 10x10 mm and 20x20 mm heat exchangers.

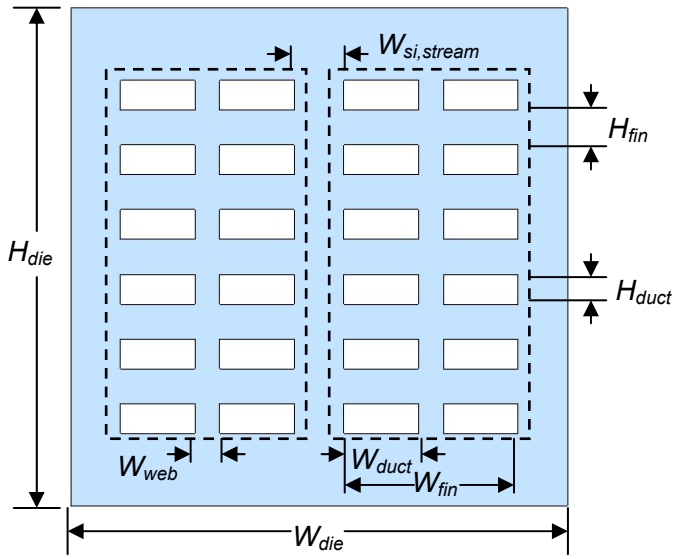

Fig. 5.1.2: Simplified drawing of the silicon plate

Table 5.1.1: Dimensions in millimeters for 10x10 mm and 20x20 mm heat exchanger silicon plates

Variable	10 mm HX Target [mm]	10 mm HX Tolerance [mm]	20 mm HX Target [mm]	20 mm HX Tolerance [mm]
W_{die}	9.77	±0.10	19.77	±0.10
H_{die}	9.77	±0.10	19.77	±0.10
$W_{si,stream}$	1.50	±0.01	1.70	±0.01
W_{duct}	1.40	+0.020/-0.00	1.00	+0.020/-0.00
H_{duct}	0.05	+0.01/-0.00	0.05	+0.01/-0.00
W_{web}	0.10	+0.00/-0.02	0.10	+0.00/-0.02
W_{fin}	2.90	+0.02/-0.00	7.60	+0.02/-0.00
H_{fin}	0.05	+0.00/-0.01	0.05	+0.00/-0.01
t_{fin}	0.50	+0.00/-0.05	0.50	+0.00/-0.05
N_{column}	2	0	7	0
N_{duct}	74	0	169	0

A simplified drawing of the glass spacer is shown in Fig. 5.1.3. The high pressure fluid flows through one rectangular hole in the spacer and the low pressure fluid returns through the other rectangular hole. The outer dimensions of the spacer, W_{die} and H_{die}, are identical to those of the silicon plate. The distance between the two fluid streams is $W_{g,stream}$. The area of the rectangular holes for fluid flow is the product of W_{gw} and H_{gw}. The thickness of the glass spacer is t_{sp}. The numerical values of each dimension and the associated tolerance are presented in Table 5.1.2 for both the 10x10 mm and 20x20 mm heat exchangers.

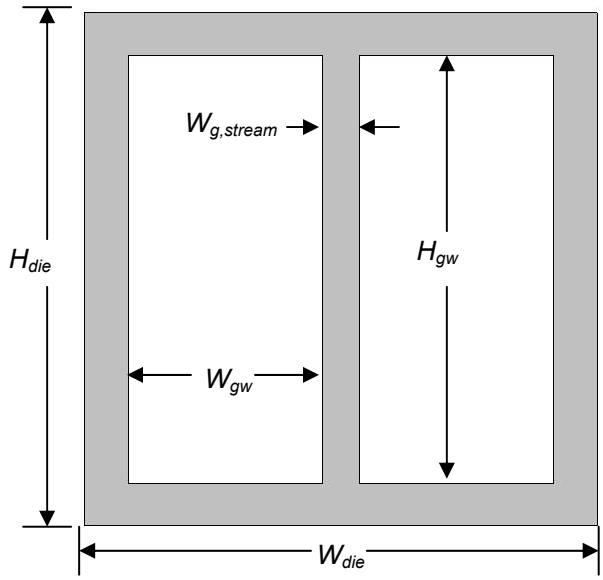

Fig. 5.1.3: Simplified drawing of glass spacer

Table 5.1.2: Dimensions in millimeters for 10x10 mm and 20x20 mm heat exchanger glass spacers

Variable	10 mm HX Target [mm]	10 mm HX Tolerance [mm]	20 mm HX Target [mm]	20 mm HX Tolerance [mm]
W_{die}	9.77	±0.10	19.77	±0.10
H_{die}	9.77	±0.10	19.77	±0.10
$W_{g,stream}$	0.70	+0.10/-0.20	0.70	+0.10/-0.20
W_{gw}	3.70	±0.10	8.60	±0.10
H_{gw}	8.15	±0.10	17.85	±0.10
t_{sp}	0.30	±0.025	0.30	±0.025

The heat transfer and pressure drop correlations used in the design model are implemented in dimensionless form so that the same correlations can be used regardless of which fluid is being tested in the heat exchanger, provided that the fluid is single phase and pure. Following the approach of Shah and London [18], the aspect ratio of the channel α is defined as the ratio of the height of the duct H_{duct} to the width of the duct W_{duct} :

$$\alpha = \frac{H_{duct}}{W_{duct}} \tag{5.1.1}$$

Most heat transfer and pressure drop correlations assume that flow is through a pipe or duct with a circular cross section; the characteristic dimension for this situation is the diameter of the duct. The concept of a hydraulic diameter was developed in order to define the characteristic

dimension for flow through non-circular duct shapes. The hydraulic diameter, D_{hyd}, can be calculated using Eq. 5.1.2, where A_{flow} is the cross sectional area for fluid flow and P_{wetted} is the "wetted" perimeter of the cross sectional area for fluid flow. Also shown on in Eq. 5.1.2 in the far right expression are the symbols from Fig. 5.1.1 that are used to calculate the hydraulic diameter of a rectangular duct.

$$D_{hyd} = \frac{4A_{flow}}{P_{wetted}} = \frac{4\left(W_{duct}\,H_{duct}\right)}{\left(2W_{duct} + 2H_{duct}\right)} \tag{5.1.2}$$

Since the ducts in the heat exchanger have such small aspect ratios, the fluid behavior in the ducts will be similar to flow between parallel plates. Parallel plates do not have a continuous perimeter, so a hydraulic diameter cannot be found using the definition of Eq. 5.1.2. However, taking the limit of Eq. 5.1.2 as W_{duct} approaches infinity, Eq. 5.1.2 reduces to Eq. 5.1.3. Since the definition of parallel plates is that the duct width is infinite, the equivalent hydraulic diameter that should be used for parallel plate ducts is Eq. 5.1.3.

$$D_{hyd,pp} = 2H_{duct} \tag{5.1.3}$$

The hydraulic diameter and aspect ratio are given for both the 10x10 mm and 20x20 mm heat exchanger in Table 5.1.3. Also shown is the hydraulic diameter of the ducts, if the ducts were approximated as parallel plates. Note that the parallel plate hydraulic diameter is only a function of the duct height.

Table 5.1.3: Hydraulic diameter and aspect ratio for both the 10x10 mm and 20x20 mm heat exchangers

	α	D_{hyd} [mm]	$D_{hyd,pp}$ [mm]
10 mm HX	0.0357	0.0966	0.100
20 mm HX	0.0500	0.0952	0.100

All of the design model geometry information discussed in Chp. 5.1 has been entered into the main program of EES as shown in Design Model Code 5.1.1. Note that either 10mm or 20mm heat exchanger geometry can be selected using the string variable DieGeom$.

Design Model Code 5.1.1: Die geometry of both 10mm and 20mm heat exchangers. This section of code is located in the main body of the EES program.

```
"*************************************************************************************************"
"HEAT EXCHANGER DIE GEOMETRY INFORMATION"
$If HX$='16die10mm'
    "Heat Exchanger used for testing in summer of 2007 with G10 headers"
    {N_die=16}                          "Check number of dies at top of program"
    DieGeom$='10mm'                     "size of dies"
    D_bolt=0.105 [in]*convert(in,m)     "minor diameter of #6 bolts"
    L_bolt=(t_sp+t_fin)*N_die#          "length of bolts"
$Endif
```

```
$If HX$='43die10mm'
    "Heat exchanger tested in the spring of 2008 with stainless steel headers"
    {N_die=43}                          "Check number of dies at top of program"
    DieGeom$='10mm'                     "size of dies"
    D_bolt=0.076 [in]*convert(in,m)     "minor diameter of #4 bolts"
    L_bolt=(t_sp+t_fin)*N_die#          "length of bolts"
$Endif


$If HX$='37die20mm'
    "Heat exchanger tested in the spring of 2008 with stainless steel headers"
    {N_die=43}                          "Check number of dies at top of program"
    DieGeom$='20mm'                     "size of dies"
    D_bolt=0.076 [in]*convert(in,m)     "minor diameter of #4 bolts"
    L_bolt=(t_sp+t_fin)*N_die#          "length of bolts"
$Endif

$If HX$='Test'
    "Fictional heat exchanger for comparing with real heat exchangers"
    {N_die=43}                          "Check number of dies at top of program"
    DieGeom$='10mm'                     "size of dies"
    D_bolt=0.076 [in]*convert(in,m)     "minor diameter of #4 bolts"
    L_bolt=(t_sp+t_fin)*N_die#          "length of bolts"
$Endif


$If DieGeom$='20mm'
    "overall dimensions"
    W_die=19.77[mm]*convert(mm,m)           "width of outer edge of HX die"
    H_die=19.77[mm]*convert(mm,m)           "height of outer edge of HX die"
    t_sp=0.3[mm]*convert(mm,m)              "thickness of glass spacer"
    t_fin=0.5[mm]*convert(mm,m)             "thickness of silicon fin"

    "silicon fin dimensions"
    W_si_stream=1.7 [mm]*convert(mm,m)      "minimum distance between fluid streams"
    H_duct=0.05[mm]*convert(mm,m)           "height of fluid duct"
    H_fin=0.05[mm]*convert(mm,m)            "height of fin"
    W_fin=7.6[mm]*convert(mm,m)             "width of fins (N_column*L_slot+N_web*L_web)"
    W_duct=1[mm]*convert(mm,m)              "width of fluid duct"
    W_web=0.1[mm]*convert(mm,m)             "width of web between slots"

    N_fin=170                               "number of fins in each column"
    N_duct=169                              "number of slots in each column"
    N_web=6                                 "number of webs"
    N_column=7                              "number of duct coulmns for each stream"

    "pryex spacer dimensions"
    W_g_stream=0.7 [mm]*convert(mm,m)       "width of spacer between streams"
    H_gw=17.85 [mm]*convert(mm,m)           "height of window"
    W_gw=8.60 [mm]*convert(mm,m)            "width of window"
$endif

$If DieGeom$='10mm'
    "overall dimensions"
    W_die=9.77[mm]*convert(mm,m)            "width of outer edge of HX die"
    H_die=9.77[mm]*convert(mm,m)            "height of outer edge of HX die"
```

```
    t_sp=0.3[mm]*convert(mm,m)                "thickness of glass spacer"
    t_fin=0.5[mm]*convert(mm,m)               "thickness of silicon fin"

    "silicon fin dimensions"
    W_si_stream=1.5[mm]*convert(mm,m)         "minimum distance between fluid streams"
    H_duct=0.05[mm]*convert(mm,m)             "height of fluid duct"
    H_fin=0.05[mm]*convert(mm,m)              "height of fin"
    W_fin=2.9[mm]*convert(mm,m)               "width of fins(N_column*L_slot+N_web*L_web)"
    W_duct=1.4[mm]*convert(mm,m)              "width of fluid duct"
    W_web=0.1[mm]*convert(mm,m)               "width of web between slots"

    N_fin=75                                  "number of fins in each column"
    N_duct=74                                 "number of slots in each column"
    N_web=1                                   "number of webs"
    N_column=2                                "number of duct coulmns for each stream"

    "pryex spacer dimensions"
    W_g_stream=0.7 [mm]*convert(mm,m)        "width of spacer between streams"
    H_gw=8.15 [mm]*convert(mm,m)             "height of window"
    W_gw=3.7 [mm]*convert(mm,m)              "width of window"
$endif

"Calculating areas and hydraulic diameters of silicon fin"
A_si_unetch=H_die*W_die                       "cross sectional area of silicon fin"
A_si_flow=N_column*N_duct*(W_duct*H_duct)     "cross sectional area for flow for one stream"
P_si_flow=N_column*N_duct*2*(W_duct+H_duct) "perimeter of flow area for one stream"
D_hyd=4*A_si_flow/P_si_flow                   "hydraulic diameter of flow area"
alpha=H_duct/W_duct                           "aspect ratio of the duct"
A_si_cond=A_si_unetch-2*A_si_flow             "cross sectional area for axial conduction"

"Calculating areas and  hydraulic diameters of glass spacer"
A_sp_unetch=W_die*H_die                       "cross sectional area of spacer before etching"
A_sp_flow=H_gw*W_gw                           "cross sectional area for flow for one stream"
P_sp_flow=2*(H_gw+W_gw)                       "perimeter of flow area for one stream"
D_hyd_sp=4*A_sp_flow/P_sp_flow                "hydraulic diameter of flow area"
A_sp_cond=A_sp_unetch-2*A_sp_flow             "cross sectional area for axial conduction"

"*****************************************************************************************************************"
```

5.2 Material Properties

The heat exchanger is being analyzed only at steady state conditions; therefore, the material property of most significant interest is the thermal conductivity. The thermal conductivity of a material often changes by an order of magnitude or more between room temperature and cryogenic temperatures. Therefore, the assumption of a constant conductivity (even one that is defined at the average temperature seen by the heat exchanger) will likely lead to large modeling errors. This section will describe how thermal conductivities are determined as a function of temperature for both the silicon and glass.

Silicon and glass are not commonly used materials for fabricating heat exchangers, so it is helpful to compare the conductivities of silicon and glass to the more common heat exchanger materials, such as copper and stainless steel. As shown in Fig. 5.2.1, the thermal conductivity of silicon is roughly comparable to that of copper and the thermal conductivity of Pyrex is roughly an order of magnitude less than stainless steel. The thermal conductivities of stainless steel and

copper are well known and can be calculated in the range of 4 K to 300 K to within 2% accuracy using curve fits supplied by the Cryogenic Technologies Group at NIST [19]. Using the values in Table 5.2.1, the thermal conductivities of copper (k_{cu}) and stainless steel (k_{ss}) can be calculated using Eq. 5.2.1 and Eq. 5.2.2 respectively. Note that RRR is the residual resistivity ratio, which is defined as the ratio of the electrical resistance at 300 K to the electrical resistance at 4.2 K. The RRR is a measure of the purity of the metal and becomes an important parameter when trying to determine the thermal conductivity of metals at low temperature, as shown in Fig. 5.2.1 for copper. The properties for pure silicon are from the Thermophysical Properties of Matter Vol. 1 [20] and the properties for Pyrex are from the Cryocomp 2.0 software package [21].

Table 5.2.1: Values used for calculating the thermal conductivity of copper and stainless steel [19]

Thermal Conductivity [W/m-K]						
Material Purity/Alloy	Copper RRR=50	Copper RRR=100	Copper RRR=150	Copper RRR=300	Copper RRR=500	Stainless Steel 304/304L/316
a	1.8743	2.2154	2.3797	1.357	2.8075	-1.4087
b	-0.41538	-0.47461	-0.4918	0.3981	-0.54074	1.3982
c	-0.6018	-0.88068	-0.98615	2.669	-1.2777	0.2543
d	0.13294	0.13871	0.13942	-0.1346	0.15362	-0.626
e	0.26426	0.29505	0.30475	-0.6683	0.36444	0.2334
f	-0.0219	-0.02043	-0.019713	0.01342	-0.02105	0.4256
g	-0.051276	-0.04831	-0.046897	0.05773	-0.051727	-0.4658
h	0.0014871	0.001281	0.0011969	0.0002147	0.0012226	0.165
i	0.003723	0.003207	0.0029988	0	0.0030964	-0.0199

$$\log_{10}(k_{cu}) = \frac{a + cT^{0.5} + eT + gT^{1.5} + iT^2}{1 + bT^{0.5} + dT + fT^{1.5} + hT^2} \tag{5.2.1}$$

$$\begin{aligned}\log_{10}(k_{ss}) &= a + b\left(\log_{10}(T)\right) + c\left(\log_{10}(T)\right)^2 + d\left(\log_{10}(T)\right)^3 + e\left(\log_{10}(T)\right)^4 \\ &+ f\left(\log_{10}(T)\right)^5 + g\left(\log_{10}(T)\right)^6 + h\left(\log_{10}(T)\right)^7 + i\left(\log_{10}(T)\right)^8\end{aligned} \tag{5.2.2}$$

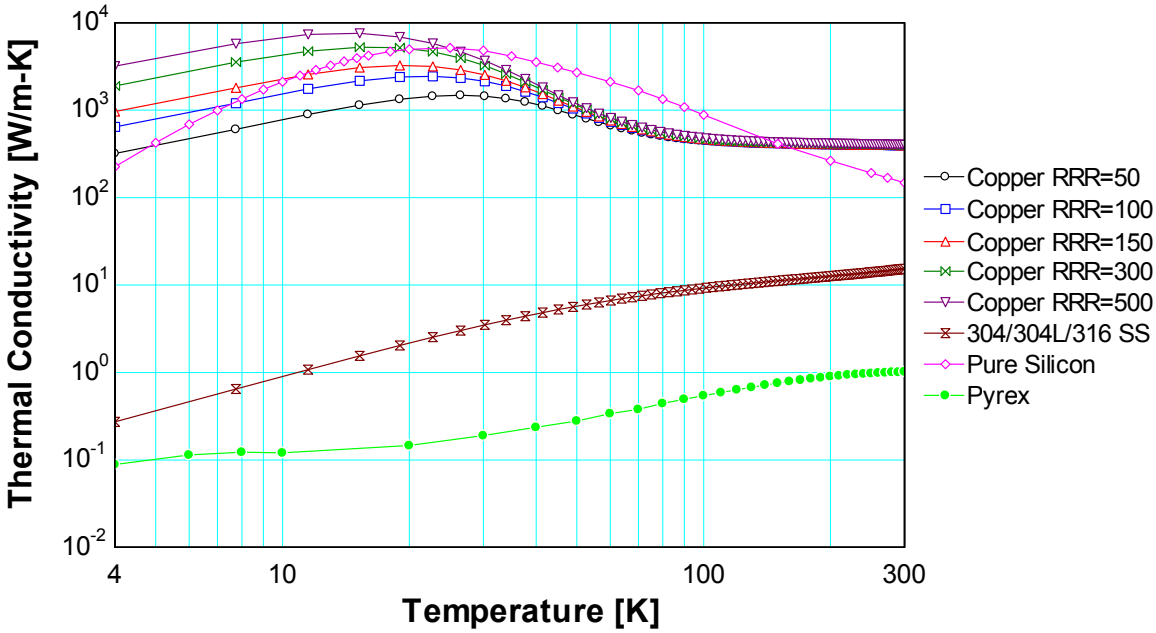

Fig. 5.2.1: Comparison of the thermal conductivity of copper [19], stainless steel [19], pure silicon [20], and pyrex [21].

Silicon, a pure element like copper, also exhibits significant changes in thermophysical properties at cryogenic temperatures that are dependent to a large degree on the purity of the sample. The silicon plates are etched and diced from a (110) P-doped silicon wafer with a resistivity range of 1 to 20 Ω-cm and a thickness of 450 to 500 µm. The (110) used to describe the silicon wafer is a crystallographic plane defined using Miller Indices [25]. The ducts are etched so that the heat is conducted through the fins parallel to the (111) plane. Doping, oxygen concentration, surface preparation, cross sectional area, and crystal orientation are all expected to have an effect the thermal conductivity of silicon [22]. However, crystal orientation has no measurable effect on thermal conductivity above 30 K and all orientations have less than a 10% difference down to 3 K [23]. Since the heat exchanger is unlikely to be used at temperatures below 100 K, the effect of crystal orientation will not be included in the design model.

Phonons are quantized vibrations in the crystal lattice structure and transport almost all of the energy associated with diffusion (i.e., conduction) in semiconductors. Metals on the other hand, transport almost all of the energy associated with diffusion by electrons [20]. The sample surface quality is important at very low temperatures where the boundaries of the sample lead to scattering of phonons [24]. Boundary scattering is not a completely understood phenomenon, but it appears that a very smooth surface leads to the specular reflection of phonons while a rougher surface leads to the diffuse reflection of phonons; Fig. 5.2.2 shows both specular and diffuse reflection of phonons. When a phonon moving from hot-to-cold is reflected specularly from a surface, the phonon is still traveling in towards the cold end of the sample after the reflection. However, when a phonon moving from hot-to-cold is reflected diffusely, it may be reflected towards the hot end of the sample or towards the cold end of the sample. Using this logic, rough surfaces will inhibit the transport of phonons and thus reduce the overall thermal conductivity.

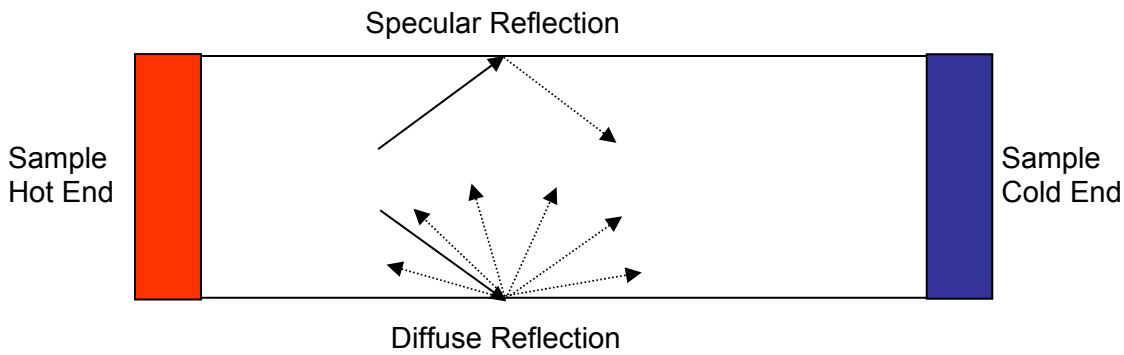

Fig. 5.2.2: Diagram of specular and diffuse reflection of phonons off the walls of a silicon sample. The solid lines represent the original trajectory of the phonon and the dashed lines represent the possible trajectories after reflection

Hurst and Frankl [24] measured the thermal conductivity between 1 K and 4 K for many samples of silicon whose only difference was the degree of polishing. They polished a number of samples with a 1 μm diamond compound and polished some of them further with an even finer abrasive called Lustrox. They found that polishing with the Lustrox can increase the silicon thermal conductivity by as much as a factor of 3 when compared to diamond polishing alone at 4 K. The samples that Hurst and Frankly used had effective diameters close to 0.9 mm, whereas the silicon fins in the 10mm and 20mm heat exchangers have an effective diameter of 0.09 mm. The effective diameter for phonon conduction is essentially identical to the hydraulic diameter used in fluid flow calculations and can be calculated using Eq. 5.2.3:

$$D_{eff,cond} = \frac{4A_{cond}}{P_{sample}} \tag{5.2.3}$$

where $D_{eff,cond}$ is the effective diameter, A_{cond} is the cross sectional area for conduction, and P_{sample} is the perimeter of the cross sectional area for conduction. Surface roughness would certainly play a large role in determining the silicon thermal conductivity near liquid helium temperatures.

The scattering of phonons at surfaces appears to be the reason that many authors report a conductivity that is dependent on the size of the sample. The smaller the sample, the more likely it is that a given phonon being transported will interact with the sample surface. Also, many authors did not measure the surface roughness or take the care to polish the surface as finely as Hurst and Frankl. The large amount of scatter that is observed between the measurements taken by different experimenters at low temperature is at least partially due to the variance of surface roughness and sample size.

The effects of surface quality and cross sectional area were not taken into account in the design model for several reasons. The first is that the silicon roughness is unknown. However, the etching processes used to create the ducts is expected to leave the surface very smooth, which should lead to a higher conductivity. In addition there is some uncertainty in the cross sectional area due to manufacturing constraints (see Tables 5.1.1 and 5.1.2). Lastly, but most importantly,

no reliable data or correlations were found that provide for the effect of surface roughness and sample size across the temperature range (100 K to 300 K) that the heat exchanger is expected to operate in.

To determine the effect that the doping has on the thermal conductivity, the doping concentration must first be calculated. Pure silicon creates free electrons and electron holes in pairs. The intrinsic density n_i of the electron holes and the free electrons in pure silicon is $1.5\text{x}10^{10}$ cm^{-3} at room temperature. By comparison, silicon at room temperature has a density of $5\text{x}10^{22}$ atoms/cm^3. Boron has only three electrons in its outermost shell, so a Boron atom in a Silicon crystal lattice will absorb an electron to create an electron hole. If the electron holes are the primary method of conduction, then a semiconductor is referred to as a p-type (positive) material. At room temperature, electron donors (such as Phosphorus) and acceptors (such as Boron) can be assumed to be fully ionized so that the hole concentration p_0 can be assumed to be equal the Boron concentration. The free electron concentration n_0 can then be calculated by Eq. 5.2.4 [25].

$$n_0 = \frac{n_i^2}{p_0} \tag{5.2.4}$$

Knowing the density of the holes and free electrons, the resistivity ρ of the doped silicon can be calculated using Eq. 5.2.5 [25].

$$\rho = \frac{1}{q\left(\mu_N \; n_0 + \mu_p \; p_0\right)} \tag{5.2.5}$$

where q is the charge of an electron ($1.6\text{x}10^{-19}$ C), μ_N is the mobility of the electrons (1350 cm^2/V-s), and μ_p is the mobility of the electron holes (480 cm^2/V-s). Using Eq. 5.2.4 and Eq. 5.2.5, the Boron concentration was determined to be between $6.7\text{x}10^{14}$ cm^{-3} and $1.5\text{x}10^{16}$ cm^{-3} for the silicon wafers used in manufacturing the MEMS heat exchanger.

The last major factor in determining the thermal conductivity of silicon is the oxygen concentration. The silicon wafers used to make the heat exchanger plates have an unknown oxygen concentration and the manufacturer is also unknown since the wafer was ordered through a distributor that contracts with many wafer manufacturers. Oxygen, like boron doping, is expected to reduce the thermal conductivity of silicon and this will become a greater effect at lower temperatures.

Figure 5.2.3 illustrates a number of experimental measurements of the thermal conductivity of silicon taken on a variety of samples [20]. Key information about each of the curves, including dopant, dopant concentration, oxygen concentration, sample size, and experimenter are included in Table 5.2.2. The plot in Fig. 5.2.3 shows that there is a wide disparity between the thermal conductivity of different samples.

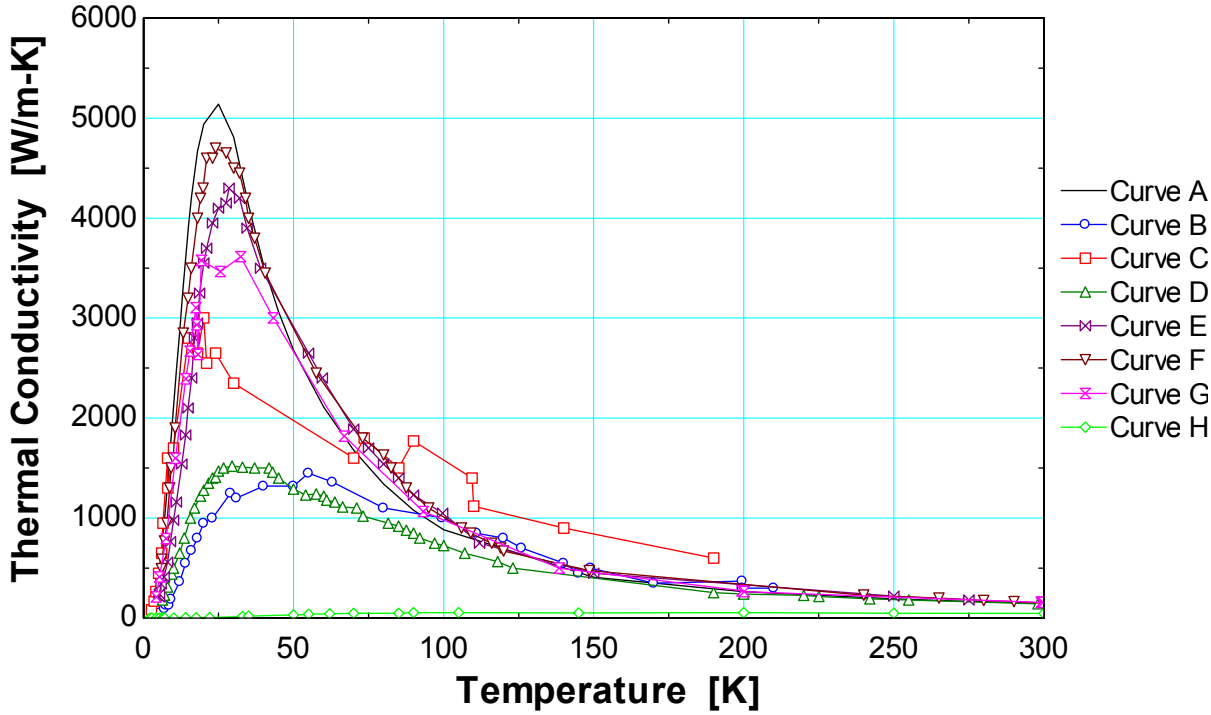

Fig. 5.2.3: Plot of the thermal conductivity of silicon for a number of different samples. The characteristics of each sample can be found in Table 5.2.2. Data from [20].

Table 5.2.2: Key characteristics of the silicon samples shown in Fig. 5.2.3. Data from [20].

Curve Letter	Dopant	Dopant Conc. [atom/cm^3]	Oxygen Conc. [atom/cm^3]	Electrical Resistivity [Ω-cm]	Temp. Range [K]	Sample Cross Section [cm]	Comments
A	None	NA	None	None	0-400	NA	TPM estimate for pure sample
B	Boron	1.0×10^{15}	2.0×10^{17}	7.2	3.5-210	0.3 x 0.3	Thompson & Younglove, 1961
C	Boron	2.0×10^{12}	$<10^{17}$	2000	2.6-190	0.3 x 0.3	Thompson & Younglove, 1961
D	Boron	4.8×10^{15}	7.0×10^{17}	3.0	6.3-298	0.616 x 0.623	Holland, 1961
E	Boron	4.0×10^{15}	$<10^{16}$	4.5	5.2-275	0.635 x 0.632	Holland, 1961
F	Boron	4.0×10^{14}	$<10^{16}$	45.5	5.9-300	0.630 x 0.640	Holland, 1961
G	Boron	High Purity	High Purity	2000	4.3-304	0.44 OD	Glassbrenner & Slack, 1964
H	Boron	3×10^{20}	?	0.0004	2.1-300	0.56 OD	Slack, 1964

As previously mentioned, the greatest scatter in the measured thermal conductivity occurs at very cold temperatures. The heat exchanger is only intended for use in the range of 100 K to 300 K. Figure 5.2.3 shows that many of the measurements converge around 100 K and therefore small variations in the silicon chemistry are unlikely to have a large effect on thermal conductivity in the operating range of the heat exchanger. The silicon wafer used to make the heat exchanger fins has an electrical resistivity range of 1 to 20 Ω-cm, which is orders of magnitude different

from the electrical resistivity of the samples that were used to generate curves C, G, and H. If these curves are removed and Fig. 5.2.3 is re-plotted over the temperature range of interest, from 100 K to 300 K, the result is Fig. 5.2.4.

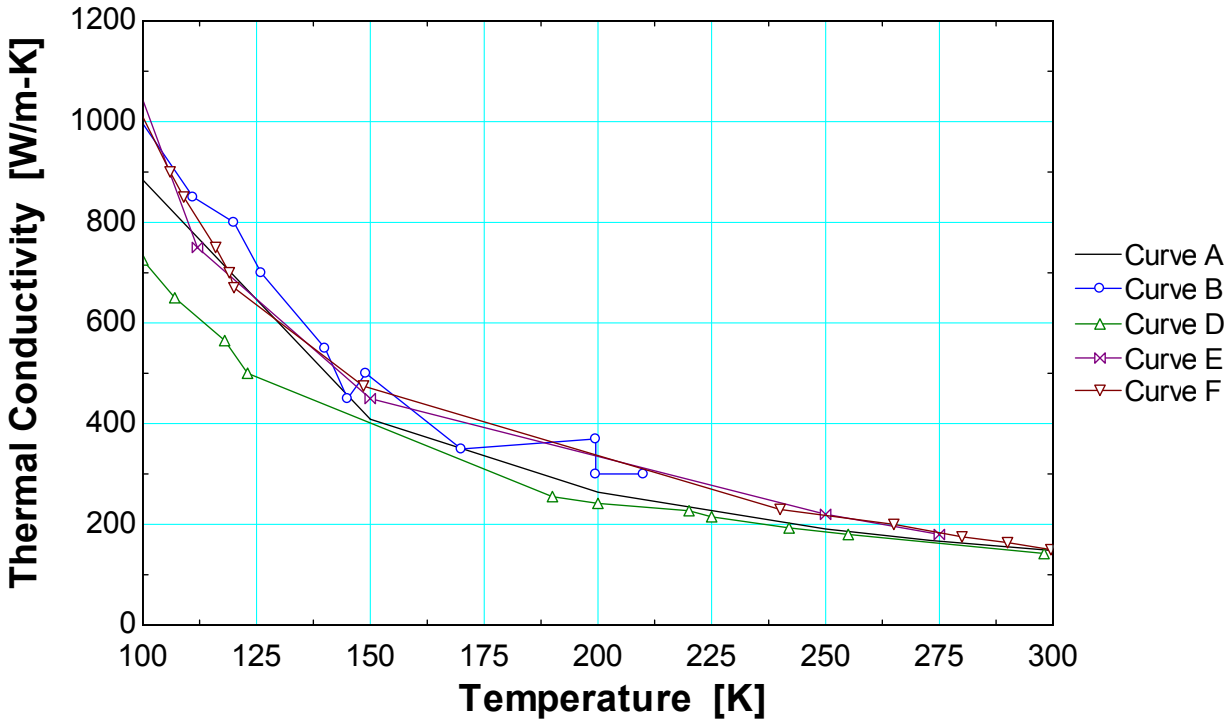

Fig. 5.2.4: Figure 5.2.2 with curves C, G, and H removed and re-plotted from 100 K to 300 K.

If curve A is considered to be the best estimate of the silicon thermal conductivity, then the relative deviation of the various samples from curve A is about 20% at 100 K. The relative deviation drops to about 10% at 300 K. The design model uses curve A to represent the silicon thermal conductivity since there is no way of determining which of the alternative curves most closely resembles the silicon in the heat exchanger fins.

The glass spacer is made from Borofloat 33, which is a borosilicate glass similar to Pyrex. The manufacturer of the glass spacer material only provides thermal conductivity values between 300 K and 450 K and is unaware of any measurements that have been taken below 300 K [26]. As shown in Fig. 5.2.5, at 300 K the conductivity provided by the Borofloat manufacturer is about 5% higher than that of Pyrex. The behavior of Pyrex provides the best available estimate of the thermal conductivity of Borofloat below 300 K. The design model uses conductivity values of Pyrex from Cryocomp [21] for temperatures below 230 K, and interpolates between the Cryocomp value at 230 K and the manufacturers data for Borofloat at 300 K for conductivity values over the temperature range of 230 K to 300 K. The conductivity curve used by the design model is also shown in Fig. 5.2.5.

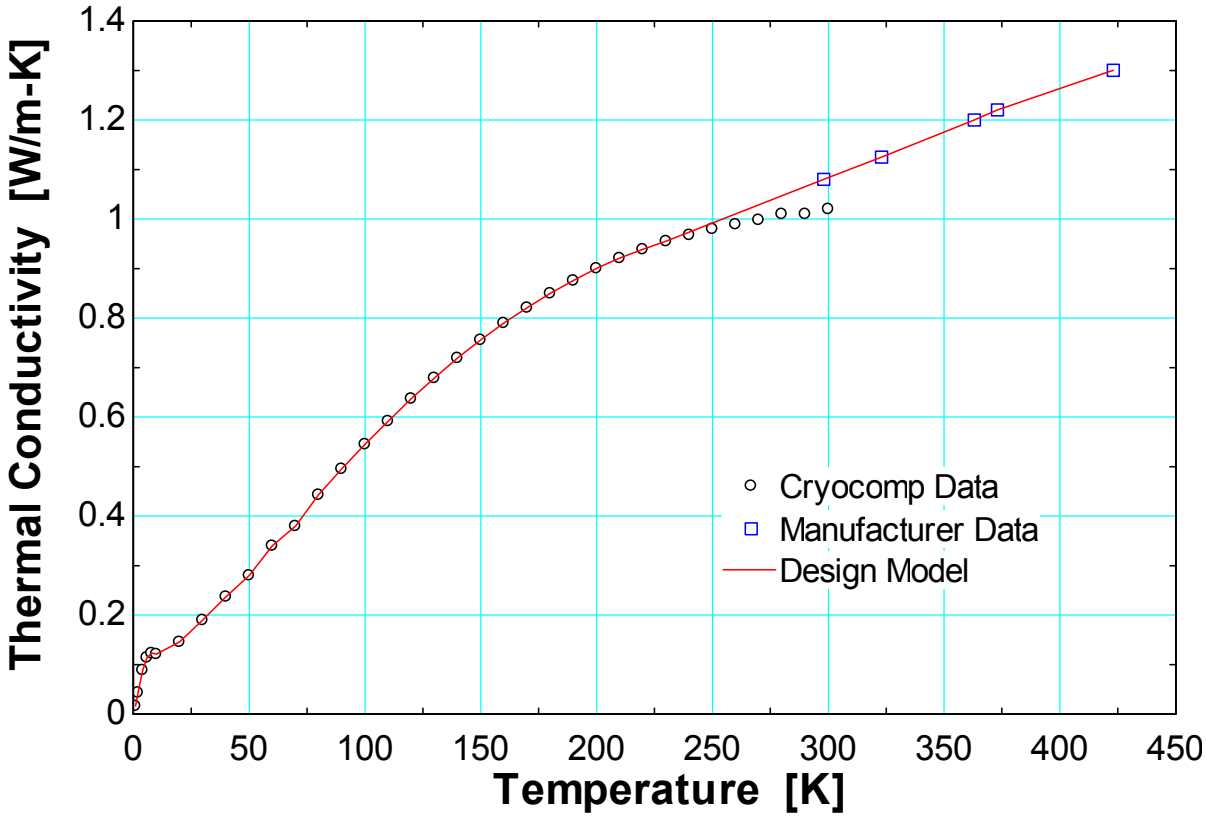

Fig. 5.2.5: Thermal conductivity of borosilicate glass as a function of temperature. Data points labeled Cryocomp Data are from [21], Data points labeled Manufacturer Data are from [26], and the line labeled Design Model shows the values that the design model will use for the glass spacer

The design model determines a material's thermal conductivity by interpolating between data points provided in a EES Lookup Table. All of the data points used for silicon, glass, and stainless steel are presented in Table 5.2.3. The thermal conductivity of stainless steel is important for calculating heat exchanger performance because there will be penalty associated with heat conducted through the bolts that hold the heat exchanger assembly together.

Table 5.2.3: The values in EES Lookup Tables used for interpolating thermal conductivity of various heat exchanger materials.

Silicon		Glass		Stainless Steel	
T [K]	k [W/m-K]	T [K]	k [W/m-K]	T [K]	k [W/m-K]
0	0	1	0.0165	10	0.9039
1	4.48	2	0.0435	20	2.169
2	31.7	4	0.0892	30	3.469
3	99.8	6	0.114	40	4.67
4	226	8	0.123	50	5.73
5	424	10	0.121	60	6.647
6	686	20	0.146	70	7.435
7	991	30	0.19	80	8.114
8	1340	40	0.237	90	8.705
9	1720	50	0.28	100	9.224
10	2110	60	0.34	110	9.685
11	2480	70	0.38	120	10.1
12	2870	80	0.443	130	10.48
13	3250	90	0.495	140	10.83
14	3600	100	0.545	150	11.17
15	3930	110	0.592	160	11.48
16	4220	120	0.637	170	11.78
18	4670	130	0.679	180	12.07
20	4940	140	0.719	190	12.35
25	5140	150	0.756	200	12.63
30	4810	160	0.79	210	12.91
35	4130	170	0.821	220	13.18
40	3530	180	0.85	230	13.45
45	3060	190	0.876	240	13.71
50	2680	200	0.9	250	13.98
60	2110	210	0.921	260	14.25
70	1680	220	0.939	270	14.51
80	1340	230	0.955	280	14.78
90	1080	298	1.08	290	15.04
100	884	323	1.125	300	15.31
150	409	363	1.2	310	15.57
200	264	373	1.22	320	15.84
250	191	423	1.3	330	16.1
273.2	168			340	16.36
300	148			350	16.62
350	119				
400	98.9				

The EES function that determines the silicon and glass conductivity for an individual die is shown in Design Model Code 5.2.2. Note that the conductivity can be determined using Lookup Table values or by manually setting the thermal conductivity. The code for determining the thermal conductivity of stainless steel is shown in the section on axial conduction, Chp. 5.7.

Design Model Code 5.2.2: The EES function used for determining the thermal conductivity of silicon and glass. This section is an internal procedure and is found at the top of the EES file before the main body of equations.

```
"*****************************************************************************************************************"
Procedure MatProp(T: k_si, k_glass)
"!Returns material properties based on temperature"

{   "constant material properties"
    k_si=200 [W/m-K]                "silicon thermal conductivity"
    k_glass=1.0 [W/m-K]             "glass thermal conductivity"}

    "variable material properties"
    k_si=Interpolate('Si Cond', T,k, T=T)                "silicon thermal conductivity"
    k_glass=Interpolate('Glass Cond', T,k, T=T)          "glass thermal conductivity"

End

"*****************************************************************************************************************"
```

5.3 Laminar Flow Heat Transfer and Pressure Drop Correlations

This section begins with a discussion on important dimensionless parameters for fluid flow. The rest of the section explains in detail how the correlations used for predicting heat transfer and pressure drop under laminar flow conditions were chosen.

The Reynolds number *Re* is the ratio of inertial forces to viscous forces and is important for prediction both heat transfer and pressure drop behavior of a fluid. The Reynolds number can be calculated by Eq. 5.3.1, where ρ is the fluid density, V_m is the mean fluid velocity, and μ is the fluid dynamic viscosity [28].

$$Re = \frac{\rho \; V_m \; D_{hyd}}{\mu} \tag{5.3.1}$$

Using the hydraulic diameter and the Reynolds number, a hydrodynamic dimensionless length x^+ at an axial distance of x along the duct can be calculated using the approach of Shah and London [18] and is shown in Eq. 5.3.2.

$$x^+ = \frac{x}{D_{hyd} \; Re} \tag{5.3.2}$$

The Peclet number *Pe* is the ratio of the thermal energy convected by the fluid to the thermal energy conducted axially through the fluid. The Peclet number can be calculated by Eq. 5.3.3 where *Cp* is the specific heat at constant pressure for the fluid, *k* is the thermal conductivity of the fluid, and *Pr* is the Prandtl number of the fluid [18].

$$Pe = \frac{\rho \; V_m \; Cp \; D_{hyd}}{k} = Re \; Pr \tag{5.3.3}$$

The thermal dimensionless length x^* can be calculated using Eq. 5.3.4 [18].

$$x^* = \frac{x}{D_{hyd}\ Pe} = \frac{x}{D_{hyd}\ Re\ Pr} \tag{5.3.4}$$

The aspect ratio α and the Reynolds number Re allow the fully developed Fanning friction factor $f_{Fanning}$ to be calculated using Eq. 5.3.5, as given by Shah and London [18]. Equation 5.3.5 is a numerical approximation to an infinite series analytical solution derived from the momentum equation for rectangular ducts with a no-slip boundary condition. The numerical approximation is reported to be within ±0.05% of the analytical solution.

$$f_{Fanning} = \frac{24}{Re}\left[1 - 1.3553\alpha + 1.9467\alpha^2 - 1.7012\alpha^3 + 0.9564\alpha^4 - 0.2537\alpha^5\right] \tag{5.3.5}$$

For the remainder of this thesis, the Darcy (Moody) friction factor f_{Darcy} will be used and all correlations will be adjusted appropriately. The Fanning friction factor is related to the Darcy friction factor as shown in Eq. 5.3.6 [18].

$$f = f_{Darcy} = 4 f_{Fanning} \tag{5.3.6}$$

Therefore, Eq. 5.3.5 can be combined with Eq. 5.3.6 to yield Eq. 5.3.7.

$$f_{fd,lam} = \frac{96}{Re}\left[1 - 1.3553\alpha + 1.9467\alpha^2 - 1.7012\alpha^3 + 0.9564\alpha^4 - 0.2537\alpha^5\right] \tag{5.3.7}$$

As the aspect ratio α approaches zero, the behavior of a rectangular duct should approach that of parallel plates. If a value of zero is input for α in Eq. 5.3.7, then Eq. 5.3.7 collapses into the analytical solution for the parallel plate fully developed friction factor $f_{fd,lam,pp}$ given in Eq. 5.3.8 [18].

$$f_{fd,lam,pp} = \frac{96}{Re} \tag{5.3.8}$$

Using the fully developed friction factor would significantly underestimate the pressure drop for short ducts (such as are found in the perforated plate heat exchanger) because it ignores the increase in the apparent friction factor that occurs while the flow is developing hydrodynamically which is related to the increase in the shear stress as well as the acceleration of the fluid core. No correlations were found in the literature for simultaneously developing flow in a rectangular duct, but Shah [18] developed a correlation for an apparent friction factor between two parallel plates. The apparent friction factor $f_{app,lam,pp}$ accounts for the higher friction factor at the duct entrance and can be calculated using Eq. 5.3.9.

$$f_{app,lam,pp} = \frac{1}{Re}\left(\frac{4\cdot 3.44}{\sqrt{x^+}} + \frac{96 + 4\left(\frac{0.674}{4\cdot x^+} - \frac{3.44}{\sqrt{\left(x^+\right)}}\right)}{1 + \frac{0.000029}{\left(x^+\right)^2}}\right) \tag{5.3.9}$$

Shah et al. [18] show the derivation of Eq. 5.3.9, which combines two previously published correlations that were valid over two different ranges of the dimensionless hydrodynamic length x^+ into one correlation. The derivation reveals that the number 96 in Eq. 5.3.9 is the product of the fully developed friction factor $f_{fd,lam,pp}$ and the Reynolds number, which is the same relationship expressed in Eq. 5.3.8. If the fully developed friction factor for parallel plates $f_{fd,lam,pp}$ is replaced with the fully developed friction factor for rectangular ducts $f_{fd,lam}$, then Eq. 5.3.7 can be combined with Eq. 5.3.9 to form Eq. 5.3.10.

$$f_{app,lam} = \frac{4}{Re}\left(\frac{3.44}{\sqrt{x^+}} + \frac{\frac{f_{fd,lam}\cdot Re}{4} + \frac{0.674}{4\cdot x^+} - \frac{3.44}{\sqrt{\left(x^+\right)}}}{1 + \frac{0.000029}{\left(x^+\right)^2}}\right) \tag{5.3.10}$$

Taking the limit of the apparent friction factor as the thermal dimensionless length approaches infinity reduces Eq. 5.3.9 and Eq. 5.3.10 to the fully developed friction factor for parallel plates and rectangular ducts respectively. In other words, the apparent friction factor approaches the fully developed friction factor as the duct length increases. Since a long duct would have fully developed flow along almost the entire length of the duct, this is the behavior that would be expected.

Another way to check the validity of Eq. 5.3.10 is to compare the equations calculated results to those tabulated for apparent friction factors in rectangular ducts. Table 5.3.1 shows the finite difference results of Curr (1972), which Shah and London report to be in excellent agreement with experimental data from Beavers et al (1970) [18]. The maximum difference between Eq. 5.3.10 and Curr's results is 9.76% for an aspect ratio of 0.2 and 17.49% for an aspect ratio of 0.5. The increase in error is expected as the rectangular duct becomes more like a square duct and less like a parallel plate duct. The aspect ratio for the ducts in both heat exchangers is less than 0.05, which is nearly the aspect ratio of a parallel plate duct, so the expected error of using Eq. 5.3.10 on the heat exchangers would likely be much less than 10%.

Table 5.3.1: Comparison of apparent friction factors derived using two different methods. The results under Curr are tabulated results using a finite difference solution. The results under Shah were obtained by modifying the parallel plate correlation to include the fully developed friction factor in rectangular ducts.

	α = 0.2				α = 0.5		
x^+ [-]	Curr f_{app} [-]	Shah f_{app} [-]	Difference [%]		Curr f_{app} [-]	Shah f_{app} [-]	Difference [%]
0.001	444	445.6	-0.36		444	445.2	-0.27
0.002	320.8	320.5	0.10		320.8	318.8	0.64
0.003	264.4	263.0	0.53		264	259.7	1.64
0.004	231.6	227.2	1.88		230.4	222.2	3.54
0.005	210	202.2	3.70		207.2	195.7	5.54
	0	0.0			0	0.0	
0.006	193.6	183.7	5.10		190.4	175.9	7.61
0.007	181.2	169.6	6.42		178.4	160.7	9.91
0.008	170.8	158.4	7.24		167.2	148.8	11.03
0.009	162.4	149.6	7.91		160	139.2	13.00
0.01	155.6	142.3	8.53		152.8	131.4	13.98
	0	0.0			0	0.0	
0.015	133.2	120.2	9.76		130	107.8	17.11
0.02	120.8	109.1	9.67		116.4	96.0	17.49
0.03	106.8	98.2	8.09		101.2	84.5	16.48
0.04	99.6	92.7	6.91		92.8	78.9	15.00
0.05	94.8	89.4	5.65		87.2	75.6	13.35
	0	0.0			0	0.0	
0.06	91.6	87.3	4.72		83.2	73.3	11.88
0.07	89.6	85.7	4.33		80.4	71.8	10.75
0.08	88	84.6	3.91		78.4	70.6	10.00
0.09	86.8	83.6	3.64		76.4	69.6	8.85
0.1	85.6	82.9	3.13		75.2	68.9	8.40

The laminar frictional pressure drop ($\Delta P_{friction,lam}$) through the duct can be calculated from Eq. 5.3.11 using the apparent friction factor, where x is the duct length, V is the mean fluid velocity in the duct, and ρ is the fluid density.

$$\Delta P_{friction,lam} = f_{app,lam}\rho \frac{x}{D_{hyd}} \frac{V_m^2}{2} \tag{5.3.11}$$

There will also be pressure drops due to fluid contraction and expansion as the fluid flows in and out of the ducts between the silicon fins. For large expansions and contractions, the fluid has little kinetic energy coming into the duct and loses almost all of its kinetic energy coming out of the duct [28]. This means that the contraction loss coefficient K_{cont} and the expansion loss coefficient K_{exp} are both nearly one, and will be conservatively assumed to have a value of one for the design model so that the pressure drop is not underestimated. The pressure drops to due to contraction and expansion can be calculated using Eq. 5.3.12 and Eq. 5.3.13 respectively,

where $V_{m,duct}$ is the mean velocity in the duct. The total pressure drop through one plate, assuming laminar flow, can be calculated using Eq. 5.3.14.

$$\Delta P_{cont} = \rho_{fluid} K_{cont} \frac{V_{m,duct}^2}{2} \tag{5.3.12}$$

$$\Delta P_{exp} = \rho_{fluid} K_{exp} \frac{V_{m,duct}^2}{2} \tag{5.3.13}$$

$$\Delta P_{tot,lam} = \Delta P_{cont} + \Delta P_{friction,lam} + \Delta P_{exp} \tag{5.3.14}$$

The Nusselt number for fully developed laminar flow through a rectangular duct is sensitive to the thermal boundary conditions applied. For a constant temperature on all surfaces of the duct and fully developed laminar flow, the Nussult number $Nu_{T,lam}$ can be calculated using Eq. 5.3.15 [11]. Eq. 5.3.15 is an approximation of the numerical results presented by Miles and Shih (1967) and Eq. 5.3.15 yields Nusselt numbers that are within ±0.1% of the numerical results.

$$Nu_{T,lam} = 7.541\left[1 - 2.610\alpha + 4.970\alpha^2 - 5.119\alpha^3 + 2.702\alpha^4 - 0.548\alpha^5\right] \tag{5.3.15}$$

Like the friction factor, the Nusselt number for parallel plates at constant temperature $Nu_{T,lam,,pp}$ should equal Eq. 5.3.15 in the limit that the aspect ratio α approaches zero. This is the case, as shown by Eq. 5.3.16 [18].

$$Nu_{T,lam,pp} = 7.541 \tag{5.3.16}$$

Another possible thermal boundary condition for fully developed laminar flow is a constant wall heat flux. Marco and Hahn (1955) derived an infinite series analytical solution for this boundary condition, and their results can be approximated to within ±0.03% using Eq. 5.3.17 [18].

$$Nu_{H,lam} = 8.235\left[1 - 2.0421\alpha + 3.0853\alpha^2 - 2.4765\alpha^3 + 1.0578\alpha^4 - 0.1861\alpha^5\right] \tag{5.3.17}$$

Again the Nusselt number for rectangular ducts approaches the Nusselt number for parallel plates $Nu_{H,pp}$ as the aspect ratio approaches zero, as shown in Eq. 5.3.18 [18].

$$Nu_{H,lam,pp} = 8.235 \tag{5.3.18}$$

The fully developed Nusselt number under constant temperature and constant heat flux boundary conditions are shown as a function of aspect ratio in Fig. 5.3.1 for both parallel plates and rectangular ducts. Since the passages through the silicon fins for both heat exchanger cross sections have a low aspect ratio, the Nusselt number is almost as high as it could have been had the passages truly been parallel plates for both thermal boundary conditions. The fully developed Nusselt numbers for both the 10 mm and 20 mm heat exchangers are tabulated in Table 5.3.2.

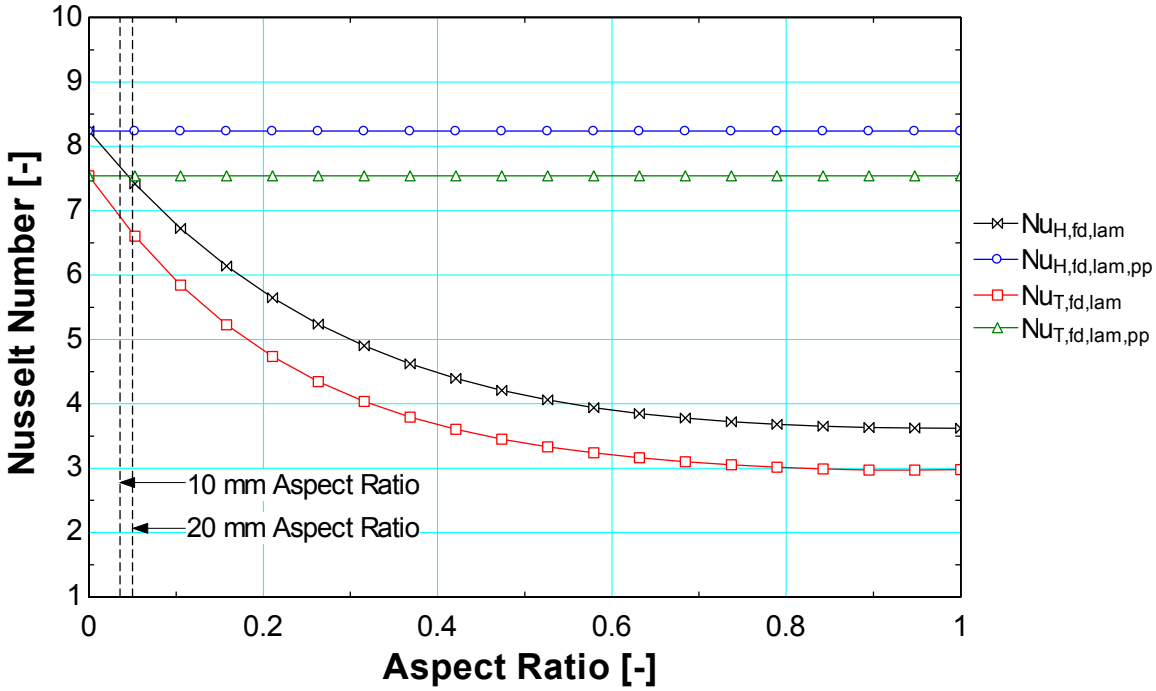

Fig. 5.3.1: Fully developed Nusselt number as a function of aspect ratio for both parallel plates and rectangular ducts

Table 5.3.2: Fully developed Nusselt numbers for constant wall temperature $Nu_{T,fd,lam}$ and constant heat flux $Nu_{H,fd,lam}$ for both the 10 mm and 20 mm heat exchangers

	α	$Nu_{T,fd,lam}$	$Nu_{H,fd,lam}$
10 mm	0.0357	6.884	7.666
20 mm	0.05	6.646	7.546

The constant wall temperature boundary condition for the fully developed Nusselt number provides a lower limit. The actual fully developed Nusselt number in the heat exchanger will be neither the constant temperature nor the constant heat flux value but somewhere in between these two values. The fully developed constant wall temperature Nusselt number was chosen in the design model in order to provide a conservative estimate of the heat exchanger performance. In any case, the very high conductivity of the silicon plates will promote a boundary condition that is closer to constant temperature than constant heat flux.

The design model accounts for the increase in the average Nusselt number that occurs while the flow is developing. No correlations were found in the literature for the simultaneously developing, average Nusselt number in rectangular ducts. However, the heat exchanger ducts have a very low aspect ratio and the behavior of fluid flow in the ducts should be similar to that of flow through parallel plates. The average Nusselt number for parallel plates with simultaneous thermally and hydrodynamically developing flow can be found using Eq. 5.3.19 [18]. Equation 5.3.19 is valid for Prandtl numbers between 0.1 and 1000 and is a correlation that approximates a series solution by Stephan (1959).

$$Nu_{T,m,pp} = 7.55 + \frac{0.024\left(x_{pp}^{*}\right)^{-1.14}}{1 + 0.0358(x_{pp}^{*})^{-0.64}\,\mathrm{Pr}^{0.17}} \tag{5.3.19}$$

Hwang and Fan (1964) also solved for the average, simultaneously developing, constant temperature Nusselt number [18]. However, they only provide tabulated results for Prandtl numbers of 0.1, 0.72, 10, and 50. Their results are shown in Table 5.3.3 and are plotted along with Eq. 5.3.19 in Fig. 5.3.2. The maximum difference of Hwang and Fan's solution from Stephan's solution is 4.3%. Two different authors using different methods were able to obtain very similar solutions, which provides some confidence as to the accuracy of these solutions. As expected, both curves in Fig. 5.3.2 converge and approach the fully developed constant temperature Nusselt number $Nu_{T,m,pp}$ for parallel plates of 7.541 as the thermal dimensionless length x^* increases.

Table 5.3.3: Average simultaneously developing constant temperature Nusselt numbers for parallel plates from two different authors

x^*	$Nu_{m,T}$ Stephan	$Nu_{m,T}$ Hwang	Difference [%]
0.00026	45.78	44.14	3.58
0.000434	35.72	35.09	1.75
0.000608	30.40	30.23	0.55
0.000955	24.61	24.91	-1.23
0.0013	21.40	21.9	-2.36
0.00174	18.83	19.52	-3.65
0.0026	15.95	16.63	-4.25
0.00347	14.28	14.9	-4.32
0.00434	13.19	13.74	-4.19
0.00608	11.82	12.24	-3.52
0.00868	10.70	10.96	-2.43
0.0148	9.50	9.593	-1.01
0.0234	8.81	8.827	-0.17
0.0321	8.48	8.474	0.03
0.0434	8.24	8.225	0.12
0.0651	8.00	7.986	0.21
0.0942	7.86	7.792	0.83
0.1519	7.73	7.707	0.36

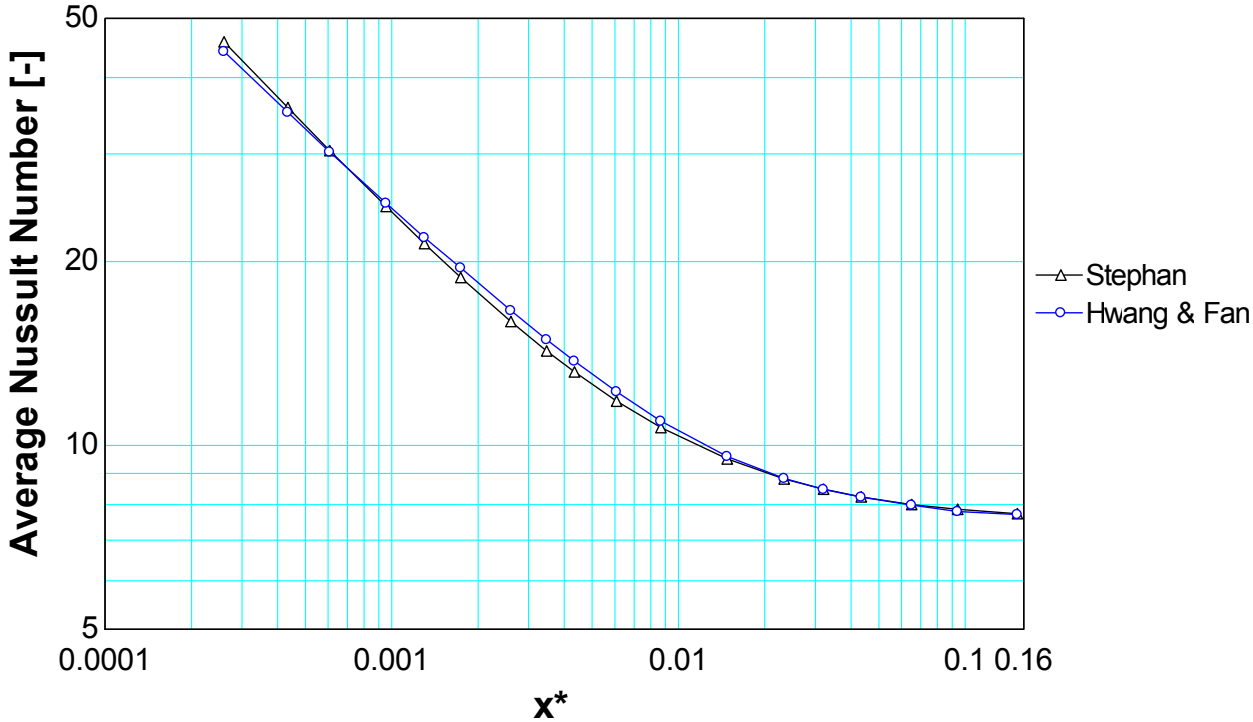

Fig. 5.3.2: Average simultaneously developing constant wall temperature Nusselt numbers for parallel plates as a function of thermal dimensionless length from two different authors

As shown in Eq. 5.3.19, the Nusselt number is a weak function of the Prandtl number for flow through a parallel plate with a constant wall temperature. The Prandtl number as a function of temperature is plotted in Fig. 5.3.3 for various fluids that are likely to be used in the heat exchanger. As Fig. 5.3.3 shows, the expected range of Prandtl numbers the heat exchanger fluids will have is between 0.65 to 0.8. The vertical lines on Fig. 5.3.3 represent the phase change from vapor to liquid. The design model allows only single phase fluids, so these correlations must be modified in order to simulate temperatures where vapor is condensing into liquid.

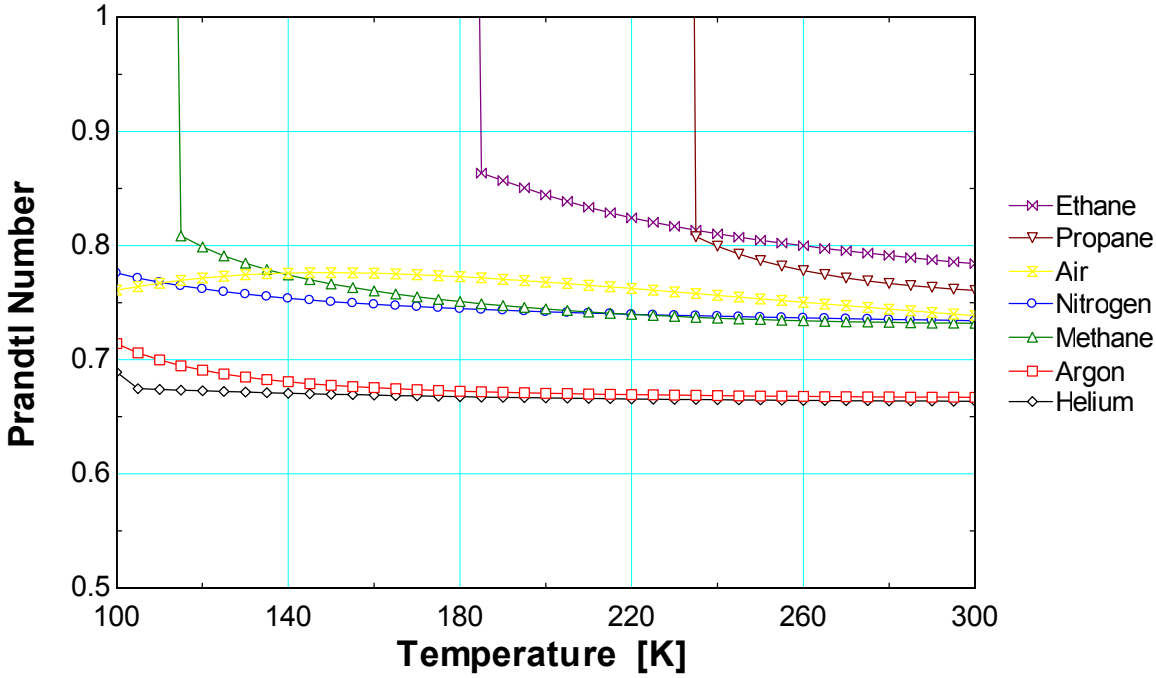

Fig. 5.3.3: Prandtl number as a function of temperature at 101.3 kPa for various fluids. The abrupt increases in Prandtl number for methane, ethane, and propane are due to the vapor condensing into liquid form at colder temperatures.

Since the axial duct length x and the hydraulic diameter $D_{hyd,pp}$ are fixed in the heat exchanger, the average parallel plate Nusselt number $Nu_{T,m,pp}$ can be plotted as a function of Reynolds number for the expected range of Prandtl numbers using Eq. 5.3.19. As shown in Fig. 5.3.4, the Nusselt number could be estimated using a Prandtl number of 0.72 with an error of no more than 5% for the entire range of 0.65 to 0.8.

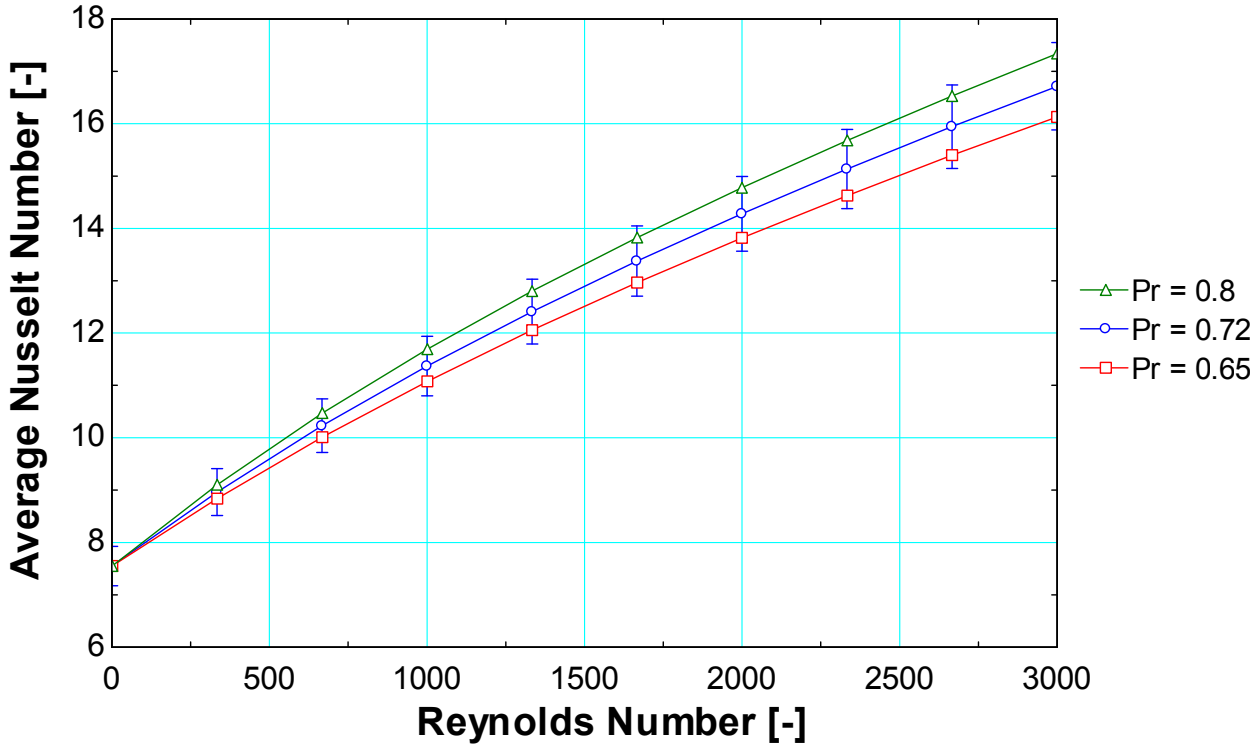

Fig. 5.3.4: Mean simultaneously developing constant temperature Nusselt number $Nu_{T,m,pp}$ for parallel plate ducts as a function of Reynolds number for Prandtl number values of 0.65, 0.72, and 0.8. The error bars on Pr = 0.72 are for a 5% relative error. The Nusselt number for any fluid with a 0.65<Pr<0.8 could be estimated to within 5% error by using Pr = 0.72

Unfortunately no correlations or tabulations for an average simultaneously developing Nusselt number with constant heat flux were found in the literature for parallel plates. No correlations were found for rectangular ducts; however, numerical simulations with air (Pr = 0.72) have been tabulated for the average Nusselt number in rectangular ducts for both constant wall temperature and constant wall heat flux assumptions [18]. The tabulated numerical solutions are presented in Table 5.3.4.

Table 5.3.4: The constant wall temperature and constant wall heat flux Nusselt numbers as a function of thermal entrance length and rectangular duct aspect ratio for air (Pr = 0.72).

x^*	α=1/6		α=1/4		α=1/3		α=1/2		α=1	
	$Nu_{T,m}$	$Nu_{H,m}$	$Nu_{T,m}$	$Nu_{H,m}$	$Nu_{T,m}$	$Nu_{H,m}$	$Nu_{T,m}$	$Nu_{H,m}$	$Nu_{T,m}$	$Nu_{H,m}$
0.00455	10.9	-	10.58	16.02	10.3	15.83	10	15.36	9.7	15.03
0.00500	10.51	-	10.18	15.49	9.91	15.21	9.6	14.88	9.3	14.55
0.00556	10.12	-	9.77	14.95	9.5	14.7	9.2	14.35	8.91	14.05
0.00625	9.72	-	9.36	14.48	9.1	14.1	8.8	13.79	8.5	13.5
0.00714	9.28	-	8.93	13.73	8.66	13.47	8.37	13.15	8.06	12.87
0.00833	8.85	-	8.48	13.03	8.18	12.78	7.91	12.48	7.61	12.19
0.01000	8.38	-	7.98	12.23	7.7	12	7.42	11.7	7.1	11.43
0.0125	7.9	-	7.47	11.35	7.17	11.13	6.88	10.83	6.57	10.53
0.0167	7.35	-	6.9	10.32	6.6	10.07	6.27	9.77	5.95	9.49
0.0200	7.07	-	6.61	9.7	6.28	9.48	5.95	9.17	5.63	8.9
0.0250	6.78	-	6.27	9.07	5.96	8.85	5.61	8.54	5.27	8.25
0.0333	6.47	-	5.93	8.37	5.6	8.13	5.23	7.83	4.88	7.52
0.0500	6.13	-	5.56	7.58	5.17	7.31	4.79	6.94	4.39	6.6
0.1000	5.72	-	5.11	6.65	4.67	6.27	4.2	5.77	3.75	5.43

The choice of whether to assume constant wall temperature or constant wall heat flux for the best accuracy is unclear. Examining the geometrical model of a 10 mm heat exchanger fin in Fig. 5.3.5 shows that the conduction resistance will be high in the *y*-direction but low in the *x*- and *z*-directions. This means that the wall temperature will be close to constant in the *x*-direction (the flow direction) at any given distance *y*, but can vary significantly for different values of *y*. If the fluid mixes perfectly while flowing through the glass spacers so that it enters the ducts at a uniform temperature then the constant heat flux assumption would be incorrect because the temperature difference between the fluid and the fin will be greater at the base of the fin than further out near the webbing. A larger temperature difference leads to a larger heat flux, so the heat flux would be larger near the fin base and smaller near the webbing. The actual average Nusselt number will be bounded between the constant heat flux and constant wall temperature results, but will be closer to the constant wall temperature due to the low resistance in the *x*-direction.

Fig. 5.3.5: Geometric model of the 10 mm heat exchanger silicon fin (drawn to scale)

The heat exchanger model is conservative if it errors on the side of smaller than actual heat transfer coefficients; therefore, for laminar flow the constant wall temperature assumption was chosen. No known correlations or tabulations exist for the aspect ratio of the 10 mm and 20 mm heat exchanger fins, but the Nusselt number $Nu_{T,m}$ could be estimated by interpolating between the Nusselt number for a parallel plate and the Nusselt number for a rectangular duct with the smallest aspect ratio for which results are available (which is still larger than the value associated with the ducts in the 10 mm or 20 mm heat exchangers). Table 5.3.5 shows the results of linear interpolation based on the aspect ratio α of the correlation for parallel plates Eq. 5.3.19 and the tabulated results for a rectangular duct with an aspect ratio of 1/6 from Table 5.3.4. The Prandtl number was assumed to be 0.72, since that was the only Prandtl number for which rectangular duct Nusselt number numerical results were found. The effect of the Prandtl number on the Nusselt number can be neglected with an approximate error of ± 5% (Fig. 5.3.4) for the gases that will likely be used for testing the heat exchanger.

Table 5.3.5: Estimated constant wall temperature Nusselt number as a function of dimensionless entrance length for both the 10 mm and 20 mm heat exchangers. The Prandtl number was assumed to be 0.72.

	Parallel Plate α=0	10 mm HX α=0.0357	20 mm HX α=0.05	Rectangular Duct α=1/6
$\hat{x}$	$Nu_{m,T}$	$Nu_{m,T}$	$Nu_{m,T}$	$Nu_{m,T}$
0.00455	12.98	12.54	12.36	10.9
0.00500	12.58	12.13	11.96	10.51
0.00556	12.16	11.72	11.55	10.12
0.00625	11.73	11.30	11.12	9.72
0.00714	11.28	10.85	10.68	9.28
0.00833	10.81	10.39	10.22	8.85
0.01000	10.33	9.91	9.74	8.38
0.0125	9.82	9.41	9.25	7.9
0.0167	9.29	8.88	8.71	7.35
0.0200	9.02	8.60	8.43	7.07
0.0250	8.73	8.32	8.15	6.78
0.0333	8.44	8.02	7.85	6.47
0.0500	8.14	7.71	7.54	6.13
0.1000	7.84	7.38	7.20	5.72

An alternative approach is to assume that the rectangular duct Nusselt number can be found by modifying the parallel plate Nusselt number correlation shown in Eq. 5.3.19. The fully developed constant temperature Nusselt number is 7.55 for parallel plates (Eq. 5.3.19), 6.88 for the 10 mm heat exchanger (Table 5.3.2), and 6.65 for the 20 mm heat exchanger (Table 5.3.2). Eq. 5.3.19 could be modified by replacing the parallel plate fully developed Nusselt number with the fully developed Nusselt number for the 10 mm or 20 mm heat exchanger ducts. In this case, the thermal dimensionless length based off the parallel plate hydraulic diameter should be replaced with the 10 mm or 20 mm heat exchanger duct hydraulic diameter. These two substitutions lead to Eq. 5.3.20 and Eq. 5.3.21 for the 10 mm and 20 mm heat exchangers respectively.

$$Nu_{T,m,10mm} = 6.88 + \frac{0.024\left(x^*_{10mm}\right)^{-1.14}}{1 + 0.0358(x^*_{10mm})^{-0.64}\,\mathrm{Pr}^{0.17}} \tag{5.3.20}$$

$$Nu_{T,m,20mm} = 6.65 + \frac{0.024\left(x^*_{20mm}\right)^{-1.14}}{1 + 0.0358(x^*_{20mm})^{-0.64}\,\mathrm{Pr}^{0.17}} \tag{5.3.21}$$

The axial length of the duct x is known to be t_{fin} and hydraulic diameter D_{hyd} is known from Table 5.1.3, so the Nusselt number $Nu_{T,m}$ can be calculated as a function of Reynolds number by using Table 5.3.5. Alternatively, the duct Nusselt number can be calculated using Eq. 5.3.20 or Eq. 5.3.21. Both approaches are plotted in Fig. 5.3.6 for the 10 mm heat exchanger.

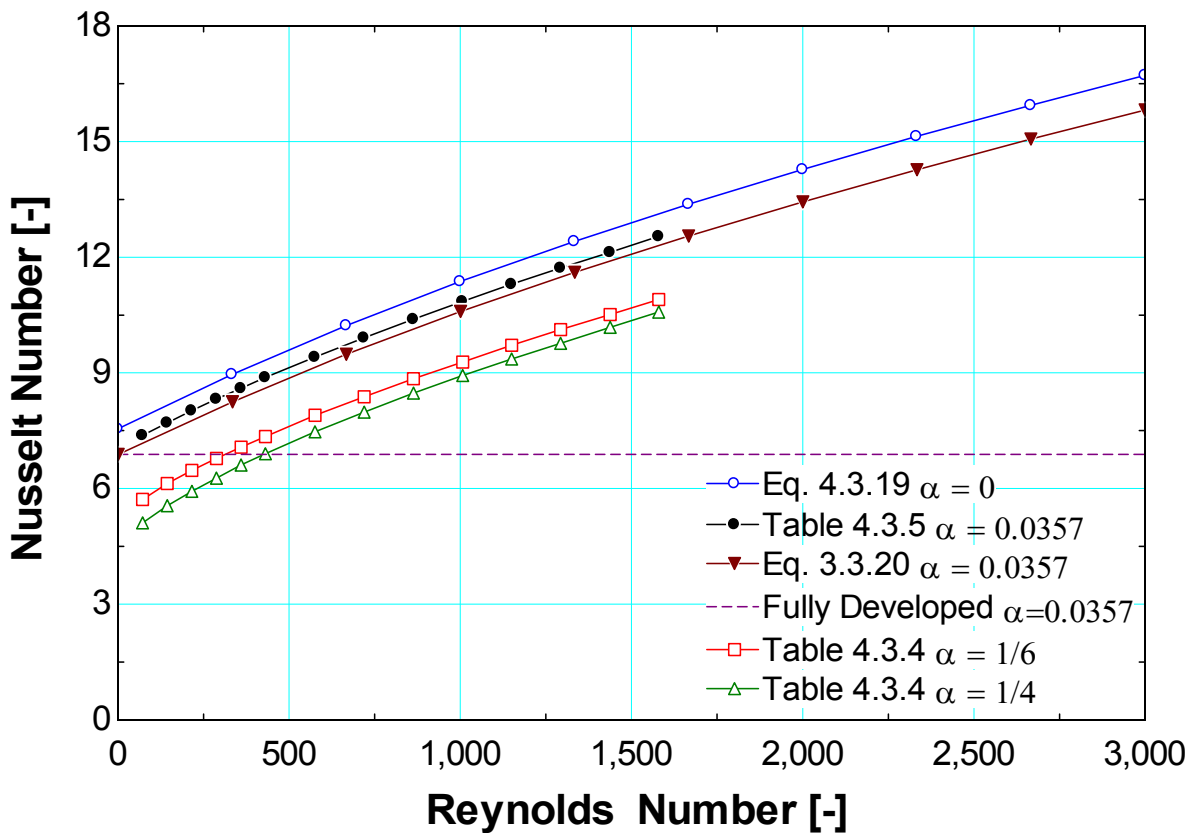

Fig. 5.3.6: Comparison of two methods for estimating the simultaneously developing Nusselt number as a function of Reynolds number for the 10 mm heat exchanger ducts. The first method, shown by the solid black dots, is to interpolate between the correlation for parallel plates and the tabulated data for an aspect ratio of 1/6. The second method, shown by the solid inverted triangles, is to modify the parallel plate Nusselt number correlation (Eq. 5.3.19) by replacing the parallel plate fully developed Nusselt number and hydraulic diameter with rectangular duct values (Eq. 5.3.20).

The modified parallel plate Nusselt number correlation was chosen for the design model for several reasons. The tabulated data for an aspect ratio of 1/6 are not sufficient for determining the Nusselt number for Reynolds numbers higher than 1600. Also, the dependence of the

Nusselt number on the Prandtl number is maintained when using the modified Nusselt number correlations, while it is neglected if the interpolation method is used. Finally, the modified Nusselt number correlations are more conservative and hence less likely to over-predict the performance of the heat exchanger.

5.4 Turbulent Flow Heat Transfer and Pressure Drop Correlations

During the process of optimizing the heat exchanger, the operating conditions and geometry may lead to turbulent rather than laminar fluid flow in some or all of the plates. Turbulent flow will generally lead to higher heat transfer coefficients, which boosts the overall stream-to-stream heat transfer inside the heat exchanger. However, turbulent flow will also lead to lead to higher frictional pressure drops. Before an optimization study can be performed, the heat transfer and pressure drop characteristics of the turbulent flow regime must be defined.

The results of a number of experimental investigations on the critical Reynolds number for transition from laminar to turbulent flow were compiled by Kakac et al. [27] and are shown in Table 5.4.1. A diagram of the two entrance types that were studied is shown in Fig. 5.4.1. Both the heat exchangers have an aspect ratio near 0.05 and a sharp entrance, so the critical Reynolds number for transition to turbulent flow is estimated to be 3000.

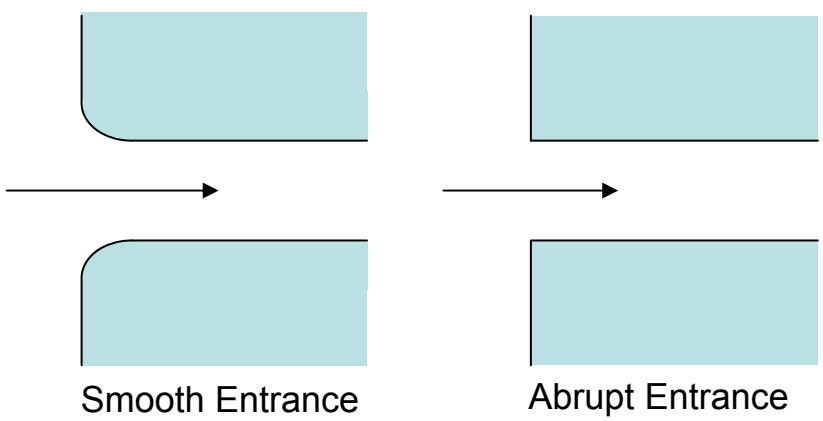

Fig. 5.4.1: Diagram of inlet geometries for rectangular ducts

Table 5.4.1: Critical Reynolds number for transition to turbulent flow in smooth rectangular ducts

Smooth Entrance		Abrupt Entrance	
α	Re_{crit}	α	Re_{crit}
0	3400	0	3100
0.1	4400	0.1	2920
0.2	7000	0.2	2500
0.333	6000	0.2555	2400
1	4300	0.3425	2360
		1	2200

To determine the fully developed turbulent friction factor in a rectangular duct, Kakac et al. recommend using the combination of Eq. 5.4.1 and Eq. 5.4.2 [27]. Equation 5.4.2 provides the friction factor for fully developed flow in smooth circular tubes (f_c) proposed by Techo et al. and Eq. 5.4.1 adjusts the circular tube friction factor to be applicable for a rectangular duct with aspect ratio α.

$$f_{fd,turb} = (1.0875 - 0.2225\alpha) f_c \tag{5.4.1}$$

$$f_c = 4\left(\frac{1}{1.7372\ln\left(\frac{Re}{1.964\ln(Re) - 3.8215}\right)}\right)^2 \tag{5.4.2}$$

The fully developed Nusselt number for turbulent flow $Nu_{fd,turb}$ can be determined from the fully developed rectangular duct friction factor $f_{fd,turb}$. Since the friction factor has already been adjusted from circular duct flow to rectangular duct flow, a standard Nusselt number correlation for smooth circular tubes can be used [27]. The recommended Nusselt number correlation is the Gnielinski equation, shown in Eq. 5.4.3. For turbulent flow the Nusselt number is the same for the constant wall temperature and constant wall heat flux conditions.

$$Nu_{fd,turb} = \frac{\left(f_{fd,turb}/8\right)\left(\mathrm{Re} - 1000\right)\mathrm{Pr}}{1 + 12.7\sqrt{f_{fd,turb}/8}\left(\mathrm{Pr}^{2/3} - 1\right)} \tag{5.4.3}$$

No correlations were found that address simultaneously developing turbulent flow for either parallel plate or rectangular ducts. However, duct shape has very little influence on turbulent flow due to the high degree of fluid mixing and the small extent of the viscous sublayer which controls the shear. In addition, the thermal boundary condition (constant wall temperature or constant heat flux) has no distinguishable effect when $t_{fin}/D_{hyd} > 8$ for Reynolds numbers less than 200,000 and only a very minor effect for smaller duct length to diameter ratios. There is no effect associated with the boundary condition for $t_{fin}/D_{hyd} > 5$ for Reynolds numbers less than 30,000 [27].

The simultaneously developing turbulent Nusselt number for smooth circular tubes can be found using Eq. 5.4.4 [27] and is valid for $t_{fin}/D_{hyd} > 3$. The ratio of t_{fin}/D_{hyd} is slightly greater than 5 for both the 10 mm and 20 mm heat exchangers. Equation 5.4.4 is a fit to experimental data for air (Pr = 0.7) from Mills (1962) and agrees with the experimental values to within 3%. Since air was the only fluid studied, Eq. 5.4.4 does not show the effect of the Prandtl number. However, some dependence of the Prandtl number is maintained through the fully developed Nusselt number term.

$$Nu_{m,turb} = Nu_{fd,turb}\left(1 + \frac{2.4254}{\left(t_{fin}/D_{hyd}\right)^{0.676}}\right) \tag{5.4.4}$$

Another correlation was found for Pr = 2.5 and is shown in Eq. 5.4.5 [27]. Equation 5.4.5 is reported to be with 5% of experimental measurements of Molki and Sparrow (1986) for t_{fin}/D_{hyd} > 2 and 9,000< Re < 88,000

$$Nu_{m,turb,MS} = Nu_{fd,turb}\left(1+\frac{23.99Re^{-0.23}}{\left(t_{fin}/D_{hyd}\right)^{\left(0.815-2.08\cdot 10^{6}Re\right)}}\right) \tag{5.4.5}$$

To determine whether neglecting the influence of the Prandtl number on the developing turbulent flow Nusselt number is a valid assumption, both Eq. 5.4.4 and Eq. 5.4.5 were plotted and are shown in Fig. 5.4.2 for a Prandtl number of 2.5. Note that Eq. 5.4.4 was developed for a Prandtl number of 0.7 and has no dependence on the Prandtl number other than the fully developed Nusselt number term. Yet Eq. 5.4.4 has only a 0.5% relative error for a Reynolds number of 10,000 and less than 12% error for a Reynolds number of 60,000. Since the expected range of Prandtl numbers for gasses to be used in testing the heat exchanger is 0.65 to 0.8 (see Fig. 3.3), the expected error from using Eq. 5.4.4 is much less than 12%. Equation 5.4.4 is used in the design model to predict simultaneously developing turbulent Nusselt numbers.

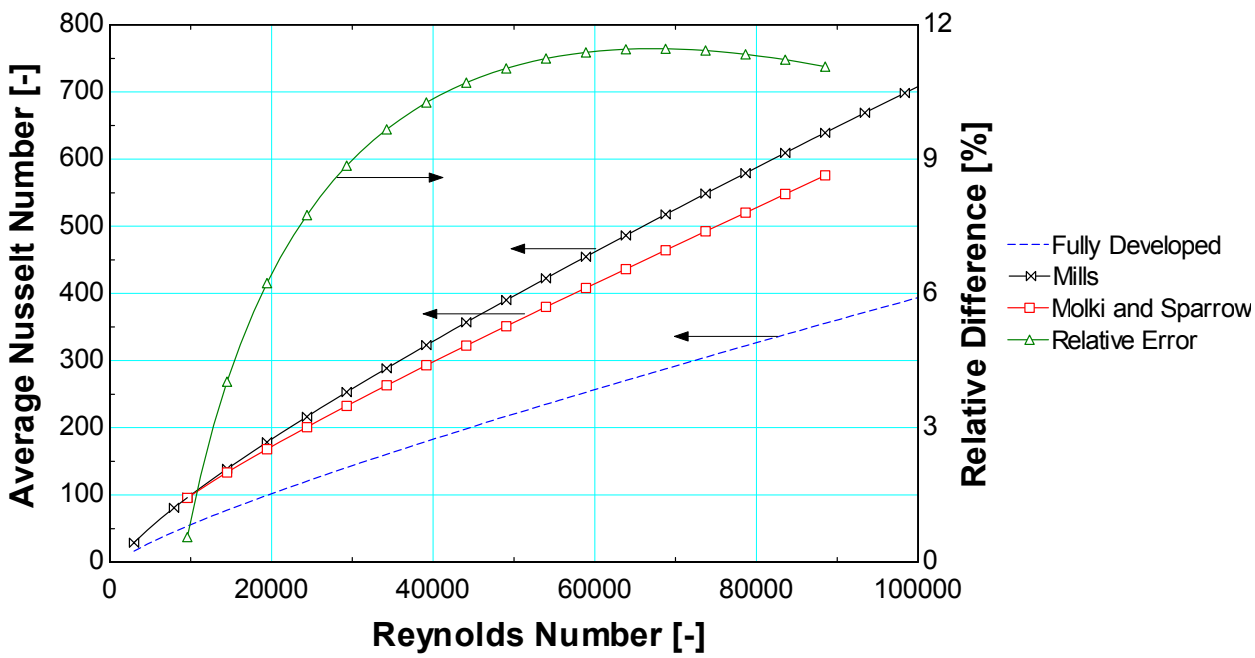

Fig. 5.4.2: Comparison of two different correlations prediction of simultaneously developing turbulent Nusselt numbers for Pr = 2.5 in the 10mm heat exchanger. The Mills correlation was developed for Pr = 0.7 and the Molki and Sparrow correlation was developed for Pr = 2.5.

No correlations were found for the apparent friction factor for developing turbulent flow for any duct shape. However, an estimate of the apparent friction factor could be obtained by replacing the fully developed Nusselt number $Nu_{fd,turb}$ in Eq. 5.4.3 with the developing Nusselt number $Nu_{m,turb}$ from Eq. 5.4.4, as shown in Eq. 5.4.6. This approach is essentially using the modified

Reynolds analogy in reverse; that is, knowledge of the Nusselt number is used to infer the friction factor. Note that Eq. 5.4.6 requires an iterative solution, but this is not a problem since the design model uses the iterative equation solver EES [17]. Equation 5.4.6 will solve reliably if the fully developed friction factor is used as the guess value for the apparent friction factor.

$$Nu_{m,turb} = \frac{\left(f_{app,turb}/8\right)\left(\mathrm{Re}-1000\right)\mathrm{Pr}}{1+12.7\sqrt{f_{app,turb}/8}\left(\mathrm{Pr}^{2/3}-1\right)} \tag{5.4.6}$$

Both the fully developed friction factor and the apparent friction factor are plotted as a function of Reynolds numbers in Fig. 5.4.3. A Prandtl number of 0.72 was chosen as a typical value for fluids that will be used in the heat exchanger. Note that the frictional pressure drop is twice as large if the developing region is taken into account when calculating the friction factor.

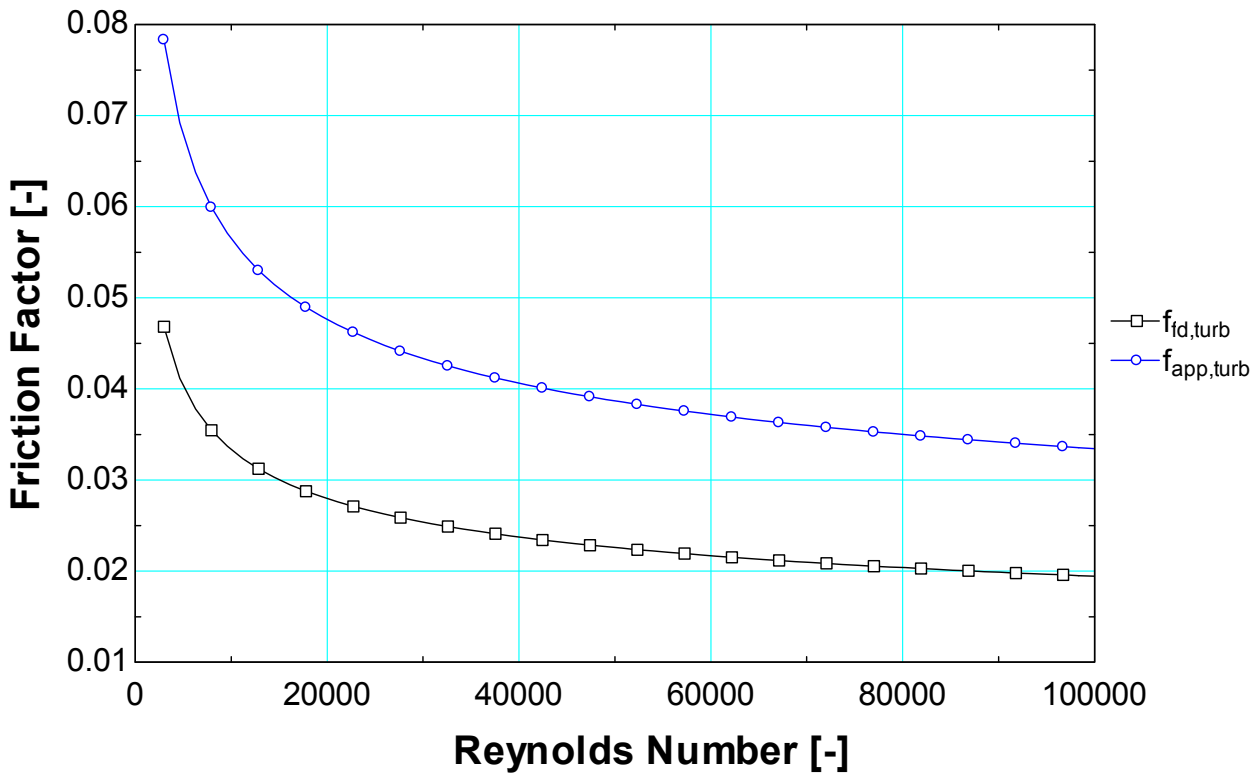

Fig. 5.4.3: Fully developed and apparent friction factors for as a function of Reynolds number for a fluid with Pr = 0.72 in the 10mm heat exchanger

The turbulent frictional pressure drop through the silicon fins can then be calculated using Eq. 5.4.7, which is just Eq. 5.3.11 with the laminar friction factor replaced by the turbulent friction factor. The total pressure drop can then be calculated using Eq. 5.4.8, which is identical to Eq. 5.3.14 with the laminar frictional pressure drop replaced with the turbulent frictional pressure drop.

$$\Delta P_{friction,turb} = f_{fd,turb}\rho_{fluid}\frac{x}{D_{hyd}}\frac{V_{m,fluid}^2}{2} \tag{5.4.7}$$

$$\Delta P_{tot,turb} = \Delta P_{cont} + \Delta P_{friction,turb} + \Delta P_{exp} \tag{5.4.8}$$

The heat transfer coefficient, *htc*, can then be determined using Eq. 5.4.9, where the Nusselt number is determined from Eq. 5.3.20 or Eq. 5.3.21 for laminar flow and from Eq. 5.4.6 for turbulent flow.

$$htc = \frac{Nu\ k}{D_{hyd}} \tag{5.4.9}$$

5.5 Fin Effectiveness

Fin effectiveness (as opposed to fin efficiency) is defined as the ratio of the actual rate of heat transfer from the fins to the maximum possible rate of heat transfer. The fin effectiveness is defined by taking the maximum rate of heat transfer to be the heat transfer that results in the fluid flowing through the fins reaching the temperature at the base of the fin through either heating or cooling (this definition is consistent with the definition of the effectiveness of a heat exchanger but inconsistent with the typical definition of the efficiency of a fin). The maximum heat transfer $\dot{q}_{fin,max}$ is defined in Eq. 5.5.1:

$$\dot{q}_{fin,max} = \dot{m}_{fluid} Cp_{fluid} \left(T_{fluid,in} - T_{fin,base} \right) \tag{5.5.1}$$

where $\dot{m}_{fluid}$ the fluid mass flow rate, Cp_{fluid} is the fluid specific heat at constant pressure, $T_{fluid,in}$ is the fluid temperature at the duct inlet, and $T_{fin,base}$ is the temperature at the base of the fin. The actual heat transfer rate, $\dot{q}_{fin,act}$, is defined in Eq. 5.5.2 through an energy balance on the fluid:

$$\dot{q}_{fin,act} = \dot{m}_{fluid} Cp_{fluid} \left(T_{fluid,in} - T_{fluid,out} \right) \tag{5.5.2}$$

where $T_{fluid,out}$ is the fluid temperature at the duct outlet. The fin effectiveness, ε_{fin}, can be found using Eq. 5.5.3:

$$\varepsilon_{fin} = \frac{\dot{q}_{fin,act}}{\dot{q}_{fin,max}} = \frac{\left(T_{fluid,in} - T_{fluid,out} \right)}{\left(T_{fluid,in} - T_{fin,base} \right)} \tag{5.5.3}$$

The actual fin heat transfer rate cannot be determined using Eq. 5.5.2 because $T_{fluid,out}$ is unknown. However, the actual heat transfer rate can be found using Eq. 5.5.4:

$$\dot{q}_{fin,act} = h\left(\eta_{fin} N_{fin} A_{fin} + A_{unfinned} \right)\left(T_{fluid,in} - T_{fin,base} \right) \tag{5.5.4}$$

where h is the heat transfer coefficient, η_{fin} is the fin efficiency, N_{fin} is the number of fins, A_{fin} is the area of an individual fin, and $A_{unfinned}$ is the heat transfer surface area that is not part of a fin. The fin efficiency term is needed because the fin temperature will increase (or decrease) with the

distance from the fin base (i.e., in the *y*-direction in Fig. 5.3.5) due to conduction resistance. The fin efficiency is the ratio of the actual heat transfer to the heat transfer that would occur if the fin surface was entirely at the fin base temperature (consistent with a fin material that has infinite thermal conductivity). Correlations for the fin efficiency of common fin shapes in the limit that the fluid temperature is constant in the flow direction can be found in many heat transfer books, such as Incropera & DeWitt [29]. The solution for the fin efficiency of a rectangular, constant cross-sectional area fin is given by Eqs. 5.5.5 and 5.5.6.

$$\beta = W_{fin}\sqrt{\frac{2htc}{k_{fin}H_{fin}}} \tag{5.5.5}$$

where β is the fin constant, W_{fin} is the width of the fin perpendicular to the direction of fluid flow, htc is the heat transfer coefficient, k_{fin} is the thermal conductivity of the fin material, and H_{fin} is the height of the fin.

$$\eta_{fin} = \frac{\tanh(\beta)}{\beta} \tag{5.5.6}$$

Conventional fin efficiency equations, such as Eq. 5.5.6, make two assumptions that are not always valid. The first is that the fluid temperature remains constant while the fluid flows across the fin. This is clearly not true in many applications since the fin is designed to transfer heat to or from the fluid and thus change the fluid temperature. However, making this assumption will generally lead to small errors if the fluid temperature change is small.

The second assumption that conventional fin efficiency equations make is that heat transfer within the fin material can be treated as if it is one-dimensional between the fin base and the fin tip. Heat transfer from the fin to the fluid will change the fluid temperature as it flows over the fin, which in turn will change the temperature distribution of the fins in the flow direction. Since there can be significant temperature gradients in two dimensions, a one-dimensional treatment of conduction can introduce significant errors in some situations.

The major advantage of using a MEMS heat exchanger over a conventional heat exchanger is the compact size of the MEMS heat exchanger. The compact size of the heat exchanger and the large temperature differences required for the cryosurgical probe will lead to fluid temperature changes that are as large as 10 K across any single die. Since the die is only 450 μm to 500 μm thick, there will certainly be large temperature gradients in the flow direction; therefore, treating the conduction through the fins as one-dimensional may not be a good assumption to make.

Nellis and Klein [31] numerically solved the problem of rectangular fins with two dimensional temperature distributions in both the fluid and the fin. They found that the fin effectiveness was a function of three non-dimensional parameters: the number of transfer units, a fin constant, and the aspect ratio of the fin. The number of transfer units *NTU* is computed according to:

$$NTU = \frac{2\ W_{fin}\ t_{fin}\ htc}{\dot{m}_{fluid}\ Cp_{fluid}} \tag{5.5.6}$$

where t_{fin} is the thickness of the fin in the flow direction and W_{fin} is the width of the fin shown in Fig. 5.1.2. The numerical results were curve fit to an analytical expression. The resulting equation is presented in Eq. 5.5.7. The maximum error between the analytical solution and the numerical solution was reported to be 3.2%, with the average rms error being 0.04%, over the range of $0.01 < NTU < 1000$ and $0.01 < \beta < 5$.

$$\varepsilon_{fin} = 1 - \exp\left[-a(\beta)\, NTU^{\left(b(\beta)+c(\beta)\ln(NTU)\right)}\right] \tag{5.5.7}$$

The terms $a(\beta)$, $b(\beta)$, and $c(\beta)$ can be found using Eq. 5.5.8-5.5.10 and Table 5.5.1.

$$a(\beta) = exp\left[-a_0 \cdot \beta^{\left(a_1 + a_2 \cdot \beta + a_3 \cdot \beta^2\right)}\right] \tag{5.5.8}$$

$$b(\beta) = \sum_{i=0}^{5} b_i \cdot \left[log_{10}(\beta)\right]^i \tag{5.5.9}$$

$$c(\beta) = \sum_{i=0}^{6} c_i \cdot \left[log_{10}(\beta)\right]^i \tag{5.5.10}$$

Table 5.5.1: Constants required for analytical solution of Eq. 5.5.7 -5.5.10

Index, *i*	a_i	b_i	c_i
0	0.297925119	0.927242296	-0.049798866
1	1.492222514	-0.071330646	-0.106555996
2	-0.081006078	0.061074063	0.020416859
3	0.002369923	0.026320276	0.141444269
4	-	-0.067908807	0.032192166
5	-	-0.03036481	-0.048599571
6	-	-	-0.018543303

Nellis and Klein's results are compared with the conventional rectangular fin equation (Eq. 5.5.6) in the limit that the fluid has an infinite fluid capacity rate (i.e., $NTU \rightarrow 0$ which leads to no temperature change in the fluid) in Fig. 5.5.1

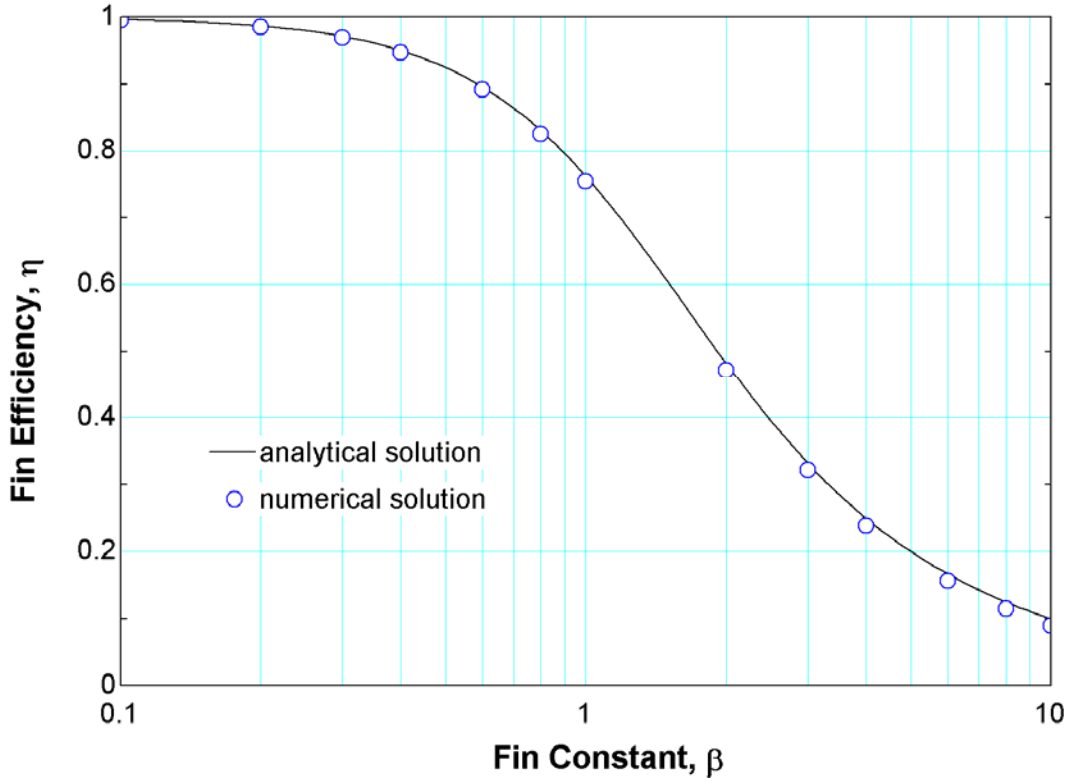

Fig. 5.5.1: Comparison of the numerical results of Nellis and Klein with the conventional rectangular fin equation Eq. 5.6 in the limit that *NTU* → 0. Figure is from [31].

The aspect ratio of the ducts between the fins does not appear in any of the equations Eq. 5.5.7-5.5.10. The dependence of the fin effectiveness on the aspect ratio was so weak that Nellis and Klein chose to neglect the aspect ratio in the analytical fit of their numerical results.

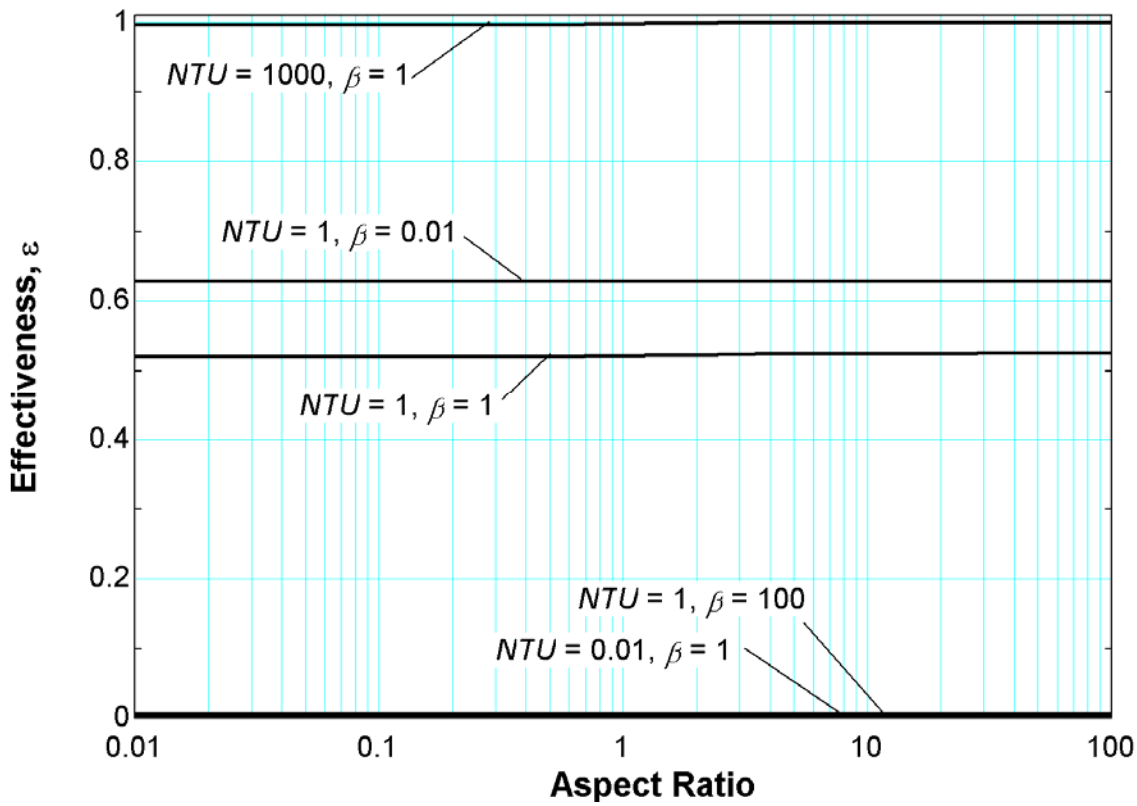

Fig. 5.5.2: Dependence of fin effectiveness on the aspect ratio of the ducts for selected values of NTU and β. Figure is from [31].

5.6 Thermal Resistances

In order to calculate the heat transfer rate between two fluid streams through a single die, the overall thermal resistance must be known. As shown in Fig. 5.6.1, there are four resistances acting in series between the hot stream to the cold stream: the resistance associated with the cold and hot fins ($R_{fin,c}$ and $R_{fin,h}$) and the resistance of the base on the cold and hot sides ($R_{cl,c}$ and $R_{cl,h}$) The variables $T_{b,h}$ and $T_{b,c}$ represent the hot and cold side fin base temperatures, respectively. The temperature at the centerline of the heat exchanger is represented by T_{cl}.

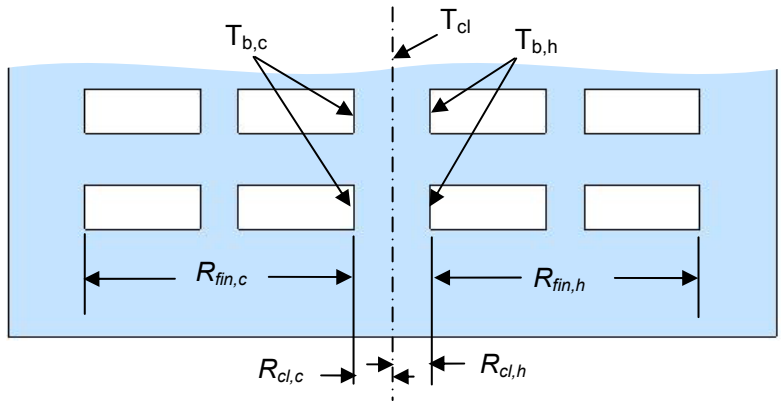

Fig. 5.6.1: Diagram of the four resistances acting series to resist heat conduction between the hot stream and cold stream in the heat exchanger

The fin resistances $R_{fin,h}$ and $R_{fin,c}$ have a thermal driving potential that is the difference between the fluid temperature and the fin base temperature. The heat transfer rate through the fins can be expressed by Eq. 5.6.1 and 5.6.2:

$$\dot{q}_{fin,h} = \frac{\left(T_{fluid,h} - T_{b,h}\right)}{R_{fin,h}} \tag{5.6.1}$$

$$\dot{q}_{fin,c} = \frac{\left(T_{b,c} - T_{fluid,c}\right)}{R_{fin,c}} \tag{5.6.2}$$

where $T_{b,h}$ and $T_{b,c}$ are the fin base temperatures shown in Fig. 5.6.1, $\dot{q}_{fin,h}$ and $\dot{q}_{fin,c}$ are the heat transfer rates through the hot and cold side fins, respectively, and $T_{fluid,h}$ and $T_{fluid,c}$ are the entering hot and cold side fluid temperatures, respectively. The fin heat transfer rates can also be expressed using the definition of fin effectiveness by combining Eq. 5.5.2 with Eq. 5.5.3, which is shown by Eq. 5.6.3 and Eq. 5.6.4, for each side of the heat exchanger.

$$\dot{q}_{fin,h} = \varepsilon_{fin,h}\dot{m}_{fluid,h}Cp_{fluid,h}\left(T_{fluid,h} - T_{b,h}\right) \tag{5.6.3}$$

$$\dot{q}_{fin,c} = \varepsilon_{fin,c}\dot{m}_{fluid,c}Cp_{fluid,c}\left(T_{b,c} - T_{fluid,c}\right) \tag{5.6.4}$$

By substituting Eq. 5.6.1 into Eq. 5.6.3 and Eq. 5.6.2 into Eq. 5.6.4, both the hot and cold side fin thermal resistances can be found. The fin resistances are then Eq. 5.6.5 and Eq. 5.6.6.

$$R_{fin,h} = \frac{1}{\varepsilon_{fin,h}\dot{m}_{fluid,h}Cp_{fluid,h}} \tag{5.6.5}$$

$$R_{fin,c} = \frac{1}{\varepsilon_{fin,c}\dot{m}_{fluid,c}Cp_{fluid,c}} \tag{5.6.6}$$

The heat transfer rate through the center strip separating the two streams is given by Eq. 5.6.7 and Eq. 5.6.8.

$$\dot{q}_{cl,h} = \frac{k_{si} t_{fin} H_{die}}{\left(W_{si,stream}/2\right)}\left(T_{b,h} - T_{cl}\right) = \frac{\left(T_{b,h} - T_{cl}\right)}{R_{cl,h}} \tag{5.6.7}$$

$$\dot{q}_{cl,c} = \frac{k_{si} t_{fin} H_{die}}{\left(W_{si,stream}/2\right)}\left(T_{cl} - T_{b,c}\right) = \frac{\left(T_{cl} - T_{b,c}\right)}{R_{cl,c}} \tag{5.6.8}$$

where k_{si} is the silicon thermal conductivity, and the dimensions t_{fin}, H_{die}, and $W_{si,stream}$ are all shown in Table 5.1.1. Since all the resistances are in series, the total resistance $R_{tot,die}$ is the sum of all the resistances shown in Fig. 5.6.1 and is expressed by Eq. 5.6.9.

$$R_{tot,die} = R_{fin,h} + R_{cl,h} + R_{cl,c} + R_{fin,c} \tag{5.6.9}$$

The total heat transfer rate between the two fluid streams in one die is therefore given by Eq. 5.6.10:

$$\dot{q}_{tot,die} = \frac{\left(T_{fluid,h} - T_{fluid,c}\right)}{R_{tot,die}} \tag{5.6.10}$$

The procedure 'StreamResistance' is shown in Design Model Code 5.6.1 and is used to calculate the thermal resistance from either fluid to the wall centerline. This procedure incorporates all the equations listed in Chap. 5.4-5.6 that are needed to calculate the hot or cold side resistances.

The procedure 'StreamResistance' begins by obtaining material properties from the procedure 'MatProp' (Design Model Code 5.2.2) and fluid properties from the procedure 'TempPress' (Design Model Code 5.6.3). The Reynolds number is calculated and used to determine whether laminar or turbulent flow correlations should be used for calculating friction factors and Nusselt numbers. The fin effectiveness is calculated using the equations described in Chp. 5.5. The fin effectiveness and wall resistance are used to calculate an overall thermal resistance between the fluid stream and the wall centerline.

Design Model Code 5.6.1: The procedure 'StreamResistance' which is used for calculating stream-to-wall centerline thermal resistance

```
"*****************************************************************************************************************"
Procedure StreamResistance(m_dot, T_av, P_av, T_h_in, T_c_in: R, Cp)
"!Calculates resistance to heat transfer and pressure drop for half a die"

$COMMON N_fluid, F$, A_si_flow, D_hyd, t_fin, alpha, W_fin, H_fin, N_fin, W_si_stream, H_die

    "!Fluid and fin material properties evaluated at average fluid temperature"
    Call TempPress(N_fluid, F$, T_av, P_av: k, mu, Cp, Pr, rho)  "fluid properties"
    Call MatProp(T_av: k_si, k_glass)                            "material properties"
```

```
"!Calculation of dimensionless parameters"
vel_av=m_dot/(rho*A_si_flow)          "average fluid velocity"
Re=vel_av*rho*D_hyd/mu                "Reynolds number"
x|plus=t_fin/(D_hyd*Re)               "hydrodynamic dimensionless length"
x|star=t_fin/(D_hyd*Re*Pr)            "thermal dimensionless length"

"!Evaluating laminar or turbulent correlations depending on Reynolds number"
If Re<3000 then
    "fully developed laminar friction factor"
    f_fd=96/Re*(1-1.3553*alpha+1.9467*alpha^2-1.7012*alpha^3+0.9564*alpha^4-0.2537*alpha^5)
    "apparent laminar friction factor"
    f_app=(4/Re)*((3.44/sqrt(x|plus)+((0.674/(4*x|plus))+(f_fd*Re)/4-3.44/sqrt(x|plus))/ &
        (1+0.00029/x|plus^2)))
    "fully developed laminar Nusselt Number with constant wall temperature"
    Nus_fd=7.541*(1-2.61*alpha+4.97*alpha^2-5.119*alpha^3+2.702*alpha^4+0.548*alpha^5)
    "average Nusselt number for laminar flow"
    Nus_m=Nus_fd+0.024*x|star^(-1.14)/(1+0.0358*x|star^(-0.64)*Pr^0.17)
Else;
    "fully developed turbulent friction factor, circular tube"
    f_c=4*(1/(1.7372*ln(Re/(1.964*ln(Re)-3.8215))))^2
    "fully developed turbulent friction factor, rectangular duct"
    f_fd=(1.0875-0.2225*alpha)*f_c
    "fully developed turbulent Nusselt number"
    Nus_fd=(f_fd/8)*(Re-1000)*Pr/(1+12.7*sqrt(f_fd/8)*(Pr^(2/3)-1))
    "average turbulent Nusselt number"
    Nus_m=Nus_fd*(1+2.4254/(t_fin/D_hyd)^0.676)
    "apparent turbulent friction factor"
    f_app=f_fd        "simplification, note that iterative sol'n not used"
    Call Error(Re)    "comment out if flow is really turbulent, serves as warning"
Endif

"!Fin effectiveness calculations"
"Coefficients from numerical analysis of fin effectiveness"
Duplicate i=1,4;  a_i[i]=Lookup('Lookup a', i, 2);End
Duplicate i=1,6;  b_i[i]=Lookup('Lookup b', i, 2);End
Duplicate i=1,7; c_i[i]=Lookup('Lookup c',i, 2);End

htc=Nus_m*k/D_hyd                                        "heat transfer coefficient"
Beta=W_fin*sqrt(2*htc/(k_si*H_fin))                      "term for fin effectiveness"
FinEff1=exp(-a_i[1]*Beta^(a_i[2]+a_i[3]*Beta+a_i[4]*Beta^2)) "term for fin effectiveness"
FinEff2=sum(b_i[j]*log10(Beta)^(j-1), j=1,6)             "term for fin effectiveness"
FinEff3=sum(c_i[j]*log10(Beta)^(j-1), j=1,7)             "term for fin effectiveness"
NTU=2*W_fin*t_fin*htc/((m_dot/N_fin)*Cp)                 "number of transfer units"
Epsilon_fin=1-exp(-FinEff1*NTU^(FinEff2+FinEff3*ln(NTU))) "fin effectiveness"

"!Stream to wall centerline thermal resistance calculation"
R=1/(Epsilon_fin*m_dot*Cp)+(W_si_stream/2)/(k_si*t_fin*H_die)

End {StreamResistance}
"*****************************************************************************************************************"
```

The procedure 'DiePressDrop', which is shown in Design Model Code 5.6.2, is used to calculate the pressure drop across one die for one stream. Similar to the procedure 'StreamResistance', the procedure 'DiePressDrop' begins by obtaining material properties from the procedure

'MatProp' (Design Model Code 5.2.2) and fluid properties from the procedure 'TempPress' (Design Model Code 5.6.3). The Reynolds number is calculated and used to determine whether laminar or turbulent flow correlations should be used for calculating the friction factor. The contraction, friction, and expansion pressure drops are calculated as described in Chap. 5.3 and 5.4 and returned to the main body of EES as a total pressure drop across one die.

If two-phase flow occurs within the heat exchanger then the procedures 'StreamResistance' and 'DiePressDrop' must be modified to include two-phase flow correlations. Two-phase flow has the advantage of higher heat transfer coefficients which would tend to improve the effectiveness of the heat exchanger. No attempt was made to model two-phase flow since no two-phase flow experimental data were collected.

Design Model Code 5.6.2: The procedure 'DiePressDrop' that is used for calculating pressure drop for a fluid across one die.

```
"*****************************************************************************************************************"
Procedure DiePressDrop(m_dot, T_av, P_av, T_h_in, T_c_in:DELTAP_die)
"!Calculates pressure drop across one die"

$COMMON N_fluid, F$, A_si_flow, D_hyd, t_fin, alpha, W_fin, H_fin, N_fin, W_si_stream, H_die

    "!Fluid and fin material properties evaluated at average fluid temperature"
    Call TempPress(N_fluid, F$, T_av, P_av: k, mu, Cp, Pr, rho)"fluid properties"
    Call MatProp(T_av: k_si, k_glass)              "material properties"

    "!Calculation of dimensionless parameters"
    vel_av=m_dot/(rho*A_si_flow)        "average fluid velocity"
    Re=vel_av*rho*D_hyd/mu              "Reynolds number"
    x|plus=t_fin/(D_hyd*Re)             "hydrodynamic dimensionless length"

    "!Evaluating laminar or turbulent correlations depending on Reynolds number"
    If Re<3000 then
        "fully developed laminar friction factor"
        f_fd=96/Re*(1-1.3553*alpha+1.9467*alpha^2-1.7012*alpha^3+0.9564*alpha^4-0.2537*alpha^5)
        "apparent laminar friction factor"
        f_app=(4/Re)*((3.44/sqrt(x|plus)+((0.674/(4*x|plus))+(f_fd*Re)/4-
3.44/sqrt(x|plus))/(1+0.00029/x|plus^2)))
    Else;
        "fully developed turbulent friction factor, circular tube"
        f_c=4*(1/(1.7372*ln(Re/(1.964*ln(Re)-3.8215))))^2
        "fully developed turbulent friction factor, rectangular duct"
        f_fd=(1.0875-0.2225*alpha)*f_c
        "apparent turbulent friction factor"
        f_app=f_fd        "simplification, note that iterative sol'n not used"
        Call Error(Re)    "comment out if flow is really turbulent, serves as warning"
    Endif

    "!Pressure drop calculations"
    K_cont=1                            "fluid has no kinetic energy coming in"
   "pressure drop due to contraction entering die"
    DELTAP_cont=(rho*(K_cont)*(vel_av^2/2))*convert(Pa,kPa)
  "frictional pressure drop across die"
    DELTAP_fric=(f_app*rho*(t_fin/D_hyd)*(vel_av^2/2))*convert(Pa,kPa)
   K_exp=1                        "fluid losses all kinetic energy in expansion"
```

```
   "pressure drop due to expansion leaving die"
    DELTAP_exp=(rho*(K_exp)*(vel_av^2/2))*convert(Pa, kPa)
    DELTAP_die=DELTAP_cont+DELTAP_fric+DELTAP_exp     "sum of all pressure drops per die"


End {DiePressDrop}
"*****************************************************************************************************"
```

The procedure 'TempPress' (Design Model Code 5.6.3) receives a temperature and pressure for a fluid and returns necessary thermophysical properties. The procedure is currently only capable of calculating the properties of pure fluids that have equations of state that are integrated into EES. However, the procedure can be easily altered so that an external routine capable (e.g., a NIST database) of calculating the properties of fluid mixtures could be integrated with the procedure 'TempPress'. The main purpose of 'TempPress' is to keep the calculation of thermophysical properties in one location so that it can be easily modified by another user if necessary.

Design Model Code 5.6.2: EES Procedure TempPress, which is used for determining fluid properties based of a given temperature and pressure

```
"*****************************************************************************************************"
Procedure TempPress(N_fluid, F$, T, P: k, mu, Cp, Pr, rho)
"!Returns fluid properties if temperature and pressure are known"

    If N_fluid =1 then
        k=conductivity(F$, T=T, P=P)  "fluid conductivity"
        mu=viscosity(F$, T=T, P=P)    "fluid viscosity"
        Cp=Cp(F$, T=T, P=P)           "fluid specific heat"
        Pr=Prandtl(F$, T=T, P=P)      "fluid Prandtl number"
        rho=density(F$, T=T, P=P)     "fluid density"
    endif

End {TempPress}

"*****************************************************************************************************"
```

5.7 Axial Conduction

Axial conduction is a loss mechanism in cryogenic heat exchangers, as discussed in detail in Chapter 4. The axial conduction resistance of a silicon perforated plate can be calculated using Eq. 5.7.1:

$$R_{ac} = \frac{t_{fin}}{k_{si}\ A_{si,cond}} \tag{5.7.1}$$

where R_{ac} is the total axial thermal resistance, t_{fin} is the thickness of the perforated plate, k_{si} is the silicon thermal conductivity determined using the procedure 'MatProp', and $A_{si,cond}$ is the surface area of the silicon perforated plate normal to the direction of axial heat flow. The silicon thermal conductivity is evaluated at the average wall temperature for the perforated plate. The axial

resistance of a single perforated plate is calculated using the procedure 'SiAxResistance', which is shown in Design Model Code 5.7.1:

Design Model Code 5.7.1: Determination of the axial conduction resistance of one silicon perforated plate

```
"*************************************************************************************************************"
Procedure SiAxResistance(T_w_av: R_ac)
"!Calculates the silicon axial conduction resistance for one die"

$COMMON t_fin, A_si_cond

    "!Calculation of axial conduction resistance perforated plate"
    Call MatProp(T_w_av: k_si, k_glass)          "avg wall temp from numerical model"
    R_ac=t_fin/(k_si*(A_si_cond))                "axial conduction resistance of silicon"

End {SiAxResistance}
"*************************************************************************************************************"
```

The axial conduction resistance of one spacer can be calculated using Eq. 5.7.2:

$$R_{sp} = \frac{t_{sp}}{k_{glass} A_{glass,cond}} \tag{5.7.2}$$

where R_{sp} is the total axial thermal resistance, t_{sp} is the thickness of the glass spacer, k_{glass} is the glass thermal conductivity determined using the procedure 'MatProp', and $A_{glass,cond}$ is the surface area of the glass spacer normal to the direction of axial heat flow. The glass thermal conductivity is evaluated at the average wall temperature for the spacer. The axial resistance of a single glass plate is calculated using the procedure GlassAxResistance, which is shown in Design Model Code 5.7.2:

Design Model Code 5.7.2: Determination of the axial conduction resistance of a single glass spacer.

```
"*************************************************************************************************************"
Procedure GlassAxResistance(T_glass: R_sp)
"!Calculates thermal axial resistance for one glass spacer"

$COMMON t_sp, A_sp_cond

    "!Calculation of axial conduction resistance for full die"
    Call MatProp(T_glass: k_si, k_glass)         "conductivity of glass"
    R_sp=(t_sp)/(k_glass*A_sp_cond)              "axial conduction resistane of silicon"

End {GlassAxResistance}

"*************************************************************************************************************"
```

As discussed in Chapter 4, conduction to and from the ends of the heat exchanger can improve or degrade the effectiveness depending on the direction of heat flow and the application of the heat exchanger. The purpose of a J-T heat exchanger is to cool the hot fluid, so any heat that is conducted to the heat exchanger ends will decrease the effectiveness and any heat conducted

away from the heat exchanger ends will improve the effectiveness. In Chapter 4 it was also shown that the hot fluid effectiveness is much more sensitive to heat flow at the cold end of the heat exchanger than heat flow at the warm end.

There is likely to be some heat conducted to and from the heat exchanger through the fluid connections; however, the tubing lengths from the headers to the Dewar wall and to the cryocooler were kept as long as space constraints allowed in order to reduce thermal conduction as much as possible. The instrumentation was much closer to the heat exchanger than it was to the cryocooler or the Dewar wall. The inlet streams are expected to be at the tube wall temperature by the time they reach the instrumentation due to the long length for heat transfer between the tube and fluid. The outlet streams are expected to absorb any heat being conducted towards the heat exchanger before it can reach the instrumentation. The design model assumes that no heat is conducted to or from the heat exchanger from the Dewar wall or the cryocooler.

However, there is one source of conduction to and from the heat exchanger ends that is significant and can be easily modeled using a few conservative assumptions. The MEMS heat exchangers assembled for experimental testing utilized support bolts that connected the warm end header to the cold end header and accepted any tensile load imposed by the internal pressure. These bolts conduct heat directly from the hot end to the cold end of the heat exchanger without any thermal interaction with the fluid.

Determining the thermal resistance of the header material from the end of the heat exchanger to the bolts is difficult due to the contact resistances and non-standard conduction shape of the header. Solving for the thermal resistance would require a numerical model of each header style that was used for experimental testing. The design model uses the simplifying and conservative assumption that the header provides no thermal resistance to heat conducted through the bolts. Therefore, the warm end temperature of the bolts is assumed to be identical to the warm end temperature of the heat exchanger wall and the cold end temperature of the bolts is assumed to be identical to the cold end temperature of the heat exchanger wall.

The bolts are assumed to have a constant cross section that matches the minor diameter of the thread. The temperature difference across the length of the bolt can be quite large, so using the thermal conductivity at the average temperature can lead to significant errors. Instead the integrated average thermal conductivity is used:

$$k_{bolt,av} = \frac{1}{\left(T_{w,h} - T_{w,c}\right)} \int_{T_{w,c}}^{T_{w,h}} k_{bolt}\left(T\right) dT \tag{5.7.3}$$

where $k_{bolt,av}$ is the integrated average thermal conductivity of the bolts, $T_{w,h}$ is the wall temperature at the hot end of the heat exchanger, and $T_{w,c}$ is the wall temperature at the cold end of the heat exchanger. The function $k_{bolt}(T)$ is equal to the $k_{ss}(T)$ presented in Eq. 5.2.2 since all of the MEMS heat exchangers used stainless steel support bolts. The solution of Eq. 5.7.3 can be expedited through the use of tabulated integrals of the thermal conductivity function from a reference temperature, T_{ref}. The mathematically equivalent form of Eq. 5.7.3 is shown in Eq. 5.7.4 in terms of integrals from a reference temperature that can easily be tabulated and looked up:

$$k_{bolt,av} = \frac{1}{\left(T_{w,h} - T_{w,c}\right)} \left(\int_{T_{ref}}^{T_{w,h}} k_{bolt}\left(T\right) dT - \int_{T_{ref}}^{T_{w,c}} k_{bolt}\left(T\right) dT \right) \tag{5.7.4}$$

A table showing integrated thermal conductivity of stainless steel based on a reference temperature of 100 K is given in Table 5.7.1. This table has been integrated into the design model as the Lookup Table 'SScond'.

Table 5.7.1: Integrated thermal conductivity values based off a reference temperature of 100 K for stainless steel. The thermal conductivity function for stainless steel is shown in Eq. 5.2.2.

T [K]	$\int_{T_{ref}}^{T} k_{bolt}\left(T\right) dT$ [W/m]
100	0
110	94.43
120	193.2
130	296
140	402.4
150	512.3
160	625.3
170	741.4
180	860.5
190	982.4
200	1107
210	1235
220	1365
230	1498
240	1633
250	1771
260	1912
270	2056
280	2202
290	2351
300	2502

The rate of heat transfer that is conducted through the bolts can be calculated using Eq. 5.7.5:

$$\dot{q}_{bolt} = \frac{N_{bolt}\ k_{bolt,av} \left(\frac{\pi}{2} D_{bolt}^2 \right) \left(T_{w,h} - T_{w,c}\right)}{L_{bolt}} \tag{5.7.5}$$

where $\dot{q}_{bolt}$ is the heat transfer rate through all of the bolts, N_{bolt} is the number of bolts, D_{bolt} is the minor diameter of the bolts, and L_{bolt} is the length of the bolts. The length of the bolts was assumed to be equal to the length of the heat exchanger. All experimentally tested heat exchangers had four support bolts. The 10 mm 16 die heat exchanger used #6 bolts (with a 2.67 mm minor diameter), while the 10 mm 43 die and 20 mm 38 die heat exchangers used #4 bolts (with a 1.93 mm minor diameter).

The quantity of heat conducted on the ends of the heat exchanger can be calculated using Eq. 5.7.6 and 5.7.7:

$$\dot{q}_{w,h} = -\dot{q}_{bolt} \tag{5.7.6}$$

$$\dot{q}_{w,c} = -\dot{q}_{bolt} \tag{5.7.7}$$

where $q_{w,h}$ is the heat conducted to the warm end of the heat exchanger and $q_{w,c}$ is the heat conducted from the cold end of the heat exchanger. The quantity of heat conducted to and from the heat exchanger ends is calculated by the procedure HeaderCond, which is shown in Design Model Code 5.7.3:

Design Model Code 5.7.3: Procedure for calculating axial conduction to and from the ends of the heat exchanger.

```
"*****************************************************************************************************************"
Procedure HeaderCond(T_w_h, T_w_c: q_dot_w_h, q_dot_w_c)
    "!Axial conduction to and from ends of heat exchanger"

$Common D_bolt, L_bolt

   "integrated conductivity to cold end temperature"
    k_int_c=interpolate('SScond', k_int, T, T=T_w_c)

   "integrated conductivity to warm end temperature"
   k_int_h=interpolate('SScond', k_int, T, T=T_w_h)

   k_bolt_av=(k_int_h-k_int_c)/(T_w_h-T_w_c)                "average conductivity of bold"
    N_bolt=4                                                "number of support bolts used"
    q_bolt=k_bolt_av*Pi/4*D_bolt^2/L_bolt*(T_w_h-T_w_c)     "heat conducted through bolts"

    q_dot_w_h=-q_bolt          "heat conducted to warm end"
    q_dot_w_c=-q_bolt          "heat conducted from cold end"

End {HeaderCond}
"*****************************************************************************************************************"
```

5.8 Parasitic Heat Loads

Heat loads that are imposed along the length of the heat exchanger on its external surface will tend to reduce the hot side effectiveness for a cryogenic heat exchanger. For J-T cycles a heat load on the heat exchanger will also tend to reduce the refrigeration capacity of the cycle. A detailed explanation of the effects of parasitic heat loads on J-T heat exchangers can be found in Chapter 4. Three heat loads on the MEMS heat exchangers were considered: radiation from the

vacuum vessel wall, thermal conduction and ohmic dissipation in the integrated PRT measurement leads, and ohmic dissipation in the integrated PRTs. All three heat loads have been estimated and included into the design model.

The MEMS heat exchangers were covered with at least 5 layers of multi-layer insulation (MLI) when tested in the cryogenic test facility. The equations used for estimating the heat load due to radiation from the wall (Eq. 5.8.1 and Eq. 5.8.3) are from Barron [32]. The heat load due to radiation on a single die can be calculated using Eq. 5.8.1:

$$\dot{q}_{rad} = F_e \; F_{12} \; \sigma \left(SA_{die} \right) \left(T_{wall}^4 - T_{die}^4 \right) \tag{5.8.1}$$

where $\dot{q}_{rad}$ is the heat load due to radiation, F_e is the emissivity factor, F_{12} is the view factor from the die surface to the shield, σ is the Stefan-Boltzmann constant, SA_{die} is the external surface area of one die, T_{wall} is the inner wall temperature of the Dewar, and T_{die} is the average wall temperature for the die. The surface area of one die can be calculated using Eq. 5.8.2:

$$SA_{die} = 4 \; W_{die} \left(t_{sp} + t_{fin} \right) \tag{5.8.2}$$

where W_{die}, t_{sp}, and t_{fin}, are listed in Table 5.1.1 and Table 5.1.2 for both the 10 mm and 20 mm dies. The emissivity factor can be calculated using Eq. 5.8.3:

$$\frac{1}{F_e} = \left(\frac{1}{e_{die}} + \frac{1}{e_{MLI}} - 1 \right) + \left(N_{MLI} - 1 \right) \left(\frac{2}{e_{MLI}} - 1 \right) + \left(\frac{1}{e_{MLI}} + \frac{1}{e_{wall}} - 1 \right) \tag{5.8.3}$$

where e_{die} is the emissivity of the die surface, e_{MLI} is the emissivity of the aluminized mylar in the MLI, e_{wall} is the emissivity of the inner wall of the Dewar, and N_{MLI} is the number of layers of MLI. The emissivity of MLI is listed as 0.025 by Barron. The inner walls of the Dewar were also covered in MLI, so the wall emissivity in Eq. 5.8.3 is also 0.025. The emissivity of the epoxy is unknown, so it is assumed to behave as a blackbody with an emissivity of one. The view factor is very close to one since nearly all radiation leaving the die will strike the inner wall of the Dewar. The view factor is assumed to be one to keep the equations simple and to overestimate rather than underestimate the heat loads.

Radiation on the heat exchanger has been included in the design model, but is unlikely to significantly effect the temperature distribution. Consider a fluid with a mass flow rate of 0.01 g/s (which is slightly lower than any experimental measured flow rates), a specific heat of 1.60 J/g-K (slightly lower than ethane at standard conditions), and a fluid temperature change of 0.25 K across one die. The total heat transfer from or to the working fluid would be 4.0×10^{-3} W. The radiation heat transfer to a single 20 mm die at 150 K with 5 radiation shields is estimated to be 6.3×10^{-6} W using Eq. 5.8.1- Eq. 5.8.3. The radiation heat load on one die is only 0.16% of the stream-to-stream heat transfer even when the mass flow rate, specific, heat, and fluid temperature change across the die are all at their expected lowest values. Therefore, radiation heat transfer that is directly incident on the heat exchanger is unlikely to have significant effects.

A simple method of estimating magnitude the heat load due to conduction and ohmic dissipation was presented in Chapter 3. This method treated the conduction and ohmic dissipation separately and summed the heat loads. The estimated heat load for a set of PRT measurement leads was estimated to be 32×10^{-6} W for a 1 m long, 0.008" diameter manganin wire with 10 μA current leads conducting between 300 K and 150 K. The 20 mm integrated PRTs used 10 μA current leads, but the 10 mm integrated PRTs used 100 μA current leads for experimental testing. If the calculations are rerun for the same wires but with 100 μA current then the total estimated heat load for a single PRT would be 3.0×10^{-3} W. Therefore, the heat load due to the PRT measurement leads is large enough to affect the heat exchanger if the capacity rate of the fluids is low and a numerical model was written to accurately account for the heat generated through ohmic dissipation and radiation from the Dewar inner wall on the total amount of heat conducted to the heat exchanger.

The length of the lead wire is broken into N_{wire} elements of equal length with temperature nodes at the center of each element. The distribution of temperature nodes and elements is shown by the schematic in Fig. 5.8.1. There are two more temperature nodes than elements so that boundary conditions can be applied to the wire ends.

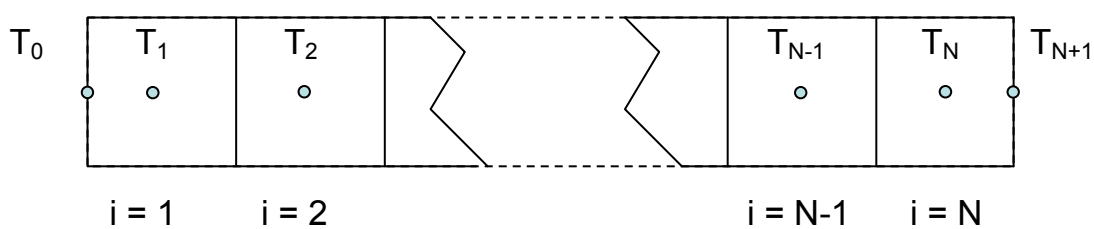

Fig. 5.8.1: Schematic showing the distribution of the temperature nodes (top text) and the element locations (bottom text).

An energy balance control volume for the *i*th element of the measurement lead wire is shown in Fig. 5.8.2 and the energy balance is shown in equation form in Eq. 5.8.4.

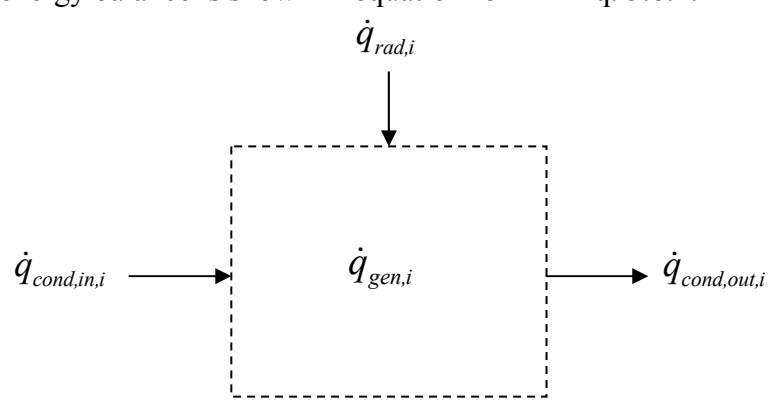

Fig. 5.8.2: Energy balance for the *i*th element of the measurement lead wire.

$$\dot{q}_{cond,in,i} + \dot{q}_{rad,i} + \dot{q}_{gen,i} = \dot{q}_{cond,out,i} \tag{5.8.4}$$

where $\dot{q}_{cond,in,i}$ is the heat conducted to the *i*th element, $\dot{q}_{cond,out,i}$ is the heat conducted from the *i*th element, $\dot{q}_{gen,i}$ is the heat generated through ohmic dissipation in the *i*th element, and $\dot{q}_{rad,i}$ is the

heat radiated onto the *i*th element. The heat conducted into the *i*th element is equal to the heat conducted from the (*i*-1)th element, as shown by Eq. 5.8.5.

$$\dot{q}_{cond,in,i} = \dot{q}_{cond,out,i-1} \text{ for } i = 2, N_{wire} \tag{5.8.5}$$

The heat conducted out of each element can be calculated using Eq. 5.8.6:

$$\dot{q}_{cond,out,i} = \frac{k_{wire,i}\left(\pi/4\right)D_{wire}{}^{2}}{\Delta x}\left(T_i - T_{i+1}\right) \quad \text{for } i = 1,\left(N_{wire}\text{-}1\right) \tag{5.8.6}$$

where Δx is the length of each element and $k_{wire,i}$ is the wire conductivity evaluated at the average of the temperatures of the *i*th and (*i*+1)th nodes. Tabulated values of the thermal conductivity for manganin as a function of temperature can be found in Chapter 3. The two boundary condition equations are presented in Eq. 5.8.7 for the warm end and in Eq. 5.8.8 for the cold end. Note that the conduction length is only half of an element for the two boundary nodes.

$$\dot{q}_{cond,in,1} = \frac{k_{wire,0}\left(\pi/4\right)D_{wire}{}^{2}}{\left(\Delta x/2\right)}\cdot\left(T_0 - T_1\right) \tag{5.8.7}$$

$$\dot{q}_{cond,out,Nwire} = \frac{k_{wire,Nwire+1}\left(\pi/4\right)D_{wire}{}^{2}}{\left(\Delta x/2\right)}\cdot\left(T_{Nwire} - T_{Nwire+1}\right) \tag{5.8.8}$$

The quantity of heat generated in the *i*th element through ohmic dissipation can be calculated using Eq. 5.8.9:

$$\dot{q}_{gen,i} = \frac{\rho_i\ \Delta x}{\left(\pi/4\right)D_{wire}^2}I_{wire}^2 \tag{5.8.9}$$

where ρ_i the electrical resistivity evaluated at the temperature of node *i* and I_{wire} is the current flowing through the wire. Tabulated values of the electrical resistivity for manganin as a function of temperature can be found in Chapter 3.

The final term of the energy balance that must be calculated is the radiation heat transfer. The surface area of an element ($SA_{element}$) can be calculated using Eq. 5.8.10:

$$SA_{element} = \pi\ D_{wire}\ \Delta x \tag{5.8.10}$$

The radiation heat load can then be calculated using Eq. 5.8.11:

$$\dot{q}_{rad,i} = F_e F_{12}\sigma\left(SA_{element}\right)\left(T_{wall}^4 - T_i^4\right) \tag{5.8.11}$$

Where the view factor F_{12} is assumed to be one since nearly all radiation leaving the wire element will strike the inner wall of the Dewar and the emissivity factor F_e can be calculated using Eq. 5.8.12:

$$\frac{1}{F_e} = \left(\frac{1}{e_{wire}} + \frac{1}{e_{MLI}} - 1\right) + \left(N_{MLI} - 1\right)\left(\frac{2}{e_{MLI}} - 1\right) + \left(\frac{1}{e_{MLI}} + \frac{1}{e_{wall}} - 1\right) \tag{5.8.12}$$

The emissivity of the wall (e_{wall}) and MLI (e_{MLI}) is 0.025 and the emissivity of the wire (e_{wire}) is assumed to be 0.5. No information was found in the literature regarding the emissivity of manganin, so the wire emissivity was chosen to match the highest emissivity for a metallic material given by Barron [31]. The application of MLI to the measurement leads was often inconsistent, with several layers being applied near the cold end and no layers being applied near the warm end. The calculations assume that one layer of MLI was applied to the entire length of the wire.

A parametric study was performed while varying the cold end temperature but maintaining the warm end temperature at 295 K. Three types of wire were studied: a 100 μA current lead (for 10 mm PRTs), a 10 μA current lead (for 20 mm PRTs), and a voltage lead with no current. All three wires were assumed to be 1 m long, have a diameter of 0.008", and fabricated out of manganin. The heat load on the heat exchanger associated with each wire is plotted as a function of the temperature difference between the wire ends in Fig. 5.8.3. The 10 μA current lead conducts roughly the same quantity of heat to the heat exchanger as the voltage lead, but the 100 μA lead conducts much larger quantities of heat even at zero temperature difference due to the ohmic dissipation.

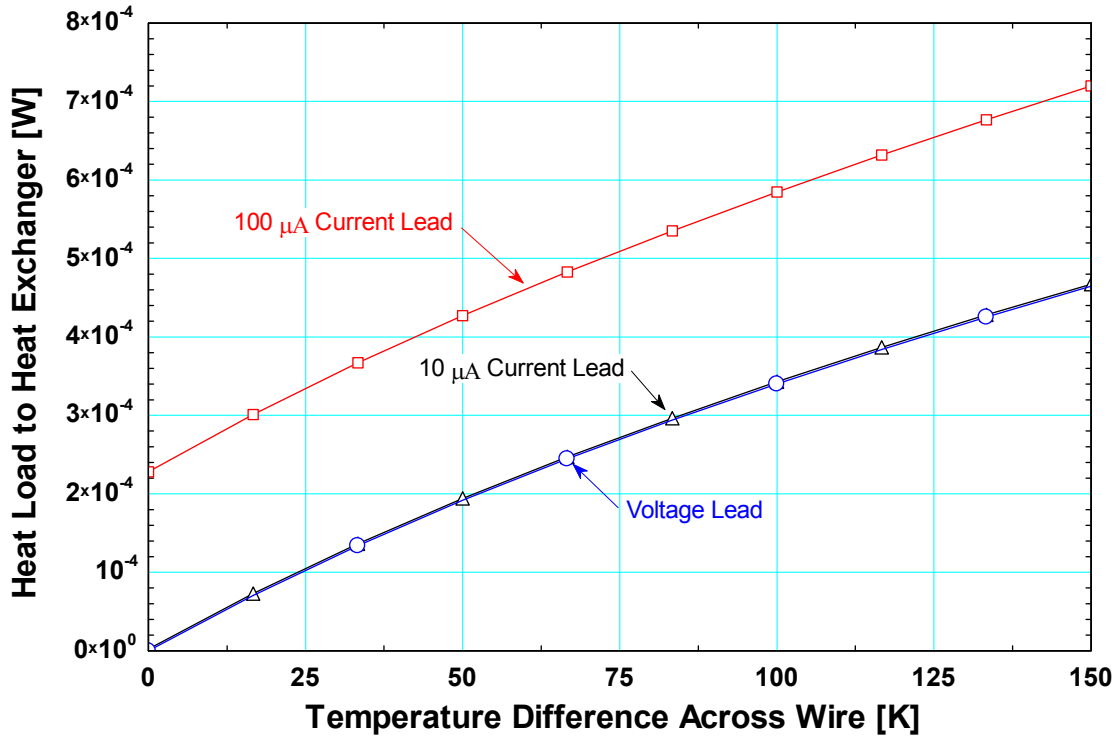

Fig. 5.8.3: Heat load to the heat exchanger as a function of the temperature difference between the ends of the lead wire. Three types of wire leads were examined: 100 μA current leads, 10 μA current leads, and voltage leads with no electrical current.

As discussed earlier in this section, at low flow rates of a fluid with small specific heats such as ethane the total stream-to-stream heat transfer could be around 4×10^{-3} W. If the temperature difference between the die and ambient is large, the quantity of heat conducted by two sets of measurement leads (2 voltage leads and 2 current leads for both the hot and cold stream PRTs) could be almost as large as the quantity of heat conducted stream-to-stream. Conduction through the measurement leads can be significant and should be included in the design model. The results shown in Fig. 5.8.3 are tabulated in Table 5.8.1. To increase the computational efficiency of the design model the data in Table 5.8.1 has been incorporated into the design model as a lookup table.

Table 5.8.1: Heat load to the heat exchanger as a function of the temperature difference between the ends of the lead wire. Three types of wire leads were examined: 100 μA current leads, 10 μA current leads, and voltage leads with no electrical current. The tabulated results are plotted in Fig. 5.8.3.

	Heat Load		
ΔT_{wire} [K]	100 μA Current [W]	10 μA Current [W]	Voltage [W]
0.0	2.28E-04	2.30E-06	8.03E-20
16.7	3.01E-04	7.31E-05	7.08E-05
33.3	3.67E-04	1.37E-04	1.34E-04
50.0	4.27E-04	1.94E-04	1.92E-04
66.7	4.83E-04	2.47E-04	2.45E-04
83.3	5.35E-04	2.97E-04	2.94E-04
100.0	5.85E-04	3.43E-04	3.40E-04
116.7	6.32E-04	3.87E-04	3.84E-04
133.3	6.77E-04	4.28E-04	4.26E-04
150.0	7.20E-04	4.67E-04	4.65E-04

The total quantity of heat conducted to the heat exchanger through the four measurement leads required for the integrated PRT can be calculated using Eq. 5.8.13:

$$\dot{q}_{wire} = 2\dot{q}_{cur} + 2\dot{q}_{volt} \tag{5.8.13}$$

where $\dot{q}_{wire}$ is the total heat conducted by all four measurement leads, $\dot{q}_{cur}$ is the heat conducted by one current lead (obtained from Table 5.8.1)., and $\dot{q}_{volt}$ is the heat conducted one voltage lead (obtained from Table 5.8.1).

The final heat load on the heat exchanger is the ohmic dissipation from the integrated PRTs. The self-heating measurement error is expected to be small due to the large bonding area to the silicon surface relative to the size of the platinum resistor. The quantity of heat generated in the integrated PRTs can be calculated using Eq. 5.8.14.

$$\dot{q}_{selfheat} = I_{wire}^2 R_{PRT} \tag{5.8.14}$$

where $\dot{q}_{selfheat}$ is the quantity of electrical power dissipated in the PRT, I_{wire} is the current flowing through the PRT, and R_{PRT} is the resistance of the PRT. The experimentally measured values of the PRT resistance as a function of temperature can be found in Chapter 6.

The total heat load on the hot stream ($\dot{q}_{h,j}$) for the *j*th die is given by Eq. 5.8.15 and the total heat load on the cold stream ($\dot{q}_{c,j}$) on the *j*th die is given by Eq. 5.8.16:

$$\dot{q}_{h,j} = \dot{q}_{rad,h,j} + \dot{q}_{wire,h,j} + \dot{q}_{selfheat,h,j} \tag{5.8.15}$$

$$\dot{q}_{c,j} = \dot{q}_{rad,c,j} + \dot{q}_{wire,c,j} + \dot{q}_{selfheat,c,j} \tag{5.8.16}$$

where $\dot{q}_{rad,j}$ is the radiation falling on half of the *j*th die (note the surface area from Eq. 5.1.2 must be divided in two), $\dot{q}_{wire,j}$ is the heat conducted through any measurement leads connected to the *j*th die, and $\dot{q}_{selfheat,j}$ is the ohmic dissipation in the PRT on the *j*th die if the PRT is being measured.

The calculation of the heat loads on the hot side, cold side, and wall have been written as EES procedures and are shown in Design Model Code 5.8.1, 5.8.2, and 5.8.3 respectively.

Design Model Code 5.8.1: Calculation of the hot side parasitic heat load

```
"*****************************************************************************************************************"
Procedure HotSideHeatLeak(N, T_h_av: q_dot_h)

$Common DieGeom$, HX$, Mode$, T_h_in, t_sp, t_fin

    "!Values dependent on die size"
    If DieGeom$='10mm' then
        I_prt=(100*10^(-6)) [A]                    "current through die PRTs"
        SA_rad=(2*0.010 [m])*(t_sp+t_fin)          "surface area for radiation"
    Endif
    If DieGeom$='20mm' then
        I_prt=(10*10^(-6)) [A]                     "current through die PRTs"
        SA_rad=(2*0.020 [m])*(t_sp+t_fin)          "surface area for radiation"
    Endif

    "!Heat load due to die PRTs, HX$ specifies name of experimental heat exchanger"
    If HX$='16die10mm' then
        q_dot_wire=0 [W]          "parasitic heat load conducted from wires"
        q_dot_selfheat=0 [W]      "parasitic heat load from PRT self heating"
    Endif
    If HX$='43die10mm' then
        If N=9 then R_PRT=interpolate1('10mmPRT9', R, T, T=T_h_av)*convert(kohm, ohm)
        If (N=14) and (Mode$='selfcool') then R_PRT=interpolate1('10mmPRT10', R, T, T=T_h_av)*convert(kohm, ohm)
        If N=22 then R_PRT=interpolate1('10mmPRT12', R, T, T=T_h_av)*convert(kohm, ohm)
        If N=27 then R_PRT=interpolate1('10mmPRT13', R, T, T=T_h_av)*convert(kohm, ohm)
        If N=36 then R_PRT=interpolate1('10mmPRT14', R, T, T=T_h_av)*convert(kohm, ohm)
        If (N=9) or ((N=14) and (Mode$='selfcool')) or (N=22) or (N=27) or (N=36) then
            q_dot_selfheat=I_prt^2/R_PRT          "parasitic  heat load from radiation"
            DELTAT=T_h_in-T_h_av                  "temperature difference between die and ambient"
            q_dot_cur=interpolate('CTF10mmPRT current', q_dot_cond, DELTAT_wire, DELTAT_wire=DELTAT)
            q_dot_volt=interpolate('CTFPRT voltage', q_dot_cond, DELTAT_wire, DELTAT_wire=DELTAT)
            q_dot_wire=2*q_dot_cur+2*q_dot_volt"four wire measurement"
        Else
            q_dot_selfheat=0 [W]                  "no PRT for self heating"
            q_dot_wire=0 [W]                      "no wire for conducting parasitic heat"
        Endif
```

```
    Endif
    If HX$='37die20mm' then
        If N=8 then R_PRT=interpolate1('20mmPRT8', R, T, T=T_h_av)*convert(kohm, ohm)
        If N=14  then R_PRT=interpolate1('20mmPRT7', R, T, T=T_h_av)*convert(kohm, ohm)
        If N=19 then R_PRT=interpolate1('20mmPRT6', R, T, T=T_h_av)*convert(kohm, ohm)
        If N=24 then R_PRT=interpolate1('20mmPRT5', R, T, T=T_h_av)*convert(kohm, ohm)
        If N=28 then R_PRT=interpolate1('20mmPRT4', R, T, T=T_h_av)*convert(kohm, ohm)
        If (N=8) or (N=14) or (N=19) or (N=24) or (N=28) then
            q_dot_selfheat=I_prt^2/R_PRT          "parasitic  heat load from radiation"
            DELTAT=T_h_in-T_h_av                  "temperature difference between die and ambient"
            q_dot_cur=interpolate('CTF20mmPRT current', q_dot_cond, DELTAT_wire, DELTAT_wire=DELTAT)
            q_dot_volt=interpolate('CTFPRT voltage', q_dot_cond, DELTAT_wire, DELTAT_wire=DELTAT)
            q_dot_wire=2*q_dot_cur+2*q_dot_volt"four wire measurement"
        Else
            q_dot_selfheat=0 [W]                  "no PRT for self heating"
            q_dot_wire=0 [W]                      "no wire for conducting parasitic heat"
        Endif
    Endif
    If HX$='Test' then
        q_dot_wire=0 [W]          "parasitic heat load conducted from wires"
        q_dot_selfheat=0 [W]      "parasitic heat load from PRT self heating"
    Endif

    "!Radiation heat load"
    e_die=1                       "die emissivity"
    e_dewar=0.025                 "emissivity of MLI on dewar innner surface"
    e_MLI=0.025                   "emissivity of MLI"
    N_MLI=1                       "number of layers of MLI"
    F_e=1/((1/e_die+1/e_MLI-1)+(N_MLI-1)*(2/e_MLI-1)+(1/E_MLI+1/E_dewar-1))          "emissivity factor"
    F_viewfactor=1                "view factor between surfaces"
    q_dot_rad=F_e*F_viewfactor*sigma#*SA_rad*(T_h_in^4-T_h_av^4)                      "parasitic  heat load from radiation"

    "!Total heat load"
    q_dot_h=q_dot_wire+q_dot_selfheat+q_dot_rad                                       "total parasitic heat load on hot stream"

End {HotSideHeatLeak}
"*****************************************************************************************************************"
```

Design Model Code 5.8.2: Calculation of the cold side parasitic heat load

```
"*****************************************************************************************************************"
Procedure ColdSideHeatLeak(N, T_c_av: q_dot_c)

$Common DieGeom$, HX$, Mode$, T_h_in, t_sp, t_fin

    "!Values dependent on die size"
    If DieGeom$='10mm' then
        I_prt=(100*10^(-6)) [A]              "current through die PRTs"
        SA_rad=(2*0.010 [m])*(t_sp+t_fin)        "surface area for radiation"
    Endif
    If DieGeom$='20mm' then
        I_prt=(10*10^(-6)) [A]               "current through die PRTs"
        SA_rad=(2*0.020 [m])*(t_sp+t_fin)        "surface area for radiation"
    Endif

    "!Heat load due to die PRTs, HX$ specifies name of experimental heat exchanger"
    If HX$='16die10mm' then
        q_dot_wire=0 [W]          "parasitic heat load conducted from wires"
        q_dot_selfheat=0 [W]      "parasitic heat load from PRT self heating"
    Endif
    If HX$='43die10mm' then
        If N=9 then R_PRT=interpolate1('10mmPRT6', R, T, T=T_c_av)*convert(kohm, ohm)
        If (N=18) and (Mode$='selfcool') then R_PRT=interpolate1('10mmPRT5', R, T, T=T_c_av)*convert(kohm, ohm)
        If N=22 then R_PRT=interpolate1('10mmPRT4', R, T, T=T_c_av)*convert(kohm, ohm)
        If N=32 then R_PRT=interpolate1('10mmPRT2', R, T, T=T_c_av)*convert(kohm, ohm)
        If N=36 then R_PRT=interpolate1('10mmPRT1', R, T, T=T_c_av)*convert(kohm, ohm)
        If (N=9) or ((N=18) and (Mode$='selfcool')) or (N=22) or (N=32) or (N=36) then
            q_dot_selfheat=I_prt^2/R_PRT         "parasitic  heat load from radiation"
            DELTAT=T_h_in-T_c_av                 "temperature difference between die and ambient"
            q_dot_cur=interpolate('CTF10mmPRT current', q_dot_cond, DELTAT_wire, DELTAT_wire=DELTAT)
            q_dot_volt=interpolate('CTFPRT voltage', q_dot_cond, DELTAT_wire, DELTAT_wire=DELTAT)
            q_dot_wire=2*q_dot_cur+2*q_dot_volt"four wire measurement"
        Else
            q_dot_selfheat=0 [W]                 "no PRT for self heating"
            q_dot_wire=0 [W]                     "no wire for conducting parasitic heat"
        Endif
```

```
    Endif
    If HX$='37die20mm' then
        If N=19 then R_PRT=interpolate1('20mmPRT1', R, T, T=T_c_av)*convert(kohm, ohm)
        If N=28 then R_PRT=interpolate1('20mmPRT2', R, T, T=T_c_av)*convert(kohm, ohm)
        If N=33 then R_PRT=interpolate1('20mmPRT3', R, T, T=T_c_av)*convert(kohm, ohm)
        If (N=19) or (N=28) or (N=33) then
            q_dot_selfheat=I_prt^2/R_PRT          "parasitic  heat load from radiation"
            DELTAT=T_h_in-T_c_av                  "temperature difference between die and ambient"
            q_dot_cur=interpolate('CTF20mmPRT current', q_dot_cond, DELTAT_wire, DELTAT_wire=DELTAT)
            q_dot_volt=interpolate('CTFPRT voltage', q_dot_cond, DELTAT_wire, DELTAT_wire=DELTAT)
            q_dot_wire=2*q_dot_cur+2*q_dot_volt"four wire measurement"
        Else
            q_dot_selfheat=0 [W]                  "no PRT for self heating"
            q_dot_wire=0 [W]                      "no wire for conducting parasitic heat"
        Endif
    Endif
    If HX$='Test' then
        q_dot_wire=0 [W]          "parasitic heat load conducted from wires"
        q_dot_selfheat=0 [W]      "parasitic heat load from PRT self heating"
    Endif

    "!Radiation heat load"
    e_die=1                       "die emissivity"
    e_dewar=0.025                 "emissivity of MLI on dewar innner surface"
    e_MLI=0.025                   "emissivity of MLI"
    N_MLI=1                       "number of layers of MLI"
    F_e=1/((1/e_die+1/e_MLI-1)+(N_MLI-1)*(2/e_MLI-1)+(1/E_MLI+1/E_dewar-1))          "emissivity factor"
    F_viewfactor=1                "view factor between surfaces"
    q_dot_rad=F_e*F_viewfactor*sigma#*SA_rad*(T_h_in^4-T_c_av^4)                      "parasitic  heat load from radiation"

    "!Total heat load"
    q_dot_c=q_dot_wire+q_dot_selfheat+q_dot_rad       "total parasitic heat load on cold stream"

End {ColdSideHeatLeak}
"*****************************************************************************************************************"
```

Design Model Code 5.8.2: Calculation of the wall parasitic heat load

```
"*****************************************************************************************************************"
Procedure WallHeatLeak(N, T_w_av: q_dot_w)
"All parasitic loads go directly to hot stream or cold stream"

    q_dot_w= 0 [W]       "parasitic heat load on wall"

End {WallHeatLeak}
"*****************************************************************************************************************"
```

5.9 Integration of General Model with MEMS Heat Exchanger Procedures

This section describes how the general numerical model of perforated plate heat exchangers covered in Chapter 4 is integrated with the MEMS heat exchanger procedures described thus far in Chapter 5. Guidelines for obtaining reliable convergence on the solution are also provided. At the conclusion of the section, some suggestions for future improvements to the model are discussed.

The section of code placed at the beginning of the EES file before any procedures is shown in Design Model Code 5.9.1. The units are specified to be in the SI system with kg, kPa, K, J being the base units of mass, pressure, temperature, and energy respectively. The $updateguesses command is included so that the previous solution can be used as the starting point to obtain the new solution. This command allows the model to converge much faster and much more reliably. The two highlighted variables *N_die#* and *N_sp#* are constants that must be specified by the user. The model should be run with constant properties while *N_die#* and *N_sp#* are being modified; otherwise the solution time will be long and the chances of the model failing to converge are high.

Design Model Code 5.9.1: Beginning of EES file

```
"!Description of Code"
"Dimensionless heat exchanger model of a perforated plate heat exchanger that includes "
"The model accounts for axial conduction, parasitic heat loads, and internal leakage"
"Model written by Michael White for M.S. Thesis at the University of Wisconsin-Madison, 2008"

$unitssystem SI mass deg kPa K J
$updateguesses
$tabstops 0.2 0.4 0.6
$constant N_die#=3      "number of dies that form the heat exchanger"
$constant N_sp#=2       "number of spacers (N_die#-1), the spacer on the end is neglected"
```

The section of code where the user selects the various options required to run the model is located at the beginning of the main body of EES code and is shown Design Model Code 5.9.2. The first step is to select the heat exchanger that is being modeled. The three experimentally tested heat exchangers are included as options, or the user can select the 'Test' option for modeling a hypothetical heat exchanger. The name is necessary so that the model can determine the heat exchanger dimensions, the location of any internal PRTs, and the size of the support bolts.

The second option requires the user to select the name of the working fluid. The number of fluids N_fluid is always one since the model is currently capable of modeling pure single phase fluids. This variable would be necessary for modeling fluid mixtures.

The third option requires the user to select whether the cooling at the cold end of the heat exchanger is provided by a cryocooler or if the heat exchanger is self-cooling through the use of a J-T cycle. If the 'cryocooler' option is selected then the cold inlet temperature must be specified and if the 'selfcool' option is selected then the orifice diameter and heater power must be specified. The model must be iterated several times in cryocooler mode so that the specified cold inlet temperature $T_{c,in}$ closely matches the temperature $T_{coldend}$ returned from the procedure 'ColdEnd' if the model is to be run in self-cooling mode.

The number of elements used for each perforated plate is specified by the variable. The hot inlet temperature and cold outlet pressure must always be specified. The hot inlet pressure is determined by adding all of the pressure drops in the heat exchanger and tubing to the cold outlet pressure. The hot and cold side pressure drops can be either specified by the user or calculated through the procedure 'DiePressDrop', which was covered in Chapter 5.6.

The mass flow rate must be specified along with the location and size of the leak. The mass flow rate inputs are passed to the procedure 'Leak', which performs the necessary mass balances and returns an array to the main EES program with the mass flow rate through each perforated plate. The mass balance equations were shown in Chapter 4 and the procedure 'Leak' is shown in Design Model Code 5.9.3.

The quantity of heat conducted to and from the ends of the heat exchanger can be either specified by the user or calculated through the use of 'HeaderCond'. The axial resistance of the silicon perforated plate and the glass spacer can be either specified or calculated through the use of 'SiAxCond' and 'GlassAxCond' respectively. The procedures 'HeaderCond', 'SiAxCond', and 'GlassAxCond', and are described in Chapter 5.7.

The stream-to-wall thermal resistances can be specified or calculated through the procedure 'StreamResistance'. The hot and cold stream specific heats can also be specified or calculated using the procedure 'StreamResistance'. Note that it is perfectly acceptable to use a constant thermal resistance and calculated specific heat or vice versa. This is accomplished by appending a '2' to the undesired variable names, as shown in the example in Design Model Code 5.9.2. The procedure 'StreamResistance' was described in Chapter 5.6.

The final variables that must be determined are the parasitic heat loads on the hot stream, the cold stream, and the wall. These variables can be either specified by the user or calculated using the procedures 'HotSideHeatLeak', 'ColdSideHeatLeak', or WallHeatLeak. The procedures used for calculating the heat loads on the length of the heat exchanger were described in Chapter 5.8.

Design Model Code 5.9.2: Beginning of main body of EES code where the user selects necessary inputs

```
"*****************************************************************************************************************"
```

```
"!Select Heat Exchanger"
{HX$='16die10mm'        "name of heat exchanger to be tested"}
HX$='43die10mm'         "name of heat exchanger to be tested"
{HX$='37die20mm'        "name of heat exchanger to be tested"}
{HX$='Test'             "name of heat exchanger to be tested"}

"!Select # of fluids and fluid name"
N_fluid=1               "number of components to working fluid"
{F$='helium'}           "the name of the working fluid(s)"
{F$='ethane'}           "the name of the working fluid(s)"

"!Select mode of operation"
Mode$='cryocooler'      "external cooling with cryocooler"
{Mode$='selfcool'}      "operation on J-T cycle"

"!Specifiy number of elements to use for each die"
N=16                                "number of nodes per die"

"!Specify hot inlet temperature and cold outlet pressure"
T_h_in=300 [K]                      "high pressure inlet temperature"
P_c_out=100 [kPa]                   "low pressure outlet pressure"

"!Specify mass flow rate"
{m_dot_g=0.005 [g/s]}                       "hot inlet mass flow rate"
m_dot=m_dot_g*convert(g/s,kg/s)             "hot inlet mass flow rate"
{Leak_pp_loc=3                              "plate adjacent to leak"
Leak_sp_loc=2                               "spacer adjacent to leak"
Frac_leak=0.2                               "fraction of mass flow rate that passes through leak"
Frac_heat=0}            "fraction max possible heat transfered between leaking fluid and wall"
Call Leak(m_dot, Leak_pp_loc, Leak_sp_loc, Frac_leak:m_dot[1..N_die#], m_dot_h_leak[1..N_die#],
m_dot_c_leak[1..N_die#])

"!Specify cold end parameters or calculate using ColdEnd"
D_orifice=0.015 [in]                "orifice diameter, only affects self-cooling mode"
Q_dot_htr=0 [W]                     "heating load on cold end in addition to parasitics"
$If Mode$='selfcool' then
    T_c_in=T_cold_end               "cold inlet temperature, for self-cooling mode"
$Else
    T_c_in=295 [K]                  "cold inlet temperature for cryocooler mode"
$Endif
DELTAP_cold_end=1100 [kPa]  "pressure drop across cold end"
{Call ColdEnd(T_h[N_die#], P_h_out, m_dot[N_die#]:T_cold_end, DELTAP_cold_end)}

"!Specify heat conducted to HX warm end and from HX cold end or calculate using HeaderCond"
q_dot_w_h=0 [W]                     "constant heat conduction into HX hot end"
q_dot_w_c=0 [W]                     "constant heat conduction out HX cold in"
{Call HeaderCond(T_h_in, T_c_in, T_w_h[1], T_w_c[N_die#]: q_dot_w_h, q_dot_w_c)}

Duplicate i=1, N_die#
    "!Specify silicon plate axial resistance or calculate using SiAxResistance"
    R_ac[i]=.05 [K/W]                                       "constant"
    {Call SiAxResistance(T_w_av[i], T_h_in, T_c_in : R_ac[i])}     "calculate"

    "!Specify hot side pressure drop or calculate using DiePressDrop"
    DELTAP_h[i]= 0.0 [kPa]                                  "constant"
    {Call DiePressDrop(m_dot[i], T_h_av[i], P_h_av[i], T_h_in, T_c_in:DELTAP_h[i])}
```

```
    "!Specify hot side thermal resistance and specific heat  or calculate using StreamResistance"
    R_h[i]=5 [K/W]                                          "constant"
    Cp_h2[i]=1700 [J/kg-K]                                  "constant"
    Call StreamResistance(m_dot[i], T_h_av[i], P_h_av[i], T_h_in, T_c_in: R_h2[i], Cp_h[i])

    "!Specify cold side pressure drop or calculate using DiePressDrop"
    DELTAP_c[i]= 0.0 [kPa]                                  "typical cold side pressure drop per die"
    {Call DiePressDrop(m_dot[i], T_c_av[i], P_c_av[i], T_h_in, T_c_in:DELTAP_c[i])}

    "!Specify cold side thermal resistance and specific heat  or calculate using StreamResistance"
    R_c[i]= 5 [K/W]                                         "constant"
    Cp_c2[i]= 1640 [J/kg-K]                                 "constant"
    Call StreamResistance(m_dot[i], T_c_av[i], P_c_av[i], T_h_in,T_c_in: R_c2[i], Cp_c[i])

    "!Specify parasitic heat load on hot stream or calculate using HotSideHeatLeak"
    q_dot_h[i]=0 [W]                                        "constant"
    {Call HotSideHeatLeak(i, T_h_av[i]: q_dot_h[i])}        "calculate"

    "!Specify parasitic heat load on cold stream or calculate using ColdSideHeatLeak"
    q_dot_c[i]=0 [W]                                        "constant"
    {Call ColdSideHeatLeak(i, T_c_av[i]: q_dot_c[i])}       "calculate"

    "!Specify parasitic heat load on wall or calculate using WallHeatLeak"
    q_dot_w[i]=0 [W]                                        "constant"
    {Call WallHeatLeak(i, T_w_av[i]: q_dot_w[i])}           "calculate"
End

Duplicate i=1, N_sp#
    "!Specify spacer axial conduction resistance or calculate using GlassAxResistance"
    R_sp[i]=10 [K/W]                                        "constant"
    T_glass[i]=(T_w_c[i]+T_w_h[i+1])/2                      "glass spacer avg temp "
    {Call GlassAxResistance(T_glass[i], T_h_in, T_c_in : R_sp[i])}                "calculate"
End
"*****************************************************************************************************************"
```

Design Model Code 5.9.3: The procedure Leak which solves the mass balance equations to generate an array which specifies the mass flow rate through each die.

```
"*****************************************************************************************************************"
Procedure Leak(m_dot, Leak_pp_loc, Leak_sp_loc, Frac_leak:m_dot[1..N_die#],
m_dot_h_leak[1..N_die#], m_dot_c_leak[1..N_die#])
"Generates array of mass flow rates that accounts for internal leakage"

"Initialize all leak rates to zero"
j=1; Repeat
    m_dot_h_leak[j]=0 [kg/s]      "leak rate on hot side of perforated plate"
    m_dot_c_leak[j]=0 [kg/s]      "leak rate on cold side of perforated plate"
j=j+1; Until (j>N_die#)

"Mass flow rate in each perforated plate"
j=1
If Leak_pp_loc=Leak_sp_loc then
    m_dot_c_leak[Leak_pp_loc]=m_dot*Frac_leak          "leak on cold side of the plate"
    Repeat
        m_dot[j]=m_dot
```

```
    j=j+1; Until (j>Leak_pp_loc)
    Repeat
        m_dot[j]=m_dot*(1-Frac_leak)
    j=j+1; Until (j>N_die#)
Else
    m_dot_h_leak[Leak_pp_loc]=m_dot*Frac_leak          "leak on hot side of the plate"
    Repeat
        m_dot[j]=m_dot
    j=j+1; Until (j=Leak_pp_loc)
    Repeat
        m_dot[j]=m_dot*(1-Frac_leak)
    j=j+1; Until (j>N_die#)
Endif

End
"*****************************************************************************************************************"
```

The procedure 'Effectiveness' is shown in Design Model Code 5.9.4. This procedure calculates the overall effectiveness of the heat exchanger as described in Chap. 4. The procedure first tests whether the specific heats are constant across the heat exchanger. If the specific heats are constant the effectiveness can be calculated using the standard definition. If the specific heats vary along the length of the heat exchanger, then enthalpies must be used to calculate the maximum possible heat transfer rate in the heat exchanger. If no leaks are present all the heat that is added or removed from a fluid stream occurs only in the perforated plates. If leaks are present then the mixing between the cold stream and the leaking fluid in the spacers must be accounted for.

Design Model Code 5.9.4: The procedure 'Effectiveness' which determines the overall effectiveness of the heat exchanger as described in Chap. 4.

```
"*****************************************************************************************************************"
Procedure Effectiveness(N_fluid, F$, Frac_leak, P_h_in, P_h_out, P_c_in, P_c_out, m_dot[1..N_die#],
Cp_h[1..N_die#], Cp_c[1..N_die#], T_h_in[1..N_die#], T_h_out[1..N_die#], T_c_in[1..N_die#],
T_c_out[1..N_die#], h_h_in[1..N_die#], h_h_out[1..N_die#], h_c_in[1..N_die#], h_c_out[1..N_die#]:
Eff_h, Eff_c, Cp_h_av, Cp_c_av)
"!Calculates the effectiveness of the heat exchanger"

Cp_h_max=max(Cp_h[1..N_die#])        "largest hot side specific  heat"
Cp_h_min=min(Cp_c[1..N_die#])        "smallest hot side specific heat"
Cp_c_max=max(Cp_h[1..N_die#])        "largest cold side specific heat"
Cp_c_min=min(Cp_c[1..N_die#])        "smallest cold side specific heat"
Cp_min=min(Cp_h_min, Cp_c_min)       "smallest specific heat for either stream"

If (Cp_h_max-Cp_h_min<1E-6) and (Cp_c_max-Cp_c_min<1E-6) then
    Cp$='Constant'                   "use constant specific  heat effectiveness equation"
Else
    Cp$='Variable'                   "use variable specific heat effectiveness equation"
Endif

If (Frac_leak=0) and (Cp$='Constant') then
    Eff_h=(Cp_h[1]*(T_h_in[1]-T_h_out[N_die#]))/(Cp_min*(T_h_in[1]-T_c_in[N_die#]))
    Eff_c=(Cp_c[1]*(T_c_out[1]-T_c_in[N_die#]))/(Cp_min*(T_h_in[1]-T_c_in[N_die#]))
    Cp_h_av=Cp_h[1]    "average hot side specific heat"
    Cp_c_av=Cp_c[1]    "aveage cold side specific heat"
Endif
```

```
h_h_out_min=enthalpy(F$, T=T_c_in[N_die#], P=P_h_out)"min possible hot outlet enthalpy"
h_c_out_max=enthalpy(F$, T=T_h_in[1], P=P_c_out)       "max possible cold outlet enthalpy"
"max possible heat transfer rate"
q_dot_max=m_dot[1]*min((h_h_in[1]-h_h_out_min), (h_c_out_max-h_c_in[N_die#]))

If (Frac_leak=0) and (Cp$='Variable') then
     "net heat removed from hot fluid"
     q_dot_h_net=sum(m_dot[i]*Cp_h[i]*(T_h_in[i]-T_h_out[i]), i=1,N_die#)
     "net heat added to cold fluid"
     q_dot_c_net=sum(m_dot[i]*Cp_c[i]*(T_c_out[i]-T_c_in[i]), i=1,N_die#)

     Eff_h=q_dot_h_net/q_dot_max        "hot side effectiveness"
     Eff_c=q_dot_c_net/q_dot_max        "cold side effectiveness"

     "average hot side specific heat"
     Cp_h_av=(h_h_in[1]-h_h_out[N_die#])/(T_h_in[1]-T_h_out[N_die#])
    "average cold side specific heat"
     Cp_c_av=(h_c_out[1]-h_c_in[N_die#])/(T_c_out[1]-T_c_in[N_die#])
Endif

If (Frac_leak>0) then
     "net heat removed from hot fluid"
     q_dot_h_net=sum(m_dot[i]*Cp_h[i]*(T_h_in[i]-T_h_out[i]), i=1,N_die#)
     "net heat added to cold fluid in perforated plates"
     q_dot_c_pp=sum(m_dot[i]*Cp_c[i]*(T_c_out[i]-T_c_in[i]), i=1,N_die#)
    "net heat added to cold fluid in spacers through mixing"
     q_dot_c_sp=sum(m_dot[i]*h_c_in[i]-m_dot[i+1]*h_c_out[i+1], i=1,N_sp#)
    "net heat added to cold fluid in perforated plates (PP) and spacers (SP)"
     q_dot_c_net=q_dot_c_pp+q_dot_c_sp

    Eff_h=q_dot_h_net/q_dot_max        "hot side effectiveness"
     Eff_c=q_dot_c_net/q_dot_max        "cold side effectiveness"

    "average hot side specific heat"
     Cp_h_av=(h_h_in[1]-h_h_out[N_die#])/(T_h_in[1]-T_h_out[N_die#])
    "average cold side specific heat"
     Cp_c_av=(h_c_out[1]-h_c_in[N_die#])/(T_c_out[1]-T_c_in[N_die#])    Endif

End {Effectiveness}
"*************************************************************************************************************"
```

The procedure 'Effectiveness' is called from the main body of EES using the code shown in Design Model Code 5.9.5. The total hot side, cold side, and overall stream-to-stream resitances are calculated for the entire heat exchanger. The axial conduction parameter, λ, is also calculated to gauge the overall effect of axial conduction on the heat exchanger. The hot side, cold side, and overall number of transfer units are calculated based on the hot inlet mass flow rate.

Design Model Code 5.9.5: Set of equations in the main body of EES used to call the procedure 'Effectiveness' and to calculate important overall heat exchanger parameters.

```
"*************************************************************************************************************"
"!Total HX effectiveness"
Call Effectiveness(N_fluid, F$, Frac_leak, P_h_in[1], P_h_out[N_die#], P_c_in[N_die#],
P_c_out[1],m_dot[1..N_die#], Cp_h[1..N_die#], Cp_c[1..N_die#], T_h_in[1..N_die#], T_h_out[1..N_die#],
T_c_in[1..N_die#], T_c_out[1..N_die#], h_h_in[1..N_die#], h_h_out[1..N_die#], h_c_in[1..N_die#],
```

```
h_c_out[1..N_die#]:Eff_h_tot, Eff_c_tot, Cp_h_av, Cp_c_av)

"total hot side resistance, each resistance in parallel"
R_h_tot=1/sum(1/R_h[i], i=1,N_die#)
"total cold side resistance, each resistance in parallel"
R_c_tot=1/sum(1/R_c[i], i=1,N_die#)
"total axial conduction resistance"
R_ac_tot=sum(R_sp[i], i=1,N_sp#)+sum(R_ac[i], i=1,N_die#)

Cp_min_av=min(Cp_h_av, Cp_c_av)                    "minimum specific heat"
lambda=1/(R_ac_tot*Cp_min_av*m_dot)                "axial conduction parameter"
NTU_h_tot=1/(m_dot*Cp_min_av*R_h_tot)              "hot side number of transfer units"
NTU_c_tot=1/(m_dot*Cp_min_av*R_c_tot)              "cold side number of transfer units"
NTU_tot=1/(m_dot*Cp_min_av*(R_h_tot+R_c_tot))      "total number of transfer units"

"*****************************************************************************************************************"
```

The set of equations in the main body of EES used for determining the spacing of the elements in each perforated plate is shown in Design Model Code 5.9.6. Note that the conduction length for the boundary nodes is only half of an element.

Design Model Code 5.9.6: Set of equations in the main body of EES used to set the spacing of the elements within the perforated plate.

```
"*****************************************************************************************************************"
"!Element spacing (identical for each die)"
gamma=1.5                    "end element slightly less than half of middle node length"
Denom=2*sum(exp(-gamma*(1-2*i/N)), i=1, N/2)
Duplicate i=1, (N/2)
    DELTAZ[i]=exp(-gamma*(1-2*i/N))/Denom
    DELTAZ[N+1-i]=DELTAZ[i]
End
DELTAZ[0]=DELTAZ[1]/2        "length for boundary equations"
DELTAZ[N+1]=DELTAZ[N]/2      "length for boundary equations"
"*****************************************************************************************************************"
```

Key variables are placed into or obtained from the ends of the fluid temperature and pressure arrays in Design Model Code 5.9.7. In addition, the calculated pressure drops from 'DiePressDrop' (Design Model Code 5.6.2) are used to construct arrays with the inlet, average, and outlet pressures for each fluid in each die.

Design Model Code 5.9.7: Set of equations in the main body of EES used to build arrays with the hot and cold side pressure profiles. Key temperatures are also placed into temperature profile arrays

```
"*****************************************************************************************************************"
"!Key variables"
T_h_in[1]=T_h_in             "hot inlet temperature"
T_h_out[N_die#]=T_h_out      "hot outlet temperature"
T_c_in[N_die#]=T_c_in        "cold inlet temperature"
T_c_out[1]=T_c_out           "cold outlet temperature"
P_h_in[1]=P_h_in             "hot inlet pressure"
P_h_out[N_die#]=P_h_out      "hot oulet pressure"
P_c_in[N_die#]=P_c_in        "cold inlet pressure"
P_c_out[1]=P_c_out           "cold outlet pressure"
```

```
"!Pressure profile"
DELTAP_cold_end=P_h_out-P_c_in      "pressure difference across cold end of heat exchanger"
Duplicate i=1, N_die#
    P_c_in[i]=P_c_out[i]+DELTAP_c[i]    "cold inlet pressure for die"
    P_c_av[i]=(P_c_in[i]+P_c_out[i])/2    "average cold side pressure for die"
    P_h_in[i]=P_h_out[i]+DELTAP_h[i]    "hot inlet pressure for die"
    P_h_av[i]=(P_h_in[i]+P_h_out[i])/2    "average hot side pressure for die"
End
Duplicate i=1, (N_die#-1)
    P_c_out[i+1]=P_c_in[i]
    P_h_out[i]=P_h_in[i+1]
End
"*****************************************************************************************************************"
```

The dimensionless variables required for the numerical model energy balances are shown in Design Model Code 5.9.8. The first set of equations defines the fluid temperature boundary equations for each die. The second set of equations calculates the capacity rates and the capacity rate ratios for each die. The third set of equations calculates the number of transfer units and the axial conduction parameter for each die. The fourth and fifth sets of equations calculate the parasitic heat load and end conduction dimensionless quantities. The sixth set of equations calculates the outlet temperature of each die, while the seventh set uses the outlet temperature to calculate the effectiveness of each die. The last set of equations is an energy balance used for error checking. If $Error_{die}$ is nonzero then there is an energy imbalance on the die that must be fixed. The model only calculates steady state conditions so there should be no net gain or loss of energy for a control volume drawn around an individual die. The $Error_{die}$ set of equations can be commented out for normal use but should be checked when changes to the numerical model have been made.

Design Model Code 5.9.8: Dimensionless variables required for numerical model energy balances

```
"*****************************************************************************************************************"
"!Dimensionless parameters"
Duplicate i=1, N_die#
    theta_h[i*N+2*i-N-2+0]=1     "hot inlet temp boundary condition"
    theta_c[i*N+2*i-N-2+N]=0     "cold inlet temp boundary condition"

    C_dot_h[i]=m_dot[i]*Cp_h[i]                    "hot side capacity rate"
    C_dot_c[i]=m_dot[i]*Cp_c[i]                    "cold side capacity rate"
    C_dot_min[i]=min(C_dot_h[i], C_dot_c[i])       "minimum capacity rate"
    mu[i]=C_dot_h[i]/C_dot_min[i]                  "hot side capacity ratio"
    nu[i]=C_dot_c[i]/C_dot_min[i]                  "cold side capacity ratio"

    NTU_h[i]=1/(R_h[i]*C_dot_min[i])               "hot side number of transfer units"
    NTU_c[i]=1/(R_c[i]*C_dot_min[i])               "cold side number of transfer units"
    lambda[i]=1/(R_ac[i]*C_dot_min[i])             "axial conduction parameter"

    chi_h[i]=q_dot_h[i]/(C_dot_min[i]*(T_h_in[i]-T_c_in[i]))"hot side parasitic heat load parameter"
    chi_c[i]=q_dot_c[i]/(C_dot_min[i]*(T_h_in[i]-T_c_in[i]))"cold side parasitic heat load parameter"
    chi_w[i]=q_dot_w[i]/(C_dot_min[i]*(T_h_in[i]-T_c_in[i]))"wall parasitic heat load parameter"

    chi_w_h[i]=q_dot_w_h[i]/(C_dot_min[i]*(T_h_in[i]-T_c_in[i]))   "warm end heat conduction"
    chi_w_c[i]=q_dot_w_c[i]/(C_dot_min[i]*(T_h_in[i]-T_c_in[i]))   "cold end heat conduction"
    chi_w_h[i]=lambda[i]*(theta_w[i*N+2*i-N-2+0]-theta_w[i*N+2*i-N-2+1])/(DELTAZ[0])
```

```
    chi_w_c[i]=lambda[i]*(theta_w[i*N+2*i-N-2+N]-theta_w[i*N+2*i-N-2+N+1])/(DELTAZ[N+1])

    theta_h[i*N+2*i-N-2+N]=(T_h_out[i]-T_c_in[i])/(T_h_in[i]-T_c_in[i])"hot outlet temp for die"
    theta_c[i*N+2*i-N-2+0]=(T_c_out[i]-T_c_in[i])/(T_h_in[i]-T_c_in[i])"cold outlet temp for die"

    Eff_h[i]=mu[i]*(T_h_in[i]-T_h_out[i])/(T_h_in[i]-T_c_in[i])        "die hot side effectiveness"
    Eff_c[i]=nu[i]*(T_c_out[i]-T_c_in[i])/(T_h_in[i]-T_c_in[i])        "die cold side effectiveness"

    "die energy balance error checking"
    {q_dot_h_net[i]=m_dot[i]*Cp_h[i]*(T_h_in[i]-T_h_out[i])  "net heat removed from hot fluid"
    q_dot_c_net[i]=m_dot[i]*Cp_c[i]*(T_c_out[i]-T_c_in[i])    "net heat added to cold fluid"
    "error check"
   Error_die[i]=q_dot_w_h[i]-q_dot_w_c[i]-q_dot_c_net[i]+q_dot_h_net[i]+ &
   q_dot_h[i]+q_dot_w[i]+ q_dot_c[i]}
End
"*****************************************************************************************************************"
```

The set of equations used for the energy balances on the spacers is shown in Design Model Code 5.9.9. There are two different choices for the energy balances on the spacers and one must be commented out before running the model. The first choice assumes that the fluid temperature remains constant across the spacer and can be used in any situation where no leakage is being modeled. The second choice has the hot fluid remain at constant temperature across the spacer, but an energy balance equation is written for the mixing of the cold fluid and leaking fluid streams. The second choice can only be used when a real fluid is being modeled due to the use of the enthalpy terms. The heat load on the wall from the leaking fluid is calculated for each die as described in Chap. 4. The quantity of heat conducted to and from each spacer is calculated using the axial resistance of the spacer and the wall temperatures at the end of the perforated plates.

Design Model Code 5.9.9: Energy balances on the spacer in the main body of EES code used to determine the change in fluid and wall temperatures across the die.

```
"*****************************************************************************************************************"
"!Choice 1: Energy balances on spacer with no internal leakage"
Duplicate j=1,N_sp#
    T_h_out[j]=T_h_in[j+1]        "no mixing or stream-to-stream heat transfer "
    T_c_in[j]=T_c_out[j+1]        "no mixing or stream-to-stream heat transfer "
End

"!Choice 2: Energy balance on spacers with possible internal leakage and a real fluid"
{Duplicate j=1,N_sp#
    T_h_out[j]=T_h_in[j+1]        "hot side"
    m_dot[j]*h_h_out[j]+q_dot_w_c[j]+m_dot[j+1]*h_c_out[j+1]=m_dot[j+1]*h_h_in[j+1]+&
          m_dot[j]*h_c_in[j]+q_dot_w_h[j+1]
End}

Duplicate j=1, N_die#
    h_h_in[j]=enthalpy(F$, T=T_h_in[j], P=P_h_in[j])
    h_h_out[j]=enthalpy(F$, T=T_h_out[j], P=P_h_out[j])
    h_c_in[j]=enthalpy(F$, T=T_c_in[j], P=P_c_in[j])
    h_c_out[j]=enthalpy(F$, T=T_c_out[j], P=P_c_out[j])
    q_dot_h_leak[j]=Frac_heat*m_dot_h_leak[j]*Cp_h[j]*(T_h_in[j]-T_w_h[j])
    q_dot_c_leak[j]=Frac_heat*m_dot_c_leak[j]*Cp_h[j]*(T_h_out[j]-T_w_c[j])
End

"!Heat conducted axially to and from each silicon plate"
```

```
q_dot_w_h[1]=q_dot_w_h+q_dot_h_leak[1]                    "heat conducted to HX warm end"
q_dot_w_c[1]=(T_w_c[1]-T_w_h[2])/R_sp[1]-q_dot_c_leak[1]"heat conducted from HX cold end"

Duplicate i=2, (N_die#-1)
    "heat conducted to HX warm end"
    q_dot_w_h[i]=(T_w_c[i-1]-T_w_h[i])/R_sp[i-1]+q_dot_h_leak[i]
    "heat conducted from HX cold end"
    q_dot_w_c[i]=(T_w_c[i]-T_w_h[i+1])/R_sp[i]-q_dot_c_leak[i]
End

"heat conducted to HX warm end"
q_dot_w_h[N_die#]=(T_w_c[-1+N_die#]-T_w_h[N_die#])/R_sp[-1+N_die#]+q_dot_h_leak[N_die#]
"heat conducted from HX cold end"
q_dot_w_c[N_die#]=q_dot_w_c-q_dot_c_leak[N_die#]
"*****************************************************************************************************************"
```

The final section of code in the main body of EES is presented in Design Model Code 5.9.10. This section contains the energy balance equations for each element in every die of the heat exchanger. The energy balances are discussed in detail in Chap. 4.

Design Model Code 5.9.10: Energy balances on the hot fluid, cold fluid, and wall for each element in each perforated plate.

```
"*****************************************************************************************************************"
"!Energy balance equations, highlighted portions account for die location in array"
Duplicate j=1, N_die#
Duplicate i=1, N
    "hot fluid energy balance"
    mu[j]*theta_h[j*N+2*j-N-2+i-1]+chi_h[j]*DELTAZ[i]=mu[j]*theta_h[j*N+2*j-N-2+i] &
        +NTU_h[j]*DELTAZ[i]*((theta_h[j*N+2*j-N-2+i]+theta_h[j*N+2*j-N-2+i-1])/2- &
        theta_w[j*N+2*j-N-2+i])
    "cold fluid energy balance"
    nu[j]*theta_c[j*N+2*j-N-2+i]+chi_c[j]*DELTAZ[i]+NTU_c[j]*DELTAZ[i]*(theta_w[j*N+2*j-N-2+i]&
        -(theta_c[j*N+2*j-N-2+i]+theta_c[j*N+2*j-N-2+i-1])/2)=nu[j]*theta_c[j*N+2*j-N-2+i-1]
End
End

Duplicate j=1, N_die#
    "first element wall energy balance"
    chi_w[j]*DELTAZ[1]+NTU_h[j]*DELTAZ[1]*((theta_h[j*N+2*j-N-2+0]+theta_h[j*N+2*j-N2+1]) &
         /2& - theta_w[j*N+2*j-N-2+1]) +lambda[j]/(DELTAZ[0])*(theta_w[j*N+2*j-N-2+0]- &
         theta_w[j*N+2*j-N-2+1])= NTU_c[j]*DELTAZ[1]*(theta_w[j*N+2*j-N-2+1]- &
         (theta_c[j*N+2*j-N-2+1]+theta_c[j*N+2*j-N-2+0])/2)+2*lambda[j]/(DELTAZ[1]+ &
         DELTAZ[2]) *(theta_w[j*N+2*j-N-2+1]-theta_w[j*N+2*j-N-2+2])

Duplicate i=2, (N-1)
    "wall energy balance"
    chi_w[j]*DELTAZ[i]+NTU_h[j]*DELTAZ[i]*((theta_h[j*N+2*j-N-2+i]+theta_h[j*N+2*j-N-2+i-1]) &
        /2-theta_w[j*N+2*j-N-2+i]) +2*lambda[j]/(DELTAZ[i]+DELTAZ[i-1])* &
        (theta_w[j*N+2*j-N-2+i-1]-theta_w[j*N+2*j-N-2+i])= NTU_c[j]*DELTAZ[i]* &
        (theta_w[j*N+2*j-N-2+i]-(theta_c[j*N+2*j-N-2+i]+theta_c[j*N+2*j-N-2+i-1])/2)+ &
         2*lambda[j]/(DELTAZ[i]+DELTAZ[i+1])*(theta_w[j*N+2*j-N-2+i]-theta_w[j*N+2*j-N-2+i+1])
End

    "last element wall energy balance"
    chi_w[j]*DELTAZ[N]+NTU_h[j]*DELTAZ[N]*((theta_h[j*N+2*j-N-2+N-1]+ &
```

```
        theta_h[j*N+2*j-N-2+N])/2-theta_w[j*N+2*j-N-2+N]) +2*lambda[j]/(DELTAZ[N-1] &
        +DELTAZ[N])*(theta_w[j*N+2*j-N-2+N-1]-theta_w[j*N+2*j-N-2+N])= &
        NTU_c[j]*DELTAZ[N]*(theta_w[j*N+2*j-N-2+N]-(theta_c[j*N+2*j-N-2+N]+ &
        theta_c[j*N+2*j-N-2+N-1])/2)+ lambda[j]/(DELTAZ[N+1])*(theta_w[j*N+2*j-N-2+N] &
        -theta_w[j*N+2*j-N-2+N+1])
End
"*****************************************************************************************************************"
```

5.10 Components External to Heat Exchanger

There are two procedures used for modeling components external to the heat exchanger. The first procedure is 'WarmEnd' (Design Model Code 5.10.1) which estimates the pressure drop between the pressure taps and the heat exchanger at the warm end of the heat exchanger. The fluid flows through smooth circular tubes with several bends. The total pressure drop is calculated using the procedure 'PipeFlow' which is included with EES.

Design Model Code 5.10.1: The procedure 'WarmEnd' which is used to calculate the pressure drop between the pressure taps and the warm end of the heat exchanger.

```
"*****************************************************************************************************************"
Procedure WarmEnd(m_dot, T_h_in, P_h_in, T_c_out, P_c_out: DELTAP_assy)

$Common F$

    ID_in=0.06 [in]*convert(in,m)          "ID of 1/8 in. tube"
    L_in=10 [in]*convert(in,m)             "Length of tube"
    L_in_elbow=4*60*ID_in                  "equivalent length of four 90 deg bends"
    L_e_in=L_in+L_in_elbow                 "total equivalent length"
    RelRough=0                             "relative roughness of smooth tube"
    call PipeFlow(F$,T_h_in,P_h_in,m_dot,ID_in, L_e_in, RelRough:h_T, h_H ,DELTAP_in, &
         Nusselt_T, f, Re_in)
    P_h_in_meas=P_h_in+DELTAP_in  "measured inlet pressure"


    ID_out=0.06 [in]*convert(in,m)         "ID of 1/8 in. tube"
    L_out=10 [in]*convert(in,m)            "Length of tube"
    L_out_elbow=4*60*ID_out                "equivalent length of four 90 deg bends"
    L_e_out=L_out+L_out_elbow              "total equivalent length"
    RelRough=0                             "relative roughness of smooth tube"
    call PipeFlow(F$,T_c_out,P_c_out,m_dot,ID_out, L_e_out, RelRough:h_T, h_H &
         ,DELTAP_out, Nusselt_T, f, Re_out)
    P_c_out_meas=P_c_out-DELTAP_out        "measured inlet pressure"

    DELTAP_assy=P_h_in_meas-P_c_out_meas          "total pressure drop in assembly"

End {WarmEnd}
"*****************************************************************************************************************"
```

The second procedure 'ColdEnd' (Design Model Code 5.10.2) is used for modeling the heat exchanger in a J-T cycle. The procedure 'ColdEnd' assumes that the hot fluid travels through a length of tubing to a valve or orifice, undergoes an isenthalpic expansion, absorbs a heat load, and travels through another length of tubing to return to the cold inlet of the heat exchanger. As previously mentioned for Design Model Code 5.9.2, the model must be iterated several times in

cryocooler mode until the cold inlet temperature $T_{c,in}$ closely matches the predicted heater outlet temperature $T_{htr,out}$.

The pressure drop in the headers and tubing is calculated using the procedure 'PipeFlow'. The radiation heat load on the tubing is calculated using the same equations described in Chap. 5.8 for calculating the radiation heat load on the heat exchanger. The pressure drop across the valve or orifice must be specified or code should be written to model the flow across the valve or orifice. The correlations supplied by the jewel orifice manufacturer predict significantly different pressure drops than those that were experimentally measured, so the orifice pressure drops will not be covered.

After undergoing an isenthalpic expansion, the fluid is assumed to pass through a heater. The heater can be an actual heater or it can simulate a refrigeration load if the J-T cycle is being used to cool an object. The radiation heat load on the tubing between the orifice/valve and the heat exchanger is assumed to be identical for both the inlet and outlet sides. The pressure drop between the orifice/valve outlet and the heat exchanger is calculated using 'PipeFlow'.

Design Model Code 5.10.2: The procedure 'ColdEnd' which is used for modeling the heat exchanger in a J-T cycle.

```
"*****************************************************************************************************************"
Procedure ColdEnd(T_h_out, P_h_out, m_dot:T_htr_out,DELTAP_cold_end)

$Common N_fluid, F$, Mode$, T_c_in, T_h_in, D_orifice, Q_dot_htr

"!Calculate orifice/valve inlet pressure"
    ID_tube=0.06 [in]*convert(in,m)        "ID of 1/8 in. tube"
    L_tube=2 [in]*convert(in,m)            "Length of tube"
    L_e_header=2*60*ID_tube                "equivalent length of two 90 deg turns in header"
    L_e_tube=L_tube+L_e_header             "total equivalent length"
    RelRough=0                             "relative roughness of smooth tube"
    call PipeFlow(F$,T_h_out,P_h_out,m_dot,ID_tube,L_e_tube, RelRough:h_T, h_H &
        ,DELTAP_tube, Nusselt_T, f, Re_tube)
    P_orif_in=P_h_out-DELTAP_tube          "orifice inlet pressure"

"!Calculate orifice/valve inlet temperature"
    Call TempPress(N_fluid, F$, T_h_out, P_h_out: k_h_out, mu_h_out, Cp_h_out, &
        Pr_h_out, rho_h_out)
    SA_tee=(Pi*(0.5 [in])*(1[in]))*2*convert(in^2,m^2)      "estimate of VCR tee joint surface area"
    e_tee=0.34                             "Barron, 304 SS emissivity"
    e_dewar=0.025                          "emissivity of MLI on dewar innner surface"
    e_MLI=0.025                            "emissivity of MLI"
    N_MLI=10                               "number of layers of MLI"
   "emissivity factor"
    F_e=1/((1/e_tee+1/e_MLI-1)+(N_MLI-1)*(2/e_MLI-1)+(1/E_MLI+1/E_dewar-1))
    F_viewfactor=1                 "view factor between surfaces"
   "parasitic  heat load from radiation"
    Q_dot_h=F_e*F_viewfactor*sigma#*SA_tee*(T_h_in^4-T_h_out^4)
    T_orif_in=T_h_out+ Q_dot_h/(m_dot*Cp_h_out)       "orifice inlet temperature"

"!Pressure and temperature drop across orifice"
    Call TempPressforEnth(N_fluid, F$, T_orif_in, P_orif_in: h_orif_in)
    DELTAP_orif=0 [kPa]                                        "constant"
    P_orif_out=P_orif_in-DELTAP_orif                           "orifice outlet pressure"
    Call EnthPressforTemp(N_fluid, F$, h_orif_in, P_orif_out: T_orif_out) "isenthalpic pressure drop"
```

```
"!Temperature gain across heater"
    Call TempPress(N_fluid, F$, T_orif_out, P_orif_out: k_orif_out, mu_orif_out, Cp_orif_out,
Pr_orif_out, rho_orif_out)
    T_htr_out=T_orif_out+(Q_dot_htr+Q_dot_h)/(Cp_orif_out*m_dot)

"!Pressure drop in tubing after orifice"
    ID_htr=0.06 [in]*convert(in,m)          "ID of 1/8 in. tube"
    L_htr=16 [in]*convert(in,m)             "Length of tube"
    L_e_htr=L_htr+L_e_header                "flow passes throught two 90 deg turns in header"
    RelRough2=0                             "relative roughness of smooth tube"
    call PipeFlow(F$,T_htr_out,P_orif_out,m_dot,ID_htr,L_e_htr, RelRough2:h_T, h_H ,DELTAP_htr,
Nusselt_T, f, Re_htr)
    P_htr_out=P_orif_out-DELTAP_htr   "orifice inlet pressure"

    DELTAP_cold_end=P_h_out-P_htr_out        "total pressure drop in cold end assembly"

End {ColdEnd}
"*****************************************************************************************************************"
```

Chapter 6: Comparison of Experimental Results with a Numerical Model

6.0 Introduction

This chapter presents the experimental results and where applicable compares the experimental data to the numerical model. The chapter begins by describing the integrated PRT calibration process and plotting the experimental results. The next two sections of the chapter show the experimental results for the pressure drop testing of the MEMS heat exchangers and micro-valve. Included in the pressure drop testing are experimental results which show the size of the internal leaks relative to the total flow rate through the heat exchanger. The next section shows the applied cooling results and compares the experimentally measured effectiveness and temperature distribution to the numerical model predictions. The last two sections of the chapter show the experimental results of testing the heat exchangers in J-T cycle in both the cryogenic test facility and in the prototype cryosurgical probe.

6.1 Integrated PRT Calibration

Two heat exchanger dies (one 10 mm and one 20 mm) with integrated PRTs were placed on top of the cryocooler heat exchanger adapter plate for calibration, as shown in Fig. 6.1.1. All of the experimental data associated with calibration of the individual dies is tabulated in Appendix E. A layer of thermal grease was used to reduce the contact resistance between the dies and the adapter plate. The heat exchanger assembly was disconnected from the adapter plate for these tests in order to reduce the thermal mass and heat loads on the cryocooler. Each die had one working PRT and the resistance of the PRT was measured by 4-wire leads that extend to the data acquisition system via a vacuum electrical feedthrough.

Two methods were used for measuring the temperature of the cryocooler adapter plate. The primary method was the thermocouple held down by cryocooler heat exchanger bolts. This is the primary method because the thermocouple is physically closest to the dies and is also mounted to the surface in a similar fashion as the dies. The secondary method is an uncalibrated commercial PRT that is inserted into a hole between the cryocooler adapter plate and the cryocooler heat exchanger with thermal grease.

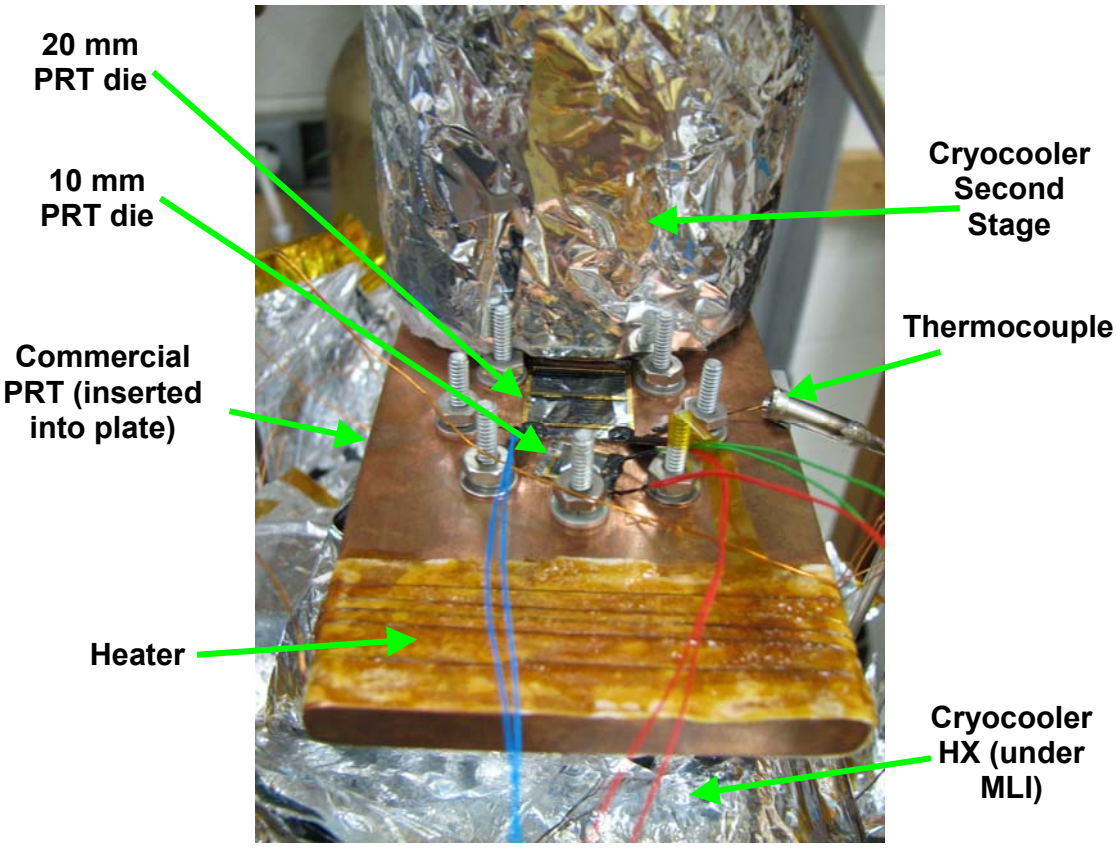

Fig. 6.1.1: Photograph of the setup used for calibrating individual dies with integrated PRTs. A commercial PRT was inserted into a small hole between the adapter plate and the cryocooler heat exchanger to measure the adapter plate temperature. A thermocouple was used to measure the temperature of the adapter plate closer to where the PRT dies were being calibrated.

The difference between the two measured temperatures was less than 1 K for the entire calibration process, as shown in Fig. 6.1.2. The cryocooler was allowed to cool at full power without activating the heater. For calibration purposes it is desirable to have the cryocooler adapter plate as isothermal as possible so that the die temperature matches the measured temperature. The heater leads to temperature gradients and was not used because of the error that it would introduce. The entire cryocooler assembly was wrapped with 5 to 10 layers of MLI depending on the location.

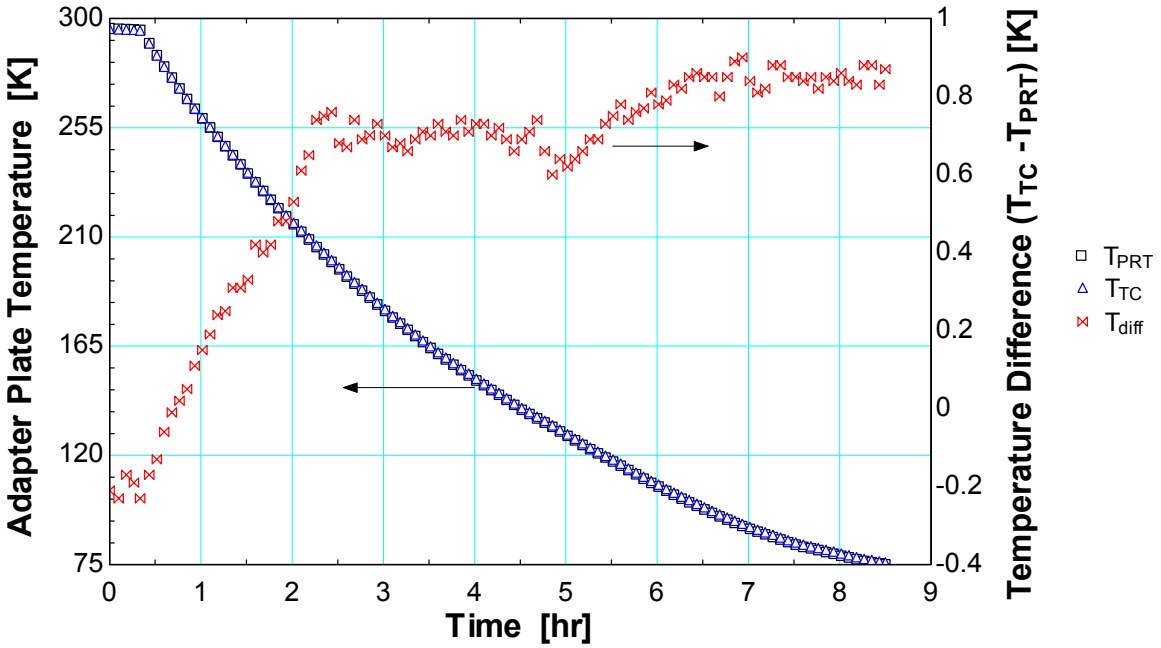

Fig. 6.1.2: Plot of the adapter plate temperature as function of time during calibration of individual dies with integrated PRTs. Two temperature measurements were made of the adapter plate using a PRT at the top of the cryocooler heat exchanger and a type E thermocouple at the top of the plate next to the dies. The maximum temperature difference between the dies was less than 1 K.

The resistance of both die PRTs as function of both the thermocouple and cryocooler PRT temperatures are plotted in Fig. 6.1.3. Since the temperature measurements agreed so closely, they produce nearly identical calibration curves. The resistance of the 20 mm die PRT at room temperature was nearly 7 times that of the 10 mm die PRT resistance, so it is difficult to compare the sensitivities of the two PRTs from Fig. 6.1.3.

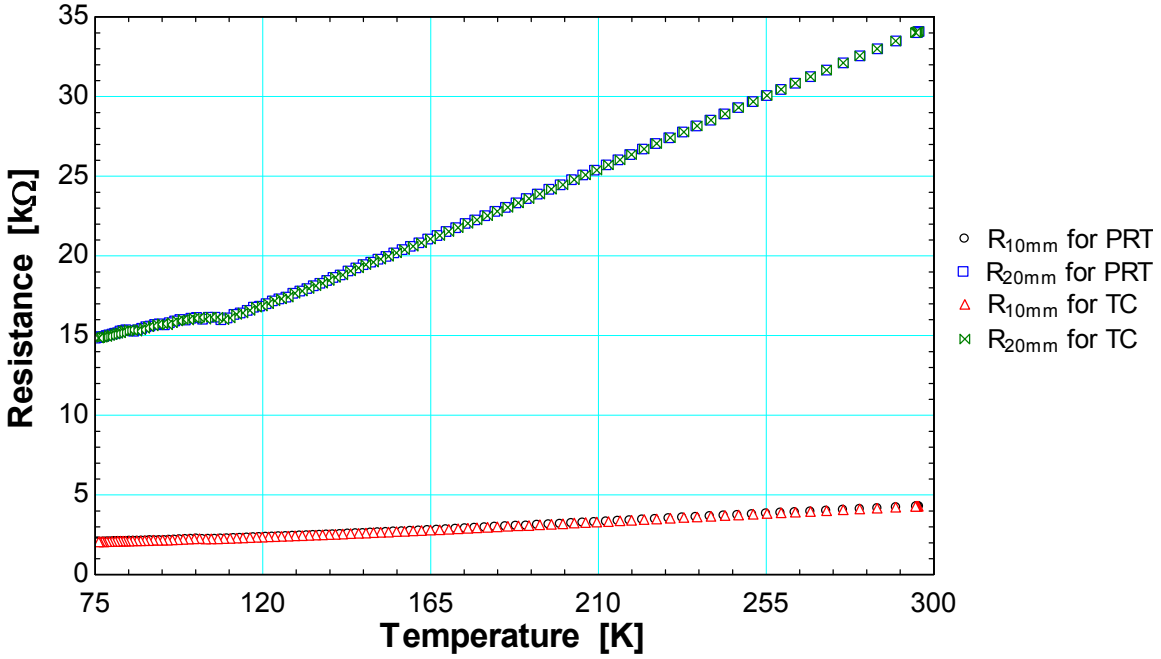

Fig. 6.1.3: PRT resistance as a function of temperature. Nearly identical results were obtained using the thermocouple or the PRT as the temperature standard.

The normalized resistance, which is defined as the resistance of the PRT divided by it's resistance at room temperature, is plotted in Fig. 6.1.4. The normalized resistance is a dimensionless quantity that allows the temperature sensitivity of the two resistors to be compared. The temperature sensitivity is the slope of the two lines shown in Fig. 6.1.4, and is defined as the ratio of the change in normalized resistance to the change in temperature.

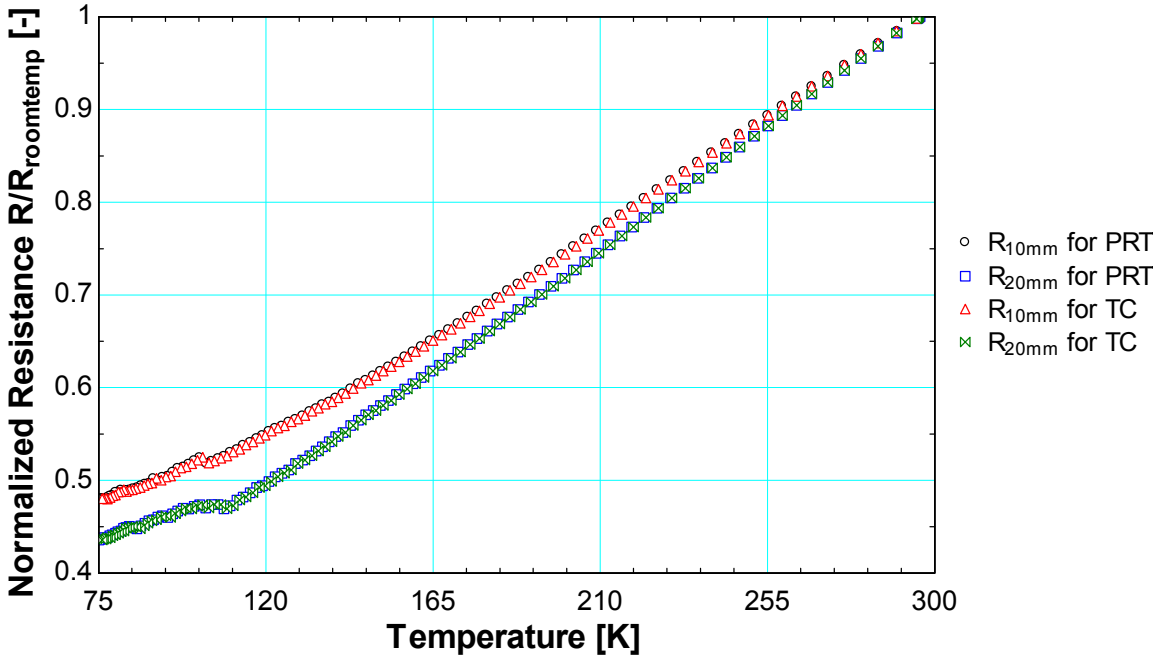

Fig. 6.1.4: Normalized resistance of integrated PRTs as a function of adapter plate temperature. The normalized resistance is defined as the resistance divided by the resistance at room temperature. The PRTs exhibit non-linear behavior below 150 K.

The normalized resistance becomes non-linear below 150 K and has an abrupt change in slope near 100 K. Just below 75 K, the resistors became open circuits. However, they started functioning again when they were warmed back up to 75 K. The cause of the open circuiting is unclear, but is unimportant for cryosurgical applications. Commercial cryosurgical probes operate with cold end temperatures down to 150 K, which happens to coincide with the linear region of the die PRTs. The two PRT resistance versus temperature curves are shown in their linear region with curve fits in Fig. 6.1.5. The 20 mm PRT is slightly more sensitive than the 10 mm PRT, with sensitivities of 0.293%/K and 0.268%/K respectively.

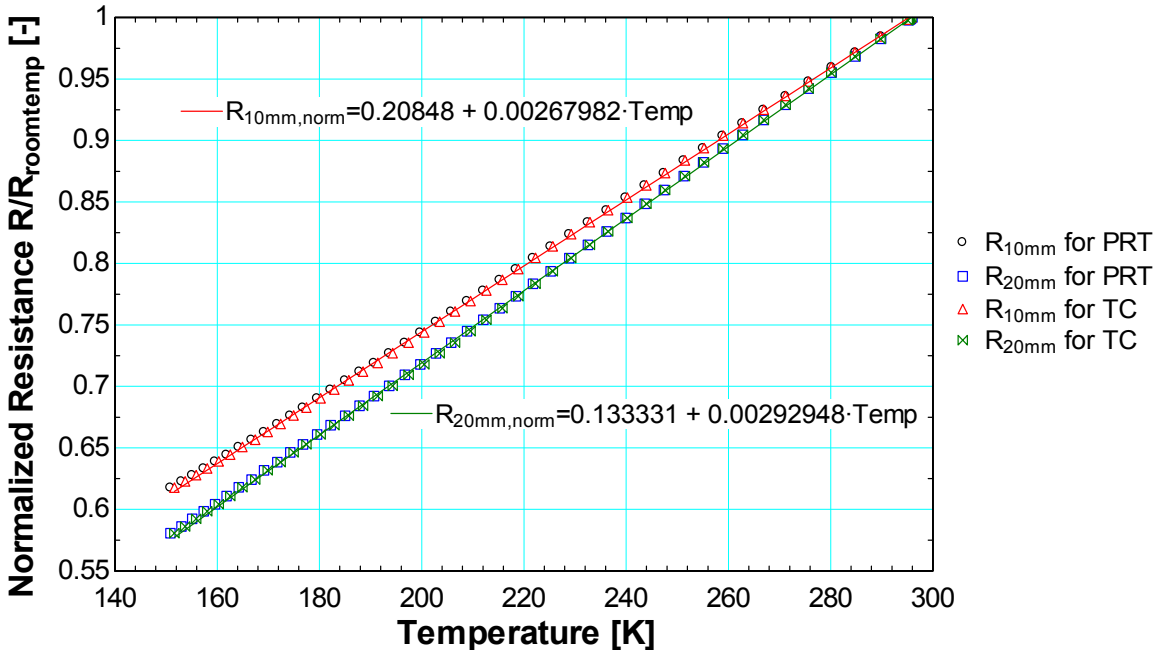

Fig. 6.1.5: Normalized resistance of integrated PRTs as a function of adapter plate temperature above 150 K. Linear curve fits were obtained using the curve fitting tools in EES.

In order to calibrate the PRTs that are integrated into the heat exchanger dies, the heat exchanger was installed into the cryogenic test facility in its typical location. However, for this experiment a bypass tube was used so that the warm incoming gas does not pass through the heat exchanger but rather goes directly to the cryocooler heat exchanger. The working fluid is cooled by the cryocooler and then flows into the low pressure side of the heat exchanger. Since no heat is exchanged in the heat exchanger, the heat exchanger should be nearly isothermal and equal to the temperature of the cryocooler. Heat leaks due to heat conduction and radiation from the environment prevent the heat exchanger from being perfectly isothermal. Heat leaks to the heat exchanger caused a temperature rise of as much as 1.5 K between the low pressure inlet and the low pressure outlet. The exact temperature distribution within the heat exchanger would be difficult to calculate and experimentally verify. For calibration purposes, the simplifying assumption was made that the axial temperature distribution was linear. The temperature at of any die (T_{die}) could then be calculated by Eq. 6.1.1:

$$T_{die} = T_{lp,out} - \frac{N_{die}}{N_{die,hx}}\left(T_{lp,out} - T_{lp,in}\right) \tag{6.1.1}$$

where $T_{lp,in}$ and $T_{lp,out}$ are the heat exchanger inlet and outlet temperatures, N_{die} is the number of dies the PRT is from the hot end of the heat exchanger, and $N_{die,hx}$ is the number of dies in the heat exchanger.

The resistance of all of the die PRTs as a function of the estimated temperature (from Eq. 6.1.1) is shown in Fig. 6.1.6. The number of experimentally measured variables exceeded the number of channels available on the mulitiplexer. Therefore each steady state point required two sets of

measurements so that all the PRT resistances could be measured. The heat exchanger was thermally cycled several times between 200 K and 300 K in order to test whether the resistance of the PRTs changed over time. No change in resistance was measurable after thermal cycling. All of the experimental data is shown in Tables F.1 through F.4 and the calibration results are shown in Tables F. 5 and F.6 in Appendix F.

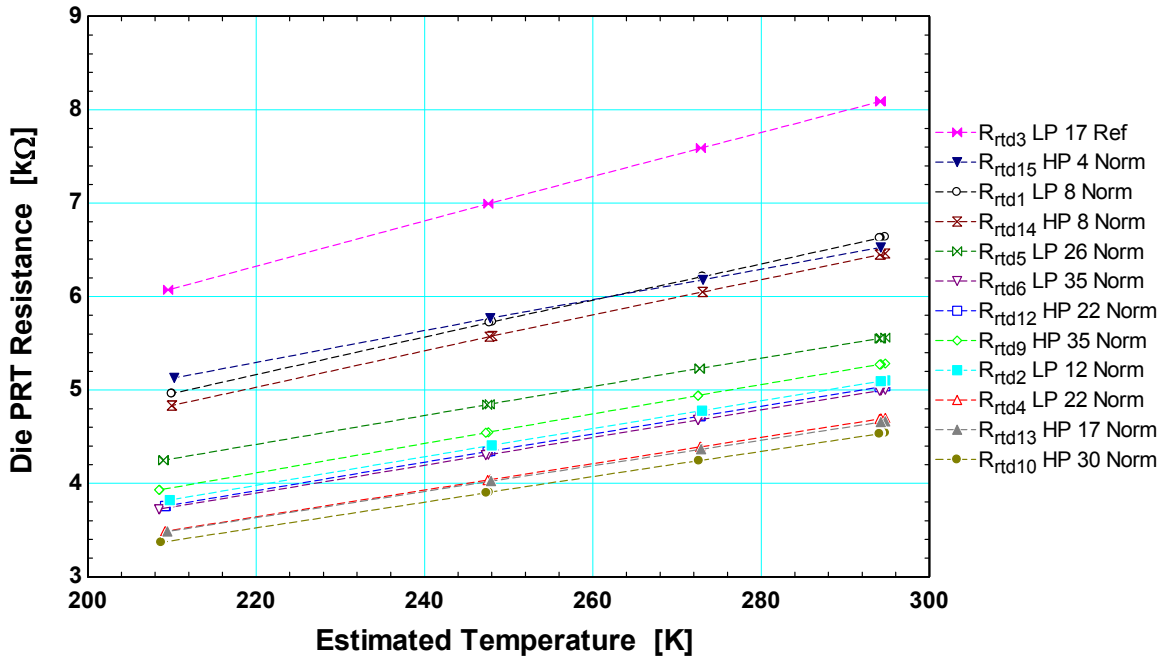

Fig. 6.1.6: Resistance of the PRTs integrated into the heat exchanger dies as function of temperature for the forty-three die 10 mm heat exchanger. The estimated temperature was calculated using Eq. 6.1.1. The legend shows which side of the heat exchanger the PRT is on, the number of dies the PRT is from the hot end of the heat exchanger, and whether it is the normal or reference type resistor.

As shown in Fig. 6.1.6, there is a wide range of resistances for all the PRTs. To see if the dies have the same sensitivity, Fig. 6.1.6 was re-plotted using the normalized resistance in Fig. 6.1.7. The normalized resistance is the resistance of a die divided by it's resistance at room temperature. All of the PRTs, with exception of PRT 15 and PRT 5, have nearly identical sensitivities. The reason why those two PRTs have different sensitivities than the other PRTs is unknown.

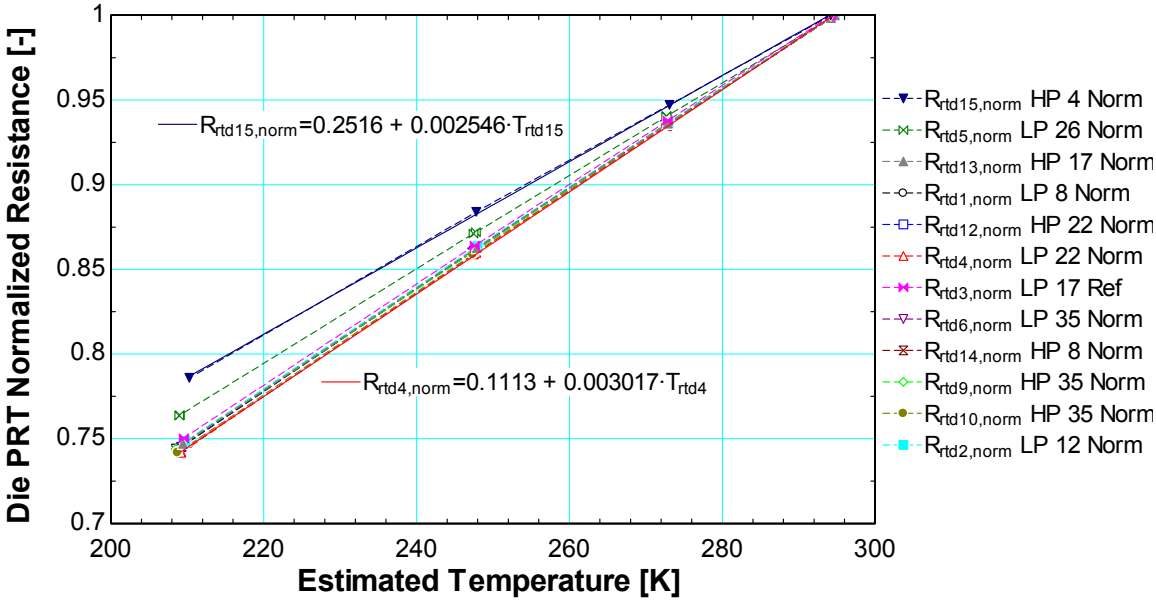

Fig. 6.1.7: Normalized resistance (PRT resistance/PRT resistance at room temperature) as a function of temperature for the forty-three die 10 mm heat exchanger. The estimated temperature was calculated using Eq. 6.1.1. The legend shows which side of the heat exchanger the PRT is on, the number of dies the PRT is from the hot end of the heat exchanger, and whether it is the normal or reference type resistor.

The measured heat leak (calculated based on the enthalpy rise of the fluid) as a function of LP inlet temperature is plotted in Fig. 6.1.8. The first data point at 295 K was obtained with both the heater and cryocooler off. The second data point at 270 K utilized a flow rate of 0.08 g/s of helium and a heater power of roughly 30 W. The third set of data points at 250 K used a flow rate of 0.08 g/s but a significantly reduced heat power. The final set of data points at 210 K used a flow rate of 0.03 g/s and no heater power. The data plotted in Fig. 6.1.8 show that the heater could have been better insulated since colder heat exchanger temperatures with smaller heater power have less heat leak than warmer heat exchanger temperatures with higher heater power.

Figure 6.1.8 suggests that a significant amount of the heat leak occurs outside the heat exchanger. The thermocouples, which are closer to the heat exchanger than the PRTs, show a smaller temperature rise across the heat exchanger. This suggests that some of the heat is picked up between the thermocouples and commercial PRTs. Later heat exchanger tests used more layers of MLI to try to reduce the heat leak further, but the calibration tests provide a rough estimate of the magnitude of the parasitic heat loads on the heat exchanger during testing.

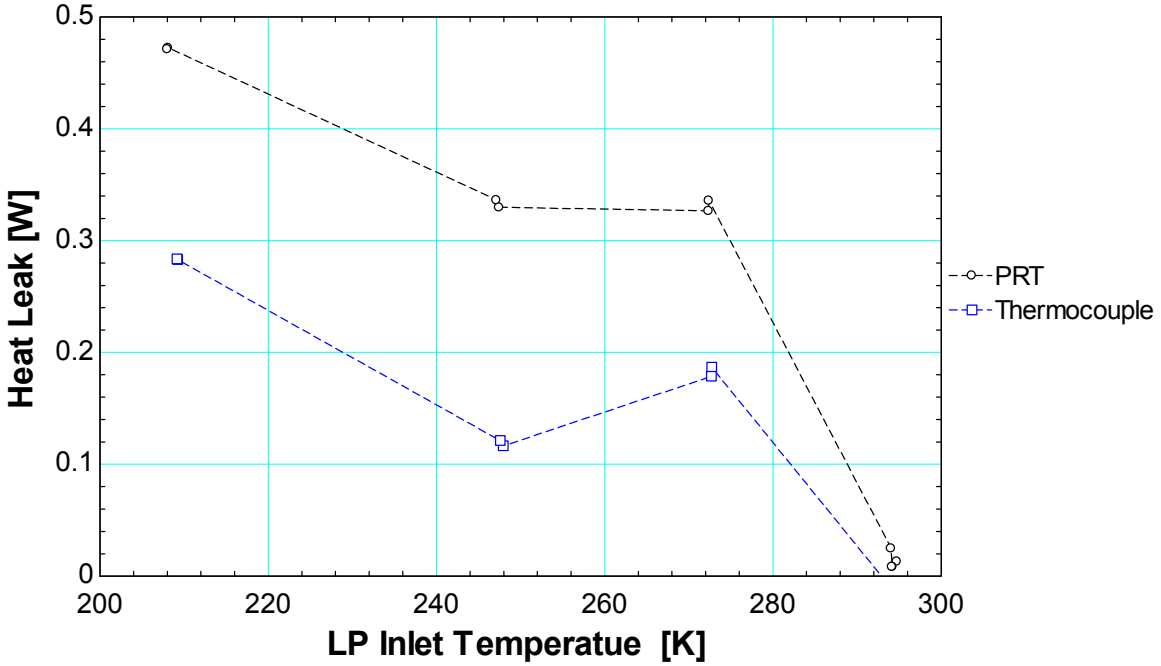

Fig. 6.1.8: Parasitic heat loads on the heat exchanger during calibration tests of the forty-three die 10 mm heat exchanger.

The calibration process for the PRTs in the thirty-seven die 20 mm heat exchanger is identical to that of the forty-three die 10 mm heat exchanger. The only difference is that there were fewer working PRTs, so there was an adequate number of multiplexer channels to measure all of the PRTs simultaneously. A linear axial temperature distribution across the heat exchanger was also assumed for the thirty-seven die 20 mm heat exchanger.

The resistance of each PRT that has been integrated into the thirty-seven die 20 mm heat exchanger is shown in Fig. 6.1.9. Similar to the forty-three die 10 mm heat exchanger, the thirty-seven die 20 mm heat exchanger also shows a significant variation in the PRT resistances. The reference location resistors all have higher resistances than the normal location resistors. The experimental data are shown in Tables G.1 and G.2 and the calibration results are shown in Tables G.3 to G.5 in Appendix G.

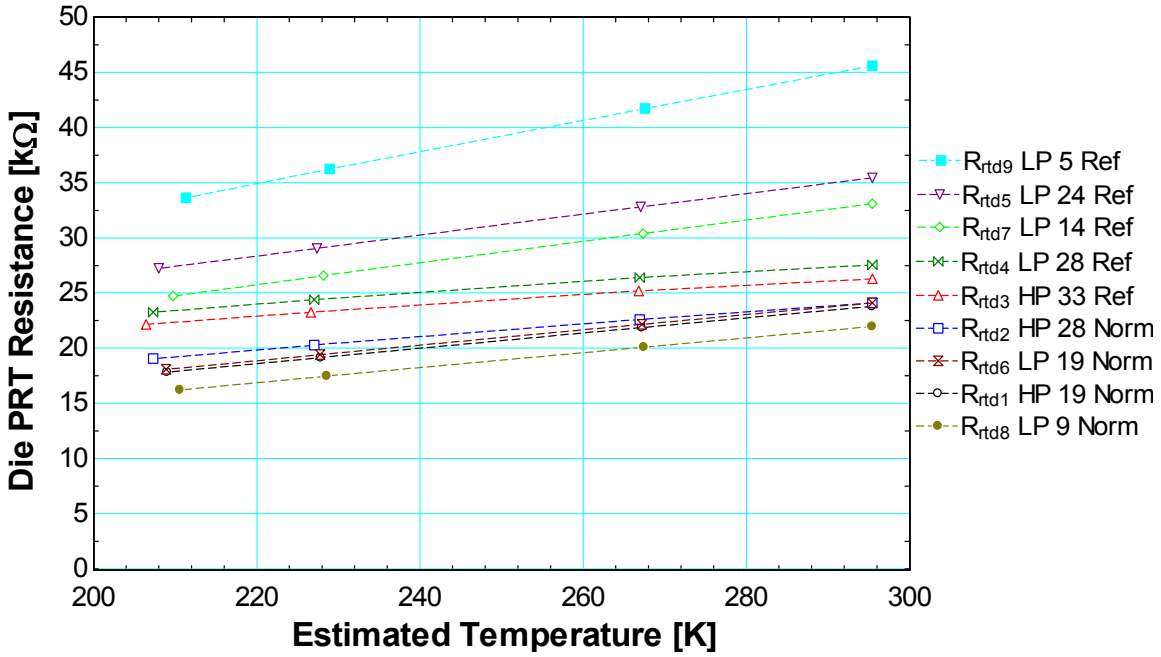

Fig. 6.1.9: Resistance of the PRTs integrated into the heat exchanger dies as function of temperature for the thirty-seven die 20 mm heat exchanger. The estimated temperature was calculated using Eq. 6.1.1. The legend shows which side of the heat exchanger the PRT is on, the number of dies the PRT is from the hot end of the heat exchanger, and whether it is the normal or reference type resistor.

The data presented in Fig. 6.1.9 were re-plotted as the normalized resistance instead of the absolute resistance to show the sensitivity of each PRT in Fig. 6.1.10. The normalized resistance is the ratio of the PRT resistance to the PRT resistance at room temperature. The sensitivity variance among the 20 mm PRTs was much greater (0.18%/K to 0.31%/K) than the 10 mm PRTs (0.25%/K to 0.30%/K). PRT 3 and PRT 4 have the lowest sensitivities and also exhibit the least linear behavior. The absolute resistance of the integrated PRTs is expected to vary due to the inconsistency of the etching process. However, the wires are all made from the same batch of platinum and should have the same resistivity and thus the same sensitivity to temperature. One possibility is that the platinum was contaminated with other materials during the manufacturing process. The reason for the differing senstivities was not examined further since the temperature dependent resistance did not change with time or thermal cycling. Since each PRT was individually calibrated it did not matter if the sensitivity varied among the PRTs.

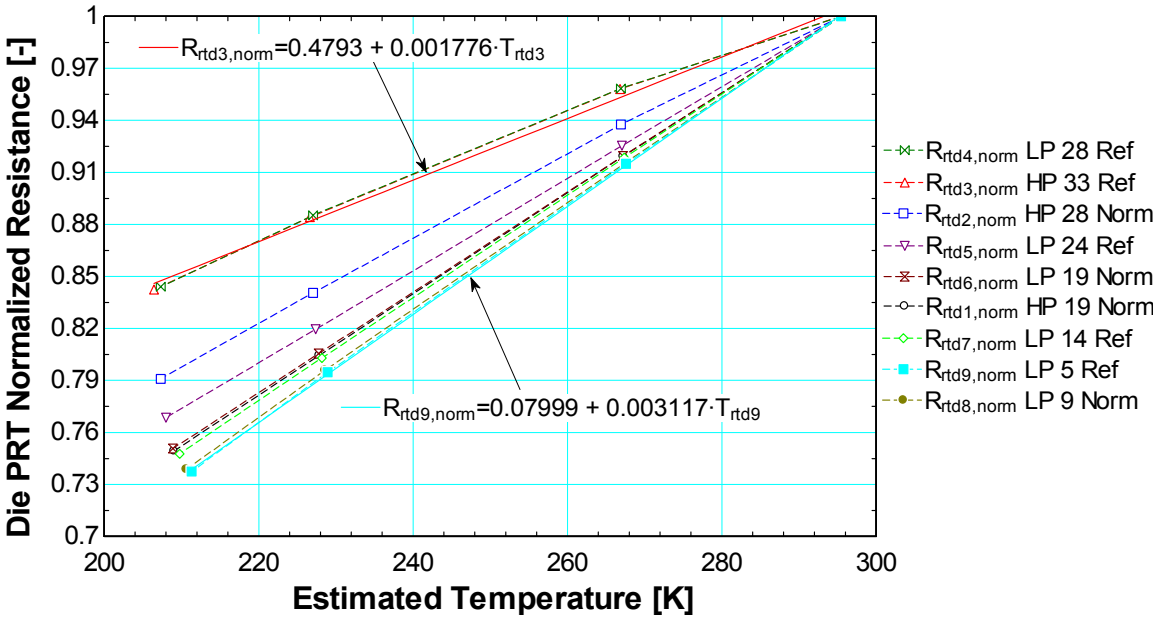

Fig. 6.1.10: Normalized resistance (PRT resistance/PRT resistance at room temperature) as a function of temperature for the thirty-seven die 20 mm heat exchanger. The estimated temperature was calculated using Eq. 6.1.1. The legend shows which side of the heat exchanger the PRT is on, the number of dies the PRT is from the hot end of the heat exchanger, and whether it is the normal or reference type resistor.

The heat leak to the 20 mm heat exchanger was approximately 20% higher than the 10 mm heat exchanger, as shown in Fig. 6.1.11. The 20 mm heat exchanger was calibrated before the 10 mm heat exchanger and was not as well insulated. Also, similar to the 10 mm heat exchanger, the 20 mm heat exchanger had a smaller temperature rise between the thermocouple measurements than between the commercial PRT measurements. Therefore, a significant part of the heat leak likely occurred outside the heat exchanger between the thermocouple and PRT temperature measurement locations. The temperature rise across the heat exchanger for the 20mm heat exchanger was much larger than the 10 mm heat exchanger (up to 7 K vs 2 K, respectively).

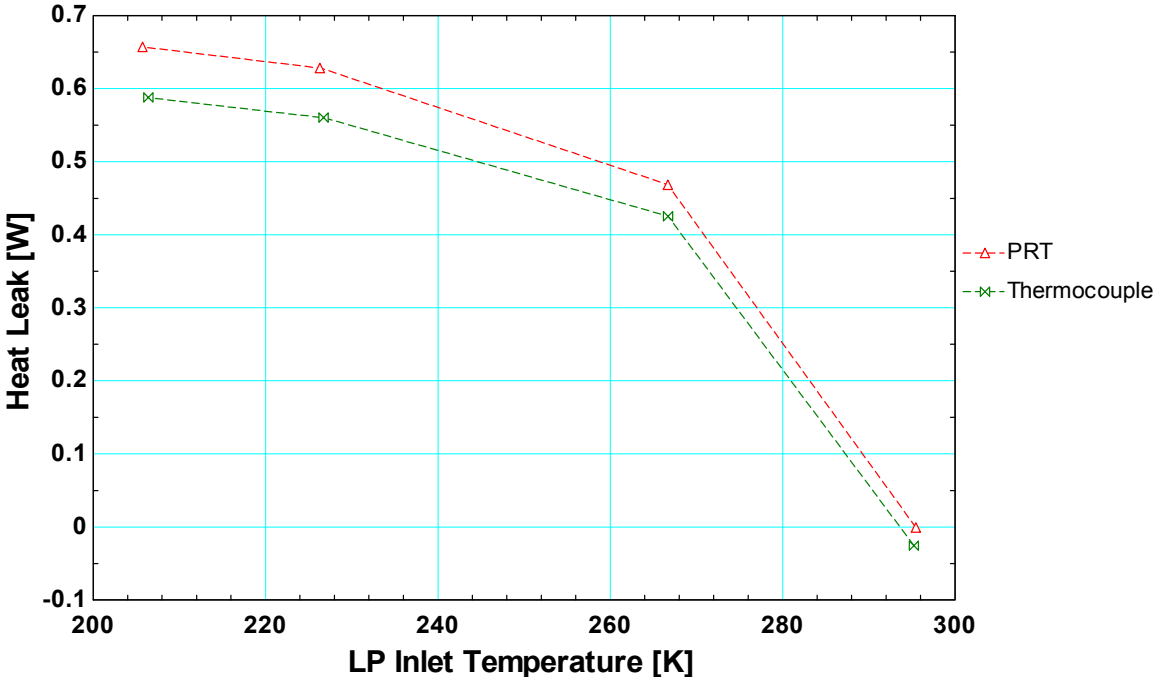

Fig. 6.1.10: Parasitic heat loads on the heat exchanger during calibration tests of the thirty-seven die 20 mm heat exchanger.

6.2 Pressure Drop Test Results for the Micro-Valve

The experimental setup used for testing the pressure drop characteristics of the micro-valve and the two heat exchangers with integrated PRTs is shown in Fig. 6.2.1. The valve was tested independently of the heat exchangers in order to determine the range of flow modulation available. If the range of possible flow rates is too small, then the valve will be too small to use in an optimal J-T cycle. However, if the flow rate can be modulated at or near the optimal flow rate then the valve becomes an attractive option for use in a J-T cycle, as discussed in Chap. 3.

The experimental setup shown in Fig. 6.2.1 is an altered form of the cryosurgical probe setup. The cryosurgical probe prototype has been removed from its stand to make room for testing the valve and heat exchangers. The inlet and outlet ports for the cryosurgical probe have been converted to the inlet and outlet ports for the micro-valve. All of the instrumentation is the same except for the addition of 0-100 VDC power supply for applying voltage to the valve. All of the experimental measurements are shown in Table H.1 and all of the results calculated from the experimental data are shown in Table H.2 in Appendix H.

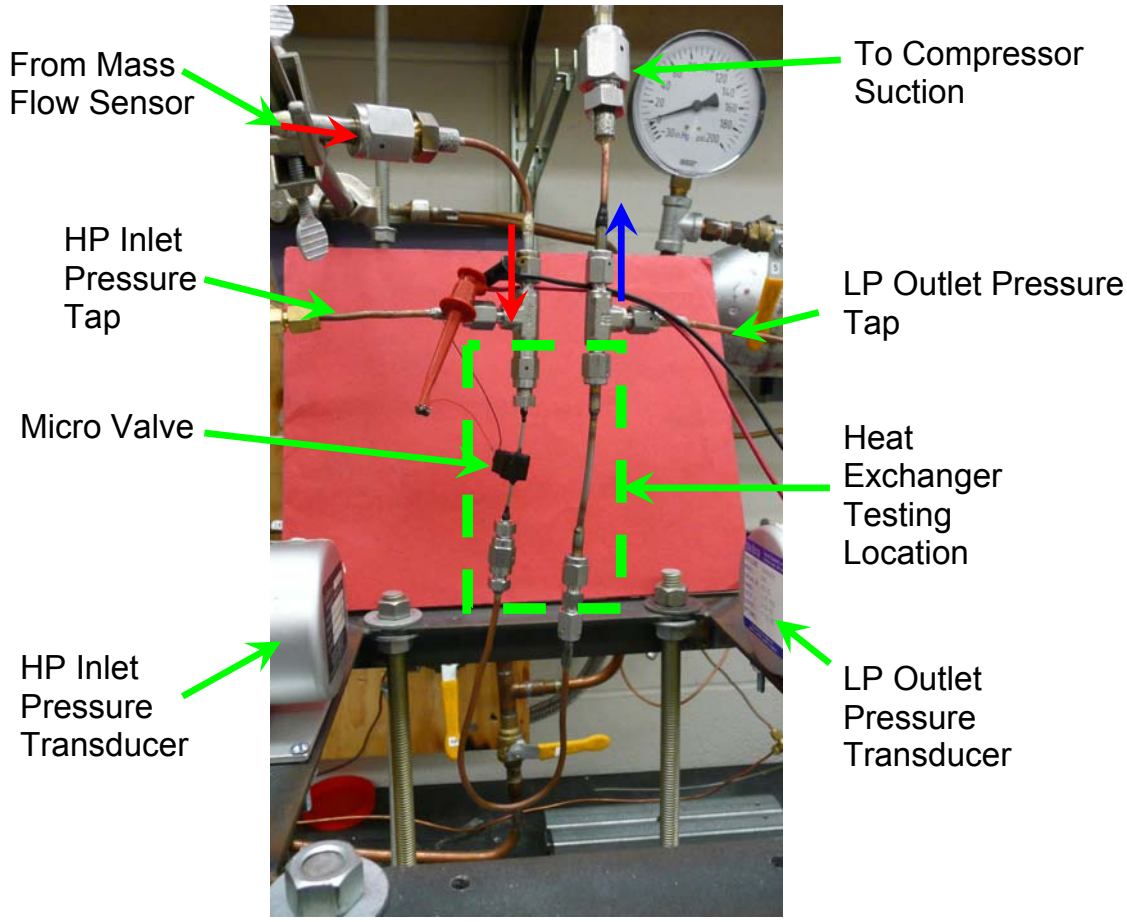

Fig. 6.2.1: Experimental setup used to test pressure drop behavior of the micro-valve, thirty-seven die 20 mm heat exchanger, and the forty-three die 10 mm heat exchanger. The cryosurgical probe was removed from the probe stand to make room for testing the valve and heat exchangers.

A plot of the mass flow rate of ethane as a function of valve voltage for various pressure differences is presented in Fig. 6.2.2. The outlet pressure was held nearly constant (between 100 kPa and 105 kPa) for all the data points shown in Fig. 6.2.2. The micro-valve is capable of reducing the flow rate when actuated by an applied voltage, but the valve is not capable of fully shutting off the flow. From the fully open position (-30 V) the valve can decrease the mass flow rate by 25% to 50% (depending on pressure) by moving to the fully closed position (100 V). The valve design would have to be modified to be normally closed when no voltage is applied if the application required a complete shutoff of fluid flow.

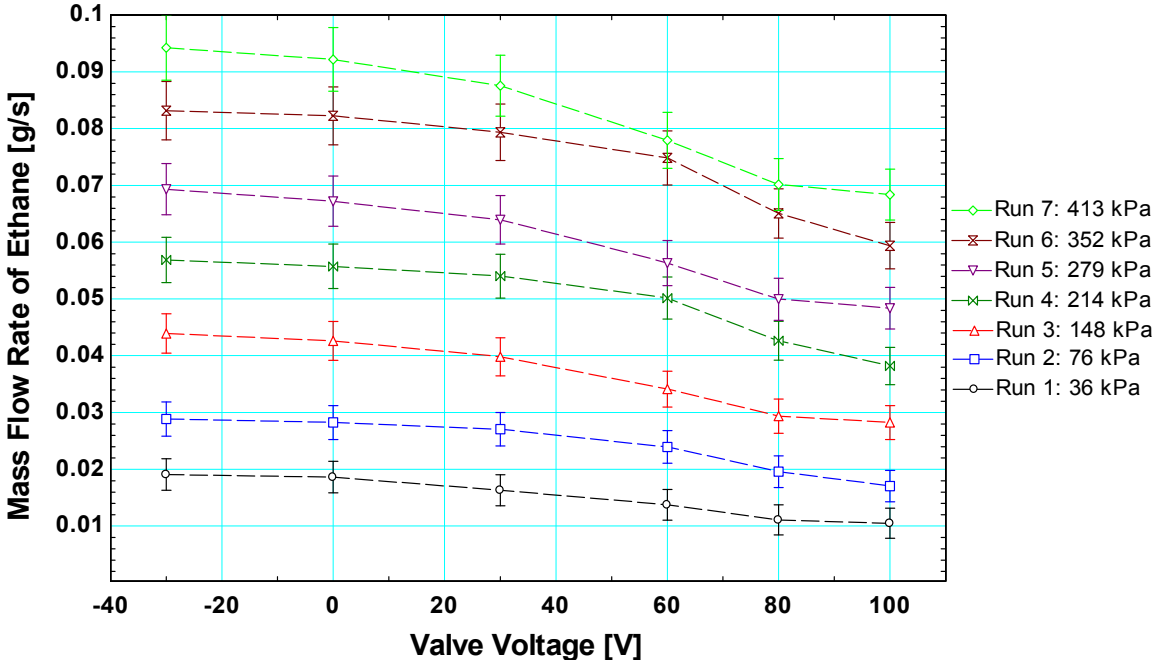

Fig. 6.2.2: Mass flow rate of ethane as a function of valve voltage for the various pressure differences shown in the legend. The valve outlet pressure ranged from 100 kPa to 105 kPa.

Visual inspection of Fig. 6.2.2 shows that there appear to be two distinct curve shapes present. One of the curves has a sharp drop off in mass flow rate at higher voltages and the other has a more gradual drop off in mass flow rate at higher voltages. These distinct curve shapes appeared to be influenced by whether the valve started in the fully open or fully closed position. Figure 6.2.3 shows how the two different curves shapes are formed. The valve started in the fully open position (-30 V) and was moved to the fully closed position (100 V), then was moved back to the fully open position. The fully open and fully closed positions appear to be unaffected by hysteresis, but the intermediate behavior depends on the applied voltage and whether the voltage is increasing or decreasing. The cause of this valve behavior is unknown but likely related to the elastic hysteresis in the PZT actuator.

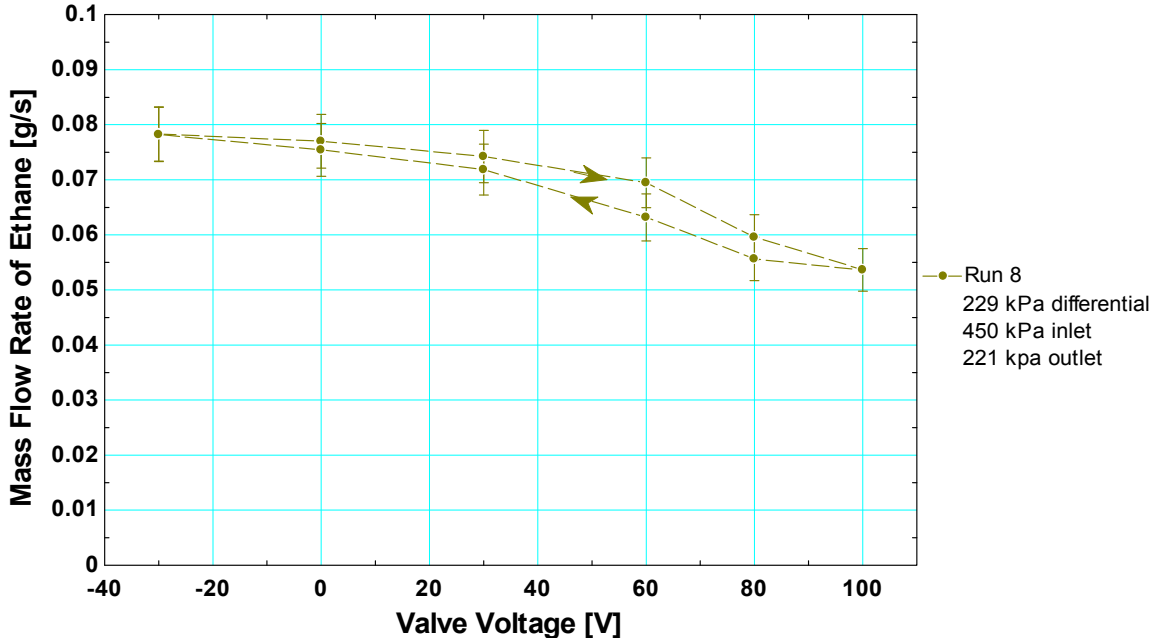

Fig. 6.2.3: Plot of mass flow rate versus valve voltage while inlet and outlet pressures are held constant. The valve began in the fully open position (-30 V). The applied voltage to the valve was increased to 100 V, which is the fully closed position. The valve voltage was then decreased to -30 V. The fully open and fully closed positions appear to be constant, but intermediate positions depend on the applied voltage and on whether the voltage is increasing or decreasing.

As the differential pressure across the valve increases, the mass flow rate also increases if a constant voltage is applied to the valve. This behavior is shown in Fig. 6.2.2. The valve outlet pressure is also important, as shown by the plot in Fig. 6.2.4. Run 8 has a smaller differential pressure than Run 5, but yet Run 8 has a higher flow rate than Run 5 due to the higher outlet pressure. This difference may be an important consideration when optimizing a J-T cycle. Increasing the valve outlet pressure increases the density of the working gas, which reduces the fluid velocity and this in turn reduces frictional pressure drop. Depending on the application, it may be beneficial to operate with higher outlet pressures in order to increase the mass flow rate if the pressure difference is fixed.

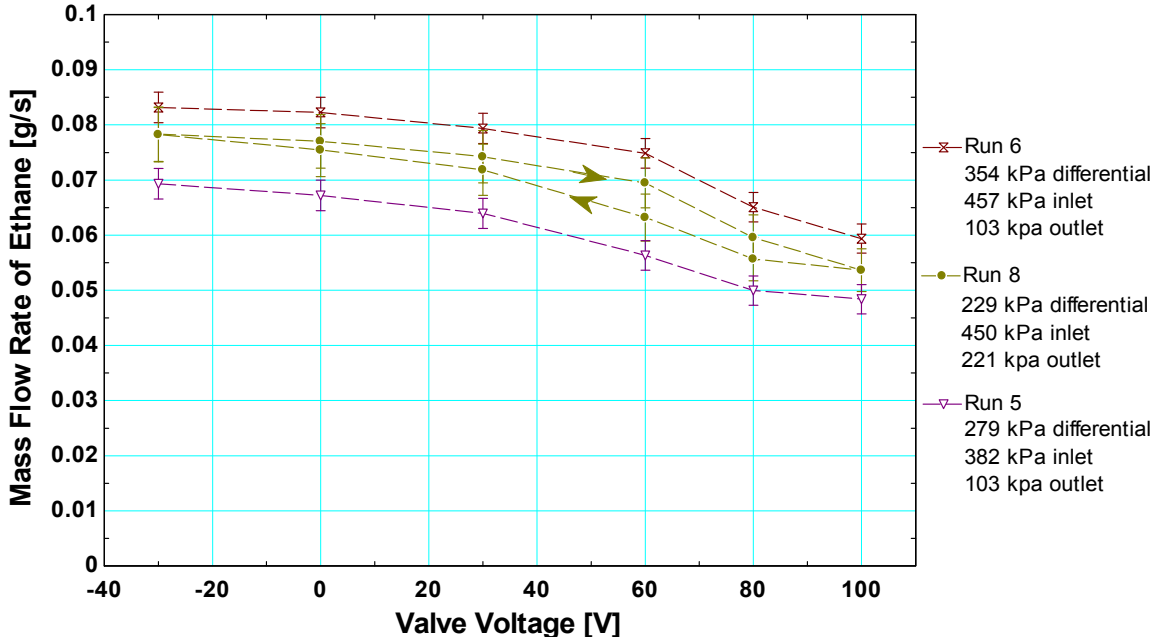

Fig. H.4: Plot of mass flow rate as a function of valve voltage. This figure shows that both the differential pressure across the valve and the outlet pressure of the valve are important. Run 8 has a smaller differential pressure than Run 5, but yet Run 8 has a higher flow rate than Run 5 due to the higher outlet pressure.

The data used to create Fig. 6.2.1 are re-plotted in Fig. 6.2.5 in order to show mass flow rate as a function of pressure difference across the valve for various valve settings. The fully open (-30 V) and the fully closed (100 V) positions have smooth curves, but the intermediate settings have jagged curves due the influence of previously applied voltages.

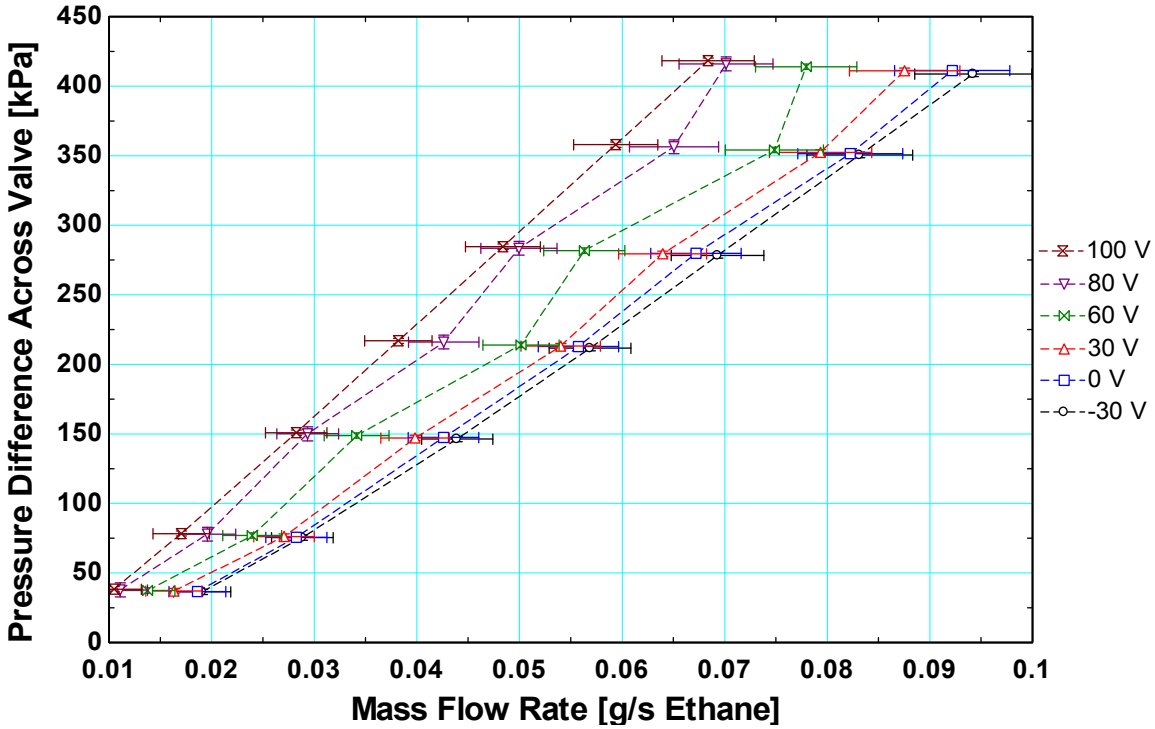

Fig. 6.2.5: Plot of mass flow rate through the valve as a function of the pressure difference across the valve for various valve settings. This plot uses the same data set as Fig. 6.2.2. The fully open (-30 V) and the fully closed (100 V) positions have smooth curves, but the intermediate settings have jagged curves due the influence of previously applied voltages. The valve outlet pressure ranged from 100 kPa to 105 kPa.

The curves for the fully open and fully closed positions were re-plotted in Fig. 6.2.6. In addition, curves showing the expected flow rate through various size orifices were plotted in Fig. 6.2.6. A detailed explanation of methods for calculating the flow rate through an orifice is included in Chap. 3. The fully open position is nearly equivalent to a 0.012" orifice at pressure differences below 50 kPa, but becomes more like a 0.010" orifice at higher pressure differences. The fully closed position corresponds to an orifice that is slightly larger than 0.008".

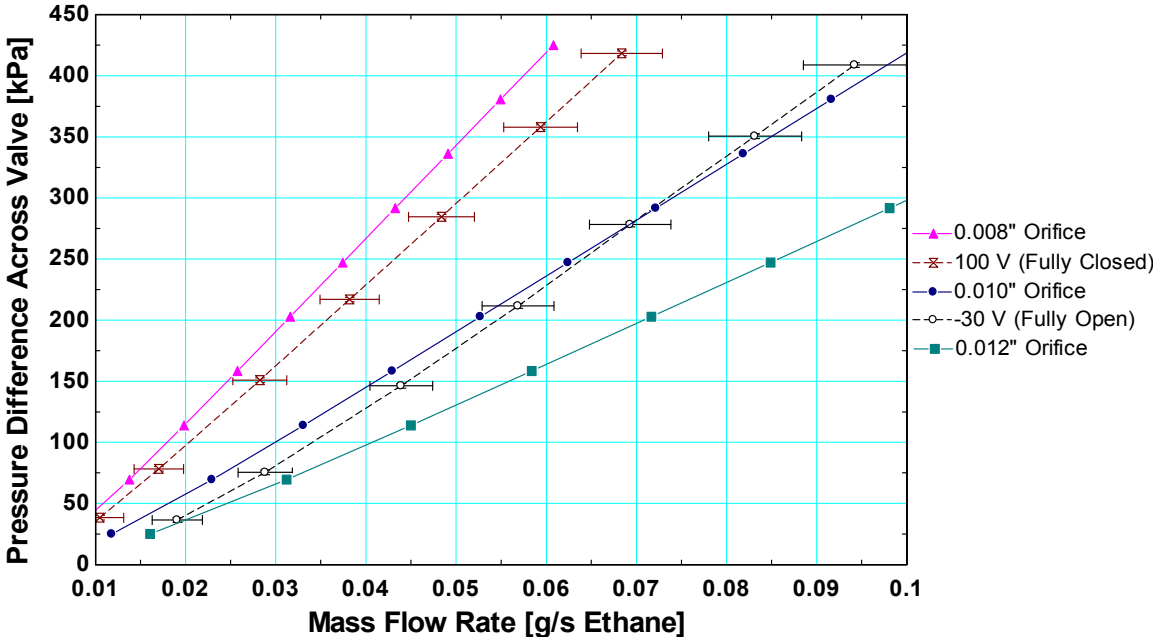

Fig. 6.2.6: Comparison of the fully open and fully closed valve positions with jewel orifice calculated flow rates. The valve outlet pressure ranged from 100 kPa to 105 kPa.

Increasing the absolute pressure at the orifice or valve outlet also increases the fluid density. The increase in density leads to larger mass flow rates for the same pressure difference across the valve or orifice. The data used in Fig. 6.2.3, which had an elevated outlet pressure of 221 kPa, are compared to jewel orifices with identical outlet pressures in Fig. 6.2.7. The fully open position flow rate is still slightly larger than a 0.010" orifice and the fully closed position flow rate is still slightly smaller than a 0.010" orifice. The effective diameter of the micro-valve does not appear to change significantly with operating pressures.

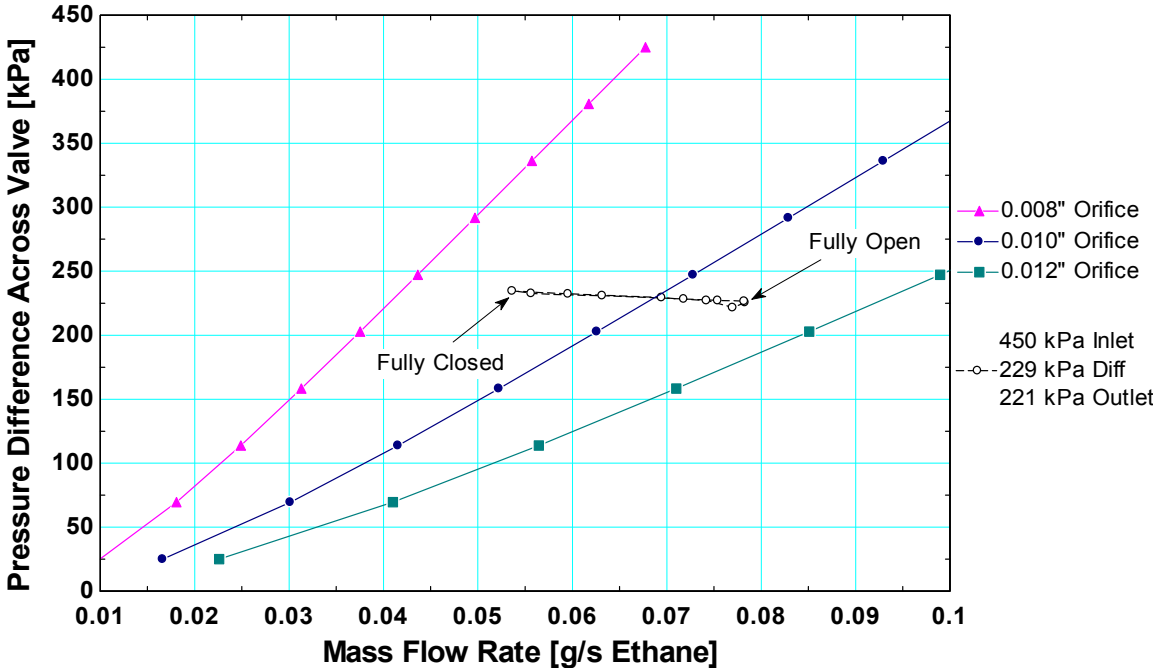

Fig. 6.2.7: The data in Fig. 6.2.3 re-plotted with the expected flow rates through a jewel orifice. The inlet pressure was kept at 450 kPa and the outlet pressure at 221 kPa for the experimental valve data points. The theoretical points for the orifices assumed an outlet pressure of 221 kPa.

6.3 Pressure Drop Test Results for the MEMS Heat Exchangers

The pressure drop tests on the sixteen die 10 mm heat exchanger were performed with the heat exchanger mounted inside the Dewar and the pressures measured at the pressure taps. Flow to the cryocooler heat exchanger was shut off using blank VCR gaskets. A VCR gasket with a large through-hole was placed in the jewel orifice location in order to connect the two sides of the heat exchanger with minimal pressure drop. All of the experimental data are shown in Tables D.1 through D.4 and the calculated results based on the experimental data are shown in Tables D.5 through D.9 in Appendix D.

Internal fluid leakage had been detected using a helium leak detector, so as part of the pressure drop testing, the internal (high-pressure to low-pressure) leak rate was also measured. By placing a blank VCR gasket in the jewel orifice location, all flow was blocked except through the internal leaks in the heat exchanger. Helium, which is commonly used for leak detection due to its small atomic radius, was used as the working fluid for this test. The leak rate was too small to be measured by the mass flow meter, as shown in Fig. 6.3.1.

Three additional curves are shown in Fig. 6.3.1. The pressure drop on the low pressure side of the heat exchanger was measured with a differential pressure gauge. A curve showing twice the measured pressure drop on the low pressure side was plotted to show the approximate total pressure drop in the heat exchanger. The final curve shown in Fig. 6.3.1 is the pressure drop in the entire assembly, which is the high pressure side inlet pressure minus the low pressure side outlet pressure.

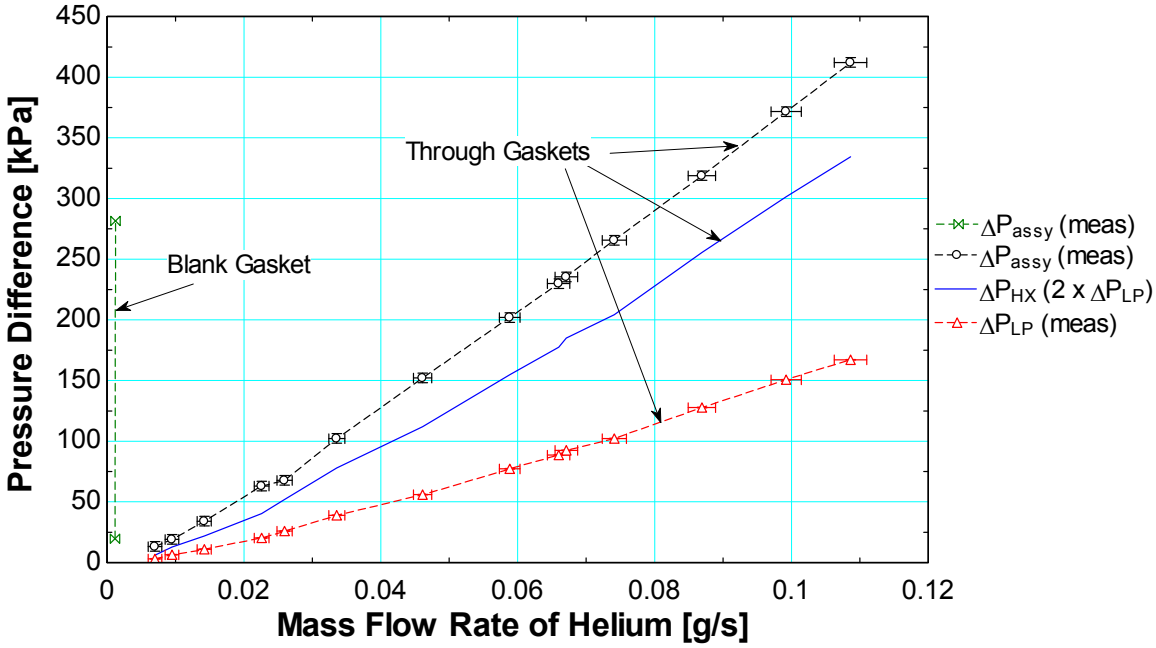

Fig. 6.3.1: Pressure drop across the sixteen die 10 mm heat exchanger using helium as the working fluid. Both the pressure drop across the entire heat exchanger assembly and across the low pressure side of the heat exchanger were measured. A line which represents twice the pressure drop on the low pressure side of the heat exchanger was plotted to show the approximate total pressure drop in the heat exchanger. A blank gasket was installed between the streams to measure the leak rate, which was negligible.

Similar pressure drop tests were also performed using air and ethane as the working fluid, shown in Figs. 6.3.2 and 6.3.3, respectively. Ethane and air showed very similar pressure drop behavior. Both fluids had a total pressure drop across the heat exchanger assembly of approximately 375 kPa at mass flow rate of 0.3 g/s. This contrasts with helium, which had total pressure drop of 375 kPa with only a 0.1 g/s mass flow rate.

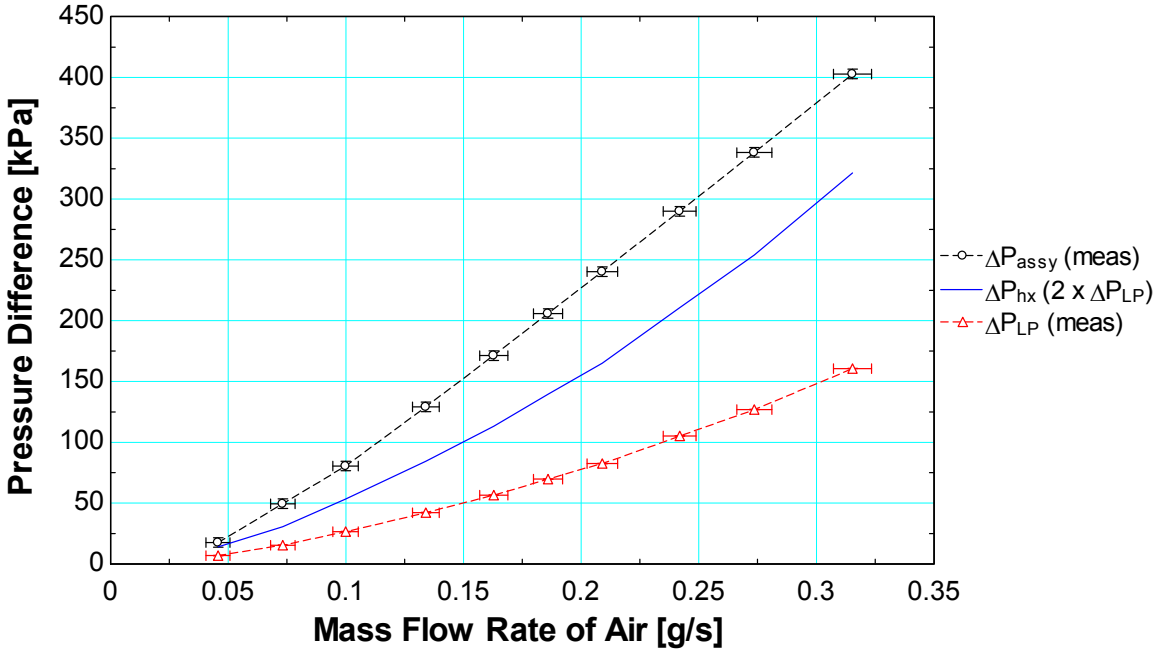

Fig. 6.3.2: Pressure drop across the sixteen die 10 mm heat exchanger using air as the working fluid. Both the pressure drop across the entire heat exchanger assembly and across the low pressure side of the heat exchanger were measured. A line which represents twice the pressure drop on the low pressure side of the heat exchanger was plotted to show the approximate pressure drop for the entire the heat exchanger.

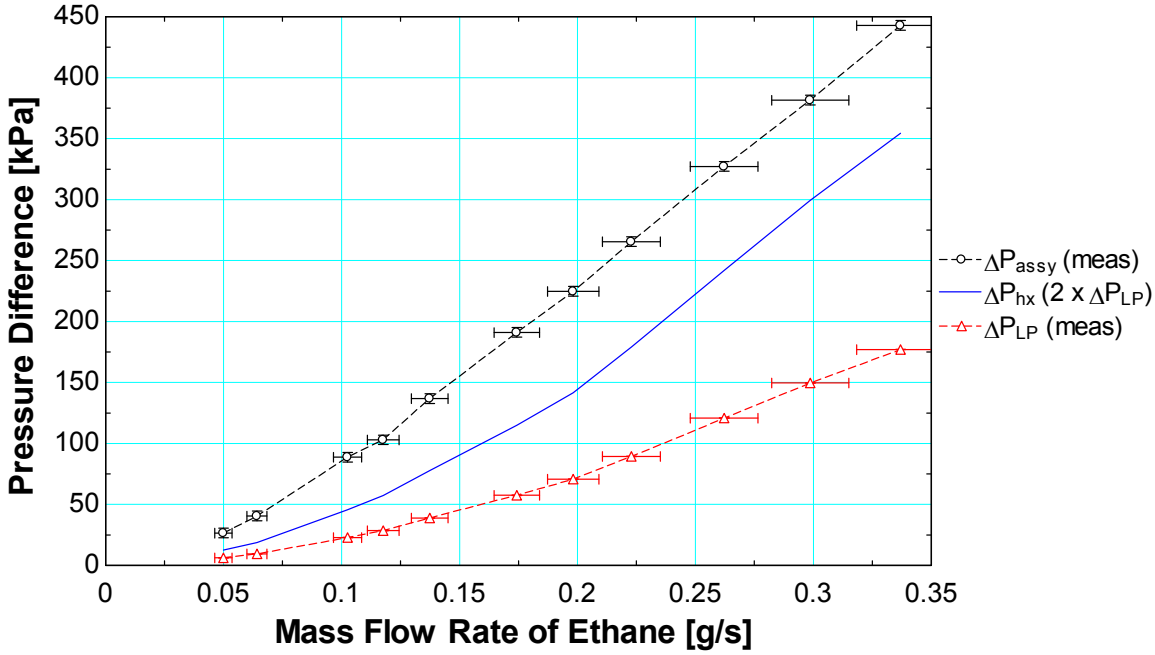

Fig. 6.3.3: Pressure drop across the sixteen die 10 mm heat exchanger using ethane as the working fluid. Both the pressure drop across the entire heat exchanger assembly and across the low pressure side of the heat exchanger were measured. A line which represents twice the pressure drop on the low pressure side of the heat exchanger was plotted to show the approximate total pressure drop in the heat exchanger.

The pressure drop behavior of the forty-three die 10 mm heat exchanger was also tested in the experimental setup shown in Fig. 6.2.1. The heat exchanger was mounted so that the high pressure inlet and low pressure outlet ports were connected to the VCR tees shown in Fig. 6.2.1. The same U-shaped copper tube was used to connect the high pressure outlet to the low pressure inlet of the heat exchanger. All of the experimental data are shown in Tables I.1 through I.3 and all of the calculated results from the experimental data are shown in Tables I.4 through I.6 in Appendix I.

Three different types of tests were performed. Each test required installation of a different VCR gasket at the high pressure outlet of the heat exchanger. The first test used a VCR gasket with a large through-hole in order to allow the maximum mass flow through the heat exchanger with the minimum pressure difference across the heat exchanger. The through-hole gasket test provides an estimate of the pressure drop behavior when the heat exchanger is tested in applied cooling mode. Performing the test at room temperature allows the pressure drop predictions of the design model to be compared to experimental data without having to account for temperature-driven changes in the fluid properties.

The next test utilized a VCR gasket with a 0.015” orifice installed in order to restrict the mass flow rate, which allows the design model to be compared to experimental data at lower flow rates and higher pressures. These conditions are present when the heat exchanger is operating in self-cooling mode. Confirming the design models pressure drop behavior in self-cooling mode is especially important because pressure drop in the heat exchanger carries the penalty of reducing

the pressure drop across the orifice and thus the available cooling from an isenthalpic pressure drop.

The last test was performed with a blank gasket at the high pressure outlet, which prevented flow through the U-shaped tube connecting the two sides of the heat exchanger. The only available flow path was through internal leaks in the heat exchanger. The mass flow rate due to internal leakage was not detectable by the mass flow meter, although internal leakage was detected when the heat exchanger was leak checked with a helium leak detector. The results of all three tests are shown in Fig. 6.3.4.

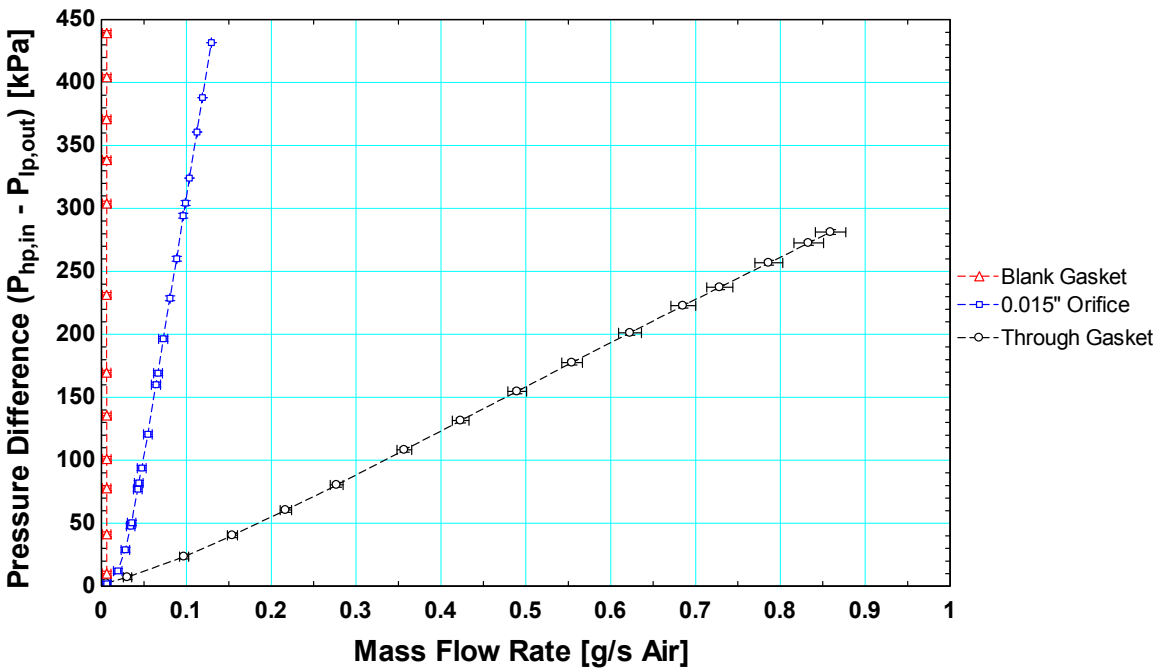

Fig. 6.3.4: Pressure difference between the high pressure inlet and the low pressure outlet of the forty-three die 10 mm heat exchanger for various configurations. The blank orifice forced entire flow rate to pass through the internal leaks in the heat exchanger. The 0.015" orifice shows pressure differentials that are typical of self-cooling tests where the majority of the pressure drop occurs at the orifice. The through gasket test shows pressure differentials that are typical for applied-cooling effectiveness tests.

The pressure drop testing of the thirty-seven die 20 mm heat exchanger was nearly identical to the forty-three die 10 mm heat exchanger. Both were tested in the same setup, both were tested with air as the working fluid, and both were tested in the same three configurations. All of the experimental data for the thirty-seven die 20 mm heat exchanger is shown in Tables J.1 through J.3 and all of the calculated results from the experimental data are shown in Tables J.4 through J.6 in Appendix J.

The thirty-seven die 20 mm heat exchanger was known to have significant leakage from leak checking with a helium leak detector. Therefore, a slightly smaller orifice, at 0.013" instead of 0.015", was used for this testing so that the orifice flow rate would more closely match the internal leakage flow rate. As shown in Fig. 6.3.5, most of the mass flow in the orifice

configuration was likely flowing through the internal leaks instead of the orifice. This is especially true at low pressure differences where the blank gasket and orifice curves lie essentially on top of each other.

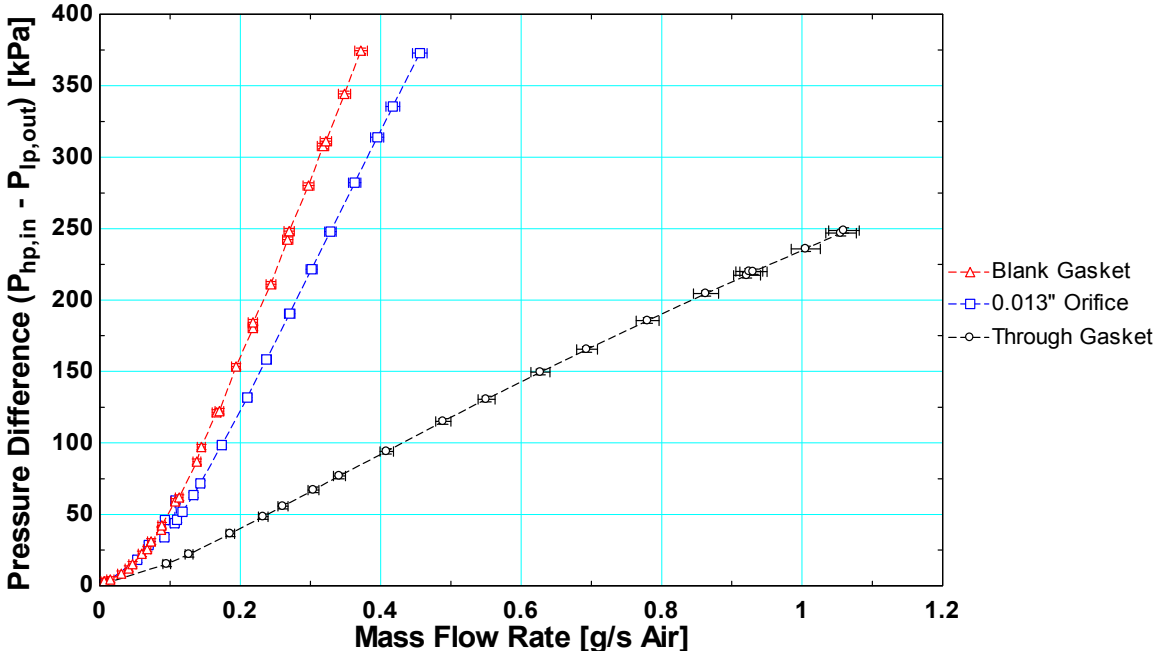

Fig. 6.3.5: Pressure difference between the high pressure inlet and the low pressure outlet of the forty-three die 10 mm heat exchanger for various configurations. The blank orifice forced entire flow rate to pass through the internal leaks in the heat exchanger. The 0.013" orifice shows pressure differentials that are typical of self-cooling tests where the majority of the pressure drop occurs at the orifice. The through gasket test shows pressure differentials that are typical for applied-cooling effectiveness tests.

6.4 Applied-Cooling Experimental Results

The first test at cryogenic temperatures on one of the MEMS heat exchangers was an external cooling test on the sixteen die 10 mm heat exchanger. The experimentally measured effectiveness as a function of mass flow rate and their corresponding uncertainties are plotted in Fig. 6.4.1. The experimental data are presented in Tables B.1 and B.2 and the results calculated from the experimental data are presented in Tables B.3 and B.4 of Appendix B. There are four different calculations of effectiveness shown in Fig. 6.4.1. The effectiveness can be defined using the cooling of the hot stream or the heating of the cold stream and each of these quantities can be calculated using the thermocouple or PRT temperature measurements.

All of the tests done on the sixteen die 10 mm heat exchanger had improper multiplexer settings. The multiplexer was set to read voltages on its fastest possible setting, which also happens to be the least accurate setting. The PRTs had slightly less than 1 K of noise. A slower but more accurate setting was used for the testing of the other two heat exchangers, which reduced the amount of noise to almost zero. Even with the noise in the PRT readings, the thermocouple and PRT temperature measurements led to similar effectiveness calculations due to the large temperature differences across the heat exchanger.

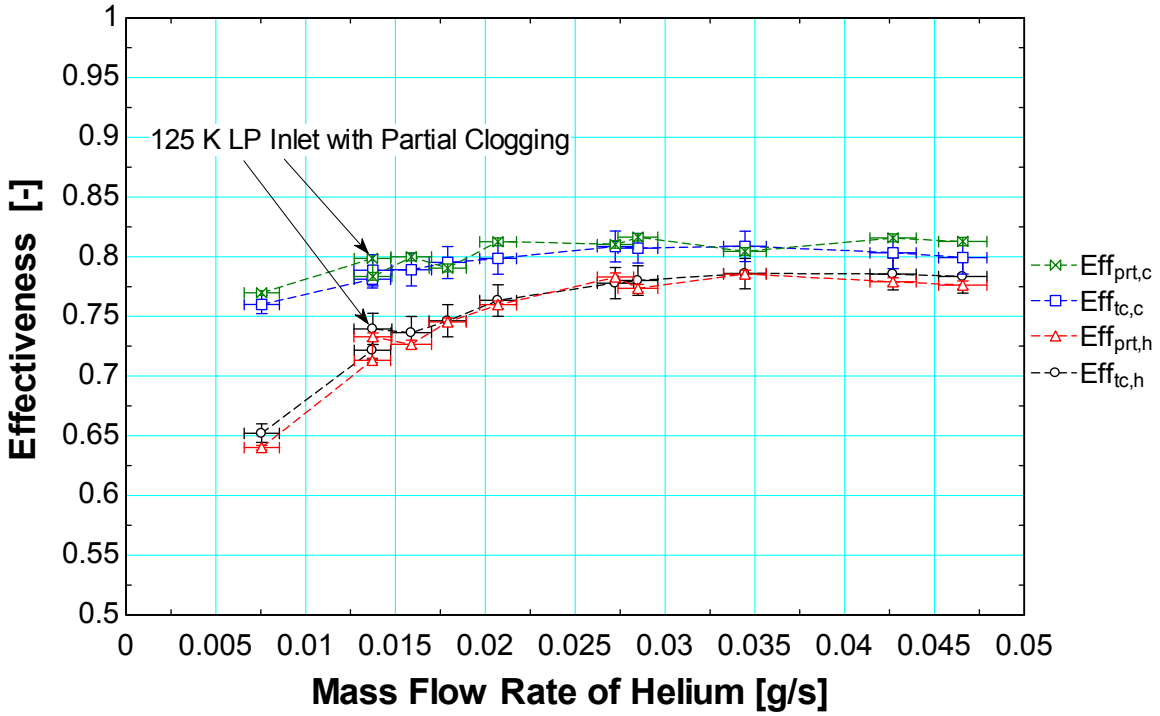

Fig. 6.4.1: Experimentally measured heat exchanger effectiveness as a function of mass flow rate for the sixteen die 10 mm heat exchanger tested in external cooling mode in the cryogenic test facility.

A contamination problem was observed when testing the heat exchanger in the applied cooling mode. When the cold end of the heat exchanger is reduced to less than approximately 210-200 K, an unknown substance begins to solidify and obstruct flow through the heat exchanger. The most likely contaminant is a volatile gas such as methane or ethane that is trapped in the oil contained in the compressor and the adsorber of the compressor's purification system. Experimental data showing the increased pressure drop due to contamination are shown in Fig. 6.4.2. The higher heat exchanger effectiveness due to the increased conductivity of silicon and the reduced conductivity of glass at the lower temperatures is labeled in Fig. 6.4.1.

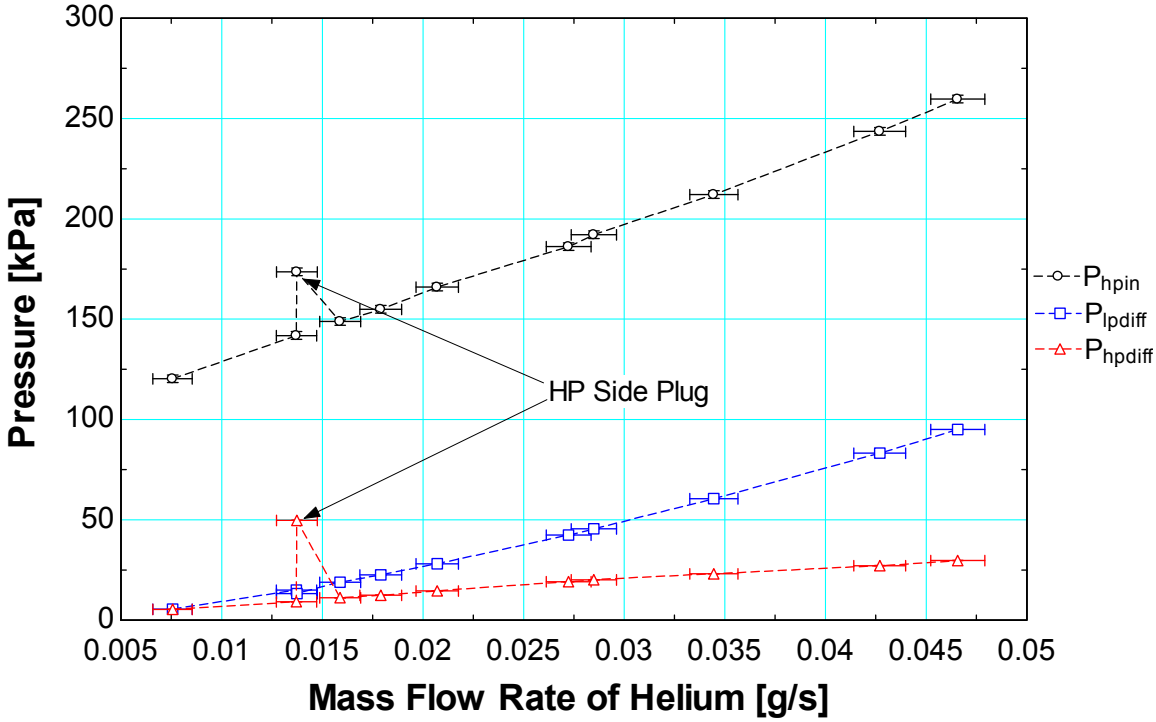

Fig. 6.4.2. Experimentally measured pressures and pressure differences as a function of mass flow rate. Contaminants from the compressor freeze out in the heat exchanger if the cold end temperature goes below 200 K.

The effectiveness of the forty-three die 10 mm heat exchanger as a function of mass flow rate was also experimentally measured in the cryogenic testing facility. The heat exchanger was tested in applied-cooling mode using two working fluids, helium and ethane. The location and type of all of the integrated PRTs are summarized in Table L.1. All of the experimental data are shown in Tables L.2-L.7 and all the calculated results are shown in Tables L.8-L.13 of Appendix L.

The results from the applied cooling test with helium are shown in Fig. 6.4.3. The high pressure inlet temperature was between 295 K and 304 K while the low pressure inlet temperature was between 237 K and 252 K. Two methods of temperature measurement were used, thermocouples (TC) and PRTs. The effectiveness can be calculated based on the heat transferred from the hot side (Eff_h) or the heat transferred to the cold side (Eff_c) of the heat exchanger.

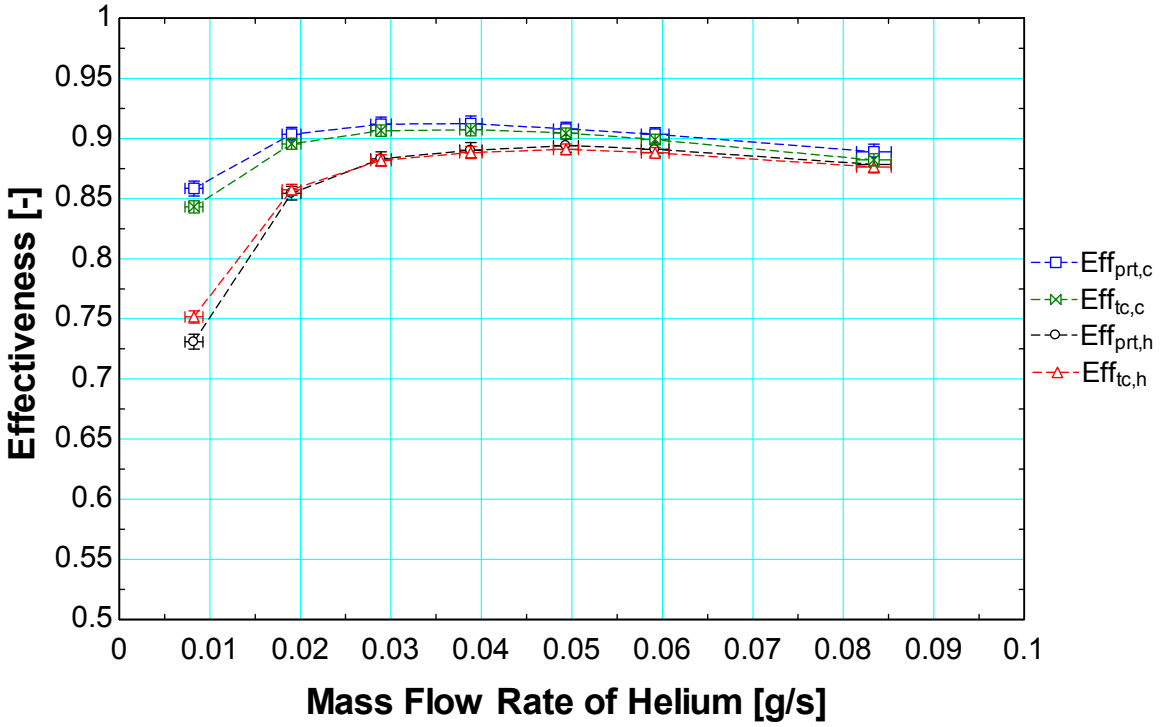

Fig. 6.4.3: Experimental measurements of heat exchanger effectiveness as a function of helium mass flow rate for the forty-three die 10 mm heat exchanger tested in applied-cooling mode in the cryogenic test facility. The high pressure inlet temperature was between 295 K and 304 K while the low pressure inlet temperature was between 237 K and 252 K.

The results from the applied-cooling test on the forty-three die 10 mm heat exchanger with ethane as the working fluid are shown in Fig. 6.4.4. The high pressure inlet temperature was between 295 K and 298 K while the low pressure inlet temperature was between 243 K and 255 K.

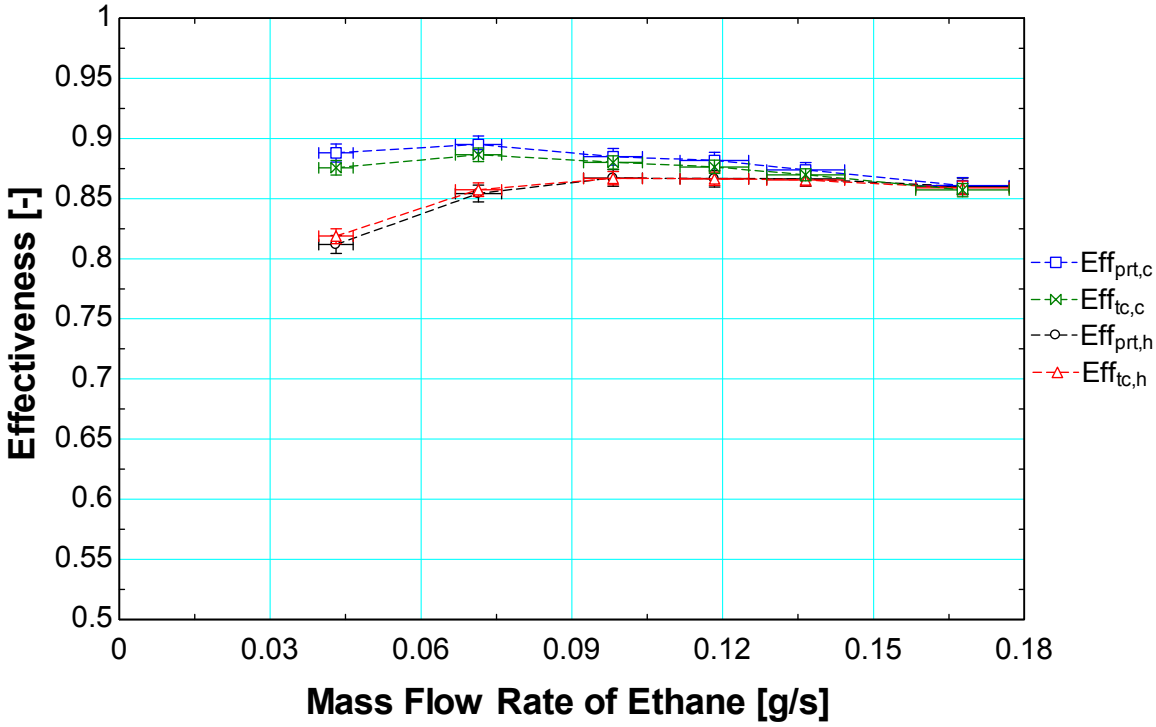

Fig. 6.4.4: Experimental measurements of heat exchanger effectiveness as a function of ethane mass flow rate for the forty-three die 10 mm heat exchanger tested in applied-cooling mode in the cryogenic test facility. The high pressure inlet temperature was between 295 K and 298 K while the low pressure inlet temperature was between 243 K and 255 K.

The pressure drop across the heat exchanger ($P_{hp,in} - P_{lp,out}$) as a function of mass flow rate during the applied-cooling tests is shown in Fig. 6.4.5. Similar to the room temperature pressure drop tests on the sixteen die 10 mm heat exchanger, the pressure drop across the heat exchanger assembly is much greater for helium than it is for ethane for a given mass flow rate.

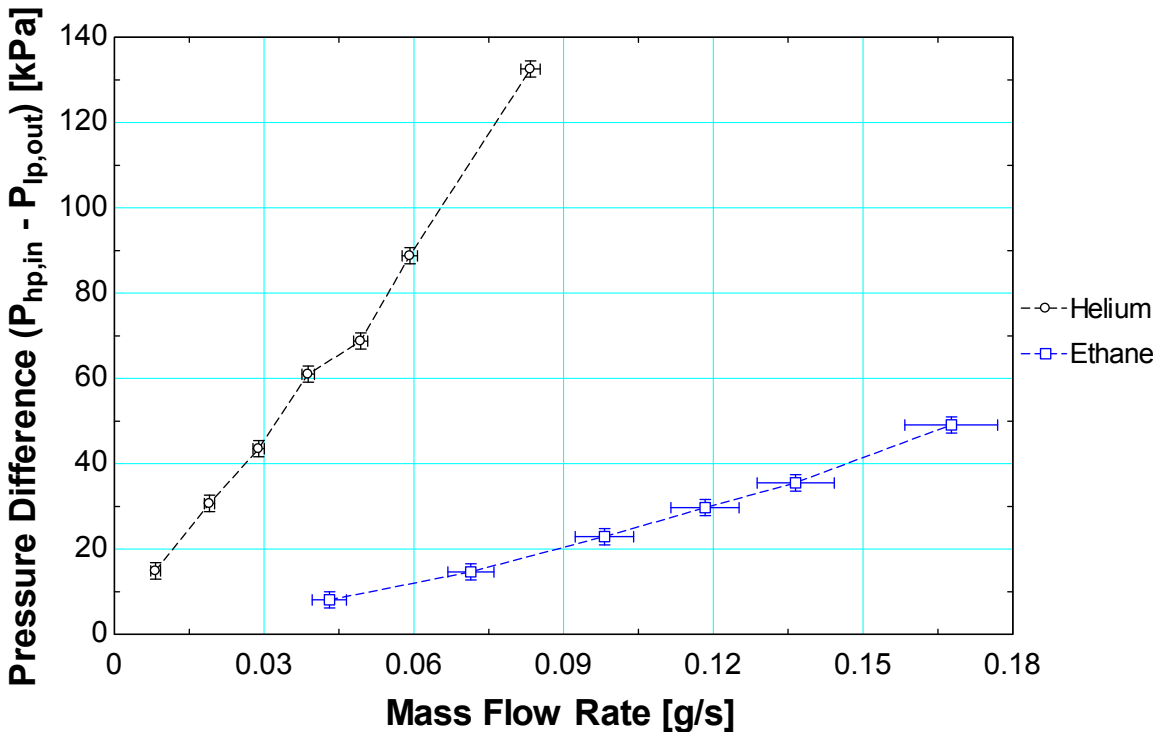

Fig. 6.4.5: Experimental measurements of the pressure difference across the heat exchanger assembly ($P_{hp,in} - P_{lp,out}$) as function of mass flow rate for both the helium and ethane applied cooling tests on the forty-three die 10 mm heat exchanger.

The temperature distribution within the forty-three die 10 mm heat exchanger was examined for four different data points. Plotted in Figs. 6.4.6 and 6.4.7 respectively are the smallest and largest mass flow rates for the applied cooling tests with helium as the working fluid. The dominant penalties on heat exchanger effectiveness for small mass flow rates are axial conduction and heat leaks. The dominant penalty on heat exchanger effectiveness for large flow rates is inadequate heat transfer area, which results in larger stream-to-stream temperature differences. Examining the smallest and largest mass flow rates, which occur on opposite sides of the peak effectiveness, allow the effects of both types of heat exchanger penalties to be experimentally studied.

The experimental temperature distributions presented in Figs. 6.4.6 and 6.4.7 qualitatively match what previous analytical and numerical models have predicted [33]. The "temperature jump" at each end that is due to axial conduction is clearly visible in Fig. 6.4.6. The temperature differences at the heat exchanger ends are large and the temperature differences in the middle of the heat exchanger are very small. The larger mass flow rate in Fig. 6.4.7 has much smaller temperature jumps at the ends of the heat exchanger and larger temperature difference in the middle of the heat exchanger.

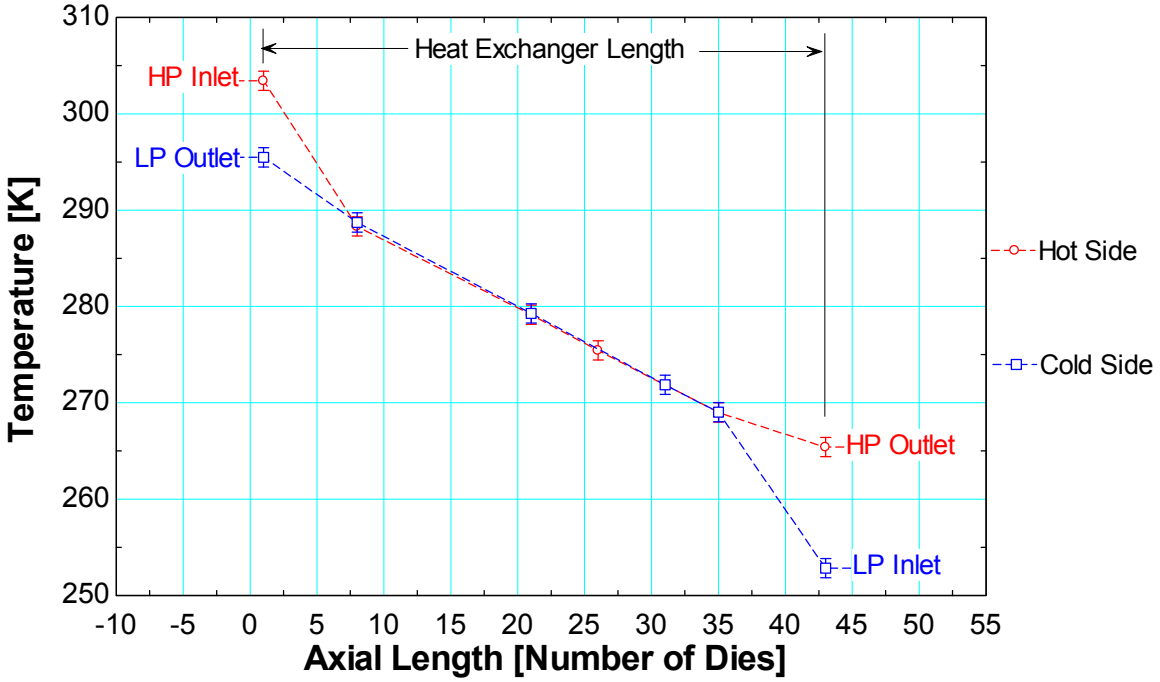

Fig. 6.4.6: Experimentally measured temperature distribution within the forty-three die 10 mm heat exchanger for the smallest helium mass flow rate (0.008 g/s) shown in Fig. 6.4.3. The inlet and outlet temperatures were measured by penetration thermocouples in the heat exchanger headers and all the internal temperatures were measured by PRTs integrated with the heat exchanger dies. The integrated PRTs were all in the normal location and were assumed to have a 1.0 K uncertainty.

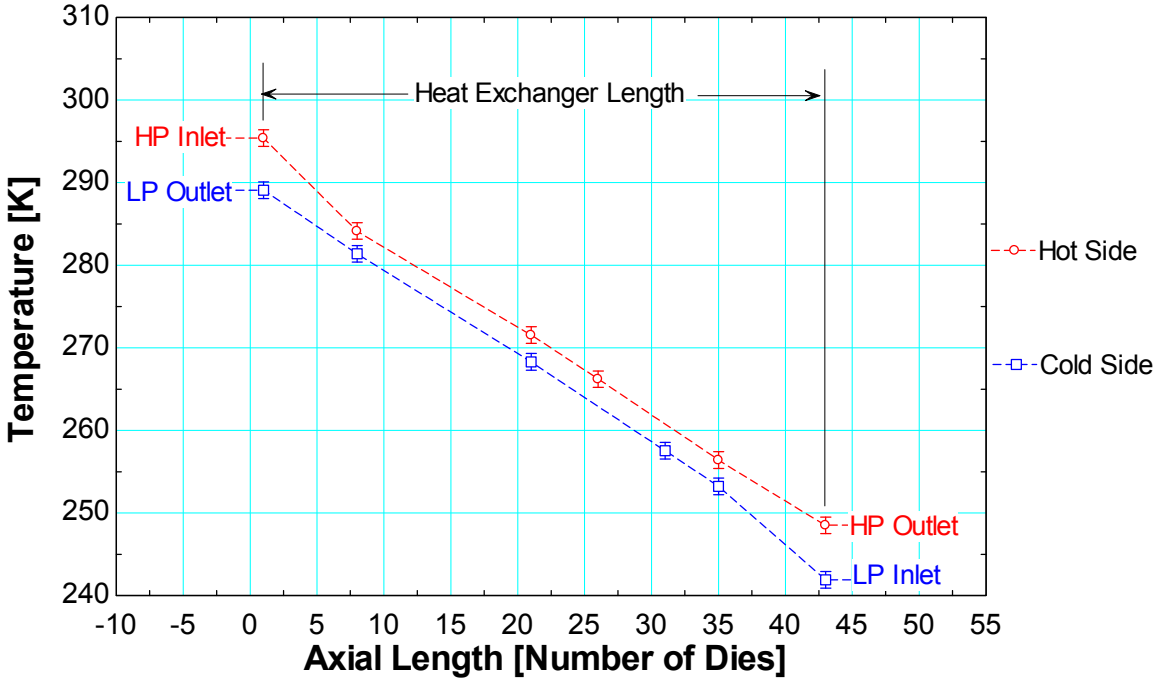

Fig. 6.4.7: Experimentally measured temperature distribution within the forty-three die 10 mm heat exchanger for the largest helium mass flow rate (0. 08 g/s) shown in Fig. 6.4.3. The inlet and outlet temperatures were measured by penetration thermocouples in the heat exchanger headers and all the internal temperatures were measured by PRTs integrated with the heat exchanger dies. The integrated PRTs were all in the normal location and were assumed to have a 1.0 K uncertainty.

Similar to Figs. 6.4.6 and 6.4.7, the temperature distributions for the smallest and largest mass flow rates from the applied-cooling tests with ethane are shown in Figs. 6.4.8 and 6.4.9 respectively. The temperature distribution trends shown by helium effectiveness tests are also shown by the ethane effectiveness tests. The temperature jumps are more pronounced in the smallest flow rate than they are with the largest flow rate. The temperature differences in the middle of the heat exchanger are much smaller for the smallest flow rate than they are for the largest flow rate.

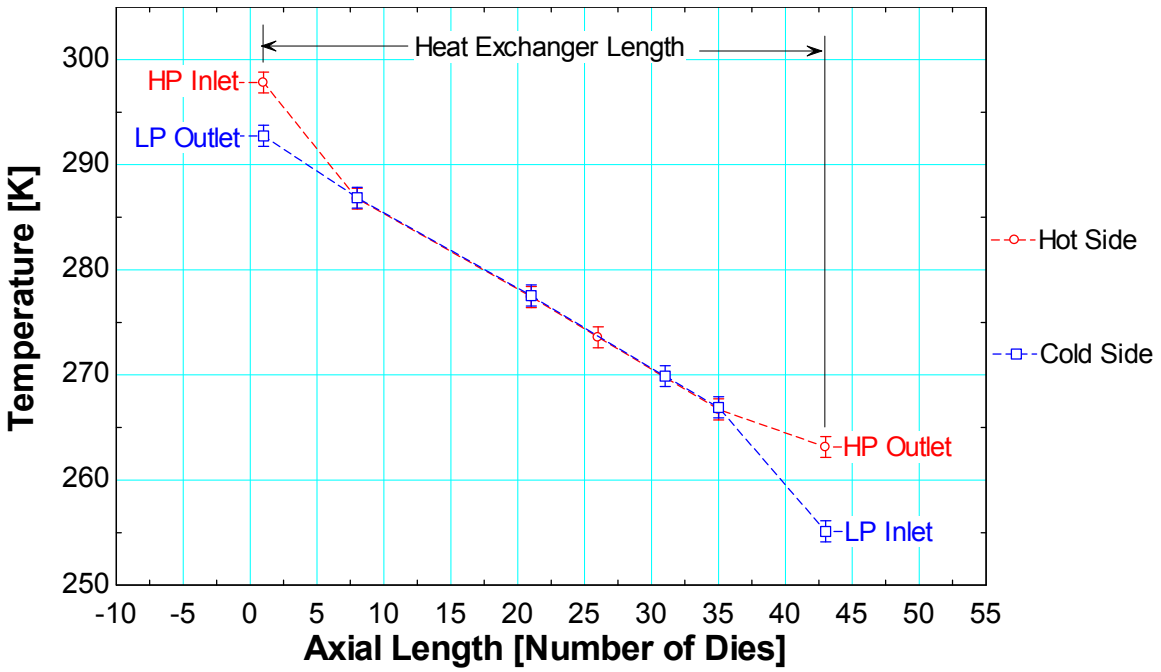

Fig. 6.4.8: Experimentally measured temperature distribution within the forty-three die 10 mm heat exchanger for the smallest ethane mass flow rate (0.04 g/s) shown in Fig. 6.4.4. The inlet and outlet temperatures were measured by penetration thermocouples in the heat exchanger headers and all the internal temperatures were measured by PRTs integrated with the heat exchanger dies. The integrated PRTs were all in the normal location and were assumed to have a 1.0 K uncertainty.

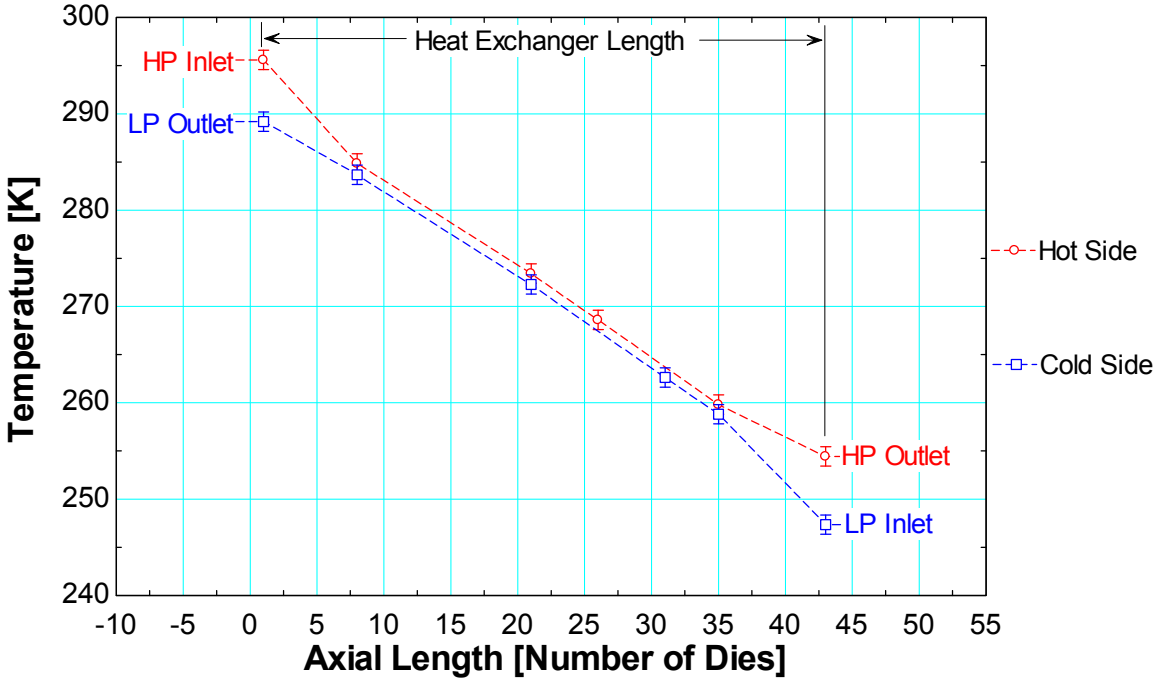

Fig. 6.4.9: Experimentally measured temperature distribution within the forty-three die 10 mm heat exchanger for the largest ethane mass flow rate (0.17 g/s) shown in Fig. 6.4.4. The inlet and outlet temperatures were measured by penetration thermocouples in the heat exchanger headers and all the internal temperatures were measured by PRTs integrated with the heat exchanger dies. The integrated PRTs were all in the normal location and were assumed to have a 1.0 K uncertainty.

The thirty-seven die 20 mm heat exchanger was tested in applied-cooling mode in the cryogenic testing facility with helium as the working fluid. The results are presented in Fig. 6.4.10. The hot inlet temperature was maintained between 296 K and 299 and the cold inlet temperature was maintained between 232 K and 242 K. The location and resistor type of all the integrated PRTs are shown in Table M.1. The experimental data are found in Tables M.2-M.4 and the calculated results based on the experimental data are found in Tables M.5-M.7 of Appendix M.

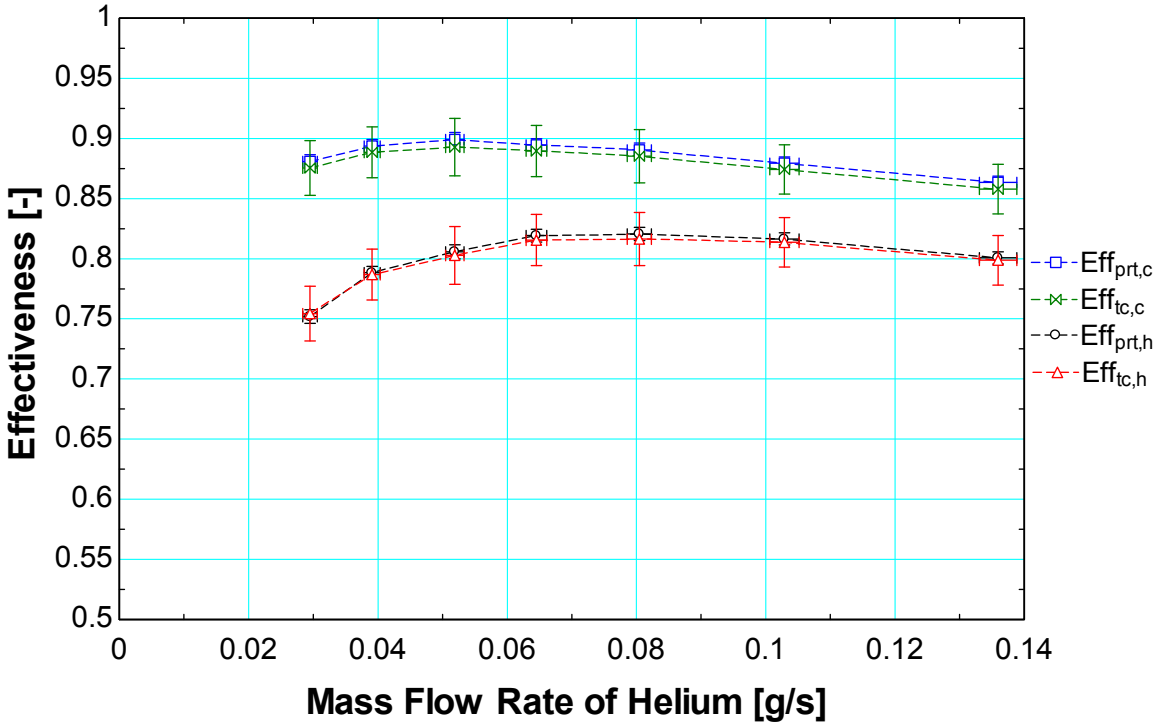

Fig. 6.4.10: Experimental measurements of heat exchanger effectiveness as a function of helium mass flow rate for the thirty-seven die 20 mm heat exchanger tested in applied-cooling mode in the cryogenic test facility. The high pressure inlet temperature was between 295 K and 299 K while the low pressure inlet temperature was between 232 K and 242 K

The pressure drop in the heat exchanger assembly ($P_{hp,in}$ - $P_{lp,out}$) during the applied-cooling tests is shown in Fig. 6.4.11. The only fluid used for testing pressure drop at room temperature was air, so direct comparisons of the pressure drop at different temperatures can not be made.

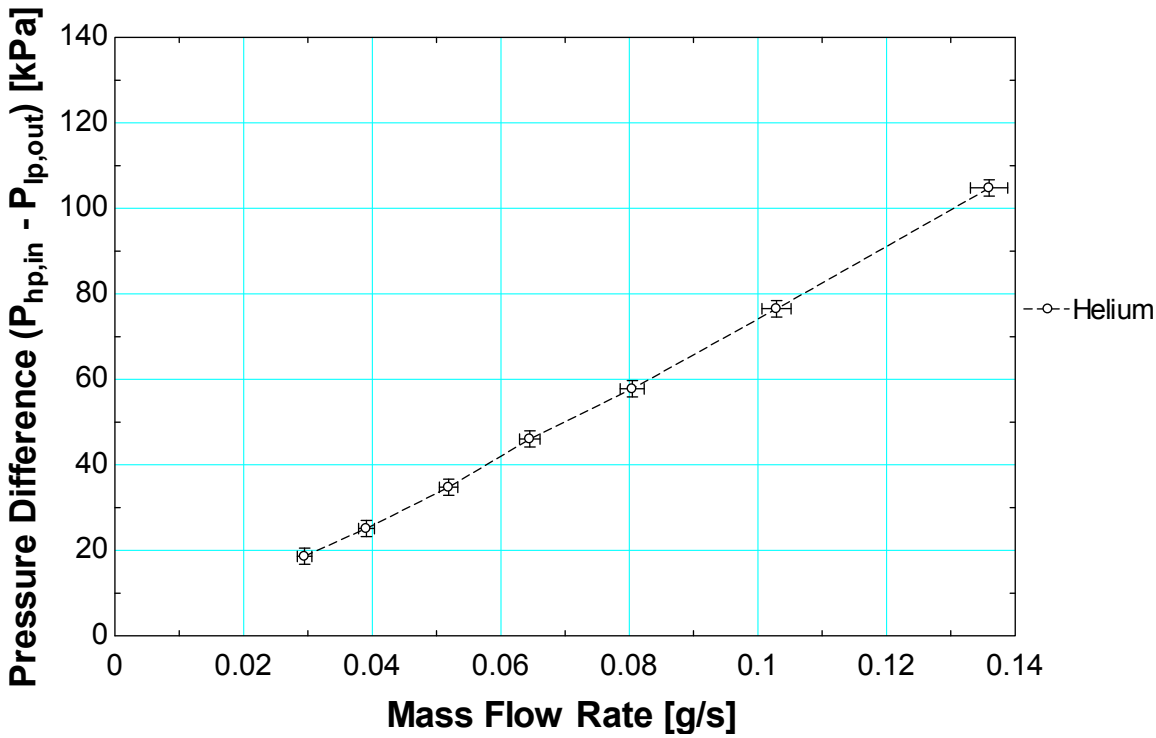

Fig. 6.4.11: Experimental measurements of the pressure difference across the heat exchanger assembly ($P_{hp,in} - P_{lp,out}$) as function of helium mass flow rate for the applied cooling tests on the thirty-seven die 20 mm heat exchanger.

The temperature distribution within the heat exchanger is shown for the smallest mass flow rate in Fig. 6.4.12 and for the largest flow rate in Fig. 6.4.13. The thirty-seven die 20 mm heat exchanger had fewer functioning integrated PRTs than the forty-three die 10 mm heat exchanger. In addition, many of the working PRTs in the thirty-seven die 20 mm heat exchanger were in the reference location.

As discussed in Appendix M, small mass flow rates generally have axial conduction as the largest penalty on heat exchanger effectiveness and large flow rates have inadequate surface area as the largest penalty on heat exchanger effectiveness. The small flow rates will have temperature jumps at the ends of the heat exchanger and small temperature differences in the middle of the heat exchanger. The large flow rates will have much smaller temperature jumps and larger temperature differences in the middle of the heat exchanger.

The smallest flow rate temperature distribution, shown in Fig. 6.4.12, shows expected behavior on the warm end but unexpected behavior on the cold end. The same unexpected cold end behavior is also present for the large mass flow rate temperature distribution shown in Fig. 6.4.12. There are several possible reasons for the unexpected temperatures at the heat exchanger cold end. One is that while the heat exchanger was being handled one or more of the fragile solder junctions on the cold end was damaged. A second is that the heat exchanger is known to have one or more large internal leaks, which can change the temperature distribution significantly. The third possible reason is that the reference location PRTs measure the fluid temperature at the outer edge of the heat exchanger but the normal location PRTs measure the average fluid temperature.

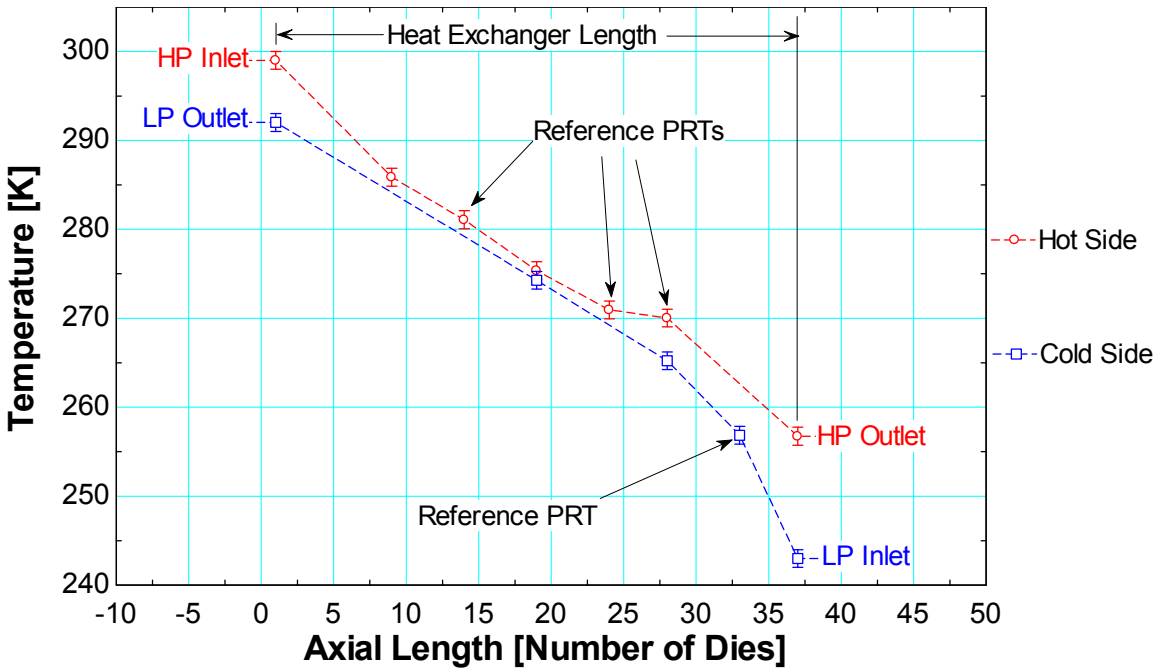

Fig. 6.4.12: Experimentally measured temperature distribution within the thirty-seven die 20 mm heat exchanger for the smallest helium mass flow rate (0.030 g/s) shown in Fig. 6.4.10. The inlet and outlet temperatures were measured by penetration thermocouples in the heat exchanger headers and all the internal temperatures were measured by PRTs integrated with the heat exchanger dies. The integrated PRTs were assumed to have the same 1 K uncertainty as the thermocouples. The reference PRTs are labeled on the plot.

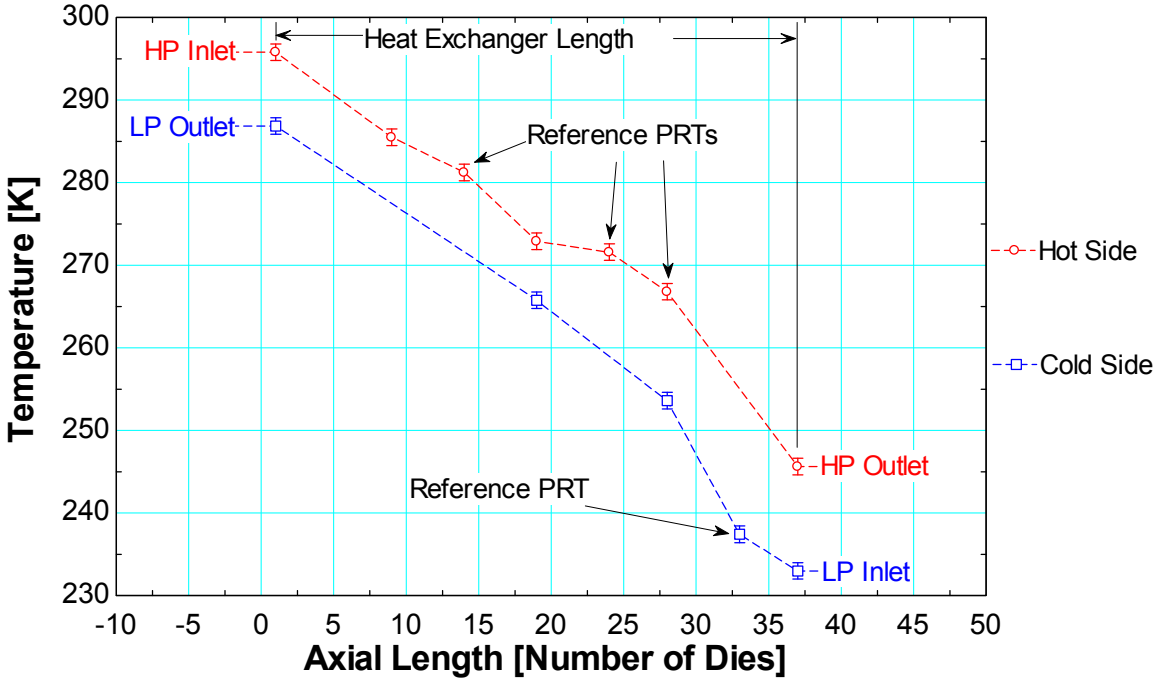

Fig. 6.4.13: Experimentally measured temperature distribution within the thirty-seven die 20 mm heat exchanger for the smallest helium mass flow rate (0.135 g/s) shown in Fig. 6.4.10. The inlet and outlet temperatures were measured by penetration thermocouples in the heat exchanger headers and all the internal temperatures were measured by PRTs integrated with the heat exchanger dies. The integrated PRTs were assumed to have the same 1 K uncertainty as the thermocouples. The reference PRTs are labeled on the plot.

6.5 Applied-Cooling Numerical Modeling Results

The applied-cooling results discussed in Chapter 6.4 are compared with the numerically modeled results in this section. The numerical model was run for the same inlet conditions as the experimental data for each steady state condition. Although the experimental effectiveness could be calculated from the PRT or thermocouple measurements, only the thermocouple measurements are shown in this section. The PRT results were not included to simplify the plots, but no information is lost because PRT and thermocouple data points were essentially identical across every experimental test condition.

A plot comparing the numerical and experimental results for the 16 die 10 mm heat exchanger is shown in Fig. 6.5.1. The numerical model is able to accurately predict experimentally measured effectiveness over the entire range of mass flow rates that were tested.

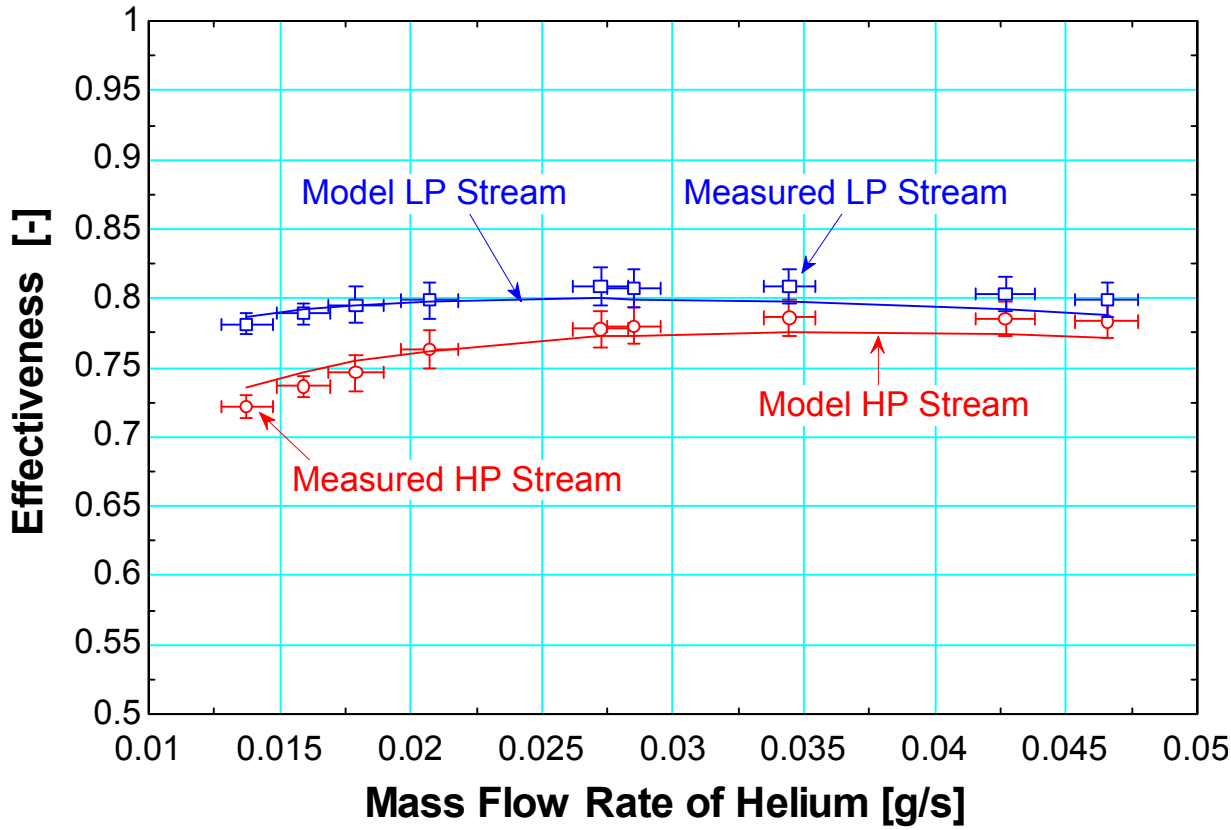

Fig. 6.5.1: Comparison of experimentally measured and numerically modeled heat exchanger effectiveness as a function of helium mass flow rate for the 16 die 10 mm heat exchanger

An applied cooling test was also performed on the forty-three die heat exchanger and the measured results are shown in Fig. 6.5.2. The forty-three die heat exchanger is nearly three times as long as the sixteen die heat exchanger and thus contains nearly three times the heat transfer surface area. As expected, the forty three die effectiveness was higher across the entire range of mass flow rates due to the increased surface area and longer length which reduces axial conduction. The numerical model is able predict the effectiveness of the longer forty-three heat exchanger with the same accuracy as for the sixteen die heat exchanger.

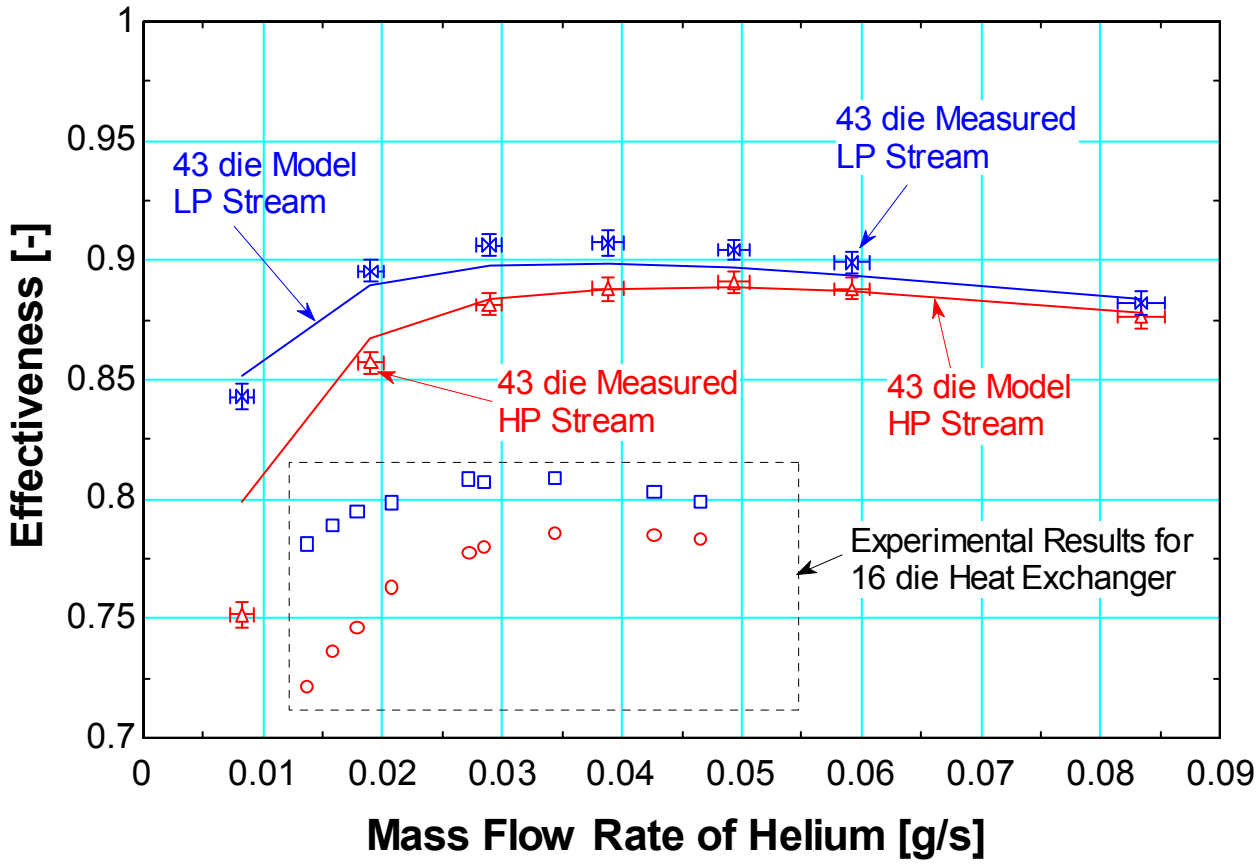

Fig. 6.5.2: Comparison of experimentally measured and numerically modeled heat exchanger effectiveness as a function of helium mass flow rate for the 43 die 10 mm heat exchanger. The experimental data points from the 16 die 10 mm heat exchanger (shown in Fig. 6.5.1) are included to show the effect of increasing the heat exchanger length.

The forty-three die heat exchanger includes dies with integrated PRTs that are used to measure the internal temperature distribution. Temperature distributions within the forty three die heat exchanger were measured during the applied cooling tests with helium as the working fluid. The internal temperature distribution is shown in Fig. 6.5.3 for the smallest mass flow rate and in Fig. 6.5.4 for the largest mass flow rate data points. The inlet and outlet temperatures shown on the plots are measured by the penetration thermocouples and the internal temperatures were measured by the integrated PRTs. The temperature distributions predicted by the numerical model are shown by the solid lines.

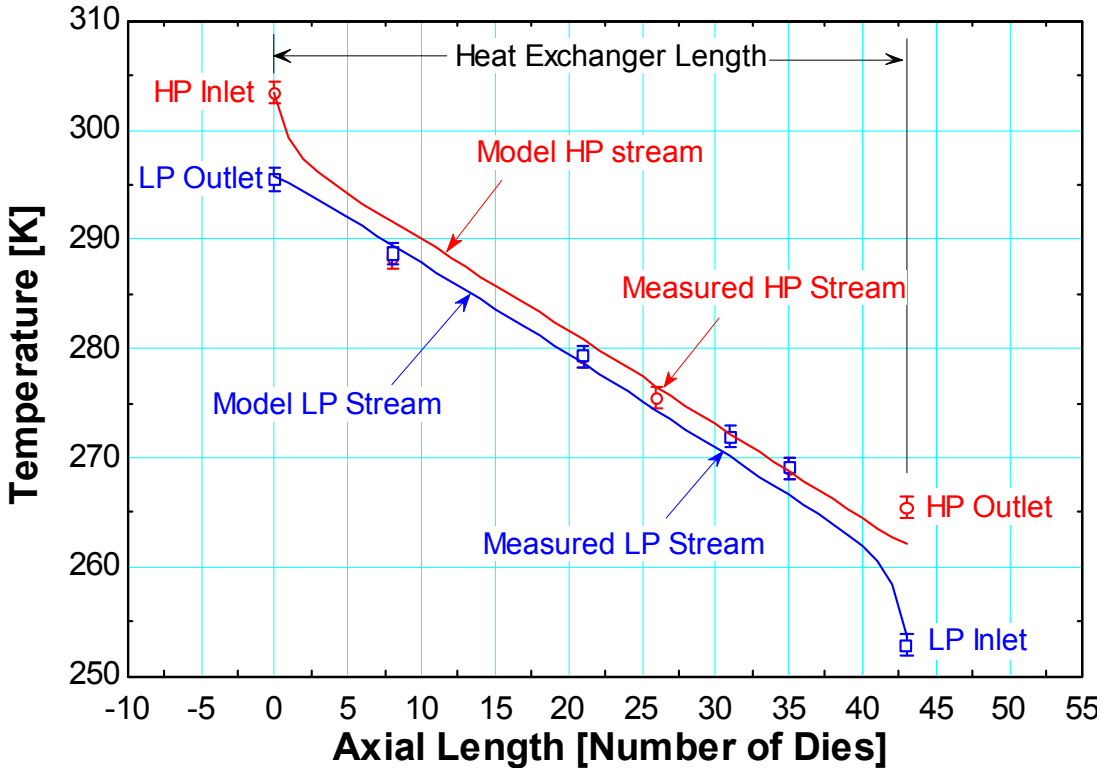

Fig. 6.5.3: Comparison of the experimentally measured and numerically modeled temperature distribution for the smallest mass flow rate data point shown in Fig. 6.5.2

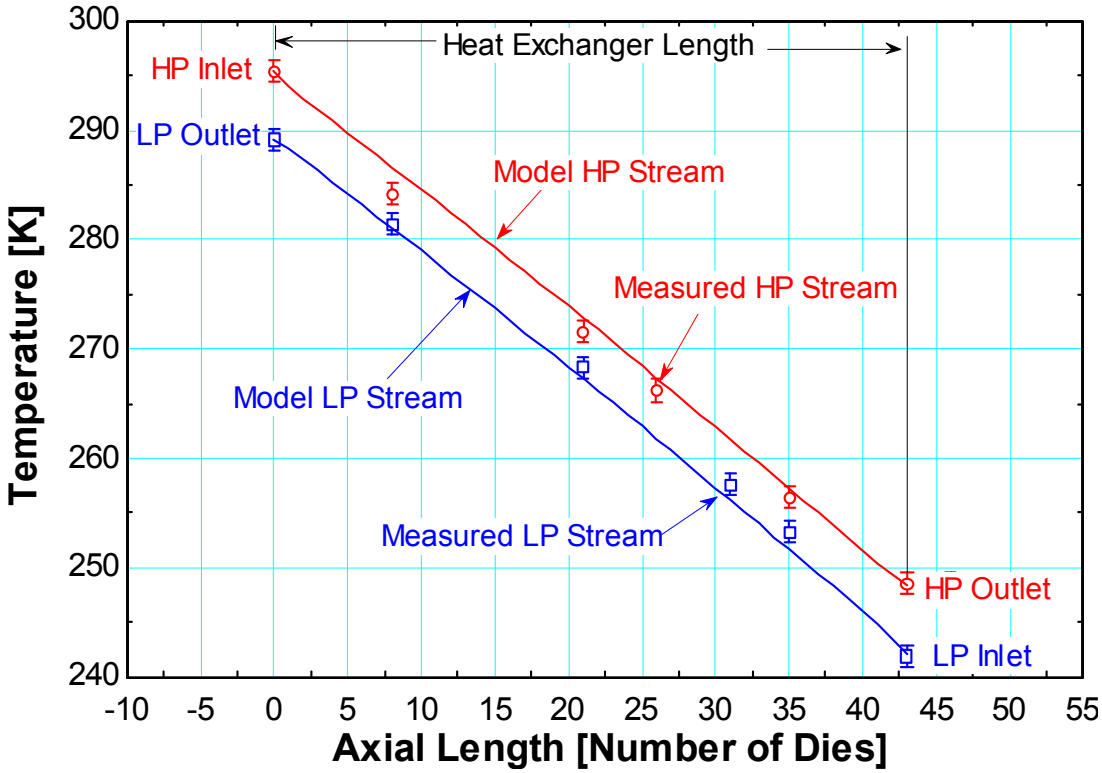

Fig. 6.5.4: Comparison of the experimentally measured and numerically modeled temperature distribution for the largest mass flow rate data point shown in Fig. 6.5.2

As the mass flow rate is decreased, the number of transfer units (*NTU*) becomes higher and therefore the average temperature difference between the two fluid streams is reduced, increasing the heat exchanger effectiveness. However, axial conduction is a major penalty at low flow rates. Analytical [14] and numerical [13] models of heat exchangers both predict abrupt "temperature jumps" at the heat exchanger ends that are related to axial conduction. These temperature jumps tend to reduce the effectiveness. As the mass flow rate increases, the *NTU* is reduced and therefore the average temperature difference between the streams increases. However, at higher mass flow rates the amount of heat conducted axially is small relative to the amount of heat transferred between the streams and therefore the penalty related to axial conduction is much lower at higher flow rates. This is evident in Figs. 6.5.3 and 6.5.4 by the reduction in the temperature jumps at the ends of the heat exchanger for the larger mass flow rate.

The experimental data and numerical model results both exhibit the trends that were expected and the measurements agree well at both high and low mass flow rates. The integrated PRTs are in better thermal contact with the silicon fins than with the fluid streams and therefore the integrated PRT measurements should be lower than the hot fluid temperature and higher than the cold fluid temperature. In each case the measured integrated PRT temperature (or part of the PRT uncertainty range) is between the predicted fluid temperatures.

An applied-cooling test was also carried out using ethane as the working fluid for the forty-three die heat exchanger. The ethane applied-cooling test was run to verify the fidelity of the numerical model with a fluid that was more typical of the working fluid within a J-T cycle. The effectiveness measurements and model predictions are shown in Fig. 6.5.5, and the temperature distributions for the smallest and largest mass flow rates are shown in Figs. 6.5.6 and 6.5.7. The model was still in good agreement with the experimental data over the range of conditions examined.

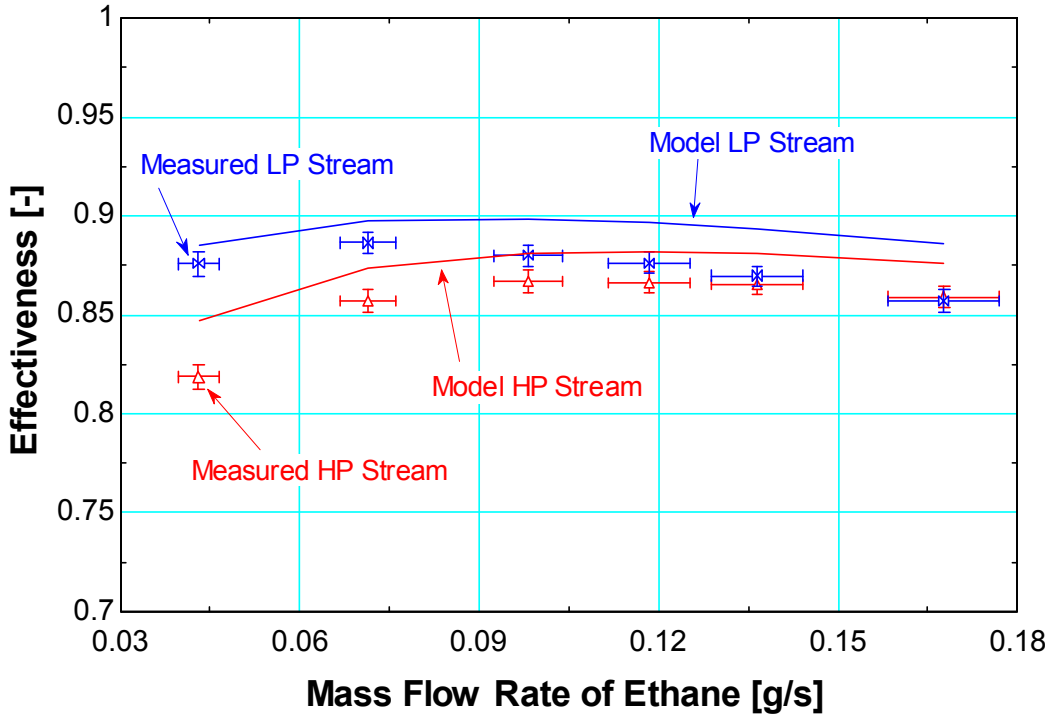

Fig. 6.5.5: Comparison of experimentally measured and numerically modeled heat exchanger effectiveness as a function of helium mass flow rate for the 43 die 10 mm heat exchanger.

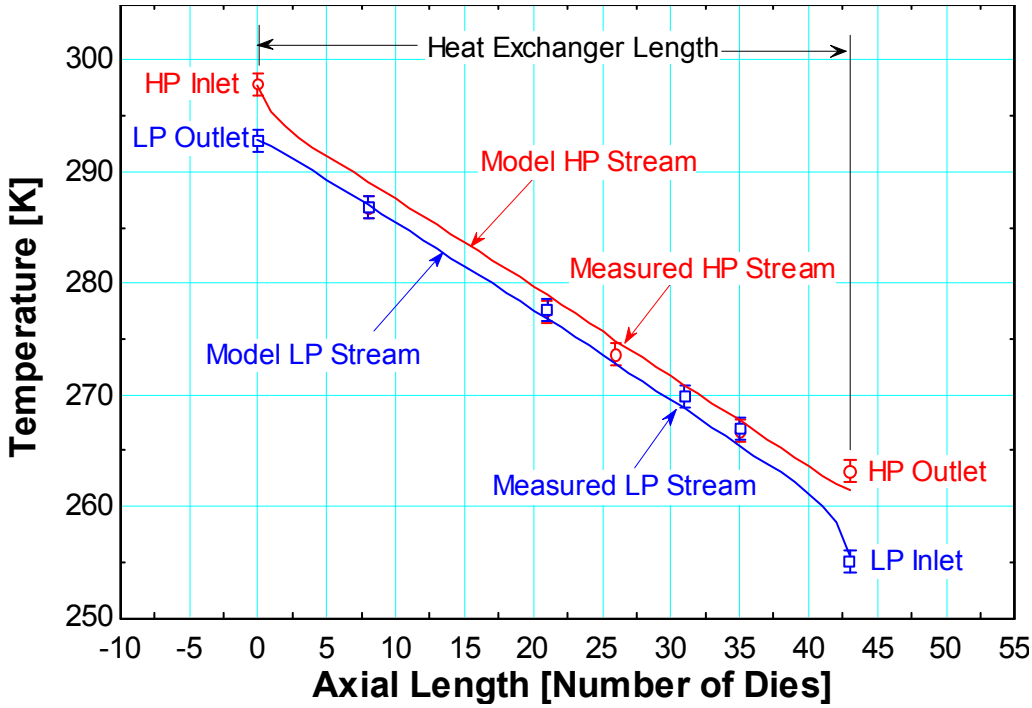

Fig. 6.5.6: Comparison of the experimentally measured and numerically modeled temperature distribution for the smallest mass flow rate data point shown in Fig. 6.5.5

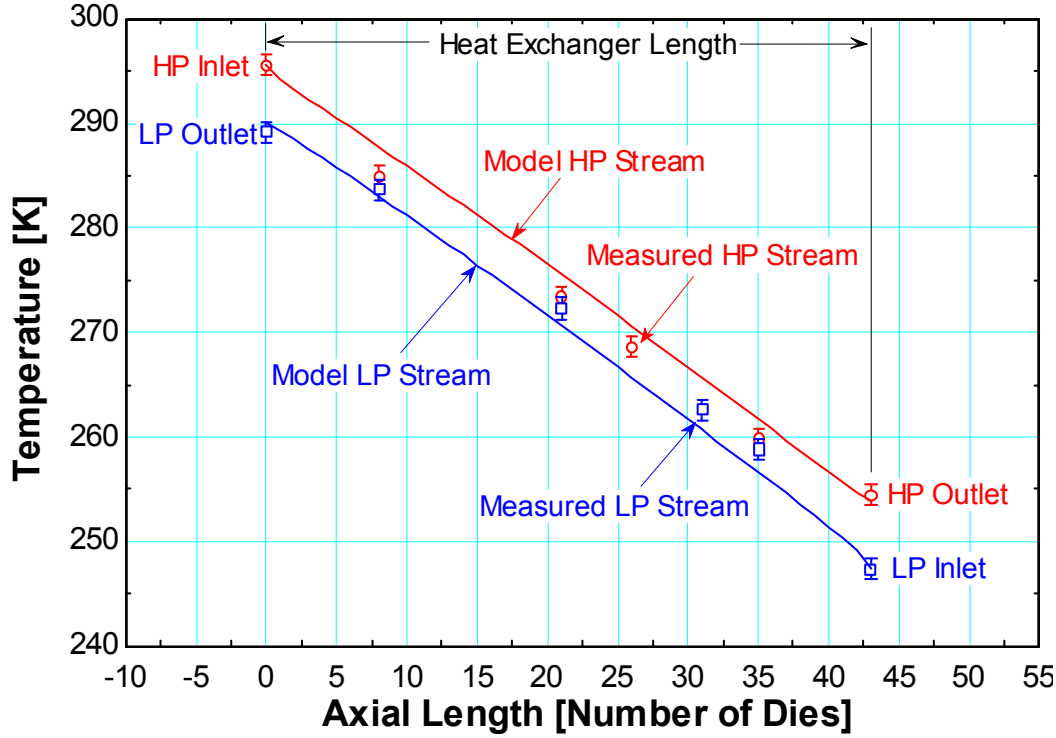

Fig. 6.5.6: Comparison of the experimentally measured and numerically modeled temperature distribution for the largest mass flow rate data point shown in Fig. 6.5.5

6.6 Cryogenic Test Facility Self-Cooling Results

The first self-cooling test performed in the cryogenic test facility was on the sixteen die 10 mm heat exchanger using ethane as the working fluid. The maximum temperature difference across the heat exchanger, which is the hot inlet temperature minus the cold inlet temperature, is plotted as a function of the pressure difference across the entire heat exchanger assembly in Fig. 6.6.1. The experimental data are presented in Table C.1 and the calculated results based on the experimental data are presented in Tables C.2 and C.3 of Appendix C.

The noise in the PRTs, which was discussed in Chapter 6.4, led to inaccurate measurements of temperature differences across the length of the heat exchanger because the temperature differences were so small. The thermocouple measurements produced a smooth curve when the temperature difference across the heat exchanger ($T_{h,in} - T_{c,in}$) is plotted against the pressure difference across the heat exchanger ($P_{h,in} - P_{c,out}$). However, the PRT temperature measurements produced results that appear to be randomly higher or lower than the thermocouple temperature difference measurements. Only the thermocouple measurements should be considered valid in Fig. 6.6.1.

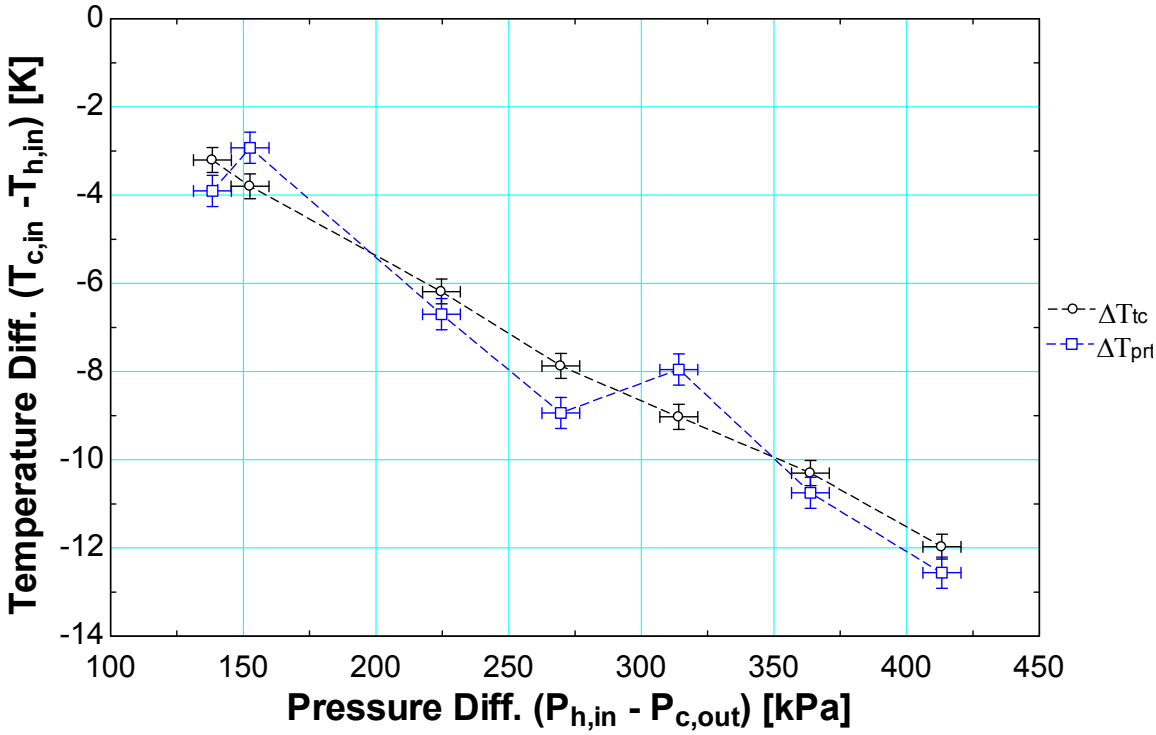

Fig. 6.6.1: Temperature difference measured across the length of the heat exchanger as a function of the pressure drop across the heat exchanger assembly. The heat exchanger was operating in self-cooling mode with ethane as the working fluid.

As discussed in Chap. 3, large temperature differences across the heat exchanger allow the heat exchanger effectiveness to be measured more accurately. Shown in Fig. 6.6.2 is a plot of heat exchanger effectiveness as a function of mass flow rate for the data set shown in Fig. 6.6.1. The error due to the noise in the PRT measurements is especially apparent in Fig. 6.6.2 with large random fluctuations in heat exchanger effectiveness. The thermocouples produced a curve the shows a steadily decreasing effectiveness with increasing mass flow rate. The data shown in Fig. 6.6.2 was re-plotted in Fig. 6.6.3 without error bars for increased clarity.

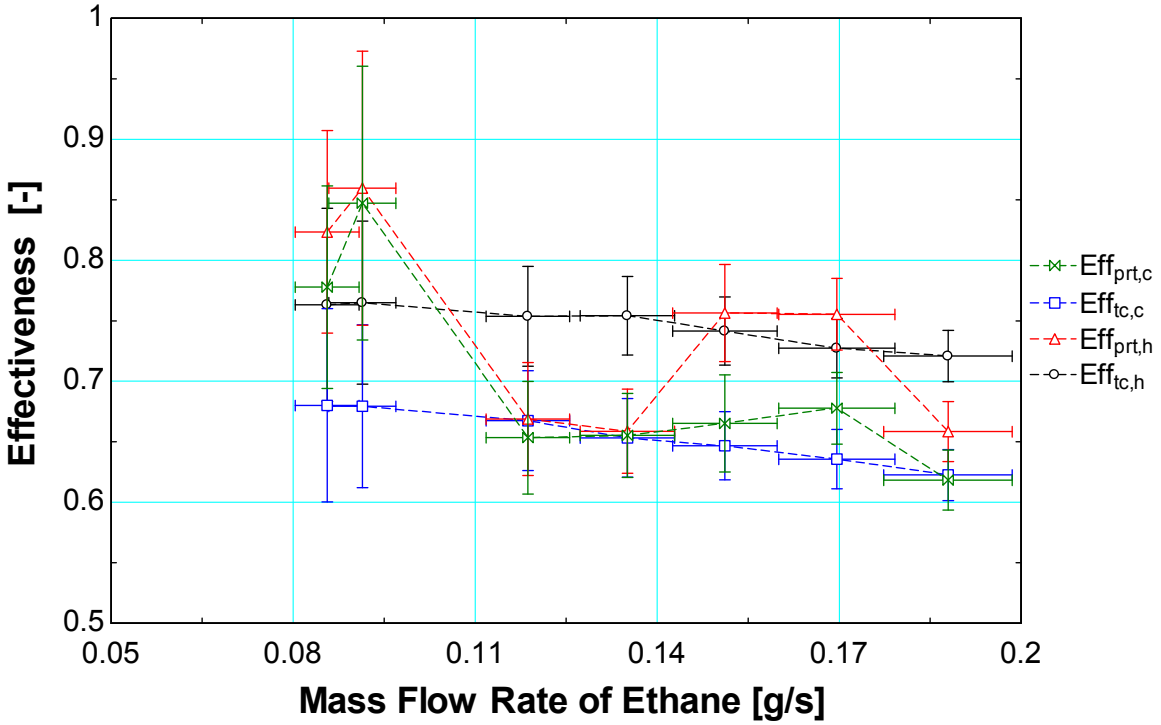

Fig. 6.6.2: Measured effectiveness as a function of the mass flow rate of ethane. Note that error bars extend off the plot due to the small temperature differences being measured.

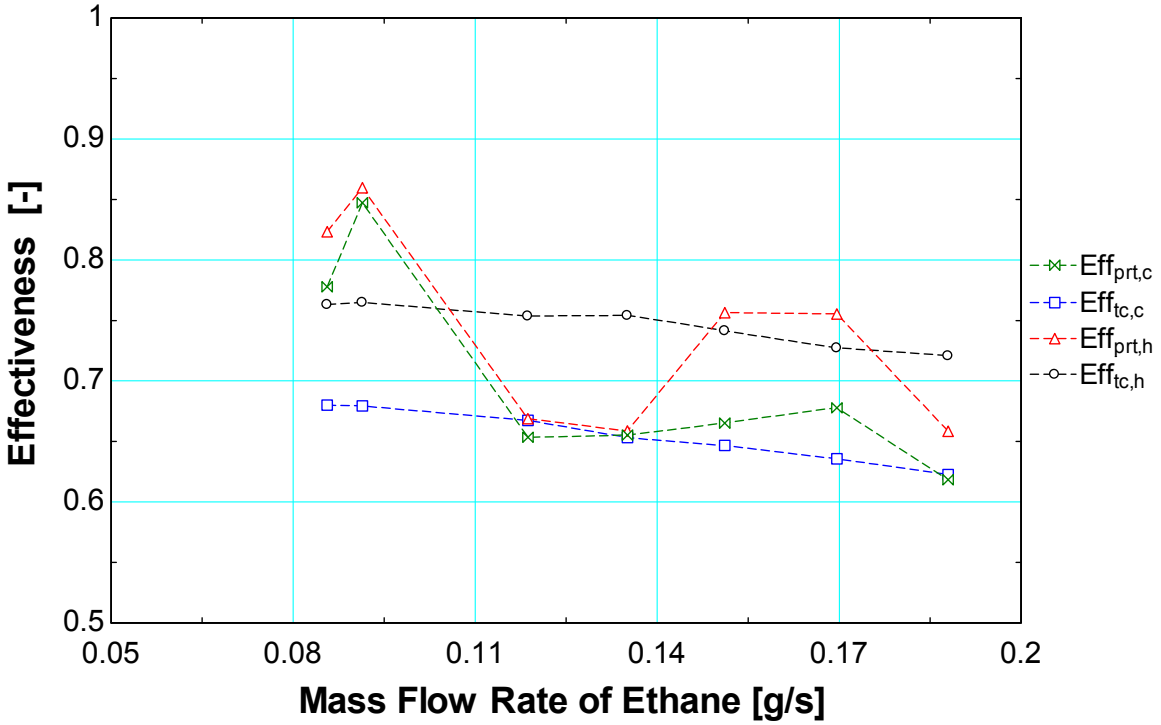

Fig. 6.6.2: Fig. 6.6.2 re-plotted without error bars for increased clarity

The forty-three die 10 mm heat exchanger was also tested in the cryogenic test facility in self-cooling mode with ethane as the working fluid. The cold end of the cryogenic test facility was

redesigned to incorporate the micro-valve and a heater, as shown in Fig. 6.6.3. There are multiple benefits to the cold end redesign in addition to the advantages associated with using a heater (which allows the measurement of a load curve) and the micro-valve (which allows flow modulation). The pressure taps that were installed in the original cold end were a source of conduction heat leak. The large amount of tubing in the old design resulted in a large thermal mass which led to a large response time for the self-cooling cycle. The tubing in the old cold end design also made it difficult to apply a large numbers of layers of MLI. The redesign reduces heat conduction and the thermal mass and provides sufficient space for the application of additional layers of MLI. The simplified self-cooling cold end design relies solely on the thermocouples for temperature measurements at the heat exchanger inlets and outlets. In previous testing, it was shown that the thermocouples provided nearly identical measurements to the commercial PRTs over the temperature range that can be obtained in self-cooling mode.

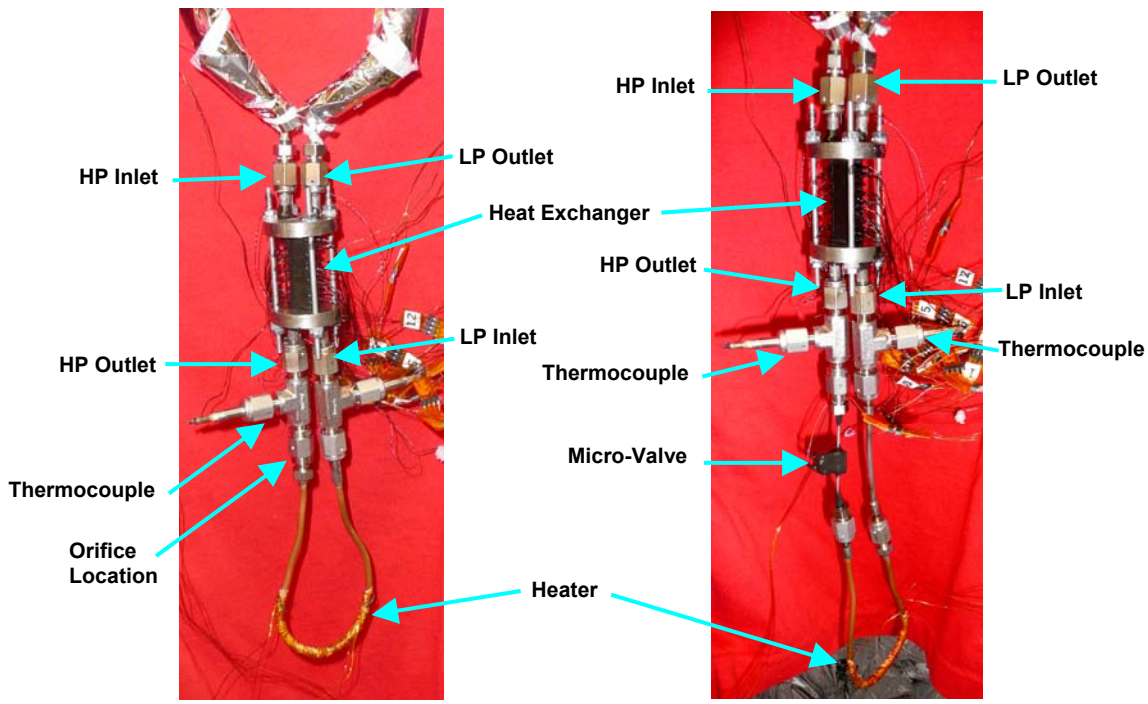

Fig. 6.6.3: Experimental setup showing the new self-cooling cold end. The setup using jewel orifices is shown to the left and the setup incorporating the micro-valve is shown to the right. The heater was fabricated from Nichrome wire with varnish used as the bonding medium.

The test results obtained in the cryogenic test facility are significantly better than were obtained using the cryosurgical probe prototype. The maximum measured temperature difference ($T_{h,in} - T_{c,in}$) in the cryogenic test facility using ethane was 43.0 K with a pressure drop of 440 kPa using a 0.015" orifice. In contrast, the maximum measured temperature difference in the cryosurgical probe was 11.4 K with a pressure drop of 436 kPa using a 0.015" orifice. The experimental results from the cryosurgical probe prototype are presented in Chapter 6.6. The locations of all of the integrated PRTs are listed in Table N.1. The experimental data for the self-cooling tests in

the cryogenic test facility are summarized in Tables N.2 - N.7 and the calculations based on the experimental data are summarized in Tables N.8 - N.13 of Appendix N.

The self-cooling measurements obtained during testing with jewel orifices and no applied heat load are shown in Fig. 6.6.4. The optimal orifice diameter is 0.015”. The 0.010” orifice provided a higher no-load cold end temperature than the 0.015” orifice for the entire range of pressure differences that were applied. The 0.020” orifice provided a slightly lower cold end temperature than the 0.015” orifice at low pressure differences, but significantly higher cold end temperatures for the largest pressure differences.

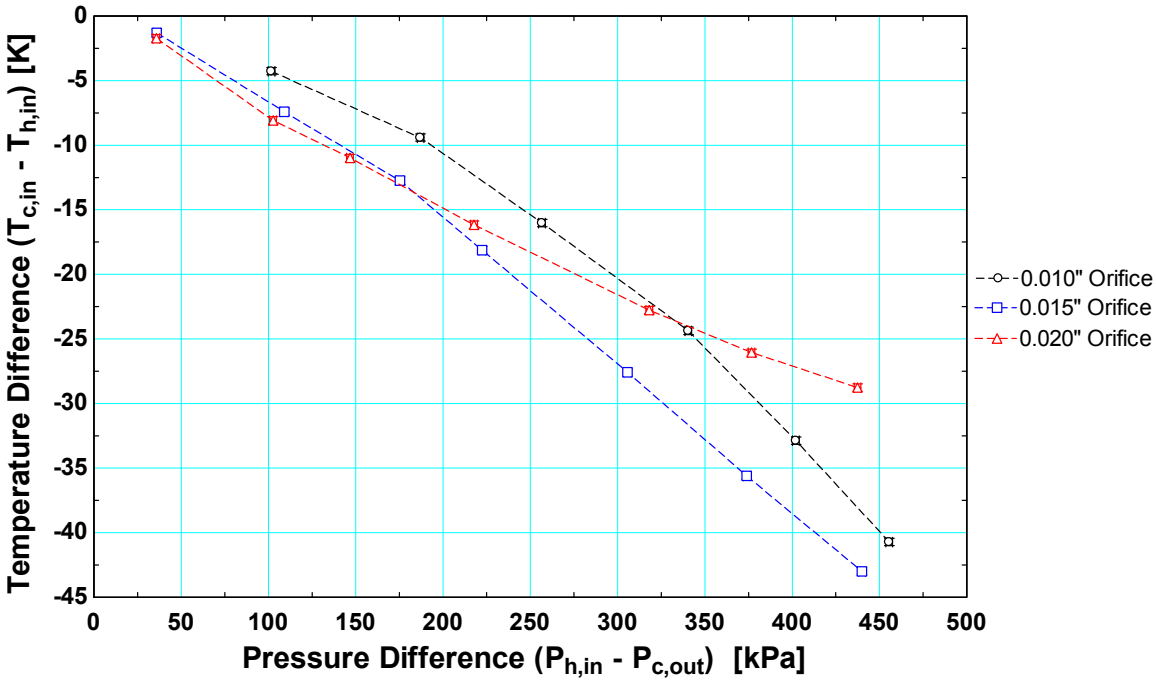

Fig. 6.6.4: Temperature difference between the heat exchanger inlet streams as a function of pressure difference applied across the forty-three die 10 mm heat exchanger assembly. The heat exchanger was tested in self-cooling mode in the cryogenic test facility with ethane as the working fluid. The optimal orifice size was 0.015”.

The forty-three die heat exchanger was also tested with the micro-valve in self-cooling mode with ethane as the working fluid. The optimal valve position (i.e., the position that produced the lowest no-load temperature) was found to be fully open (-30 V), as shown in Fig. 6.6.5. The smallest temperature difference produced across the heat exchanger occurred when the valve was in the fully closed position (100 V); recall that the "fully-closed" position allows a substantial flow due to the action of the pressure difference on the valve seat. The results from an applied voltage of 60 V were much closer to the 0 V results than the 100 V results. This behavior is likely due to the hysteresis exhibited by the PZT actuator; the voltage was consistently adjusted from 0 V to 60 V for each 60 V data point.

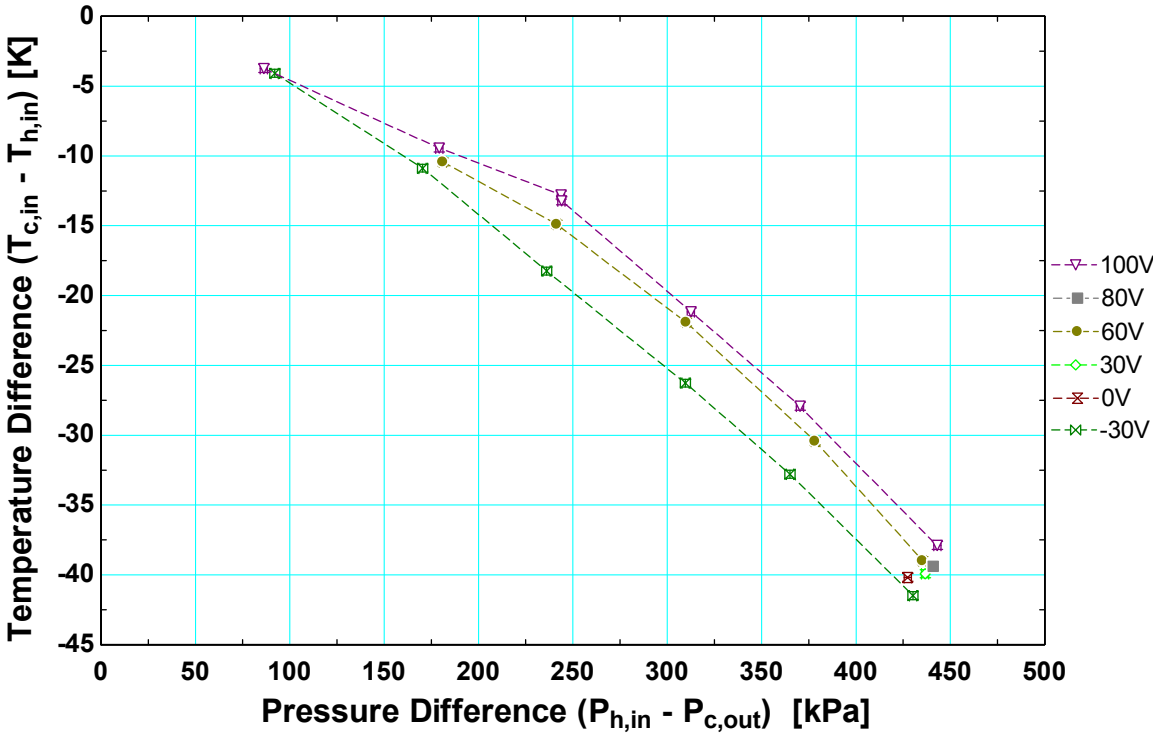

Fig. 6.6.5: Temperature difference between the heat exchanger inlet streams as a function of pressure difference applied across the forty-three die 10 mm heat exchanger assembly. The heat exchanger was tested in self-cooling mode in the cryogenic test facility with ethane as the working fluid. The optimal valve position was fully open (-30 V).

The valve and orifice self-cooling results are compared on the plot shown in Fig. 6.6.6. The fully open valve position (-30 V) provides approximately the same performance as the 0.015" orifice and the fully closed valve position (100 V) provides approximately the same performance as the 0.010" orifice.

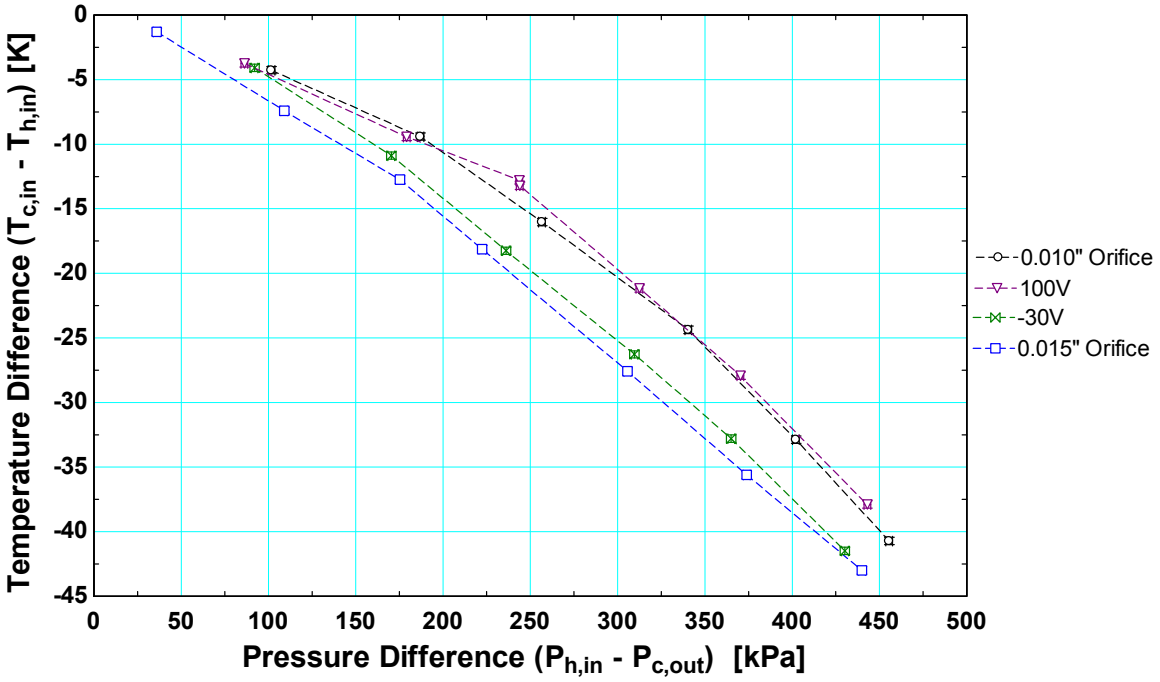

Fig. 6.6.6: Temperature difference between the heat exchanger inlet streams as a function of pressure difference applied across the forty-three die 10 mm heat exchanger assembly. The heat exchanger was tested in self-cooling mode in the cryogenic test facility with ethane as the working fluid. The valve in the fully open position (-30 V) has roughly the same performance as a 0.015" orifice and the valve in the fully closed position (100 V) has roughly the same performance as a 0.010" orifice.

The effectiveness of the heat exchanger as a function of mass flow rate is shown in Fig. 6.6.7 and is re-plotted in Fig. 6.6.8 without the error bars for increased clarity. The top group of curves in Fig. 6.6.7 consists of the hot side measurements of effectiveness for the orifice tests. The bottom group of curves consists of the hot side effectiveness measurements for the micro-valve tests and all of the cold side effectiveness measurements.

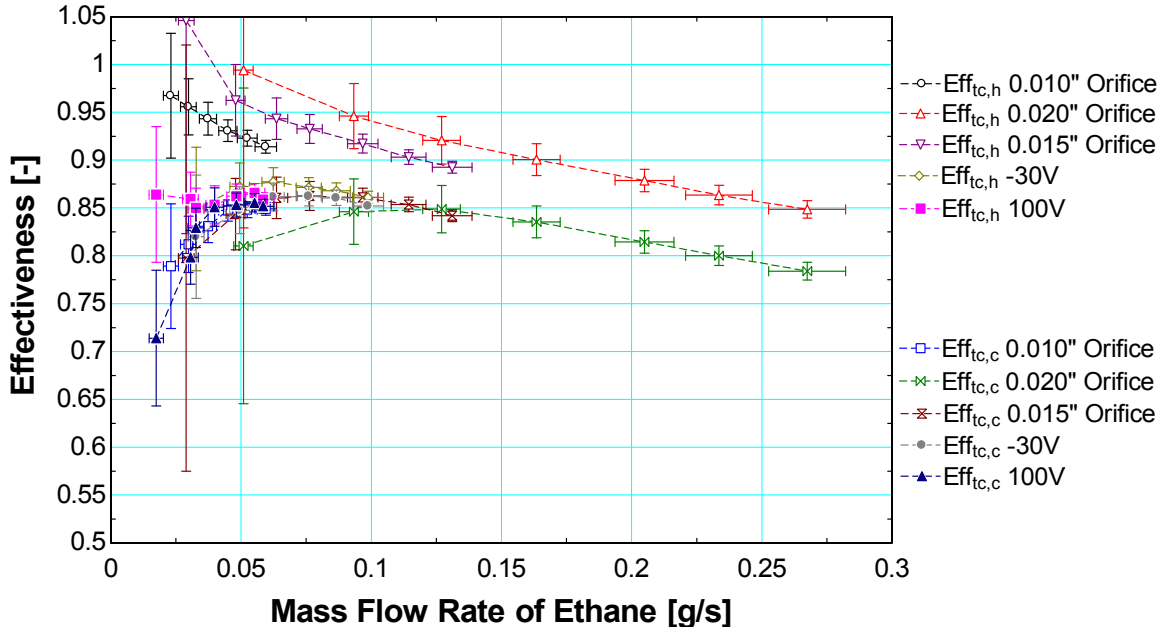

Fig. 6.6.7: Heat exchanger effectiveness as a function of mass flow rate for the data set shown in Figs. 6.6.4 and 6.6.5. All effectiveness calculations utilized the thermocouples built in to the cryogenic test facility. The curves based on the effectiveness of cooling the high pressure stream are shown in the top group and the curves based on the effectiveness of heating the low pressure stream are shown in the bottom group.

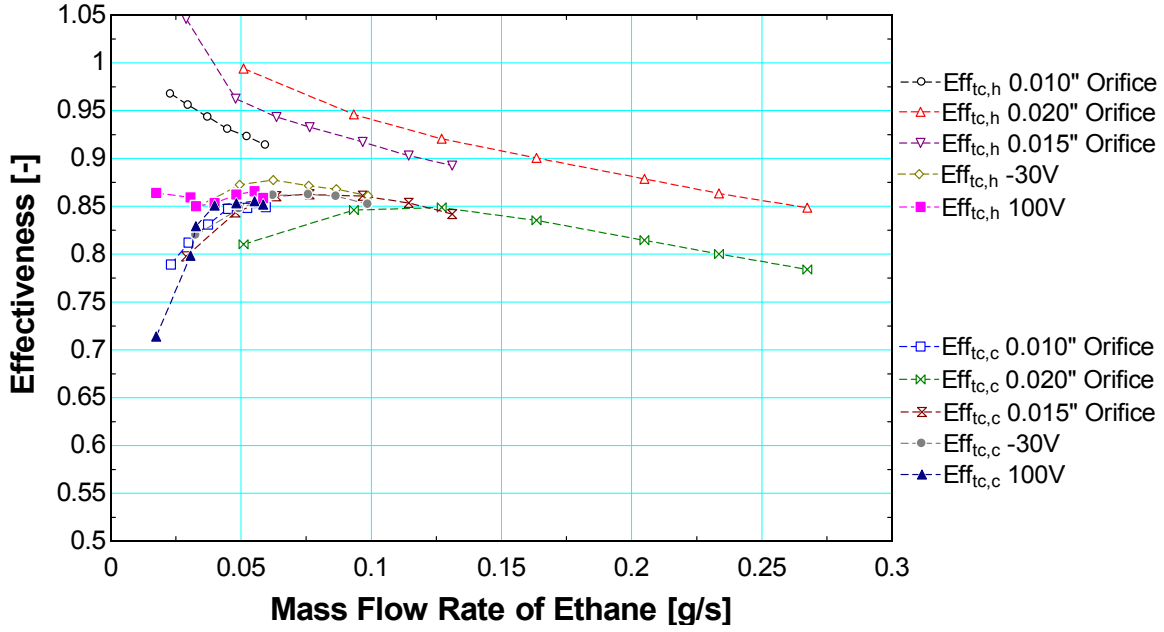

Fig. 6.6.8: Fig. 6.6.7 re-plotted without error bars for increased clarity

The temperature distribution measured by the integrated PRTs within the forty-three die heat exchanger is shown in Figures 6.6.9, 6.6.10, and 6.6.11. In each case, the temperature distribution obtained for the tests in which the maximum pressure difference is applied are shown. Figures 6.6.9 through 6.6.11 correspond to the 0.010”, 0.015”, and 0.020” orifice,

respectively. Each of the plots clearly show a characteristic temperature "jump" at both ends of the heat exchanger, this suggests that axial conduction is one of the biggest penalties on the heat exchanger performance. The 0.010" orifice test has the smallest temperature difference in the midsection of the heat exchanger because it has the smallest mass flow rate and therefore the highest number of transfer units. The 0.020" orifice test has the largest temperature difference in the midsection due to the significantly higher mass flow rates which reduces the number of transfer units.

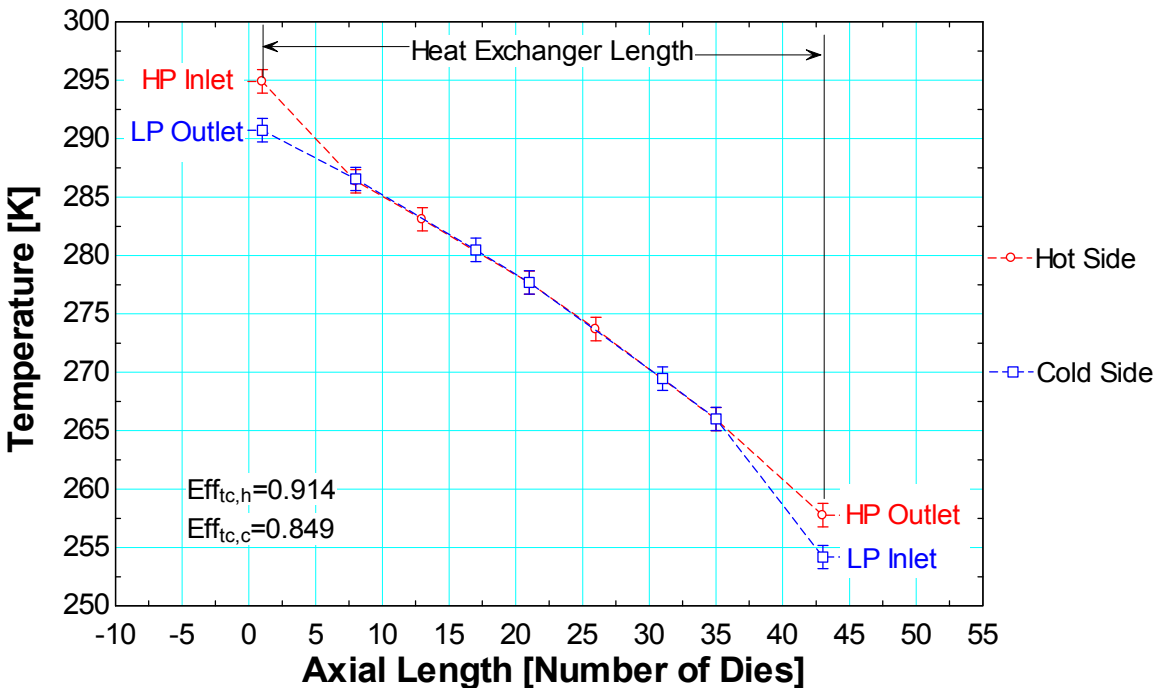

Fig. 6.6.9: Plot of the temperature distribution with the forty-three die 10 mm heat exchanger when tested with a 0.010" orifice for the data point with the maximum temperature difference. The inlet and outlet temperatures were measured with thermocouples built in to the cryogenic test facility. The temperatures within the heat exchanger were measured using the die PRTs. All of the die PRTs were located in the normal PRT position.

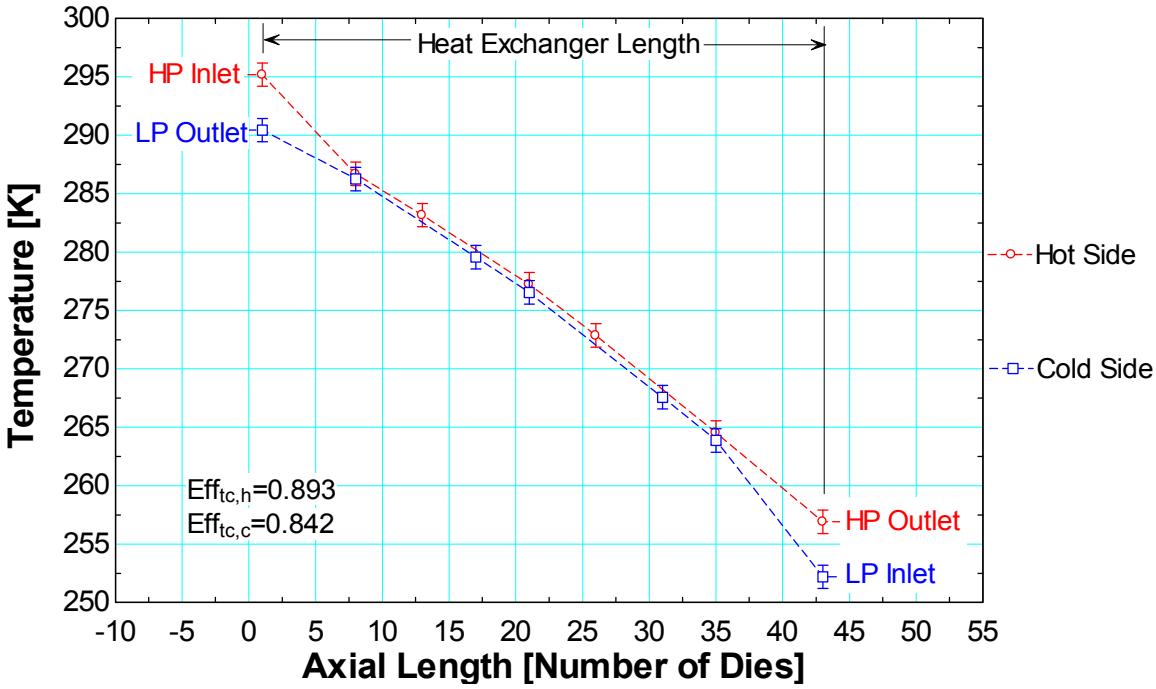

Fig. 6.6.10: Plot of the temperature distribution with the forty-three die 10 mm heat exchanger when tested with a 0.015" orifice for the data point with the maximum temperature difference. The inlet and outlet temperatures were measured with thermocouples built in to the cryogenic test facility. The temperatures within the heat exchanger were measured using the die PRTs. All of the die PRTs were located in the normal PRT position.

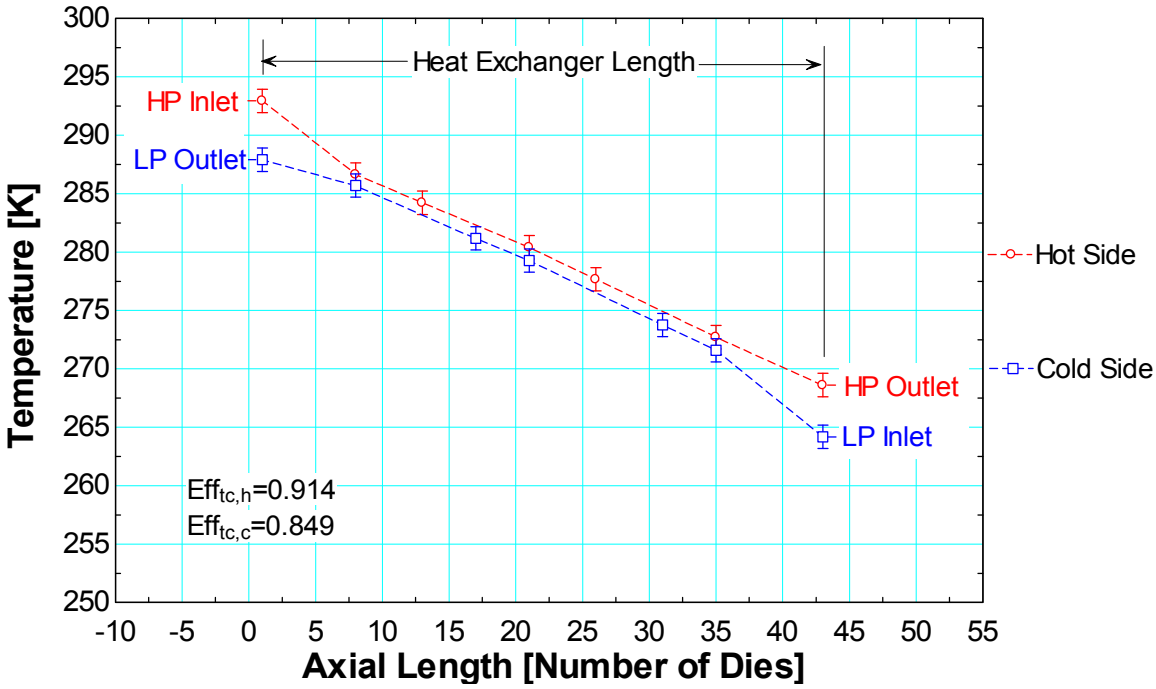

Fig. 6.6.11: Plot of the temperature distribution with the forty-three die 10 mm heat exchanger when tested with a 0.020" orifice for the data point with the maximum temperature difference. The inlet and outlet temperatures were measured with thermocouples built in to the cryogenic test facility. The temperatures within the heat exchanger were measured using the die PRTs. All of the die PRTs were located in the normal PRT position.

For cryosurgical applications it is important that the probe tip be able to reach cryogenic temperatures while absorbing a heat load. The setup in Fig. 6.5.3 was used to measure the performance of the forty-three die 10 mm heat exchanger under an applied load. The micro-valve in the fully open position was shown in Fig. 6.5.6 to provide nearly the optimal flow restriction. The heater shown in Fig. 6.5.3 was used to provide a range of applied heat loads to the cold end of the cycle and the changes in cycle temperatures were measured in order to produce a load curve.

The load curve for the forty-three die 10 mm heat exchanger is presented in Fig. 6.5.12. The temperature difference across the heat exchanger is nearly a linear function of the heat load supplied by the heater. The cycle operated with the micro-valve in the fully open position (-30 V). For the load curve tests, the warm inlet pressure was held at 535 kPa, the pressure difference across the heat exchanger assembly was held at 435 kPa, and the mass flow rate of ethane was 0.098 g/s. The location of all of the PRTs that are integrated with the heat exchanger is listed in Table O.1. The experimental data for the self-cooling tests in the cryogenic test facility are shown in Tables O.2 and O.3 and the calculations based on the experimental data are listed in Tables O.4 and O.5 of Appendix O.

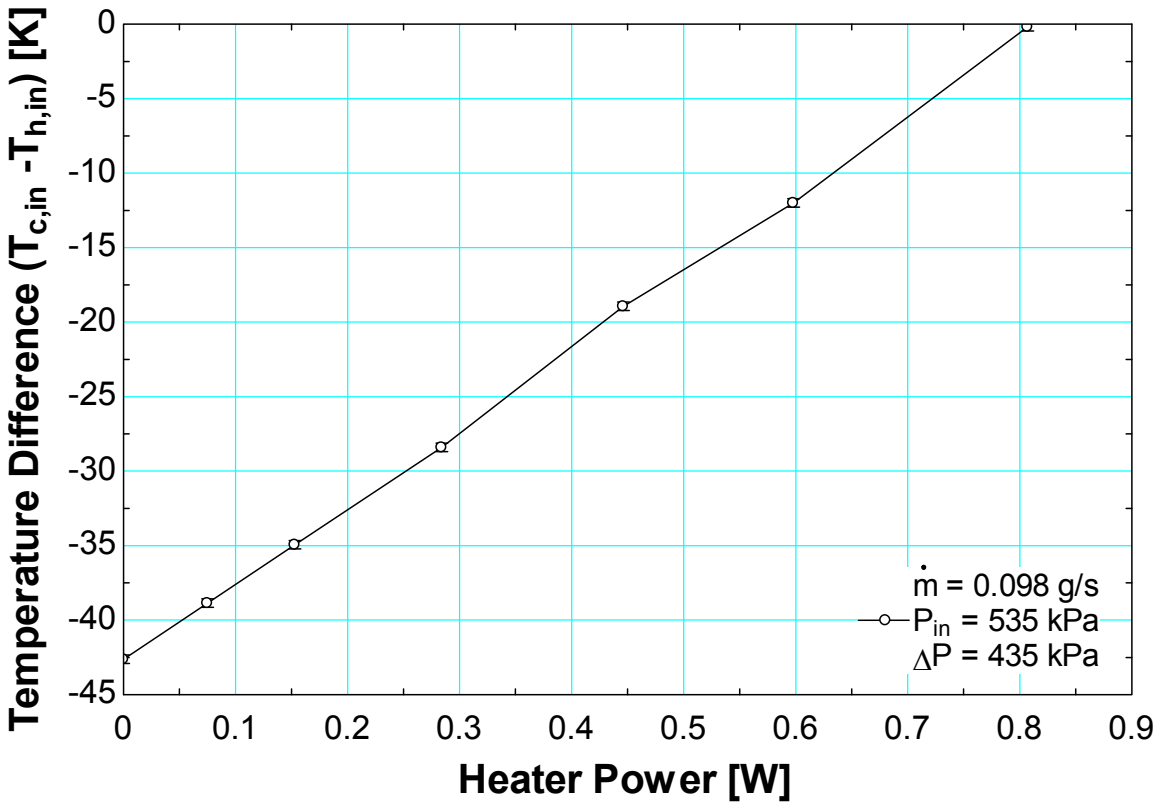

Fig. 6.6.12: Temperature difference across the heat exchanger ($T_{c,in} - T_{h,in}$) as a function of heater power. For the load curve tests the warm inlet pressure was held at 535 kPa, the pressure difference across the heat exchanger assembly was held at 435 kPa, and the mass flow rate of ethane was 0.098 g/s.

The effectiveness of the heat exchanger was nearly constant for most of the load curve tests. This is expected because the pressures and mass flow were both held nearly constant. The data point for a heater power of 0.8 W shows a drop in effectiveness, but the uncertainty is very large (greater than 1) due to the small temperature differences that characterize this data point. The difference between the effectiveness measurements on the hot stream and on the cold stream is likely due to conduction from the heater through the tube to the heat exchanger and temperature sensors. Parasitic heat loads from the environment are present for the 0 W heating load and these parasitics will tend to decrease as the heat exchanger cold end is warmed to near ambient temperature by increasing heater power. Notice that as the heater power increases, the difference between the hot and cold side effectiveness also increases. This observation suggests that the heater itself is responsible for the difference in measured effectiveness on the hot and cold sides of the heat exchanger, not a parasitic heat load.

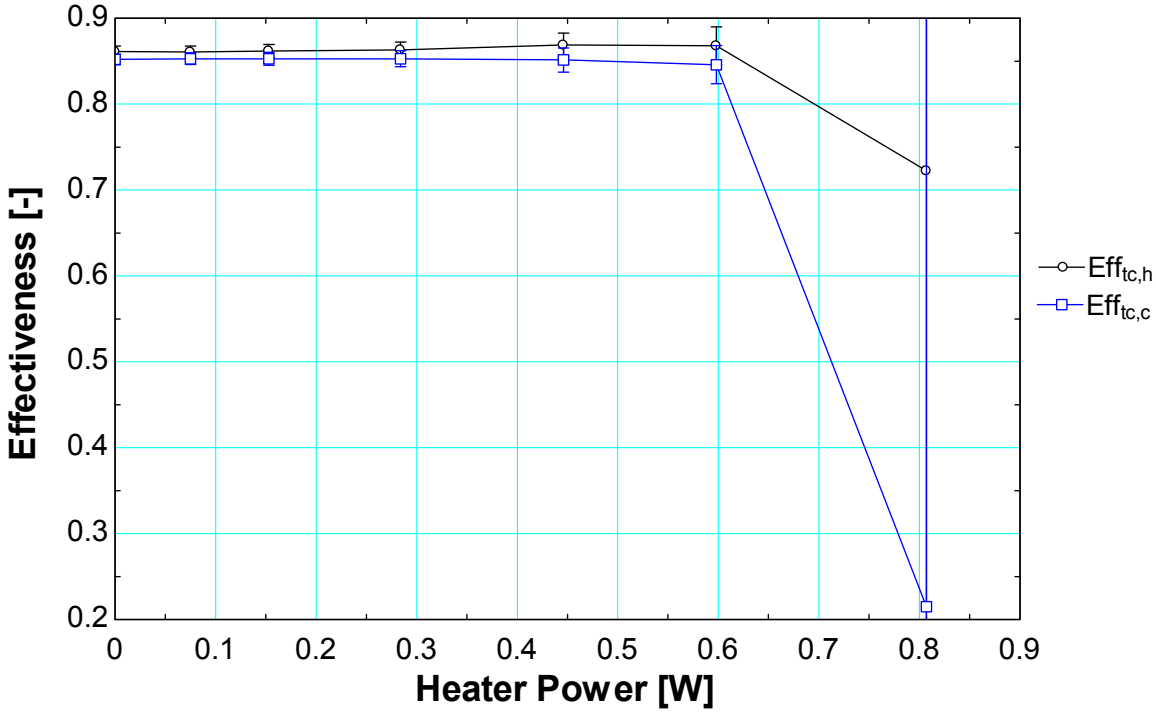

Fig. 6.6.13: Heat exchanger effectiveness as a function of heater power for the data shown in Fig. 6.5.12. The effectiveness is nearly constant until the heater power is equal to the isenthalpic pressure drop cooling power. The effectiveness at a heater power of 0.8 has an uncertainty of over 1 due to the small temperature differences across the heat exchanger.

6.7 Cryosurgical Probe Prototype Results

The cryosurgical probe was originally designed with the idea that the valve was likely to be too small to allow for the optimal operation of the J-T cycle. The cryosurgical probe was therefore designed so that an orifice and the micro-valve could be used in parallel. However, experimental testing on the valve suggests that when the valve is in the fully open position it has an effective orifice diameter that is very close to the optimum. Therefore, no tests were actually performed with the micro-valve and an orifice in parallel. The location and resistor type of all the integrated PRTs is shown in Table K.1. All of the experimental data is shown in Tables K.2-K.7 and all the calculated results are shown in Tables K.8-K.13 in Appendix K.

The cryosurgical probe prototype was tested with three different orifice diameters (0.010”, 0.013”, and 0.015”) and multiple applied voltages on the valve. As shown in Fig. 6.7.1, the temperature difference across the heat exchanger for a given pressure difference was much larger for the 0.013” diameter orifice than for the 0.010” orifice. However, there is almost no temperature difference increase between the 0.013” and the 0.015” orifice sizes, which suggests that optimal orifice is likely close to 0.015”. Had the optimal orifice size been significantly bigger than 0.015”, then the increase in performance associated with moving from the 0.013” to the 0.015” orifice should have been bigger. Another limitation was that this corresponded to the largest jewel orifice that was available at the time. Larger orifices were subsequently ordered for testing in the cryogenic testing facility.

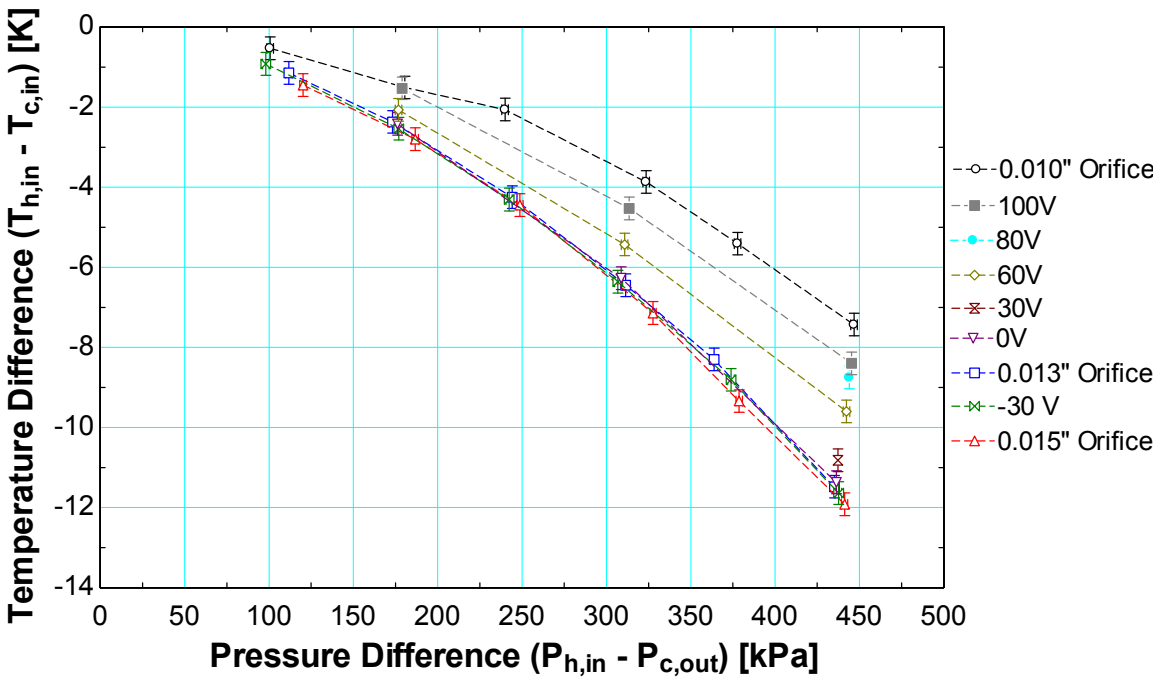

Fig. 6.7.1: Temperature difference between the heat exchanger inlet streams as a function of pressure difference applied across the forty-three die 10 mm heat exchanger assembly. The heat exchanger was tested in self-cooling mode with ethane as the working fluid.

The data shown in Fig. 6.7.1 was also used to determine the heat exchanger effectiveness as a function of mass flow rate; these results are shown in Fig. 6.7.2. All effectiveness calculations utilized the thermocouples inserted into the headers of the forty-three die 10 mm heat exchanger. The effectiveness of cooling the high pressure stream is shown in the top grouping of curves and the effectiveness of warming the low pressure stream in shown in the bottom grouping of curves for various orifice sizes and valve voltages. Error bars were plotted in Fig. 6.7.2 but the same data is shown without the error bars in Fig. 6.7.3 to make the plot less cluttered. As discussed in Chap. 3, measuring the effectiveness of a heat exchanger with small temperature difference leads to much larger uncertainties than measuring effectiveness with large temperature differences.

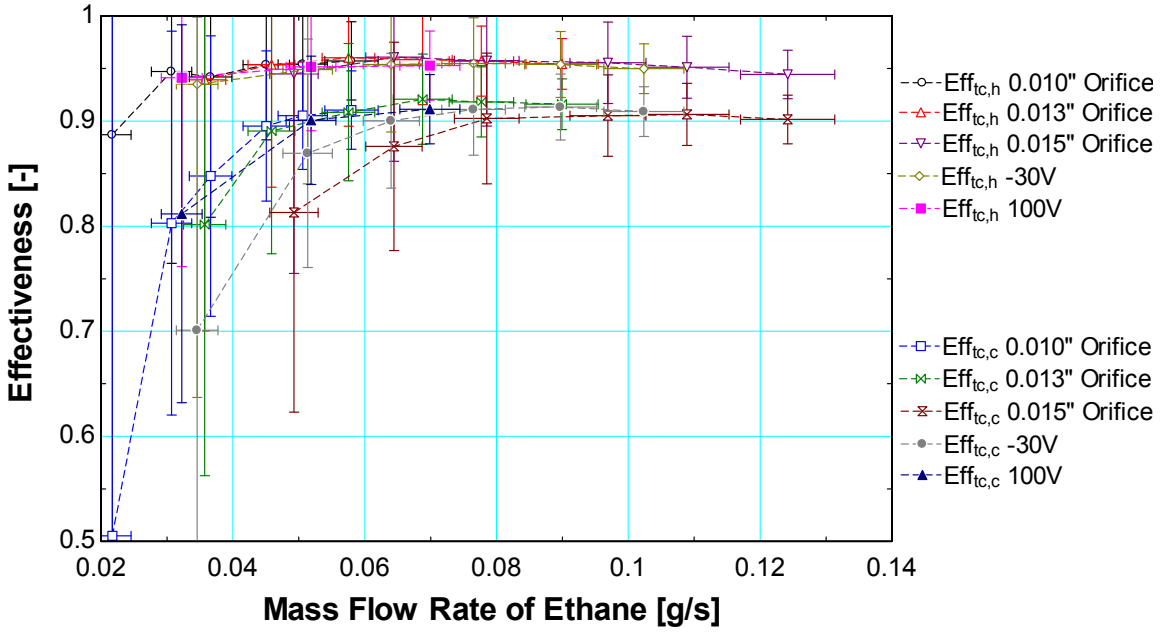

Fig. 6.7.2: Heat exchanger effectiveness as a function of mass flow rate for the data set shown in Fig. 6.7.1. All effectiveness calculations utilized the thermocouples inserted into the headers of the forty-three die 10 mm heat exchanger. The curves based on the effectiveness of cooling the high pressure stream are shown in the top group and the curves based on the effectiveness of heating the low pressure stream are shown in the bottom group.

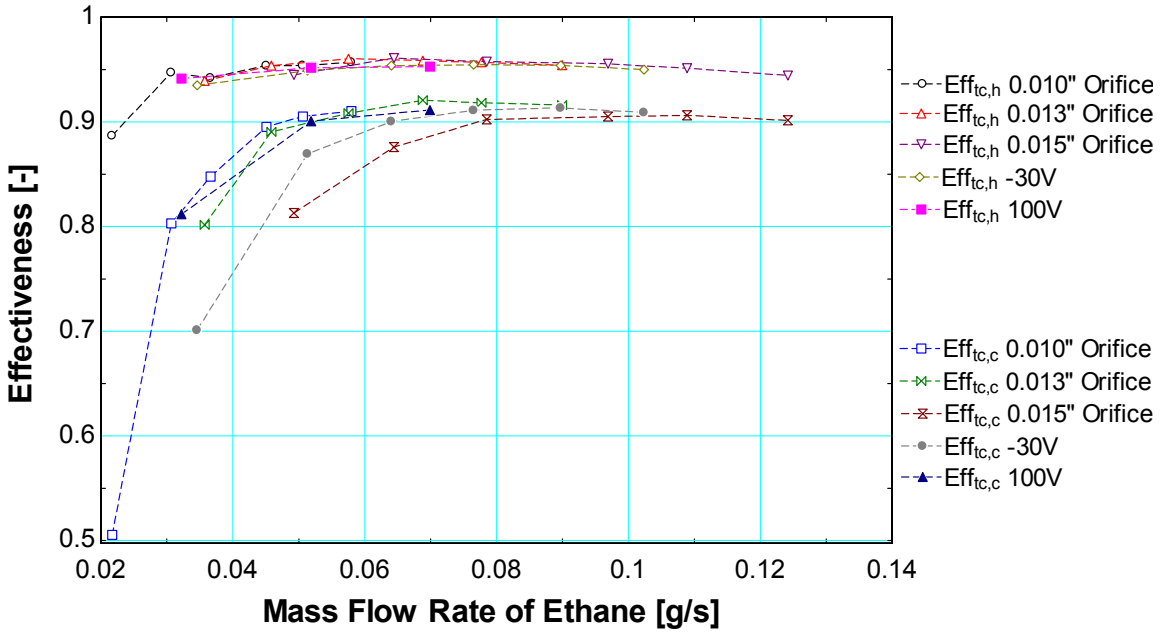

Fig. 6.7.3: Figure 6.7.2 re-plotted with out error bars for increased clarity

This was the first test performed on a heat exchanger with integrated PRTs. The test was done before the die PRTs had been calibrated, but the resistances were recorded so that they could be converted to temperatures at a later time. The plots presented in Figs. 6.7.4 to 6.7.6 show the

temperature distributions within the heat exchanger for various size orifices. The inlet and outlet temperatures of the heat exchanger were measured by thermocouples inserted directly into the headers. The internal temperatures were measured by the integrated PRTs. The internal PRTs were assumed to have an absolute uncertainty of ±1.0 K, which is slightly greater than maximum axial temperature difference across the heat exchanger during calibration for the points above 250 K.

All of the integrated PRTs were in the normal location with the exception of the data point labeled reference PRT. The reference PRT, which is located on the outer edge of the high pressure side of the heat exchanger, had a higher temperature reading than would be expected from the rest of the hot side temperature profile. The explanation for this higher reading is that the reference PRT measures the temperature of the silicon furthest from the heat exchanger wall separating the fluid streams, whereas the normal location PRT measures the average temperature of the fins. On the hot side of the heat exchanger, the reference PRTs are at a higher temperature than the normal location PRTs and on the cold side of the heat exchanger the reference location PRTs are colder than the normal location PRTS.

The plots shown in Figs. 6.7.4 through 6.7.6 show very similar trends. The reference location PRT shows a temperature that is higher than would be expected based on interpolating between the normal PRT measurements. All three plots show that there a temperature difference between the two fluid streams of approximately 3 K across the length of the heat exchanger. However, there is only a 1 K temperature difference between the streams at the heat exchanger headers. The discrepancy between the two measurement methods falls within the experimental uncertainty of the temperature measurements.

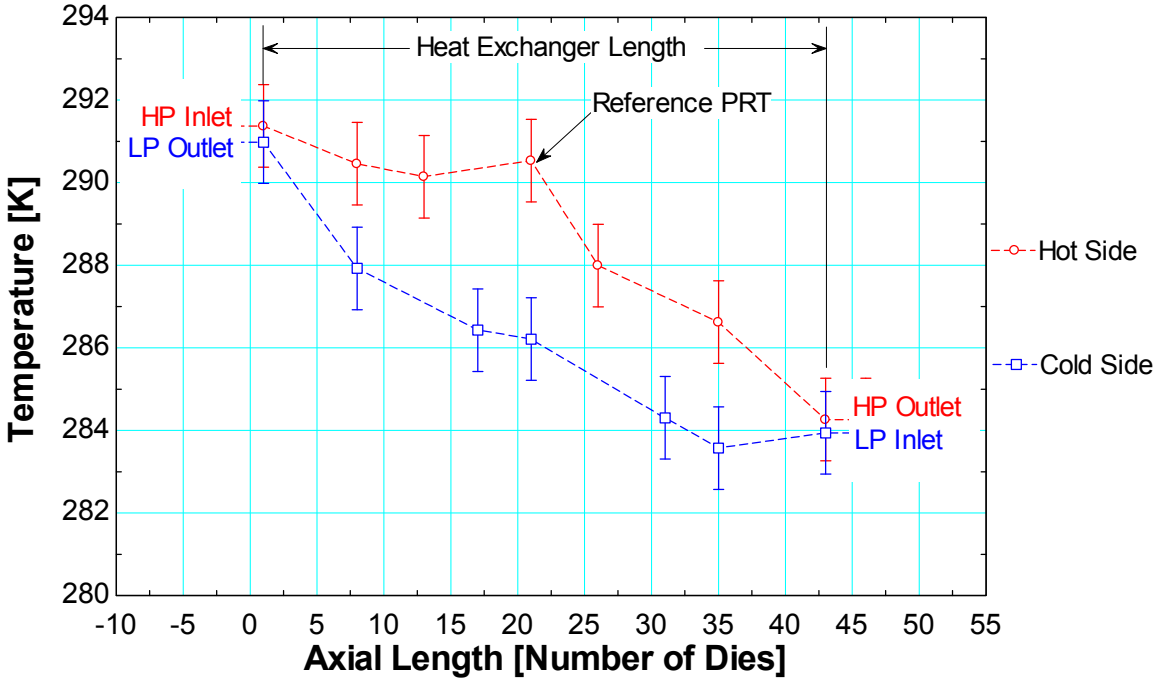

Fig. 6.7.4: Plot of the temperature distribution with the forty-three die 10 mm heat exchanger when tested with a 0.010" orifice for the data point with the maximum temperature difference. The inlet and outlet temperatures were measured with thermocouples inserted into the heat exchanger headers. The temperatures within the heat exchanger were measured using the die PRTs. All of the PRTs were located in the normal PRT position except for the point labeled "Reference PRT".

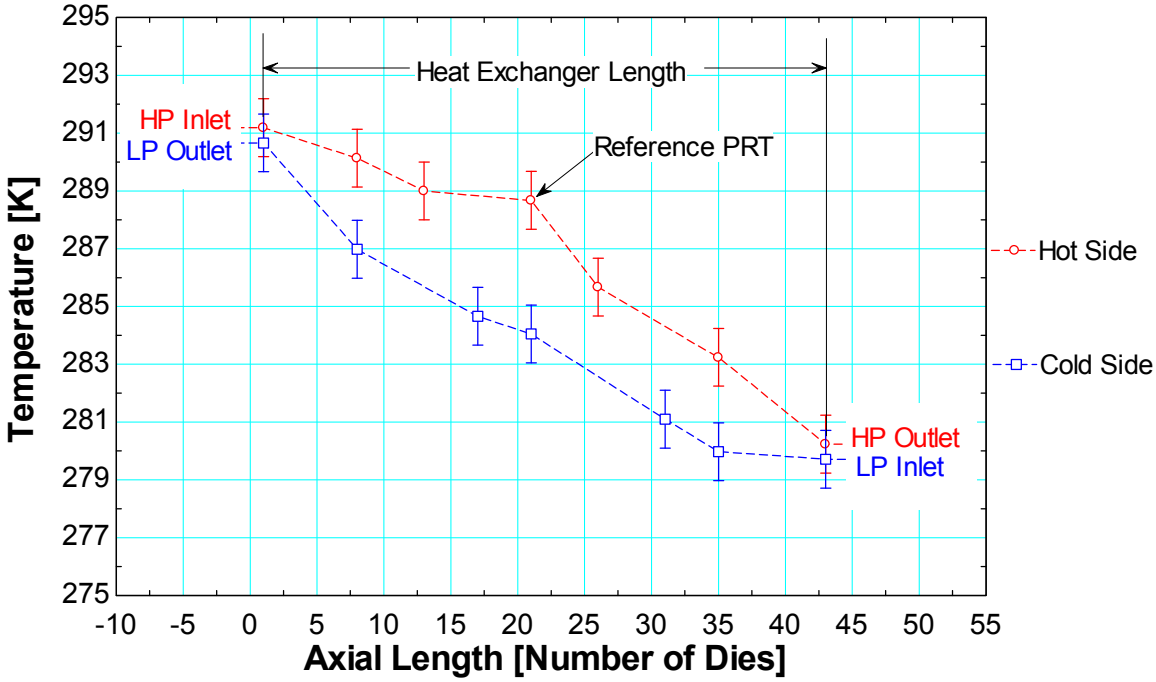

Fig. 6.7.5: Plot of the temperature distribution with the forty-three die 10 mm heat exchanger when tested with a 0.013" orifice for the data point with the maximum temperature difference. The inlet and outlet temperatures were measured with thermocouples inserted into the heat exchanger headers. The temperatures within the heat exchanger were measured using the die PRTs. All of the PRTs were located in the normal PRT position except for the point labeled "Reference PRT".

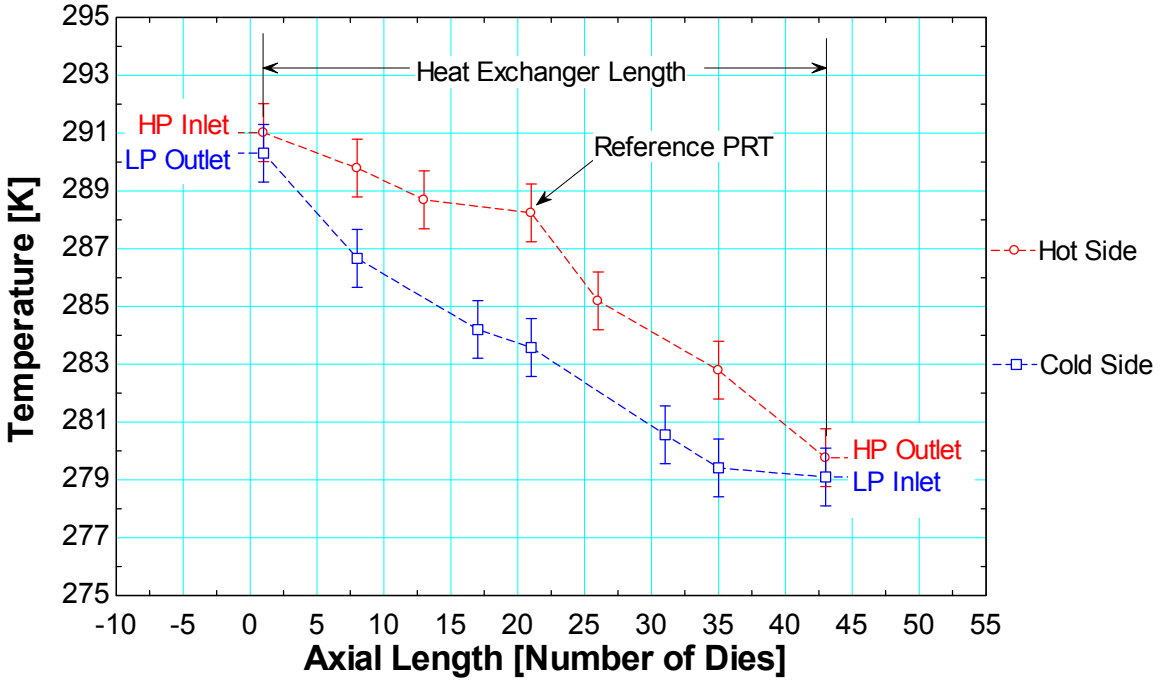

Fig. 6.7.6: Plot of the temperature distribution with the forty-three die 10 mm heat exchanger when tested with a 0.015" orifice for the data point with the maximum temperature difference. The inlet and outlet temperatures were measured with thermocouples inserted into the heat exchanger headers. The temperatures within the heat exchanger were measured using the die PRTs. All of the PRTs were located in the normal PRT position except for the point labeled "Reference PRT".

References

1. Dobak, J., "A Review of Cryobiology and Cryosurgery," *Advances in Cryogenic Engineering*, Vol. 43 (1998), pp. 889-896
2. University of Wisconsin-Madison General Surgery Website, http://www.surgery.wisc.edu/general/patients/uwmhpscryo.shtml
3. Fredrickson, K.L, *Optimization of Cryosurgical Probes for Cancer Treatment*, M.S. Thesis, University of Wisconsin-Madison (2004), http://sel.me.wisc.edu/publications/theses/theses2.html
4. Frank, M..T., *Recuperative Heat Exchanger for a MEMS Cryoprobe*, M.S. Thesis, University of Wisconsin-Madison (2004), http://sel.me.wisc.edu/publications/theses/theses2.html
5. Hoch, D.W. et al., "Progress Towards a Micromachined Heat Exchanger for a Cryosurgical Probe", *Cryocoolers 14*, Annapolis, Maryland (2006), pp. 505-514
6. Zhu, W. et al., "A Planar Glass/Si Micromachining Process for the Heat Exchanger in a J-T Cryosurgical Probe", *Proc. Solid State Sensors, Actuators and Microsystems*, Hilton Head (2006), pp. 51-55
7. Zhu, W. et al., "Two Approaches to Micromachining Si Heat Exchangers for Joule-Thomson Cryosurgical Probes", *Proc. IEEE MEMS*, Kobe, Japan (2007), pp. 317-320.
8. Lakeshore Cryotronics Inc., Temperature and Measurement Control Catalog, http://www.lakeshore.com/temp/acc/am_wirets.html.
9. Brosten, T.R., *Model and Test of an Actively Controlled Cryogenic Micro Valve*, M.S. Thesis, University of Wisconsin-Madison, 2006.
10. Incropera, F.P., and DeWitt, D.P., *Fundamentals of Heat and Mass Transfer*, Fourth edition, John Wiley and Sons, New York, 2002
11. Taylor, B.N., and Kuyatt, C.E., *Guidelines for Evaluating and Expressing the Uncertainty of NIST Measurement Results*, National Institute of Standards and Technology Technical Note 1297, 1994
12. Huges, C., *Experimental Measurement of Heat Transfer Coefficients for Mixed Gas Working Fluids in Joule-Thomson Systems*, M.S. Thesis, University of Wisconsin-Madison, 2004.
13. Nellis, G.F., "A Heat Exchanger Model that Includes Axial Conduction, Parasitic Heat Loads, and Property Variations", *Cryogenics* 43(2003), pp. 523-538.
14. Kroeger, P.G., "Performance Deterioration in High Effectiveness Heat Exchangers due to Axial Heat Conduction Effects", *Advances in Cryogenic Engineering*, Vol. 12 (1967), pp. 363-372
15. Chowdhury, K., and Sarangi, S., "Performance of cryogenic heat exchangers with heat leak from the surroundings", *Advances in Cryogenic Engineering*, Vol. 29 (1984), pp.273-280.
16. Barron, R.F., "Effect of heat transfer from ambient on cryogenic heat exchanger performance", *Advances in Cryogenic Engineering*, Vol. 29 (1984), pp.273-280.
17. Engineering Equation Solver (EES), www.fchart.com, Version 8.120 (05/07/08)
18. Shah, R.K., and London, A.L., "Laminar Flow Forced Convection in Ducts", Academic Press, 1978
19. Cryogenic Material Properties Database, *Cryogenic Technologies Group of the National Institute of Standards and Technology (NIST)*, http://cryogenics.nist.gov/MPropsMAY/material%20properties.htm
20. "Thermophysical Properties of Matter Vol. 1: Thermal Conductivity Metallic Elements and

Alloys", edited by Touloukian et. al., IFI/Plenum, 1970

21. Cryocomp 2.0, Cryodata Inc., www.cryodata.com
22. "Properties of Crystalline Silicon", 2nd edition, edited by Robert Hull et al., Institution of Electrical Engineers, London, UK, 1999
23. McKurdy, A.K., Maris, H.J., Elbaum, C. "Anisotropic Heat Conduction in Cubic Crystals in the Boundary Scattering Regime", Physical Review B, Vol. 2, Num. 10, 1970
24. Hurst, W.S., and Frankl, D.R., "Thermal Conductivity of Silicon in the Boundary Scattering Regime", Physical Review, Vol. 186, Num. 3, 1969
25. Liu, C. "Foundations of MEMS", Pearson Prentice Hall, 2006
26. Schott North America Website, Borofloat Product Properties, http://www.us.schott.com/hometech/english/download/thermal_conduct.pdf
27. Kakac, S., Shah, R.K., Aung, W., "Handbook of Single-Phase Convective Heat Transfer", John Wiley & Sons, 1987
28. Fox, R.W, and McDonald, A.T., "Introduction to Fluid Mechanics", 5th edition, John Wiley & Sons, 1998
29. Incropera, F.P., and DeWitt, D.P., "Fundamentals of Heat and Mass Transfer", 5th edition, John Wiley & Sons, 2002
30. Rosenhow, W.M. et al., "Handbook of Heat Transfer", 3rd edition, McGraw-Hill, 1998
31. Nellis, G.F., Klein, S.A., "Approximate Solution for Rectangular Fins in Contact with Flowing Fluid", UW-Madison Internal Technical Report, 2006
32. Barron, R.F., "Cryogenic Heat Transfer", Taylor & Francis, 1999
33. Nellis, G.F., Klein, S.A., "Heat Transfer Book Info ????????

Appendix A: Experimental Uncertainty Review

The purpose of these appendices is to archive all of the experimental data that were collected over the course of the project. The tables that contain these data are too long to include in the main body of the thesis, but the raw experimental data may be valuable to others working on MEMS heat exchangers. The analysis of this data is discussed in Chapter 6 where it is also compared with the design model predictions. Only the experimental data and model results will be provided in these appendices. Common abbreviations that are used in tables and figures are listed in Table A.1.

Table A.1: Common abbreviations used in tables and figures in the appendices

Abbreviation	Definition
PRT	Platinum Reistance Thermometer
TC	Thermocouple
H	Hot side
C	Cold side of heat exchanger
HP	High pressure side of heat exchanger
LP	Low pressure side of heat exchanger
U	Uncertainty
Eff	Effectiveness
MLI	Multi-Layer Insulation

Appendix A provides a review of the methods used to determine experimental uncertainties. Additional details are covered in Chapter 3. The review covers the equations used to estimate the uncertainty in the temperature, mass flow rate, and pressure measurements and concludes with the details of the heat exchanger effectiveness uncertainty calculation.

The PRTs were all calibrated by the manufacturer with the exception of the PRT used to measure the cryocooler temperature, which was taken from an old experimental apparatus in the laboratory. The cryocooler PRT was not labeled with a serial number and therefore could not be linked to any calibration. The temperature of the cryocooler was not used for any calculations and therefore a high degree of accuracy was not required. The cryocooler PRT was assumed to have a temperature dependent resistance that was the average of the four calibrated PRTs. The resistances for each PRT as a function of temperature are shown in Table A.2. The uncertainty of the calibrated PRTs is ±0.25 K.

An Agilent 34970A multiplexer with an internal thermistor was used to measure the thermocouple voltage and convert these measurements to temperature. The absolute uncertainty of the thermocouples is assumed to be 1.0 K. However, the thermocouples were all fabricated from the same spool of thermocouple wire. Therefore, they should all have nearly identical bias (absolute errors). Thus, the thermocouples should be capable of making much more accurate temperature differential measurements than absolute temperature measurements. This capability was verified by placing all of the thermocouples into an ice bath and observing that they all read between -0.3 °C and -0.1 °C. Therefore, whenever an absolute temperature measurement is

shown within the appendices, a ±1.0 K measurement uncertainty is assigned to it whereas whenever a differential temperature measurement is shown a measurement uncertainty of ±0.2 K is assigned to it.

The mass flow meter used in the test facility has a voltage output of 0 to 5 V corresponding to a range of flow rates from 0 to 100 standard liters/min of nitrogen. The mass flow meter manufacturer recommends using Eq. A.1 to determine the mass flow rate ($\dot{m}$) based on output voltage (V_{signal}).

$$\dot{m} = V_{signal}\ K\ C_{convert} \tag{A.1}$$

where $\dot{m}$ is the mass flow rate of the fluid in standard liters per minute, K is the conversion factor from voltage to flow rate (100 standard liters per minute divided by 5 volts), and $C_{convert}$ is the conversion factor used when operating the flow meter for fluids, temperatures, and pressures other than the calibration conditions. The conversion factor can be calculated by Eq. A.2.

$$C_{convert} = \frac{Cp_1\ \rho_1}{Cp_2\ \rho_2} \tag{A.2}$$

where Cp_1 is the specific heat of nitrogen evaluated at 400 bar and 70°C (the calibration temperature plus 50°C), ρ_1 is the density of nitrogen evaluated at 20°C and 101.325 kPa, Cp_2 is the specific heat of the test fluid evaluated at the inlet pressure and inlet temperature plus 50°C, and ρ_2 is the density of the test fluid evaluated at 20°C and 101.325 kPa. The mass flow meter is calibrated for nitrogen at 400 bar absolute and 20°C. The reason that the specific heat capacities are evaluated at 50°C higher than the average fluid temperature is because of the heater in the capillary tube raises the fluid temperature. The 50°C is used so that the specific heat is evaluated at the average fluid temperature in the capillary tube. The percent error associated with the conversion factor is shown by Eq. A.3:

$$U_{convert} = (2\%) \cdot C_{convert} \quad \text{if } C_{convert} > 1$$

$$U_{convert} = \frac{(2\%)}{C_{convert}} \quad \text{if } C_{convert} < 1 \tag{A.3}$$

To calculate the total uncertainty of the mass flow rate it is necessary to calculate the partial derivative of the mass flow rate with respect to the conversion factor, as shown in Eq. A.4:

$$\frac{\partial \dot{m}}{\partial C_{convert}} = V_{signal}\ K \tag{A.4}$$

The mass flow sensor has been calibrated to within ±0.2% of the full scale mass flow rate ($\dot{m}_{max}$) under calibration conditions. The uncertainty due to the calibration error (U_{calib}) can be calculated using Eq. A.5:

$$U_{calib} = 0.002\ \dot{m}_{max} \tag{A.5}$$

The total uncertainty in the mass flow rate ($U_{\dot{m},tot}$), since the uncertainties are uncorrelated and random, can then be calculated using Eq. A.6 [11]:

$$U_{\dot{m},tot} = \sqrt{\left(U_{calib}\right)^2 + \left(\frac{\partial m}{\partial C_{convert}}\right)^2 \left(U_{convert}\right)^2} \tag{A.6}$$

Note that there is no partial derivative associated with the calibration uncertainty term because the calibration uncertainty is constant.

Four different pressure sensors were used. Each of these sensors has ±0.11% full scale uncertainty. A pressure sensor capable of measuring 0-250 psia with a 0-5 VDC readout was always used to measure the hot inlet pressure of the heat exchanger. The pressure transducer used to measure the high pressure side differential pressure was a 0-5 psid with a 0-5 VDC output. The results from this pressure sensor are seldom used because the pressure differences were often too high for the pressure transducer to measure. A third pressure transducer with a ± 25 psid range and ± 2.5 VDC output was used; this transducer was sometimes used to measure the differential pressure across the low pressure side of the heat exchanger and sometimes used to measuring the gauge pressure at the low pressure outlet. When the third pressure transducer was used to measure the gauge pressure at the low pressure outlet, a mercury barometer was used to measure atmospheric pressure so that an absolute pressure could be calculated. The mercury barometer had a resolution of 0.1 mm Hg and was assumed to have an uncertainty of 1 mm Hg because no information on the uncertainty of the barometer could be found. The ability of these three transducers to measure pressures or pressure differences accurately was verified using mechanical pressure gauges. The fourth pressure transducer that was intended to be used to measure the cold side outlet pressure was found to functioning improperly and therefore was not used.

A pressure difference (ΔP) can be calculated using Eq. A.7:

$$\Delta P = P_1 - P_2 \tag{A.7}$$

where P_1 and P_2 are the pressures of interest. The square of both partial derivatives of ΔP (with respect to P_1 and P_2) are equal to one; therefore the uncertainty of a pressure difference can be calculated using Eq. A.8:

$$U_{\Delta P} = \sqrt{\left(U_{P1}\right)^2 + \left(U_{P2}\right)^2} \tag{A.8}$$

As shown in Chap. 3, the heat exchanger effectiveness can be calculated using Eq. A.9.

$$\varepsilon = \frac{\dot{q}_{act}}{\dot{q}_{\max}} = \frac{\dot{C}_h (T_{h,in} - T_{h,out})}{\dot{C}_{min} (T_{h,in} - T_{c,in})} \tag{A.9}$$

where ε is the heat exchanger effectiveness, $\dot{q}_{act}$ is the actual amount of heat transferred in the heat exchanger, $\dot{q}_{max}$ is the maximum possible heat transfer rate in the heat exchanger, $\dot{C}_h$ is the hot fluid capacity rate, $\dot{C}_{min}$ is the minimum capacity rate of the two fluids, $T_{h,in}$ is the inlet temperature of the hot fluid, $T_{h,out}$ is the outlet temperature of the hot fluid, and $T_{c,in}$ is the inlet temperature of the cold fluid. The capacity rate for a fluid is defined as the product of its mass flow rate and the specific heat at constant pressure.

The heat exchanger effectiveness is a function of three different temperatures and each of the temperature measurements has an uncertainty associated with it. The sensitivity of heat exchanger effectiveness to changes in temperature can be found by taking the partial derivative of Eq. A.9 with respect to each of the individual fluid temperatures, which yields Eqs. A.10-A.12:

$$\frac{\partial \varepsilon}{\partial T_{h,in}} = \frac{\dot{C}_h}{\dot{C}_{min} (T_{h,in} - T_{c,in})} - \frac{\dot{C}_h (T_{h,in} - T_{h,out})}{\dot{C}_{min} (T_{h,in} - T_{c,in})^2} \tag{A.10}$$

$$\frac{\partial \varepsilon}{\partial T_{h,out}} = -\frac{\dot{C}_h}{\dot{C}_{min} (T_{h,in} - T_{c,in})} \tag{A.11}$$

$$\frac{\partial \varepsilon}{\partial T_{c,in}} = \frac{\dot{C}_h (T_{h,in} - T_{h,out})}{\dot{C}_{min} (T_{h,in} - T_{c,in})^2} \tag{A.12}$$

As the temperature difference between the two fluid inlet temperatures increases, each of the partial derivatives shown in Eq. A.10-A.12 decreases. Therefore, the sensitivity of the effectiveness to changes in measured fluid temperature decreases with larger temperature differences across the heat exchanger. If the measurement uncertainties are random and uncorrelated, the total uncertainty in heat exchanger effectiveness can be calculated using Eq. A.13:

$$U_\varepsilon = \sqrt{\left(\frac{\partial \varepsilon}{\partial T_{h,in}}\right)^2 \left(U_{T_{h,in}}\right)^2 + \left(\frac{\partial \varepsilon}{\partial T_{h,out}}\right)^2 \left(U_{T_{h,out}}\right)^2 + \left(\frac{\partial \varepsilon}{\partial T_{c,in}}\right)^2 \left(U_{T_{c,in}}\right)^2} \tag{A.13}$$

Where U_ε is the total uncertainty in heat exchanger effectiveness and $U_{Th,in}$, $U_{Th,out}$, and U_{Tcin} are the temperature measurement uncertainties of the hot inlet, hot outlet, and cold inlet fluid streams respectively.

Table A.2: Table of PRT resistances as a function of temperature. Calibration was performed by the PRT manufacturer for all PRTs except the one mounted to the cryocooler which is uncalibrated.

	PRTs				
Location:	HP Inlet	HP Outlet	LP Inlet	LP Outlet	Cryocooler
Serial #:	P13053	P12971	P13054	P12972	Unknown
T [K]	R_{HPIN} [kΩ]	R_{HPOUT} [kΩ]	R_{LPIN} [kΩ]	R_{LPOUT} [kΩ]	R_{cc} [kΩ]
70	16.90581	16.90104	16.90415	16.90576	16.90419
75	19.07889	19.07130	19.08293	19.07873	19.07796
80	21.24260	21.23229	21.25216	21.24235	21.24235
85	23.39722	23.38428	23.41214	23.39688	23.39763
90	25.54304	25.52756	25.56314	25.54262	25.54409
95	27.68033	27.66239	27.70543	27.67982	27.68199
100	29.80935	29.78904	29.83930	29.80876	29.81161
105	31.93037	31.90776	31.96499	31.92970	31.93321
110	34.04364	34.01882	34.08277	34.04289	34.04703
115	36.14940	36.12245	36.19288	36.14857	36.15333
120	38.24789	38.21890	38.29566	38.24700	38.25236
125	40.33935	40.30839	40.39105	40.33839	40.34430
130	42.42400	42.39115	42.47958	42.22970	42.38111
135	44.50207	44.46741	44.56137	44.50098	44.50796
140	46.57377	46.53737	46.63664	46.57262	46.58010
145	48.63930	48.60125	48.70560	48.63809	48.64606
150	50.69887	50.65924	50.76844	50.69671	50.70582
155	52.75267	52.71153	52.82537	52.75136	52.76023
160	54.80090	54.75832	54.87657	54.79954	54.80883
165	56.84373	56.79979	56.92223	56.84231	56.85202
170	58.88133	58.83610	58.96252	58.87987	58.88996
175	60.91388	60.86743	60.99762	60.91238	60.92283
180	62.94154	62.89394	63.02768	62.94000	62.95079
185	64.96446	64.91579	65.05287	64.96288	64.97400
190	66.98280	66.93312	67.07333	66.98118	66.99261
195	68.99669	68.94608	69.08921	68.99504	69.00676
200	71.00627	70.95480	71.10065	71.00460	71.01658
205	73.01168	72.95941	73.10777	73.00998	73.02221
210	75.01304	74.96003	75.11071	75.01131	75.02377
215	77.01046	76.95679	77.10958	77.00871	77.02139
220	79.00405	78.94979	79.10448	79.00228	79.01515
225	80.99392	80.93914	81.09554	80.99213	81.00518
230	82.98017	82.92492	83.08283	82.97836	82.99157
235	84.96259	84.90724	85.06647	84.96106	84.97434
240	86.94216	86.88618	87.04652	86.94032	86.95380

Table A.2: (continued)

	PRTs				
Location:	HP Inlet	HP Outlet	LP Inlet	LP Outlet	Cryocooler
Serial #:	P13053	P12971	P13054	P12972	Unknown
T [K]	R_{HPIN} [Ω]	R_{HPOUT} [Ω]	R_{LPIN} [Ω]	R_{LPOUT} [Ω]	R_{cc} [Ω]
245	88.91806	88.86182	89.02308	88.91621	88.92979
250	90.89066	90.83423	90.99621	90.88881	90.90248
255	92.86003	92.80346	92.96598	92.85817	92.87191
260	94.82623	94.76959	94.93245	94.82437	94.83816
265	96.78931	96.73267	96.89567	96.78744	96.80127
270	98.74932	98.69273	98.85569	98.74745	98.76130
275	100.70629	100.64983	100.81256	100.70443	100.71828
280	102.66025	102.60397	102.76628	102.65839	102.67222
285	104.61120	104.55517	104.71687	104.60935	104.62315
290	106.55913	106.50343	106.66433	106.55729	106.57105
295	108.50406	108.44873	108.60865	108.50223	108.51592
300	110.44598	110.39109	110.54983	110.44417	110.45777
305	112.38490	112.33050	112.48789	112.38310	112.39660
310	114.32080	114.26696	114.42282	114.31902	114.33240
315	116.25369	116.20048	116.35462	116.25193	116.26518
320	118.18358	118.13105	118.28328	118.18184	118.19494
325	120.11046	120.05868	120.20883	120.10875	120.12168
330	122.03434	121.98336	122.13124	122.03265	122.04540
335	123.95521	123.90509	124.05053	123.95354	123.96609
340	125.87307	125.82388	125.96669	125.87144	125.88377
345	127.78793	127.73973	127.87974	127.78633	127.79843
350	129.69978	129.65263	129.78966	129.69822	129.71007
355	131.60863	131.56258	131.69645	131.60710	131.61869
360	133.51448	133.46959	133.60013	133.51299	133.52430
365	135.41732	135.37365	135.50069	135.41587	135.42688
370	137.31716	137.27477	137.39813	137.31575	137.32645
375	139.21400	139.17295	139.29245	139.21263	139.22301
380	141.10784	141.06818	141.18366	141.10652	141.11655
385	142.99867	142.96047	143.07175	142.99740	143.00707
390	144.88651	144.84982	144.95673	144.88528	144.89459
395	146.77134	146.73622	146.83859	146.77017	146.77908
400	148.65317	148.61968	148.71734	148.65206	148.66056
405	150.53201	150.50020	150.59298	150.53095	150.53904
410	152.40784	152.37777	152.46551	152.40684	152.41449
415	154.28068	154.25240	154.33493	154.27974	154.28694

Table A.2: (continued)

	PRTs				
Location:	HP Inlet	HP Outlet	LP Inlet	LP Outlet	Cryocooler
Serial #:	P13053	P12971	P13054	P12972	Unknown
T [K]	R_{HPIN} [Ω]	R_{HPOUT} [Ω]	R_{LPIN} [Ω]	R_{LPOUT} [Ω]	R_{cc} [Ω]
420	156.15052	156.12409	156.20125	156.14964	156.15638
425	158.01736	157.99284	158.06445	158.01654	158.02280
430	159.88121	159.85864	159.92455	159.88045	159.88621
435	161.74205	161.72150	161.78154	161.74137	161.74662
440	163.59991	163.58142	163.63543	163.59929	163.60401
445	165.45476	165.43840	165.48622	165.45422	165.45840
450	167.30662	167.29244	167.33390	167.30615	167.30978
455	169.15549	169.14353	169.17848	169.15509	169.15815
460	171.00136	170.99169	171.01996	171.00103	171.00351
465	172.84423	172.83690	172.85835	172.84399	172.84587
470	174.68412	174.67918	174.69363	174.68395	174.68522
475	176.52101	176.51851	176.52582	176.52092	176.52157
480	178.35490	178.35490	178.35490	178.35490	178.35490

Appendix B: Sixteen Die 10 mm Heat Exchanger External Cooling Results

Table B.1: Experimental temperature measurements for the sixteen die 10 mm heat exchanger operating in external cooling mode with helium as the working fluid

Run #	TC HP IN [K]	TC HP OUT [K]	TC LP IN [K]	TC LP OUT [K]	PRT HP IN [V]	PRT HP OUT [V]	PRT LP IN [V]	PRT LP OUT [V]	PRT CC [V]
1	291.87	186.93	130.97	253.26	0.10673	0.06534	0.04138	0.09202	0.02940
2	296.13	169.87	125.40	260.09	0.10945	0.05881	0.03975	0.09475	0.03376
3	300.27	225.44	202.24	280.54	0.11031	0.08110	0.07188	0.10318	0.06861
4	300.55	225.98	204.95	282.15	0.11080	0.08134	0.07274	0.10389	0.07047
5	300.09	229.10	204.97	280.63	0.11080	0.08242	0.07275	0.10291	0.06892
6	300.52	229.39	203.93	280.17	0.11074	0.08279	0.07227	0.10313	0.06813
7	300.77	230.81	203.84	279.57	0.11058	0.08333	0.07236	0.10296	0.06742
8	299.95	219.60	196.66	280.22	0.11036	0.07851	0.06969	0.10275	0.06684
9	300.27	220.45	198.69	280.88	0.11085	0.07895	0.07025	0.10302	0.06828
10	300.11	224.33	203.63	281.20	0.11036	0.08073	0.07235	0.10345	0.07064
11	300.52	227.44	207.23	281.86	0.11058	0.08199	0.07378	0.10378	0.07233

Table B.2: Experimental measurements of the mass flow rate and pressures for the sixteen die 10 mm heat exchanger operating in external cooling mode with helium as the working fluid.

Run #	Mass Flow Rate [V]	HP IN Press [V]	HP DIFF Press [V]	LP DIFF Press [V]
1	0.078	0.34903	0.79173	0.08113
2	0.142	0.50368	7.21321	0.19167
3	0.213	0.48153	2.11545	0.40756
4	0.294	0.55724	2.92514	0.66129
5	0.184	0.44944	1.81215	0.32695
6	0.164	0.43187	1.62320	0.27473
7	0.141	0.41158	1.33406	0.21784
8	0.281	0.53995	2.78193	0.61609
9	0.355	0.61517	3.35150	0.87794
10	0.440	0.70682	3.94992	1.20883
11	0.480	0.75349	4.31638	1.37926

Table B.3: Calculation of heat exchanger effectiveness based on the experimental measurements shown in Table B.1

Run	Hot Side		Cold Side		Uncertainty	
	TC [-]	PRT [-]	TC [-]	PRT [-]	TC [-]	PRT [-]
1	0.652	0.640	0.760	0.770	0.00155	0.00190
2	0.740	0.733	0.789	0.784	0.00149	0.00182
3	0.763	0.760	0.799	0.813	0.00261	0.00327
4	0.780	0.774	0.807	0.816	0.00269	0.00332
5	0.746	0.746	0.795	0.791	0.00268	0.00329
6	0.737	0.727	0.789	0.800	0.00263	0.00323
7	0.722	0.713	0.781	0.799	0.00261	0.00324
8	0.778	0.783	0.809	0.810	0.00249	0.00312
9	0.786	0.786	0.809	0.805	0.00254	0.00313
10	0.786	0.779	0.804	0.816	0.00267	0.00333
11	0.783	0.776	0.800	0.813	0.00276	0.00343

Table B.4: Calculation of mass flow rate and pressures based on the experimental data shown in Table B.2.

Run	Mass Flow Rate		Pressures					
			HP IN		HP Diff		LP Diff	
	Value [g/s]	Uncertainty [g/s]	Value [kPa]	Uncertainty [kPa]	Value [kPa]	Uncertainty [kPa]	Value [kPa]	Uncertainty [kPa]
1	0.0076	0.00098	120.3	1.90	5.5	0.04	5.6	0.19
2	0.0137	0.00101	173.6	1.90	49.7	0.04	13.2	0.19
3	0.0207	0.00106	166	1.90	14.6	0.04	28.1	0.19
4	0.0285	0.00113	192.1	1.90	20.2	0.04	45.6	0.19
5	0.0179	0.00103	154.9	1.90	12.5	0.04	22.5	0.19
6	0.0159	0.00102	148.9	1.90	11.2	0.04	18.9	0.19
7	0.0137	0.00101	141.9	1.90	9.2	0.04	15.0	0.19
8	0.0272	0.00111	186.1	1.90	19.2	0.04	42.5	0.19
9	0.0345	0.00119	212.1	1.90	23.1	0.04	60.5	0.19
10	0.0427	0.00129	243.7	1.90	27.2	0.04	83.4	0.19
11	0.0466	0.00135	259.8	1.90	29.8	0.04	95.1	0.19

Appendix C: Sixteen Die 10 mm Heat Exchanger Self-Cooling Results

Table C.1: Experimental measurements for the self-cooling test on the sixteen die 10 mm heat exchanger. The working fluid was ethane and the orifice size was 0.020". The cold side outlet pressure was held at 115 kPa.

Run #	Mass Flow Rate [V]	TC HP IN [K]	TC HP OUT [K]	TC LP IN [K]	TC LP OUT [K]	PRT HP IN [V]	PRT HP OUT [V]	PRT LP IN [V]	PRT LP OUT [V]	Press HP IN [V]
1	0.3343	297.00	294.55	293.79	296.00	0.10949	0.10819	0.10808	0.10916	0.735
2	0.3560	295.52	292.62	291.72	294.34	0.10857	0.10753	0.10753	0.10840	0.776
3	0.4631	294.92	290.27	288.74	292.95	0.10862	0.10683	0.10612	0.10775	0.985
4	0.5298	296.44	290.52	288.57	293.84	0.10927	0.10693	0.10590	0.10813	1.116
5	0.5936	296.17	289.49	287.15	293.16	0.10878	0.10639	0.10579	0.10780	1.245
6	0.6659	295.05	287.57	284.75	291.52	0.10873	0.10552	0.10465	0.10748	1.389
7	0.7395	294.99	286.38	283.02	290.78	0.10862	0.10536	0.10383	0.10688	1.532

Table C.2: Calculations of maximum temperature difference ($T_{h,in} - T_{c,in}$) and pressure difference ($P_{h,in} - P_{c,in}$) based on the experimental data in Table C.1.

Run	Temperature Difference		Temperature Difference Uncertainty		Pressure Difference	
	TC [K]	PRT [K]	TC [K]	PRT [K]	Value [kPa]	Uncertainty [kPa]
1	-3.20	-3.91	0.28	0.35	138.4	7.151
2	-3.80	-2.93	0.28	0.35	152.5	7.151
3	-6.19	-6.70	0.28	0.35	224.7	7.151
4	-7.87	-8.94	0.28	0.35	269.6	7.151
5	-9.03	-7.96	0.28	0.35	314.1	7.151
6	-10.30	-10.75	0.28	0.35	363.7	7.151
7	-11.97	-12.56	0.28	0.35	413.2	7.151

Table C.3: Calculations of heat exchanger effectiveness and mass flow rate based on the experimental data in Table C.1.

Run	Mass Flow Rate		Hot Side Effectiveness		Cold Side Effectiveness		Effectiveness Uncertainty	
	Value	Uncertainty	TC [-]	PRT [-]	TC [-]	PRT [-]	TC [-]	PRT [-]
1	0.0856	0.0053	0.763	0.824	0.680	0.778	0.080	0.084
2	0.0914	0.0055	0.765	0.860	0.679	0.847	0.067	0.113
3	0.1187	0.0069	0.754	0.669	0.667	0.653	0.041	0.047
4	0.1351	0.0078	0.754	0.659	0.653	0.655	0.032	0.035
5	0.1512	0.0086	0.742	0.756	0.647	0.665	0.028	0.040
6	0.1696	0.0096	0.727	0.755	0.636	0.678	0.025	0.030
7	0.1879	0.0106	0.721	0.658	0.623	0.618	0.021	0.025

Appendix D: Sixteen Die 10 mm Heat Exchanger Pressure Drop Results

Table D.1: Experimental data collected for the pressure drop testing of the sixteen die 10 mm heat exchanger with helium as the working fluid

Helium - Through Gasket							
Labview					*Handwritten*		
TC HP IN [K]	Mass Flow Rate [V]	HP In Pressure [V]	HP Diff Pressure [V]	LP Diff Pressure [V]	LP Inlet [psig]	LP Outlet [psig]	Room Pressure [mm Hg]
293.69	0.0720	0.323	0.707	0.044	0.9	0	736.4
293.89	0.0977	0.340	1.639	0.093	0.9	0	736.4
293.92	0.1462	0.388	2.815	0.158	2	0.2	736.4
293.88	0.2328	0.478	5.234	0.293	4	0.5	736.4
294.27	0.2672	0.481	7.015	0.376	3.8	0	736.4
294.00	0.3459	0.581	8.476	0.565	5.2	0	736.4
294.08	0.4750	0.726	10.074	0.812	8.1	0	736.4
294.15	0.6062	0.871	12.580	1.122	10.3	0	736.4
294.35	0.6798	0.952	13.379	1.287	11.9	0	736.4
294.23	0.6915	0.968	13.221	1.341	12.2	0	736.4
294.31	0.7637	1.055	13.633	1.481	14.2	0	736.4
294.34	0.8955	1.210	14.210	1.853	17.5	0	736.4
294.42	1.0225	1.363	14.541	2.186	21	0	736.4
294.41	1.1195	1.480	14.721	2.425	23.8	0	736.4

Table D.2: Experimental data collected for the pressure drop testing of the sixteen die 10 mm heat exchanger with air as the working fluid

Air - Through Gasket							
Labview					*Handwritten*		
TC HP IN [K]	Mass Flow Rate [V]	HP In Pressure [V]	HP Diff Pressure [V]	LP Diff Pressure [V]	LP Inlet [psig]	LP Outlet [psig]	Room Pressure [mm Hg]
294.00	0.0915	0.336	2.552	0.101	0.5	0	736.4
294.00	0.1467	0.428	5.506	0.222	1.2	0	736.4
294.04	0.2002	0.518	8.371	0.387	2.2	0	736.4
294.08	0.2688	0.659	10.074	0.612	5	0	736.4
294.10	0.3267	0.782	12.181	0.821	7.5	0	736.4
294.12	0.3731	0.882	12.974	1.012	9.5	0	736.4
294.16	0.4196	0.982	13.533	1.196	11.6	0	736.4
294.18	0.4858	1.126	14.148	1.527	14	0	736.4
294.19	0.5498	1.266	14.451	1.841	17.9	0	736.4
294.24	0.6341	1.453	14.733	2.331	23.5	0	736.4

Table D.3: Experimental data collected for the pressure drop testing of the sixteen die 10 mm heat exchanger with ethane as the working fluid

Ethane - Through Gasket							
Labview					*Handwritten*		
TC HP IN [K]	Mass Flow Rate [V]	HP In Pressure [V]	HP Diff Pressure [V]	LP Diff Pressure [V]	LP Inlet [psig]	LP Outlet [psig]	Room Pressure [mm Hg]
294.03	0.1926	0.362	2.795	0.092	0.8	0	736.4
294.02	0.2477	0.413	4.122	0.137	1.8	0.5	736.4
293.94	0.3968	0.542	8.442	0.331	3.5	0	736.4
294.00	0.4500	0.616	8.791	0.363	6.1	4	736.4
293.97	0.4557	0.604	9.173	0.416	4.5	1	736.4
293.85	0.5325	0.682	10.625	0.564	5.5	0	736.4
293.98	0.6772	0.839	12.698	0.834	8.1	0	736.4
294.00	0.7715	0.947	13.401	1.027	10.4	0.5	736.4
294.00	0.8687	1.055	13.902	1.298	12.5	0	736.4
293.97	1.0247	1.234	14.395	1.754	16.8	0	736.4
293.92	1.1701	1.391	14.660	2.170	20.5	0	736.4
293.92	1.3234	1.569	14.869	2.569	25	0	736.4

Table D.4: Experimental data collected for the leak testing of the sixteen die 10 mm heat exchanger with helium as the working fluid

Helium - Blank Gasket							
Labview					*Handwritten*		
TC HP IN [K]	Mass Flow Rate [V]	HP In Pressure [V]	HP Diff Pressure [V]	LP Diff Pressure [V]	LP Inlet [psig]	LP Outlet [psig]	Room Pressure [mm Hg]
293.61	0.0118	0.342	0.080	-0.004	0	0	735.2
293.66	0.0126	1.161	0.086	-0.004	0	0	735.2

Table D.5: Calculated results from Table D.1

Mass Flow Rate		Assembly Pressure Drop		LP Side Pressure Drop		HX Pressure Drop
Value [g/s]	Uncertainty [g/s]	Value [kPa]	Uncertainty [kPa]	Value [kPa]	Uncertainty [kPa]	Value [kPa]
0.0070	0.0010	13.23	3.93	3.06	0.19	6.12
0.0095	0.0010	19.10	3.93	6.43	0.19	12.86
0.0142	0.0010	34.12	3.93	10.90	0.19	21.81
0.0226	0.0011	63.03	3.93	20.22	0.19	40.44
0.0259	0.0011	67.78	3.93	25.92	0.19	51.84
0.0336	0.0012	102.30	3.93	38.94	0.19	77.87
0.0461	0.0013	152.20	3.93	55.99	0.19	112.00
0.0588	0.0015	201.90	3.93	77.34	0.19	154.70
0.0660	0.0016	229.90	3.93	88.70	0.19	177.40
0.0671	0.0017	235.40	3.93	92.45	0.19	184.90
0.0741	0.0018	265.60	3.93	102.10	0.19	204.30
0.0869	0.0020	318.80	3.93	127.80	0.19	255.50
0.0992	0.0022	371.70	3.93	150.70	0.19	301.50
0.1086	0.0024	412.10	3.93	167.20	0.19	334.40

Table D.6: Calculated results from Table D.2

Mass Flow Rate		Assembly Pressure Drop		LP Side Pressure Drop		HX Pressure Drop
Value [g/s]	Uncertainty [g/s]	Value [kPa]	Uncertainty [kPa]	Value [kPa]	Uncertainty [kPa]	Value [kPa]
0.0457	0.0051	17.64	3.93	6.98	0.19	13.95
0.0732	0.0052	49.50	3.93	15.33	0.19	30.65
0.0999	0.0054	80.50	3.93	26.65	0.19	53.30
0.1341	0.0057	129.10	3.93	42.21	0.19	84.42
0.1629	0.0060	171.30	3.93	56.59	0.19	113.20
0.1859	0.0062	205.80	3.93	69.75	0.19	139.50
0.2090	0.0065	240.30	3.93	82.49	0.19	165.00
0.2419	0.0069	289.90	3.93	105.30	0.19	210.60
0.2736	0.0074	338.30	3.93	127.00	0.19	253.90
0.3153	0.0080	402.80	3.93	160.70	0.19	321.40

Table D.7: Calculated results from Table D.3

Mass Flow Rate		Assembly Pressure Drop		LP Side Pressure Drop		HX Pressure Drop
Value [g/s]	Uncertainty [g/s]	Value [kPa]	Uncertainty [kPa]	Value [kPa]	Uncertainty [kPa]	Value [kPa]
0.0499	0.0037	26.61	3.93	6.32	0.19	12.63
0.0641	0.0043	40.65	3.93	9.47	0.19	18.94
0.1025	0.0060	88.79	3.93	22.84	0.19	45.68
0.1177	0.0067	103.00	3.93	28.68	0.19	57.36
0.1374	0.0077	136.80	3.93	38.89	0.19	77.78
0.1742	0.0096	191.10	3.93	57.52	0.19	115.00
0.1982	0.0109	224.80	3.93	70.82	0.19	141.60
0.2228	0.0122	265.50	3.93	89.52	0.19	179.00
0.2621	0.0144	327.10	3.93	120.90	0.19	241.90

Table D.8: Calculated results from Table D.4

Mass Flow Rate		Assembly Pressure Drop	
Value [g/s]	Uncertainty [g/s]	Value [kPa]	Uncertainty [kPa]
0.0011	0.0010	19.72	3.93
0.0012	0.0010	281.5	3.93

Appendix E: Integrated PRT Die Calibration

Table E.1: Experimental data from the calibration of individual dies with integrated PRT dies. The current flowing through the PRTs was 100 µA.

Relative Time [hh:mm:ss]	PRT [K]	TC [K]	Voltage 10mm [V]	Voltage 20mm [V]	Resistance 10mm [kΩ]	Resistance 20mm [kΩ]
0:00:00	296.00	295.79	0.42871	3.40833	4.28709	34.08328
0:05:59	295.73	295.50	0.42835	3.40518	4.28352	34.05178
0:10:59	295.60	295.43	0.42827	3.40432	4.28268	34.04316
0:15:59	295.49	295.30	0.42814	3.40297	4.28140	34.02970
0:20:04	295.31	295.08	0.42794	3.40096	4.27943	34.00957
0:25:59	289.89	289.72	0.42208	3.34862	4.22076	33.48618
0:30:59	284.87	284.74	0.41657	3.30029	4.16574	33.00291
0:35:59	280.18	280.12	0.41139	3.25523	4.11385	32.55231
0:40:59	275.69	275.68	0.40639	3.21101	4.06390	32.11008
0:45:59	271.17	271.19	0.40134	3.16626	4.01341	31.66262
0:50:59	266.87	266.92	0.39653	3.12419	3.96525	31.24194
0:55:59	262.74	262.85	0.39188	3.08302	3.91876	30.83016
1:00:59	258.86	259.01	0.38751	3.04494	3.87508	30.44935
1:05:59	255.05	255.24	0.38319	3.00674	3.83193	30.06736
1:10:59	251.25	251.49	0.37888	2.96875	3.78880	29.68746
1:15:59	247.36	247.61	0.37448	2.92989	3.74475	29.29893
1:20:59	243.65	243.96	0.37022	2.89189	3.70223	28.91891
1:25:59	239.90	240.21	0.36595	2.85244	3.65945	28.52437
1:30:59	236.17	236.50	0.36151	2.81498	3.61511	28.14983
1:35:59	232.49	232.91	0.35729	2.77812	3.57293	27.78117
1:40:59	228.87	229.27	0.35312	2.74153	3.53118	27.41526
1:45:59	225.23	225.65	0.34890	2.70469	3.48903	27.04686
1:50:59	221.78	222.26	0.34489	2.66998	3.44888	26.69976
1:55:59	218.43	218.91	0.34096	2.63542	3.40961	26.35423
2:00:59	215.27	215.80	0.33726	2.60266	3.37256	26.02661
2:05:59	212.05	212.66	0.33352	2.57054	3.33516	25.70539
2:10:59	208.90	209.55	0.32987	2.53856	3.29870	25.38560
2:15:59	205.78	206.52	0.32621	2.50722	3.26214	25.07222
2:20:59	202.77	203.52	0.32263	2.47741	3.22629	24.77413
2:25:59	199.71	200.47	0.31893	2.44664	3.18931	24.46637
2:30:59	196.72	197.40	0.31532	2.41799	3.15323	24.17991
2:35:59	193.62	194.29	0.31169	2.38731	3.11694	23.87307
2:40:59	190.66	191.40	0.30834	2.35937	3.08338	23.59366
2:45:59	187.84	188.53	0.30525	2.33229	3.05252	23.32289
2:50:59	185.01	185.71	0.30221	2.30479	3.02210	23.04793
2:55:59	182.18	182.91	0.29898	2.27846	2.98982	22.78460
3:00:59	179.53	180.23	0.29595	2.25268	2.95950	22.52676
3:05:59	176.78	177.45	0.29275	2.22526	2.92750	22.25259
3:10:59	174.28	174.96	0.28996	2.20294	2.89959	22.02938
3:15:59	171.72	172.38	0.28696	2.17624	2.86959	21.76239

Table E.1: Experimental data from the calibration of individual dies with integrated PRT dies. The current flowing through the PRTs was 100 µA (cont.)

Relative Time [hh:mm:ss]	PRT [K]	TC [K]	Voltage 10mm [V]	Voltage 20mm [V]	Resistance 10mm [kΩ]	Resistance 20mm [kΩ]
3:20:59	169.16	169.85	0.28421	2.15316	2.84214	21.53160
3:25:59	166.70	167.41	0.28150	2.12745	2.81504	21.27454
3:30:59	164.23	164.93	0.27897	2.10636	2.78968	21.06362
3:35:59	161.82	162.55	0.27634	2.08192	2.76339	20.81924
3:40:59	159.56	160.27	0.27396	2.05943	2.73960	20.59434
3:45:59	157.33	158.03	0.27154	2.03957	2.71544	20.39570
3:50:59	155.12	155.86	0.26920	2.01920	2.69201	20.19196
3:55:59	152.98	153.69	0.26699	1.99753	2.66992	19.97529
4:00:59	150.85	151.58	0.26485	1.97929	2.64847	19.79285
4:05:59	148.91	149.64	0.26282	1.96103	2.62816	19.61028
4:10:59	146.89	147.59	0.26074	1.94486	2.60735	19.44863
4:15:59	144.93	145.65	0.25918	1.92456	2.59179	19.24555
4:20:59	142.82	143.51	0.25677	1.90557	2.56773	19.05566
4:25:59	140.77	141.43	0.25453	1.88007	2.54528	18.80070
4:30:59	138.80	139.49	0.25252	1.86492	2.52523	18.64924
4:35:59	137.07	137.78	0.25069	1.84591	2.50693	18.45909
4:40:59	135.25	135.99	0.24955	1.82761	2.49554	18.27613
4:45:59	133.51	134.17	0.24763	1.81163	2.47625	18.11631
4:50:59	131.77	132.37	0.24633	1.79483	2.46333	17.94825
4:55:59	129.89	130.53	0.24435	1.77901	2.44348	17.79012
5:00:59	127.98	128.60	0.24268	1.76556	2.42675	17.65564
5:05:59	126.17	126.81	0.24139	1.74192	2.41387	17.41924
5:10:59	124.32	124.98	0.23959	1.72986	2.39593	17.29862
5:15:59	122.52	123.21	0.23859	1.71707	2.38589	17.17068
5:20:59	120.82	121.51	0.23710	1.69973	2.37098	16.99726
5:25:59	119.09	119.82	0.23523	1.68427	2.35226	16.84266
5:30:59	117.51	118.26	0.23385	1.67790	2.33845	16.77902
5:35:59	115.76	116.54	0.23201	1.65822	2.32010	16.58221
5:40:59	113.91	114.65	0.23069	1.64242	2.30689	16.42421
5:45:59	112.19	112.95	0.22875	1.63208	2.28745	16.32084
5:50:59	110.42	111.19	0.22739	1.61086	2.27394	16.10861
5:55:59	108.71	109.52	0.22560	1.59949	2.25603	15.99492
6:00:59	107.13	107.91	0.22452	1.61521	2.24521	16.15213
6:05:59	105.37	106.16	0.22333	1.61538	2.23329	16.15383
6:10:59	103.82	104.65	0.22235	1.60216	2.22350	16.02157
6:15:59	102.18	103.00	0.22500	1.61392	2.25004	16.13919
6:20:59	100.70	101.55	0.22362	1.60888	2.23617	16.08875
6:25:59	99.19	100.05	0.22206	1.59852	2.22061	15.98524
6:30:59	97.73	98.58	0.22062	1.60116	2.20619	16.01164
6:35:59	96.29	97.14	0.22000	1.59147	2.20003	15.91468
6:40:59	94.89	95.69	0.21832	1.58074	2.18317	15.80739
6:45:59	93.54	94.39	0.21639	1.56727	2.16393	15.67265

Table E.1: Experimental data from the calibration of individual dies with integrated PRT dies. The current flowing through the PRTs was 100 µA (cont.)

Relative Time [hh:mm:ss]	PRT [K]	TC [K]	Voltage 10mm [V]	Voltage 20mm [V]	Resistance 10mm [kΩ]	Resistance 20mm [kΩ]
6:50:59	92.18	93.07	0.21592	1.57376	2.15921	15.73760
6:55:59	90.92	91.82	0.21442	1.56942	2.14418	15.69421
7:00:59	89.72	90.56	0.21530	1.55929	2.15301	15.59293
7:05:59	88.55	89.36	0.21306	1.55503	2.13057	15.55033
7:10:59	87.45	88.27	0.21281	1.54608	2.12810	15.46081
7:15:59	86.35	87.23	0.21199	1.53704	2.11988	15.37038
7:20:59	85.31	86.19	0.21103	1.52645	2.11027	15.26452
7:25:59	84.19	85.04	0.21061	1.53199	2.10605	15.31993
7:30:59	83.24	84.09	0.20993	1.53560	2.09928	15.35600
7:35:59	82.35	83.19	0.20985	1.53080	2.09848	15.30804
7:40:59	81.65	82.50	0.20916	1.52782	2.09155	15.27824
7:45:59	80.98	81.80	0.20998	1.51736	2.09981	15.17357
7:50:59	80.21	81.06	0.20903	1.51487	2.09031	15.14874
7:55:59	79.49	80.33	0.20889	1.50978	2.08894	15.09777
8:00:59	78.66	79.52	0.20753	1.50396	2.07534	15.03962
8:05:59	77.97	78.81	0.20718	1.50051	2.07178	15.00511
8:10:59	77.24	78.07	0.20638	1.49310	2.06382	14.93102
8:15:59	76.50	77.38	0.20568	1.49339	2.05679	14.93389
8:20:59	76.04	76.92	0.20599	1.48862	2.05993	14.88619
8:25:59	75.48	76.31	0.20602	1.48785	2.06015	14.87848
8:29:59	75.09	75.96	0.20576	1.48422	2.05763	14.84215

Appendix F: Forty-three Die 10 mm Heat Exchanger Integrated PRT Calibration

Table F.1: Mass flow rate, temperature, and pressure measurements for the PRTs that were tested in both wiring arrangements during the calibration of the forty-three die 10 mm heat exchanger.

Run	Mass Flow Rate	Thermocouples			Commercial PRT				Pressure		
	[V]	HP IN [K]	LP IN [K]	LP Out [K]	HP IN [V]	LP IN [V]	LP OUT [V]	Cryo-cooler [V]	HP IN [V]	LP OUT [V]	ATM [mmHg]
1	0.7495	294.3	294.0	294.0	0.1083	0.1083	0.1082	0.1082	0.6733	0.8199	743.0
2	0.7486	294.4	294.1	294.0	0.1083	0.1083	0.1082	0.1082	0.6723	0.8041	744.4
3	0.8988	296.5	247.9	248.2	0.1092	0.0900	0.0902	0.0896	0.7092	0.9453	744.4
4	0.9012	294.5	247.6	247.8	0.1084	0.0899	0.0901	0.0894	0.7093	0.9418	744.4
5	0.3917	296.0	209.2	210.6	0.1090	0.0743	0.0752	0.0731	0.4705	0.4821	746.1
6	0.3921	296.3	209.2	210.7	0.1091	0.0743	0.0752	0.0731	0.4708	0.4822	746.1
7	0.7644	298.1	272.7	273.2	0.1097	0.0998	0.1000	0.0993	0.6630	0.8102	742.2
8	0.7655	297.7	272.7	273.1	0.1095	0.0998	0.1000	0.0993	0.6626	0.7951	742.2
9	0.7478	294.7	294.6	294.5	0.1084	0.1085	0.1084	0.1084	0.6634	0.7568	739.3
10	0.7497	293.4	293.9	293.8	0.1079	0.1082	0.1082	0.1082	0.6627	0.7557	738.4

Table F.2: The voltages of every die PRT that was tested in both wiring arrangements during the calibration of the forty-three die 10 mm heat exchanger. The current flow through the PRTs was 100 µA.

Run	Die PRTS							
	RTD 1 [V]	RTD 12 [V]	RTD 4 [V]	RTD 5 [V]	RTD 6 [V]	RTD 14 [V]	RTD 9 [V]	RTD 10 [V]
1	0.6629	0.5033	0.4692	0.5552	0.4994	0.6451	0.5273	0.4533
2	0.6630	0.5034	0.4692	0.5553	0.4994	0.6452	0.5274	0.4533
3	0.5729	0.4346	0.4040	0.4847	0.4306	0.5577	0.4547	0.3903
4	0.5723	0.4341	0.4035	0.4842	0.4301	0.5571	0.4542	0.3899
5	0.4962	0.3756	0.3485	0.4246	0.3721	0.4831	0.3929	0.3368
6	0.4964	0.3757	0.3486	0.4247	0.3722	0.4833	0.3930	0.3369
7	0.6215	0.4719	0.4392	0.5228	0.4678	0.6049	0.4939	0.4244
8	0.6214	0.4718	0.4391	0.5228	0.4677	0.6048	0.4939	0.4243
9	0.6638	0.5041	0.4698	0.5559	0.5001	0.6461	0.5281	0.4540
10	0.6626	0.5030	0.4689	0.5549	0.4992	0.6448	0.5271	0.4531

Table F.3: The voltages of every die PRT that was tested only in the first wiring arrangement during the calibration of the forty-three die 10 mm heat exchanger. The current flow through the PRTs was 100 µA.

Run	PRT 2 [V]	RTD 13 [V]
1	0.5094	0.4657
3	0.4406	0.4024
5	0.3819	0.3484
7	0.4778	0.4366
9	0.5101	0.4664

Table F.4: The voltages of every die PRT that was tested only in the second wiring arrangement during the calibration of the forty-three die 10 mm heat exchanger. The current flow through the resistors was 100 µA.

Run	PRT 2 [V]	RTD 13 [V]
2	0.8092	0.6527
4	0.6992	0.5767
6	0.6072	0.5128
8	0.7589	0.618
10	0.8088	0.6524

Table F.5: PRT resistances as a function of temperature for PRTs 1 through 6 on the forty-three die 10 mm heat exchanger.

PRT 1		PRT 2		PRT 3		PRT 4		PRT 5		PRT 6	
T [K]	R [kΩ]	T [K]	R [kΩ]	T [K]	R [kΩ]	T [K]	R [kΩ]	T [K]	R [kΩ]	T [K]	R [kΩ]
294.8	6.638	294.7	5.101	294.2	8.092	294.7	4.698	294.7	5.559	294.7	5.001
294.2	6.629	294.2	5.094	294.1	8.088	294.2	4.692	294.2	5.552	294.2	4.994
294.2	6.63	273	4.778	272.8	7.589	294.2	4.692	294.2	5.553	294.2	4.994
294.1	6.626	248	4.406	247.6	6.992	294.1	4.689	294.1	5.549	294.1	4.992
273.1	6.215	209.7	3.819	209.5	6.072	272.8	4.392	272.7	5.228	272.5	4.677
273	6.214					272.7	4.391	272.7	5.228	272.5	4.678
248	5.729					247.8	4.04	247.7	4.847	247.6	4.306
247.7	5.723					247.5	4.035	247.4	4.842	247.3	4.301
210	4.964					209.2	3.486	209	4.247	208.5	3.722
209.9	4.962					209.2	3.485	208.9	4.246	208.4	3.721

Table F.6: PRT resistances as a function of temperature for PRTs 9 through 15 on the forty-three die 10 mm heat exchanger.

PRT 9		PRT 10		PRT 12		PRT 13		PRT 14		PRT 15	
T [K]	R [kΩ]	T [K]	R [kΩ]	T [K]	R [kΩ]	T [K]	R [kΩ]	T [K]	R [kΩ]	T [K]	R [kΩ]
294.7	5.281	294.7	4.54	294.7	5.041	294.7	4.664	294.8	6.461	294.2	6.524
294.2	5.273	294.2	4.533	294.2	5.033	294.2	4.657	294.2	6.451	294.2	6.527
294.2	5.274	294.2	4.533	294.2	5.034	272.9	4.366	294.2	6.452	273.1	6.18
294.1	5.271	294.1	4.531	294.1	5.03	247.9	4.024	294.1	6.448	247.8	5.767
272.5	4.939	272.6	4.243	272.8	4.719	209.4	3.484	273.1	6.049	210.2	5.128
272.5	4.939	272.6	4.244	272.7	4.718			273	6.048		
247.6	4.547	247.7	3.903	247.8	4.346			248	5.577		
247.3	4.542	247.4	3.899	247.5	4.341			247.7	5.571		
208.5	3.93	208.8	3.369	209.2	3.757			210	4.833		
208.4	3.929	208.7	3.368	209.2	3.756			209.9	4.831		

Table F.7: Mass flow rate, heat leak, and temperatures for all calibration points

Mass Flow Rate		Heat Leak		Commerical PRT				Thermocouples		
Value [g/s]	Uncertainty [g/s]	PRT [W]	TC [W]	CC [K]	HP IN [K]	LP IN [K]	LP OUT [K]	HP IN [K]	LP IN [K]	LP OUT [K]
0.0726	0.0017	0.01	-0.02	294.8	294.8	294.7	294.8	294.7	294.6	294.5
0.0727	0.0017	0.01	-0.02	294.3	294.5	294.2	294.2	294.4	294.1	294.0
0.0727	0.0017	0.01	-0.02	294.2	294.4	294.2	294.2	294.3	294.0	294.0
0.0728	0.0017	0.02	-0.01	294.1	293.5	294.0	294.1	293.4	293.9	293.8
0.0742	0.0018	0.34	0.19	271.3	298.0	272.4	273.2	298.1	272.7	273.2
0.0743	0.0018	0.33	0.18	271.3	297.7	272.3	273.2	297.7	272.7	273.1
0.0872	0.0020	0.33	0.12	246.6	296.7	247.5	248.2	296.5	247.9	248.2
0.0875	0.0020	0.34	0.12	246.3	294.7	247.1	247.9	294.5	247.6	247.8
0.0381	0.0012	0.47	0.28	205.2	296.6	208.1	210.5	296.3	209.2	210.7
0.0380	0.0012	0.47	0.28	205.1	296.2	208.0	210.4	296.0	209.2	210.6

Appendix G: Thirty-Seven Die 20 mm Heat Exchanger Integrated PRT Calibration

Table G.1: Steady-state mass flow rate, temperature, and pressure measurements for the thirty-seven die 20 mm heat exchanger during the calibration test.

Mass Flow Rate	Thermocouples			Commercial PRT				Pressure		
	HP IN	LP IN	LP Out	HP IN	LP IN	LP OUT	Cryo-cooler	HP IN	LP OUT	ATM
[V]	[K]	[K]	[K]	[V]	[V]	[V]	[V]	[V]	[V]	[mmHg]
0.8579	295.4	295.2	295.2	0.1087	0.1088	0.1087	0.1087	0.7039	1.2500	729.8
0.8818	301.4	266.7	267.7	0.1110	0.0976	0.0979	0.0971	0.6998	1.2330	729.8
0.4105	297.2	226.7	229.4	0.1095	0.0816	0.0827	0.0805	0.5088	0.8259	729.8
0.2016	294.7	206.4	212.2	0.1085	0.0734	0.0759	0.0712	0.4370	0.6227	734.9

Table G.2: Measured steady-state voltages on the integrated PRTs of the thirty-seven die 20 mm heat exchanger during the calibration test.

Die PRTS								
RTD 1 [V]	RTD 2 [V]	RTD 3 [V]	RTD 4 [V]	RTD 5 [V]	RTD 6 [V]	RTD 7 [V]	RTD 8 [V]	RTD 9 [V]
0.2380	0.2411	0.2629	0.2756	0.3545	0.2411	0.3310	0.2196	0.4561
0.2188	0.2261	0.2519	0.2641	0.3281	0.2217	0.3040	0.2010	0.4173
0.1914	0.2027	0.2325	0.2440	0.2905	0.1942	0.2658	0.1748	0.3624
0.1783	0.1907	0.2215	0.2326	0.2724	0.1810	0.2475	0.1622	0.3363

Table G.3: PRT resistances as a function of temperature for PRTs 1 through 5 on the thirty-seven die 20 mm heat exchanger.

PRT 1		PRT 2		PRT 3		PRT 4		PRT 5	
T [K]	R [kΩ]	T [K]	R [kΩ]	T [K]	R [kΩ]	T [K]	R [kΩ]	T [K]	R [kΩ]
295.4	23.8	295.4	24.11	295.4	26.29	295.4	27.56	295.4	35.45
267.2	21.88	266.9	22.61	266.8	25.19	266.9	26.41	267	32.81
227.9	19.14	227	20.27	226.6	23.25	227	24.4	227.4	29.05
209	17.83	207.3	19.07	206.4	22.15	207.3	23.26	208	27.24

Table G.4: PRT resistances as a function of temperature for PRTs 6 through 9 on the thirty-seven die 20 mm heat exchanger.

PRT 6		PRT 7		PRT 8		PRT 9	
T [K]	R [kΩ]	T [K]	R [kΩ]	T [K]	R [kΩ]	T [K]	R [kΩ]
295.4	24.11	295.4	33.1	295.4	21.96	295.4	45.61
267.2	22.17	267.3	30.4	267.5	20.1	267.6	41.73
227.8	19.42	228.2	26.58	228.6	17.48	228.9	36.24
208.9	18.1	209.7	24.75	210.6	16.22	211.3	33.63

Table G.5: Mass flow rate, heat leak, and temperatures for all calibration points

Mass Flow Rate		Heat Leak		Commerical PRTs				Thermocouples		
Value [g/s]	Uncertainty [g/s]	PRT [W]	TC [W]	CC [K]	HP IN [K]	LP IN [K]	LP OUT [K]	HP IN [K]	LP IN [K]	LP OUT [K]
0.0833	0.0019	0.00	-0.03	295.4	295.5	295.4	295.4	295.4	295.2	295.2
0.0856	0.0020	0.47	0.43	265.7	301.6	266.7	267.7	301.4	266.7	267.7
0.0398	0.0013	0.63	0.56	223.8	297.4	226.3	229.3	297.2	226.7	229.4
0.0196	0.0010	0.66	0.59	200.5	295.1	205.7	212.2	294.7	206.4	212.2

Appendix H: Micro-Valve Flow Rate Testing

Table H.1: Experimental data measuring the pressure drop characteristics of the micro-valve.

Run	Valve Voltage [V]	Mass Flow Rate [V]	HP IN Pressure [V]	LP OUT Pressure [V]	Atm Pressure [mmHg]
1	-30	0.0735	0.397	0.048	727.9
1	0	0.0717	0.397	0.045	727.9
1	30	0.0628	0.398	0.044	727.9
1	60	0.0529	0.399	0.045	727.9
1	80	0.0427	0.401	0.047	727.9
1	100	0.0404	0.401	0.040	727.9
2	-30	0.1113	0.511	0.051	727.9
2	0	0.109	0.512	0.052	727.9
2	30	0.1044	0.512	0.048	727.9
2	60	0.0924	0.514	0.044	727.9
2	80	0.0755	0.515	0.039	727.9
2	100	0.0657	0.516	0.035	727.9
3	-30	0.17	0.718	0.061	727.9
3	0	0.1649	0.723	0.067	727.9
3	30	0.1541	0.720	0.059	727.9
3	60	0.1321	0.723	0.050	727.9
3	80	0.1136	0.726	0.047	727.9
3	100	0.1093	0.728	0.042	727.9
4	-30	0.2208	0.911	0.078	727.9
4	0	0.2164	0.913	0.071	727.9
4	30	0.2097	0.914	0.071	727.9
4	60	0.1947	0.916	0.069	727.9
4	80	0.1655	0.920	0.058	727.9
4	100	0.1483	0.921	0.053	727.9
5	-30	0.2699	1.106	0.086	727.9
5	0	0.2617	1.111	0.089	727.9
5	30	0.249	1.108	0.081	727.9
5	60	0.2193	1.113	0.071	727.9
5	80	0.1945	1.117	0.066	727.9
5	100	0.1884	1.120	0.064	727.9

Table H.1: Experimental data measuring the pressure drop characteristics of the micro-valve (cont.)

Run	Valve Voltage [V]	Mass Flow Rate [V]	HP IN Pressure [V]	LP OUT Pressure [V]	Atm Pressure [mmHg]
6	-30	0.3249	1.320	0.111	727.9
6	0	0.3213	1.322	0.104	727.9
6	30	0.31	1.324	0.099	727.9
6	60	0.2924	1.327	0.093	727.9
6	80	0.2542	1.332	0.082	727.9
6	100	0.232	1.333	0.069	727.9
7	-30	0.3691	1.490	0.116	727.9
7	0	0.3611	1.497	0.113	727.9
7	30	0.3429	1.495	0.106	727.9
7	60	0.3053	1.501	0.093	727.9
7	80	0.2748	1.506	0.087	727.9
7	100	0.2679	1.510	0.078	727.9
8	-30	0.3058	1.299	1.814	727.9
8	0	0.3007	1.301	1.882	727.9
8	30	0.2899	1.300	1.800	727.9
8	60	0.2713	1.306	1.795	727.9
8	80	0.2327	1.312	1.782	727.9
8	100	0.2096	1.316	1.771	727.9
8	80	0.2174	1.311	1.773	727.9
8	60	0.2468	1.307	1.777	727.9
8	30	0.2806	1.300	1.784	727.9
8	0	0.2946	1.298	1.785	727.9
8	-30	0.3055	1.296	1.786	727.9

Table H.2: Calculated values from the experimental data shown in Table H.1.

Run	Valve Voltage [V]	Mass Flow Rate [g/s]	Flow Rate Uncertainty [g/s]	HP IN Pressure [kPa]	LP OUT Pressure [kPa]	Pressure Difference [kPa]	Pressure Difference Uncertainty [kPa]
1	-30	0.0191	0.0028	136.8	100.4	36.5	1.9
1	0	0.0186	0.0028	136.9	100.2	36.7	1.9
1	30	0.0163	0.0027	137.2	100.1	37.1	1.9
1	60	0.0137	0.0027	137.6	100.1	37.5	1.9
1	80	0.0111	0.0027	138.2	100.3	37.9	1.9
1	100	0.0105	0.0027	138.1	99.8	38.3	1.9
2	-30	0.0288	0.0030	176.0	100.5	75.5	1.9
2	0	0.0282	0.0030	176.3	100.7	75.7	1.9
2	30	0.0271	0.0030	176.6	100.4	76.2	1.9
2	60	0.0239	0.0029	177.1	100.1	77.0	1.9
2	80	0.0196	0.0028	177.6	99.8	77.9	1.9
2	100	0.0170	0.0027	177.9	99.4	78.4	1.9
3	-30	0.0439	0.0035	247.5	101.2	146.3	1.9
3	0	0.0426	0.0034	249.2	101.7	147.5	1.9
3	30	0.0398	0.0033	248.2	101.1	147.1	1.9
3	60	0.0341	0.0032	249.3	100.5	148.8	1.9
3	80	0.0293	0.0030	250.3	100.3	150.0	1.9
3	100	0.0282	0.0030	250.8	100.0	150.8	1.9
4	-30	0.0569	0.0040	314.1	102.4	211.7	1.9
4	0	0.0557	0.0039	314.8	102.0	212.9	1.9
4	30	0.0540	0.0039	315.1	102.0	213.2	1.9
4	60	0.0501	0.0037	315.8	101.8	214.0	1.9
4	80	0.0426	0.0034	317.1	101.0	216.0	1.9
4	100	0.0382	0.0033	317.6	100.7	216.9	1.9
5	-30	0.0693	0.0045	381.2	103.0	278.2	1.9
5	0	0.0672	0.0044	383.0	103.2	279.8	1.9
5	30	0.0639	0.0043	382.1	102.6	279.4	1.9
5	60	0.0563	0.0040	383.6	101.9	281.7	1.9
5	80	0.0499	0.0037	385.1	101.6	283.4	1.9
5	100	0.0484	0.0036	386.0	101.4	284.5	1.9

Table H.2: Calculated values from the experimental data shown in Table H.1 (cont.)

Run	Valve Voltage [V]	Mass Flow Rate [g/s]	Flow Rate Uncertainty [g/s]	HP IN Pressure [kPa]	LP OUT Pressure [kPa]	Pressure Difference [kPa]	Pressure Difference Uncertainty [kPa]
6	-30	0.0832	0.0052	455.2	104.7	350.5	1.9
6	0	0.0823	0.0051	455.7	104.2	351.4	1.9
6	30	0.0794	0.0050	456.3	103.8	352.5	1.9
6	60	0.0748	0.0048	457.6	103.4	354.1	1.9
6	80	0.0651	0.0043	459.1	102.7	356.4	1.9
6	100	0.0594	0.0041	459.7	101.8	357.9	1.9
7	-30	0.0942	0.0057	513.7	105.0	408.7	1.9
7	0	0.0922	0.0056	516.1	104.9	411.2	1.9
7	30	0.0875	0.0054	515.3	104.4	411.0	1.9
7	60	0.0779	0.0049	517.4	103.5	413.9	1.9
7	80	0.0701	0.0046	519.0	103.0	416.0	1.9
7	100	0.0684	0.0045	520.7	102.4	418.2	1.9
8	-30	0.0783	0.0049	447.6	222.1	225.6	1.9
8	0	0.0770	0.0049	448.4	226.8	221.6	1.9
8	30	0.0742	0.0047	448.3	221.2	227.1	1.9
8	60	0.0695	0.0045	450.2	220.8	229.4	1.9
8	80	0.0596	0.0041	452.2	219.9	232.2	1.9
8	100	0.0537	0.0039	453.7	219.2	234.5	1.9
8	80	0.0557	0.0039	452.0	219.3	232.7	1.9
8	60	0.0632	0.0043	450.5	219.5	230.9	1.9
8	30	0.0719	0.0046	448.3	220.1	228.2	1.9
8	0	0.0754	0.0048	447.3	220.1	227.2	1.9
8	-30	0.0782	0.0049	446.8	220.2	226.6	1.9

Appendix I: Forty-three Die 10 mm Heat Exchanger Pressure Drop Testing

Table I.1: Experimental data collected for the through gasket pressure drop test on the forty-three die 10 mm heat exchanger

Mass Flow Rate [V]	HP Inlet Pressure [V]	LP Outlet Pressure [V]	Atm Press [mmHg]
0.0117	0.2908	0.01523	727.2
0.0613	0.3117	0.0501	727.2
0.1947	0.3797	0.1513	727.2
0.3091	0.4423	0.2201	727.2
0.4352	0.5214	0.3261	727.2
0.5557	0.6003	0.4286	727.2
0.7157	0.7082	0.5655	727.2
0.8492	0.8006	0.69	727.2
0.983	0.8934	0.8182	727.2
1.114	0.985	0.9424	727.2
1.251	1.082	1.084	727.2
1.377	1.17	1.215	727.2
1.464	1.231	1.306	727.2
1.581	1.313	1.434	727.2
1.676	1.381	1.547	727.2
1.728	1.417	1.602	727.2
1.766	1.423	1.349	727.2

Table I.2: Experimental data collected for the 0.015" orifice gasket pressure drop test on the forty-three die 10 mm heat exchanger

Mass Flow Rate [V]	HP Inlet Pressure [V]	LP Outlet Pressure [V]	Atm Press [mmHg]
0.0123	0.2558	-0.1656	734.8
0.0383	0.2927	-0.132	734.8
0.0563	0.3451	-0.1133	734.8
0.0711	0.4081	-0.1095	734.8
0.0854	0.4862	-0.1053	734.8
0.0948	0.535	-0.1047	734.8
0.1094	0.6154	-0.0932	734.8
0.1287	0.729	-0.0966	734.8
0.1458	0.8368	-0.0865	734.8
0.1616	0.9337	-0.0674	734.8
0.1774	1.027	-0.0543	734.8
0.1933	1.128	-0.0462	734.8
0.2081	1.217	-0.0362	734.8
0.2259	1.326	-0.0224	734.8
0.2394	1.407	-0.0159	734.8
0.2603	1.537	-0.0002	734.8
0.1985	1.158	-0.0457	734.8
0.1334	0.758	-0.0833	734.8
0.0877	0.4984	-0.117	734.8
0.0687	0.3961	-0.1319	734.8

Table I.3: Experimental data collected for the blank gasket pressure drop test on the forty-three die 10 mm heat exchanger

Mass Flow Rate [V]	HP Inlet Pressure [V]	LP Outlet Pressure [V]	Atm Press [mmHg]
0.0123	0.2808	-0.1601	734.8
0.0122	0.3731	-0.153	734.8
0.0122	0.4794	-0.1513	734.8
0.0124	0.5448	-0.1608	734.8
0.0124	0.6417	-0.1777	734.8
0.0121	0.7412	-0.1745	734.8
0.0121	0.9208	-0.1712	734.8
0.0123	1.132	-0.1671	734.8
0.0123	1.232	-0.1716	734.8
0.0121	1.327	-0.1682	734.8
0.0124	1.422	-0.1738	734.8
0.0124	1.524	-0.1743	734.8

Table I.4: Calculated results from the experimental data listed in Table I.1

Mass Flow Rate		Pressure Difference ($P_{hp,in}$ - $P_{lp,out}$)	
Value [g/s]	Uncertainty [g/s]	Value [kPa]	Uncertainty [kPa]
0.0058	0.0050	2.2	1.9
0.0306	0.0050	7.0	1.9
0.0972	0.0054	23.5	1.9
0.1543	0.0059	40.4	1.9
0.2172	0.0066	60.3	1.9
0.2772	0.0075	80.4	1.9
0.3569	0.0087	108.2	1.9
0.4233	0.0098	131.5	1.9
0.4898	0.0110	154.6	1.9
0.5546	0.0122	177.6	1.9
0.6229	0.0134	201.2	1.9
0.6855	0.0146	222.7	1.9
0.7286	0.0154	237.5	1.9
0.7863	0.0165	256.9	1.9
0.8334	0.0174	272.6	1.9
0.8591	0.0179	281.2	1.9

Table I.5: Calculated results from the experimental data listed in Table I.2

Mass Flow Rate		Pressure Difference ($P_{hp,in}$ - $P_{lp,out}$)	
Value [g/s]	Uncertainty [g/s]	Value [kPa]	Uncertainty [kPa]
0.0061	0.0050	1.6	1.9
0.0191	0.0050	12.0	1.9
0.0281	0.0050	28.8	1.9
0.0355	0.0050	50.3	1.9
0.0426	0.0051	76.9	1.9
0.0473	0.0051	93.7	1.9
0.0546	0.0051	120.6	1.9
0.0642	0.0051	160.0	1.9
0.0727	0.0052	196.5	1.9
0.0805	0.0052	228.6	1.9
0.0884	0.0053	260.0	1.9
0.0962	0.0053	294.1	1.9
0.1036	0.0054	324.0	1.9
0.1124	0.0055	360.6	1.9
0.1190	0.0055	388.2	1.9
0.1294	0.0056	431.8	1.9

Table I.6: Calculated results from the experimental data listed in Table I.3

Mass Flow Rate		Pressure Difference ($P_{hp,in}$ - $P_{lp,out}$)	
Value [g/s]	Uncertainty [g/s]	Value [kPa]	Uncertainty [kPa]
0.0061	0.0050	9.876	1.906
0.0061	0.0050	41.21	1.906
0.0061	0.0050	77.73	1.906
0.0062	0.0050	100.9	1.906
0.0062	0.0050	135.5	1.906
0.0060	0.0050	169.6	1.906
0.0060	0.0050	231.3	1.906
0.0061	0.0050	303.9	1.906
0.0061	0.0050	338.6	1.906
0.0060	0.0050	371	1.906
0.0062	0.0050	404.2	1.906
0.0062	0.0050	439.4	1.906

Appendix J: Thirty-Seven Die 20 mm Heat Exchanger Pressure Drop Testing

Table J.1: Experimental data collected for the through gasket pressure drop test on the thirty-seven die 20 mm heat exchanger

Mass Flow Rate [V]	HP Inlet Pressure [V]	LP Outlet Pressure [V]	Atm Press [mmHg]
0.0123	0.173	-0.581	736.4
0.2544	0.267	-0.407	736.4
0.1908	0.235	-0.470	736.4
0.3722	0.328	-0.315	736.4
0.4660	0.379	-0.230	736.4
0.5224	0.413	-0.170	736.4
0.6094	0.464	-0.079	736.4
0.6837	0.507	-0.005	736.4
0.8189	0.588	0.151	736.4
0.9809	0.688	0.345	736.4
1.1044	0.763	0.499	736.4
1.2591	0.859	0.699	736.4
1.3924	0.941	0.879	736.4
1.5666	1.047	1.119	736.4
1.7341	1.149	1.351	736.4
1.8705	1.231	1.541	736.4
2.0209	1.320	1.754	736.4
2.1221	1.380	1.898	736.4
1.8521	1.218	1.514	736.4
1.8585	1.220	1.483	736.4
2.1305	1.385	1.894	736.4

Table J.2: Experimental data collected for the 0.013" orifice gasket pressure drop test on the thirty-seven die 20 mm heat exchanger

Mass Flow Rate [V]	HP Inlet Pressure [V]	LP Outlet Pressure [V]	Atm Press [mmHg]
0.0125	0.196	-0.448	727.4
0.1069	0.259	-0.375	727.4
0.1390	0.293	-0.354	727.4
0.1852	0.351	-0.319	727.4
0.2154	0.394	-0.300	727.4
0.2205	0.449	0.170	727.4
0.2668	0.507	0.206	727.4
0.2872	0.534	0.224	727.4
0.3482	0.617	0.251	727.4
0.4210	0.727	0.320	727.4
0.4760	0.814	0.364	727.4
0.5425	0.919	0.424	727.4
0.6053	1.019	0.477	727.4
0.6596	1.105	0.524	727.4
0.7291	1.216	0.580	727.4
0.7943	1.320	0.640	727.4
0.8388	1.391	0.680	727.4
0.9169	1.514	0.756	727.4
0.2358	0.469	0.187	727.4
0.2136	0.442	0.169	727.4
0.1839	0.410	0.149	727.4
0.1495	0.380	0.121	727.4
0.1018	0.336	0.086	727.4
0.0121	0.293	0.033	727.4

Table J.3: Experimental data collected for the blank gasket pressure drop test on the thirty-seven die 20 mm heat exchanger

Mass Flow Rate [V]	HP Inlet Pressure [V]	LP Outlet Pressure [V]	Atm Press [mmHg]
0.0125	0.350	0.283	733.4
0.0299	0.355	0.293	733.4
0.0821	0.382	0.318	733.4
0.1349	0.427	0.345	733.4
0.1749	0.470	0.365	733.4
0.2264	0.540	0.384	733.4
0.2770	0.618	0.412	733.4
0.3414	0.729	0.455	733.4
0.3890	0.822	0.465	733.4
0.4376	0.909	0.510	733.4
0.4890	1.004	0.538	733.4
0.5370	1.102	0.575	733.4
0.5973	1.219	0.613	733.4
0.6472	1.316	0.648	733.4
0.7008	1.419	0.684	733.4
0.7481	1.510	0.700	733.4
0.6387	1.299	0.612	733.4
0.5413	1.109	0.529	733.4
0.4377	0.908	0.449	733.4
0.3331	0.711	0.376	733.4
0.2899	0.634	0.345	733.4
0.2149	0.514	0.295	733.4
0.1766	0.460	0.268	733.4
0.1463	0.423	0.246	733.4
0.1197	0.395	0.230	733.4
0.0930	0.370	0.214	733.4
0.0609	0.346	0.188	733.4
0.0122	0.325	0.161	733.4

Table J.4: Calculated results from the experimental data listed in Table J.1

Mass Flow Rate		Pressure Difference ($P_{hp,in}$ - $P_{lp,out}$)	
Value [g/s]	Uncertainty [g/s]	Value [kPa]	Uncertainty [kPa]
0.0061	0.0050	1.4	1.9
0.1271	0.0056	22.0	1.9
0.0953	0.0053	15.3	1.9
0.1859	0.0062	36.5	1.9
0.2327	0.0068	48.4	1.9
0.2608	0.0072	55.7	1.9
0.3041	0.0079	67.1	1.9
0.3412	0.0085	76.8	1.9
0.4085	0.0096	94.1	1.9
0.4891	0.0110	115.0	1.9
0.5506	0.0121	130.6	1.9
0.6274	0.0135	149.7	1.9
0.6936	0.0147	165.5	1.9
0.7801	0.0164	185.6	1.9
0.8632	0.0180	204.6	1.9
0.9308	0.0193	219.8	1.9
1.0050	0.0207	235.8	1.9
1.0550	0.0217	246.8	1.9
0.9217	0.0191	217.4	1.9
0.9248	0.0192	220.1	1.9
1.0600	0.0218	248.7	1.9

Table J.5: Calculated results from the experimental data listed in Table J.2

Mass Flow Rate		Pressure Difference ($P_{hp,in}$ - $P_{lp,out}$)	
Value [g/s]	Uncertainty [g/s]	Value [kPa]	Uncertainty [kPa]
0.0062	0.0050	1.4	1.9
0.0534	0.0051	18.2	1.9
0.0694	0.0052	28.6	1.9
0.0925	0.0053	46.0	1.9
0.1075	0.0054	59.5	1.9
0.1101	0.0055	46.1	1.9
0.1331	0.0057	63.5	1.9
0.1433	0.0058	71.7	1.9
0.1737	0.0061	98.5	1.9
0.2099	0.0065	131.7	1.9
0.2372	0.0069	158.3	1.9
0.2703	0.0074	190.6	1.9
0.3014	0.0078	221.5	1.9
0.3284	0.0082	247.9	1.9
0.3628	0.0088	282.2	1.9
0.3951	0.0093	314.0	1.9
0.4171	0.0097	335.5	1.9
0.4558	0.0104	372.9	1.9
0.1177	0.0055	51.8	1.9
0.1066	0.0054	43.8	1.9
0.0918	0.0053	34.0	1.9

Table J.6: Calculated results from the experimental data listed in Table J.3

Mass Flow Rate		Pressure Difference ($P_{hp,in}$ - $P_{lp,out}$)	
Value [g/s]	Uncertainty [g/s]	Value [kPa]	Uncertainty [kPa]
0.0062	0.0050	3.3	1.9
0.0149	0.0050	4.4	1.9
0.0410	0.0051	12.1	1.9
0.0673	0.0052	25.6	1.9
0.0873	0.0053	39.2	1.9
0.1130	0.0055	61.7	1.9
0.1382	0.0057	86.9	1.9
0.1702	0.0060	122.2	1.9
0.1939	0.0063	153.5	1.9
0.2180	0.0066	180.5	1.9
0.2435	0.0070	211.1	1.9
0.2674	0.0073	242.3	1.9
0.2972	0.0078	280.2	1.9
0.3219	0.0081	311.2	1.9
0.3485	0.0086	344.3	1.9
0.3719	0.0089	374.5	1.9
0.3177	0.0081	307.8	1.9
0.2695	0.0073	248.2	1.9
0.2181	0.0066	184.4	1.9
0.1661	0.0060	121.4	1.9
0.1446	0.0058	97.1	1.9
0.1072	0.0054	59.0	1.9
0.0881	0.0053	42.4	1.9
0.0730	0.0052	31.0	1.9
0.0598	0.0051	22.4	1.9
0.0464	0.0051	15.2	1.9
0.0304	0.0050	8.5	1.9
0.0061	0.0050	3.1	1.9

Appendix K: Forty-three Die 10 mm Heat Exchanger Cryosurgical Probe Tests

Table K.1: Locations of the integrated PRTs within the forty-three die 10 mm heat exchanger during the self-cooling tests performed in the cryosurgical probe prototype

Die	HP Inlet	LP Outlet
1		
2		
3		
4		
5		
6		
7		
8		
9	PRT 9 (Norm)	PRT 6 (Norm)
10		
11		
12		
13		
14	PRT 10 (Norm)	
15		
16		
17		
18		PRT 5 (Norm)
19		
20		
21		
22	PRT 12 (Norm)	PRT 4 (Norm)
23		
24		
25		
26		
27	PRT 13 (Norm)	
28		
29		
30		
31		
32		PRT 2 (Norm)
33		
34		
35		
36	PRT 14 (Norm)	PRT 1 (Norm)
37		
38		
39		
40		
41		
42		
43		
	HP Outlet	**LP Inlet**

Table K.2: Experimental data for the cryosurgical probe with the forty-three die 10 mm heat exchanger installed. The working fluid was ethane and the orifice diameters tested include 0.010", 0.013", and 0.015"

0.010" Orifice - No Valve											
	Mass	*Thermocouples*							*Pressures*		
Point	Flow Rate [V]	HP IN [K]	HP OUT [K]	LP IN [K]	LP OUT [K]	ORIFICE OUT [K]	VALVE OUT [K]	TIP [K]	HP IN [V]	LP OUT [V]	ATM [mm Hg]
1	0.0836	291.94	291.47	291.41	291.68	290.47	290.63	290.82	0.5911	0.0733	735.7
2	0.1187	292.17	290.74	290.66	291.89	289.04	289.49	289.58	0.8175	0.0605	729.1
3	0.1425	293.51	291.57	291.45	293.23	289.30	289.98	290.05	0.9980	0.0818	738.2
4	0.1755	292.06	288.37	288.19	291.75	285.21	286.34	286.22	1.2377	0.0680	738.2
5	0.1972	291.18	286.02	285.77	290.83	282.21	283.63	283.40	1.3940	0.0629	738.4
6	0.2267	291.37	284.26	283.94	290.98	279.65	281.42	281.07	1.5964	0.0789	735.7

0.013" Orifice - No Valve											
	Mass	*Thermocouples*							*Pressures*		
Point	Flow Rate [V]	HP IN [K]	HP OUT [K]	LP IN [K]	LP OUT [K]	ORIFICE OUT [K]	VALVE OUT [K]	TIP [K]	HP IN [V]	LP OUT [V]	ATM [mm Hg]
1	0.1378	292.14	291.06	290.99	291.92	289.99	290.20	290.34	0.6218	0.0616	737.8
2	0.1776	292.61	290.35	290.24	292.38	288.71	289.11	289.31	0.8087	0.1056	737.8
3	0.2231	291.70	287.62	287.45	291.39	285.21	285.91	286.29	1.0166	0.1154	737.8
4	0.2676	291.69	285.51	285.24	291.34	282.32	283.35	283.89	1.2131	0.1243	736.4
5	0.3030	291.71	283.77	283.41	291.28	279.97	281.23	281.88	1.3689	0.1414	737.8
6	0.3515	291.19	280.24	279.71	290.66	275.46	277.12	277.91	1.5771	0.1510	736.4

0.015" Orifice - No Valve											
	Mass	*Thermocouples*							*Pressures*		
Point	Flow Rate [V]	HP IN [K]	HP OUT [K]	LP IN [K]	LP OUT [K]	ORIFICE OUT [K]	VALVE OUT [K]	TIP [K]	HP IN [V]	LP OUT [V]	ATM [mm Hg]
1	0.1903	292.62	291.25	291.17	292.36	290.05	290.28	290.39	0.6278	-0.0250	735.4
2	0.2492	291.71	289.02	288.91	291.40	287.16	287.68	287.75	0.8271	0.0051	736.2
3	0.3046	291.92	287.66	287.47	291.57	285.13	285.94	285.91	1.0126	0.0301	737.4
4	0.3771	291.61	284.79	284.47	291.12	281.34	282.57	282.39	1.2469	0.0571	737.0
5	0.4243	291.09	282.21	281.75	290.51	278.06	279.55	279.29	1.3951	0.0548	738.3
6	0.4852	291.02	279.77	279.10	290.30	274.78	276.51	276.17	1.5806	0.0729	740.0

Table K.3: Integrated RTD voltages for the cryosurgical probe prototype with the forty-three die 10 mm heat exchanger installed. The working fluid was ethane and the orifice diameters tested include 0.010”, 0.013”, and 0.015”

0.010" Orifice - No Valve										
	HP PRTs					*LP PRTs*				
Point	PRT 9 [V]	PRT 10 [V]	PRT 12 [V]	PRT 13 [V]	PRT 14 [V]	PRT 1 [V]	PRT 2 [V]	PRT 4 [V]	PRT 5 [V]	PRT 6 [V]
1	0.52445	0.45094	0.50304	0.46312	0.64180	0.65358	0.50239	0.46273	0.54777	0.49269
2	0.52392	0.45066	0.50245	0.46245	0.64053	0.65242	0.50167	0.46236	0.54747	0.49259
3	0.52630	0.45246	0.50434	0.46404	0.64242	0.65418	0.50309	0.46393	0.54926	0.49454
4	0.52355	0.44992	0.50105	0.46076	0.63713	0.64868	0.49923	0.46097	0.54618	0.49205
5	0.52169	0.44818	0.49872	0.45841	0.63318	0.64470	0.49639	0.45878	0.54410	0.49037
6	0.52150	0.44780	0.49779	0.45722	0.63059	0.64199	0.49465	0.45790	0.54339	0.49019

0.013" Orifice - No Valve										
	HP PRTs					*LP PRTs*				
Point	PRT 9 [V]	PRT 10 [V]	PRT 12 [V]	PRT 13 [V]	PRT 14 [V]	PRT 1 [V]	PRT 2 [V]	PRT 4 [V]	PRT 5 [V]	PRT 6 [V]
1	0.52494	0.45105	0.50302	0.46299	0.64118	0.65289	0.50197	0.46255	0.54773	0.49285
2	0.52539	0.45128	0.50296	0.46274	0.64028	0.65194	0.50142	0.46247	0.54780	0.49325
3	0.52353	0.44938	0.50037	0.46007	0.63580	0.64726	0.49815	0.46003	0.54542	0.49143
4	0.52284	0.44851	0.49879	0.45828	0.63236	0.64372	0.49572	0.45854	0.54407	0.49077
5	0.52246	0.44801	0.49777	0.45701	0.62976	0.64087	0.49387	0.45744	0.54320	0.49036
6	0.52100	0.44627	0.49507	0.45405	0.62417	0.63495	0.48988	0.45489	0.54074	0.48882

0.015" Orifice - No Valve										
	HP PRTs					*LP PRTs*				
Point	PRT 9 [V]	PRT 10 [V]	PRT 12 [V]	PRT 13 [V]	PRT 14 [V]	PRT 1 [V]	PRT 2 [V]	PRT 4 [V]	PRT 5 [V]	PRT 6 [V]
1	0.52552	0.45153	0.50347	0.46335	0.64160	0.65331	0.50233	0.46299	0.54822	0.49342
2	0.52377	0.44983	0.50122	0.46109	0.63789	0.64948	0.49960	0.46088	0.54612	0.49176
3	0.52371	0.44957	0.50049	0.46014	0.63586	0.64731	0.49819	0.46017	0.54555	0.49167
4	0.52251	0.44818	0.49832	0.45770	0.63129	0.64249	0.49482	0.45803	0.54360	0.49050
5	0.52119	0.44676	0.49610	0.45534	0.62713	0.63801	0.49184	0.45591	0.54156	0.48914
6	0.52048	0.44585	0.49444	0.45340	0.62332	0.63386	0.48907	0.45423	0.54006	0.48836

Table K.4: Experimental data for the cryosurgical probe with the forty-three die 10 mm heat exchanger installed. The working fluid was ethane and the voltages applied to the valve include -30 V, 0 V, and 30 V.

No Orifice - Valve Voltage -30 V											
	Mass	*Thermocouples*							*Pressures*		
	Flow		HP		LP	ORIFICE	VALVE			LP	
Point	Rate	HP IN	OUT	LP IN	OUT	OUT	OUT	TIP	HP IN	OUT	ATM
	[V]	[K]	[K]	[K]	[K]	[K]	[K]	[K]	[V]	[V]	[mm Hg]
1	0.1331	291.49	290.63	290.57	291.22	289.76	289.63	289.92	0.5932	0.1230	734.3
2	0.1987	292.12	289.71	289.58	291.82	288.14	287.96	288.48	0.8287	0.1587	734.3
3	0.2481	291.34	287.23	287.03	290.99	285.06	284.82	285.54	1.0176	0.1473	737.7
4	0.2974	291.42	285.35	285.06	291.01	282.54	282.24	283.13	1.2066	0.1470	743.0
5	0.3499	291.48	283.08	282.67	290.99	279.57	279.21	280.31	1.4064	0.1747	741.9
6	0.4005	291.63	280.58	279.99	291.01	276.27	275.85	277.13	1.5952	0.1942	741.9

No Orifice - Valve Voltage 0 V											
	Mass	*Thermocouples*							*Pressures*		
	Flow		HP		LP	ORIFICE	VALVE			LP	
Point	Rate	HP IN	OUT	LP IN	OUT	OUT	OUT	TIP	HP IN	OUT	ATM
	[V]	[K]	[K]	[K]	[K]	[K]	[K]	[K]	[V]	[V]	[mm Hg]
1	0.1931	291.59	289.30	289.17	291.29	287.76	287.56	288.09	0.8242	0.1455	735.2
2	0.2884	291.42	285.44	285.15	291.02	282.62	282.33	283.24	1.2116	0.1517	739.0
3	0.3909	291.97	281.18	280.60	291.38	276.92	276.51	277.78	1.5901	0.1910	740.2

No Orifice - Valve Voltage 30 V											
	Mass	*Thermocouples*							*Pressures*		
	Flow		HP		LP	ORIFICE	VALVE			LP	
Point	Rate	HP IN	OUT	LP IN	OUT	OUT	OUT	TIP	HP IN	OUT	ATM
	[V]	[K]	[K]	[K]	[K]	[K]	[K]	[K]	[V]	[V]	[mm Hg]
1	0.3728	291.40	281.12	280.58	290.83	276.87	276.45	277.75	1.5916	0.1912	737.1

Table K.5: Integrated RTD voltages for the cryosurgical probe prototype with the forty-three die 10 mm heat exchanger installed. The working fluid was ethane and the voltages applied to the valve include -30 V, 0 V, and 30 V.

No Orifice - Valve Voltage -30 V										
	HP PRTs					*LP PRTs*				
Point	PRT 9 [V]	PRT 10 [V]	PRT 12 [V]	PRT 13 [V]	PRT 14 [V]	PRT 1 [V]	PRT 2 [V]	PRT 4 [V]	PRT 5 [V]	PRT 6 [V]
1	0.52287	0.44990	0.50177	0.46191	0.64002	0.65200	0.50126	0.46178	0.54676	0.49170
2	0.52336	0.45011	0.50157	0.46146	0.63870	0.65061	0.50044	0.46158	0.54675	0.49214
3	0.52171	0.44833	0.49913	0.45899	0.63432	0.64635	0.49747	0.45942	0.54458	0.49043
4	0.52134	0.44766	0.49782	0.45753	0.63116	0.64325	0.49540	0.45823	0.54347	0.48983
5	0.52088	0.44688	0.49636	0.45576	0.62758	0.63946	0.49292	0.45678	0.54224	0.48926
6	0.52051	0.44620	0.49488	0.45394	0.62380	0.63538	0.49025	0.45527	0.54096	0.48879

No Orifice - Valve Voltage 0 V										
	HP PRTs					*LP PRTs*				
Point	PRT 9 [V]	PRT 10 [V]	PRT 12 [V]	PRT 13 [V]	PRT 14 [V]	PRT 1 [V]	PRT 2 [V]	PRT 4 [V]	PRT 5 [V]	PRT 6 [V]
1	0.52256	0.44940	0.50082	0.46081	0.63781	0.64984	0.49983	0.46097	0.54604	0.49138
2	0.52142	0.44770	0.49790	0.45759	0.63150	0.64341	0.49554	0.45828	0.54370	0.49002
3	0.52109	0.44672	0.49554	0.45459	0.62480	0.63644	0.49102	0.45591	0.54160	0.48931

No Orifice - Valve Voltage 30 V										
	HP PRTs					*LP PRTs*				
Point	PRT 9 [V]	PRT 10 [V]	PRT 12 [V]	PRT 13 [V]	PRT 14 [V]	PRT 1 [V]	PRT 2 [V]	PRT 4 [V]	PRT 5 [V]	PRT 6 [V]
1	0.52032	0.44611	0.49502	0.45422	0.62449	0.63621	0.49076	0.45548	0.54106	0.48858

Table K.6: Experimental data for the cryosurgical probe with the forty-three die 10 mm heat exchanger installed. The working fluid was ethane and the voltages applied to the valve include 60 V, 80 V, and 100 V.

No Orifice - Valve Voltage 60 V											
	Mass	*Thermocouples*							*Pressures*		
Point	Flow Rate [V]	HP IN [K]	HP OUT [K]	LP IN [K]	LP OUT [K]	ORIFICE OUT [K]	VALVE OUT [K]	TIP [K]	HP IN [V]	LP OUT [V]	ATM [mm Hg]
1	0.1655	291.73	289.78	289.66	291.45	288.24	288.05	288.60	0.8243	0.1366	735.2
2	0.2465	291.37	286.19	285.94	291.00	283.39	283.09	284.04	1.2155	0.1390	739.8
3	0.3134	290.79	281.66	281.19	290.29	277.42	276.99	278.38	1.5998	0.1585	737.1

No Orifice - Valve Voltage 80 V											
	Mass	*Thermocouples*							*Pressures*		
Point	Flow Rate [V]	HP IN [K]	HP OUT [K]	LP IN [K]	LP OUT [K]	ORIFICE OUT [K]	VALVE OUT [K]	TIP [K]	HP IN [V]	LP OUT [V]	ATM [mm Hg]
1	0.2869	290.97	282.63	282.22	290.53	278.46	278.03	279.44	1.6021	0.1431	738.0

No Orifice - Valve Voltage 100 V											
	Mass	*Thermocouples*							*Pressures*		
Point	Flow Rate [V]	HP IN [K]	HP OUT [K]	LP IN [K]	LP OUT [K]	ORIFICE OUT [K]	VALVE OUT [K]	TIP [K]	HP IN [V]	LP OUT [V]	ATM [mm Hg]
1	0.1246	291.77	290.33	290.24	291.50	288.86	288.66	289.23	0.8275	0.1226	735.2
2	0.2017	291.59	287.28	287.06	291.25	284.53	284.23	285.22	1.2202	0.1223	739.8
3	0.2731	291.02	283.02	282.62	290.59	278.86	278.43	279.86	1.6042	0.1285	741.0

Table K.7: Integrated RTD voltages for the cryosurgical probe prototype with the forty-three die 10 mm heat exchanger installed. The working fluid was ethane and the voltages applied to the valve include 60 V, 80 V, and 100 V.

No Orifice - Valve Voltage 60 V										
	HP PRTs					*LP PRTs*				
Point	PRT 9 [V]	PRT 10 [V]	PRT 12 [V]	PRT 13 [V]	PRT 14 [V]	PRT 1 [V]	PRT 2 [V]	PRT 4 [V]	PRT 5 [V]	PRT 6 [V]
1	0.52286	0.44968	0.50122	0.46125	0.63851	0.65063	0.50039	0.46137	0.54642	0.49163
2	0.52161	0.44801	0.49843	0.45820	0.63266	0.64471	0.49634	0.45891	0.54403	0.49022
3	0.51972	0.44575	0.49495	0.45437	0.62518	0.63707	0.49125	0.45552	0.54092	0.48807

No Orifice - Valve Voltage 80 V										
	HP PRTs					*LP PRTs*				
Point	PRT 9 [V]	PRT 10 [V]	PRT 12 [V]	PRT 13 [V]	PRT 14 [V]	PRT 1 [V]	PRT 2 [V]	PRT 4 [V]	PRT 5 [V]	PRT 6 [V]
1	0.52018	0.44626	0.49573	0.45523	0.62672	0.63871	0.49238	0.45628	0.54164	0.48852

No Orifice - Valve Voltage 100 V										
	HP PRTs					*LP PRTs*				
Point	PRT 9 [V]	PRT 10 [V]	PRT 12 [V]	PRT 13 [V]	PRT 14 [V]	PRT 1 [V]	PRT 2 [V]	PRT 4 [V]	PRT 5 [V]	PRT 6 [V]
1	0.52307	0.44991	0.50162	0.46171	0.63933	0.65156	0.50104	0.46179	0.54678	0.49180
2	0.52211	0.44852	0.49929	0.45918	0.63434	0.64652	0.49770	0.45967	0.54490	0.49069
3	0.52032	0.44640	0.49600	0.45554	0.62728	0.63931	0.49279	0.45655	0.54188	0.48864

Table K.8: Calculated results from Table K.1

0.010" Orifice - No Valve											
	Mass Flow Rate		*Temperatures*		*Effectiveness*			*Pressures*			
Point	Value [g/s]	Uncertainty [g/s]	ΔT Assy [K]	U ΔT [K]	Hot Side [K]	Cold Side [K]	U Eff [K]	HP IN [kPa]	LP OUT [kPa]	ΔP Assy [kPa]	U ΔP [kPa]
1	0.0217	0.0028	-0.53	1.41	0.89	0.51	2.53	203.80	103.10	100.60	1.91
2	0.0307	0.0031	-1.51	1.41	0.95	0.80	0.91	281.80	101.40	180.40	1.91
3	0.0366	0.0032	-2.06	1.41	0.94	0.85	0.67	344.00	104.10	240.00	1.91
4	0.0451	0.0035	-3.87	1.41	0.95	0.90	0.36	426.70	103.10	323.60	1.91
5	0.0506	0.0037	-5.41	1.41	0.95	0.91	0.26	480.60	102.80	377.80	1.91
6	0.058	0.0040	-7.43	1.41	0.96	0.91	0.19	550.30	103.50	446.80	1.91

0.013" Orifice - No Valve											
	Mass Flow Rate		*Temperatures*		*Effectiveness*			*Pressures*			
Point	Value [g/s]	Uncertainty [g/s]	ΔT Assy [K]	U ΔT [K]	Hot Side [K]	Cold Side [K]	U Eff [K]	HP IN [kPa]	LP OUT [kPa]	ΔP Assy [kPa]	U ΔP [kPa]
1	0.0357	0.0032	-1.15	1.41	0.94	0.80	1.19	214.40	102.60	111.70	1.91
2	0.0459	0.0035	-2.37	1.41	0.95	0.89	0.58	278.80	105.60	173.10	1.91
3	0.0575	0.0040	-4.25	1.41	0.96	0.91	0.33	350.50	106.30	244.10	1.91
4	0.0688	0.0045	-6.45	1.41	0.96	0.92	0.21	418.20	106.70	311.50	1.91
5	0.0777	0.0049	-8.30	1.41	0.96	0.92	0.17	471.90	108.10	363.80	1.91
6	0.0899	0.0055	-11.48	1.41	0.95	0.92	0.12	543.70	108.60	435.10	1.91

0.015" Orifice - No Valve											
	Mass Flow Rate		*Temperatures*		*Effectiveness*			*Pressures*			
Point	Value [g/s]	Uncertainty [g/s]	ΔT Assy [K]	U ΔT [K]	Hot Side [K]	Cold Side [K]	U Eff [K]	HP IN [kPa]	LP OUT [kPa]	ΔP Assy [kPa]	U ΔP [kPa]
1	0.0493	0.0037	-1.45	1.41	0.94	0.81	0.95	216.40	96.32	120.10	1.91
2	0.0644	0.0043	-2.80	1.41	0.96	0.88	0.50	285.10	98.50	186.60	1.91
3	0.0785	0.0049	-4.45	1.41	0.96	0.90	0.31	349.10	100.40	248.70	1.91
4	0.0969	0.0058	-7.14	1.41	0.96	0.91	0.19	429.90	102.20	327.70	1.91
5	0.1089	0.0064	-9.34	1.41	0.95	0.91	0.15	480.90	102.20	378.70	1.91
6	0.1242	0.0072	-11.92	1.41	0.94	0.90	0.12	544.90	103.70	441.20	1.91

Table K.9: Calculated results from Table K.2

0.010" Orifice - No Valve										
	HP PRTs					*LP PRTs*				
Point	PRT 9 [K]	PRT 10 [K]	PRT 12 [K]	PRT 13 [K]	PRT 14 [K]	PRT 1 [K]	PRT 2 [K]	PRT 4 [K]	PRT 5 [K]	PRT 6 [K]
1	292.4	292.5	294.1	292.3	292.5	289.5	289.5	289.7	289.3	289.6
2	292.0	292.3	293.7	291.8	291.9	288.9	289.0	289.4	289.1	289.6
3	293.6	293.6	294.9	293.0	292.8	289.8	290.0	290.5	290.3	290.9
4	291.8	291.7	292.8	290.6	290.1	287.0	287.4	288.4	288.3	289.2
5	290.6	290.4	291.2	288.9	288.0	285.0	285.5	286.8	286.9	288.0
6	290.5	290.1	290.5	288.0	286.6	283.6	284.3	286.2	286.4	287.9

0.013" Orifice - No Valve										
	HP PRTs					*LP PRTs*				
Point	PRT 9 [K]	PRT 10 [K]	PRT 12 [K]	PRT 13 [K]	PRT 14 [K]	PRT 1 [K]	PRT 2 [K]	PRT 4 [K]	PRT 5 [K]	PRT 6 [K]
1	292.7	292.6	294.1	292.2	292.2	289.1	289.2	289.5	289.3	289.7
2	293.0	292.7	294.1	292.0	291.7	288.7	288.8	289.5	289.4	290.0
3	291.8	291.3	292.3	290.1	289.4	286.3	286.7	287.7	287.8	288.8
4	291.3	290.7	291.2	288.8	287.6	284.5	285.0	286.7	286.9	288.3
5	291.1	290.3	290.5	287.8	286.2	283.0	283.8	285.9	286.3	288.0
6	290.1	289.0	288.7	285.7	283.2	280.0	281.1	284.1	284.7	287.0

0.015" Orifice - No Valve										
	HP PRTs					*LP PRTs*				
Point	PRT 9 [K]	PRT 10 [K]	PRT 12 [K]	PRT 13 [K]	PRT 14 [K]	PRT 1 [K]	PRT 2 [K]	PRT 4 [K]	PRT 5 [K]	PRT 6 [K]
1	293.1	292.9	294.3	292.5	292.4	289.4	289.5	289.9	289.6	290.1
2	291.9	291.7	292.9	290.8	290.5	287.4	287.6	288.3	288.2	289.0
3	291.9	291.5	292.4	290.1	289.4	286.3	286.7	287.8	287.9	288.9
4	291.1	290.4	290.9	288.3	287.0	283.8	284.4	286.3	286.6	288.1
5	290.3	289.4	289.4	286.6	284.8	281.5	282.4	284.8	285.2	287.2
6	289.8	288.7	288.2	285.2	282.8	279.4	280.6	283.6	284.2	286.7

Table K.10: Calculated results from Table K.3

No Orifice - Valve Voltage -30 V											
	Mass Flow Rate		***Temperatures***		***Effectiveness***			***Pressures***			
Point	Value [g/s]	Uncertainty [g/s]	ΔT Assy [K]	U ΔT [K]	Hot Side [K]	Cold Side [K]	U Eff [K]	HP IN [kPa]	LP OUT [kPa]	ΔP Assy [kPa]	U ΔP [kPa]
1	0.0346	0.0032	-0.92	1.41	0.93	0.70	1.49	204.50	106.40	98.12	1.91
2	0.0513	0.0037	-2.54	1.41	0.95	0.87	0.54	285.70	108.80	176.80	1.91
3	0.064	0.0043	-4.31	1.41	0.95	0.90	0.32	350.80	108.50	242.30	1.91
4	0.0765	0.0048	-6.36	1.41	0.95	0.91	0.22	416.00	109.20	306.80	1.91
5	0.0897	0.0055	-8.81	1.41	0.95	0.91	0.16	484.80	111.00	373.90	1.91
6	0.1024	0.0061	-11.64	1.41	0.95	0.91	0.12	549.90	112.30	437.60	1.91
No Orifice - Valve Voltage 0 V											
	Mass Flow Rate		***Temperatures***		***Effectiveness***			***Pressures***			
Point	Value [g/s]	Uncertainty [g/s]	ΔT Assy [K]	U ΔT [K]	Hot Side [K]	Cold Side [K]	U Eff [K]	HP IN [kPa]	LP OUT [kPa]	ΔP Assy [kPa]	U ΔP [kPa]
1	0.05	0.0037	-2.42	1.41	0.95	0.86	0.57	284.10	108.10	176.10	1.91
2	0.0742	0.0047	-6.27	1.41	0.95	0.91	0.22	417.70	109.00	308.70	1.91
3	0.0999	0.0060	-11.37	1.41	0.95	0.91	0.12	548.20	111.90	436.30	1.91
No Orifice - Valve Voltage 30 V											
	Mass Flow Rate		***Temperatures***		***Effectiveness***			***Pressures***			
Point	Value [g/s]	Uncertainty [g/s]	ΔT Assy [K]	U ΔT [K]	Hot Side [K]	Cold Side [K]	U Eff [K]	HP IN [kPa]	LP OUT [kPa]	ΔP Assy [kPa]	U ΔP [kPa]
1	0.0953	0.0057	-10.82	1.41	0.95	0.91	0.13	548.70	111.50	437.20	1.91

Table K.11: Calculated results from Table K.4

No Orifice - Valve Voltage -30 V										
	HP PRTs					*LP PRTs*				
Point	PRT 9 [K]	PRT 10 [K]	PRT 12 [K]	PRT 13 [K]	PRT 14 [K]	PRT 1 [K]	PRT 2 [K]	PRT 4 [K]	PRT 5 [K]	PRT 6 [K]
1	291.3	291.7	293.3	291.4	291.6	288.7	288.7	289.0	288.7	289.0
2	291.7	291.9	293.1	291.1	290.9	288.0	288.2	288.9	288.7	289.3
3	290.6	290.5	291.4	289.3	288.6	285.8	286.2	287.3	287.2	288.1
4	290.4	290.0	290.6	288.2	286.9	284.2	284.8	286.4	286.5	287.7
5	290.1	289.5	289.6	286.9	285.0	282.3	283.1	285.4	285.7	287.3
6	289.8	288.9	288.5	285.6	283.0	280.2	281.4	284.3	284.8	287.0

No Orifice - Valve Voltage 0 V										
	HP PRTs					*LP PRTs*				
Point	PRT 9 [K]	PRT 10 [K]	PRT 12 [K]	PRT 13 [K]	PRT 14 [K]	PRT 1 [K]	PRT 2 [K]	PRT 4 [K]	PRT 5 [K]	PRT 6 [K]
1	291.1	291.3	292.6	290.6	290.4	287.6	287.8	288.4	288.2	288.7
2	290.4	290.1	290.6	288.3	287.1	284.3	284.9	286.5	286.6	287.8
3	290.2	289.3	289.0	286.1	283.6	280.7	281.9	284.8	285.2	287.3

No Orifice - Valve Voltage 30 V										
	HP PRTs					*LP PRTs*				
Point	PRT 9 [K]	PRT 10 [K]	PRT 12 [K]	PRT 13 [K]	PRT 14 [K]	PRT 1 [K]	PRT 2 [K]	PRT 4 [K]	PRT 5 [K]	PRT 6 [K]
1	289.7	288.9	288.6	285.8	283.4	280.6	281.7	284.5	284.9	286.8

Table K.12: Calculated results from Table K.5

No Orifice - Valve Voltage 60 V											
	Mass Flow Rate		***Temperatures***		***Effectiveness***			***Pressures***			
Point	Value [g/s]	Uncertainty [g/s]	ΔT Assy [K]	U ΔT [K]	Hot Side [K]	Cold Side [K]	U Eff [K]	HP IN [kPa]	LP OUT [kPa]	ΔP Assy [kPa]	U ΔP [kPa]
1	0.0428	0.0034	-2.07	1.41	0.94	0.85	0.66	284.20	107.40	176.70	1.91
2	0.0634	0.0042	-5.43	1.41	0.95	0.91	0.25	419.00	108.20	310.80	1.91
3	0.0802	0.0050	-9.60	1.41	0.95	0.91	0.14	551.50	109.20	442.30	1.91
No Orifice - Valve Voltage 80 V											
	Mass Flow Rate		***Temperatures***		***Effectiveness***			***Pressures***			
Point	Value [g/s]	Uncertainty [g/s]	ΔT Assy [K]	U ΔT [K]	Hot Side [K]	Cold Side [K]	U Eff [K]	HP IN [kPa]	LP OUT [kPa]	ΔP Assy [kPa]	U ΔP [kPa]
1	0.0734	0.0047	-8.75	1.41	0.95	0.91	0.16	552.30	108.30	444.00	1.91
No Orifice - Valve Voltage 100 V											
	Mass Flow Rate		***Temperatures***		***Effectiveness***			***Pressures***			
Point	Value [g/s]	Uncertainty [g/s]	ΔT Assy [K]	U ΔT [K]	Hot Side [K]	Cold Side [K]	U Eff [K]	HP IN [kPa]	LP OUT [kPa]	ΔP Assy [kPa]	U ΔP [kPa]
1	0.0322	0.0031	-1.53	1.41	0.94	0.81	0.90	285.30	106.50	178.80	1.91
2	0.0519	0.0038	-4.53	1.41	0.95	0.90	0.30	420.60	107.10	313.60	1.91
3	0.0699	0.0046	-8.40	1.41	0.95	0.91	0.16	553.00	107.70	445.40	1.91

Table K.13: Calculated results from Table K.6

No Orifice - Valve Voltage 60 V										
	HP PRTs					*LP PRTs*				
Point	PRT 9 [K]	PRT 10 [K]	PRT 12 [K]	PRT 13 [K]	PRT 14 [K]	PRT 1 [K]	PRT 2 [K]	PRT 4 [K]	PRT 5 [K]	PRT 6 [K]
1	291.3	291.5	292.9	290.9	290.8	288.0	288.2	288.7	288.4	288.9
2	290.5	290.3	291.0	288.7	287.7	285.0	285.4	286.9	286.9	287.9
3	289.3	288.6	288.6	285.9	283.8	281.1	282.0	284.5	284.8	286.5

No Orifice - Valve Voltage 80 V										
	HP PRTs					*LP PRTs*				
Point	PRT 9 [K]	PRT 10 [K]	PRT 12 [K]	PRT 13 [K]	PRT 14 [K]	PRT 1 [K]	PRT 2 [K]	PRT 4 [K]	PRT 5 [K]	PRT 6 [K]
1	289.6	289.0	289.1	286.5	284.6	281.9	282.8	285.0	285.3	286.8

No Orifice - Valve Voltage 100 V										
	HP PRTs					*LP PRTs*				
Point	PRT 9 [K]	PRT 10 [K]	PRT 12 [K]	PRT 13 [K]	PRT 14 [K]	PRT 1 [K]	PRT 2 [K]	PRT 4 [K]	PRT 5 [K]	PRT 6 [K]
1	291.5	291.7	293.2	291.3	291.2	288.5	288.6	289.0	288.7	289.0
2	290.9	290.7	291.6	289.4	288.6	285.9	286.4	287.5	287.4	288.3
3	289.7	289.1	289.3	286.8	284.9	282.2	283.1	285.2	285.4	286.9

Appendix L: Forty-three Die 10 mm Heat Exchanger Effectiveness Tests

Table L.1: Locations of the integrated PRTs within the forty-three die 10 mm heat exchanger applied-cooling tests performed in the cryogenic testing facility

Die	HP Inlet	LP Outlet
1		
2		
3		
4		
5		
6		
7		
8		
9	PRT 9 (Norm)	PRT 6 (Norm)
10		
11		
12		
13		
14		
15		
16		
17		
18		
19		
20		
21		
22	PRT 12 (Norm)	PRT 4 (Norm)
23		
24		
25		
26		
27	PRT 13 (Norm)	
28		
29		
30		
31		
32		PRT 2 (Norm)
33		
34		
35		
36	PRT 14 (Norm)	PRT 1 (Norm)
37		
38		
39		
40		
41		
42		
43		
	HP Outlet	**LP Inlet**

Table L.2: Experimental temperature measurements at the inlets and outlets for the forty-three die 10 mm heat exchanger as it was being tested in applied-cooling mode in the cryogenic test facility. Helium was the working fluid.

Point	PRTs					Thermocouples			
	HP IN [V]	HP OUT [V]	LP IN [V]	LP OUT [V]	CC [V]	HP IN [K]	HP OUT [K]	LP IN [K]	LP OUT [K]
1	0.11163	0.09701	0.09177	0.10882	0.08737	303.43	265.40	252.83	295.49
2	0.11019	0.09060	0.08740	0.10800	0.08528	299.59	249.62	241.30	293.50
3	0.10900	0.08919	0.08671	0.10704	0.08526	296.38	246.14	239.40	291.05
4	0.10904	0.09039	0.08824	0.10722	0.08714	296.45	249.19	243.25	291.52
5	0.10964	0.08819	0.08579	0.10745	0.08485	297.93	243.68	237.04	292.11
6	0.10866	0.09015	0.08773	0.10634	0.08716	295.39	248.51	241.89	289.09
7	0.10966	0.08833	0.08586	0.10737	0.08503	297.96	243.99	237.19	291.83

Table L.3: Experimental mass flow rate and pressure measurements for the forty-three die 10 mm heat exchanger as it was being tested in applied-cooling mode in the cryogenic test facility. Helium was the working fluid.

Point	Mass Flow Rate [V]	Pressures		
		HP IN [V]	LP OUT [V]	ATM [mm Hg]
1	0.0849	0.2847	-0.2133	735.0
2	0.1961	0.3817	0.0407	735.8
3	0.2979	0.4410	0.1386	742.1
4	0.4002	0.4847	0.1159	735.8
5	0.5085	0.5820	0.4776	742.1
6	0.8591	0.7116	0.2002	742.1
7	0.6100	0.6042	0.3105	735.8

Table L.4: Experimental temperature measurements for the integrated PRTs of the forty-three die 10 mm heat exchanger as it was being tested in applied-cooling mode in the cryogenic test facility. Helium was the working fluid.

Point	Die PRTs							
	PRT 1 [V]	PRT 2 [V]	PRT 12 [V]	PRT 4 [V]	PRT 9 [V]	PRT 6 [V]	PRT 13 [V]	PRT 14 [V]
1	0.61371	0.47614	0.48118	0.44824	0.51819	0.49134	0.44008	0.59726
2	0.58837	0.45893	0.47053	0.43694	0.51326	0.48578	0.42777	0.57424
3	0.58196	0.45426	0.46717	0.43300	0.51013	0.48211	0.42445	0.56880
4	0.58677	0.45768	0.46986	0.43543	0.51220	0.48359	0.42741	0.57405
5	0.57773	0.45175	0.46796	0.43228	0.51324	0.48299	0.42436	0.56639
6	0.58303	0.45479	0.47008	0.43289	0.51180	0.48064	0.42744	0.57353
7	0.57733	0.45154	0.46789	0.43210	0.51314	0.48281	0.42443	0.56680

Table L.5: Experimental temperature measurements at the inlets and outlets for the forty-three die 10 mm heat exchanger as it was being tested in applied-cooling mode in the cryogenic test facility. Ethane was the working fluid.

Point	PRTs					Thermocouples			
	HP IN [V]	HP OUT [V]	LP IN [V]	LP OUT [V]	CC [V]	HP IN [K]	HP OUT [K]	LP IN [K]	LP OUT [K]
1	0.10948	0.09582	0.09266	0.10768	0.09028	297.81	263.14	255.11	292.74
2	0.10907	0.09338	0.09072	0.10725	0.08917	296.65	256.86	249.91	291.63
3	0.10932	0.09310	0.09064	0.10730	0.08948	297.16	256.15	249.54	291.79
4	0.10901	0.09268	0.09019	0.10693	0.08919	296.42	255.04	248.34	290.86
5	0.10898	0.09087	0.08807	0.10654	0.08717	296.31	250.48	242.97	289.87
6	0.10872	0.09248	0.08986	0.10629	0.08913	295.58	254.44	247.36	289.19

Table L.6: Experimental mass flow rate and pressure measurements for the forty-three die 10 mm heat exchanger as it was being tested in applied-cooling mode in the cryogenic test facility. Ethane was the working fluid.

Point	Mass Flow Rate [V]	Pressures		
		HP IN [V]	LP OUT [V]	ATM [mm Hg]
1	0.1676	0.3746	0.3351	734.7
2	0.2774	0.4023	0.3784	734.7
3	0.3819	0.4315	0.4045	735
4	0.4598	0.4556	0.4290	733.4
5	0.5304	0.4795	0.4526	739.6
6	0.6509	0.5226	0.4851	732.2

Table L.7: Experimental temperature measurements for the integrated PRTs of the forty-three die 10 mm heat exchanger as it was being tested in applied-cooling mode in the cryogenic test facility. Ethane was the working fluid.

Point	Die PRTs							
	PRT 1 [V]	PRT 2 [V]	PRT 12 [V]	PRT 4 [V]	PRT 9 [V]	PRT 6 [V]	PRT 13 [V]	PRT 14 [V]
1	0.60959	0.47316	0.47863	0.44582	0.51582	0.48864	0.43752	0.59296
2	0.59936	0.46626	0.47462	0.44158	0.51411	0.48658	0.43270	0.58355
3	0.59825	0.46565	0.47502	0.44159	0.51513	0.48713	0.43280	0.58299
4	0.59586	0.46390	0.47378	0.44012	0.51404	0.48579	0.43156	0.58101
5	0.58778	0.45837	0.47031	0.43642	0.51227	0.48362	0.42762	0.57372
6	0.59391	0.46237	0.47279	0.43852	0.51289	0.48397	0.43073	0.57997

Table L.8: Calculated results from experimental data shown in Table L.2

Point	Commercial PRTs					Thermocouple Effectiveness			Commercial PRT Effectiveness		
	HP IN [K]	HP OUT [K]	LP IN [K]	LP OUT [K]	CC [K]	Hot Side [-]	Cold Side [-]	U_{Eff} [-]	Hot Side [-]	Cold Side [-]	U_{Eff} [-]
1	303.1	265.7	252.0	295.8	241.1	0.752	0.843	0.005	0.731	0.858	0.006
2	299.3	249.4	240.9	293.7	235.8	0.857	0.896	0.005	0.854	0.904	0.006
3	296.3	245.8	239.1	291.2	235.7	0.882	0.907	0.005	0.883	0.912	0.006
4	296.4	248.9	243.0	291.7	240.5	0.888	0.907	0.005	0.890	0.912	0.006
5	297.9	243.3	236.8	292.3	234.7	0.891	0.904	0.004	0.894	0.908	0.006
6	298.0	243.7	237.0	292.1	235.1	0.888	0.899	0.004	0.891	0.904	0.006
7	295.4	248.3	241.7	289.4	240.5	0.876	0.882	0.005	0.878	0.889	0.006

Table L.9: Calculated results from experimental data shown in Table L.3

Point	Mass Flow Rate		Pressures			
	Value [g/s]	Uncertainty [g/s]	HP IN [kPa]	LP OUT [kPa]	ΔP [kPa]	$U_{\Delta P}$ [kPa]
1	0.0082	0.0010	98.2	83.3	14.9	1.9
2	0.0190	0.0010	131.6	100.9	30.7	1.9
3	0.0289	0.0011	152.0	108.5	43.5	1.9
4	0.0388	0.0012	167.1	106.1	61.0	1.9
5	0.0494	0.0014	200.6	131.9	68.8	1.9
6	0.0592	0.0015	208.3	119.5	88.8	1.9
7	0.0834	0.0019	245.3	112.7	132.6	1.9

Table L.10: Calculated results from experimental data shown in Table L.4

Point	Die PRT Temperatures							
	HP Side				LP Side			
	PRT 9 [K]	PRT 12 [K]	PRT 13 [K]	PRT 14 [K]	PRT 1 [K]	PRT 2 [K]	PRT 4 [K]	PRT 6 [K]
	288.3	279.2	275.4	269.0	269.0	271.9	279.3	288.7
1	285.1	271.8	266.4	256.8	256.0	260.3	271.2	284.9
2	283.1	269.6	264.0	253.9	252.7	257.2	268.4	282.4
3	284.4	271.4	266.2	256.7	255.1	259.5	270.1	283.4
4	285.1	270.1	264.0	252.6	250.5	255.5	267.9	283.0
5	285.0	270.1	264.0	252.8	250.3	255.4	267.7	282.9
6	284.1	271.5	266.2	256.4	253.2	257.5	268.3	281.4

Table L.11: Calculated results from experimental data shown in Table L.5

Point	Commercial PRTs					Thermocouple Effectiveness			Commercial PRT Effectiveness		
	HP IN [K]	HP OUT [K]	LP IN [K]	LP OUT [K]	CC [K]	Hot Side [-]	Cold Side [-]	U_{Eff} [-]	Hot Side [-]	Cold Side [-]	U_{Eff} [-]
1	297.5	262.7	254.2	292.9	248.4	0.819	0.876	0.006	0.812	0.888	0.007
2	296.5	256.5	249.3	291.8	245.6	0.857	0.886	0.006	0.854	0.895	0.007
3	297.1	255.8	249.1	291.9	246.4	0.867	0.880	0.006	0.867	0.885	0.007
4	296.3	254.7	248.0	291.0	245.7	0.866	0.876	0.006	0.867	0.882	0.007
5	296.2	250.1	242.6	290.0	240.5	0.866	0.870	0.005	0.866	0.874	0.006
6	295.6	254.2	247.1	289.3	245.5	0.859	0.857	0.005	0.860	0.861	0.007

Table L.12: Calculated results from experimental data shown in Table L.6

Point	Mass Flow Rate		Pressures			
	Value [g/s]	Uncertainty [g/s]	HP IN [kPa]	LP OUT [kPa]	ΔP [kPa]	$U_{\Delta P}$ [kPa]
1	0.0431	0.0035	129.1	121.1	8.1	1.9
2	0.0714	0.0046	138.7	124.0	14.7	1.9
3	0.0982	0.0058	148.8	125.9	22.9	1.9
4	0.1184	0.0068	157.1	127.4	29.7	1.9
5	0.1365	0.0077	165.3	129.8	35.5	1.9
6	0.1677	0.0093	180.2	131.1	49.1	1.9

Table L.13: Calculated results from experimental data shown in Table L.7

Point	Die PRT Temperatures							
	HP Side				LP Side			
	PRT 9 [K]	PRT 12 [K]	PRT 13 [K]	PRT 14 [K]	PRT 1 [K]	PRT 2 [K]	PRT 4 [K]	PRT 6 [K]
1	286.8	277.4	273.6	266.7	266.9	269.9	277.5	286.9
2	285.6	274.7	270.0	261.7	261.6	265.2	274.5	285.4
3	286.3	274.9	270.1	261.4	261.1	264.8	274.5	285.8
4	285.6	274.1	269.2	260.4	259.8	263.7	273.5	284.9
5	284.5	271.7	266.3	256.5	255.7	259.9	270.8	283.4
6	284.9	273.4	268.6	259.8	258.8	262.6	272.3	283.7

Appendix M: Thirty-seven Die 20 mm Heat Exchanger Effectiveness Tests

Table M.1: Locations of the integrated PRTs within the thirty-seven die 20 mm heat exchanger for the applied-cooling tests performed in the cryogenic testing facility

Die	HP Inlet	LP Outlet
1		
2		
3		
4		
5		
6		
7		
8	PRT 8 (Norm)	
9		
10		
11		
12		
13		
14	PRT 7 (Ref)	
15		
16		
17		
18		
19	PRT 6 (Norm)	PRT 1 (Norm)
20		
21		
22		
23		
24	PRT 5 (Ref)	
25		
26		
27		
28	PRT 4 (Ref)	PRT 2 (Norm)
29		
30		
31		
32		
33		PRT 3 (Ref)
34		
35		
36		
37		
38		
39		
40		
41		
42		
43		
	HP Outlet	**LP Inlet**

Table M.2: Experimental temperature measurements at the inlets and outlets for the thirty-seven die 20 mm heat exchanger as it was being tested in applied-cooling mode in the cryogenic test facility. Helium was the working fluid.

Point	PRTs					Thermocouples			
	HP IN [V]	HP OUT [V]	LP IN [V]	LP OUT [V]	CC [V]	HP IN [K]	HP OUT [K]	LP IN [K]	LP OUT [K]
1	0.11001	0.09327	0.08788	0.10738	0.08575	298.99	256.74	242.98	292.01
2	0.10929	0.09028	0.08530	0.10675	0.08363	297.09	249.20	236.22	290.30
3	0.10902	0.09173	0.08770	0.10687	0.08646	296.42	252.88	242.18	290.60
4	0.10961	0.08972	0.08546	0.10707	0.08436	297.83	247.79	236.47	291.05
5	0.10900	0.08987	0.08582	0.10647	0.08490	296.28	248.13	237.30	289.51
6	0.10950	0.08893	0.08443	0.10649	0.08368	297.51	245.74	233.88	289.51
7	0.10885	0.08891	0.08407	0.10548	0.08349	295.79	245.62	232.98	286.86

Table M.3: Experimental mass flow rate and pressure measurements for the thirty-seven die 20 mm heat exchanger as it was being tested in applied-cooling mode in the cryogenic test facility. Helium was the working fluid.

Point	Mass Flow Rate [V]	Pressures		
		LP IN [V]	LP OUT [V]	ATM [mm Hg]
1	0.3040	0.3785	0.1953	738.0
2	0.4030	0.4125	0.2715	738.0
3	0.5346	0.4626	0.3843	736.8
4	0.6647	0.5092	0.4509	738.0
5	0.8288	0.5745	0.6098	736.8
6	1.0602	0.6726	0.8286	736.8
7	1.4006	0.8068	1.0904	736.4

Table M.4: Experimental temperature measurements for the integrated PRTs of the thirty-seven die 20 mm heat exchanger as it was being tested in applied-cooling mode in the cryogenic test facility. Helium was the working fluid.

Point	Die PRTs							
	PRT 1 [V]	PRT 2 [V]	PRT 3 [V]	PRT 4 [V]	PRT 5 [V]	PRT 6 [V]	PRT 7 [V]	PRT 8 [V]
1	0.22361	0.22512	0.24709	0.26573	0.33091	0.22731	0.31724	0.21324
2	0.22073	0.22160	0.24293	0.26329	0.32669	0.22485	0.31485	0.21195
3	0.22213	0.22324	0.24460	0.26525	0.32954	0.22660	0.31695	0.21295
4	0.22075	0.22102	0.24141	0.26429	0.32781	0.22590	0.31703	0.21333
5	0.22020	0.22072	0.24116	0.26487	0.32804	0.22584	0.31690	0.21297
6	0.21923	0.21929	0.23895	0.26526	0.32790	0.22594	0.31778	0.21361
7	0.21779	0.21830	0.23772	0.26599	0.32790	0.22562	0.31739	0.21299

Table M.5: Calculated results from the experimental data in Table M.2

Point	Commercial PRTs					Thermocouple Effectiveness			Commercial PRT Effectiveness		
	HP IN [K]	HP OUT [K]	LP IN [K]	LP OUT [K]	CC [K]	Hot Side [-]	Cold Side [-]	U_{Eff} [-]	Hot Side [-]	Cold Side [-]	U_{Eff} [-]
1	298.9	256.2	242.1	292.1	237.0	0.754	0.875	0.023	0.752	0.881	0.006
2	297.0	248.6	235.6	290.5	231.6	0.787	0.889	0.021	0.788	0.894	0.005
3	296.3	252.3	241.7	290.8	238.8	0.803	0.893	0.024	0.806	0.899	0.006
4	297.8	247.2	236.0	291.3	233.4	0.816	0.89	0.021	0.819	0.894	0.005
5	296.3	247.6	236.9	289.8	234.8	0.816	0.885	0.022	0.821	0.891	0.005
6	297.6	245.2	233.4	289.8	231.7	0.814	0.874	0.02	0.817	0.879	0.005
7	295.9	245.1	232.5	287.2	231.3	0.799	0.858	0.021	0.801	0.864	0.005

Table M.6: Calculated results from the experimental data in Table M.3

Point	Mass Flow Rate		Pressures			
	Value [g/s]	Uncertainty [g/s]	HP IN [kPa]	LP OUT [kPa]	ΔP [kPa]	$U_{\Delta P}$ [kPa]
1	0.0295	0.0011	130.5	111.9	18.6	1.9
2	0.0391	0.0012	142.2	117.1	25.1	1.9
3	0.0519	0.0014	159.5	124.7	34.8	1.9
4	0.0645	0.0016	175.5	129.5	46.1	1.9
5	0.0804	0.0019	198.1	140.3	57.8	1.9
6	0.1029	0.0023	231.9	155.4	76.5	1.9
7	0.1359	0.0029	278.1	173.4	104.8	1.9

Table M.7: Calculated results from the experimental data in Table M.4

	Die PRT Temperatures							
	HP Side					LP Side		
Point	PRT 8 [K]	PRT 7 [K]	PRT 6 [K]	PRT 4 [K]	PRT 5 [K]	PRT 1 [K]	PRT 2 [K]	PRT 3 [K]
1	285.9	281.1	275.4	270.9	270.0	274.3	265.2	256.8
2	283.9	278.6	271.8	265.3	265.5	270.0	259.2	248.2
3	285.4	280.8	274.3	269.8	268.5	272.1	262.0	251.7
4	286.0	280.9	273.3	267.4	266.7	270.1	258.2	245.1
5	285.5	280.7	273.2	268.8	266.9	269.3	257.7	244.5
6	286.4	281.6	273.4	269.8	266.8	267.8	255.3	240.0
7	285.5	281.2	272.9	271.6	266.8	265.8	253.6	237.4

Appendix N: Forty-three Die 10 mm Heat Exchanger Self-Cooling Tests

Table N.1: Locations of the integrated PRTs within the forty-three die 10 mm heat exchanger self-cooling tests performed in the cryogenic testing facility

Die	HP Inlet	LP Outlet
1		
2		
3		
4		
5		
6		
7		
8		
9	PRT 9 (Norm)	PRT 6 (Norm)
10		
11		
12		
13		
14	PRT 10 (Norm)	
15		
16		
17		
18		PRT 5 (Norm)
19		
20		
21		
22	PRT 12 (Norm)	PRT 4 (Norm)
23		
24		
25		
26		
27	PRT 13 (Norm)	
28		
29		
30		
31		
32		PRT 2 (Norm)
33		
34		
35		
36	PRT 14 (Norm)	PRT 1 (Norm)
37		
38		
39		
40		
41		
42		
43		
	HP Outlet	LP Inlet

Table N.2: Experimental data for the forty-three die 10 mm heat exchanger installed in the cryogenic test facility. The working fluid was ethane and the orifice diameters tested include 0.010", 0.015", and 0.020"

0.010" Orifice - No Valve								
	Mass	*Thermocouples*				*Pressures*		
	Flow		HP		LP		LP	
Point	Rate	HP IN	OUT	LP IN	OUT	HP IN	OUT	ATM
	[V]	[K]	[K]	[K]	[K]	[V]	[V]	[mm Hg]
1	0.0892	293.00	288.87	288.73	292.13	0.6143	0.1619	742
2	0.1158	294.73	285.74	285.32	293.09	0.8062	-0.1112	739
3	0.1455	294.71	279.60	278.68	292.33	1.0123	-0.0962	742
4	0.1754	293.20	270.55	268.83	290.23	1.2103	-0.3215	742
5	0.2056	294.89	264.61	262.02	291.18	1.4032	-0.2453	739
6	0.2340	294.90	257.76	254.18	290.72	1.5735	-0.1693	739

0.015" Orifice - No Valve								
	Mass	*Thermocouples*				*Pressures*		
	Flow		HP		LP		LP	
Point	Rate	HP IN	OUT	LP IN	OUT	HP IN	OUT	ATM
	[V]	[K]	[K]	[K]	[K]	[V]	[V]	[mm Hg]
1	0.1116	294.04	292.68	292.74	293.78	0.4030	0.0903	726
2	0.1862	295.82	288.68	288.40	294.72	0.6191	0.1033	730
3	0.2482	296.06	284.05	283.32	294.46	0.8155	0.1314	726
4	0.2977	294.70	277.81	276.57	292.55	0.9714	0.1984	741
5	0.3788	295.01	269.75	267.42	291.96	1.2141	0.2050	741
6	0.4479	293.64	261.56	258.03	289.80	1.4100	0.1940	741
7	0.5163	295.18	256.91	252.19	290.44	1.5949	0.1818	730

0.020" Orifice - No Valve								
	Mass	*Thermocouples*				*Pressures*		
	Flow		HP		LP		LP	
Point	Rate	HP IN	OUT	LP IN	OUT	HP IN	OUT	ATM
	[V]	[K]	[K]	[K]	[K]	[V]	[V]	[mm Hg]
1	0.1969	294.39	292.69	292.68	294.07	0.4073	0.0968	735.3
2	0.3639	297.07	289.43	288.99	295.89	0.6128	0.1622	731.3
3	0.4917	292.48	282.37	281.49	290.95	0.7918	0.3990	740.6
4	0.6349	292.69	278.16	276.53	290.33	0.9872	0.3512	737.9
5	0.7991	292.80	272.84	270.03	289.22	1.2310	0.1205	734.6
6	0.9123	292.53	270.09	266.47	288.22	1.3892	0.0644	733.3
7	1.0487	292.94	268.61	264.18	287.90	1.5799	0.1411	731.3

Table N.3: Integrated RTD voltages for the forty-three die 10 mm heat exchanger installed in the cryogenic test facility. The working fluid was ethane and the orifice diameters tested include 0.010”, 0.015”, and 0.020”

0.010" Orifice - No Valve										
	HP PRTs					*LP PRTs*				
Point	PRT 9 [V]	PRT 10 [V]	PRT 12 [V]	PRT 13 [V]	PRT 14 [V]	PRT 1 [V]	PRT 2 [V]	PRT 4 [V]	PRT 5 [V]	PRT 6 [V]
1	0.52282	0.44892	0.49789	0.46030	0.63632	0.65500	0.50378	0.46470	0.55088	0.49607
2	0.52346	0.44890	0.49684	0.45867	0.63248	0.65095	0.50123	0.46362	0.55023	0.49661
3	0.52110	0.44608	0.49240	0.45365	0.62330	0.64135	0.49467	0.45929	0.54625	0.49429
4	0.62674	0.48461	0.48522	0.45230	0.51637	0.48967	0.44581	0.60934	0.53958	0.44106
5	0.51680	0.44053	0.48292	0.44245	0.60140	0.61826	0.47931	0.44993	0.53790	0.48990
6	0.51518	0.43836	0.47901	0.43769	0.59158	0.60783	0.47252	0.44602	0.53447	0.48819

0.015" Orifice - No Valve										
	HP PRTs					*LP PRTs*				
Point	PRT 9 [V]	PRT 10 [V]	PRT 12 [V]	PRT 13 [V]	PRT 14 [V]	PRT 1 [V]	PRT 2 [V]	PRT 4 [V]	PRT 5 [V]	PRT 6 [V]
1	0.52592	0.45197	0.50179	0.46414	0.64234	0.66124	0.50830	0.46833	0.55455	0.49900
2	0.52629	0.45153	0.50001	0.46168	0.63697	0.65557	0.50464	0.46654	0.55326	0.49924
3	0.52501	0.44978	0.49693	0.45805	0.63003	0.64820	0.49967	0.46347	0.55052	0.49789
4	0.52149	0.44611	0.49180	0.45246	0.62037	0.63794	0.49252	0.45836	0.54562	0.49438
5	0.51932	0.44315	0.48656	0.44625	0.60813	0.62481	0.48375	0.45301	0.54084	0.49196
6	0.51511	0.43864	0.48004	0.43908	0.59513	0.61082	0.47416	0.44642	0.53454	0.48759
7	0.51572	0.43844	0.47839	0.43655	0.58887	0.60369	0.46972	0.44442	0.53309	0.48775

0.020" Orifice - No Valve										
	HP PRTs					*LP PRTs*				
Point	PRT 9 [V]	PRT 10 [V]	PRT 12 [V]	PRT 13 [V]	PRT 14 [V]	PRT 1 [V]	PRT 2 [V]	PRT 4 [V]	PRT 5 [V]	PRT 6 [V]
1	0.52640	0.45225	0.50192	0.44041	0.64245	0.66132	0.50840	0.46855	0.55480	0.49948
2	0.52828	0.45308	0.50143	0.46289	0.63836	0.65680	0.50569	0.46785	0.55471	0.50104
3	0.52033	0.44585	0.49292	0.45458	0.62583	0.64361	0.49596	0.45952	0.54604	0.49328
4	0.51901	0.44409	0.48996	0.45112	0.61932	0.63635	0.49102	0.45631	0.54310	0.49165
5	0.51712	0.44172	0.48608	0.44667	0.61097	0.62688	0.48455	0.45202	0.53909	0.48924
6	0.51579	0.44024	0.48388	0.44422	0.60655	0.62172	0.48097	0.44951	0.53667	0.48756
7	0.51564	0.43986	0.48301	0.44312	0.60425	0.61865	0.47892	0.44822	0.53550	0.48694

Table N.4: Experimental data for the forty-three die 10 mm heat exchanger installed in the cryogenic test facility. The working fluid was ethane and the voltages applied to the valve include -30 V, 0 V, and 30 V.

No Orifice - Valve Voltage -30 V								
	Mass	***Thermocouples***				***Pressures***		
	Flow		HP		LP		LP	
Point	Rate	HP IN	OUT	LP IN	OUT	HP IN	OUT	ATM
	[V]	[K]	[K]	[K]	[K]	[V]	[V]	[mm Hg]
1	0.1267	294.11	290.64	290.02	293.40	0.5798	0.1427	735.2
2	0.1941	298.81	289.33	287.93	297.29	0.8173	0.1935	736.1
3	0.2450	298.35	282.37	280.10	296.17	1.0085	0.1967	735.8
4	0.2975	294.69	271.86	268.42	291.82	1.2206	0.1763	742.8
5	0.3404	295.92	267.55	263.13	292.51	1.3837	0.2095	731.7
6	0.3895	296.01	260.41	254.52	291.77	1.5734	0.2215	727.2

No Orifice - Valve Voltage 0 V								
	Mass	***Thermocouples***				***Pressures***		
	Flow		HP		LP		LP	
Point	Rate	HP IN	OUT	LP IN	OUT	HP IN	OUT	ATM
	[V]	[K]	[K]	[K]	[K]	[V]	[V]	[mm Hg]
1	0.3719	298.41	263.83	258.23	294.32	1.5682	0.2394	725.8

No Orifice - Valve Voltage 30 V								
	Mass	***Thermocouples***				***Pressures***		
	Flow		HP		LP		LP	
Point	Rate	HP IN	OUT	LP IN	OUT	HP IN	OUT	ATM
	[V]	[K]	[K]	[K]	[K]	[V]	[V]	[mm Hg]
1	0.2994	294.76	260.54	254.85	290.8	1.5864	0.1875	730.0

Table N.5: Integrated RTD voltages for the forty-three die 10 mm heat exchanger installed in the cryogenic test facility. The working fluid was ethane and the voltages applied to the valve include -30 V, 0 V, and 30 V.

No Orifice - Valve Voltage -30 V										
	HP PRTs					*LP PRTs*				
Point	PRT 9 [V]	PRT 10 [V]	PRT 12 [V]	PRT 13 [V]	PRT 14 [V]	PRT 1 [V]	PRT 2 [V]	PRT 4 [V]	PRT 5 [V]	PRT 6 [V]
1	0.52491	0.45076	0.49995	0.46208	0.63873	0.65749	0.50571	0.46655	0.55284	0.49804
2	0.52968	0.45406	0.50210	0.46311	0.63786	0.65639	0.50566	0.46847	0.55562	0.50243
3	0.52672	0.45062	0.49679	0.45712	0.62691	0.64482	0.49776	0.46322	0.55074	0.49945
4	0.51895	0.44298	0.48678	0.44666	0.60934	0.62633	0.48473	0.45343	0.54105	0.49184
5	0.51922	0.44253	0.48497	0.44405	0.60316	0.61961	0.48046	0.45147	0.53959	0.49188
6	0.51731	0.44000	0.48052	0.43869	0.59231	0.60792	0.47272	0.44689	0.53550	0.48975
No Orifice - Valve Voltage 0 V										
	HP PRTs					*LP PRTs*				
Point	PRT 9 [V]	PRT 10 [V]	PRT 12 [V]	PRT 13 [V]	PRT 14 [V]	PRT 1 [V]	PRT 2 [V]	PRT 4 [V]	PRT 5 [V]	PRT 6 [V]
1	0.52125	0.44355	0.48464	0.44269	0.59846	0.61430	0.47747	0.45088	0.53969	0.49355
No Orifice - Valve Voltage 30 V										
	HP PRTs					*LP PRTs*				
Point	PRT 9 [V]	PRT 10 [V]	PRT 12 [V]	PRT 13 [V]	PRT 14 [V]	PRT 1 [V]	PRT 2 [V]	PRT 4 [V]	PRT 5 [V]	PRT 6 [V]
1	0.51565	0.43879	0.47961	0.43813	0.59223	0.60823	0.47283	0.44634	0.53473	0.48848

Table N.6: Experimental data for the forty-three die 10 mm heat exchanger installed in the cryogenic test facility. The working fluid was ethane and the voltages applied to the valve include 60 V, 80 V, and 100 V.

No Orifice - Valve Voltage 60 V								
	Mass	*Thermocouples*				*Pressures*		
	Flow	HP		LP		LP		
Point	Rate	HP IN	OUT	LP IN	OUT	HP IN	OUT	ATM
	[V]	[K]	[K]	[K]	[K]	[V]	[V]	[mm Hg]
1	0.2148	297.08	278.18	275.18	294.62	1.2190	0.1677	740.0
2	0.2728	296.87	263.32	257.89	292.94	1.5832	0.1826	734.8
3	0.1501	295.41	286.43	284.98	293.87	0.8326	0.1058	740.0
4	0.1638	293.33	280.52	278.43	291.37	1.0049	0.0996	735.6
5	0.2145	293.57	267.37	263.15	290.22	1.4035	0.1217	728.8

No Orifice - Valve Voltage 80 V								
	Mass	*Thermocouples*				*Pressures*		
	Flow	HP		LP		LP		
Point	Rate	HP IN	OUT	LP IN	OUT	HP IN	OUT	ATM
	[V]	[K]	[K]	[K]	[K]	[V]	[V]	[mm Hg]
1	0.2599	294.43	260.66	255.05	290.51	1.5929	0.1471	736.1

No Orifice - Valve Voltage 100 V								
	Mass	*Thermocouples*				*Pressures*		
	Flow	HP		LP		LP		
Point	Rate	HP IN	OUT	LP IN	OUT	HP IN	OUT	ATM
	[V]	[K]	[K]	[K]	[K]	[V]	[V]	[mm Hg]
1	0.0680	297.39	294.16	293.65	296.34	0.5656	0.1568	735.0
2	0.1192	295.93	287.83	286.49	294.15	0.8339	0.1470	736.8
3	0.1560	295.92	284.66	282.70	294.20	1.0248	0.1629	735.8
4	0.1890	296.11	277.90	274.94	293.56	1.2225	0.1547	736.9
5	0.2180	298.26	274.15	270.33	295.14	1.3946	0.1815	734.6
6	0.2299	293.85	261.42	255.96	290.00	1.5971	0.1312	738.4
7	0.1272	293.30	282.44	280.50	291.36	1.0118	0.1005	736.8

Table N.7: Integrated RTD voltages for the forty-three die 10 mm heat exchanger installed in the cryogenic test facility. The working fluid was ethane and the voltages applied to the valve include 60 V, 80 V, and 100 V.

No Orifice - Valve Voltage 60 V										
	HP PRTs					*LP PRTs*				
Point	PRT 9 [V]	PRT 10 [V]	PRT 12 [V]	PRT 13 [V]	PRT 14 [V]	PRT 1 [V]	PRT 2 [V]	PRT 4 [V]	PRT 5 [V]	PRT 6 [V]
1	0.52359	0.44756	0.49279	0.45296	0.61991	0.63756	0.49266	0.45939	0.54697	0.49647
2	0.51891	0.44172	0.48303	0.44147	0.59737	0.61366	0.47679	0.44968	0.53823	0.49165
3	0.52431	0.44948	0.49734	0.45880	0.63223	0.65064	0.50117	0.46396	0.55068	0.49740
4	0.51957	0.44487	0.49140	0.45268	0.62223	0.64024	0.49376	0.45823	0.54496	0.49284
5	0.51554	0.43969	0.48257	0.44233	0.60210	0.61902	0.47961	0.44955	0.53720	0.48874

No Orifice - Valve Voltage 80 V										
	HP PRTs					*LP PRTs*				
Point	PRT 9 [V]	PRT 10 [V]	PRT 12 [V]	PRT 13 [V]	PRT 14 [V]	PRT 1 [V]	PRT 2 [V]	PRT 4 [V]	PRT 5 [V]	PRT 6 [V]
1	0.51498	0.43831	0.47926	0.43796	0.59235	0.60854	0.47294	0.44615	0.53444	0.48796

No Orifice - Valve Voltage 100 V										
	HP PRTs					*LP PRTs*				
Point	PRT 9 [V]	PRT 10 [V]	PRT 12 [V]	PRT 13 [V]	PRT 14 [V]	PRT 1 [V]	PRT 2 [V]	PRT 4 [V]	PRT 5 [V]	PRT 6 [V]
1	0.52965	0.45498	0.50473	0.46664	0.64534	0.66432	0.51083	0.47114	0.55769	0.50257
2	0.52518	0.45041	0.49859	0.46019	0.63461	0.65316	0.50292	0.46520	0.55188	0.49825
3	0.52427	0.44916	0.49640	0.45758	0.62956	0.64784	0.49936	0.46303	0.54996	0.49731
4	0.52206	0.44634	0.49168	0.45209	0.61910	0.63682	0.49195	0.45839	0.54579	0.49508
5	0.52352	0.44687	0.49086	0.45035	0.61410	0.63142	0.48875	0.45745	0.54548	0.49632
6	0.51432	0.43793	0.47922	0.43819	0.59340	0.60980	0.47364	0.44621	0.53433	0.48744
7	0.51999	0.44552	0.49264	0.45421	0.62526	0.64345	0.49589	0.45948	0.54605	0.49329

Table N.8: Calculated results from Table N.2

0.010" Orifice - No Valve											
	Mass Flow Rate		*Temperatures*		*Effectiveness*			*Pressures*			
Point	Value [g/s]	Uncertainty [g/s]	ΔT Assy [K]	U ΔT [K]	Hot Side [K]	Cold Side [K]	U Eff [K]	HP IN [kPa]	LP OUT [kPa]	ΔP Assy [kPa]	U ΔP [kPa]
1	0.0231	0.0029	-4.27	0.28	0.79	0.97	0.07	211.80	110.10	101.70	1.91
2	0.0298	0.0030	-9.41	0.28	0.81	0.96	0.03	277.90	90.86	187.10	1.91
3	0.0373	0.0033	-16.03	0.28	0.83	0.94	0.02	349.00	92.29	256.70	1.91
4	0.045	0.0035	-24.37	0.28	0.85	0.93	0.01	417.20	76.76	340.50	1.91
5	0.0524	0.0038	-32.87	0.28	0.85	0.92	0.01	483.70	81.61	402.10	1.91
6	0.0595	0.0041	-40.72	0.28	0.85	0.91	0.01	542.40	86.85	455.60	1.91

0.015" Orifice - No Valve											
	Mass Flow Rate		*Temperatures*		*Effectiveness*			*Pressures*			
Point	Value [g/s]	Uncertainty [g/s]	ΔT Assy [K]	U ΔT [K]	Hot Side [K]	Cold Side [K]	U Eff [K]	HP IN [kPa]	LP OUT [kPa]	ΔP Assy [kPa]	U ΔP [kPa]
1	0.0289	0.0030	-1.30	0.28	0.80	1.05	0.22	138.90	103.00	35.91	1.91
2	0.0479	0.0036	-7.42	0.28	0.84	0.96	0.04	213.40	104.40	109.00	1.91
3	0.0636	0.0043	-12.74	0.28	0.86	0.94	0.02	281.10	105.90	175.30	1.91
4	0.0763	0.0048	-18.13	0.28	0.86	0.93	0.02	334.90	112.50	222.40	1.91
5	0.0967	0.0058	-27.59	0.28	0.86	0.92	0.01	418.50	112.90	305.60	1.91
6	0.1144	0.0067	-35.61	0.28	0.85	0.90	0.01	486.10	112.20	373.90	1.91
7	0.1311	0.0076	-42.99	0.28	0.84	0.89	0.01	549.80	109.90	440.00	1.91

0.020" Orifice - No Valve											
	Mass Flow Rate		*Temperatures*		*Effectiveness*			*Pressures*			
Point	Value [g/s]	Uncertainty [g/s]	ΔT Assy [K]	U ΔT [K]	Hot Side [K]	Cold Side [K]	U Eff [K]	HP IN [kPa]	LP OUT [kPa]	ΔP Assy [kPa]	U ΔP [kPa]
1	0.0509	0.0037	-1.71	0.28	0.81	0.99	0.16	140.40	104.70	35.71	1.91
2	0.0933	0.0056	-8.08	0.28	0.85	0.95	0.03	211.30	108.70	102.60	1.91
3	0.127	0.0072	-10.99	0.28	0.85	0.92	0.02	273.00	126.20	146.70	1.91
4	0.1634	0.0091	-16.16	0.28	0.84	0.90	0.02	340.30	122.60	217.70	1.91
5	0.2049	0.0113	-22.77	0.28	0.81	0.88	0.01	424.40	106.20	318.10	1.91
6	0.2335	0.0128	-26.06	0.28	0.80	0.86	0.01	478.90	102.20	376.70	1.91
7	0.2674	0.0147	-28.76	0.28	0.78	0.85	0.01	544.70	107.20	437.40	1.91

Table N.9: Calculated results from Table N.3

0.010" Orifice - No Valve										
	HP PRTs					*LP PRTs*				
Point	PRT 9 [K]	PRT 10 [K]	PRT 12 [K]	PRT 13 [K]	PRT 14 [K]	PRT 1 [K]	PRT 2 [K]	PRT 4 [K]	PRT 5 [K]	PRT 6 [K]
1	291.3	291.0	290.6	290.2	289.6	290.2	290.4	291.1	291.4	292.0
2	291.7	291.0	289.9	289.1	287.6	288.1	288.7	290.3	291.0	292.3
3	290.2	288.9	286.8	285.4	282.8	283.2	284.3	287.2	288.3	290.7
4	356.4	316.6	281.9	284.4	226.9	206.6	251.5	411.0	283.9	254.6
5	287.4	284.7	280.3	277.2	271.2	271.4	274.0	280.5	282.8	287.7
6	286.3	283.1	277.7	273.7	266.0	266.0	269.5	277.7	280.5	286.6

0.015" Orifice - No Valve										
	HP PRTs					*LP PRTs*				
Point	PRT 9 [K]	PRT 10 [K]	PRT 12 [K]	PRT 13 [K]	PRT 14 [K]	PRT 1 [K]	PRT 2 [K]	PRT 4 [K]	PRT 5 [K]	PRT 6 [K]
1	293.3	293.3	293.3	293.1	292.8	293.4	293.5	293.7	293.9	294.0
2	293.6	292.9	292.1	291.3	290.0	290.5	291.0	292.4	293.0	294.1
3	292.7	291.6	289.9	288.6	286.3	286.7	287.7	290.2	291.2	293.2
4	290.5	288.9	286.4	284.5	281.2	281.5	282.9	286.5	287.9	290.8
5	289.0	286.7	282.8	280.0	274.8	274.8	277.0	282.7	284.7	289.1
6	286.3	283.3	278.4	274.7	267.9	267.5	270.6	278.0	280.5	286.1
7	286.7	283.2	277.2	272.9	264.5	263.9	267.6	276.5	279.6	286.2

0.020" Orifice - No Valve										
	HP PRTs					*LP PRTs*				
Point	PRT 9 [K]	PRT 10 [K]	PRT 12 [K]	PRT 13 [K]	PRT 14 [K]	PRT 1 [K]	PRT 2 [K]	PRT 4 [K]	PRT 5 [K]	PRT 6 [K]
1	293.6	293.5	293.4	275.7	292.9	293.4	293.5	293.8	294.0	294.3
2	294.8	294.1	293.0	292.1	290.7	291.1	291.7	293.3	294.0	295.4
3	289.7	288.7	287.2	286.1	284.1	284.4	285.2	287.4	288.2	290.0
4	288.8	287.4	285.2	283.5	280.7	280.7	281.9	285.1	286.2	288.9
5	287.6	285.6	282.5	280.3	276.3	275.8	277.5	282.0	283.6	287.3
6	286.7	284.5	281.0	278.5	274.0	273.2	275.1	280.2	281.9	286.1
7	286.6	284.2	280.4	277.7	272.7	271.6	273.8	279.3	281.2	285.7

Table N.10: Calculated results from Table N.4

No Orifice - Valve Voltage -30 V											
	Mass Flow Rate		***Temperatures***		***Effectiveness***			***Pressures***			
Point	Value [g/s]	Uncertainty [g/s]	ΔT Assy [K]	U ΔT [K]	Hot Side [K]	Cold Side [K]	U Eff [K]	HP IN [kPa]	LP OUT [kPa]	ΔP Assy [kPa]	U ΔP [kPa]
1	0.0327	0.0031	-4.09	0.28	0.82	0.85	0.06	199.90	107.90	92.02	1.91
2	0.0495	0.0037	-10.88	0.28	0.85	0.87	0.02	281.80	111.50	170.30	1.91
3	0.0623	0.0042	-18.25	0.28	0.86	0.88	0.01	347.70	111.70	236.00	1.91
4	0.076	0.0048	-26.27	0.28	0.86	0.87	0.01	420.80	111.20	309.60	1.91
5	0.0866	0.0054	-32.79	0.28	0.86	0.87	0.01	477.00	112.00	365.00	1.91
6	0.0987	0.0060	-41.49	0.28	0.85	0.86	0.01	542.40	112.20	430.20	1.91
No Orifice - Valve Voltage 0 V											
	Mass Flow Rate		***Temperatures***		***Effectiveness***			***Pressures***			
Point	Value [g/s]	Uncertainty [g/s]	ΔT Assy [K]	U ΔT [K]	Hot Side [K]	Cold Side [K]	U Eff [K]	HP IN [kPa]	LP OUT [kPa]	ΔP Assy [kPa]	U ΔP [kPa]
1	0.0938	0.0058	-40.18	0.28	0.86	0.86	0.01	540.60	113.30	427.30	1.91
No Orifice - Valve Voltage 30 V											
	Mass Flow Rate		***Temperatures***		***Effectiveness***			***Pressures***			
Point	Value [g/s]	Uncertainty [g/s]	ΔT Assy [K]	U ΔT [K]	Hot Side [K]	Cold Side [K]	U Eff [K]	HP IN [kPa]	LP OUT [kPa]	ΔP Assy [kPa]	U ΔP [kPa]
1	0.0761	0.0049	-39.92	0.28	0.86	0.86	0.01	546.90	110.30	436.60	1.91

Table N.11: Calculated results from Table N.5

No Orifice - Valve Voltage -30 V										
	HP PRTs					*LP PRTs*				
Point	PRT 9 [K]	PRT 10 [K]	PRT 12 [K]	PRT 13 [K]	PRT 14 [K]	PRT 1 [K]	PRT 2 [K]	PRT 4 [K]	PRT 5 [K]	PRT 6 [K]
1	292.7	292.4	292.0	291.6	290.9	291.5	291.7	292.4	292.7	293.3
2	295.7	294.7	293.5	292.3	290.4	290.9	291.7	293.8	294.5	296.4
3	293.9	292.2	289.8	287.9	284.7	285.0	286.4	290.0	291.3	294.2
4	288.8	286.5	283.0	280.3	275.4	275.6	277.6	283.0	284.9	289.1
5	289.0	286.2	281.8	278.4	272.1	272.1	274.8	281.6	283.9	289.1
6	287.7	284.3	278.7	274.4	266.4	266.1	269.6	278.3	281.2	287.6

No Orifice - Valve Voltage 0 V										
	HP PRTs					*LP PRTs*				
Point	PRT 9 [K]	PRT 10 [K]	PRT 12 [K]	PRT 13 [K]	PRT 14 [K]	PRT 1 [K]	PRT 2 [K]	PRT 4 [K]	PRT 5 [K]	PRT 6 [K]
1	290.3	287.0	281.5	277.4	269.6	269.3	272.8	281.2	284.0	290.2

No Orifice - Valve Voltage 30 V										
	HP PRTs					*LP PRTs*				
Point	PRT 9 [K]	PRT 10 [K]	PRT 12 [K]	PRT 13 [K]	PRT 14 [K]	PRT 1 [K]	PRT 2 [K]	PRT 4 [K]	PRT 5 [K]	PRT 6 [K]
1	286.7	283.4	278.1	274.0	266.3	269.7	266.2	277.9	280.7	286.7

Table N.12: Calculated results from Table N.6

No Orifice - Valve Voltage 60 V											
	Mass Flow Rate		***Temperatures***		***Effectiveness***			***Pressures***			
Point	Value [g/s]	Uncertainty [g/s]	ΔT Assy [K]	U ΔT [K]	Hot Side [K]	Cold Side [K]	U Eff [K]	HP IN [kPa]	LP OUT [kPa]	ΔP Assy [kPa]	U ΔP [kPa]
1	0.0385	0.0033	-10.43	0.28	0.84	0.86	0.03	287.00	106.00	181.10	1.91
2	0.0421	0.0034	-14.90	0.28	0.85	0.86	0.02	346.40	104.90	241.50	1.91
3	0.0546	0.0039	-21.90	0.28	0.86	0.87	0.01	420.20	110.20	310.00	1.91
4	0.0548	0.0039	-30.42	0.28	0.85	0.86	0.01	483.80	105.60	378.30	1.91
5	0.069	0.0046	-38.98	0.28	0.86	0.86	0.01	545.80	110.60	435.20	1.91

No Orifice - Valve Voltage 80 V											
	Mass Flow Rate		***Temperatures***		***Effectiveness***			***Pressures***			
Point	Value [g/s]	Uncertainty [g/s]	ΔT Assy [K]	U ΔT [K]	Hot Side [K]	Cold Side [K]	U Eff [K]	HP IN [kPa]	LP OUT [kPa]	ΔP Assy [kPa]	U ΔP [kPa]
1	0.0661	0.0044	-39.38	0.28	0.85	0.86	0.01	549.10	108.30	440.90	1.91

No Orifice - Valve Voltage 100 V											
	Mass Flow Rate		***Temperatures***		***Effectiveness***			***Pressures***			
Point	Value [g/s]	Uncertainty [g/s]	ΔT Assy [K]	U ΔT [K]	Hot Side [K]	Cold Side [K]	U Eff [K]	HP IN [kPa]	LP OUT [kPa]	ΔP Assy [kPa]	U ΔP [kPa]
1	0.0174	0.0027	-3.74	0.28	0.71	0.86	0.07	195.00	108.80	86.18	1.91
2	0.0306	0.0030	-9.44	0.28	0.80	0.86	0.03	287.50	108.40	179.10	1.91
3	0.0327	0.0031	-12.80	0.28	0.83	0.85	0.02	348.80	105.20	243.60	1.91
4	0.0399	0.0033	-13.22	0.28	0.85	0.85	0.02	353.30	109.30	244.00	1.91
5	0.0482	0.0037	-21.17	0.28	0.85	0.86	0.01	421.40	108.90	312.50	1.91
6	0.0552	0.0040	-27.93	0.28	0.86	0.87	0.01	480.80	110.50	370.30	1.91
7	0.0585	0.0041	-37.89	0.28	0.85	0.86	0.01	550.60	107.50	443.10	1.91

Table N.13: Calculated results from Table N.7

No Orifice - Valve Voltage 60 V										
	HP PRTs					*LP PRTs*				
Point	PRT 9 [K]	PRT 10 [K]	PRT 12 [K]	PRT 13 [K]	PRT 14 [K]	PRT 1 [K]	PRT 2 [K]	PRT 4 [K]	PRT 5 [K]	PRT 6 [K]
1	292.3	291.4	290.2	289.1	287.5	288.0	288.7	290.6	291.3	292.9
2	289.2	288.0	286.2	284.7	282.2	282.7	283.7	286.4	287.5	289.7
3	291.8	290.0	287.1	284.9	281.0	281.3	283.0	287.3	288.8	292.2
4	286.6	284.1	280.1	277.1	271.6	271.8	274.2	280.2	282.3	286.9
5	288.8	285.6	280.4	276.5	269.1	269.0	272.3	280.3	283.0	288.9

No Orifice - Valve Voltage 80 V										
	HP PRTs					*LP PRTs*				
Point	PRT 9 [K]	PRT 10 [K]	PRT 12 [K]	PRT 13 [K]	PRT 14 [K]	PRT 1 [K]	PRT 2 [K]	PRT 4 [K]	PRT 5 [K]	PRT 6 [K]
1	286.2	283.1	277.8	273.9	266.4	266.4	269.7	277.8	280.5	286.4

No Orifice - Valve Voltage 100 V										
	HP PRTs					*LP PRTs*				
Point	PRT 9 [K]	PRT 10 [K]	PRT 12 [K]	PRT 13 [K]	PRT 14 [K]	PRT 1 [K]	PRT 2 [K]	PRT 4 [K]	PRT 5 [K]	PRT 6 [K]
1	295.7	295.4	295.1	294.9	294.3	295.1	295.2	295.8	296.0	296.5
2	292.9	292.1	291.1	290.2	288.7	289.3	289.9	291.4	292.1	293.4
3	289.5	288.4	287.0	285.8	283.8	284.3	285.1	287.3	288.2	290.0
4	292.3	291.2	289.6	288.3	286.1	286.6	287.5	289.9	290.8	292.8
5	290.8	289.1	286.3	284.2	280.6	280.9	282.5	286.6	288.0	291.3
6	291.8	289.4	285.8	283.0	277.9	278.2	280.3	285.9	287.8	292.1
7	285.8	282.8	277.8	274.1	266.9	267.0	270.2	277.8	280.4	286.0

Appendix O: Forty-three Die 10 mm Heat Exchanger Load Curve Tests

Table O.1: Locations of the integrated PRTs within the forty-three die 10 mm heat exchanger self-cooling tests performed in the cryogenic testing facility

Die	HP Inlet	LP Outlet
1		
2		
3		
4		
5		
6		
7		
8		
9	PRT 9 (Norm)	PRT 6 (Norm)
10		
11		
12		
13		
14	PRT 10 (Norm)	
15		
16		
17		
18		PRT 5 (Norm)
19		
20		
21		
22	PRT 12 (Norm)	PRT 4 (Norm)
23		
24		
25		
26		
27	PRT 13 (Norm)	
28		
29		
30		
31		
32		PRT 2 (Norm)
33		
34		
35		
36	PRT 14 (Norm)	PRT 1 (Norm)
37		
38		
39		
40		
41		
42		
43		
	HP Outlet	LP Inlet

Table O.2: Experimental data for the forty-three die 10 mm heat exchanger installed self-cooling mode in the cryogenic test facility with ethane as the working fluid.

No Orifice - Valve Voltage -30 V									
	Mass Flow	*Thermocouples*				*Pressures*			
Point	Rate [V]	HP IN [K]	HP OUT [K]	LP IN [K]	LP OUT [K]	HP IN [V]	LP OUT [V]	ATM [mm Hg]	Heater [W]
1	0.3872	295.58	259.00	252.96	291.27	1.5806	0.1898	728.8	0.000
2	0.3885	294.43	261.11	255.58	290.50	1.5838	0.1824	726.8	0.075
3	0.3894	293.77	263.74	258.82	290.18	1.5822	0.1848	724.4	0.153
4	0.3914	293.29	268.83	264.87	290.30	1.5846	0.1451	735.4	0.284
5	0.3926	296.72	280.29	277.77	294.58	1.5754	0.1588	735.4	0.446
6	0.3928	294.69	284.28	282.68	293.25	1.5824	0.1591	735.4	0.598
7	0.3899	296.33	296.20	296.15	296.19	1.5683	0.1738	736.3	0.807

Table O.3: Integrated RTD voltages for the forty-three die 10 mm heat exchanger installed in self-cooling mode in the cryogenic test facility with ethane as the working fluid.

No Orifice - Valve Voltage -30 V										
	HP PRTs					*LP PRTs*				
Point	PRT 9 [V]	PRT 10 [V]	PRT 12 [V]	PRT 13 [V]	PRT 14 [V]	PRT 1 [V]	PRT 2 [V]	PRT 4 [V]	PRT 5 [V]	PRT 6 [V]
1	0.51634	0.43903	0.47924	0.43734	0.59005	0.60549	0.47111	0.44566	0.53431	0.48881
2	0.51558	0.43878	0.47972	0.43832	0.59286	0.60852	0.47292	0.44622	0.53453	0.48819
3	0.51568	0.43927	0.48107	0.44011	0.59678	0.61273	0.47560	0.44759	0.53560	0.48838
4	0.51676	0.44091	0.48417	0.44391	0.60452	0.62095	0.48102	0.45071	0.53831	0.48957
5	0.52464	0.44877	0.49468	0.45499	0.62342	0.64084	0.49494	0.46099	0.54841	0.49728
6	0.52364	0.44869	0.49604	0.45722	0.62902	0.64692	0.49871	0.46248	0.54930	0.49653
7	0.52977	0.45536	0.50576	0.46790	0.64801	0.66709	0.51264	0.47215	0.55847	0.50270

Table O.4: Calculated results from Table O.2

No Orifice - Valve Voltage -30 V											
	Mass Flow Rate		*Temperatures*		*Effectiveness*			*Pressures*			
Point	Value [g/s]	Uncertainty [g/s]	ΔT Assy [K]	U ΔT [K]	Hot Side [K]	Cold Side [K]	U Eff [K]	HP IN [kPa]	LP OUT [kPa]	ΔP Assy [kPa]	U ΔP [kPa]
1	0.09823	0.0060	-42.62	0.28	0.86	0.85	0.01	544.9	110.3	434.6	1.91
2	0.09877	0.0060	-38.85	0.28	0.86	0.85	0.01	546.0	109.5	436.5	1.91
3	0.09913	0.0060	-34.95	0.28	0.86	0.85	0.01	545.4	109.3	436.1	1.91
4	0.09973	0.0060	-28.42	0.28	0.86	0.85	0.01	546.3	108.0	438.2	1.91
5	0.09938	0.0060	-18.95	0.28	0.87	0.85	0.01	543.1	109.0	434.1	1.91
6	0.09982	0.0060	-12.01	0.28	0.87	0.85	0.02	545.5	109.0	436.5	1.91
7	0.09878	0.0060	-0.18	0.28	0.72	0.22	1.41	540.7	110.1	430.5	1.91

Table O.5: Calculated results from Table O.2

No Orifice - Valve Voltage -30 V										
	HP PRTs					*LP PRTs*				
Point	PRT 9 [K]	PRT 10 [K]	PRT 12 [K]	PRT 13 [K]	PRT 14 [K]	PRT 1 [K]	PRT 2 [K]	PRT 4 [K]	PRT 5 [K]	PRT 6 [K]
1	287.1	283.6	277.8	273.4	265.2	264.8	268.5	277.4	280.4	287.0
2	286.6	283.4	278.2	274.2	266.7	266.4	269.7	277.8	280.5	286.6
3	286.7	283.8	279.1	275.5	268.7	268.5	271.5	278.8	281.2	286.7
4	287.4	285.0	281.2	278.3	272.9	272.8	275.2	281.1	283.0	287.5
5	292.5	290.9	288.4	286.4	282.8	283.0	284.5	288.4	289.8	292.8
6	291.8	290.8	289.3	288.0	285.8	286.1	287.0	289.5	290.4	292.3
7	295.7	295.7	295.7	295.8	295.9	297.0	296.5	296.7	296.5	296.6